UNIVERSIDADE FEDERAL DO RIO GRANDE DO SUL
PROGRAMA DE PÓS-GRADUAÇÃO EM FÍSICA
Tese de Doutorado

Uma nova visão sobre a periferia das Nuvens de Magalhães

A new view of the Magellanic Clouds outskirts

Adriano Pieres

Tese realizada sob a orientação do Dr. Basílio Xavier Santiago e apresentada ao Programa de Pós-Graduação do Instituto de Física da Universidade Federal do Rio Grande do Sul para a obtenção de Título de Doutor em Ciências, na Área de Astrofísica.

Porto Alegre, RS, Brasil
Outubro de 2017

⋆ Trabalho financiado pelo CNPq

Folha de Aprovação

Esta folha certifica que a Tese preparada por Adriano Pieres, entitulada "Uma nova visão sobre a periferia das Nuvens de Magalhães" sob a orientação do Dr. Basílio Xavier Santiago e apresentada ao Programa de Pós-Graduação do Instituto de Física da Universidade Federal do Rio Grande do Sul para a obtenção de Título de Doutor em Ciências, na Área de Astrofísica cumpre com a regulamentação deste Departamento, Instituto e Universidade e alcança o padrão concernente à originalidade.

Assinado pela banca examinadora

Nome	**Assinatura**	**Data**
(**Dr. Basílio Xavier Santiago**)		
(**Dr. Jacques Raymond Daniel Lepine**)		
(**Dr. Horácio Alberto Dottori**)		
(**Dra. Ana Leonor Chies Santiago Santos**)		
(**Dr. Roberto Kalbusch Saito**)		

Agradecimentos

Agradeço à minha família, aos amigos que me deram suporte e incentivo durante este período do doutorado.

Agradeço ao meu orientador Basílio Santiago Xavier, pela paciência e grande conhecimento demonstrado.

Agradeço às pessoas que fazem do Instituto de Física da Universidade Federal do Rio Grande do Sul (IF-UFRGS) esta instituição de respeito. Foi neste instituto que completei minha graduação, tive várias bolsas de iniciação científica, concluí meu mestrado e doutorado. Tive e sempre vou ter os exemplos de dedicação. Agradeço principalmente aos professores Sílvio Cunha, João Edgar Schmidt, Fernando Lang da Silveira, Claudio Schneider, Kepler de Souza Oliveira Filho, Horácio Dottori e Ana Chies-Santos. Cada conversa com cada um de vocês é um Universo que se desvela.

Graças à bolsa de mestrado e doutorado do Conselho Nacional de Pesquisa (CNPq) pude me dedicar integralmente ao mestrado e doutorado. Sem esta instituição, num momento tão fragilizado da pesquisa no Brasil, nada do que foi desenvolvido aqui estaria escrito nem teria sido publicado.

Agradeço às instituições LIneA e do DES-Brazil, sem os quais os dados em que trabalhamos não teriam chegado até nós. Agradeço à equipe destas instituições, que me forneceram instrutivos exemplos e conhecimento. Principalmente Luis Nicolaci da Costa, Marcio Maia, Aurelio Carnero, Ricardo Ogando e Júlia de Figueiredo Gschwend.

Também aos membros internacionais do DES, pelo exemplo de dedicação, cordialidade e oportunidades propiciadas. Foi um tempo intenso de aprendizado. Agradeço principalmente aos pós-docs Alexander Drlica-Wagner, Keith Bechtol e Ting Li e ao professor Brian Yanny. Me mostraram que a rapidez não é necessariamente inimiga da perfeição.

Resumo

Nossa amostra de trabalho consistiu das cercanias das Nuvens de Magalhães dentro da área amostrada pelo Dark Energy Survey. Nos concentramos na amostra de aglomerados da Grande Nuvem de Magalhães e na descoberta de uma sobredensidade estelar associada à Pequena Nuvem de Magalhães, sobre as quais faremos aqui uma breve descrição, baseada nos resumos já publicados.

A Grande Nuvem de Magalhães possui um sistema rico e diversificado de aglomerados estelares, cujas idades, abundâncias químicas e posições oferecem informação a respeito do histórico de formação estelar desta galáxia. Nós usamos as imagens dos dados de verificação científica do Dark Energy Survey para aumentar o censo de aglomerados conhecidos na região externa da Grande Nuvem de Magalhães e para determinar os parâmetros físicos de uma grande número destes objetos usando uma amostra homogênea, tanto fotométrica quanto espacialmente.

Nossa amostra contém 255 aglomerados identificados visualmente, dos quais 109 não estão listados em nenhum catálogo prévio. Nós quantificamos o efeito de adensamento estelar para a amostra produzida pela equipe de gerenciamento dos dados do Dark Energy Survey e concluímos que a completeza da amostra estelar é $< 10\%$ no centro de aglomerados típicos da Grande Nuvem de Magalhães. Desenvolvemos então um arranjo de tarefas para amostrar e medir as magnitudes e posições das estrelas nos candidatos a aglomerados da Grande Nuvem de Magalhães utilizando o conjunto de pacotes DAOPHOT. Também implementamos um método de máxima probabilidade para ajustar perfis de densidade individuais, bem como diagramas cor-magnitude. Para 117 aglomerados (de um total de 255) dos candidatos, sendo 28 aglomerados até então não catalogados, obtivemos idades, metalicidades, módulo de distância e parâmetros estruturais confiáveis, confirmando sua natureza de sistemas físicos. A distribuição de metalicidades para os aglomerados mostra uma dependência radial, com uma ausência de aglomerados quimicamente mais ricos que $[\mathrm{Fe/H}] \simeq -0,7$ além de 8 kpc do centro da Grande Nuvem. A distribuição de idade mostra dois picos em $\simeq$ 1,2 e $\simeq$ 2,7 bilhões de anos. A relação idade-metalicidade mostra que mesmo sendo uma amostra externa, há uma concordância global com outros trabalhos que amostraram regiões mais centrais desta galáxia. Além disso a relação idade-metalicidade da amostra de aglomerados é bem descrita tendo como limites o modelo analítico de Pagel & Tautvaisiene (1998) e o modelo empírico de Harris & Zaritsky (2009), embora nenhum deles descreva bem o conjunto de aglomerados aqui amostrados.

Aqui também reportamos a descoberta de uma sobredensidade estelar batizada de

SMCNOD (acrônimo do inglês *Small Magellanic Cloud Northern Over-Density*), utilizando dados dos primeiros dois anos do Dark Energy Survey e do primeiro ano do *MAGellanic SatelLITEs Survey - MagLiteS*. A SMCNOD é indistinguível em idade, metalicidade e distância das estrelas vizinhas da Pequena Nuvem de Magalhães, sendo primariamente composta por estrela de idade intermediária (6 bilhões de anos e Z=0.001), juntamente com uma pequena fração de estrelas jovens (1 Gyr, Z=0.01). A SMCNOD tem uma forma alongada com uma elipticidade $\epsilon = 0.6$ e um tamanho aproximado de 6 $\times$ 2 graus, uma magnitude absoluta de $M_V \cong$ -7.7, $r_h = 2.1$ kpc e $\mu_V(r < r_h) = 31.2$ mag arcsec^{-2}. Estimamos uma massa estelar de $\sim 10^5$ massas solares, seguindo uma função de massa inicial de Kroupa. A SMCNOD foi provavelmente removida do disco da Pequena Nuvem de Magalhães via *tidal stripping*, pois é localizada próximo da extremidade da Corrente de Magalhães (*Magellanic Stream*) e, segundo a literatura, houve recentes encontros entre a LMC e a SMC. Este cenário é apoiado pela significante falta de Hidrogênio neutro. Outros cenários potenciais para a origem da SMCNOD são: uma sobredensidade transitória dentro do raio de maré ou uma satélite primordial em estado avançado de ruptura.

Abstract

Our working sample comprised the outskirts of the Magellanic Clouds encompassed by the Dark Energy Survey. We focused in the star cluster system of the Large Magellanic Cloud and on the discovery of a stellar over-density associated to the Small Magellanic Cloud, which we will briefly describe here, based on already published abstracts.

The Large Magellanic Cloud harbors a rich and diverse system of star clusters, whose ages, chemical abundances, and positions provide information about the Large Magellanic Cloud history of star formation. We use Science Verification imaging data from the Dark Energy Survey to increase the census of known star clusters in the outer Large Magellanic Cloud and to derive physical parameters for a large sample of such objects using a spatially and photometrically homogeneous data set. Our sample contains 255 visually identified cluster candidates, of which 109 were not listed in any previous catalog. We quantify the crowding effect for the stellar sample produced by the Dark Energy Survey Data Management pipeline and conclude that the stellar completeness is $< 10\%$ inside typical Large Magellanic cluster cores. We therefore develop a pipeline to sample and measure stellar magnitudes and positions around the cluster candidates using DAOPHOT. We also implement a maximum-likelihood method to fit individual density profiles and colour-magnitude diagrams. For 117 (from a total of 255) of the cluster candidates (28 uncatalogued clusters), we obtain reliable ages, metallicities, distance moduli and structural parameters, confirming their nature as physical systems. The distribution of cluster metallicities shows a radial dependence, with no clusters more metal-rich than $[\mathrm{Fe/H}] \simeq -0.7$ beyond 8 kpc from the center of that galaxy. The age distribution has two peaks at $\simeq$ 1.2 Gyr and $\simeq$ 2.7 Gyr. The age-metallicity relation shows that even with an external sample, there is a global agreement with other studies that sampled more central regions of the Large Magellanic Cloud. In addition, this age-metallicity relation is well described as bounded by the analytical model from Pagel & Tautvaisiene (1998) and the empirical model from Harris & Zaritsky (2009). But neither of them describes accurately the clusters set.

We also report here the discovery of a stellar over-density 8° north of the center of the Small Magellanic Cloud, baptized as SMCNOD (Small Magellanic Cloud Northern Over-Density), using data from the first two years of the Dark Energy Survey (DES) and the first year of the MAGellanic SatelLITEs Survey (MagLiteS). The SMCNOD is indistinguishable in age, metallicity and distance from the nearby SMC stars, being primarly composed of intermediate-age stars (6 Gyr, Z=0.001), with a small

fraction of young stars (1 Gyr, Z=0.01). The SMCNOD has an elongated shape with an ellipticity $\epsilon = 0.6$ and a size of $\sim$ 6x2 deg. It has an absolute magnitude of $M_V \cong -7.7$, $r_h = 2.1$ kpc, and $\mu_V(r < r_h) = 31.2$ mag arcsec^{-2}. We estimate a stellar mass of $\sim 10^5$ $M_\odot$, following a Kroupa mass function. The SMCNOD was probably removed from the SMC disk by tidal stripping, since it is located near the head of the Magellanic Stream, and the literature indicates likely recent LMC-SMC encounters. This scenario is supported by the lack of significant HI gas. Other potential scenarios for the SMCNOD origin are a transient over-density within the Small Magellanic Cloud tidal radius or a primordial SMC satellite in advanced stage of disruption.

Conteúdo

Lista de Figuras

Lista de Tabelas

Abreviações

ΛCDM Lambda Cold Dark Matter

ACS Advanced Camera for Surveys

AMR Age Metalicity Relationship ou Relação Idade Metalicidade

BIC Bayesian Information Criteria

CCD Charge-Coupled Device

CFR Cluster Formation Rate

CMD Color Magnitude Diagram

CTIO Cerro Tololo Inter-american Observatory

DECam Dark Energy Camera

DES Dark Energy Survey

DES-GA Dark Energy Survey Galactic Archeology

DES-Y2Q1 Dark Energy Survey Quick Release of the Second Year

DESDM Dark Energy Data Management

GMC Giant Mollecular Cloud

HST Hubble Space Telescope

LIneA Laboratório Interinstitucional de e-Astronomia

LMC Large Magellanic Cloud

M NNN Messier, onde N são algarismos

MagLiteS Magellanic Satellites Survey

MB Magellanic Bridge

MS Magellanic Stream

MW Milky-Way ou Via Láctea

NGC NNNN New General Catalogue, onde N são algarismos

NOAO National Optical Astronomy Observatory

PSFEx PSF Extractor

RC Red Clump

RGB Red Giant Branch

SExtractor Source-Extractor

SFH Star Formation History

SFR Star Formation Rate

SMASH Survey of the MAgellanic Stellar History

SMC Small Magellanic Cloud

SMCNOD Small Magellanic Cloud Northern Over-Density

SPT South Polar Telescope

SV Science Verification

TDG Tidal Dwarf Galaxy

UFDG Ultra Faint Dwarf Galaxies

Capítulo 1

Introdução Geral - Estrelas, aglomerados de estrelas e galáxias

1.1 Introdução

Ao longo do trabalho vamos repetidamente mencionar os termos estrelas, associações e aglomerados estelares, galáxias-anãs e galáxias. Definir estes tópicos e seus limites não é uma tarefa fácil, dada a existência de objetos muito próximos das interfaces da definição (por exemplo, aglomerados muito luminosos e galáxias com baixa luminosidade). Muitos trabalhos já foram publicados tentando cristalizar estas definições (Trumpler, 1930, Mateo, 1998, Sparke & Gallagher, 2000, Lada & Lada, 2003, Forbes & Kroupa, 2011, Misgeld & Hilker, 2011, Gieles & Portegies Zwart, 2011, Willman & Strader, 2012)[1]. Enquanto existe um relativo consenso para a definição de estrela, associação e aglomerado, para galáxias e galáxias-anãs há uma grande gama de definições propostas na literatura, bem como uma mudança destas definições ao longo do tempo, principalmente nas últimas décadas. Nossa intenção ao ventilar este assunto aqui é mais contextualizá-las do que perseguir uma definição estática e atemporal. Mesmo com estas dificuldades, expomos aqui uma breve revisão bibliográfica das definições destes objetos.

As estrelas são os blocos formadores das associações, aglomerados estelares e galáxias. No tocante aos limites em massa, a estrela mais massiva conhecida é a estrela R136a1 do aglomerado R136 na Nebulosa da Tarântula, localizada na Grande Nuvem de Magalhães. Crowther et al. (2016) estimou a massa de R136a1 como de

[1]A referência de Forbes e Kroupa 2011 possui um questionário on-line ainda ativo onde você pode votar a sua própria definição de galáxia: `https://www.surveymonkey.com/r/WLRJMWS?sm=NHpXx4P8WdQDhcLJ9kxJNg%3d%3d`

315^{+60}_{-50} massas solares ($M_\odot$). Embora esta medida esteja próximo do que se acredita ser o limite atual para a massa de uma estrela, é esperado que as primeiras estrelas formadas no Universo, as estrelas de população III, tenham alcançado mais de 1000 $M_\odot$ (Bromm & Larson, 2004, Glover, 2005). No outro extremo, o limite inferior de massa para a definição de estrela é o minimo necessário para que o núcleo da estrela sustente reações nucleares de conversão de Hidrogênio em Hélio como o ciclo próton-próton. Este limite é de 0,072-0,09 $M_\odot$ (Baraffe et al., 1998, Kutner, 2003, Carroll & Ostlie, 2007) dependendo da metalicidade, sendo adotado geralmente o valor de 0,08 $M_\odot$. A maior parte do tempo de vida da estrela (em torno de 90% do período em que a estrela sustenta reações nucleares) é gasto transformando Hidrogênio em Hélio no seu centro. Esse período é conhecido como Sequência Principal (em inglês *Main Sequence* ou *MS*).

Na atual visão da formação estelar (Jeans, 1902), as estrelas se formam a partir de uma nuvem molecular gigante (em inglês *GMC* ou *Giant Molecular Cloud*), com no mínimo uma massa de aproximadamente 10^5 $M_\odot$, que colapsa gravitacionalmente. Seguindo o colapso da nuvem, há a fragmentação, formando um grande número de glóbulos de gás e poeira que mais tarde originarão as estrelas. A formação das estrelas em número ocorre de forma desigual para diferentes massas: há sempre um número maior de estrelas com baixa massa do que com altas massas (Kroupa, 2001, Chabrier, 2003). Assim, são formadas no mínimo alguns milhares de estrelas, dados os limites de massa das estrelas e da nuvem molecular. Depois de formadas as estrelas, o objeto dará origem a um aglomerado, uma associação ou a um conjunto de estrelas dispersas no campo das galáxias (Gieles & Portegies Zwart, 2011). As estrelas de campo que povoam as galáxias são então estrelas que se formaram a partir destas nuvens, mas que se desligaram gravitacionalmente de seus objetos formadores, devido a processos dinâmicos como evaporação, efeitos de maré e interação com outros objetos, com troca de energia cinética entre as estrelas (Gerhard, 2000). Outros processos impactam significativamente a massa do objeto inicial, facilitando a saída das estrelas, como por exemplo a expulsão de gás pelos ventos das estrelas supernovas, mais massivas e portanto as primeiras estrelas deste objeto a terminar seu ciclo evolutivo. Estes objetos formadores de estrelas (ou os seus remascentes, se ainda existentes numa configuração coesa) são chamados de aglomerados, quando mais precisamente as estrelas possuem uma grande energia gravitacional de ligação. Quando esta energia de ligação é muito baixa, tem-se o que se denomina de associação estelar(Gieles & Portegies Zwart, 2011). Como é difícil quantificar a massa de um sistema estelar aparentemente ligado, um critério proposto por Gieles & Por-

tegies Zwart (2011) para a distinção entre aglomerado e associação estelar é a razão Π entre a idade e o tempo de cruzamento (T_{cr}, em inglês *crossing time*). O tempo de cruzamento pode ser definido em termos dos parâmetros empíricos do objeto: seu raio de meia-luz R_{eff} (o raio do círculo que engloba a metade da luminosidade projetada do objeto), sua massa M e a constante gravitacional G:

$$T_{cr} = 10 \left(\frac{R_{eff}^2}{GM} \right)^{3/2}. \tag{1.1}$$

Se o objeto possui $\Pi > 1$ é considerado um aglomerado, caso contrário, as estrelas encontram-se unidas em uma associação estelar. Aqui cabe uma consideração sobre esta classificação, pois pode haver aglomerados jovens massivos e que continuariam coesos por alguns bilhões de anos, mas que por serem muito jovens, podem ter um valor de $\Pi < 1$ e portanto, seriam classificados como associações. Utilizando Binney & Tremaine 2011, para um aglomerado globular com 10^5 $M_\odot$, a uma distância de 10 parsecs o T_{cr} é igual a 1 milhão de anos, o que diminui bastante (mas não exclui) a chance de uma classificação errônea. Diminuindo a massa para 10^4 $M_\odot$, o *crossing time* aumenta para 10 milhões de anos. Adicionalmente, aglomerados menos massivos do que 10^5 $M_\odot$ perdem o gás residual em um tempo muito menor do que o *crossing time*, dissolvendo-se, enquanto que aglomerados com esta massa ou acima respondem adiabaticamente à perda de gás da nuvem. tendo uma maior chance de sobrevivência (Baumgardt et al., 2008).

Os valores empíricos para a massa são deduzidos da luminosidade do aglomerado e portanto, também de uma função de massa assumida para o objeto. Embora haja esta distinção entre aglomerado e associação, ao longo do trabalho vamos utilizar o termo aglomerado estelar para englobar aglomerado e associação estelares. Isso evitará a repetição de termos e a distinção de objetos que em muitos casos é ainda impossível de ser feita (visto os dados empíricos ainda insuficientes). Haja vista também o fato de que muitas referências são mais antigas do que a distinção proposta entre estes dois objetos.

Embora a ideia de aglomerado seja a de um objeto com intenso apinhamento de fontes estelares, apenas uma em cada quatro estrelas nasce em um ambiente onde há interação na formação e/ou evolução de estrelas (Gieles & Portegies Zwart, 2011). Quanto à homogeneidade, é esperado que as estrelas de um aglomerado tenham uma mesma composição química primordial (pois nasceram de uma mesma nuvem de gás homogênea) e uma idade semelhante. A idade pode variar em poucos milhões de anos, dependendo do tempo que o disco protoestelar leva para a formação das

estrelas, sendo que o esperado é que as estrelas menos massivas sejam mais jovens que as mais massivas, pois estas últimas se formam mais rapidamente do que as anteriores. Embora observações dentro das duas últimas décadas (apenas para citar alguns trabalhos Lee et al., 1999, Milone et al., 2008, 2009, Marino et al., 2009, Sbordone et al., 2011, Piotto et al., 2012) tenham levantado e comprovado divergências quanto à composição química das estrelas dentro de um mesmo aglomerado globular na Galáxia, e também mostrado que em alguns casos há um espalhamento em idade maior do que o esperado, a ideia que temos dos aglomerados estelares ainda é a de um conjunto de estrelas com basicamente a mesma composição química e mesma idade[2]. Mesmo coesos, dinamicamente os aglomerados estelares perdem estrelas ao longo do tempo, fazendo com que suas componentes venham a povoar o ambiente de campo das galáxias (disco, halo ou bojo).

Englobando um grande conjunto de estrelas temos uma galáxia. Ela pode ser definida em grandes linhas como um sistema de estrelas e seu campo de radiação, remanescentes de estrelas, seus prováveis (ou comprovados) planetas, um meio interestelar de gás e poeira, um campo magnético comum à galáxia, raios cósmicos e um componente conhecido como matéria escura que interage gravitacionalmente com os outros componentes, porém com interações eletromagnéticas muito restritas (Navarro et al., 1996). Este sistema pode ter de vários quiloparsecs (1kpc=3,0857 $\times 10^{19}$ m) de extensão (como no caso das galáxias gigantes) até apenas uma centena de parsecs de extensão (caso de algumas galáxias anãs) e encontra-se gravitacionalmente ligado. A galáxia que melhor conhecemos é a Via-Láctea, galáxia onde o Sol ocupa uma região periférica, distando do centro $8,33 \pm 0,35$ kpc (Gillessen et al., 2009), e com diâmetro próximo de 30 kpc (Schneider, 2006). Na próxima subseção faremos um estudo sobre a classificação das galáxias.

1.1.1 Denominação, taxonomia e evolução das galáxias

Historicamente a primeira classificação de galáxias foi morfológica (elípticas, lenticulares, espirais e espirais barradas), seguindo o diapasão de Hubble (Hubble, 1926), como na figura 1.1. Seguindo esta classificação, as galáxias elípticas têm isofotas que lhes dão o nome, enquanto as galáxias espirais têm formato de disco, com

[2]Importante citar a definição que temos hoje da classificação de aglomerado globular Galáctico. Inicialmente, com os trabalhos de Sandage 1958, os aglomerados globulares foram o protótipo de populações estelares simples: uma única idade e uma mesma composição química. Mais tarde, com as diferentes populações que foram descobertas nos aglomerados globulares Galácticos, principalmente a anti-correlação Na-O, a melhor definição é a de que os aglomerados globulares Galácticos têm ao menos uma população estelar (Carretta et al., 2010).

braços espirais curvos. A presença de uma barra próxima do centro da galáxia leva à denominação de galáxia barrada, seguindo uma classificação conforme a distinção entre a barra e os braços espirais (a, b ou c), indo de uma galáxia com braços muito enrolados em torno do núcleo (a) para uma galáxia com braços quase na posição radial (c), sendo a classificação b um caso intermediário. Por fim, e não presentes na figura 1.1, as galáxias com formas irregulares ou não usuais são chamadas de galáxias irregulares.

Embora com grande valor histórico, esta classificação de galáxias de Edwin Hubble mostra-se atualmente um tanto defasada tendo em vista a grande variedade de galáxias elípticas e de anãs. Obviamente à época ela se destinava a galáxias luminosas e cobrindo vários kiloparsecs. Ela é insuficiente para a grande gama de galáxias de baixo brilho, quer sejam elas anãs ou mesmo galáxias gigantes. Historicamente é compreensível que estas galáxias de baixo brilho superficial (geralmente com brilho superficial menor do que magnitude 25 por segundo de arco quadrado segundo Bothun et al. 1986) tenham sido excluídas da classificação de Hubble, sendo que a previsão de sua existência se deu primeiramente em Disney 1976 e a observação de um destes objetos (Malin 1) foi feita pela primeira vez por Bothun et al. (1986).

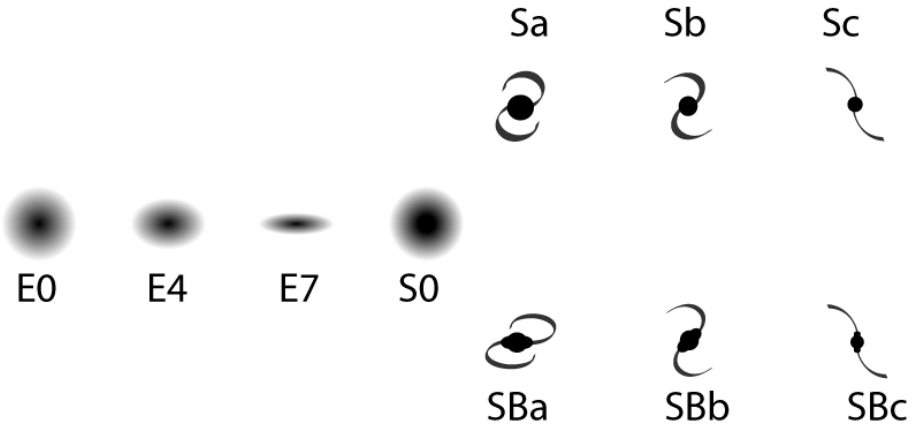

Figura 1.1: Diagrama de Hubble em forma de diapasão para a classificação de galáxias segundo a forma. À esquerda as galáxias elípticas, com elipticidade crescente até a forma lenticular (S0), bifurcando-se em espirais normais (braço superior) e espirais barradas (braço inferior). Retirado de https://dept.astro.lsa.umich.edu/ugactivities/Labs/GalClass/GalClassShort.html. Acessado 14 de abril de 2016.

Um comentário importante é que a classificação das galáxias pela sua forma é feita geralmente pela análise de imagens nas bandas B e/ou V. No entanto, a forma das galáxias pode mudar drasticamente dependendo do intervalo de comprimento de onda utilizado para observação (Kutner, 2003).

A forma das galáxias não só traz informação sobre sua aparência, mas também sobre seu histórico de formação e evolução estelar (Schneider, 2006), donde se imagina que as galáxias sigam trajetórias evolutivas semelhantes nestes dois quesitos. As galáxias elípticas apresentam uma cor avermelhada quando são observadas no óptico, o que sugere uma população estelar velha (12-13 bilhões de anos). Um exemplo de galáxia elíptica é a galáxia M49 (ou NGC 4472, Figura 1.2). Inicialmente se pensou que, devido à população jovem não significativa, as galáxias elípticas tivessem exaurido completamente sua quantidade de gás e poeira (Hubble, 1926, Sandage, 1961). Hoje se sabe que esta quantidade não é relativamente tão pequena quanto se imaginava, em torno de 3% da massa estelar total da galáxia (Young et al., 2011), mas ainda bem menor do que nas galáxias espirais (Schneider, 2006). A Via-Láctea, como exemplo de uma galáxia espiral, possui em torno de 10-20% de matéria bariônica na forma de gás e poeira (Friaça, 2000). Essa quantidade de gás e poeira maior nas galáxias espirais e irregulares pode explicar a fração de população estelar jovem significativa, ao contrário das galáxias elípticas. As galáxias irregulares e espirais apresentam uma taxa de formação estelar (em inglês *Star Formation Rate - SFR*) atual significativa em relação à taxa de formação estelar média (Schneider, 2006) ao longo de sua existência. A razão da massa de gás em relação à massa de poeira para uma amostra de 14 galáxias espirais próximas é de 120±60 segundo Stevens et al. (2005).

As interações entre galáxias induzem o aumento significativo de incidentes de formação estelar, levando às galáxias *Starburst* ou galáxias com surto de formação estelar (Schneider, 2006). Esta interação ou *merger* pode ser um processo envolvendo galáxias de aproximadamente mesma massa (então sendo chamado de *major merger*) ou galáxias com massas muito diferentes (*minor merger*). No entanto, existem galáxias *Starburst* isoladas, o que evidencia que a interação gravitacional com outra galáxia não é o único mecanismo que pode induzir a intensa formação estelar ou a surtos de formação estelar (Tacconi et al., 2010, Daddi et al., 2010).

Quanto ao tamanho, um limite inferior para as galáxias gigantes é proposto por Forbes & Kroupa (2011) como 100 parsecs para o raio de meia-luz, a partir do qual (para tamanhos menores) a galáxia é chamada de galáxia anã, uma nomenclatura já comum para as galáxias não tão massivas e nem tão extensas. Elas consistem de sistemas menores, que podem apresentar ou não grande concentração de matéria escura e população estelar simples (valores únicos ou muito próximos para a idade e metalicidade) ou variada.

No entanto, não há um consenso na literatura para esta diferenciação entre galáxia

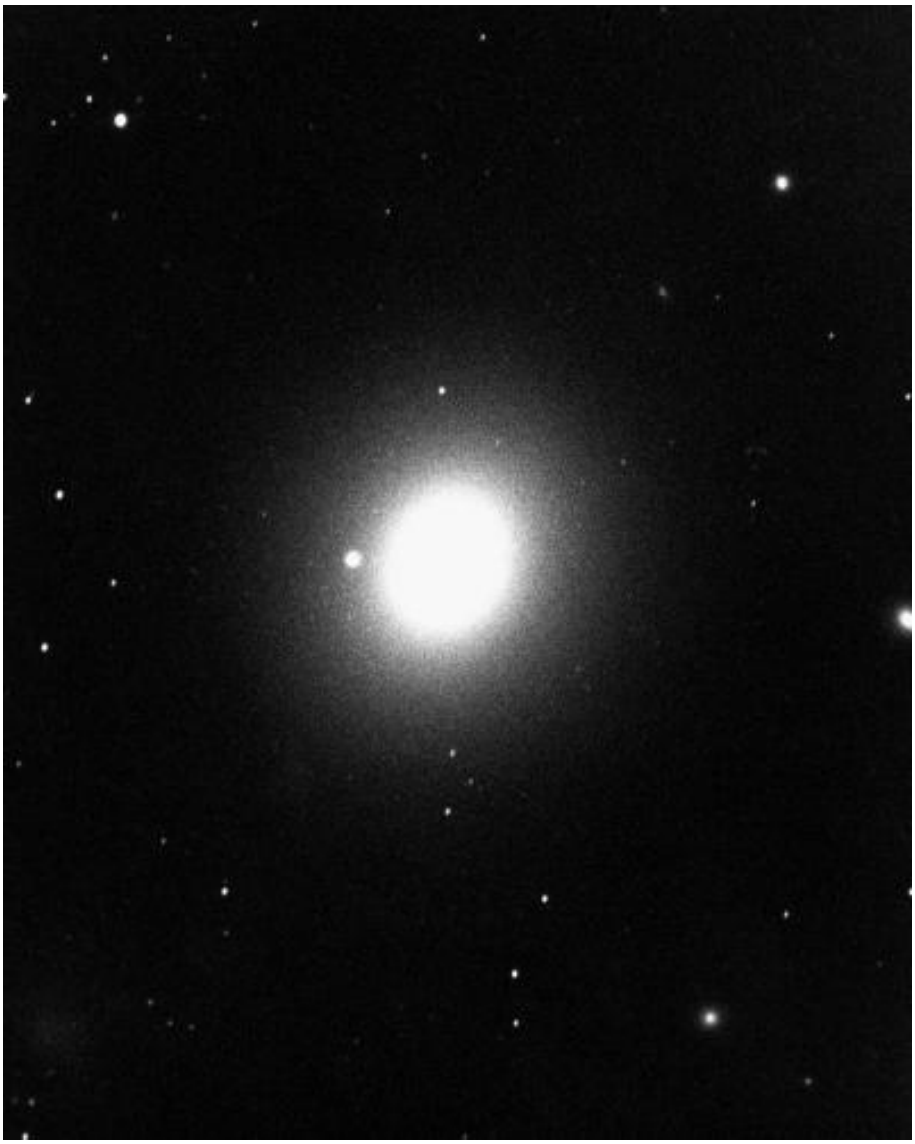

Figura 1.2: Galáxia elíptica típica M49, em uma imagem na banda V observada com o telescópio Mayall KPNO de 4 metros de abertura. Retirado de https://www.noao.edu/image_gallery/html/im0088.html. Acessado 21 de agosto de 2017.

anã e gigante, sendo que as galáxias anãs tem tamanho típico de 0.1-10kpc em comparação com galáxias gigantes como a Via-Láctea, com diâmetro em torno de 30kpc. Por exemplo, McConnachie (2012) classifica arbitrariamente as galáxias com $M_V > -18$ como galáxias anãs (*dwarf*) e um estudo mais completo no espaço massa-raio-luminosidade é feito por Tollerud et al. (2011), para a classificação de uma série de objetos (incluindo aglomerados globulares). A massa típica das anãs seguindo este último estudo está em torno de $10^7 - 10^9$ $M_\odot$ e para as gigantes o limite de massa vai até próximo de 10^{14} $M_\odot$, que é a massa esperada para as galáxias que se encontram próximas dos centros de aglomerados de galáxias.

Uma subdivisão das galáxias anãs é feita levando-se em conta diferentes características como por exemplo o tamanho e brilho superficial para as galáxias anãs conhecidas como compactas ou ultra compactas, o baixo brilho superficial para as galáxias anãs classificadas como ultra-débeis e a forma para as anãs esferoidais, elípticas ou irregulares.

As anãs compactas ou *Compact Dwarfs* foram definidas originalmente por Zwicky 1970, referindo-se a objetos fortemente compactados e portanto com alto brilho superficial (magnitude por segundo de arco quadrado <20 nas bandas B, V, R e I). Zwicky ainda classificou as *Compact Dwarfs* como azuis (*blue*) caso elas satisfizessem a condição anterior de densidade de brilho nas bandas B e R (Zwicky & Zwicky, 1971). Mais tarde, Thuan & Martin 1981 cunharam o termo *Blue Compact Dwarf* referente a galáxias anãs com alto brilho superficial e alta taxa de formação estelar recente, com cor *(B-V)* entre 0,0 e 0,3 (Schneider, 2006). Já as *Ultra-Compact Dwarfs* ou *UCDs* foram primeiramente observadas na década de 1990 (Hilker et al., 1999) e são classificadas por Mieske et al. 2008 como galáxias com raio de meia-luz (r_h) entre 7 e 100 parsecs e massa $\geq 2 \times 10^6 M_\odot$. Uma classificação diferente é feita por Baumgardt & Mieske 2008: ($-10,5 \geq M_V \geq -14$), r_h entre 10-100 parsecs, massas entre 10^7 a 10^8 $M_\odot$ e conteúdo bariônico (todo o conteúdo que não é matéria escura) de no mínimo metade da massa dinâmica. A origem das *UCDs* é atribuída ao *tidal stripping* de galáxias anãs nucleadas quando se aproximam de galáxias gigantes massivas (Pfeffer & Baumgardt, 2013). Seguindo esta mesma referência, para a galáxia M87 no aglomerado de Virgo esta distância deve ser menor que 10 kpc na máxima aproximação.

As galáxias-anãs muito débeis (em inglês *Ultra-Faint Dwarf Galaxies* ou *UFDG*) são galáxias com brilho superficial muito baixo, objetos dominados em grande parte pela matéria escura, $r_h \geq 20$ pc, $-2,5 \geq M_V \geq -7,5$ (McConnachie et al., 2005), geralmente apresentando populações velhas e pobres em metais (Drlica-Wagner et al.,

2015).

As galáxias anãs esferoidais (em inglês *Dwarf Spheroidals* ou simplesmente *dSph*) são mais brilhantes do que as *UFDG*, com $-7,5 \geq M_V \geq -12,5$, forma aparente esferoidal, não possuem quantidade expressiva de gás, poeira, nem tampouco formação estelar recente (Gilmore et al., 2007), e têm valores de razão massa dinâmica sobre luminosidade em relação à razão solar ($[M/L]/[M/L]_{\odot}$) acima de 10 (Walker & Peñarrubia, 2011). O último parâmetro é um forte indicador da presença de matéria escura. Esta classificação não significa que não haja outros objetos, como por exemplo aglomerados globulares Galácticos, que sejam mais brilhantes do que algumas UFDG ou mesmo dSph, como por exemplo ωCen, com $M_V = -10.26$. Para uma lista destes objetos bem como uma maior discussão da questão da classificação de objetos em galáxias, referimo-nos aos trabalhos de Forbes & Kroupa (2011) e de Willman & Strader (2012).

Na classificação quanto ao formato, as anãs elípticas são galáxias tipicamente com $-8 \geq M_B \geq -18$, perfis de brilho superficial muito suaves mesmo mostrando um núcleo mais brilhante (Ferguson & Binggeli, 1994), exceto para as anãs elípticas mais débeis (Sandage et al., 1985). Por vezes na literatura há uma sobreposição na classificação de anãs elípticas com anãs esferoidais, sendo que uma segura classificação na região de interface muito difícil (Binggeli & Cameron, 1991, Prugniel et al., 1992, Vader & Chaboyer, 1994, Zaritsky et al., 2006a,b).

Por último, as anãs irregulares são amorfas, embora apresentem uma curva de rotação bem definida. Geralmente apresentam grandes quantidades de Hidrogênio neutro formando um grande componente gasoso (Battaner & Florido, 2000).

As galáxias contêm quantidades variadas de sistemas, como aglomerados estelares e nuvens interestelares (Karttunen et al., 2003). Nas galáxias, entre as estrelas, existe um meio interestelar (na sigla em inglês *ISM - Interestellar medium*) esparso de gás e poeira (Karttunen et al., 2003). Em nossa Galáxia, o gás e a poeira concentram-se no disco da Galáxia, o que ocorre comumente também nas outras galáxias (Schneider, 2006). As estimativas em massa para o gás e a poeira nas galáxias variam, geralmente como menos de 10% da quantidade total em massa de estrelas é estimada para o gás (Schneider, 2006). Outros autores Kutner (2003) citam dados da ordem de 1% para o gás. Outros autores ainda listam as chamadas galáxias ricas em gás (*gas-rich galaxy*), galáxias com até mais de 70% de seu conteúdo bariônico ainda na forma de gás (Lutz et al., 2017), mas onde por razões cinemáticas (grande momento angular) associadas à falta de interações com as galáxias próximas, há uma baixa eficiência na formação estelar (Chowdhury & Chengalur, 2017). Há

ainda galáxias muito distantes, onde a grande quantidade de gás ainda não foi convertida em estrelas, sendo também classificadas como galáxias ricas em gás, mas geralmente com uma alta taxa de formação estelar (Salim et al., 2007, Gowardhan et al., 2017). Há ainda as galáxias HII, ricas em gás, dominadas por alta formação estelar, apresentando baixa metalicidade e aparentemente tiveram o seu conteúdo em gás tardiamente convertido em estrelas (Telles & Terlevich, 1994).

Há ainda as galáxias ultra difusas, descobertas em 1984 por Sandage e Bingelli (Sandage & Binggeli, 1984). Segundo esta referência, são galáxias que podem ter o tamanho da Galáxia, mas que possuem apenas 1% de seu brilho superficial. Este baixo brilho superficial é devido a uma quase completa falta de formação estelar, possuindo apenas uma pequena fração de massa em estrelas muito velhas. Um exemplo conhecido é o da galáxia Dragonfly no aglomerado de galáxias de Coma, confirmada espectroscopicamente (van Dokkum et al., 2015).

Outro tipo de galáxia descoberto nos últimos anos são as galáxias *jellyfish* (ou em português 'água-viva'). Como o próprio nome sugere, são galáxias com brilho superficial muio baixo, encontradas em aglomerados de galáxias. Elas são caracterizadas pelo gás de galáxias retirado de suas hospedeiras (Ebeling et al., 2014) por *ram pressure* (mecanismo onde o meio intergaláctico oferece resistência à passagem do gás de uma galáxia que se desloca em relação ao meio) (Gunn & Gott, 1972). Este gás violentamente retirado rapidamente forma estrelas, geralmente ao longo de uma cauda ou em forma de nós (Owers et al., 2012).

Como último tipo de galáxia, citamos as anãs de maré *Tidal Dwarf Galaxy*, galáxias constituídas por estrelas que se formaram *in situ* durante a colisão, interação ou fusão de galáxias espirais massivas, com massa acima de $10^8 M_\odot$ (Duc, 2012).

Com uma variedade tão grande de galáxias, muitas destas descobertas nas últimas décadas, há uma sobreposição entre as galáxias com tamanhos de algumas dezenas de parsecs e objetos como os aglomerados globulares (veja por exemplo a figura 1.3, retirada de Misgeld & Hilker 2011). Para exemplificar, esse é o caso da galáxia anã Tucana V (Drlica-Wagner et al., 2015)[3] e do aglomerado globular Palomar 5 (Abell, 1955). A galáxia anã tem $r_h = 17 \pm 6$ pc (Drlica-Wagner et al., 2015), enquanto que Palomar 5 tem $r_h = 18,42$ pc (Harris, 1996b). Enquanto que o critério de raio de meia luz certamente colocaria ambos na mesma classificação, a dispersão de velocidades das estrelas é maior para uma galáxia anã (devido à presença de matéria escura) do que para o aglomerado, para o qual não é necessária a hipótese

[3]Embora seja listada como galáxia anã, ainda não há comprovação espectroscópica da dispersão de velocidades deste objeto.

da matéria escura para explicar sua dinâmica estelar. O teste de separação entre aglomerado estelar e galáxia proposto por Willman & Strader 2012 é exatamente este: um aglomerado seria um objeto cuja dinâmica é explicada pelas leis de Newton e por seu conteúdo bariônico, enquanto que para uma galáxia, o conteúdo bariônico associado às leis de Newton não são suficientes para explicar sua dinâmica. Embora eficaz para a definição de galáxia, este critério não dá conta das múltiplas divisões e classificações das galáxias propostas acima.

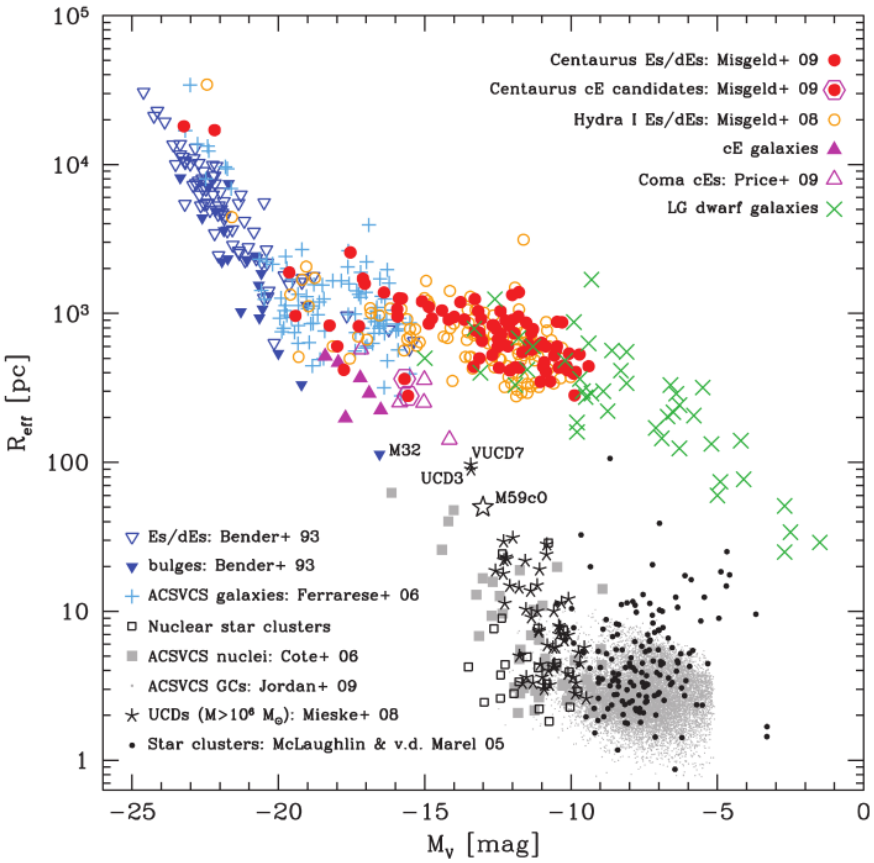

Figura 1.3: Distribuição de sistemas estelares quentes, segundo Misgeld & Hilker 2011, onde o raio efetivo é plotado contra a magnitude absoluta na banda *V*.

1.1.2 O estudo das galáxias através dos aglomerados estelares

A interação gravitacional com uma galáxia vizinha ou um *merger* (Sanders et al., 1988, Keel et al., 1985, Duc et al., 1997, Lawrence et al., 1989) pode fazer com que o gás presente na galáxia colapse, levando à formação de aglomerados estelares, num

surto de formação estelar. Este surto pode ser causado também por outros fatores ainda desconhecidos, como já citamos.

É muito mais fácil estimar os parâmetros físicos das estrelas (idades, metalicidades e distâncias) quando elas se encontram em aglomerados ou associações do que quando dispersas na galáxia. No entanto, os aglomerados tendem a dissipar suas estrelas. Dessa forma, quando se vai avaliar o histórico de formação estelar em uma galáxia a partir de uma amostra de aglomerados, deve se corrigir o histórico de formação estelar tendo em conta que há um número muito maior de aglomerados velhos do que de aglomerados jovens que se dissiparam pela galáxia. Esta correção pode (e certamente vai) introduzir uma série de incertezas na determinação do histórico de formação estelar. Assim, a reconstrução do histórico de formação estelar (na sigla em inglês *SFH - Star Formation History*) é facilitada pelo rastreio destes aglomerados estelares na galáxia estudada, mas privilegia os aglomerados jovens, pois a taxa de formação estelar será mais precisa para estes objetos. As estrelas de campo também padecem de uma deficiência semelhante, pois as estrelas massivas evoluem rapidamente, se tornando remanescentes estelares em um lapso de tempo curto em comparação com a idade da galáxia.

Além da idade, a metalicidade nos aglomerados fornece importante informação a respeito da evolução química de uma galáxia. Com a determinação da idade e da metalicidade dos aglomerados (ou relação idade-metalicidade - em inglês AMR) pode-se procurar por gradientes radiais de metalicidade e inferir se a formação destes aglomerados ocorreu sequencialmente do centro para as bordas (formação *inside-out*) ou da periferia para o centro *outside-in*. Além disso, pode-se traçar áreas predominantes de formação estelar, como por exemplo os braços de galáxias espirais. Ou ainda inferir a relação idade-metalicidade para os aglomerados, traçando mais claramente o histórico de enriquecimento químico da galáxia, inclusive podendo dizer se há chance de algum aglomerado fazer parte daquela galáxia ou ter acrescido mais tarde (dependendo se obedece ou não à relação idade metalicidade para os aglomerados daquela galáxia).

1.2 O Grupo Local

O Grupo Local é o nome dado ao conjunto de galáxias existentes dentro de uma distância de aproximadamente 1 Mpc da Via-Láctea (Kutner, 2003). Graças a esta distância relativamente pequena é possível com a instrumentação atual resolver as estrelas que constituem as galáxias do Grupo Local, de forma que se pode estudar

em maior detalhe as suas populações estelares.

Antes da virada do milênio, haviam apenas 35 galáxias como confirmadamente pertencentes ao Grupo Local (Mateo, 1998). Depois do advento do SDSS (York et al., 2000), dezenas de galáxias-anãs foram adicionadas, muitas das quais classificadas como *UFDG* (Willman et al., 2005b,a, Zucker et al., 2006b,a, Belokurov et al., 2006, 2007, 2008, 2009, 2010, Grillmair, 2006, 2009, Sakamoto & Hasegawa, 2006, Irwin et al., 2007, Walsh et al., 2007). O Dark Energy Survey (DES) tem também importante papel no aumento do número de galáxias anãs do Grupo Local, pois até o momento foram descobertas na área do céu amostrada pelo DES um total de 18 candidatas a galáxias anãs (Kim et al., 2015, Koposov et al., 2015, Bechtol et al., 2015, Drlica-Wagner et al., 2015), sendo que 16 foram descobertas e publicadas pela colaboração (Bechtol et al., 2015, Drlica-Wagner et al., 2015).

O grupo de galáxias do qual faz parte a Via-Láctea compreende também duas galáxias anãs irregulares próximas, chamadas Nuvens de Magalhães (a Grande Nuvem de Magalhães na sigla em inglês *Large Magellanic Cloud - LMC* - e a Pequena Nuvem de Magalhães, em inglês *Small Magellanic Cloud - SMC*), além dos componentes mais brilhantes e massivos como a Galáxia de Andrômeda e a M33 (Sparke & Gallagher, 2000).

As duas Nuvens de Magalhães são consideradas galáxias satélites da Via-Láctea (Sparke & Gallagher, 2000), embora alguns artigos recentes não consigam comprovar se o sistema magalhânico orbita a Via-Láctea ou está passando por uma primeira aproximação da Galáxia. Kallivayalil et al. (2013) indica que, embora haja incertezas razoáveis na determinação das massas destes corpos, períodos orbitais das Nuvens (como um todo) em relação à Via-Láctea menores do que 4 bilhões de anos estão descartados. Um estudo recente (James & Ivory, 2011) revelou que é relativamente rara a frequência de satélites de galáxias como as nuvens de Magalhães no entorno de galáxias com luminosidades comparáveis com a da Via-Láctea. Para uma amostra de 143 galáxias luminosas (distantes de nós até 30 Mpc), dois terços não apresentam satélites com formação estelar (para luminosidades e taxas de formação estelar bem abaixo daquelas das Nuvens de Magalhães). Apenas 47 galáxias (um terço da amostra) têm um sistema de satélites com formação estelar associado, com separação média de 81kpc. Já o conjunto das Nuvens de Magalhães e a Via-Láctea tem uma separação média de 56kpc - $49,9 \pm 2,0$ kpc para a LMC segundo (de Grijs et al., 2014) e 62,1±1,9 kpc para a SMC segundo (Graczyk et al., 2014). Este estudo comprova que o sistema da Via-Láctea e das Nuvens de Magalhães é realmente um sistema atípico, com baixa probabilidade de ocorrência.

Outro sistema importante no Grupo Local é o sistema da galáxia de Andrômeda (M31), cujo principal componente que dá nome ao sistema é a galáxia de Andrômeda, e que possui massa e tamanho ligeiramente maiores que os da nossa Galáxia (Peñarrubia et al., 2014). M31 é uma galáxia espiral distante 780 kpc da Via-Láctea (McConnachie et al., 2005) e que também possui um sistema de galáxias satélites (McConnachie et al., 2005). As quatro galáxias satélites de Andrômeda mais brilhantes são M32, M110, NGC185 e NGC147, com $M_V = -16,4$, -16,5, -14,8 e -14,6, respectivamente (McConnachie, 2012). Comparando com as galáxias anãs da Via-Láctea, segundo o mesmo autor, as mais brilhantes são a LMC, a SMC, e as anãs de Canis Major e de Sagitário, com M_V = -18,1, -16,8, -14,4 e -13,5, respectivamente. A maioria das galáxias anãs de Andrômeda (29 de um total de 33, ou seja, todas exceto as quatro já citadas) foi descoberta depois da década de 1970 (McConnachie et al., 2005). Analogamente a alguns trabalhos que indicam um plano preferencial para a distribuição de galáxias satélites na Via-Láctea (Pawlowski et al., 2012, 2013, Pawlowski & Kroupa, 2013), também na galáxia de Andrômeda parece haver um grande e delgado plano de galáxias-anãs corrotantes (Ibata et al., 2013). Sobre o histórico de formação estelar, segundo Davidge et al. (2012) na parte externa da galáxia (mais distantes do centro que 21kpc) a taxa de formação estelar é constante, enquanto que para distâncias menores do que 21 kpc houve um aumento de 2 a 3 vezes na taxa de formação estelar nos últimos 10 milhões de anos em comparação com o precedente 100 milhões de anos (ou seja, uma relativa aceleração na taxa de formação estelar). Seguindo esta mesma referência, estas regiões de formação estelar são dispostas em forma de anéis de gás frio com estrelas de idade em torno de 100 milhões de anos. Além disso a distribuição de estrelas vermelhas evoluídas é diferente para os dois braços da galáxia, sendo que a densidade projetada destas estrelas no braço norte é duas vezes maior do que no braço sul. Essa característica parece indicar que esta estrutura é a consequência de interações com uma galáxia companheira ou possivelmente NGC 205.

Agora faremos um apanhado mais detalhado a respeito dos principais objetos no entorno Galáctico: A Via-Láctea e as Nuvens de Magalhães.

1.2.1 A Via-Láctea

O Sol encontra-se entre os braços espirais de Perseus e Sagittarius (Kutner, 2003), na galáxia chamada Via-Láctea ou simplesmente Galáxia (com inicial maiúscula). Os componentes estruturais da Galáxia são o bojo - a parte central da Galáxia, o disco fino, o disco espesso e o halo (Sparke & Gallagher, 2000). Há ainda uma barra

no centro da Via-Láctea (Bissantz & Gerhard, 2002, Wegg et al., 2015).

Acredita-se que o bojo da Galáxia tenha alguns décimos da massa visível da Galáxia (Carroll & Ostlie, 2007). As estrelas do bojo são de difícil observação pois a quantidade de gás e poeira diminui o brilho das estrelas nesta região em até 30 magnitudes na banda V (Lebofsky & Rieke, 1987, Catchpole et al., 1990). Uma das soluções para contornar este problema é o uso de filtros no infravermelho como os filtros *J, H* e *K* do 2MASS (Huchra et al., 1994) ou *W1* e *W2* do WISE (Wright et al., 2010), diminuindo assim a extinção interestelar. Grande parte das estrelas presentes no bojo tem idades de $10 \pm 2,5$ bilhões de anos (Minniti & Zoccali, 2008), e alta metalicidade, entre [Fe/H]=0 e +0,5. O diagrama cor-magnitude mais profundo das estrelas do bojo foi produzido por Sahu et al. (2006) utilizando a ACS a bordo do HST (na busca por exoplanetas hospedados em estrelas em frente ao bojo Galáctico) e é perfeitamente compatível com a idade de 10 bilhões de anos e a metalicidade solar como população predominante. Segundo van Loon et al. 2003, as estrelas mais jovens (em torno de 200 milhões de anos) estão confinadas ao plano Galáctico e representam uma pequena parcela da população do bojo, juntamente com uma população intermediária de algumas centenas de estrelas no ramo assintótico das gigantes (em inglês *Asymptotic Ginat Branch* ou *AGB*), as quais sofrem grande perda de massa.

O perfil vertical de densidade de estrelas na Galáxia pode ser ajustado à superposição de dois discos exponenciais, mas não a um único disco (Gilmore & Reid, 1983). Estes dois componentes dão origem ao que chamamos hoje de disco fino e de disco espesso da Galáxia, melhor descrito por leis de densidade exponenciais (Bahcall & Soneira, 1980, Gilmore & Reid, 1983), tanto para a distribuição radial (ao longo do disco) como para a distribuição em altura (ortogonal ao plano do disco). A escala de altura (altura onde a densidade de estrelas cai a 1/e em relação à densidade no disco) e a escala de comprimento determinados por Jurić et al. (2008) são de 300 e 2600 parsecs para o disco fino e de 900 e 3600 parsecs para o disco espesso, utilizando o método de paralaxe fotométrica em 48 milhões de estrelas do SDSS (DR5). Novos estudos (por exemplo Bovy et al. 2016) utilizando dados de levantamentos espectroscópicos como o APOGEE (do inglês *APO Galactic Evolution Experiment*) estão mostrando que existem diferenças significativas deste modelo simplificado para o disco da Galáxia. As estrelas que compõe o disco e que apresentam um alto valor de $[\alpha/Fe]$ e baixa metalicidade se distribuem seguindo um perfil exponencial de densidade para distâncias entre 4 e 14 kpc do centro Galáctico. Já as estrelas com baixo [α/Fe] (basicamente [α/Fe]$\leq$0,1) e -0,6$\leq$[Fe/H]$\leq$+0,3 em pas-

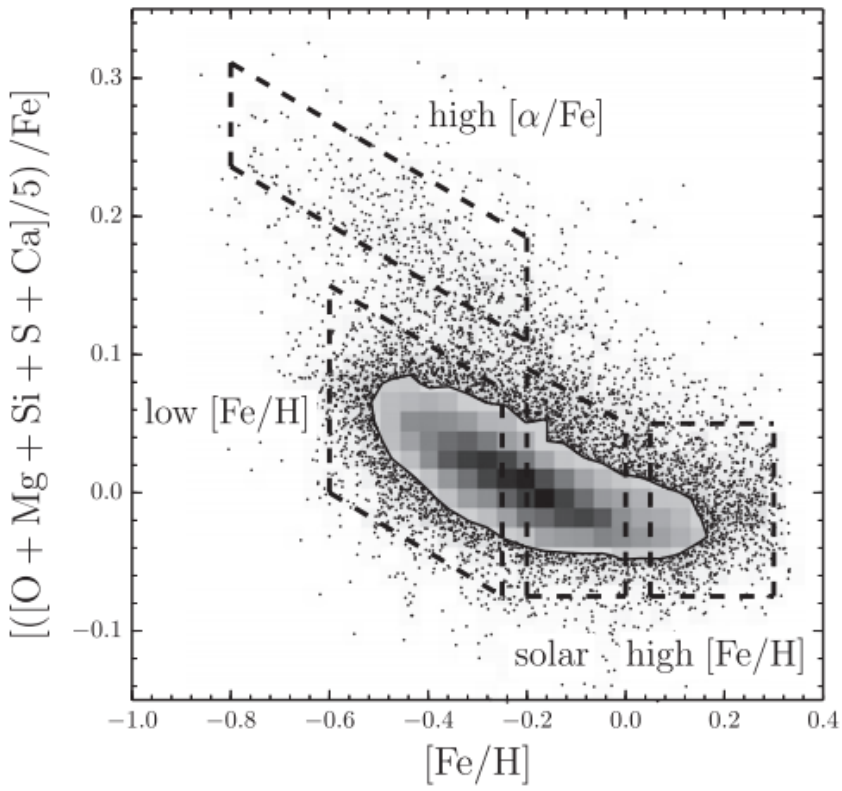

Figura 1.4: Distribuição de 14.699 estrelas na amostra do APOGEE-RC usada em Bovy et al. (2016), no plano definida pela abundância de [Fe/H] e a abundância média de elementos α. Uma representação de densidade linear binada é usada para os 68% de distribuição que é contida dentro do contorno mostrado. Maiores detalhes no referido artigo.

sos de [Fe/H]=0,1 apresentam um pico de densidade que vai se afastando do centro Galáctico à medida que a metalicidade vai diminuindo. Veja a Figura 5 de Bovy et al. (2016) aqui representada na Figura 1.4 para uma melhor definição dos limites de alta e baixa metalicidade e [α/Fe].

É no disco fino que ocorre a atual formação estelar, sendo que a maioria dos aglomerados abertos se encontra nesta região (Magrini et al., 2017). A região onde há uma maior concentração de gás e poeira no disco fino possui espessura média de 90pc (Carroll & Ostlie, 2007), embora possa ser tão fina quanto 35pc. Seguindo as conclusões de Jurić et al. (2008), a razão do número de estrelas entre o disco espesso e fino é em torno de 12%, enquanto que a razão entre as estrelas do halo e do disco fino é de 0,5%. Alguns autores propõem que o disco espesso seja formado pelas estrelas do disco fino que se aqueceram cinematicamente, tendo portanto uma dispersão de velocidades maior do que o disco fino e também estrelas mais velhas (como citado por

Carroll & Ostlie, 2007). Embora se possa compreender que o disco espesso possa ter sido criado pelo aquecimento cinemático das estrelas com a interação gravitacional com aglomerados, associações e nuvens moleculares gigantes, ainda outros cenários são propostos para a formação do disco espesso, como a fusão da Via-Láctea com uma galáxia anã ou mesmo a acreção destas galáxias-anãs com a Galáxia proposta por Beers & Sommer-Larsen (1995), dada a diferença cinemática entre o disco fino e o espesso para uma população estelar pobre em metais encontrada por estes autores. Além disso, Schönrich & Binney (2009) demonstraram que a mistura de estrelas com diferentes distâncias radiais em relação ao centro da galáxia (uma consequência inevitável de uma estrutura espiral) leva a dois componentes discoidais como modelo mais simples, nos quais a taxa de formação estelar é uma função monotonicamente decrescente.

Além do disco, existe o halo da Galáxia, uma região aproximadamente esférica que circunda a Galáxia e é composto por aglomerados globulares e estrelas de campo (Carroll & Ostlie, 2007). Quimica e dinamicamente os aglomerados globulares Galácticos formam dois conjuntos primeiramente identificados por Zinn (1985): os mais pobres em metais distribuem-se esfericamente em torno do centro galáctico e são associados ao halo galáctico, enquanto que o conjunto dos mais ricos em metais é achatado e pode ser associado ao disco espesso, com poucas exceções. Usualmente o divisor de metalicidade é [Fe/H] = -0,8 (Carroll & Ostlie, 2007).

Além destes componentes, devemos citar o halo de matéria escura aproximadamente esférico (ou triaxial segundo Law et al. 2009) que se estende pelo menos até 230kpc (Carroll & Ostlie, 2007) do centro da Galáxia e com massa total mínima de 10 vezes a massa visível da Galáxia. A massa estelar da Galáxia é estimada por McMillan 2017 como sendo $5,43 \pm 0,57 \times 10^{10}$ $M_\odot$ e a massa virial total de $1,30 \pm 0,30 \times 10^{12}$ $M_\odot$. Resultado similar é encontrado por Kafle et al. (2014): $1,041^{+0,27}_{-0,34} \times 10^{11}$ $M_\odot$ para a massa estelar e $0,80^{+0,31}_{-0,16} \times 10^{12} M_\odot$ para a massa total.

Próximo da Via-Láctea, encontram-se as duas galáxias mais extensas no céu e maiores em tamanho, classificadas como companheiras ou satélites da Via-Láctea: a SMC e a LMC. Ambas podem ser vistas na figura 1.5, em um campo de 60 × 20 graus.

1.2.2 A Pequena Nuvem de Magalhães

A SMC é uma galáxia irregular, situada na constelação de Tucana, com distância estimada de 62,1±1,9 kpc (Graczyk et al., 2014). Sua metalicidade média está próxima de um décimo da metalicidade solar no centro e diminui em direção às

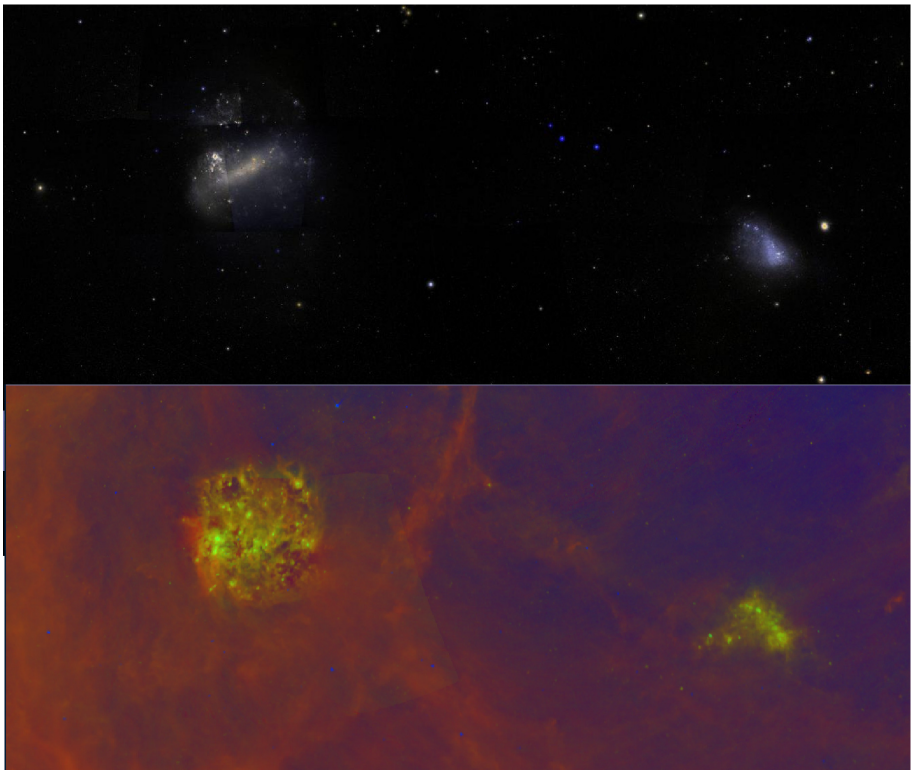

Figura 1.5: As galáxias LMC (esquerda) e SMC (direita) em (topo) uma composição utilizando as chapas fotográficas do Digital Sky Survey (DSS), nas bandas B, V e I e (abaixo) como visto pelo IRAS (InfraRed Astronomical Satellite) no infravermelho próximo. O Norte está para cima e o Leste à esquerda. Fonte: GoogleSky. Acessado: 29 de agosto de 2017.

regiões periféricas (Carrera et al., 2008). Embora classificada como *dIrr - dwarf irregular*, uma estrutura elongada na direção Noroeste-Sudoeste, semelhante a uma barra, é notável, juntamente com uma Asa na direção da LMC e da Ponte Magalhânica (conjunto de estrelas e aglomerados que liga as duas nuvens). A massa da SMC é em torno de um quinto da massa da LMC (embora a medida da massa possa variar muito dependendo da referência) e se encontra um pouco mais distante do que aquela. Seu tamanho, embora considerada uma galáxia irregular, é também motivo de muitas discrepâncias. Enquanto simulações predizem para a SMC um raio de truncagem de 5kpc (Bekki & Chiba, 2005), Noël & Gallart (2007) encontraram estrelas de idade intermediária e velhas até 6,5 kpc (5,8°) do centro da SMC, não detectando um limite ou raio de truncagem para a população estelar. Nidever et al. (2011) detectam estrelas gigantes vermelhas, pobres em metais (características da população da SMC) e à mesma distância que a SMC a 11kpc de distância do centro da SMC, numa distribuição azimutalmente simétrica. A população da região do *Main Sequence Turn Off*, velha (6 bilhões de anos) e pobre em metais é bem ajustada a um perfil exponencial até 7,3°, e em algumas direções até 8,4°. Além deste limite há uma quebra no perfil de densidade estelar, diminuindo a taxa de queda radial de densidade de estrelas, provavelmente devido a um halo de estrelas ou a estrelas situadas além do raio de maré.

Subramanian & Subramaniam (2011) utilizaram estrelas variáveis RR Lyrae para determinar um plano médio de distância para a SMC, encontrando uma ajuste para um elipsóide com semi-eixos na razão 1:1,3:6,2, sendo o semi-eixo maior praticamente alinhado com a linha de visada. Assim como as RR Lyrae, as estrelas do Red Clump (RC) também se distribuem formando uma figura semelhante. Assim como na LMC, na SMC são visíveis muitas regiões de emissão HII, evidenciando uma intensa formação estelar.

Embora distante 24 graus da Grande Nuvem de Magalhães, a Pequena Nuvem está em interação física com esta e com a Via-Láctea, orbitando a Grande Nuvem em um período em torno de 1,5 bilhões de anos (Bekki & Chiba, 2005), sendo que atualmente encontra-se muito próximo de um mínimo de distância em relação a LMC.

Quanto à taxa de formação estelar, o trabalho de Piatti et al. (2015) mostra picos de formação estelar em 1.5 e 5 bilhões de anos, sendo que a taxa de formação estelar para idades maiores do que 5 bilhões de anos é muito modesta (abaixo de 0,015 $M_{\odot}$ por ano em comparação com 0,05 há 5 bilhões de anos atrás). Este trabalho mostra também que há variações locais, sendo que a taxa de formação atual é muito maior

no centro da SMC (na região que se assemelha a uma barra) do que na periferia.

Quanto à população de aglomerados estelares da Pequena Nuvem, Piatti et al. (2015) demonstraram que os aglomerados mais velhos (idade maior do que 2,5 bilhões de anos) estão mais distantes do centro da SMC do que os aglomerados mais jovens. Por outro lado, há um excesso de aglomerados com idades de 1,5 e 5 bilhões de anos, correspondente à mesma análise feita com as estrelas de campo da SMC. A comparação entre a taxa de formação de aglomerados e a taxa de formação de estrelas de campo mostrou que há um acréscimo quanto ao número de aglomerados observados para idades mais jovens que 2,5 bilhões de anos. Quanto à posição, há um acúmulo de aglomerados jovens (com idades de 20 milhões de anos) e de idade intermediária (em torno de um bilhão de anos) em direção à Ponte Magalhânica e à estrutura conhecida como Asa (em inglês *wing*) da SMC.

Recentemente Olsen et al. (2011) demonstraram através da análise cinemática e de metalicidade de estrelas da LMC que 376 estrelas de sua amostra apresentam fortes indícios de terem sido retiradas da SMC, o que reforça a intensa interação gravitacional entre estas duas galáxias. Também resultado desta interação é a Ponte de Magalhães (ou *MB - Magellanic Bridge*), ao passo que a formação da Corrente de Magalhães (ou *MS - Magellanic Stream*) sofreu intensa influência gravitacional da Via-Láctea (Diaz & Bekki, 2012). Além destas estruturas há ainda o *Leading Arm*, uma extensão de gás na direção oposta à ponte de Magalhães.

O MS é uma corrente de gás Hidrogênio neutro (HI), que se extende por pelo menos 200° no céu, como mostra a figura 1.6. Sua idade é estimada como de 2,5 bilhões de anos (Nidever et al., 2010) e as densidades colunares do gás variam até 10^{21} átomos de gás cm^{-2}. Segundo a mesma referência o gás parece ter sido arrancado da LMC devido a uma forte aproximação da SMC, disparando a formação do MS e também a formação estelar nestas duas galáxias.

A MB é como o próprio nome diz uma ponte com 14° de extensão contendo gás neutro (HI) em uma rica estrutura de cascas, bolhas e filamentos (Muller et al., 2003). Além do gás há uma contrapartida estelar, com estrelas e aglomerados muito jovens (Bica et al., 2015).

1.2.3 A Grande Nuvem de Magalhães

A Grande Nuvem de Magalhães, assim como a Pequena Nuvem de Magalhães, também é geralmente classificada como uma galáxia irregular, embora tenha uma estrutura semelhante a uma barra, e também um disco. O NED (Nasa Extragalactic Database) classifica a LMC como uma galáxia espiral barrada [SB(s)m], baseado

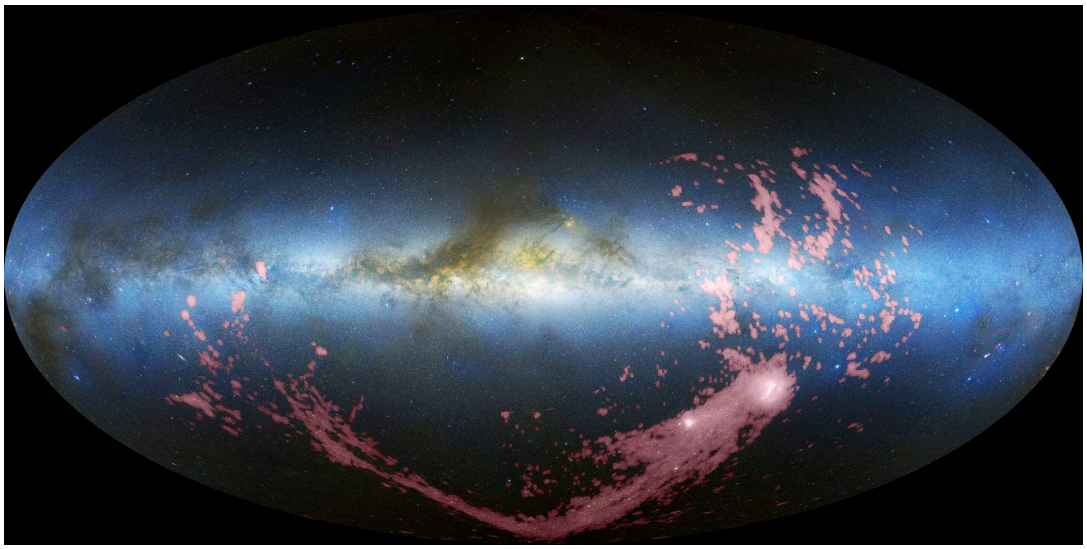

Figura 1.6: *Magallanic Stream* em coordenadas galácticas, tendo o centro da Via-Láctea no centro da figura. A concentração de HI é mostrada como uma faixa em magenta que se extende desde a LMC (maior concentração de gás, próximo do plano galáctico), passando próximo do pólo galáctico e indo até a direção oposta. A ponte de Magalhães também é visível como uma faixa ligando as duas nuvens. O *Leading Arm* aparece na direção oposta à ponte de Magalhães. Figura retirada de Nidever et al. (2010).

no trabalho de de Vaucouleurs et al. (1991). Nesta nomenclatura descendente da nomenclatura de Hubble, o autor acrescenta um "s" indicando que a galáxia não tem anéis. A letra "m" indica que a galáxia não possui bojo aparente, embora o formato irregular, típica da LMC. Em outras palavras, a letra "m" denota que esta galáxia é o modelo de seu subtipo. Assim como a SMC, os elipsóides de isodensidades de estrelas apresentados por Klein et al. (2014) mostram uma galáxia alongada na nossa direção, certamente mostrando indícios da interação gravitacional com a Via-Láctea.

A distância da LMC até nós é de $49,9 \pm 2,0$ kpc ou $(\text{m-M})_0 = 18,49 \pm 0,09$ (de Grijs et al., 2014) e as estrelas de população velha (população que se distribui mais externamente à nuvem) sugerem um raio de truncagem de $13,5 \pm 0,8$ kpc (Balbinot et al., 2015). A inclinação da LMC está em torno de 37 graus, propiciando, assim como a SMC, uma análise das estruturas estelares desta galáxia. O ângulo de posição das linhas dos nodos (linha que intersecta o disco da LMC e o plano do céu) está muito provavelmente entre 130-145°. Estes valores de inclinação e ângulo de posição diferem levemente segundo a referência, embora alguns valores extremos para o ângulo de posição na literatura como 122,5±8,3 de van der Marel & Cioni (2001) e $168° \pm 4°$, conforme Feitzinger et al. (1977) existam na literatura. Su-

bramanian & Subramaniam (2010), utilizando estrelas do agrupamento vermelho (mais conhecido pela denominação em inglês *Red Clump* ou *RC*), mostraram que há variações de inclinação no plano do disco (ao menos utilizando estas estrelas), justificando o porquê de se encontrarem diferentes valores de inclinação e diferentes ângulos de posição para diferentes regiões amostradas. Os diferentes métodos utilizados também contribuem para diferentes medidas de inclinação. Esta inclinação varia de $22,0^{\circ} \pm 6,0^{\circ}$ de Kim et al. (1998) até $38,14 \pm 0,08^{\circ}$ de Balbinot et al. (2015). Esta última referência utilizou a amostra estelar externa do primeiro catálogo dos dados de verificação científica do DES (DES-SVA1, na sigla em inglês).

Além desta variação de inclinação ao longo do disco, suas bordas não são completamente planas, apresentando um empenamento nas suas partes mais externas (Nikolaev et al., 2001, Subramanian & Subramaniam, 2010, Balbinot et al., 2015). É importante notar que este empenamento na borda noroeste da LMC tente a fazer com que as estrelas estejam mais afastadas de um observador na Via-Láctea. Este empenamento certamente se deve a uma interação gravitacional e não é produto recente da interação gravitacional LMC-Via-Láctea. Afinal se fosse esta a causa do empenamento, este deveria estar voltado para a Via-Láctea.

A massa estimada da LMC possui várias medidas, muitas com grande imprecisão. As estimativas vão de $3,5 \pm 1,4 \times 10^{10} \mathrm{M}_{\odot}$ (van der Marel & Kallivayalil, 2014) para um raio de maré de 13.5 kpc até $2,5^{+0.9}_{-0.8} \times 10^{11}$ $\mathrm{M}_{\odot}$ (Peñarrubia et al., 2016). A metalicidade média da LMC é mais alta do que a SMC, em torno de [Fe/H] = -0.3. Obviamente este é um valor médio, mas podemos com isso estimar que as estrelas da LMC possuem em média 5 vezes mais metais do que as estrelas da SMC.

A LMC é rica em gás e poeira e também passa por uma intensa formação estelar. Embora um completo estudo sobre a formação estelar da LMC ainda não existe, alguns artigos como o de Meschin et al. (2014) nos dão alguns indícios. Este artigo determina a SFR para três campos situados a 4, 5,5 e 7,1 graus do centro da LMC. Os campos mais internos apresentam uma taxa de formação estelar ao longo da linha de visada muito mais intensa do que os campos externos. No campo externo, como podemos ver na figura 1.7 retirada de Meschin et al. (2014), há o predomínio de idades maiores do que 10 bilhões de anos e um decréscimo para idades mais jovens. Para os outros campos é de se notar uma diminuição na SFR, formando um mínimo para idades entre 4 e 6 bilhões de anos. Já para o campo mais central (distando 4° do centro da LMC), a taxa de formação estelar recente chega a quatro vezes a taxa de formação estelar para as regiões amostradas mais internas, com máximos locais correspondentes a idade de $\simeq$0.7 e $\simeq$ 3 bilhões de anos. A idade para a qual

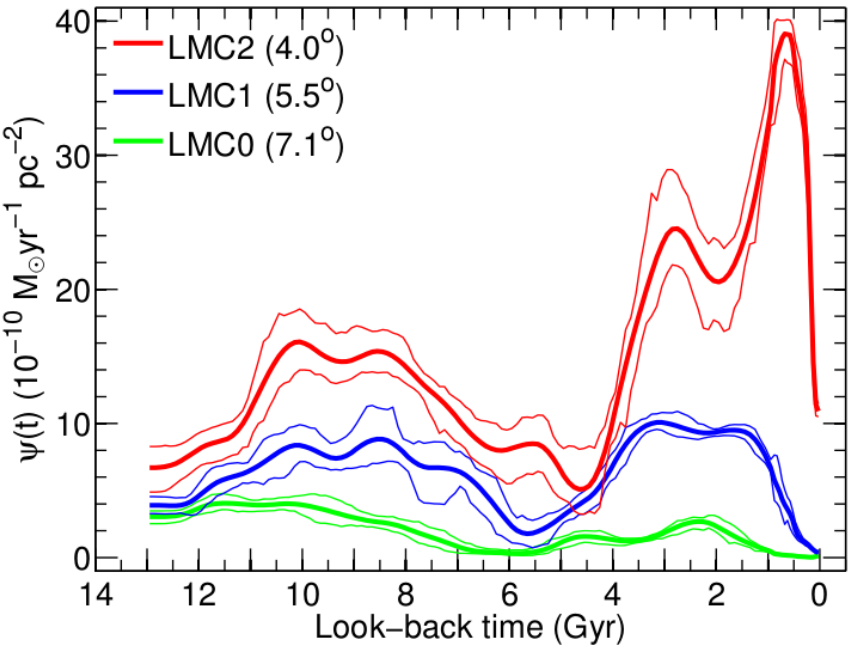

Figura 1.7: Figura 6 de Meschin et al. (2014) mostrando o Histórico de formação estelar na Grande Nuvem de Magalhães integrado nos campos cuja distância em relação ao centro da LMC são indicados na legenda. As linhas mais finas representam a incerteza estimada pelo método apresentado no artigo.

metade da massa foi formada é de 4.0, 6.8 e 9.3 bilhões de anos para 4,0, 5,5 e 7,1 graus. Estes dados favorecem uma formação de fora para dentro (em inglês *outside-in formation*), onde se formaram primeiro as estrelas nas regiões externas da galáxia (portanto existindo hoje uma população velha) e depois nas regiões internas, como se pode notar pela idade recente das estrelas nesta região.

1.2.4 A Grande Nuvem e seu sistema de aglomerados

Como já citamos antes, para determinar taxas de formação estelar e gradientes radiais de metalicidade de uma galáxia, é muito mais fácil analisar aglomerados estelares do que determinar a porcentagem de estrelas de campo que pertencem a uma determinada idade e/ou metalicidade. A grande questão se baseia na sobrevivência dos aglomerados velhos como entidades coesas no disco (Baumgardt & Makino, 2003, Baumgardt & Kroupa, 2007). Fenômenos como a evaporação, ejeção de estrelas, segregação de massa e consequente perda de massa, choques com o disco, bem como a própria evolução das estrelas, emitindo grande parte da massa no ramo assimptótico das gigantes, faz com que grande parte dos aglomerados abertos mais

velhos do que um bilhão de anos na Galáxia não mais exista (Lamers et al., 2005). A exceção em nossa Galáxia são os aglomerados globulares, sobrevivendo graças ao fato de serem muito mais massivos do que os aglomerados abertos, embora simulações mostrem que entre 53-67% dos aglomerados globulares não vão sobreviver dentro de mais uma idade do Universo ou mais um tempo de Hubble (Baumgardt & Makino, 2003). Para uma comparação entre as massas dos aglomerados abertos e globulares, indicamos Dias et al. (2002) e Harris (1996a), respectivamente.

Na LMC é esperado que com um potencial gravitacional bem menor (como citado anteriormente, a massa da LMC é estimada por muitos autores entre 0,25 e menos de 0,1 vezes a massa da Via-Láctea), o tempo de dissolução (ou *disruption time*) dos aglomerados seja maior, podendo ser observados aglomerados muito mais velhos do que aqui na Galáxia. Com base nisso, é esperado que o número de aglomerados na LMC obedeça a uma lei que seja muito próxima da taxa de formação estelar, visto que muitos aglomerados (mesmo os mais velhos) devem ter sobrevivido coesos. O fato mais notável que se observa é um intervalo de idade (entre os 4 e os 10 bilhões de anos) onde não há aglomerados (Girardi et al., 1995, Piatti & Geisler, 2013, de Grijs & Anders, 2006). Alguns candidatos são elencados para estarem neste intervalo, no entanto as incertezas nas determinações de idade os colocam como limitadores do intervalo ou então são descartados como populando este intervalo (Sarajedini, 1998, Rich et al., 2001, Balbinot et al., 2010). Embora este intervalo seja relativamente bem definido para os aglomerados ou associações, o histórico de formação estelar mostra que, para as estrelas de campo, houve formação estelar durante este período (Figura 1.7). Interessante notar que neste intervalo houve formação de estrelas, como mostra a análise de 5,5 milhões de estrelas de campo da LMC, de Piatti & Geisler (2013), que adotaram o *age gap* como entre 5 e 12 bilhões de anos. Com base nestes dados, podemos presumir que houve formação de aglomerados durante o *age gap* que passaram pelo processo de rompimento. Ainda que exista alguns aglomerados mais velhos que 10 bilhões de anos na LMC, seu número é muito pequeno (Geisler et al., 1997). Um exemplo de aglomerado velho na LMC é o Aglomerado do Retículo, afastado cerca de 10 graus do centro da LMC. Outro aglomerado velho e que poderia estar localizado dentro do *age gap* é o aglomerado ESO121-SC003, para o qual já se cogitou da possibilidade de ter sido acretado pela LMC (Bica et al., 1998). No entanto, vários autores (inclusive nós), pudemos notar que este aglomerado obedece muito bem a relação idade-metalicidade para os aglomerados da LMC (Meschin et al. 2014e referências), o que o coloca como altamente provável de ter sido sido produzido pelo gás da própria LMC.

Sobre a relação idade-metalicidade dos aglomerados da LMC, Livanou et al. (2013) trabalharam com observações de 15 aglomerados da LMC, numa amostra razoavelmente distribuída sobre o disco da LMC (sete próximos do centro e oito distantes 6-7 kpc do centro). Os autores notaram que os aglomerados mais jovens que 6×10^8 anos apresentam uma metalicidade muito maior que o restante mais velho e que os aglomerados mais pobres em metais estão situados nas regiões mais distantes da LMC, favorecendo uma formação estelar *inside-out*. Podemos comparar este resultado com o trabalho de Carollo et al. (2016), que encontrou um gradiente radial negativo para a idade do halo da Galáxia, estudando as estrelas do ramo horizontal azul (em inglês *Blue Horizontal Branch*) do SDSS. As estrelas mais próximas da vizinhança solar (até 15 kpc do centro Galáctico) tem mais de 12 bilhões de anos, enquanto que as com idade média em torno de 9 bilhões de anos estão situadas até 45-50 kpc de distância do centro Galáctico. Vemos que o último resultado favorece claramente uma formação de dentro para fora para o halo galáctico, enquanto que o resultado de Livanou et al. (2013) justifica um modelo de fora para dentro. Se os aglomerados de Livanou et al. (2013) estão claramente identificados com o disco, deve haver mecanismos completamente diferentes para a formação do halo Galáctico e para o disco da LMC,

1.2.5 A periferia das Nuvens de Magalhães

É na periferia das Nuvens de Magalhães que concentraremos o nosso estudo. Basicamente a tese irá focar nos aglomerados estelares periféricos da LMC e no conteúdo estelar dos campos vizinhos à SMC.

Com o sistema de aglomerados da LMC, começamos com a detecção visual, passando pela redução, confirmação como sobredensidade e finalmente a comparação com modelos e discussão de resultados. O sistema de aglomerados nos traz informação sobre como se deu a formação estelar naquela galáxia - seguindo ou não modelos teóricos ou inferindo por gradientes de idade e metalicidade naquela galáxia. Da formação estelar podemos determinar em quais intervalos de tempo ocorreu um abrandamento ou mesmo supressão da formação estelar, e como foi o enriquecimento químico da Nuvem em si. A região amostrada pelo DES nos seus dados de verificação científica foi relativamente pouco explorada, dada a grande distância angular do centro da LMC. Uma busca na literatura mostra que grande parte dos artigos publicados centraliza a amostragem na própria LMC, sendo que a periferia vai sendo melhor explorada à medida que os dados são amostrados em maior profundidade. Explorar esta amostra de aglomerados, externa e pouco explorada, é

parcialmente nosso objetivo neste trabalho.

Sobre a periferia da SMC, começamos selecionando uma amostra estelar em toda a amostra do DES, procurando por sobredensidades extendidas e por estrelas presentes no MS. Embora não tenhamos detectado nenhuma sobredensidade de estrelas no MS, uma conjunto significativo de estrelas com características semelhantes às da SMC em idade e metalicidade apresentou-se próxima à borda do halo extendido da SMC, antes detectado por Nidever et al. (2011). Ao unir com dados de outro levantamento, este conjunto de estrelas revelou-se como uma sobredensidade significantemente acima da densidade do halo extendido, e deu origem à segunda parte de nosso trabalho aqui apresentado: a SMCNOD.

Capítulo 2

Descrição dos Levantamentos aplicados nesta tese

2.1 Dark Energy Survey

Para realizar a análise dos aglomerados externos da Grande Nuvem de Magalhães e a descoberta da sobredensidade próxima à Pequena Nuvem de Magalhães utilizamos as imagens nos filtros g, r e i na região imageada pelo Dark Energy Survey. As seções seguintes deste capítulo falarão um pouco mais sobre este levantamento e sobre os dados disponibilizados pela/para a colaboração.

A partir da descoberta da expansão acelerada do Universo em 1998, graças à análise de brilho de um grande conjunto de supernovas tipo Ia, tornou-se uma necessidade a melhor compreensão da energia escura, responsável por esta expansão. Para tanto, foi proposto pela comunidade astrofísica dos Estados Unidos e está sendo executado no Chile pelo NOAO (*National Optical Astronomy Observatory* ou Observatório Astronômico Óptico Norte-Americano) um levantamento de parte do céu austral com a finalidade de se estudar e definir a natureza e distribuição da energia escura no Universo - o *Dark Energy Survey* ou *DES*. Sediada em solo americano, mas com cientistas espalhados por praticamente todo o mundo, a colaboração inicialmente envolvia 120 cientistas dos Estados Unidos, Espanha, Reino Unido, Brazil, Alemanha e Suíça. Hoje envolve muitos países mais.

O DES portanto está mapeando o Hemisfério Galáctico Sul, numa extensão de 5000 graus quadrados, nas bandas *g, r, i, z e Y* (figura 2.1) (cobrindo um intervalo em comprimento de onda de 400-1065 nm) em 525 noites. A magnitudes limite esperadas ao final do survey são de g=24.45, r=24.30, i=23.50, z=22.90 e Y=21.70 com razão sinal-ruído de 10 para as fontes puntuais (Dark Energy Survey Collaboration

et al., 2016). Um breve prospecto temporal coloca o DES com duração de 5 anos, a partir de 2013. As imagens para os dados de verificação científica foram tomadas de outubro/novembro de 2012 até fevereiro de 2013. Posteriormente (iniciando-se em 31 de agosto de 2013) foram tomados os dados do ano 1 (Y1) e assim tem ocorrido sucessivamente, com as imagens sendo tomadas em agosto/setembro de um dado ano até o final de fevereiro do ano seguinte.

O tempo de exposição para as imagens da banda g, r, i e z é de 90 segundos e para a banda Y é de 45 segundos. A escolha dos filtros se deve a que o propósito do levantamento (como o próprio nome já diz) é a observação de galáxias, muitas com um deslocamento para o vermelho sensível (altos *redshifts*), portanto deslocando a emissão destas galáxias para as bandas do infravermelho.

Em torno de 10% do tempo observacional do Dark Energy Survey está destinado ao imageamento de um mesmo campo de 40 graus quadrados de forma a vigiar o aparecimento de supernovas. O planejamento inicial era de 100 supernovas to tipo Ia que seriam descobertas no intervalo de redshift entre 0,25-0,75 ao longo do levantamento (Tucker et al., 2007). Atualmente (depois do terceiro ano de observações ter sido reduzido) já foram confirmadas 228 supernovas apenas do tipo Ia, a grande maioria no intervalo de redshift de 0,2 a 0,8.

2.1.1 DECam - Dark Energy Camera

Para as observações foi selecionado o telescópio Victor M. Blanco de 4 metros, situado no Cerro Tololo Inter-american Observatory (CTIO), Chile. A câmera especialmente construída para as observações é a DECam, com 570 Megapixels distribuídos em 74 CCDs, sendo que 12 deles (2k$\times$ 2k pixels) são utilizados para guiagem e foco e os CCDs restantes (62 com 2k$\times$ 4k pixels) para imageamento. A área coberta pelos pixels neste conjunto de CCDs (total) tem um formato hexagonal e cobre 3 graus quadrados. A escala é de 0,263 segundos de arco por pixel. A câmera foi instalada em 2012 e teve a sua primeira luz neste mesmo ano.

A DECam está montada no foco primário do telescópio Blanco e possui cinco lentes corretoras que possibilitam seu amplo campo. Os CCDs da DECam são resfriados a -100°C graças a um circuito fechado de nitrogênio líquido. O conjunto que consiste nas lentes corretoras e os CCDs estão dispostos em uma estrutura de forma cilíndrica, onde é feito vácuo, sendo que a primeira lente corretora serve de janela a esta estrutura. O conjunto também compreende os filtros, o obturador, sistema óptico ativo e a parte eletrônica da DECam. Os CCDs que compõem a DECam foram fabricados pelo *Lawrence Berkeley National Laboratory* (LBNL), e

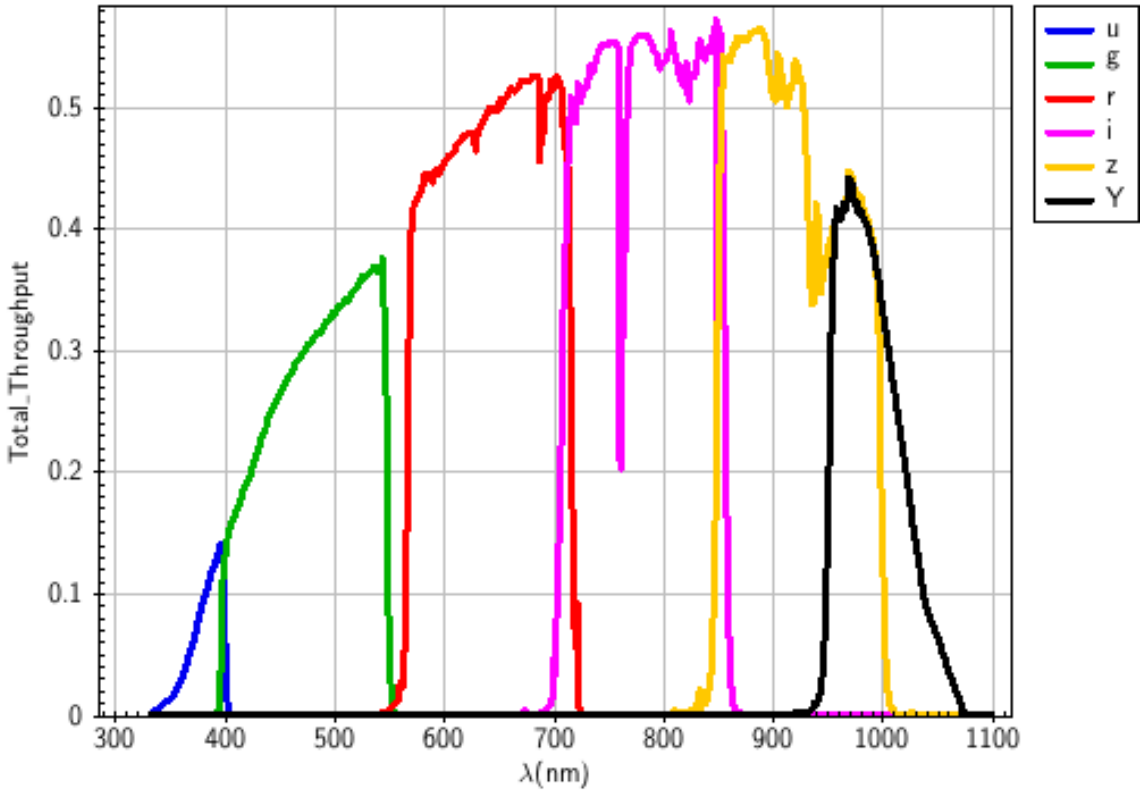

Figura 2.1: Curvas de transmissão da DECam (incluindo a atmosfera). Aqui está incluída a banda u, não utilizada pelo DES. Retirada de http://www.ctio.noao.edu/noao/sites/default/files/DECam/decam_filters.gif em 08 de novembro de 2017.

enviados para o Fermilab, onde os CCDs foram montados no circuito e escolhidos para compor o conjunto de CCDs da DECam. Maiores detalhes técnicos sobre a DECam podem ser encontrados em Flaugher et al. (2015).

2.1.2 DESDM (DES Data Management)

Depois de observadas pela DECam, as imagens são transmitidas através de um link de microondas para o National Center for Science Computer Applications (NCSA), em Illinois, Estados Unidos. Lá ficam armazenadas e posteriormente são tratadas pelo DESDM ou Gerenciamento de Dados do DES.

As imagens são primeiramente reduzidas, chip a chip e exposição a exposição. Depois disso é feita a detecção de fontes, junto com a calibração astro e fotométrica preliminar. Com esta classificação o processo é repetido, utilizando os dados da primeira redução para as soluções astro e fotométricas, vinculando os chips e exposições. Por último, as imagens são coadicionadas e finalmente é produzido o catálogo final.

As imagens coadicionadas são disponibilizadas em formatos chamados de *tiles* (significando ladrilho), com dimensões de 0,75 graus x 0,75 graus. Maiores detalhes podem ser encontrados em Mohr et al. (2012) e Desai et al. (2012). Sobre a nomenclatura, os tiles são chamados pelo prefixo 'DES' seguido de dois algarismos correspondentes à hora e mais dois ao minutos da ascenção reta do centro do 'tile', mais o sinal da declinação e quatro algarismos correspondentes à declinação (dois para graus e dois para os minutos). Um exemplo para a nomenclatura é DES0516-6414, correspondente ao 'tile' centrado na ascenção reta 5h 16min e declinação -64° 14'.

Para a redução, a priorização de objetos foi dada às galáxias, sendo escolhido o SEXTRACTOR (Bertin & Arnouts, 1996), um pacote que determina quais regiões que estão acima das contagens de fundo para uma imagem do céu. Uma série de parâmetros acompanha a detecção das fontes em uma imagem astronômica, assim como o catálogo final para um *tile* também possui uma série de medidas para as fontes luminosas. Um parâmetro particularmente importante para a seleção estrela/galáxia é o parâmetro *blend*, que irá determinar como será o tratamento de fontes muito próximas, sendo estas fundidas em apenas uma só (como por exemplo regiões de formação estelar muito próximas nos braços de uma galáxia muito distante) ou tratadas como separadas (neste caso, como seria o esperados para estrelas próximas do centro de um aglomerado globular). Como o levantamento tem um viés extra-galáctico, foram priorizados os parâmetros para a redução de galáxias, sendo que as estrelas dos aglomerados estelares não são muito representadas nos catálogos

liberados pelo levantamento. Este caso particular levou-nos a fazer uma avaliação da completeza estelar nas imagens do DES.

A classificação estrela-galáxia é dada praticamente por um parâmetro saído do SEXTRACTOR, chamado de SPREAD MODEL. Ele é baseado na diferença entre a medida (em magnitudes) dada pelo modelo da função de espalhamento puntual e a medida dada por um modelo ligeiramente mais extendido, feito pela mesma função de espalhamento puntual convoluída com um disco exponencial com comprimento de escala igual à largura-a-meia-altura (da fonte, em contagens) dividido por 16.

2.1.3 Participação brasileira no DES

A participação brasileira no DES se deu através do Laboratório Interinstitucional de e-Astronomia (LIneA), com a tarefa de desenvolver e organizar o portal científico para acesso virtual (visualização, informação sobre os dados, bem como funções de registro de análise e incorporação de códigos científicos) aos dados do DES. O LIneA constituiu e gerencia um consórcio de pesquisadores brasileiros no DES, o DES-Brazil, o qual tem a tarefa de desenvolver e organizar melhorias neste portal científico.

Uma das ferramentas inicialmente desenvolvida e que foi muito utilizada por nós para a detecção de aglomerados na Grande Nuvem de Magalhães é o *TileViewer*, onde as imagens nas bandas g, r e i são combinadas para gerar uma imagem com o acompanhamento de coordenadas equatoriais e posterior registro.

2.1.4 Os dados de Verificação Científica (SV) do DES

As observações dos dados de verificação científica do DES (SV) foram feitas entre outubro/novembro de 2012 e fevereiro de 2013, somando um total de 427 horas de observação. Os dados foram tomados para conjuntamente determinar as capacidades e levantar possíveis problemas com a DECam e com o conjunto de tarefas de redução de dados do DESDM quanto à qualidade das imagens, calibração, astrometria, fotometria, apontamento, guiagem, questões operacionais e conjunto de programas para os campos de supernova.

A maior área dos dados de verificação científica do DES compreende uma área em comum com o Telescópio Polar Austral ou *South Pole Telescope* - SPT (Carlstrom et al., 2011). O *SPT* é um telescópio com 10 metros de diâmetro destinado a amostrar o céu nas bandas de 3, 2 e 1,3 mm, desenhado para o estudo das anisotropias na radiação cósmica de fundo e a descoberta de aglomerados de galáxias (Reichardt

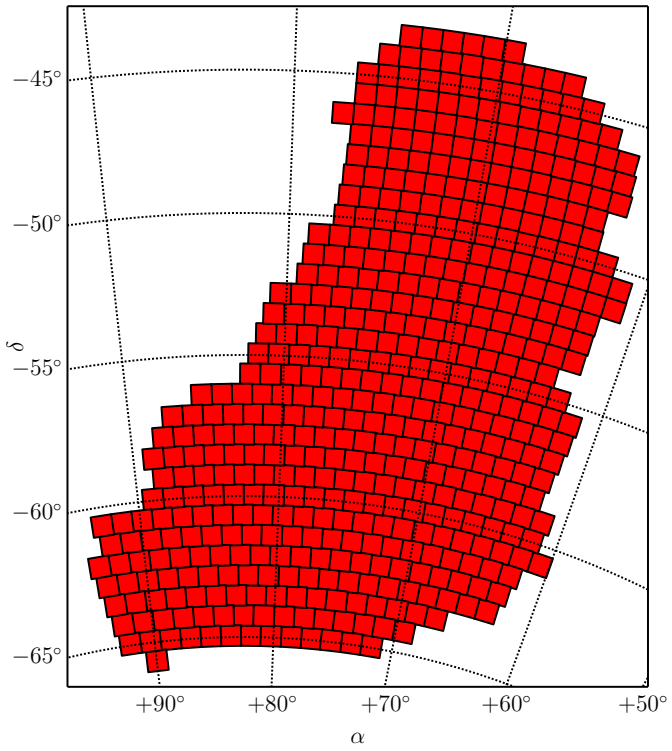

Figura 2.2: Os *tiles* (polígonos em magenta) imageados pelo SV-SPTE são mostrados na figura, acompanhados das coordenadas equatoriais em seus respectivos eixos.

et al., 2013) usando o efeito Sunyaev-Zel'dovich. Este último consiste no espalhamento e polarização da radiação de fundo de microondas do Universo (*Cosmic Microwave Background*) pelos elétrons em alta temperatura do meio intergaláctico, via efeito Compton inverso (Hanson et al., 2013), onde o fóton recebe energia de uma partícula carregada. Com a sobreposição entre as áreas do SPT e do DES, a equipe do *SPT* pode se beneficiar dos dados nas bandas do visível do Dark Energy Survey.

Aqui neste trabalho não iremos tratar de dados processados pelo SPT. Daqui por diante, o termo 'SPT' irá se referir à área do céu também amostrada pelo *South Polar Telescope*, mas imageada pelo DES. Ou seja, vai se referir à área do céu (como um sítio) e não ao levantamento (ou aos dados) em si.

A área a leste do SPT recebeu o nome de SPT-E ou *SPT-East*, estando localizada imediatamente a norte da LMC. Na figura 2.2 são mostrados os *tiles* do SVA1-SPTE (primeira liberação de dados da área do SPT), sendo que alguns tiles muito pouco amostrados foram excluídos da visualização. O trabalho sobre os aglomerados da Grande Nuvem de Magalhães (apresentado no Cap. 3) é baseado nas imagens do DES desta região do céu e na primeira liberação de catálogos dos dados de verificação científica pela colaboração. Esta região soma 157 graus quadrados e é formada por 2537 imagens de exposição individual, sendo que cada exposição individual tem duração de 90 segundos para todas as bandas g, r e i, exceto para a banda Y, com exposição de 45s. Maiores detalhes sobre os dados de verificação científica podem ser encontrados em Rykoff & DES Cluster Working Group (2014). Embora os dados de verificação científica sejam os primeiros dados do DES, eles já possuem a profundidade fotométrica esperada pelo levantamento ao final do projeto.

Os dados utilizados na descoberta da SMCNOD foram o catálogo da liberação rápida do segundo ano do DES (DES-Y2Q1) e o primeiro catálogo do MagLiteS (do inglês *Magellanic Satellites Survey*), levantamento ainda em andamento que visa imagear uma área contígua de 1200 graus quadrados próximo ao Pólo Celeste Sul no entorno das Nuvens de Magalhães, também utilizando a DECam.

2.1.5 O catálogo DES-Y1A1

Depois dos dados de verificação científica, o primeiro catálogo (Y1A1) contendo os dados do primeiro ano do DES foi liberado para a colaboração dia 21 de dezembro de 2014. Este catálogo cobria em torno de 50% da área total do levantamento. A área do Y1A1 na verdade cobre a área do SPT e a área próxima do equador celeste conhecida como Stripe 82. Mesmo com uma área menor, as fontes são oriundas

da extração da imagem coadicionada, aumentando a profundidade do catálogo. A figura 2.3, produzida com o catálogo de estrelas do Y1A1, ilustra a cobertura e a densidade de estrelas do catálogo do primeiro ano do DES.

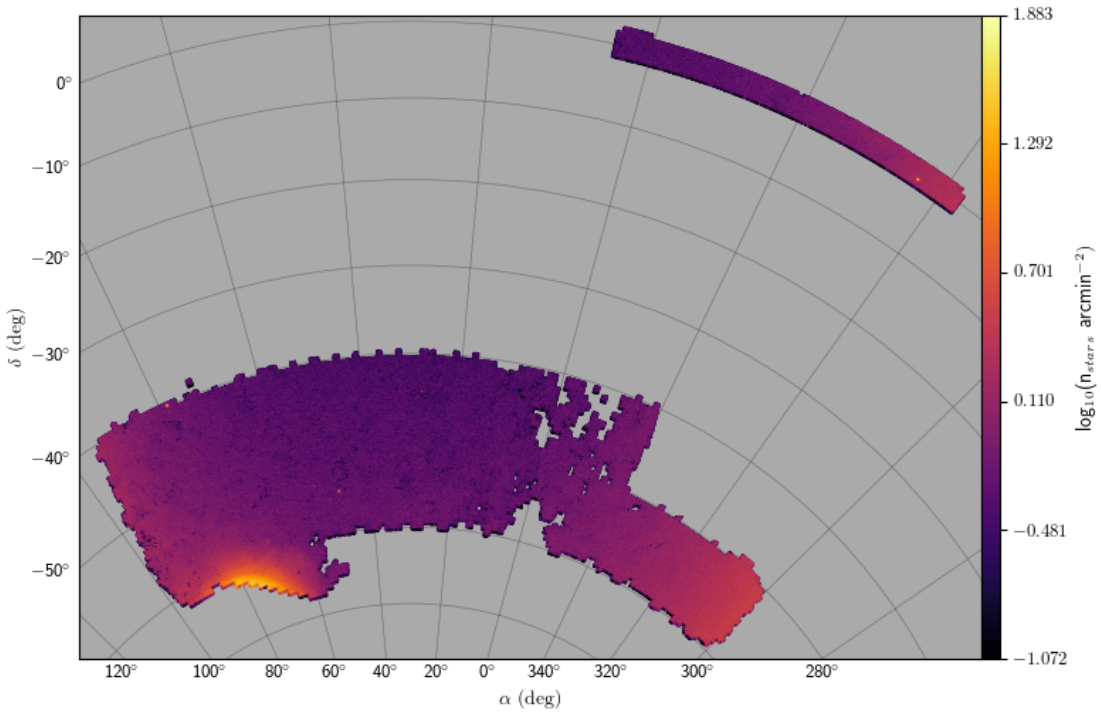

Figura 2.3: Densidade de estrelas e cobertura do catálogo Y1A1 em coordenadas equatoriais para estrelas, em projeção cônica de Albers. Algumas caracacterísticas podem ser notadas, como o campo limite com a LMC (embaixo, à esquerda), e algumas galáxias anãs clássicas. O campo superior é o Stripe82, enquanto que o campo retangular mais austral é o SPT.

2.1.6 O catálogo DES-Y2Q1

Como seria esperado que o próximo catálogo depois do Y1A1 fosse liberado depois de um ano, alguns integrantes do DES resolveram utilizar uma fotometria a partir das imagens não-coadicionadas, unicamente das imagens de exposição única, de forma a se ter um catálogo estelar mais rapidamente. Este catálogo foi batizado de Y2Q1 - um catálogo rápido (*quick release*) para os dois primeiros anos do levantamento. A cobertura deste catálogo é de praticamente todo o survey. Embora a profundidade deste catálogo não seja otimizada pela coadição das imagens, a cobertura foi ampliada pela utilização da fotometria em apenas duas bandas (g e r).

Desta forma, depois de pouco mais de seis meses do primeiro artigo de descoberta de galáxias-anãs no DES (Bechtol et al., 2015), houve a liberação do segundo artigo, utilizando a cobertura de praticamente todo o levantamento (Drlica-Wagner et al., 2015).

O catálogo Y2Q1 foi o catálogo utilizado para a descoberta da SMCNOD (Capítulo 4), onde mais tarde, para a análise, foi combinado com o catálogo do MagLiteS (Drlica-Wagner et al., 2016). A figura 2.4 mostra um mapa de cobertura e de densidade das estrelas do catálogo Y2Q1 (magnitude $17,0 < g < 23,0$ e cor $-0,5 < g - r < 1,2$).

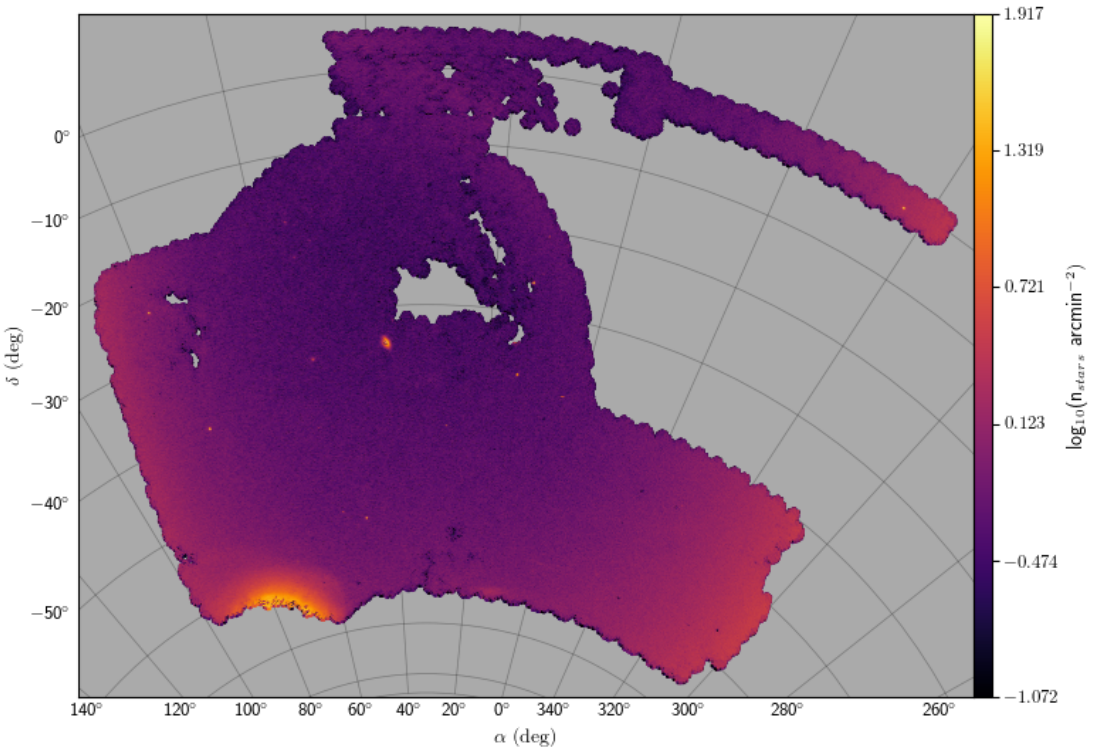

Figura 2.4: Densidade de estrelas e cobertura do catálogo Y2Q1 em coordenadas equatoriais, em projeção cônica de Olbers. Algumas caracacterísticas podem ser notadas, como o campo limite com a LMC (embaixo, à esquerda), os limites do levantamento mais próximos do plano Galáctico (à esquerda e à direita), algumas galáxias anãs clássicas e mesmo algumas recentemente descobertas, algumas centenas de graus quadrados não cobertas (no centro da figura) e o Stream de Sagitário, que cruza a parte superior de cima para baixo e da esquerda para a direita (em baixo contraste).

Maiores informações sobre este catálogo podem ser encontradas em (Drlica-Wagner et al., 2015), onde há uma detalhada descrição do catálogo, incluindo a comparação com o catálogo CFHTLens, para análise de completeza/pureza da amostra.

2.1.7 Análise preliminar da completeza estelar nos Dados de Verificação Científica (SV) do DES

Com os catálogos dos dados de verificação científica em mãos, o grupo procurou por sobredensidades estelares, através do programa FindSat (Balbinot et al., 2013). No entanto, as sobredensidades vistas nas imagens coadicionadas não correspondiam a sobredensidades nos catálogos liberados pela colaboração, evidenciando a baixa completeza estelar em regiões densamente povoadas.

Assim, devido ao fato de os primeiros catálogos do DES terem uma falta de fontes estelares detectadas associadas a sobredensidades, utilizamos uma fotometria alternativa (em muito menor escala) para determinar a completeza estelar do método de redução do DES. Foi este conjunto de tarefas que mais tarde deu origem ao método de redução utilizado para os aglomerados da LMC.

A princípio utilizamos pequenas áreas de 1500 x 1500 pixels ou 6,575 x 6.575 minutos de arco quadrados para a redução alternativa, nas bandas g, r e i. Depois de uma busca visual nas imagens de verificação científica liberadas pela colaboração (maiores detalhes na seção 3.2), detectando 299 candidatos a sobredensidades, escolhemos alguns candidatos para fazermos testes sobre a qualidade da redução alternativa e sobre a completeza dos dados do catálogo do DES.

As imagens foram recortadas tendo ao centro alguns candidatos a aglomerados da LMC, dois deles com grande densidade de estrelas (o candidato número 119, no tile correspodente DES0551-6331 e o candidato 1 no tile DES0516-6414) e outros dois com baixa densidade de estrelas (candidatos 8 e 10 nos tiles DES0510-6441 e DES0516-6414). A figura 2.5 mostra o conjunto com os quatro candidatos e os respectivos anéis para a determinação da completeza dos dados em relação da distância do centro do candidato.

A fotometria alternativa seguiu tarefas-padrão do DAOPHOT (Stetson, 1987), como *daofind, phot, psf* e *allstar*. A comparação com o catálogo do DES em posição resultou em um ponto-zero o qual foi determinado como a média das diferenças entre os dois catálogos para estrelas com $g < 19$ e posteriormente somado ao catálogo do DAOPHOT. Como um teste de comparação, plotamos os CMDsjá calibrados com o ponto-zero para a imagem em torno do candidato 119 na figura 2.6 em ambos os catálogos, sendo que o critério de seleção para a fonte foi a de que as fontes do catálogo DAOPHOT tivessem contrapartida no catálogo do DES dentro de 1 pixel na imagem (0,263 segundos de arco na imagem).

De forma a evitar artifícios das imagens, utilizamos como critério de seleção (basicamente para excluir detecções espúrias no entorno de estrelas saturadas) a

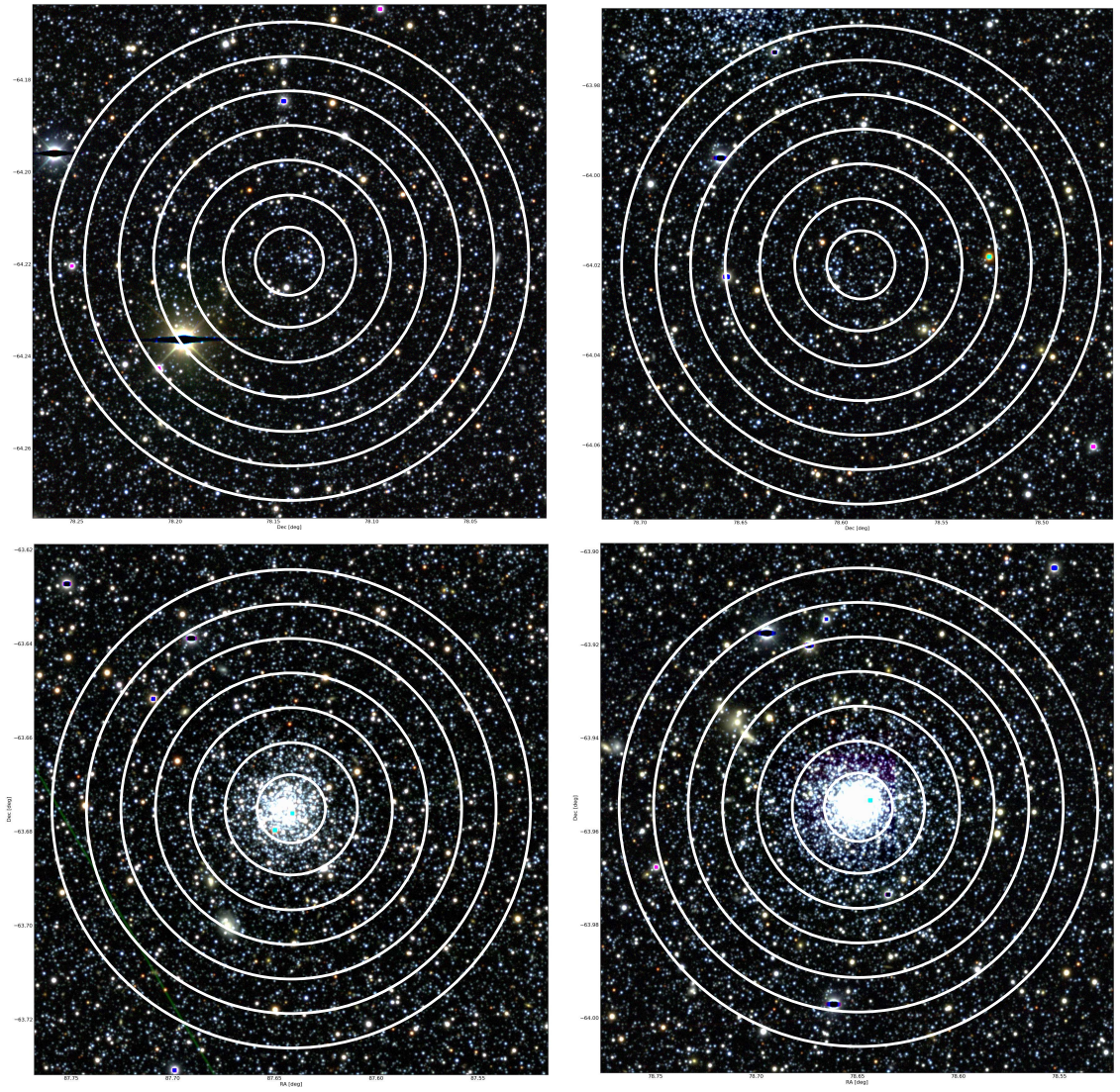

Figura 2.5: Mosaico de imagens a partir das imagens nas bandas g, r e i de quatro candidatos a aglomerados estelares nas imagens do DES (da esquerda para a direita e de cima para baixo): DES0551-6331_119, DES0516-6414_1, DES0510-6441_8 e DES0516-6414_10. Cada imagem tem 6,575 x 6,575 minutos de arco, centrado no aglomerado. O Norte está indicado na direção para cima e o Leste para a esquerda. O nome de cada candidato é composto pelo nome do tile (no primeiro caso, DES0551-6331) adicionado por um número de ordem (no primeiro caso, 119). Os anéis representados servem de delimitadores para os campos onde a completeza estelar foi sondada. Utilizando a distância de 49,9 kpc para a LMC (de Grijs et al., 2014), cada campo possui a extensão de 95,4 × 95,4 parsecs.

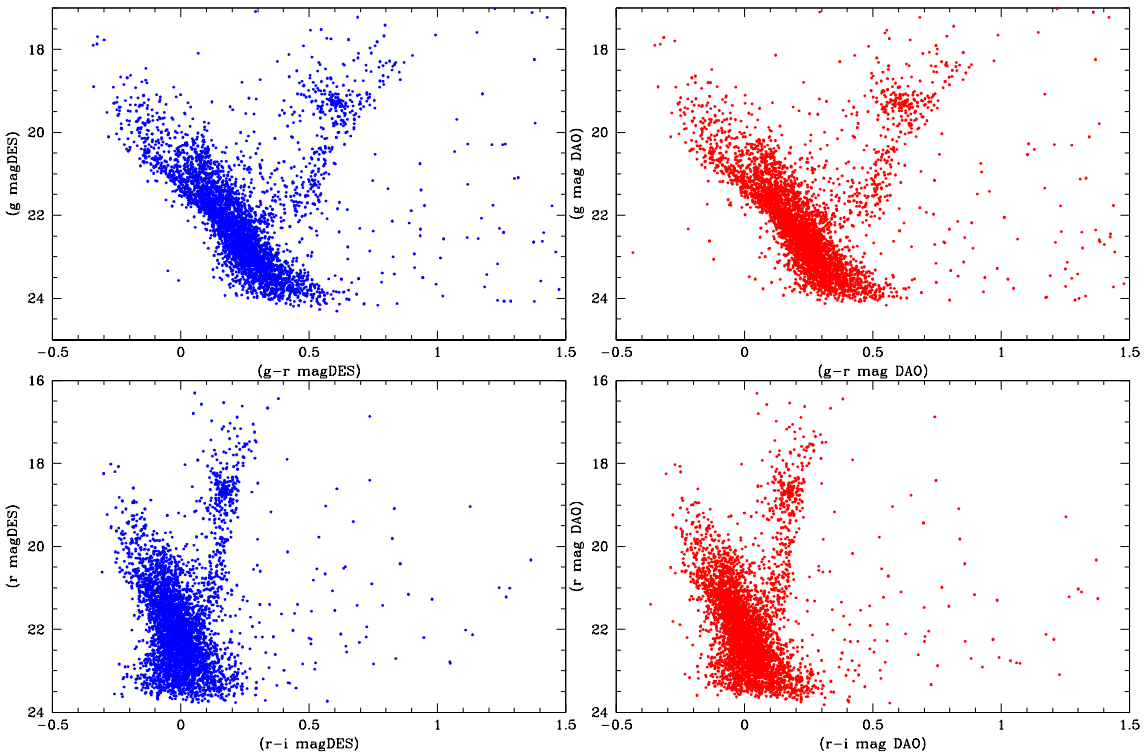

Figura 2.6: CMDs do candidato a aglomerado estelar no tile DES0551-6331_119 para estrelas com a mesma posição dentro de 1 pixel (0,263 segundo de arco em ascenção reta e declinação) no catálogo do DES e produzido por nós. *Painel superior:* CMD (g-r,g) usando o catálogo do DES (à esquerda) e DAOPHOT (à direita); *Painel inferior:* CMD (r-i,r) seguindo a mesma ordem. Os CMDs para ambos os catálogos são muito parecidos, atestando a qualidade da redução.

incerteza na magnitude, tipicamente em 0.1 para as três bandas. Para a separação estrela / galáxia, utilizamos o parâmetro *sharpness* nas três bandas, apresentando valores (em módulo) menores que 1 para estrelas.

Aqui enumeramos as principais conclusões na análise de completeza estelar para os dados do SVA1:

1. Uma fotometria independente via PSF nas imagens coadicionadas do DES leva a medidas fotométricas coerentes com os catálogos liberados pelo DESDM, adicionando uma simples correção de ponto zero.

2. Em geral os diagramas cor-magnitude baseados na amostra estelar do DAOPHOT, selecionada usando erros em magnitude e *sharpness*, são similares àqueles do DESDM (utilizando a fotometria baseada em SExtractor e PSFEx), com cortes em *spread_model*. Estes resultados são obtidos para regiões do SPT-E que cobrem a região externa da LMC, sendo ricas em estrelas, muitas das quais pertencem ao campo da LMC. Em ambas as amostras estelares, as características principais são próprias da LMC, com o campo dominado por uma sequência principal entre $18 < g < 24$, um ponto de saída da sequência principal em $g \sim 22{,}5$, $g\text{-}r \sim 0{,}2$, um ramo de gigantes e um RC com $g < 22$ e $g\text{-}r > 0{,}3$.

3. O catálogo alternativo, por utilizar o DAOPHOT, não possui um separador estrela / galáxia muito robusto. Os catálogos do DES utilizam o *spread_model*, que se baseia na forma da PSF da fonte. Desta forma, a pureza estelar do catálogo alternativo não é facilmente alcançável utilizando critérios de seleção como incerteza na magnitude e *sharpness*;

4. Contudo, a amostra estelar do DESDM é muito incompleta em campos populados, como aqueles próximos a aglomerados ricos da LMC. Nestas regiões, o catálogo do DESDM amostra menos que 50% dos objetos detectados pelo DAOPHOT, mesmo com magnitudes brilhantes como ($g < 19$). No centro destes aglomerados, a incompleteza do DESDM é grande o suficiente para que haja supressões locais de estrelas na distribuição da densidade superficial de fontes puntuais no céu.

5. Nas vizinhanças dos aglomerados da LMC ou mesmo dentro de aglomerados mais pobres, a completeza do DESDM relativa ao DAOPHOT é próxima de 1 até $g \cong 20$. Contudo, DESDM ainda amostra menos fontes puntuais que o DAOPHOT para magnitudes fracas.

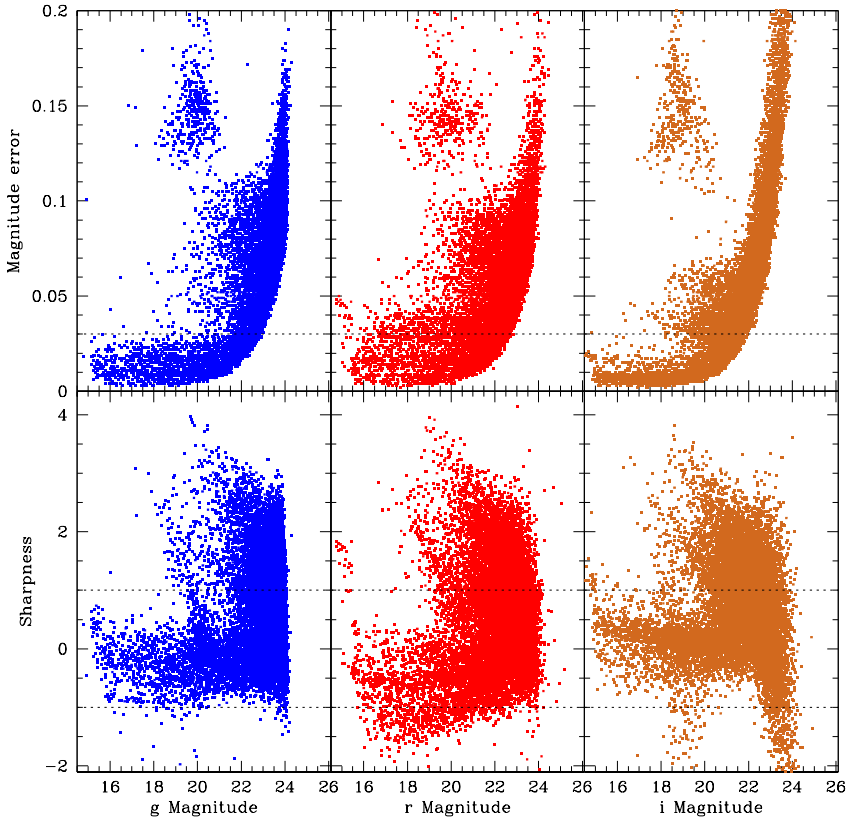

Figura 2.7: Painéis superiores, da esquerda para a direita: erro em magnitude para o catálogo DAOPHOT via ajuste de PSF como função das magnitudes nos filtros g, r and i, respectivamente. Painéis inferiores: parâmetro *sharpness* como função também das magnitudes, seguindo a mesma ordem que os painéis superiores. O filtro r apresenta um espalhamento incomum e foi excluído do critério de seleção. Comportamento similar ocorre para *spread_model* no filtro r. Estes dados são relacionados ao *tile* DES0419-4914.

6. A completeza estelar do DESDM é uma forte função da densidade de fontes, caindo abruptamente de $\sim$ 0,3 to $<$ 0,1 para densidade superficiais $>$ 1,2 $\times$ stars/minuto de arco^2.

7. Nós também comparamos amostras estelares entre os dois catálogos em regiões mais típicas amostradas pelo DES, longe dos campos da LMC. Nesta regiões a densidade de pontos é em torno de um décimo da densidade de fontes previamente analisada.

8. Dados os mesmos cortes para fontes puntuais para os catálogos DESDM e DAOPHOT, o último ainda encontra mais de três vezes mais fontes do que o primeiro. As estrelas em comum entre as duas reduções correspondem a >80% da amostra do DESDM.

9. Consistentes com os resultados encontrados para campos próximos da LMC, a incompleteza do DESDM em um típico *tile* é uma forte função da magnitude, rapidamente diminuindo para $g > 20$.

10. A amostra estelar do DESDM é muito mais pura do que aquela baseada no DAOPHOT. Isso é evidenciado pelos diagramas cor-cor. Como uma inevitável contra-partida, o catálogo DAOPHOT é muito mais completo. Portanto. medidas quantitativas de completeza estelar do DESDM relativo ao DAOPHOT, ambas como uma função da magnitude e densidade, dependem da quantidade de contaminação de galáxias em ambas as amostras. Usar estrelas próximas do *locus* estelar em um diagrama cor-cor leva a um grande aumento da completeza estelar do DESDM relativo ao DAOPHOT. Ainda, medimos como em torno de $\simeq 70\%$ para estrelas mais brilhantes do que $g = 23$ e $41,5\%$ até $g = 24$.

Ainda como exemplos de como a completeza afeta a amostra estelar, os mapas de densidade mostrados na figura 2.8 referem-se aos mesmos campos amostrados na figura 2.9. Pode-se notar como a amostra estelar ficaria gravemente comprometida com o uso do catálogo DESDM.

Assim, analisando os resultados da completeza do DESDM decidimos por efetuar a redução dos aglomerados fazendo a transferência das imagens coadicionadas nas três bandas e combinando os resultados em uma fotometria alternativa. O uso das três bandas (portanto duas cores) nos permitiu uma sensível descontaminação das estrelas da LMC em relação a galáxias e possíveis objetos espúrios. Além disso,

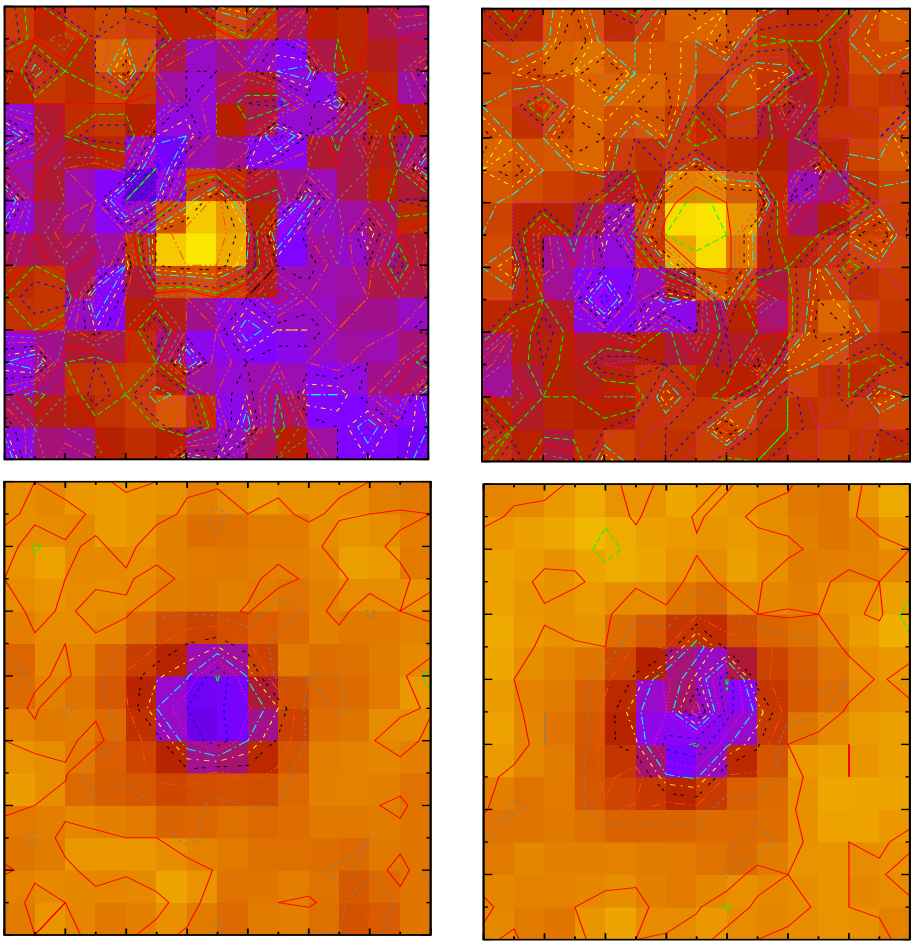

Figura 2.8: Mapas de densidades para aglomerados ricos da LMC. A cor tendendo ao azul representa um aumento de densidade. Painéis superiores: catálogos do DESDM. Painéis inferiores: catálogo alternativo utilizando o DAOPHOT.

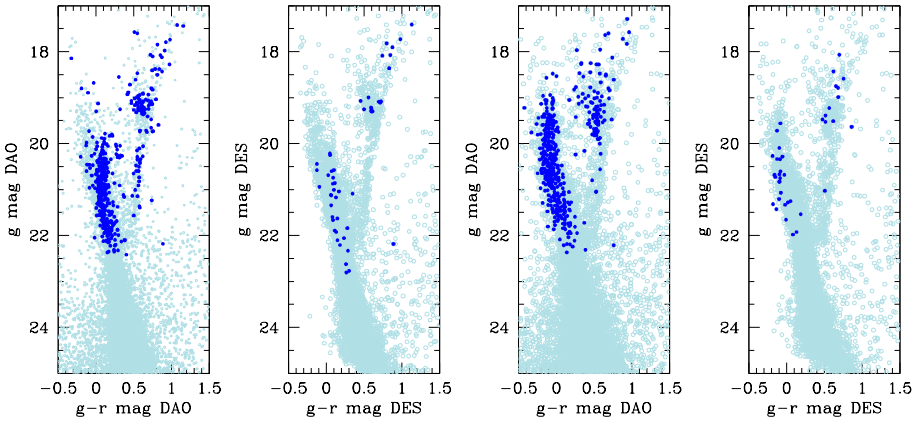

Figura 2.9: Diagramas cor-magnitude dos aglomerados com as estrelas localizadas dentro do segundo anel (azul escuro) amostrado na Fig. 2.1 e dentro da imagem (azul claro). O painel mais à esquerda mostra os dados do DAOPHOT para o aglomerado DES0551-6331_119. O segundo a partir da esquerda mostra os dados do DESDM para a mesma imagem. Os dois painéis à direita mostram a mesma sequência de CMDs mas para o outro candidato: DES0516-6414_11.

estas três bandas foram as mais amostradas pelo levantamento, aumentando a completeza dos aglomerados identificados. Os métodos utilizados para a identificação e caracterização destas sobredensidades estelares são descritos no próximo capítulo.

2.2 MagLiteS

Com a composição do Grupo de Trabalho da Galáxia no DES, foi feita a proposta por um dos colaboradores (Keith Bechtol) de se realizar um levantamento no entorno das Nuvens de Magalhães, onde os participantes deste novo levantamento seriam os membros do DES e do SMASH Nidever et al. 2017. Esta proposta objetiva estudar uma área em torno do Pólo Celeste Sul (veja a figura 2.10), sendo que serão utilizadas apenas imagens nas bandas g e r, com a DECam. Maiores detalhes sobre este *survey* podem ser encontradas em Drlica-Wagner et al. 2016. Com a descoberta de um número significativo de galáxias anãs próximas às Nuvens (Jethwa et al., 2016, Koposov et al., 2015), este levantamento se consolida como uma fonte de novas descobertas de galáxias anãs, aumentando o censo destes objetos e melhor caracterizando o problemas das satélites faltantes (em inglês *missing satellites*) e da probabilidade de algumas anãs da Galáxia pertencerem originalmente às Nuvens.

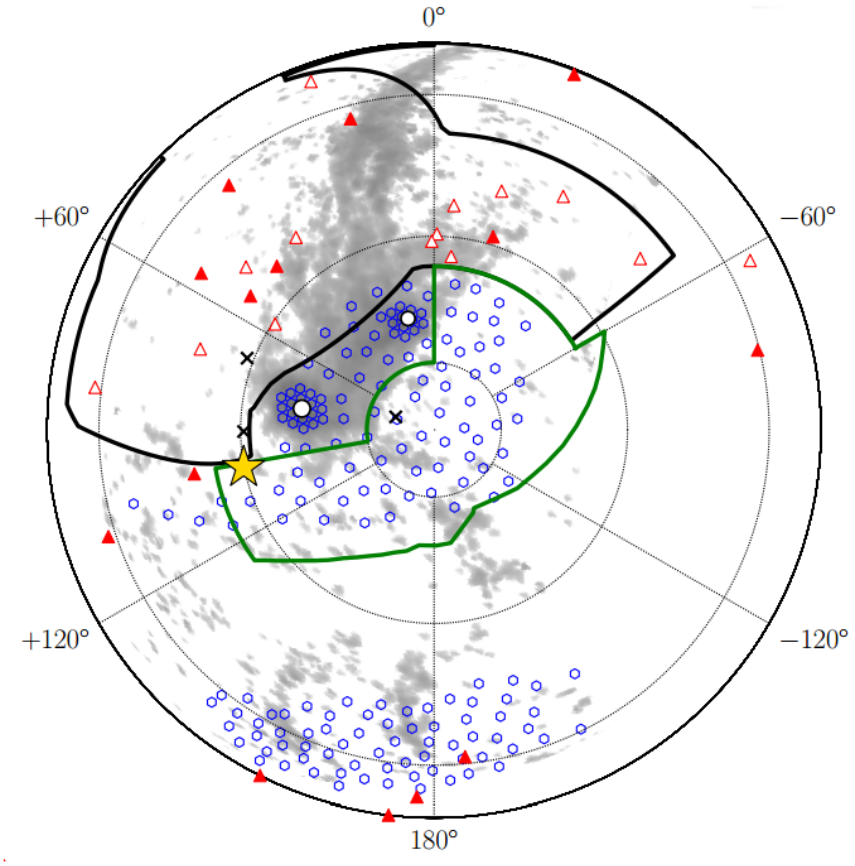

Figura 2.10: A linha preta contorna a área amostrada pelo DES, enquanto que a linha verde representa a área amostrada pelo MagLiteS e os hexágonos em azul as regiões do SMASH (áreas não contíguas). Candidatos a galáxias anãs são marcados como triângulos preenchidos (confirmados espectroscopicamente) e não-preenchidos (ainda não confirmados). A área em cinza representa a densidade colunar de gas (HI) segundo Nidever et al. 2010. Os 'xis' marcam a posição dos aglomerados mais externos da LMC (ESO121SC003, Retículo e NGC 1841). Retirado de Drlica-Wagner et al. 2016 (Painel esquerdo da figura 1 deste artigo).

Capítulo 3

Os aglomerados da LMC

3.1 Introdução

Aqui fazemos uma breve apresentação dos métodos utilizados para a identificação, caracterização e análise dos aglomerados da LMC, tais como a identificação dos aglomerados nas imagens, a caracterização dos perfis de densidade e a comparação com isócronas para a determinação dos parâmetros destes objetos. De certa forma, aqui é o espaço onde detalhamos um pouco mais os métodos aplicados e as comparações com a literatura. Ao leitor que preferir a leitura do artigo, indicamos a seção 3.4 como sumário das atividades desenvolvidas.

3.2 Busca por sobredensidades estelares nas imagens de Verificação Científica do DES

Para a prévia identificação dos aglomerados da Grande Nuvem de Magalhães nos dados SV-DES, inicialmente foi feita uma varredura visual. O grupo de imagens mais próximas da Grande Nuvem de Magalhães (SPT-E) compõe-se de 280 imagens de 0,75 graus $\times$ 0,75 graus cada uma (*tile*). As imagens foram divididas em cinco subgrupos com overlap parcial entre si, para serem escaneadas por cada um dos integrantes do grupo DES-GA Brasil (Dark Energy Survey Galactic Archeology Brasil) àquela época (Basílio X. Santiago, Eduardo Balbinot, Adriano Pieres, Anna Bárbara Queiróz de Andrade e Douglas Oscar).

Depois da busca por sobredensidades estelares, as posições dos candidatos a aglomerados estelares foram comparadas para evitar duplas entradas. Foi feita uma avaliação para a determinação de um raio visual prévio e foram listados alguns

comentários. O total de candidatos associados a sobredensidades estelares foi de 299.

3.3 Métodos probabilísticos para determinação das propriedades físicas dos aglomerados

Na escolha do método probabilístico, preferimos a Máxima Verossimilhança (em inglês *Maximum Likelihood*), ainda chamado de Força Bruta, com as incertezas nos parâmetros sendo dadas pela técnica de análise do perfil de verossimilhança ou probabilidade (Sprott, 2000, Fisher, 1925). Esta últimas obras citadas podem ainda ser utilizadas como uma fonte para uma descrição formal do método, que pode ser aplicado a praticamente qualquer comparação entre dados e modelos. Para determinar a máxima verossimilhança, varremos as grades contendo os valores numéricos dos parâmetros dos perfis e posteriormente das isócronas, guardando os valores de probabilidade para cada um dos conjuntos dos parâmetros. Com isso, basta sondarmos o espaço de parâmetros para determinar os máximos ou as incertezas.

São necessários alguns comentários para essa técnica. Como os parâmetros são elencados por uma grade (não são utilizados valores interpolados), o conjunto dos parâmetros mais prováveis faz parte do conjunto de parâmetros da grade, sendo que para todas as combinações de parâmetros da grade são calculadas as verossimilhanças. Isso faz com que o tempo computacional seja estimado com o número de parâmetros e de intervalos em que estes são amostrados. Num exemplo simples, se a probabilidade para uma grade com dimensão 3 (igual ao número de parâmetros) contendo 20 pontos em cada dimensão (ou seja, 20 valores para cada parâmetro) demora 10 minutos para rodar em um computador, ao aumentarmos o número de parâmetros para 4, teremos um tempo computacional esperado de 10min $\times$ 20 = 200 min = 3,33 horas. Se dobrarmos o número de valores para cada parâmetro o tempo esperado vai para $40^4/20^4 = 2^4$ ou 16 vezes maior. A superamostragem da grade ou o aumento do número de parâmetros torna o método pouco eficiente no tocante ao tempo computacional. Métodos como o as cadeias de Markov amostradas por Monte-Carlo (MCMC) de Foreman-Mackey et al. (2013) diminuem este tempo computacional, ao avaliar a probabilidade dos caminhantes se dispersarem pelo espaço de parâmetros. No entanto, estes últimos métodos não são muito indicados quando o espaço de parâmetros é truncado (por exemplo em idade e metalicidade para objetos velhos e pobres em metais), pois os caminhantes (na abordagem MCMC) não podem se difundir pela barreira no espaço de parâmetros. Testes anteriores utili-

zando a probabilidade marginalizada também tiveram os mesmos resultados que o método MCMC. Outra diferença é que o método de Força Bruta não trabalha com a probabilidade marginalizada (como o MCMC), sendo que a probabilidade é determinada apenas para um ponto do espaço (enquanto que a probabilidade marginalizada é a soma das probabilidades que contém aquele respectivo valor para o parâmetro, colapsada para os outros parâmetros).

Para a determinação da incerteza, utilizamos o método de análise do perfil do logaritmo da probabilidade (Sprott, 2000). Este método consiste em se amostrar o logaritmo da probabilidade ao longo do parâmetro para o qual se quer determinar a incerteza. No caso de se determinar a incerteza para a idade, se fixa a idade em um determinado valor e se determina o valor máximo de probabilidade. Os parâmetros restantes podem ser mantidos fixos nos valores mais prováveis (neste caso não levando em conta a variância entre os parâmetros), ou se pode fazer variar os outros parâmetros, de forma a se amostrar a máxima verossimilhança para aquele valor de idade (em nosso exemplo). Nossa escolha, depois de uma longa discussão com os revisores da colaboração, foi a de se levar em conta a variância na determinação da incerteza, sendo que esta é ligeiramente maior do que quando se mantém os parâmetros restantes fixos nos valores mais prováveis. No entanto, este método é bem mais robusto e formal, sem custo computacional exagerado (menos do que duas vezes o método computacional quando não se leva em conta a variãncia).

A determinação da incerteza ocorre ao longo da curva de $2 \times \log \mathcal{L}$ da seguinte forma: o pico informa o valor mais provável para aquele parâmetro. A diferença (ao longo do eixo do parâmetro escolhido) entre este pico e o valor de $2 \times \log \mathcal{L}$ do pico subtraído de k^2 informa o valor de k intervalos de confiança, ou de $k\sigma$, onde σ corresponde ao intervalo de confiança. Se k=1, o intervalo de confiança é de 68%. Desta forma, em um exemplo simples, para um pico de $2 \times \log \mathcal{L}$ com valor máximo em zero para uma idade de 10 bilhões de anos, a diferença entre a idade do pico de probabilidade e a idade onde $2 \times \log \mathcal{L}$ cai para -1 será a incerteza (no limite de 68%) para a idade. Vale lembrar que, como dito no parágrafo acima, esta curva de $2 \times \log \mathcal{L}$ foi construída levando em conta a variação dos parãmetros restantes, tendendo a um maior valor para a incerteza quando comparada com valores de probabilidade sem levar em conta a variância. Como existem dois valores para os parâmetros onde $2 \times \log \mathcal{L}$ atinge o valor de -1 (um antes do pico e outro depois do pico), na avaliação da incerteza recorremos a uma média entre os dois valores para informar a incerteza. Ressaltamos ainda que a curva de $2 \times \log \mathcal{L}$ deve ser suave e bem comportada em torno do máximo, como lembra Martin et al. (2008). No caso

dos aglomerados reais, onde a incerteza calculada ficou menor do que o valor do passo na grade mais fina, a incerteza assumida é o valor médio entre os passos (em ambas as direções).

As incertezas informadas ao final do trabalho refletem portanto a variação de probabilidade dos parâmetros para um intervalo de confiança de 1 σ (68,3%).

Para o caso dos perfis de densidade dos aglomerados da LMC, utilizamos o perfil de densidade está somado à densidade do fundo de estrelas da Via-Láctea e da LMC, como na Figura 4 do artigo. Isso evita densidades muito pequenas na escala logaritmica.

3.3.1 Aplicações aos dados do DES

Como resultados, durante o período da descoberta das galáxias anãs do ano 1 (Bechtol et al., 2015) e 2 (Drlica-Wagner et al., 2015) dentro da colaboração, aplicamos os métodos para o ajuste de perfil exponencial e melhor modelo (isócrona) para os objetos descobertos, apresentando os resultados em telecons dentro da colaboração. Desta forma, nosso trabalho foi validado, aproveitando as críticas e sugestões dos colaboradores, muito importante para o desenvolvimento dos métodos. As figuras 3.1 e 3.2 mostram dois exemplos da aplicação dos métodos para a galáxia anã Reticulum II, trabalho feito anteriormente à publicação das descobertas do ano 1 da colaboração.

Além disso, também incluimos o artigo de descoberta do aglomerado estelar DES1, onde também aplicamos os métodos aqui desenvolvidos, bem como para a caracterização deste objeto (perfil e isócrona).

3.4 Resumo das atividades desenvolvidas em relação aos aglomerados da LMC

- Busca visual por sobredensidades estelares na periferia da LMC;
- Confecção de uma *pipeline* utilizando as tarefas do IRAF para efetuar a fotometria de imagens;
- Aplicação da *pipeline* aos candidatos a aglomerados estelares utilizando as imagens de verificação científicas do DES (fotometria dos candidatos);
- Análise dos candidatos a aglomerados estelares;

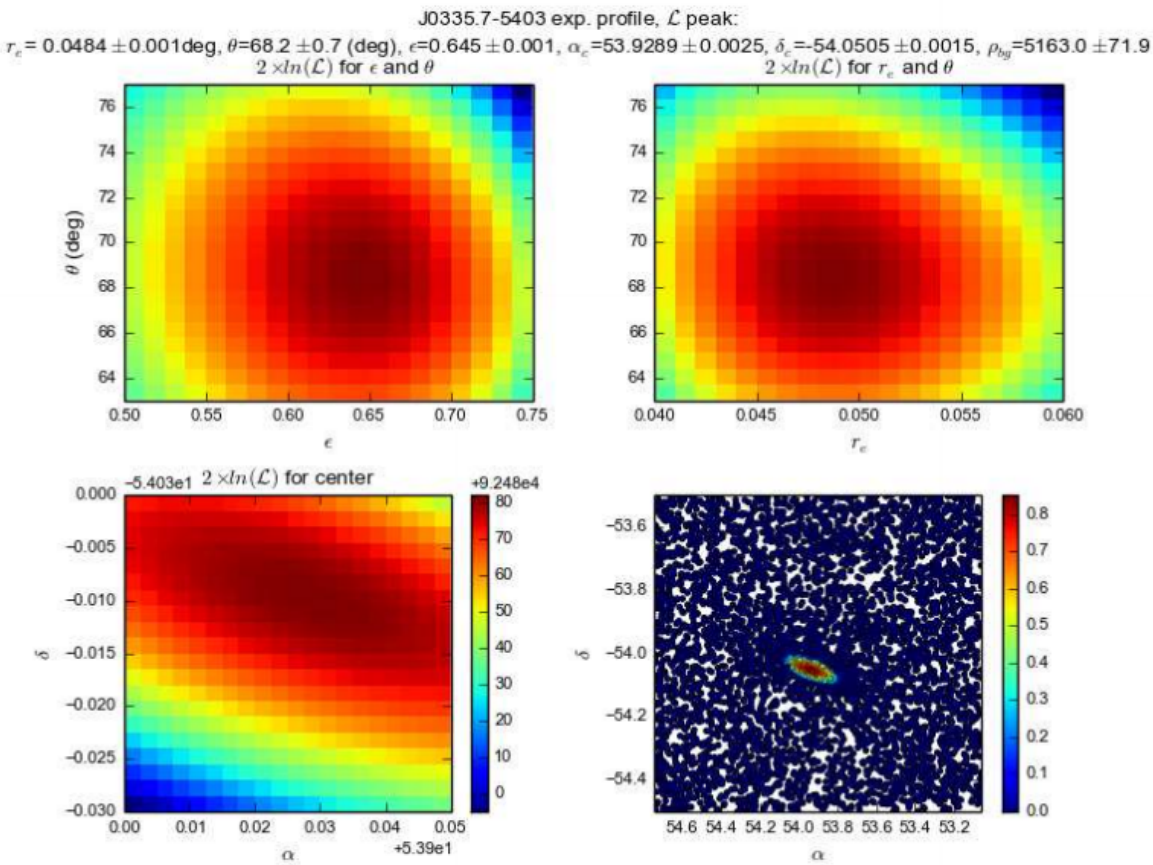

Figura 3.1: Ajuste do perfil exponencial com cinco parâmetros (raio exponencial, elipticidade, ângulo de posição e centro (ascenção reta (α) e declinação (δ)) para a galáxia-anã Reticulum II. Os melhores valores são informados no título da figura.

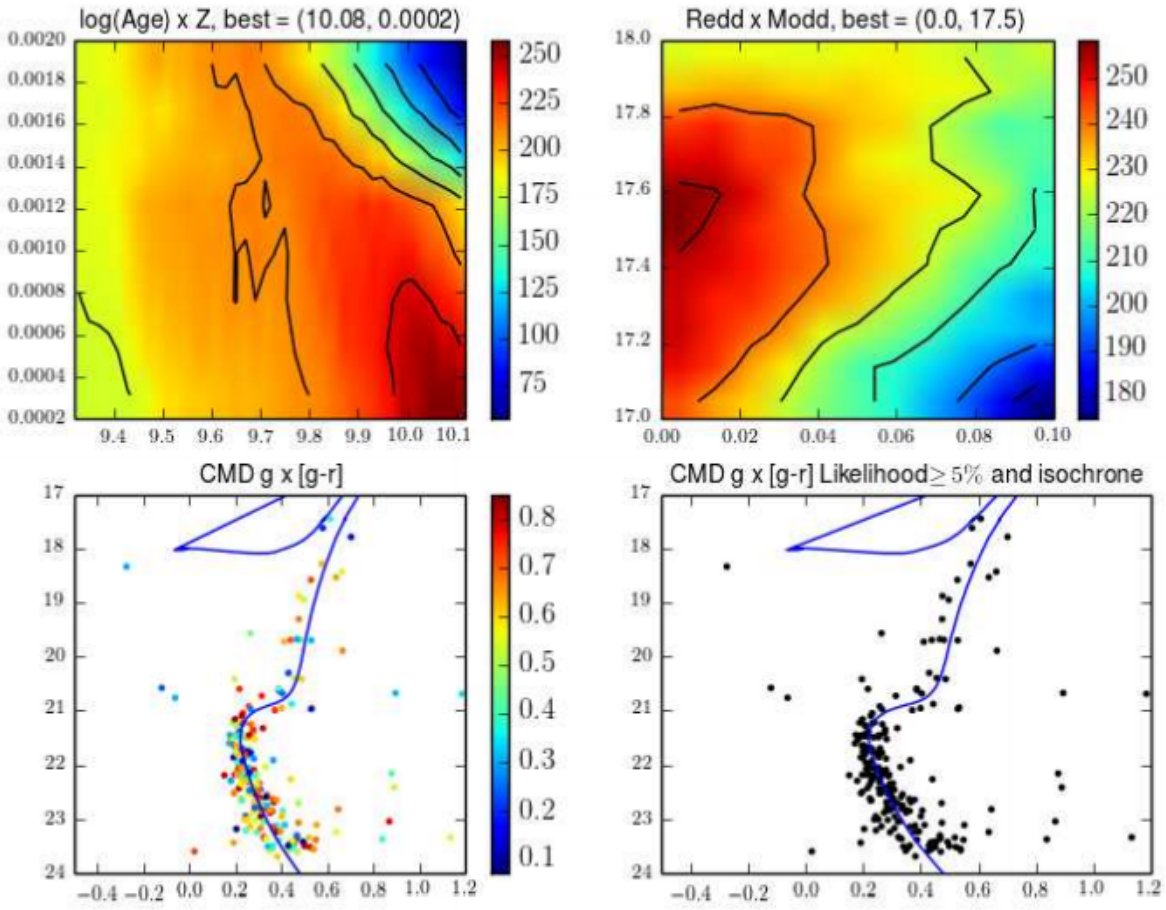

Figura 3.2: Ajuste para idade, metalicidade, avermelhamento e módulo de distância para as estrelas com probabilidade de pertencimento (dada pelo perfil exponencial) maior do que 5%, para a galáxia-anã Reticulum II. Os valores mais prováveis são informados no título da figura.

- Determinação das propriedades estruturais dos candidatos a aglomerados, bem como idade, metalicidades, avermelhamento e módulo de distância;
- Validação dos métodos utilizando aglomerados simulados;
- Comparação com os dados da literatura;

Monthly Notices of the ROYAL ASTRONOMICAL SOCIETY

MNRAS (2016) doi:10.1093/mnras/stw1260
Advance Access publication 2016 May 26

Physical properties of star clusters in the outer LMC as observed by the DES

A. Pieres,[1,2⋆] B. Santiago,[1,2⋆] E. Balbinot,[3⋆] E. Luque,[1,2] A. Queiroz,[1,2] L. N. da Costa,[2,4] M. A. G. Maia,[2,4] A. Drlica-Wagner,[5] A. Roodman,[6,7] T. M. C. Abbott,[8] S. Allam,[5] A. Benoit-Lévy,[9,10,11] E. Bertin,[9,11] D. Brooks,[10] E. Buckley-Geer,[5] D. L. Burke,[6,7] A. Carnero Rosell,[2,4] M. Carrasco Kind,[12,13] J. Carretero,[14,15] C. E. Cunha,[6] S. Desai,[16,17] H. T. Diehl,[5] T. F. Eifler,[18] D. A. Finley,[5] B. Flaugher,[5] P. Fosalba,[14] J. Frieman,[5,6] D. W. Gerdes,[19] D. Gruen,[6,7] R. A. Gruendl,[12,13] G. Gutierrez,[5] K. Honscheid,[20,21] D. J. James,[8] K. Kuehn,[22] N. Kuropatkin,[5] O. Lahav,[10] T. S. Li,[23] J. L. Marshall,[23] P. Martini,[20,24] C. J. Miller,[19,25] R. Miquel,[15,26] R. C. Nichol,[27] B. Nord,[5] R. Ogando,[2,4] A. A. Plazas,[18] A. K. Romer,[28] E. Sanchez,[29] V. Scarpine,[5] M. Schubnell,[19] I. Sevilla-Noarbe,[29] R. C. Smith,[8] M. Soares-Santos,[5] F. Sobreira,[2,30] E. Suchyta,[31] M. E. C. Swanson,[13] G. Tarle,[19] J. Thaler,[32] D. Thomas,[27] D. L. Tucker[5] and A. R. Walker[8]

Affiliations are listed at the end of the paper

Accepted 2016 May 23. Received 2016 May 23; in original form 2015 November 26

ABSTRACT

The Large Magellanic Cloud (LMC) harbours a rich and diverse system of star clusters, whose ages, chemical abundances and positions provide information about the LMC history of star formation. We use Science Verification imaging data from the Dark Energy Survey (DES) to increase the census of known star clusters in the outer LMC and to derive physical parameters for a large sample of such objects using a spatially and photometrically homogeneous data set. Our sample contains 255 visually identified cluster candidates, of which 109 were not listed in any previous catalogue. We quantify the crowding effect for the stellar sample produced by the DES Data Management pipeline and conclude that the stellar completeness is <10 per cent inside typical LMC cluster cores. We therefore reanalysed the DES co-add images around each candidate cluster and remeasured positions and magnitudes for their stars. We also implement a maximum-likelihood method to fit individual density profiles and colour–magnitude diagrams. For 117 (from a total of 255) of the cluster candidates (28 uncatalogued clusters), we obtain reliable ages, metallicities, distance moduli and structural parameters, confirming their nature as physical systems. The distribution of cluster metallicities shows a radial dependence, with no clusters more metal rich than [Fe/H] $\simeq -0.7$ beyond 8 kpc from the LMC centre. The age distribution has two peaks at $\simeq$1.2 and $\simeq$2.7 Gyr.

Key words: methods: statistical – Magellanic Cloud – galaxies: star clusters: general.

1 INTRODUCTION

The Large Magellanic Cloud (LMC) is a nearby dynamically active satellite galaxy, exhibiting multiple epochs of star formation, while also suffering from tidal interactions with the Small Magellanic Cloud (SMC) and the Milky Way (MW). Given its proximity, stellar populations in the LMC are easily resolved in deep surveys, allowing us to obtain information such as ages, chemical abundances, kinematics and distances to individual stars and star clusters. Thus, the LMC represents an excellent local laboratory to study the effects of gravitational forces on the evolution of a satellite galaxy,

⋆ E-mail: adriano.pieres@ufrgs.br (AP); basilio.santiago@ufrgs.br (BS); e.balbinot@surrey.ac.uk (EB)

including its star formation history (SFH) and age–metallicity relation (AMR).

A wealth of data describing the structure and stellar populations of the LMC has been accumulated over decades of research. The LMC is known to have a stellar disc inclined relative to the line of sight towards its centre by $i = 36$–38° with a position angle of $\theta = 130$–145°. This disc also seems to have a warp and to be flared (Caldwell & Coulson 1986; Alves & Nelson 2000; Olsen & Salyk 2002; Subramanian & Subramaniam 2010; Balbinot et al. 2015). A large number of studies have tried to reconstruct its SFH and/or AMR, often in connection to the SMC (Carrera et al. 2008, 2011; Harris & Zaritsky 2009; Glatt, Grebel & Koch 2010; Indu & Subramaniam 2011; Rubele et al. 2012; Piatti & Geisler 2013; Weisz et al. 2013; Meschin et al. 2014).

Regarding the stellar populations and their variation as a function of position, many studies attempt to reconstruct the SFH and/or AMR of the LMC, based on field stars (Carrera et al. 2008, 2011; Meschin et al. 2014), clusters in the relatively central region (<10 kpc) (Olszewski et al. 1991; Kontizas, Kontizas & Michalitsianos 1993; Geisler et al. 1997, 2007; Kerber, Santiago & Brocato 2007; Glatt, Grebel & Koch 2010) or both (Piatti & Geisler 2013). The results have been inconsistent, as no single SFH and AMR applies to the entire LMC body or to clusters and field stars alike (Carrera et al. 2011; Piatti & Geisler 2013). In a recent paper, Piatti & Geisler (2013) analyse 5.5 million LMC field stars and present age and metallicity trends with distance from the LMC centre (out to 8 kpc) and an AMR. Their results are more consistent with outside-in star formation and chemical enrichment. They also find larger spreads in age and metallicity in the outer regions and no clear age gap in the field star formation. Carrera et al. (2011) investigate fields stars farther out, from 5.2 to 9.2 kpc from the LMC centre, and find age and metallicity gradients only for the youngest and the most metal-rich stars. For the star clusters, Glatt et al. (2010) fit Padova (Girardi et al. 2002) and Geneva (Lejeune & Schaerer 2001) isochrones to a sample of 1193 young LMC clusters within 4 deg of its centre and find two periods of enhanced cluster formation, at 125 and 800 Myr. They argue that these peaks in the cluster formation rate may be connected with the last encounter of the LMC and SMC.

In contrast with our knowledge of the inner structure and stellar populations of the LMC, much less is known about the periphery at distances >10 kpc. Covering the extended outer LMC regions requires a large-area, photometric and homogeneous sample. This has recently been provided by the early data taken as part of the Dark Energy Survey (DES) Science Verification (SV). In this work we aim to probe clusters in the outer LMC field in DES-SV footprint, using a homogeneous data sample.

This paper is organized as follows: Section 2 is a brief introduction presenting the data (the DES-SV data set, its reduction and the resulting LMC clusters sample). Section 3 describes the methods we applied to recover cluster structural parameters and cluster stellar populations. In Section 4 we tested the limits of the methods, simulating clusters, recovery of parameters and determining uncertainties. Section 5 presents our results and compares to available literature. Section 6 provides a discussion and summary.

2 DATA

2.1 DES and SV

The DES (The Dark Energy Survey Collaboration 2005) is a 5000 deg^2 imaging survey in *grizY* bands currently being carried out using DECam, a 3 deg^2 (2.°2 diameter) wide-field mosaic camera on the CTIO Blanco 4 m telescope with a pixel scale of 0.263 arcsec pixel^{-1} (Flaugher et al. 2015). DES will reach a characteristic photometric depth of 24th magnitude (with S/N $\simeq$ 10 for *g* band, point-like sources) and enable accurate photometry and morphology of objects 10 times fainter than the Sloan Digital Sky Survey. The exposure times for DES single exposures are 90 s for *g, r, i, z* and 45 s for *Y* band.

The DECam images are reduced by the DES Data Management (DESDM) team, which has a pipeline to co-add and calibrate (astrometrically and photometrically) images and finally catalogue and classify the objects in the images. The final co-add images are called *tiles*, with a size of 0.75 deg × 0.75 deg ($10^4 \times 10^4$ pixels). More details can be found in Mohr et al. (2012) and Desai et al. (2012).

A substantial challenge for deep ground-based surveys is the star/galaxy separation. DESDM performs photometric analysis with SEXTRACTOR (Bertin & Arnouts 1996), a software package which identifies and selects sources above a threshold based on the image background. The blend parameter determines whether a group of neighbouring pixels must be classified as a single source or multiple objects (Bertin 2011). The final catalogue produces several magnitude measurements (*mag_auto* and *mag_psf*, for example) and *spread_model* as the main star/galaxy separator. This is based on the difference between the best-fitting local point spread function (PSF) model and a slightly more extended model made from the same PSF convolved with a circular exponential disc model with scalelength equal to FWHM/16 (where FWHM is the full width half-maximum of the PSF model).

The DES-SV data were taken from November 2012 to February 2013 for a total of 427 h of observation. The data were intended to test DECam capabilities and the DESDM data pipeline (calibration and photometry, astrometry, image quality, pointing and guiding, operational readiness and pipelines for supernova). The largest contiguous area of the SV campaign was the South Pole Telescope East field (SPT-E), which is located immediately to the north of the LMC. This work is based on the co-add data products from the first release processing of the SV observations (SVA1), which includes the SPT-E region (157 deg^2) in 2537 exposures.

2.2 LMC star clusters

An initial sample of LMC star clusters in the SPT-E region was obtained by a visual inspection of the SV co-add images [Red Giant Branch (RGB) images made co-added exposures in the *g*, *r* and *i* bands], on a tile by tile basis. We used the Tile Viewer tool available at the DES Science portal (Balbinot et al. 2012), which is a web-based facility. The list of SPT-E tiles was initially split among five of the authors with an overlap region among them. Almost all LMC clusters were found in the southern part of the field, which was inspected by two of us. The overlapping region included 10 clusters found by one of the authors, eight of which comprised the sample found by the other. Not unexpectedly, the two extra objects were poor clusters. Despite the low numbers, this sample overlap suggests a uniform sampling among the richer systems analysed in Section 5.2.

After eliminating repeats from the individual searches, the original cluster list contained 294 candidates. We then matched our candidates with the Bica et al. (2008) LMC clusters catalogue. Our list contains a total of 109 previously uncatalogued objects. Seven objects included in the Bica et al. (2008) catalogue were not in our original list. By visually inspecting their images, one of these

objects was clearly a galaxy and another was very close to a bright star, leaving a total of 299 cluster candidates in the SPT-E region.

The sample was further refined using the g versus $g-r$ colour–magnitude diagrams (CMDs; from DAOPHOT, see Section 2.4). 44 out of the 299 visually inspected candidates had CMDs that were not consistent with simple or composite stellar populations, usually containing a large fraction of faint red sources, more consistent with galaxy clusters. The filtered subsample has 255 candidates consistent with being star clusters. The full list is available in VizieR database.

2.3 DES-SV stellar sample

Since the DES main goals are cosmological in nature, the science requirements for the data are related to detecting, measuring and characterizing galaxies, not stars. Therefore, we ran a complementary diagnostic of the DES-SV stellar catalogue. Our main concern was to investigate the completeness of the SVA1 stellar catalogue as a function of S/N and crowding, since this aspect is crucial to the analysis of LMC clusters presented here. For that purpose, we used routines from IRAF/DAOPHOT (Stetson 1987), which is the benchmark program to detect and measure stellar data in crowded fields. Details about our DAOPHOT reduction and photometry pipeline are provided in Section 2.4. A full description of stellar completeness in SVA1 catalogues can be found in a future technical paper (Pieres et al., in preparation). Below we summarize our basic conclusions:

(i) CMDs based on the stellar samples drawn from standard DAOPHOT selection, using PSF magnitude errors and sharpness, are similar to those from SVA1, based on *spread_model* cuts. In the SPT-E fields covering the outer LMC, the CMDs from both SVA1 and DAOPHOT clearly display the main features of the LMC field population, such as an Main Sequence (MS) ranging from $18 < g < 24$, an old Main Sequence Turnoff at $g\sim22.5$, $g-r\sim0.2$, a red giant branch and a red clump with $g < 22$ and $g-r > 0.3$.

(ii) In typical DES regions, well away from the LMC, the source density is about 1/10 of that found in regions where most star clusters are found. In this low-density regime, as well as inside poor LMC clusters, SVA1 completeness relative to DAOPHOT is close to 1 down to $g \cong 20$. SVA1 catalogues tend to sample fewer point sources than DAOPHOT at fainter magnitudes, but the relative completeness varies depending on how we separate stars from galaxies in either case.

(iii) SVA1 stellar completeness is a strong function of source density, dropping abruptly from $\sim$0.3 to $<$0.1 for surface densities $>$260 stars arcmin^{-2}. In particular, the SVA1 stellar sample is very incomplete in crowded fields, such as those close to the centres of rich LMC star clusters. In these regions, SVA1 samples less than 50 per cent of the objects detected by DAOPHOT, even at bright magnitudes ($g < 19$). Inside rich cluster cores, the SVA1 incompleteness is large enough to cause local holes in the surface density distribution of point sources on the sky. This result is robust to the way we separate stars from galaxies.

With these results in mind, we decided that we could not use the SVA1 catalogues inside and around the LMC clusters. However, we used SVA1 co-add images to identify cluster candidates and its catalogs to fit zero-points to DAOPHOT photometry. We also decided to use three bands (two colours) instead of two, to better describe the stellar locus of each cluster candidate. For reference, a comparison of both software packages (SExtractor with PSFEX and DAOPHOT with ALLSTAR) can be found in Annunziatella et al. (2013). In Section 2.4 we describe in detail the data reduction and analysis based on our DAOPHOT pipeline.

2.4 DAOPHOT data reduction

As mentioned earlier, the SVA1 catalogue is incomplete in crowded regions, such as inside LMC star clusters. To bypass this problem, we used the SVA1 co-add image products in the vicinity of each of our candidate clusters as inputs for our own photometric extraction based on DAOPHOT. For each object we made an image cutout with 6.75 arcmin on a side, visually centred on the candidate, in three bands: g, r and i.

The IRAF/DAOPHOT routines were combined into a pipeline to reduce DES co-add cutouts (Fig. 1). This pipeline is a set of scripts using the tasks *daofind*, *phot*, *pstselect*, *psf*, *allstar* and works as follows. First, we combined g and r images and ran *daofind* to detect sources on these combined images; we rejected sources that were less than 3.0σ above the background. We then picked the 50 brightest sources to use as a starting template for PSF modelling (running *psf* task). With the initial PSF model, we ran *allstar* over all sources found and refined our initial list of stars used for PSF fitting by choosing those whose local background is $\leq$3 counts, and which have low magnitude error ($\leq$0.01 mag) and low chi-square ($\leq$0.2). This procedure of refining the PSF after an initial *allstar* run is meant to make the process subject to minimal human interference (although some human decisions were still needed at times). PYTHON and FORTRAN routines were made to select the stars and convert their α and δ coordinates to/from x and y coordinates. This conversion, whenever needed, uses the WCS of the DESDM co-adds, therefore preserving DESDM astrometry. The SVA1 catalogue has a typical accuracy of 200 mas per coordinate when compared to UCAC-4, and 100 mas for nearby sources. Using a program similar to the *join* Linux command, we then composed the DAOPHOT catalogues from each filter. We then added g, r and i zero-points, by taking DES catalogue photometry as reference, and created the final DAOPHOT catalogue. The stars used for this calibration were those that satisfied the following criteria: $magerr_{DAO} \leq 0.03$, $|sharp| \leq 1.00$ in g, r and i filters, brighter than 20 (in g and r filters) and 19 (for i *filter*). The corresponding sources in SVA1 had to have $|\ spread\_model\ | \leq 0.002$ and magnitude error $\leq$0.03. The standard deviation for these difference ($|mag_{DAO} - mag_{SVA1}|$) has typical values $\leq$0.02 for the three filters. This small random scatter after the zero-point correction precludes the need of adopting colour terms in the calibration.

After the reduction, diagnostic plots were made to evaluate the DAOPHOT catalogue completeness level and to make reduction sanity checks. An example of these diagnostic plots is shown in Fig. 2. Example $g \times [g-r]$ CMDs of clusters of different ages and richness are shown in Fig. 3. Details about parameters fitting are provided in Section 3.

The criteria we used to define sources as stars from the DAOPHOT catalogue were magnitude error $\leq$0.1 and |sharpness| $\leq$1.00 in g, r and i bands simultaneously. Stars used for refining the PSF model or for calibration purposes were subject to more stringent selection criteria, as explained earlier. Our DAOPHOT based selection of stars is still prone to substantial contamination by galaxies. However, within a typical visual cluster radius this contamination amounts to less than 2 per cent.

A parallel analysis of relative completeness (SVA1 and DAOPHOT catalogues, using the same pipeline reduction presented here) has been reported by Balbinot et al. (2015) in their section 3.3.

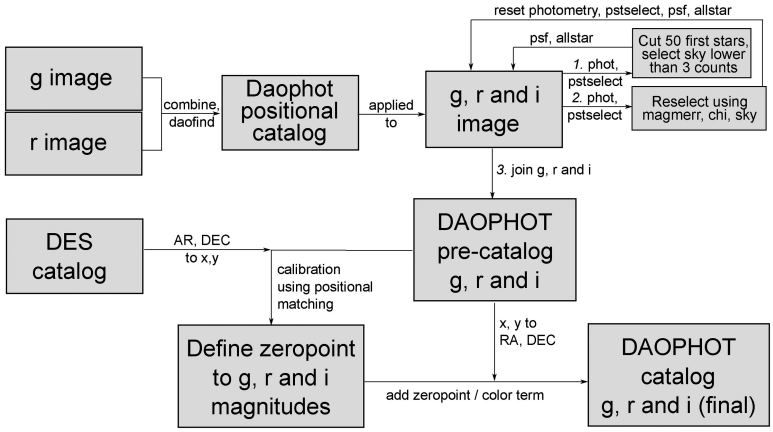

Figure 1. Flow chart describing the DAOPHOT based reduction and photometry pipeline developed as part of this work. As final products, it yields a catalogue using *g, r* and *i* magnitudes from co-add image cutouts. First, the *g* and *r* images are combined to generate a positional sources catalogue (using *daofind*). This catalogue is a starting point to run *phot* (for aperture measurements) and *pstselect* (for producing a list of stars to be used in the PSF model) routines for each filter. We pick the 50 brightest sources and run *psf* (that does the actual PSF modelling) and *allstar* (PSF fitting to all detected sources) tasks. A cleaner set of psf stars is selected as those sources with the lowest values of *chi, magerror, sky*, making up a new PSF list. We reset the list and rerun *psf* and *allstar*. The zero-point for each filter are determined comparing magnitudes of SVA1 (DESDM) and DAOPHOT after a positional match to the DES catalogue. Last, these calibration terms are added and the coordinates converted to α and δ, generating the final composite DAOPHOT catalogue.

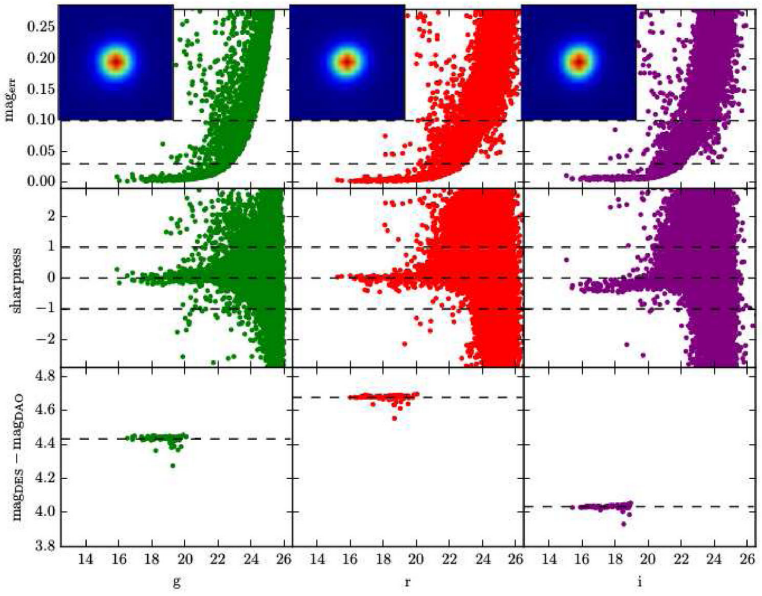

Figure 2. Diagnostic plot for the image reduction around our LMC cluster candidate 67. The three columns refer to *g*, *r* and *i* filters, from left to right. The upper row shows the DAOPHOT magnitude errors increasing towards fainter stars. The upper dashed line is the maximum magnitude error adopted to classify an object as a star. The lower dashed line is the cut-off used for calibration purposes. The model PSF images are shown at the top left of these panels. In the middle row, the sharpness parameter is plotted against the magnitudes. Again, the dashed lines limit the assumed stellar locus. The lower row shows the magnitude differences ($\mathrm{mag_{DES}} - \mathrm{mag_{DAO}}$) for classified stars that were used for calibration (the zero-point added to DAOPHOT was based in a mean of these stars). The outliers in the bottom panels were ruled out using a 3σ clipping algorithm.

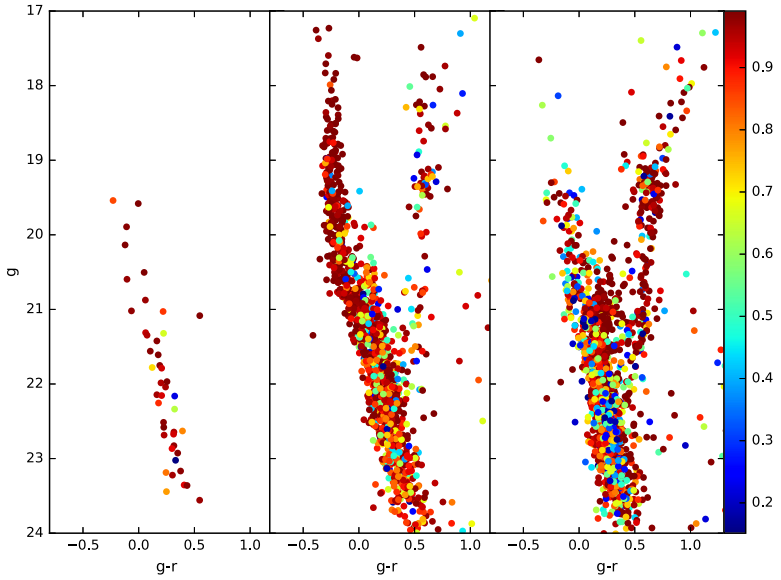

Figure 3. In order to illustrate the clusters richness in this sample, we show $g \times [g-r]$ CMDs for (leftmost panel) the poorest cluster in this sample (DES001SC17 with 44 stars and 1.26 Gyr as fitted age), the young (480 Myr) BSDL2976 cluster (central panel) and the intermediate-age (2.57 Gyr) SL388 cluster (rightmost panel). Stars are colour coded by their likelihood being cluster members assuming a King profile as described in equation (9).

3 METHODS

3.1 Radial density profiles

We used the King azimuthally symmetric profile (King 1962) as the standard model to describe the surface density profile of the star cluster candidates:

$$\rho_{\rm cl}(r) = k\left(\frac{1}{[1+(r/r_{\rm c})^2]^{1/2}} - \frac{1}{[1+(r_{\rm t}/r_{\rm c})^2]^{1/2}}\right)^2, \quad (1)$$

where $\rho_{\rm cl}$ is the surface number density of cluster stars, r is the angular distance from the centre ($\alpha_{\rm c}$ and $\delta_{\rm c}$ in cutout), $r_{\rm c}$ is the cluster *core radius* and $r_{\rm t}$ is the cluster *tidal radius*. The parameter k is the profile normalization and is related to the central surface density. The King density profile is widely used for both high and low-mass Galactic clusters (Kharchenko et al. 2012; Miocchi et al. 2013).

The King parameters $r_{\rm c}$, $r_{\rm t}$ and centroid were determined using a maximum likelihood estimate (MLE). First, we determined the background density of stellar sources in the cutout image, $\rho_{\rm bg}$. We do that by counting stars farther than two times a visually determined cluster radius and dividing this number count by the corresponding area. After we determined the background density, we estimated the number of stars ($N_\star$) belonging to the cluster by following the recipe by Martin, de Jong & Rix (2008)

$$N_\star = N_{\rm tot} - \rho_{\rm bg} \times A, \quad (2)$$

where A is the cutout area and $N_{\rm tot}$ is the total number of stars in the cutout. The profile normalization constant k is determined for each profile by dividing the number of cluster stars ($N_\star$) by the integral of the King profile from the centre to $r_{\rm t}$:

$$k = \frac{N_\star}{\int_0^{r_{\rm t}} 2\pi r {\rm d}r \left(\frac{1}{[1+(r/r_{\rm c})^2]^{1/2}} - \frac{1}{[1+(r_{\rm t}/r_{\rm c})^2]^{1/2}}\right)^2}. \quad (3)$$

In the fitting process, we varied the centre position ($\alpha_{\rm c}$ and $\delta_{\rm c}$) and the parameters $r_{\rm c}$ and $r_{\rm t}$ (these parameters are determined from the model profile grid), evaluating the initial estimates by eye.

The likelihood that star i belongs to the full model (King profile) with radii $r_{\rm c}$ and $r_{\rm t}$ and centred at $\alpha_{\rm c}$ and $\delta_{\rm c}$ and normalized to k is

$$\ell_i = k\left(\frac{1}{[1+(r_i/r_{\rm c})^2]^{1/2}} - \frac{1}{[1+(r_{\rm t}/r_{\rm c})^2]^{1/2}}\right)^2 + \rho_{\rm bg}, \quad (4)$$

where r_i is the radial distance of the given star from that model centre. The most likely model (defined by parameters $r_{\rm c}$, $r_{\rm t}$ and position $\alpha_{\rm c}$, $\delta_{\rm c}$) is the one which maximizes the log-likelihood summed over all stars:

$$\log \mathcal{L}(r_{\rm c}, r_{\rm t}, \alpha_{\rm c}, \delta_{\rm c}) = \sum_{i=1}^{N} \log(\ell_i), \quad (5)$$

where N is $N_{\rm tot}$ in equation (2). Note that, in practice, stars located outside the tidal radius of each model profile contribute to the likelihood with $\ell_i = \rho_{\rm bg}$.

3.2 Isochrone fits

We also used a maximum-likelihood approach to determine the cluster simple stellar populations: age, metallicity, distance modulus and reddening. As in the fit for the density profiles, the basic step is to measure the likelihood that each star is taken from a modelled isochrone displaced by a given distance modulus and extinction

vector. In this work, we are using three magnitudes, g, r and i. Thus, the distance from the isochrone in magnitude space must be evaluated in 3D space. For this purpose, we used the PARSEC isochrones (Bressan et al. 2012) and adopted the Galactic extinction law of Cardelli, Clayton & Mathis (1989). The reddening is used to constrain extinction as measured in each magnitude. As a result of our choice, extinction is then given as

$$A_g = 3.318E(g-r) \tag{6}$$

$$A_r = 2.318E(g-r) \tag{7}$$

$$A_i = 1.758E(g-r). \tag{8}$$

Note that this choice of extinction law leads to very similar results (within the uncertainties) to a typical LMC extinction curve (Gordon et al. 2003) for g, r and i DECam filters.

The isochrone fitting works as follows. Given the best-fitting density profile, we first assigned a probability that star i belongs to the candidate cluster as

$$P_i^{\rm kp} = \left(\frac{\rho_{\rm cl}(r_i)}{\rho_{\rm bg}+\rho_{\rm cl}(r_i)}\right), \tag{9}$$

where $\rho_{\rm bg}$ is the background star density, as described in the previous section. We applied a threshold cut in $P^{\rm kp} > 0.05$ to select the stars to use in the fit. We then computed the Gaussian likelihood that a given isochrone is the correct one describing this set of stars. We first determined the distance of star i to isochrone j, d_{ij}. This is the minimum distance of the star in the M-dimensional photometric space (in this case, g, r and i magnitudes) to the isochrone:

$$d_{ij}^2 = \min\left[\sum_{l=1}^{M}\left(\frac{m_{li}-m_{lj}}{\sigma_{m_{li}}}\right)^2\right], \tag{10}$$

where the sum is over all photometric bands, (m_{lj}) is the closest isochrone magnitude in band l to the observed magnitude of star i (m_{li}), and $\sigma_{m_{li}}$ is the uncertainty in m_{li}. The isochrone magnitudes are already displaced by the distance modulus and reddening, both of which are free fit parameters. To avoid numerical limitations, we interpolate the isochrone points when determining d_{ij}, instead of using the discrete set of isochrone points.

Note that d_{ij} corresponds to the highest likelihood term that the star i is drawn from isochrone model j, which is then given by

$$P_{ij} = \frac{1}{(2\pi)^{M/2}}\left(\prod_{l=1}^{M}\frac{1}{\sigma_{mli}}\right)\exp\left(\frac{-d_{ij}^2}{2}\right). \tag{11}$$

Finally, the logarithmic likelihood that the set of N stars that satisfies the $P^{\rm kp} > 0.05$ criterion are drawn from isochrone model j can be written as

$$\log\mathcal{L}_j = \log\prod_{i=1}^{N}(P_{ij}\,P_i^{\rm kp}) = \sum_{i=1}^{N}\log(P_{ij}) + \sum_{i=1}^{N}\log(P_i^{\rm kp}). \tag{12}$$

3.3 Optimization methods

We are dealing with a maximization problem where we want to find the model which best describes the set of likely cluster stars. Given a grid in parameter space of age, metallicity, distance and reddening, we found the peak of $\mathcal{L}$ ($\mathcal{L}_{\rm max}$), and we probe the $2\log(\mathcal{L})$ space around this global maximum. The $2\log(\mathcal{L})$ values behave similarly to a χ^2 distribution, assuming that uncertainties have Gaussian (or similar) behaviour close to the peak. In this way we estimate the $k\sigma$ confidence level in the same manner as the χ^2 distribution (Lupton 1993, section 10.3). The main difference is that we include the covariance among parameters using the profile likelihood technique (Fisher 1956; Sprott 2000). For example, when determining the uncertainty in the age we perform a likelihood scan where at each value of cluster age we maximizing the likelihood with respect to the other parameters. Thus, the $k\sigma$ confidence intervals are determined when the log of the profile likelihood drops by $(k^2)/2$ from its maximum value. The uncertainties quoted in this work correspond to 1σ confidence level (68 per cent).

In the cases where the quoted uncertainties are smaller than the half-bin size (as is the cases for a few metal-poor clusters), we take the error to be the maximum of the uncertainty as computed by the likelihood method and half of the bin size at the grid point corresponding to maximum likelihood. The uncertainties quoted here reflect the statistical uncertainty in the model fit, and do not include any systematic uncertainties in the derivation of synthetic isochrone models (e.g. Bressan et al. 2012).

We test our profile and isochrone fitting in simulated star clusters in Section 4. The next section presents the model grids to do that.

3.4 Model grids

The likelihood optimization methods outlined in the previous sections require a grid of models, both for the structure (profile fitting) and for the other physical parameters (CMD fitting).

The LMC clusters vary in size by about an order of magnitude, as will be shown later in this paper. Therefore, it was not possible to use a single grid in $r_{\rm c}$ and $r_{\rm t}$ for all clusters. Furthermore, initial guesses from visual estimates were not always useful in constraining an optimal range in core and tidal radii. As a result, the profile fits were carried out interactively, with a size grid that varied from one cluster to the other. The central positions were allowed to vary within $\pm r_{\rm t}/4$ as taken from the previous iteration, until convergence. We define convergence to occur when the algorithm indicates a likelihood maximum close to the centre of the parameter's range. For some candidates, the range in $r_{\rm t}$ continuously increased and reached the limit of the cutout (much greater than the visual radius), which means the set of stars does not present a clear overdensity. These cases were removed from our catalogue.

The CMD fits were carried out with a fixed initial set of isochrones from which we built a likelihood map for each cluster. This initial grid covers the range 8.12 $\leq$log[age(yr)] $\leq$10.12 with 10 equally spaced age steps of Δ log[age(yr)] = 0.2. Metallicity varies within 0.0002 $\leq Z \leq$0.019 in 23 values: 0.0002 $\leq Z \leq$0.0008, step=0.0002; 0.001 $\leq Z \leq$0.019, step=0.001. The other dimensions are 18.2 $\leq (m-M)_0 \leq$18.8 with $\Delta(m-M)_0 = 0.03$ and $0 \leq E(g-r) \leq 0.2$ with $\Delta E(g-r) = 0.02$. This grid is the same for real and simulated clusters.

We scanned the entire initial grid, searching for a global likelihood maximum. We then defined another model grid around this maximum, which is narrower in log[age(yr)], covering $\log[\mathrm{age(yr)}]_{\rm max} - 0.4 \leq \log[\mathrm{age(yr)}] \leq \log[\mathrm{age(yr)}]_{\rm max} + 0.4$ with Δ log[age(yr)] = 0.02, where $\log[\mathrm{age(yr)}]_{\rm max}$ is the age corresponding to the likelihood peak in the initial grid. Metallicity in this thinner grid was restricted to ± 4 steps around the maximum likelihood value in the initial grid. Reddening and distance modulus were allowed to vary by ± 0.05 and ± 0.1, respectively, with 10 steps in each axis, from their initial best solution.

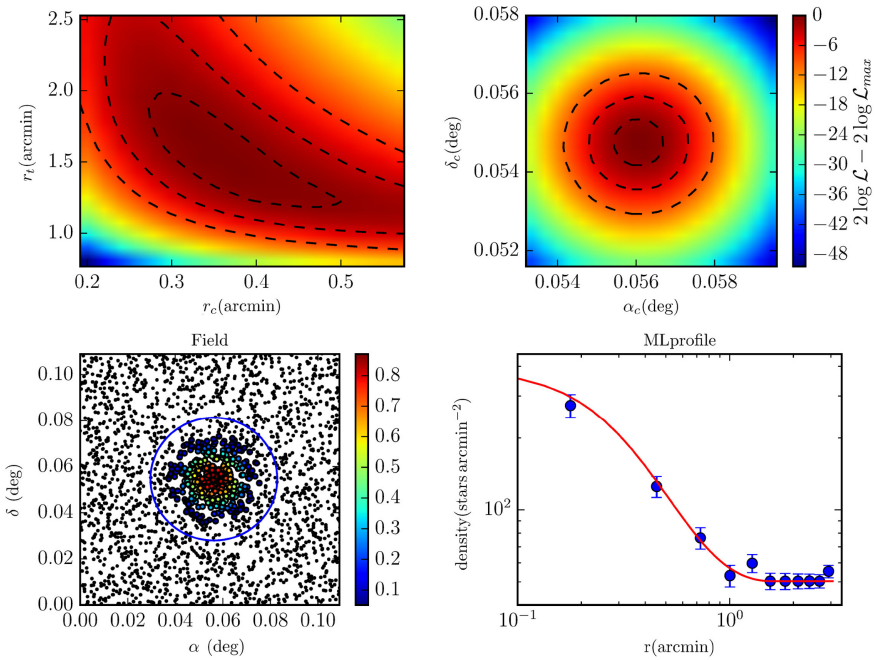

Figure 4. Example of the recovery of structural parameters for a simulated cluster ($\tau = 1$Gyr and $Z = 0.010$). The most likely parameters (using the DECam plate scale = 0.263 arcsec pixel^{-1}) are $r_c = 0.33$ arcmin, $r_t = 1.60$ arcmin, $k = 536$ stars arcmin^{-2}. Top left: likelihood maps for grid in r_c and r_t. Top right: $2\log\mathcal{L}$ map for centre position (top-left and right-hand plots share same colour bar). Black dashed lines in both top panels show limits for 1σ, 2σ and 3σ confidence levels. Bottom left: on-sky distribution of stars, colour coded according to likelihood. Bottom right: binned profile (blue circles) and the best-fitting model profile (solid red line).

4 CLUSTER SIMULATIONS

We first tested the fitting methods for density profiles and isochrones described above using simulated data.

We built artificial star clusters using GENCMD[1] and we inserted the synthetic stars into a typical LMC field. This code generates simple stellar populations (α, δ, magnitudes and magnitudes errors) given an initial number of stars, a mass function, a spatial density profile, a set of isochrones, filters and typical magnitude uncertainties. Here we used the Kroupa mass function (Kroupa 2001), King profile (King 1962) and PARSEC models (Bressan et al. 2012) for DECam filters (g, r and i). The positions of the synthetic stars are randomly chosen from the King profile for some choice of r_c, r_t and density normalization k. Their magnitudes are also randomly picked given the chosen isochrone model (age, metallicity, distance and reddening) and mass function. We used the same extinction law as cited above for DES bands and a typical magnitude error curve for each filter.

We simulated star clusters at a fixed distance modulus of $(m - M)_0 = 18.5$ and no reddening. The simulated clusters were all cut at $g \leq 24$ and $\sigma_{g,r,i} \leq 0.1$. These photometric uncertainties were assigned to the synthetic stars following empirical curves as a function of *gri* magnitudes taken from Balbinot et al. (2015). For simplicity, we did not simulate unresolved binaries. We also used a fixed concentration parameter typical of LMC clusters for all the simulations, $\log_{10}(r_t/r_c) = 0.6$ (Werchan & Zaritsky 2011).

We produced sets of clusters with different richness levels, varying the number of stars but keeping tidal radius constant (for a same set of simulations). Each set had six clusters, resulting from the combination of two bins in metallicity (metal-poor, $Z = 0.0002$; and metal-rich, $Z = 0.010$) with three bins in age (young, 1 Gyr; intermediate age, 5 Gyr; and old, 10 Gyr).

All clusters in a set were simulated with a variable number of input stars in GENCMD. The final number depends on several factors, including distance, magnitude and colour cut-offs, photometric errors, age and metallicity. A first set was run for clusters with a total of 1200–5400 input stars following a King profile with $r_t = 94$ arcsec. The number of stars in the output varied from 88 to 151. Fig. 4 presents the results for application of the method for a simulated cluster with $\tau = 5$ Gyr, $Z = 0.010$, $r_c = 20$ arcsec, $r_t = 94$ arcsec and 137 stars, centred in the image centre. The recovered structural parameters are $r_c = 20$ arcsec and $r_t = 96$ arcsec and the best-fitting centre is offsets $\Delta x = 4.3$ arcsec and $\Delta y = 0.6$ arcsec, using the method described above (Section 3). The method is also very efficient in recovering the input isochrone (Fig. 5, upper panels).

To probe the limitations of the methods to cluster richness we simulated additional, poorer clusters. One of these runs simulated six small clusters ($r_t = 48$ arcsec), with 21–38 stars in the output, following the same ratio ρ_c/N (ρ_c = central density and N the cluster total star count). As shown in the bottom panel

[1] https://github.com/balbinot/genCMD

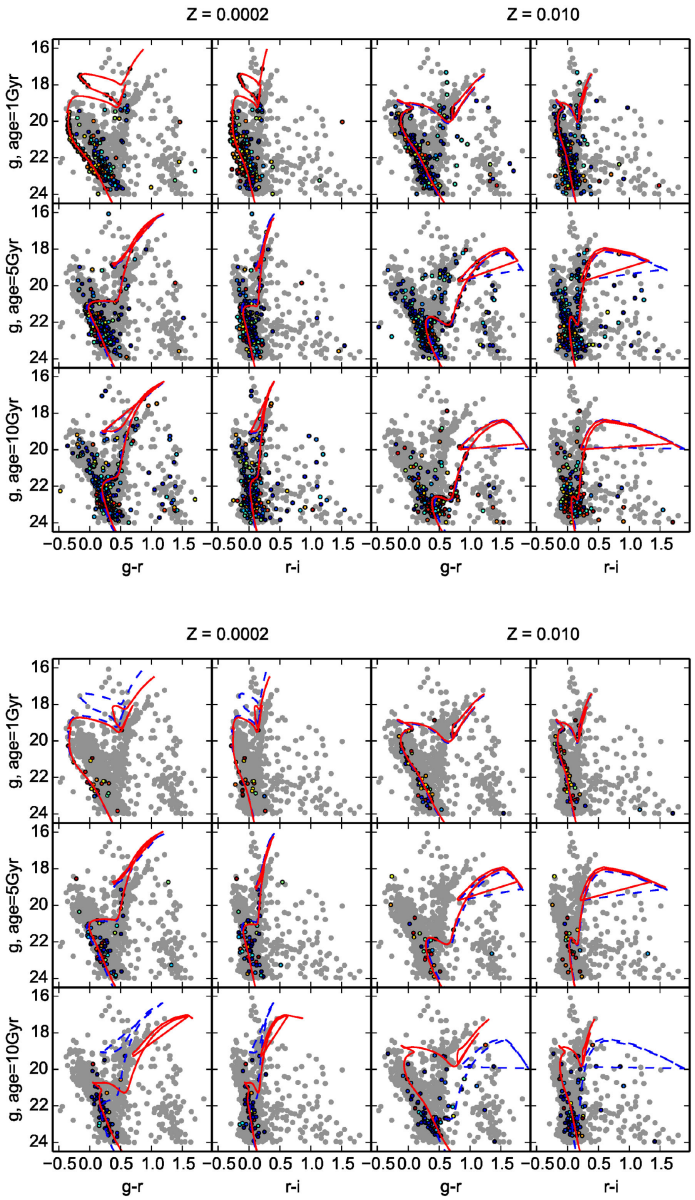

Figure 5. Synthetic CMDs for six clusters inserted in an LMC field in three bands (g, r and i). The clusters are combinations of young (1 Gyr), intermediate age (5 Gyr) and old ages (10 Gyr) with two metallicities ($Z = 0.0002$ and 0.010). Stars whose likelihood to belong to a cluster is greater than 0.05 are shown in colour (and black outline), while background stars are shown in grey. The generating isochrone (dashed blue line) and the recovered isochrone (solid red line) are overlaid to the data. Top: clusters with 88–151 stars. Bottom: clusters with 21–38 stars. The method fails to recover cluster parameters of old and sparse clusters (clusters with 22 and 36 stars, respectively). Young and intermediate age clusters (which represent the majority of LMC clusters sample) are well recovered even for a small number of stars.

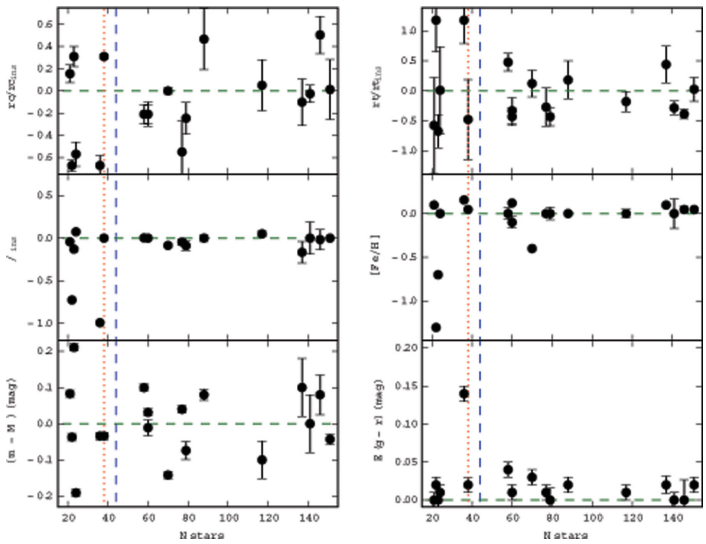

Figure 6. Errors in parameter recovery as a function of number of stars in simulated clusters. Top panels: relative errors in core radius and tidal radius; middle panels: relative errors in age and absolute error in metallicity; bottom panels: errors in distance modulus and $E(g-r)$, in magnitude units. The dashed blue line shows the adopted minimum cluster richness of 44 stars in the actual LMC sample.

of Fig. 5, the method fails to correctly recover the old clusters (which have, respectively, 22 and 36 stars for the low and high metallicities).

The errors in recovering cluster parameters for all our simulated sets are addressed in Fig. 6; we show the relative parameter errors, as well as the estimated uncertainties. For the vast majority of simulated clusters, the figure shows errors of <20 per cent in age and metallicity, <10 per cent in distance, and <0.05 in extinction. The structural parameters are recovered with somewhat larger errors, ≃40 per cent. There is a weak dependence of the error amplitude on cluster richness in most panels. This trend is more visible in the r_t, age and [Fe/H] plots, where errors significantly larger than those quoted above occur for simulated clusters poorer than $N \simeq 40$–50. A similar behaviour is also seen in the CMD fits presented in Fig. 5, as discussed earlier. To prevent lower quality fits from contaminating our results, we adopt a somewhat arbitrary lower limit in richness of $N = 44$ in our LMC sample. We note, however, that we have only 20 clusters (≃17 per cent of the sample) in the range 44–100 stars, and that no visible trend in age, [Fe/H], distance modulus, redenning or structural parameters is seen in this richness range. This renders the results of our upcoming analysis (Section 5.2) robust to the exact richness threshold adopted.

5 DES-SV DATA

In this section, we show the results of our profile and isochrone fitting methods to the sample of LMC clusters. We first carried out the profile fit as described in Section 3.1. Only clusters with a $\mathcal{L}$ peak corresponding to $r_t < 6.5$ arcsec and with a minimum of $N_{star} = 44$ member stars were used in the subsequent analyses. The upper bound in the tidal radius is the size of the co-add image cutout around each cluster candidate. The only exception to this rule is the Reticulum cluster, whose tidal radius is larger than the image cutout size but was kept in our sample for comparison with results from the literature (Section 5.1). The richness criterion is guided by our simulation results, as discussed in Section 4. Of the 255 cluster candidates mentioned in Section 2.2, only 121 had their structural parameters successfully determined by the likelihood fit. Including the Reticulum cluster (122 candidates), the final sample available for isochrone fitting and analysis amounts to 117 clusters. Five clusters have less than the adopted minimum number of member stars and are therefore below the threshold limit.

Fig. 7 presents their on-sky distribution colour coded by their most likely tidal radius.

5.1 Comparison to literature

Before proceeding with an LMC cluster system analysis, we first validated the methods outlined in Section 3 with DES-SV data by comparing our LMC clusters parameters to those found in the literature. Our comparison sample is made up of six relatively rich clusters for which data of comparable or superior quality are available. For NGC 1868 and NGC 2162, there are parameter estimates from more than one source in the literature, while for Hodge 4, ESO 121-03, NGC 2193 and Reticulum cluster only one reference was found. The results are summarized in Table 1 and Fig. 8.

The results listed in Table 1 come from a variety of different methods and data. Most of them are based on CMD analysis, like our own. In this sense, the fits found in previous works are not necessarily more accurate than ours. In particular, none of those papers are based on the same set of PARSEC isochrones used in this work and some of them are not based on optical data, as is the case of Grocholski et al. (2007). These issues, coupled with variations in methodology, are probably the cause of the spread in the parameters from different authors, or even among the same authors, as attested by the compilation of NGC 1868 and NGC 2162 results. Even with this spread, there is a clear correlation

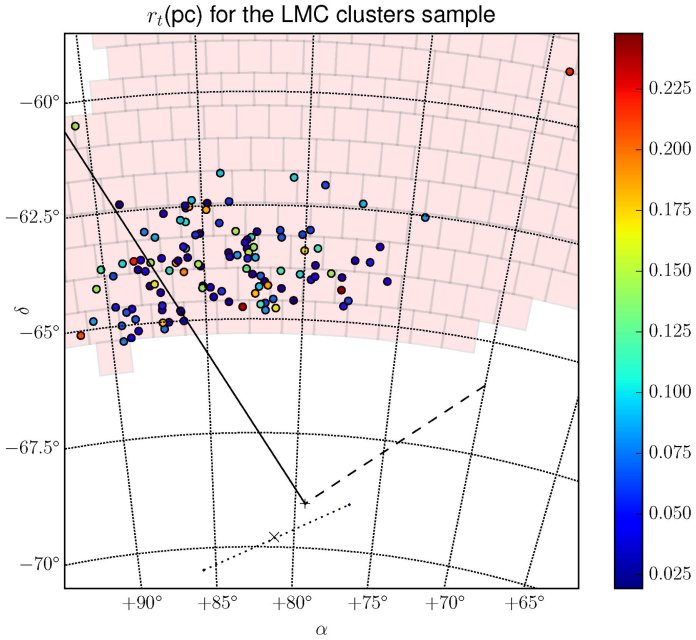

Figure 7. On-sky cluster sample (circles), showing the distribution of tidal radius (in parsecs, colour coded) and the tiles sampled (complete or incompletely) in SV campaign (red boxes). The cross (bottom) indicates the LMC centre as assumed here. The dashed line is the LMC line of nodes and solid line is the maximum gradient distance line. From van der Marel (2001), we present the location of LMC bar (dotted line as the major axis) and its centre ('x') in the maximum star surface density. The Reticulum cluster is the upper rightmost cluster.

between our fits and literature, as one can see in Fig. 8 for all the parameters. Fig. 8 testifies that there is no strong systematic trends in our determinations. Therefore, we conclude that the soundness of our methodology is further corroborated based on these real data comparisons.

For the structural parameters, we had no overlap with the large sample of clusters measured by Werchan & Zaritsky (2011). The only paper with a common sample is Mackey & Gilmore (2003), who measure surface brightness profiles compared to our star density profiles. The authors describe how it is difficult to reconcile their results with density profiles in the literature. A possible explanation for this discrepancy is incompleteness, which affects the density profile much more than surface brightness profiles, since fainter stars have low weight in surface brightness profile while in density profiles all stars have the same weight. The incompleteness severely affects crowded systems, as NGC 1868 and NGC 2162, for which we find core radii 15 and 5 times larger, respectively, than Mackey & Gilmore (2003). For Hodge 4 (a less crowded cluster), this ratio decreases to 3 times larger.

In Fig. 9, we show completeness curves in *gri* bands integrated over the entire cutout of SL 262. We also show completeness curves in the centres of moderately and severely crowded clusters, namely SL 262 and NGC 1868. For that purpose, we picked a square image (54 × 54 arcsec) centred in each cluster. For clarity, curves are only presented for g band, but are similar at other bands. The completeness levels shown correlate well with the strong discrepancies we find with respect to Mackey & Gilmore (2003) and suggests further that incompleteness is the dominant source of these discrepancies. Note that rich clusters which have crowded centres make up about 15 per cent of our sample.

The completeness was estimated in our data by inserting 2.4 × 10^4 artificial stars in 10 realizations of the image in each band (g, r and i) for the two clusters cited above. We then proceeded to reduce the artificial stars in the same manner as the DES-SV data. The inserted stars vary in the range $21.0 \leq g \leq 25.0$. The criteria to recover stars are the same used to classify a source as star: $\mathrm{error}_{g,r,i} \leq 0.1$ and $|\mathrm{sharpness}_{g,r,i}| \leq 1.0$, and a maximum deviation from initial position equal to 0.8 arcsec.

To test whether the differences between our estimate of the core radius and those in the literature might stem from completeness, we used the same maximum likelihood method for the NGC 1868 profile, but selecting only stars with $g < 21.5$. The corresponding core radius using the latter sample (less affected by incompleteness) decreased to 0.58 of the value initially measured (using stars with $g < 24$). The tidal radius increased 10 per cent (certainly due to statistical variations, given the lower star counts in cluster outer regions). We then conclude the completeness is the main cause of difference between our determinations and those from Mackey & Gilmore (2003).

5.2 DES-SV LMC clusters

In this section, we analyse the distribution of LMC clusters as a function of size, age, metallicity and position in space.

Figs 10 and 11 show the results of the ML method for SL126, which is a typical cluster from our sample. Fig. 10 has a clear

Table 1. Table comparing literature data and our determinations. Numbers in superscript indicate the references, while the last line to each cluster shows the values determined in this paper.

Cluster	log(age)	[Fe/H]	$E(g-r)$	$(m-M)_0$	r_c(arcsec)
NGC 1868	8.87 ± 0.10^a				6.67^b
	8.74 ± 0.30^c	-0.50 ± 0.20^d			
	8.95 ± 0.03^e	-0.40 ± 0.10^e			
	8.97 ± 0.04^f	-0.32 ± 0.71^f			
	8.95^g	-0.38^g	0.00^g	18.70^g	
	8.93^h	-0.38^h	0.04^h	18.45^h	
	9.05 ± 0.03^i	-0.70 ± 0.10^i	0.04 ± 0.01^i	18.33 ± 0.06^i	
	9.10 ± 0.01	-0.88 ± 0.04	0.09 ± 0.02	18.35 ± 0.01	99
NGC 2162	8.95 ± 0.10^a				10.13^b
	9.20 ± 0.12^j	-0.40^k			
	9.32 ± 0.06^f	-0.90 ± 0.03^f			
	$9.11^{+0.12l}_{-0.16}$	-0.23 ± 0.20^k			
	9.10 ± 0.03^i	-0.38^i	0.03 ± 0.02^i	18.35 ± 0.08^i	
	9.15^m	-0.46 ± 0.07^m	0.03^m	18.58 ± 0.18^m	
	9.11 ± 0.01	-0.88 ± 0.06	0.08 ± 0.02	18.36 ± 0.01	55
Hodge 4	9.33^m	-0.55 ± 0.06^m	0.04^m	18.37 ± 0.03^m	15.2^b
	9.37 ± 0.02	-0.88 ± 0.06	0.01 ± 0.02	18.53 ± 0.02	50
ESO121-03	9.95^m	-0.91 ± 0.16^m	0.03^m	18.12 ± 0.06^m	
	9.99 ± 0.01	-1.40 ± 0.05	0.07 ± 0.01	18.35 ± 0.01	
NGC 2193	9.30^m	-0.49 ± 0.05^m	0.04^m	18.45 ± 0.04^m	
	9.38 ± 0.01	-0.70 ± 0.04	0.03 ± 0.01	18.35 ± 0.01	
Reticulum cluster		-1.70 ± 0.10^h	0.00^h	18.37 ± 0.07^h	
	$10.11 - 10.18^n$	-1.44^n	0.016^n	18.40^n	
	10.10 ± 0.01	-1.88 ± 0.10	0.00 ± 0.01	18.49 ± 0.01	

[a]Girardi et al. (1995) (CMD fitting),
[b]Mackey & Gilmore (2003) (Surface brightness profiles),
[c]Elson & Fall (1988) (CMD fitting),
[d]Olszewski et al. (1991) (spectroscopy of red giants),
[e]Kerber & Santiago (2005) (HST/CMD fitting),
[f]Leonardi & Rose (2003) (integrated spectra),
[g]Kerber & Santiago (2006) (HST/CMD fitting),
[h]Li, de Grijs & Deng (2014) (CMD fitting and simulations),
[i]Kerber et al. (2007) (HST/CMD fitting),
[j]Piatti et al. (2014) (HST/CMD fitting),
[k]Piatti et al. (2013) (CMD fitting),
[l]Geisler et al. (1997) (CMD fitting),
[m]Grocholski et al. (2007) (RC and CMD fitting),
[n]Kuehn et al. (2013) (Variable stars).

$\log(\mathcal{L})$ maximum for the profile and indicates that we successfully recovered the centre and the structural parameters of this cluster. The CMDs in Fig. 11 are well described by the best-fitting isochrone that resulted from the method described in Section 3.2.

The concentration and $\log_{10}(\frac{\rho_c}{\rho_{bg}})$ histograms are shown in Fig. 12 for all clusters. The concentration distribution is very similar to the one shown by Werchan & Zaritsky (2011, top panel of their fig. 14), which is based on fits to radial luminosity profiles. Both display a broad peak around $c = 0.6$, and another peak at very low concentration values. In our analysis this latter peak is not as pronounced, probably attesting a strong selection bias in favour of clusters with high contrast to background (in this work), which will tend to be more concentrated at a fixed richness. Another reason for this mild discrepancy is that the authors used a radius encompassing 90 per cent of luminosity rather than the tidal radius.

The central density relative background histogram has a peak $\simeq$3.5 times background density. A small number of clusters have densities near the background value; these are mainly located closer to the LMC centre. In contrast, the high values for central densities usually occur for clusters located farther from the LMC centre. The most notable cluster in this sense is the Reticulum cluster, which is located in a region where the stellar density is very low. This cluster does not have a crowded central region, allowing for good photometric parameter estimation.

The age distribution of the LMC clusters in our sample presents two main peaks, at $\sim$1.2 and $\sim$2.7 Gyr. This can be seen in Fig. 13 (top-right panel). The same figure also shows ages as a function of position on the sky (top-left panel) and distance to the LMC centre (r; bottom-left panel). No obvious age gradient is seen in this latter plot.

To assess the significance of the observed bimodality, we carried out Kolmogorov–Smirnov (KS) tests based on the null hypotheses that the observed distribution is either single or doubled peaked. We limited the test to clusters with <4 Gyr (114 clusters from the total of 117 clusters). We fitted the observed age distribution to models with one and two Gaussians. We then created 1000 random

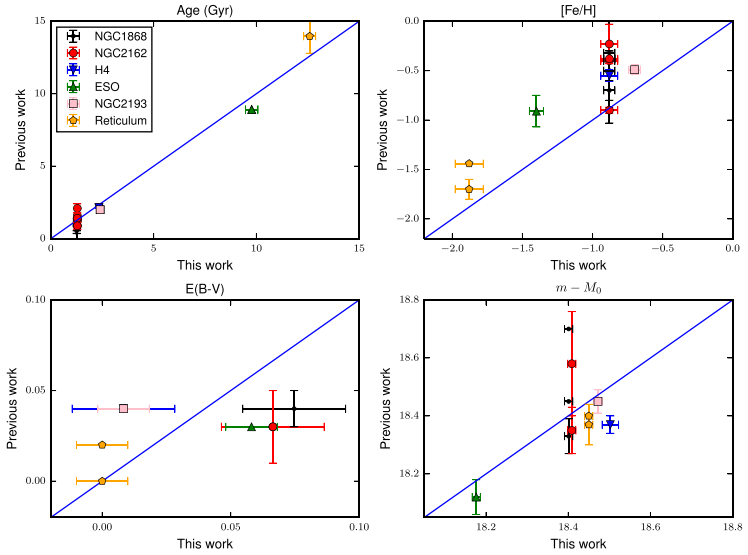

Figure 8. Comparison between our fits and previous works for age (upper left), metallicity (upper right), reddening (lower left) and distance modulus (lower right). The identify line is also plotted. The uncertainties are shown in the cases they were quoted in the references.

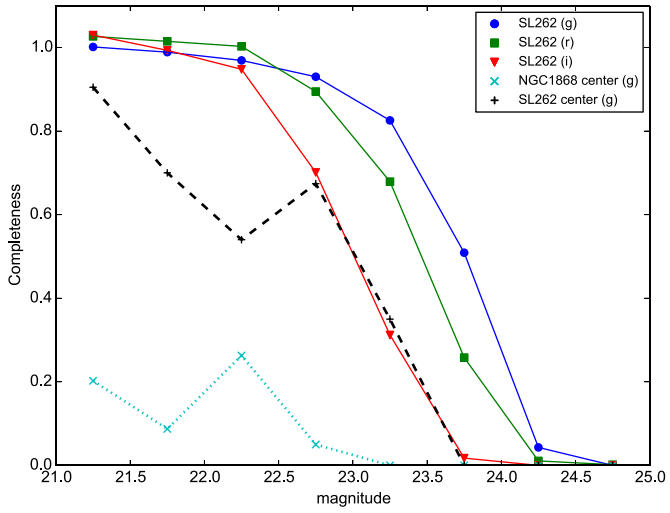

Figure 9. Completeness curves integrated over all positions in the SL 262 cutout ($\simeq$6.6 arcmin) are shown for *g*, *r* and *i* bands (solid lines: circles, squares and triangles, respectively). Completeness covering central regions (a square with 53 $\times$ 53 arcsec) of SL262 (moderate crowding, dashed line and plus symbols) and NGC 1868 (severe crowding, dotted line and cross symbols) is shown just for *g* band as dotted lines, plus and star symbols, respectively.

samples of ages with the same size as the real sample and following each of these models, and applied the KS test comparing each realization to the real distribution. The average result over 1000 realizations indicates that the real clusters do not originate from a unimodal distribution ($\bar{p} = 0.009$ or $\simeq 3\sigma$). Therefore, we can reject the hypothesis that the real age distribution comes from a unimodal distribution.

For the double Gaussian model, the best-fitting age peaks confirm the visual estimates, corresponding to 1.2 and 2.7 Gyr, respectively. And the average *p*-value over 1000 realizations is 0.25, showing that the observed distribution is consistent with the adopted null hypothesis in this case.

The Gaussian mixture model fit indicates two Gaussian for the age distribution (114 clusters with age <4 Gyr) using Bayesian

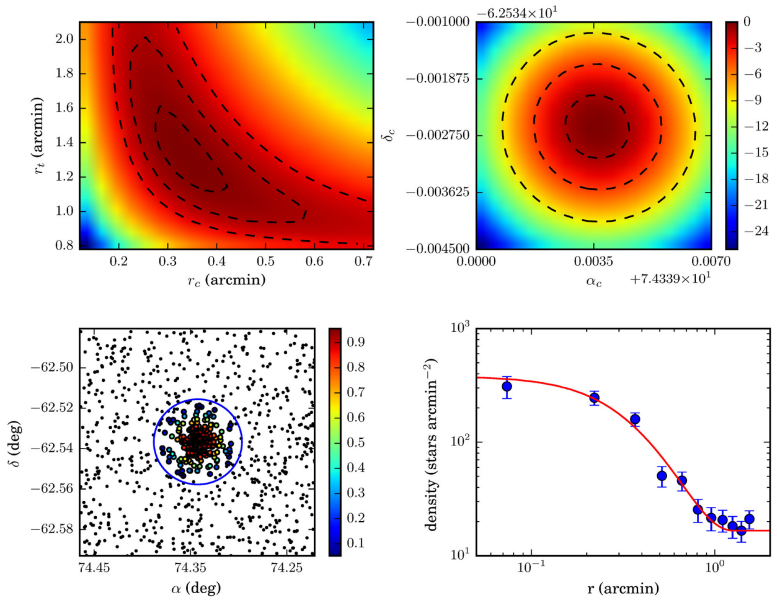

Figure 10. Maximum likelihood method applied to the cluster SL126. The most likely parameters for this cluster are $r_c = 19$ arcsec, $r_t = 79$ arcsec, $\alpha_c = 74.^{\circ}3424$, $\delta = -62.^{\circ}5356$, $k = 0.14$ stars arcsec^{-2}. Top panels: likelihood distribution (normalized by maximum) over r_c and r_t (left) and over cluster centre coordinates (right). Lower left: field stars ($P^{kp} < 0.05$, black dots) and likelihood (colour bar) that each star belongs to the cluster. Lower right: density profile binned in 11 rings (blue dots) and the fitted density profile (solid red line).

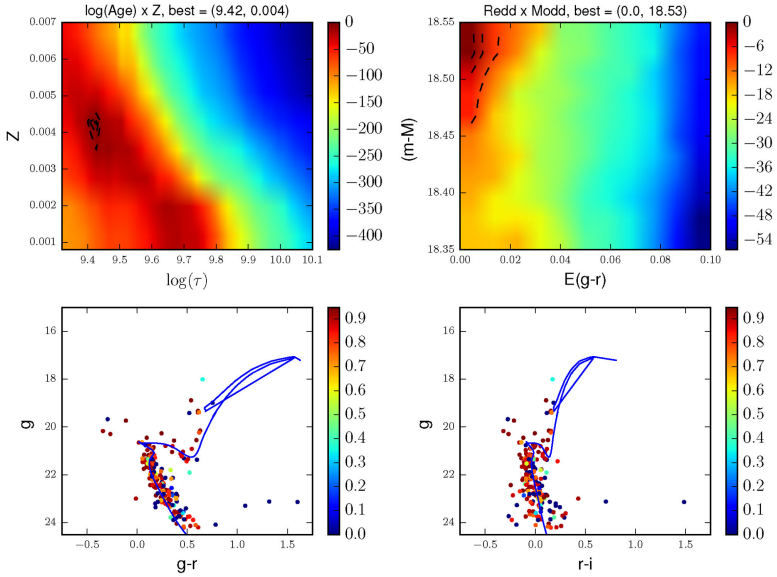

Figure 11. 2 log($\mathcal{L}$) distribution for age and metallicity (top-left panel) and for reddening and distance modulus (top-right panel) for cluster SL 126 (scaled as coded in the colour bars). The bottom panels show g versus $(g - r)$ and g versus $(r - i)$ CMDs. Only stars with membership probability, $P^{kp} > 0.05$, are shown. The best-fitting isochrone (given by MLE) is also overlaid.

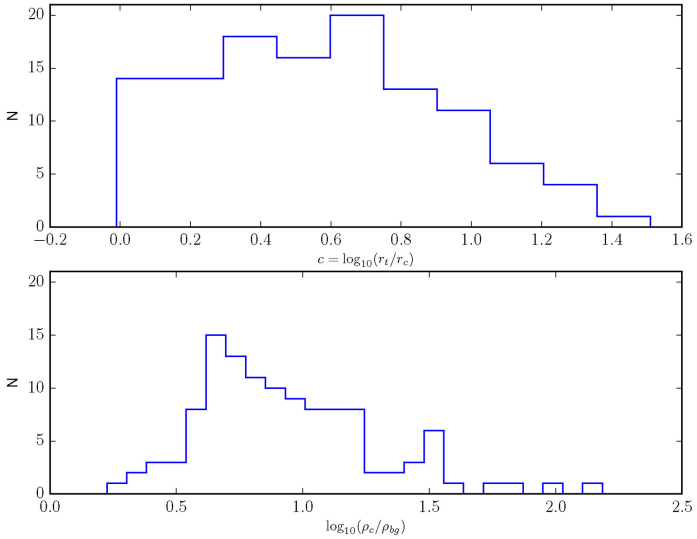

Figure 12. Distribution of concentration parameter (top) and of the logarithm of central density contrast over the background (bottom) for the LMC clusters sample.

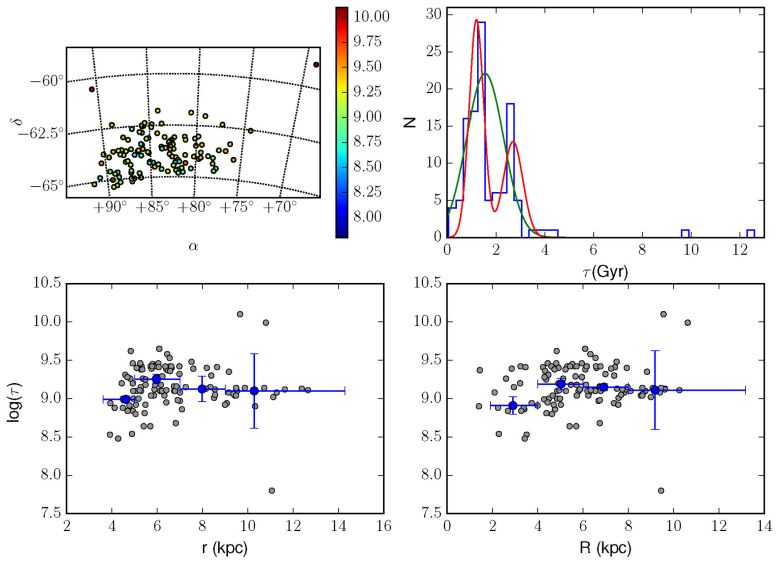

Figure 13. Top left: on-sky cluster distribution colour coded according to log(age). Top right: histogram of cluster ages shown along with unimodal and bimodal Gaussians fitted using the method presented in Ashman, Bird & Zepf (1994). Bottom left: age versus radial distance from LMC centre. Blue circles present the median age in four non-equal subsamples. Horizontal bars indicate the coordinate range. Vertical bars represent the standard deviation in age for each subsample. Bottom right: age versus cylindrical coordinate *R*.

information criteria (BIC). We found relative weights of 0.63 and 0.37 for these Gaussians centred in 1.1 and 2.3 Gyr with standard deviations of 0.4 and 0.6 Gyr, respectively. BIC returns as best values 258.8 for two Gaussians against 268.2 for three and 270.4 for only one Gaussian.

We also tried to follow the recipe in Ashman et al. (1994) to investigate the best-fitting multipeak model for the observed age distribution in the sample. However, our fits for one, two and three Gaussians resulted in different standard deviations: 0.43 and 0.3 Gyr for two peaks, and 0.44, 0.12 and 0.16 Gyr for three peaks. The lack

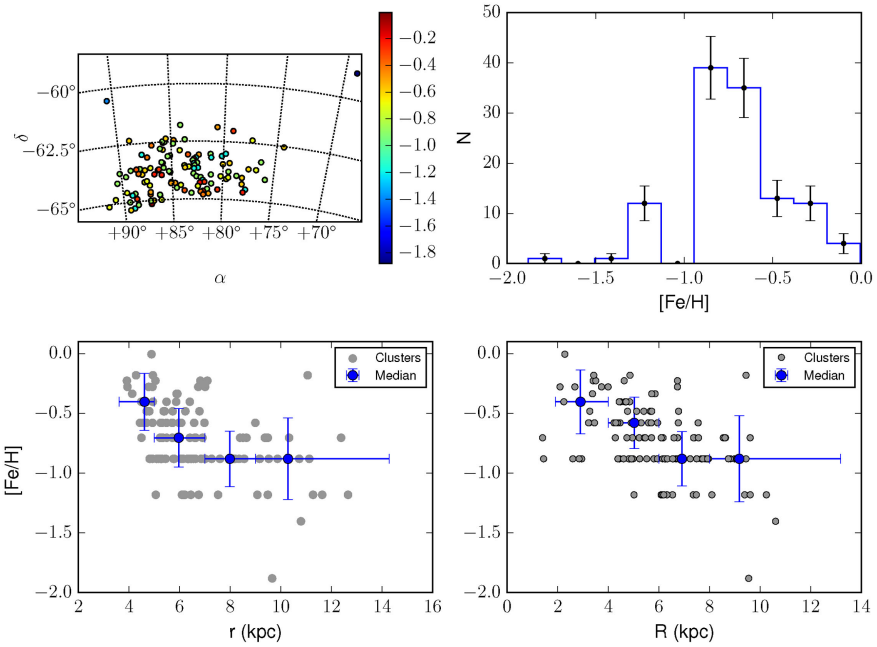

Figure 14. Top left: on-sky cluster metallicity distribution (colour coded). Top right: metallicity histogram. Bottom left: [Fe/H] versus radial distance from LMC centre (grey circles). Filled circles present the median for metallicity, dividing the distance range in four non-equal subsamples (blue dots are placed at each subsample median distance). Vertical bars represent the metallicity dispersion (standard deviation) for each subsample. Horizontal bars are the subsample range in radial coordinate (r or R). Bottom right: metallicity (Fe/H) for cylindrical coordinate R (radial distance projected on disc).

of homoscedastic distributions in the current situation rendered any the results from the method by Ashman et al. (1994) less reliable, as discussed in Ashman et al. (1994) and Nemec & Nemec (1991).

Given the observed bimodality in the age distribution, we split the sample into two classes, of clusters younger and older than 2 Gyr. We calculated a mean r for these two age classes, obtaining $\overline{r} = 6.87$ and 6.42 kpc, respectively.

We also computed cylindrical coordinates of each cluster based on an LMC disc model from Balbinot et al. (2015). These authors fit the DES-SV field stars distribution and derive the disc position angle and inclination with respect to the sky. The LMC centre and heliocentric distances were kept fixed in the fit at $\alpha_0 = 79.^{\circ}40$, $\delta_0 = -69.^{\circ}03$ (Nikolaev et al. 2004) and $D_{\rm LMC} = 49.9$ kpc (de Grijs, Wicker & Bono 2014). To determine the cylindrical coordinates, we used the transformations presented in Weinberg & Nikolaev (2001). In the lower-right panel of Fig. 13, we plot the ages against the R coordinate, along the disc plane, and again infer an essentially flat relation. The $\overline{R}$ values for our two age subsamples are 5.92 and 5.79 kpc for the younger and older clusters, respectively.

Our sample covers an unprecedented range in distances from the LMC (from $\simeq$4 kpc out to $\simeq$13 kpc), reaching out to previously unexplored outer LMC regions. The clusters age distribution presented here is complementary to that shown by Piatti & Geisler (2013), who study field stars in regions corresponding to deprojected distances in the range from $\simeq$0.5 kpc out to $\simeq$8 kpc. Those authors favour an outside-in star formation in the sense that old (and metal-poor) stars tend to be located in the outer disc, whereas younger stars (also more metal-rich) tend to inhabit the inner LMC regions. This age trend with distance, however, is largely restricted to the inner 4 kpc. Beyond that, their relation between age and distance is flat, similar to what is found with the LMC clusters studied here.

Fig. 14 shows similar plots for metallicity. Most clusters in our sample are metal poor $Z < 0.004$ ([Fe/H] < -0.7) as Fig. 14 shows in upper-right panel. Unlike age, there is a clear trend in metallicity as a function of distance from the LMC centre (bottom panels). The two-sided p-value for a statistical hypothesis test (whose null hypothesis is that the slope is zero) is 10^{-8} for R and 10^{-6} for r. We conclude we can reject the null hypothesis.

The median metallicity systematically drops by a factor of $\simeq$2 from $r = 5$ to 10 kpc. Clusters with $-1.5 <$(Fe/H)< -1.0 are distributed over the entire radial distance range. On the other hand, $Z > 0.005$ clusters ([Fe/H] > -0.6) are only found for $r < 8$ kpc. A larger metallicity spread in inner fields has also been found by Piatti & Geisler (2013) for LMC field star population. However, for the range of distances in common with their study, our results are in disagreement in the sense that the clusters have a larger spread than the field stars at a fixed distance from the LMC centre.

The AMR is plotted in Fig. 15, where we compare the AMR from our data (blue filled dots) to the one from Piatti & Geisler (2013, open boxes for LMC field stars and filled boxes for LMC clusters). In general, the AMR from those authors corresponds to an upper envelope to the cluster AMR presented here. In particular, our sample includes young clusters with a very large range in metallicities, reaching down to [Fe/H] $\simeq -1.2$. These are mainly the clusters belonging to the 1.2 Gyr age peak. This young and metal-poor sample is consistent with a recent cluster formation epoch in the outer

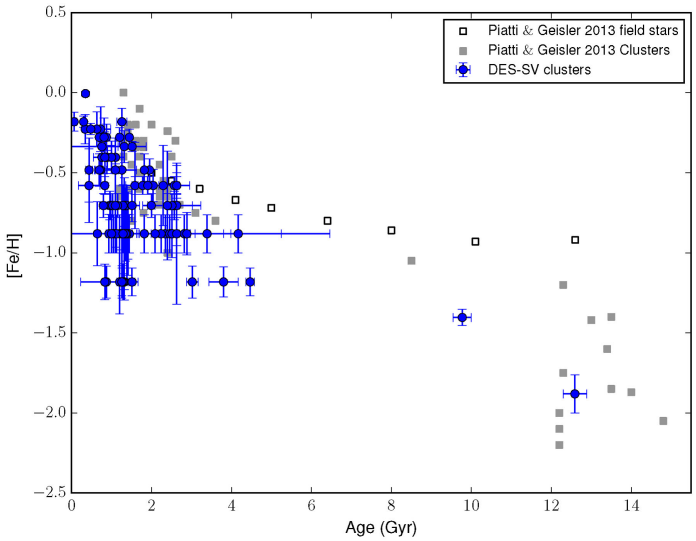

Figure 15. AMR for LMC clusters sample (filled circles). Open boxes (field) and filled boxes (clusters) are from Piatti & Geisler (2013, fig. 6 in that paper).

regions of the LMC sampled in this paper, contrasting a relative low SFR in these areas (Meschin et al. 2014). This large spread at relatively young ages contrasts with the lack of metal-rich clusters at larger ages.

Our results are in agreement with Livanou et al. (2013), who analysed a sample of 15 LMC clusters spread all over the galaxy. On the other hand, the field stars AMR relation from Carrera et al. (2011) lead to higher metallicities at a fixed age than those typically inferred for our sample of outer LMC clusters, at least for ages >3 Gyr. The discrepancy is not caused by the different ranges in distance to the LMC centre, since most of our clusters are closer to 8 kpc, similarly to their sample. This is another example of a discrepancy between results based on field and cluster stars.

In Fig. 16, we compare the AMR for our sample of outer LMC star clusters to the most accepted models used in literature for the LMC chemical evolution. Briefly, the model from Pagel & Tautvaisiene (1998) is based on a bursting model assuming a constant star formation rate for clusters in the range 1.6 $<\tau<$3.2 Gyr. In that model, the metallicity increases for clusters younger than 1.6 Gyr and this feature reasonably describes the upper metallicity limit for the younger clusters studied here, as well as the old and most metal-poor clusters. The Harris & Zaritsky (2009) model is based on the STARFISH analysis code, using bright field stars. Their results describe an initial burst of star formation and a quiescent epoch from approximately 12 to 5 Gyr ago. Star formation then resumed and has proceeded until the current time at an average rate of roughly 0.2 $M_\odot$ yr^{-1}. Among the global variations in the recent star formation rate they identify peaks at roughly 2 Gyr, 500, 100 and 12 Myr. This latter model better represents the younger clusters in our sample. Palma et al. (2015) study a sample of clusters located in an inner LMC region and whose AMR is bracketed by the two models. Those authors argue that a combination of both models is a more adequate description of their sample than a single model. Our sample, on the other hand, shows a sizable fraction of relatively young clusters with lower metallicities than predicted by either model.

Fig. 17 shows the results for the reddening values obtained from the ML fits. The sample of clusters is systematically decreasing towards larger extinction. The majority of the clusters have $E(g-r)\leq$0.10. Using the maps from Schlegel, Finkbeiner & Davis (1998) and the reddening law from Cardelli et al. (1989), the typical values towards these clusters are in the range 0.04 $\leq E(g-r)\leq$0.10, which is in general agreement with the fitted values. There is no strong trend in $E(g-r)$ values with distance from the LMC centre.

6 DISCUSSION AND SUMMARY

Here we summarize our main results.

(i) We scanned the DES-SV images to search for stellar overdensities in fields close to the LMC, identifying 255 cluster candidates. We catalogued and matched this sample to the star clusters catalogue from Bica et al. (2008), adding clusters already discovered and identifying unknown clusters. We used DES-SV co-add images in *g, r* and *i* bands to make square cutouts (with 6.75 arcmin on a side) around each candidate.

(ii) We found that stellar completeness in DES-SVA1 catalogue is a strong function of source density, sharply dropping to <0.1 for surface densities >260 stars arcmin^{-2}. The DES-SVA1 stellar sample is very incomplete in crowded fields, such as those close to centres of rich LMC star clusters, where DESDM detects less than 50 per cent of the objects detected by DAOPHOT.

(iii) To reduce stellar incompleteness in crowded fields, we developed a pipeline to reduce data using DAOPHOT. The pipeline combines *g* and *r* images and runs PSF selection and photometry in a largely automatic way. Using stars with good photometry in both catalogues, we compared the final DAOPHOT magnitudes to DES-SVA1, determining a zero-point. The agreement is very good and on average DES-SVA1 and DAOPHOT photometry agree within

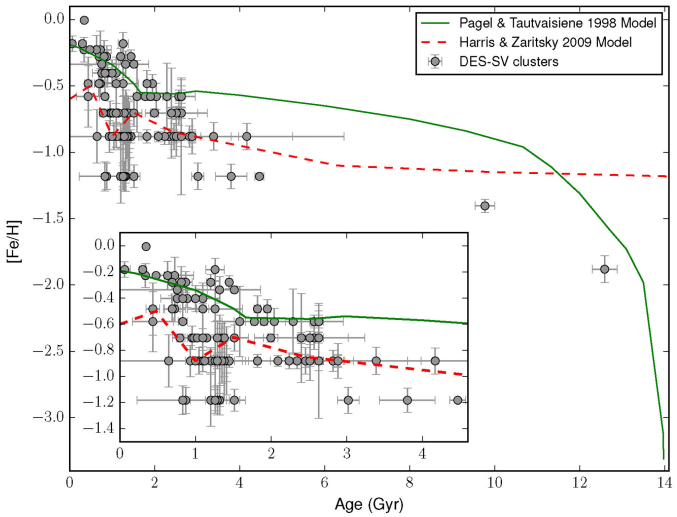

Figure 16. Two models for the LMC chemical evolution history are compared to the AMR for outer LMC clusters (filled circles). The model from Harris & Zaritsky (2009) is shown as a dashed red line, whereas the solid green line shows the Pagel & Tautvaisiene (1998) model. Box: zoom in over the region indicated, showing the young and metal-rich clusters compared to both models.

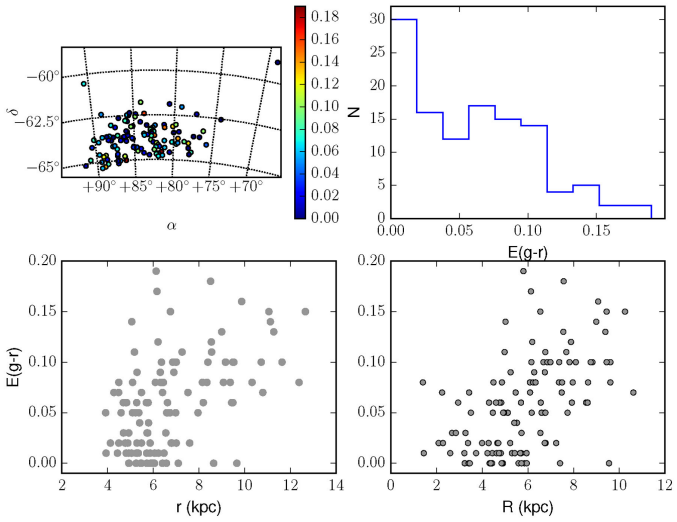

Figure 17. Top left: on-sky cluster distribution colour coded according to $E(g-r)$. Top right: distribution of $E(g-r)$. Bottom: reddening versus radial distance from LMC centre (left) and versus cylindrical coordinate R (radial distance projected on disc) at right.

0.02 in three bands, without the need for a colour term. We selected stars as sources from DAOPHOT reductions with g,r,i errors <0.1 and $|\mathrm{sharpness}_{g,r,i}|$ <1.

(iv) We applied a maximum likelihood estimation approach to fit the stellar density profile to a King model (King 1962), following a recipe similar to that of Martin et al. (2008). This method is robust to determine centre position, core and tidal radii. As output, for each cluster candidate we listed the stars within the tidal radius, along with their probability to belong to cluster candidate (P^{kp}). From the initial sample containing 255 cluster candidates, only 121 had their structural parameters successfully determined by the profile likelihood fit.

(v) We compared the stars with P^{kp} >0.05 to Bressan et al. (2012) isochrones, varying reddening and distance moduli in a two-step refined grid search. The final grid allows a more refined scan of parameters space around the MLE peak given by the initial grid.

The uncertainties are estimated from the likelihood distribution around peak. We used the results from this method for both global and structural parameters.

(vi) We tested our inference methods, by inserting simulated cluster stars (using GENCMD) in a typical LMC field and proceeding through the same steps as for real clusters. We varied the input number of simulated stars, reaching a minimal number of $\simeq$40–50 cluster stars necessary to recover the generating isochrone. When a threshold on the minimum number of stars is applied, the LMC cluster sample decreases from 121 to 117 clusters, which is the final number of clusters used in the analysis.

(vii) We compared our method to results from data from the literature. The agreement is usually within the uncertainties, with a few exceptions in distance modulus, metallicity and core radii, and an excellent agreement for ages and reddenings. None of the comparison papers from the literature are based on the same set of PARSEC isochrones used in this work or even in optical data. These issues and the variations in methodology, are probably the cause of the discrepancy in the parameters from different authors. Given we are dealing with a homogeneous photometric sample, we conclude that our method is corroborated based on these real data comparisons (literature and our results).

(viii) The cluster age distribution presents two main peaks in 1.2 and 2.7 Gyr. We run statistical KS tests to probe the bimodality significance. The tests confirm that a two-peaked age distribution is more consistent with the observed distribution, and rule out that the data follow a single peak age distribution. Splitting the sample in clusters younger and older than 2 Gyr and calculating a mean radial distance to each subsample, the difference is not sensitive whether considering $\bar{R}$ (5.92 and 5.79 kpc) or $\bar{r}$ (6.87 and 6.46 kpc). This conclusion agrees to Piatti & Geisler (2013), who found a flat age-distribution for fields with radial distances >4 kpc.

(ix) Metallicity presents a clearer radial trend, both in terms of the average metallicity or its dispersion. Metal-rich clusters ([Fe/H] >-0.6) are concentrated within $r<8$ kpc, whereas the most metal-poor clusters are found over the entire distance range.

(x) The AMR for LMC clusters differs from LMC field stars AMR (from Piatti & Geisler 2013) in the sense that the latter form an upper envelope in metallicity for age distribution. The same feature is shown in Livanou et al. (2013), as the presence of young clusters (1 Gyr) filling the range from most metal rich down to [Fe/H] $\simeq-1.2$.

(xi) Regarding the LMC chemical evolution model, our sample shows more young metal-poor clusters than are predicted by the models of Pagel & Tautvaisiene (1998) and Harris & Zaritsky (2009). Apart from this, our results are in broader agreement with the models.

The discovery of 28 previously uncatalogued clusters (with profiles and models determined here) is proof that the list of LMC clusters is not complete, mainly in its less scrutinized outskirts.

It is expected that the final DES release will provide deeper photometry, reaching further into the clusters' MS and decreasing uncertainties for their SubGiant Branch and RGB stars, even the final release footprint will not cover same SV footprint. We plan to explore these data in greater depth, extracting more information about the LMC clusters, including the identification of extended main-sequence turnoffs, modelling binarism, better constraining their shapes and assessing the correlations among different cluster properties.

The cluster (and star) formation rate may be enhanced by tidal gravitational interactions (in this case, SMC-LMC or Galaxy-LMC). While the gravitational interaction between the Galaxy and the LMC is a controversial issue (see for example Kroupa & Bastian 1997; Kallivayalil et al. 2013), there is a consensus for the SMC-LMC orbit period being $\simeq$2 Gyr. In this sense, the age distribution of clusters as shown in Fig. 13 favours a strong gravitational interaction that occurred 1.5 Gyr ago, coinciding with the SMC-LMC pericentric passage predicted by the 'best orbital model' described in Bekki & Chiba (2005). The secondary peak at 3 Gyr is less pronounced, likely as a result of clusters disruption effects. Therefore, the relative peak heights provide an estimate of the half-life for these outer LMC clusters. As for the older clusters, they may result from processes taking place during the early evolution of the host. A problem of this scenario is that the metallicity predicted for clusters in the aforementioned simulations (where clusters formed from gas clouds pre-enriched by the formation of field stars) is higher than for LMC field stars, which is in disagreement with the results presented here. This discrepancy may be attenuated considering an inefficient gas mixing at the LMC outskirts.

Other photometric surveys are currently focused on the Magellanic Clouds, such as the Vista Magellanic Survey (Cioni & the VMC team 2015) and the Survey of the Magellanic Stellar History (Nidever & Smash Team 2015). Merging these data sets should result in a more complete picture of the Magellanic star clusters system and outer stellar populations. As these more remote regions should be strongly affected by the gravitational interaction involving the Galaxy, the LMC, the SMC and other dwarf galaxies sharing similar orbits and location, these combined surveys should be useful constraints to *N*-body simulations describing the origin and evolution of the Magellanic System.

ACKNOWLEDGEMENTS

We would like to thank the anonymous referee for many useful suggestions. This paper has gone through internal review by the DES collaboration.

AdP acknowledges financial support from the Brazilian Institution CNPq. EdB acknowledges financial support from the European Research Council (ERC-StG-335936, CLUSTERS).

We are grateful for the extraordinary contributions of our CTIO colleagues and the DECam Construction, Commissioning and Science Verification teams in achieving the excellent instrument and telescope conditions that have made this work possible. The success of this project also relies critically on the expertise and dedication of the DES Data Management group.

Funding for the DES Projects has been provided by the US Department of Energy, the US National Science Foundation, the Ministry of Science and Education of Spain, the Science and Technology Facilities Council of the United Kingdom, the Higher Education Funding Council for England, the National Center for Supercomputing Applications at the University of Illinois at Urbana-Champaign, the Kavli Institute of Cosmological Physics at the University of Chicago, the Center for Cosmology and Astro-Particle Physics at the Ohio State University, the Mitchell Institute for Fundamental Physics and Astronomy at Texas A&M University, Financiadora de Estudos e Projetos, Fundação Carlos Chagas Filho de Amparo à Pesquisa do Estado do Rio de Janeiro, Conselho Nacional de Desenvolvimento Científico e Tecnológico and the Ministério da Ciência, Tecnologia e Inovação, the Deutsche Forschungsgemeinschaft and the Collaborating Institutions in the Dark Energy Survey.

The Collaborating Institutions are Argonne National Laboratory, the University of California at Santa Cruz, the University of Cambridge, Centro de Investigaciones Enérgeticas,

Medioambientales y Tecnológicas-Madrid, the University of Chicago, University College London, the DES-Brazil Consortium, the University of Edinburgh, the Eidgenössische Technische Hochschule (ETH) Zürich, Fermi National Accelerator Laboratory, the University of Illinois at Urbana-Champaign, the Institut de Ciències de l'Espai (IEEC/CSIC), the Institut de Física d'Altes Energies, Lawrence Berkeley National Laboratory, the Ludwig-Maximilians Universität München and the associated Excellence Cluster Universe, the University of Michigan, the National Optical Astronomy Observatory, the University of Nottingham, The Ohio State University, the University of Pennsylvania, the University of Portsmouth, SLAC National Accelerator Laboratory, Stanford University, the University of Sussex and Texas A&M University.

The DES data management system is supported by the National Science Foundation under Grant Number AST-1138766. The DES participants from Spanish institutions are partially supported by MINECO under grants AYA2012-39559, ESP2013-48274, FPA2013-47986 and Centro de Excelencia Severo Ochoa SEV-2012-0234. Research leading to these results has received funding from the European Research Council under the European Union's Seventh Framework Programme (FP7/2007-2013) including ERC grant agreements 240672, 291329 and 306478.

REFERENCES

Alves D. R., Nelson C. A., 2000, ApJ, 542, 789
Annunziatella M., Mercurio A., Brescia M., Cavuoti S., Longo G., 2013, PASP, 125, 68
Ashman K. M., Bird C. M., Zepf S. E., 1994, AJ, 108, 2348
Balbinot E., Santiago B. X., Girardi L., da Costa L. N., Maia M. A. G., Pellegrini P. S. S., Makler M., 2012, in Ballester P., Egret D., Lorente N. P. F., eds, ASP Conf. Ser. Vol. 461, Astronomical Data Analysis Software and Systems XXI. Astron. Soc. Pac., San Francisco, p. 287
Balbinot E. et al., 2015, MNRAS, 449, 1129
Bekki K., Chiba M., 2005, MNRAS, 356, 680
Bertin E., 2011, in Evans I. N., Accomazzi A., Mink D. J., Rots A. H., eds, ASP Conf. Ser. Vol. 442, Astronomical Data Analysis Software and Systems XX. Astron. Soc. Pac., San Francisco, p. 435
Bertin E., Arnouts S., 1996, A&AS, 117, 393
Bica E., Bonatto C., Dutra C. M., Santos J. F. C., 2008, MNRAS, 389, 678
Bressan A., Marigo P., Girardi L., Salasnich B., Dal Cero C., Rubele S., Nanni A., 2012, MNRAS, 427, 127
Caldwell J. A. R., Coulson I. M., 1986, MNRAS, 218, 223
Cardelli J. A., Clayton G. C., Mathis J. S., 1989, ApJ, 345, 245
Carrera R., Gallart C., Hardy E., Aparicio A., Zinn R., 2008, AJ, 135, 836
Carrera R., Gallart C., Aparicio A., Hardy E., 2011, AJ, 142, 61
Cioni M.-R. L., the VMC team 2015, preprint (arXiv:1503.06972)
de Grijs R., Wicker J. E., Bono G., 2014, AJ, 147, 122
Desai S. et al., 2012, ApJ, 757, 83
Elson R. A., Fall S. M., 1988, AJ, 96, 1383
Fisher R. A., 1956, Statistical Methods and Scientific Inference. Oliver and Boyd, Edinburgh, UK
Flaugher B. et al., 2015, AJ, 150, 150
Geisler D., Bica E., Dottori H., Claria J. J., Piatti A. E., Santos J. F. C., Jr, 1997, AJ, 114, 1920
Geisler D., Grocholski A. J., Sarajedini A., Cole A. A., Smith V. V., 2007, in Combes F., Palous J., eds, Proc. IAU Symp. 235, Galaxy Evolution Across the Hubble Time. Cambridge Univ. Press, Cambridge, p. 92
Girardi L., Chiosi C., Bertelli G., Bressan A., 1995, A&A, 298, 87
Girardi L., Bertelli G., Bressan A., Chiosi C., Groenewegen M. A. T., Marigo P., Salasnich B., Weiss A., 2002, A&A, 391, 195
Glatt K., Grebel E. K., Koch A., 2010, A&A, 517, AA50
Gordon K. D., Clayton G. C., Misselt K. A., Landolt A. U., Wolff M. J., 2003, ApJ, 594, 279
Grocholski A. J., Sarajedini A., Olsen K. A. G., Tiede G. P., Mancone C. L., 2007, AJ, 134, 680
Harris J., Zaritsky D., 2009, AJ, 138, 1243
Indu G., Subramaniam A., 2011, A&A, 535, A115
Kallivayalil N., van der Marel R. P., Besla G., Anderson J., Alcock C., 2013, ApJ, 764, 161
Kerber L. O., Santiago B. X., 2005, A&A, 435, 77
Kerber L. O., Santiago B. X., 2006, A&A, 452, 155
Kerber L. O., Santiago B. X., Brocato E., 2007, A&A, 462, 139
Kharchenko N. V., Piskunov A. E., Schilbach E., Röser S., Scholz R.-D., 2012, A&A, 543, A156
King I., 1962, ApJ, 67, 471
Kontizas M., Kontizas E., Michalitsianos A. G., 1993, A&A, 269, 107
Kroupa P., 2001, MNRAS, 322, 231
Kroupa P., Bastian U., 1997, New Astron., 2, 77
Kuehn C. A. et al., 2013, AJ, 145, 160
Lejeune T., Schaerer D., 2001, A&A, 366, 538
Leonardi A. J., Rose J. A., 2003, AJ, 126, 1811
Li C., de Grijs R., Deng L., 2014, ApJ, 784, 157
Livanou E., Dapergolas A., Kontizas M., Nordström B., Kontizas E., Andersen J., Dirsch B., Karampelas A., 2013, A&A, 554, A16
Lupton R., 1993, Statistics in Theory and Practice. Princeton Univ. Press, Princeton, NJ
Mackey A. D., Gilmore G. F., 2003, MNRAS, 338, 85
Martin N. F., de Jong J. T. A., Rix H.-W., 2008, ApJ, 684, 1075
Meschin I., Gallart C., Aparicio A., Hidalgo S. L., Monelli M., Stetson P. B., Carrera R., 2014, MNRAS, 438, 1067
Miocchi P. et al., 2013, ApJ, 774, 151
Mohr J. J. et al., 2012, in Radziwill N. M., Chiozzi G., eds, Proc. SPIE Conf. Ser. Vol. 8451, Software and Cyberinfrastructure for Astronomy II. SPIE, Bellingham, p. 84510D
Nemec J., Nemec A. F. L., 1991, PASP, 103, 95
Nidever D., Smash Team 2015, in Points S., Kunder A., eds, ASP Conf. Ser. Vol. 491, Fifty Years of Wide Field Studies in the Southern Hemisphere: Resolved Stellar Populations of the Galactic Bulge and Magellanic Clouds. Astron. Soc. Pac., San Francisco, p. 325
Nikolaev S., Drake A. J., Keller S. C., Cook K. H., Dalal N., Griest K., Welch D. L., Kanbur S. M., 2004, ApJ, 601, 260
Olsen K. A. G., Salyk C., 2002, AJ, 124, 2045
Olszewski E. W., Schommer R. A., Suntzeff N. B., Harris H. C., 1991, AJ, 101, 515
Pagel B. E. J., Tautvaisiene G., 1998, MNRAS, 299, 535
Palma T., Clariá J. J., Geisler D., Gramajo L. V., Ahumada A. V., 2015, MNRAS, 450, 2122
Piatti A. E., Geisler D., 2013, AJ, 145, 17
Piatti A. E., Keller S. C., Mackey A. D., Da Costa G. S., 2013, Bol. Asoc. Argentina Astron., 56, 275
Piatti A. E., Keller S. C., Mackey A. D., Da Costa G. S., 2014, MNRAS, 444, 1425
Schlegel D. J., Finkbeiner D. P., Davis M., 1998, ApJ, 500, 525
Sprott D. A., 2000, Statistical Inference in Science. Springer, Berlin,
Stetson P. B., 1987, PASP, 99, 191
Subramanian S., Subramaniam A., 2010, A&A, 520, A24
The Dark Energy Survey Collaboration 2005, preprint (astro-ph/0510346)
Weinberg M. D., Nikolaev S., 2001, ApJ, 548, 712
Weisz D. R., Dolphin A. E., Skillman E. D., Holtzman J., Dalcanton J. J., Cole A. A., Neary K., 2013, MNRAS, 431, 364
Werchan F., Zaritsky D., 2011, AJ, 142, 48

APPENDIX A: CLUSTERS LIST

We append the list of clusters for which we fit profiles and isochrones. We match cluster centroids (columns 2 and 3) to Bica et al. (2008) within a radius of 1 arcmin. The name of the nearest match is listed in column (1). In the case there are more than one object in the match, we assigned the nearest object. Columns (4) and (5) are the King profile core and tidal radius. Concentration $[c = \log(r_t/r_c)]$ is listed in column (6). The age, metallicity, reddening and distance modulus are listed in the remaining columns, along with their associated uncertainties (for a 68 per cent confidence level).

Cluster name	α_c	δ_c	r_c(arcmin)	r_t(arcmin)	c	Age(Gyr)	Fe/H	$E(g-r)$	$m-M_0$
Reticulum cluster	69.042 30	−58.859 67	1.94 ± 0.01	3.40 ± 0.01	0.24	12.59 ± 0.29	−1.88 ± 0.12	0.00 ± 0.01	18.49 ± 0.01
SL126,ESO85SC21,KMHK322	74.342 42	−62.535 62	0.31 ± 0.02	1.31 ± 0.35	0.63	2.63 ± 0.06	−0.58 ± 0.06	0.00 ± 0.01	18.53 ± 0.01
DES001SC01	75.818 22	−64.029 76	0.18 ± 0.03	0.72 ± 0.73	0.59	2.82 ± 0.13	−0.88 ± 0.12	0.04 ± 0.02	18.32 ± 0.05
SL214,LW130,ESO85SC41,KMHK512	76.351 51	−63.287 54	0.50 ± 0.05	0.75 ± 0.48	0.17	1.20 ± 0.03	−0.88 ± 0.12	0.10 ± 0.01	18.12 ± 0.01
SL233,ESO85SC45,KMHK543	76.766 07	−63.647 70	0.42 ± 0.03	0.99 ± 0.28	0.37	2.57 ± 0.06	−0.70 ± 0.09	0.00 ± 0.02	18.14 ± 0.04
SL262,LW146,ESO119SC40,KMHK582	77.340 28	−62.379 69	0.56 ± 0.03	1.49 ± 0.23	0.42	2.63 ± 0.06	−0.70 ± 0.08	0.01 ± 0.01	18.45 ± 0.01
SL273,KMHK597	77.474 75	−63.638 29	0.36 ± 0.03	0.61 ± 0.34	0.23	1.58 ± 0.07	−0.58 ± 0.06	0.00 ± 0.01	18.42 ± 0.02
DES001SC02	77.709 62	−64.528 80	0.42 ± 0.10	1.24 ± 0.34	0.47	0.87 ± 0.64	−1.18 ± 0.10	0.08 ± 0.01	18.09 ± 0.16
BSDL818	77.925 11	−64.653 23	0.17 ± 0.07	0.74 ± 0.80	0.64	0.72 ± 0.25	−0.23 ± 0.14	0.00 ± 0.10	18.73 ± 0.18
SL303,LW158,KMHK644	78.085 93	−64.303 82	0.36 ± 0.05	3.67 ± 0.17	1.01	2.63 ± 0.06	−0.58 ± 0.08	0.00 ± 0.01	18.62 ± 0.04
DES001SC03	78.102 03	−64.027 77	0.27 ± 0.06	0.65 ± 0.52	0.38	0.83 ± 0.06	−0.58 ± 0.06	0.13 ± 0.01	18.11 ± 0.13
NGC1868,SL330,LW169,ESO85SC56,	78.652 51	−63.957 14	1.65 ± 0.01	2.35 ± 0.01	0.15	1.26 ± 0.03	−0.88 ± 0.12	0.09 ± 0.02	18.35 ± 0.01
ESO119SC50,KMHK705	79.173 49	−62.023 92	0.12 ± 0.02	1.10 ± 0.60	0.94	1.45 ± 0.03	−0.28 ± 0.05	0.05 ± 0.01	18.34 ± 0.04
SL354,LW177,ESO85SC63,KMHK712	79.384 39	−63.420 73	0.89 ± 0.08	1.79 ± 0.12	0.30	2.63 ± 0.06	−0.58 ± 0.06	0.01 ± 0.01	18.39 ± 0.01
H88-257,H80F4-6	79.453 94	−64.044 71	0.22 ± 0.05	0.75 ± 0.53	0.52	2.63 ± 0.61	−0.70 ± 0.25	0.05 ± 0.03	18.25 ± 0.01
H88-258,H80F4-7,KMHK720	79.465 27	−63.795 10	0.39 ± 0.05	0.71 ± 0.48	0.26	1.05 ± 0.07	−0.88 ± 0.12	0.14 ± 0.01	17.99 ± 0.07
SL372,LW180,KMHK730	79.659 56	−64.112 18	0.71 ± 0.13	1.06 ± 0.46	0.17	1.35 ± 0.06	−0.70 ± 0.11	0.08 ± 0.06	17.90 ± 0.02
NGC1900,SL376,LW184,ESO85SC68,	79.740 75	−63.024 12	0.49 ± 0.05	1.30 ± 0.04	0.43	1.32 ± 0.09	−1.18 ± 0.11	0.10 ± 0.01	17.97 ± 0.01
SL388,LW186,ESO85SC72,KMHK773	80.023 39	−63.480 33	0.54 ± 0.03	2.55 ± 0.14	0.68	2.57 ± 0.06	−0.58 ± 0.06	0.00 ± 0.01	18.61 ± 0.02
OHSC10,KMHK782	80.162 00	−63.135 00	0.17 ± 0.04	1.30 ± 0.56	0.89	1.20 ± 0.03	−1.18 ± 0.20	0.13 ± 0.01	17.99 ± 0.01
SL401,LW190,KMHK791	80.209 39	−64.003 91	0.28 ± 0.03	1.74 ± 0.36	0.80	2.40 ± 0.06	−0.70 ± 0.08	0.07 ± 0.01	18.27 ± 0.03
KMHK815	80.492 40	−64.598 99	0.35 ± 0.06	0.36 ± 0.14	0.02	0.87 ± 0.08	−0.28 ± 0.08	0.01 ± 0.02	18.46 ± 0.15
LW195,ESO119SC61,KMHK821	80.647 59	−61.879 43	0.33 ± 0.03	1.59 ± 0.32	0.68	1.95 ± 0.05	−0.48 ± 0.07	0.01 ± 0.01	18.48 ± 0.09
DES001SC04	81.132 15	−64.325 42	0.12 ± 0.04	0.47 ± 0.26	0.61	4.17 ± 1.08	−0.88 ± 0.12	0.06 ± 0.05	18.37 ± 0.10
KMHK854	81.170 56	−63.203 52	0.12 ± 0.04	1.46 ± 0.60	1.07	1.29 ± 0.16	−1.18 ± 0.11	0.15 ± 0.02	17.90 ± 0.12
NGC1942,SL445,LW203,ESO85SC81,	81.179 74	−63.939 37	0.80 ± 0.06	1.69 ± 0.23	0.32	1.41 ± 0.03	−0.88 ± 0.16	0.06 ± 0.01	18.60 ± 0.01
SL448,LW205,ESO85SC82,KMHK859	81.248 78	−63.048 50	0.28 ± 0.04	1.16 ± 0.38	0.62	2.45 ± 0.06	−0.88 ± 0.12	0.02 ± 0.01	18.22 ± 0.01
LW208,KMHK878	81.394 92	−64.758 10	0.08 ± 0.01	2.70 ± 0.53	1.52	0.72 ± 0.15	−0.48 ± 0.10	0.06 ± 0.02	18.35 ± 0.01
LW212,KMHK882,BSDL1630	81.537 31	−64.565 97	0.48 ± 0.07	1.33 ± 0.28	0.44	1.26 ± 0.19	−0.88 ± 0.30	0.19 ± 0.01	18.27 ± 0.14
BSDL1735	81.816 36	−64.261 48	0.16 ± 0.04	2.77 ± 0.45	1.25	0.69 ± 0.02	−0.28 ± 0.06	0.03 ± 0.02	18.59 ± 0.01
DES001SC05	81.921 98	−64.807 29	0.16 ± 0.05	1.28 ± 0.88	0.91	0.76 ± 0.07	−0.40 ± 0.10	0.07 ± 0.04	18.59 ± 0.11
SL484,LW216,KMHK918	81.946 00	−64.649 97	0.24 ± 0.05	1.04 ± 0.54	0.64	0.34 ± 0.03	−0.23 ± 0.09	0.05 ± 0.01	18.47 ± 0.14
DES001SC08	81.973 49	−64.175 41	0.39 ± 0.02	0.39 ± 0.19	0.01	1.26 ± 0.40	−1.18 ± 0.10	0.10 ± 0.04	18.08 ± 0.12
KMHK938	82.182 39	−64.680 12	0.16 ± 0.03	1.83 ± 0.40	1.06	1.00 ± 0.26	−0.40 ± 0.07	0.08 ± 0.04	18.38 ± 0.16
DES001SC07	82.188 70	−64.058 64	0.22 ± 0.06	1.29 ± 0.48	0.77	1.41 ± 0.10	−0.88 ± 0.12	0.11 ± 0.04	18.21 ± 0.08
HS317,KMHK947	82.254 36	−64.288 81	0.12 ± 0.04	1.51 ± 0.70	1.12	0.30 ± 0.04	−0.18 ± 0.03	0.07 ± 0.05	18.51 ± 0.01

Cluster name	α_c	δ_c	r_c(arcmin)	r_t(arcmin)	c	Age(Gyr)	Fe/H	$E(g-r)$	$m-M_0$
DES001SC06	82.371 92	−63.083 30	0.46 ± 0.01	0.48 ± 0.32	0.01	1.82 ± 0.04	−0.48 ± 0.10	0.05 ± 0.01	18.43 ± 0.04
SL509,LW221,ESO85SC91,KMHK957	82.450 45	−63.649 79	0.88 ± 0.07	1.59 ± 0.12	0.25	1.26 ± 0.03	−1.18 ± 0.09	0.15 ± 0.01	18.26 ± 0.02
SL511,LW222,KMHK959	82.453 66	−64.438 82	0.26 ± 0.07	3.29 ± 0.37	1.10	2.00 ± 0.09	−0.70 ± 0.08	0.10 ± 0.01	18.14 ± 0.01
SL515,LW223,ESO85SC92,KMHK965	82.534 06	−63.426 85	0.55 ± 0.05	2.15 ± 0.19	0.59	1.26 ± 0.03	−0.88 ± 0.12	0.08 ± 0.01	18.43 ± 0.01
SL525,LW225,KMHK973	82.593 68	−64.017 76	0.47 ± 0.02	0.49 ± 0.40	0.03	2.88 ± 1.10	−0.88 ± 0.13	0.01 ± 0.03	18.30 ± 0.02
NGC1997,SL520,LW226,ESO86SC1,	82.643 48	−63.204 79	0.85 ± 0.05	1.79 ± 0.20	0.33	4.47 ± 0.10	−1.18 ± 0.09	0.08 ± 0.01	18.33 ± 0.01
SL529,LW229,ESO86SC5,KMHK992	82.780 57	−63.540 49	0.41 ± 0.05	2.31 ± 0.23	0.76	2.88 ± 0.07	−0.88 ± 0.12	0.01 ± 0.01	18.47 ± 0.02
OHSC20	82.833 36	−63.670 46	0.18 ± 0.03	0.96 ± 0.63	0.71	3.80 ± 0.37	−1.18 ± 0.09	0.08 ± 0.07	18.28 ± 0.06
LW230	82.847 62	−63.261 48	0.30 ± 0.04	0.66 ± 0.48	0.35	0.06 ± 0.07	−0.18 ± 0.06	0.15 ± 0.04	18.00 ± 0.16
DES001SC10	82.856 39	−63.453 56	0.27 ± 0.04	0.50 ± 0.44	0.27	1.51 ± 0.15	−1.18 ± 0.09	0.17 ± 0.06	18.32 ± 0.16
SL540,LW232,KMHK1003	82.893 60	−63.887 14	0.16 ± 0.04	2.19 ± 0.51	1.13	0.93 ± 0.07	−0.88 ± 0.12	0.10 ± 0.01	18.24 ± 0.19
DES001SC09	82.956 84	−63.322 52	0.32 ± 0.07	0.84 ± 0.56	0.42	1.20 ± 0.18	−0.88 ± 0.12	0.09 ± 0.03	18.31 ± 0.10
H4,SL556,LW237,ESO86SC9,KMHK1034	83.107 91	−64.736 54	0.83 ± 0.05	3.44 ± 0.03	0.62	2.34 ± 0.11	−0.88 ± 0.12	0.01 ± 0.02	18.70 ± 0.02
DES001SC12	83.340 19	−63.596 30	0.12 ± 0.05	1.43 ± 0.76	1.06	2.40 ± 0.62	−0.70 ± 0.34	0.02 ± 0.04	18.39 ± 0.04
DES001SC13	83.404 47	−63.071 90	0.12 ± 0.03	2.36 ± 0.73	1.28	1.32 ± 0.16	−0.34 ± 0.10	0.00 ± 0.06	18.37 ± 0.10
DES001SC16	83.701 46	−62.422 95	0.34 ± 0.06	1.15 ± 0.76	0.53	1.38 ± 0.32	−0.88 ± 0.30	0.16 ± 0.01	18.10 ± 0.20
OHSC22,KMHK1089	83.714 19	−63.632 54	0.23 ± 0.03	0.61 ± 0.66	0.43	0.44 ± 0.27	−0.58 ± 0.23	0.06 ± 0.03	18.35 ± 0.20
DES001SC11	83.770 45	−63.538 94	0.08 ± 0.03	0.52 ± 0.66	0.79	0.95 ± 0.09	−0.70 ± 0.09	0.09 ± 0.02	18.26 ± 0.02
DES001SC14	83.803 42	−64.618 81	0.12 ± 0.05	0.47 ± 0.89	0.61	0.76 ± 1.10	−0.34 ± 0.06	0.02 ± 0.06	18.49 ± 0.18
E2,ESO120SC08,KMHK1119	84.090 11	−61.788 61	0.46 ± 0.04	1.74 ± 0.32	0.58	2.24 ± 0.05	−0.88 ± 0.12	0.10 ± 0.01	18.17 ± 0.01
LW250,KMHK1129	84.158 28	−64.386 28	0.37 ± 0.04	0.97 ± 0.40	0.42	0.98 ± 0.05	−0.70 ± 0.08	0.02 ± 0.01	18.43 ± 0.01
SL604,LW251,KMHK1127	84.192 08	−62.884 30	0.42 ± 0.03	0.99 ± 0.30	0.37	2.63 ± 0.06	−0.70 ± 0.08	0.01 ± 0.01	18.43 ± 0.01
DES001SC15	84.572 19	−64.505 97	0.67 ± 0.17	0.68 ± 0.34	0.00	2.63 ± 3.83	−0.88 ± 0.44	0.10 ± 0.06	18.27 ± 0.18
LW260,KMHK1168	84.721 74	−64.292 17	0.16 ± 0.07	0.65 ± 0.69	0.62	0.44 ± 0.09	−0.48 ± 0.20	0.04 ± 0.04	18.35 ± 0.12
DES001SC17	84.745 72	−62.456 73	0.32 ± 0.01	0.33 ± 0.36	0.01	1.26 ± 0.36	−0.48 ± 0.21	0.02 ± 0.09	18.33 ± 0.02
DES001SC20	84.798 94	−62.585 97	0.39 ± 0.08	3.07 ± 0.55	0.89	1.45 ± 0.03	−0.88 ± 0.12	0.10 ± 0.01	18.32 ± 0.02
KMHK1195	85.096 80	−64.248 33	0.61 ± 0.02	0.62 ± 0.31	0.00	1.26 ± 0.12	−0.18 ± 0.09	0.00 ± 0.04	18.40 ± 0.10
LW266,KMHK1198	85.131 32	−64.298 48	0.20 ± 0.08	2.12 ± 0.70	1.02	0.69 ± 0.10	−0.48 ± 0.10	0.03 ± 0.03	18.53 ± 0.10
DES001SC19	85.144 43	−63.100 33	0.15 ± 0.03	0.35 ± 0.21	0.37	1.41 ± 0.21	−0.88 ± 0.26	0.08 ± 0.08	18.18 ± 0.01
DES001SC18	85.172 62	−63.818 72	0.13 ± 0.05	0.53 ± 0.49	0.62	1.32 ± 0.30	−0.88 ± 0.25	0.12 ± 0.01	18.15 ± 0.06
SL649,LW269,KMHK1214	85.288 48	−63.771 32	0.31 ± 0.04	2.11 ± 0.33	0.83	2.45 ± 0.12	−0.88 ± 0.12	0.03 ± 0.02	18.60 ± 0.02
BSDL2771	85.366 40	−63.132 42	0.32 ± 0.14	1.12 ± 0.75	0.55	1.26 ± 0.19	−0.88 ± 0.20	0.10 ± 0.08	18.11 ± 0.01
DES001SC22	85.474 93	−62.361 56	0.13 ± 0.03	1.44 ± 0.74	1.03	2.29 ± 0.40	−0.58 ± 0.25	0.00 ± 0.06	18.57 ± 0.18
LW272,KMHK1241	85.607 24	−62.501 70	0.14 ± 0.05	3.08 ± 0.63	1.33	2.09 ± 0.10	−0.88 ± 0.12	0.10 ± 0.01	18.32 ± 0.05
DES001SC21	85.764 33	−62.528 62	0.20 ± 0.06	1.01 ± 0.58	0.70	2.51 ± 0.06	−0.70 ± 0.08	0.05 ± 0.02	18.35 ± 0.09
LW276,KMHK1269	85.801 17	−63.617 29	0.50 ± 0.01	0.51 ± 0.22	0.00	2.88 ± 0.07	−0.88 ± 0.12	0.01 ± 0.01	18.45 ± 0.03
LW278,KMHK1265	85.801 60	−62.470 70	0.26 ± 0.03	0.79 ± 0.53	0.49	2.63 ± 0.06	−0.88 ± 0.12	0.06 ± 0.01	18.36 ± 0.01
SL670,LW277,ESO86SC25,KMHK1268	85.808 29	−62.833 91	0.33 ± 0.02	1.59 ± 0.29	0.68	2.57 ± 0.06	−0.58 ± 0.06	0.01 ± 0.01	18.55 ± 0.02
KMHK1278	85.868 77	−63.414 79	0.13 ± 0.04	2.02 ± 0.59	1.20	1.38 ± 0.28	−0.88 ± 0.12	0.10 ± 0.02	18.03 ± 0.12
SL677,LW280,KMHK1286	85.981 55	−63.373 42	0.29 ± 0.04	0.86 ± 0.44	0.47	0.65 ± 0.05	−0.88 ± 0.20	0.00 ± 0.02	18.50 ± 0.01
SL680,LW281,KMHK1290	86.017 61	−63.924 66	0.31 ± 0.12	3.07 ± 0.37	0.99	0.63 ± 0.05	−0.23 ± 0.11	0.01 ± 0.03	18.45 ± 0.11

Cluster name	α_c	δ_c	r_c(arcmin)	r_t(arcmin)	c	Age(Gyr)	Fe/H	$E(g-r)$	$m-M_0$
NGC2097,SL682,LW282,ESO56SC28,	86.029 48	−62.783 51	0.85 ± 0.02	1.61 ± 0.02	0.28	1.10 ± 0.03	−0.88 ± 0.12	0.08 ± 0.01	18.37 ± 0.01
SL689,LW284,KMHK1310	86.142 88	−65.001 71	0.23 ± 0.08	0.84 ± 0.34	0.56	1.02 ± 0.02	−0.70 ± 0.08	0.18 ± 0.01	18.13 ± 0.01
SL694,LW287,KMHK1318	86.278 04	−63.676 21	0.21 ± 0.03	0.40 ± 0.09	0.27	1.20 ± 0.06	−0.28 ± 0.06	0.02 ± 0.02	18.67 ± 0.04
KMHK1322	86.288 98	−64.797 39	0.20 ± 0.05	1.22 ± 0.50	0.80	1.58 ± 0.23	−0.58 ± 0.27	0.01 ± 0.05	18.52 ± 0.08
SL696,LW286,KMHK1324	86.312 40	−64.772 44	0.19 ± 0.04	0.69 ± 0.51	0.57	1.12 ± 0.03	−0.88 ± 0.12	0.11 ± 0.01	18.13 ± 0.02
SL701,LW289,ESO56SC30,KMHK1330	86.391 15	−63.715 73	0.43 ± 0.06	3.29 ± 0.28	0.89	1.38 ± 0.03	−0.70 ± 0.08	0.06 ± 0.01	18.10 ± 0.06
BSDL2976	86.743 97	−63.863 92	0.80 ± 0.08	1.86 ± 0.17	0.37	0.48 ± 0.01	−0.23 ± 0.03	0.02 ± 0.01	18.27 ± 0.02
OHSC26	86.848 54	−62.622 15	0.11 ± 0.04	0.54 ± 0.30	0.68	0.89 ± 0.06	−0.40 ± 0.07	0.00 ± 0.07	18.55 ± 0.01
SL720,LW299,KMHK1373	86.945 25	−65.011 15	0.44 ± 0.02	0.64 ± 0.36	0.16	2.04 ± 0.15	−0.58 ± 0.10	0.05 ± 0.07	18.41 ± 0.01
KMHK1381	87.038 43	−63.598 45	0.23 ± 0.03	0.93 ± 0.06	0.60	1.15 ± 0.03	−0.70 ± 0.08	0.08 ± 0.01	18.11 ± 0.02
DES001SC23	87.196 62	−65.152 52	0.33 ± 0.07	1.13 ± 0.22	0.54	0.35 ± 0.01	−0.01 ± 0.01	0.02 ± 0.01	18.58 ± 0.01
SL724,LW305,KMHK1388	87.222 06	−64.633 12	0.24 ± 0.04	0.94 ± 0.35	0.60	1.10 ± 0.08	−0.48 ± 0.20	0.03 ± 0.04	18.33 ± 0.18
SL726,LW306,KMHK1390	87.245 26	−64.733 59	0.34 ± 0.04	0.69 ± 0.41	0.31	1.00 ± 0.32	−0.40 ± 0.10	0.00 ± 0.06	18.40 ± 0.13
KMHK1391	87.258 21	−64.348 38	0.55 ± 0.02	0.57 ± 0.35	0.01	1.51 ± 0.18	−0.70 ± 0.10	0.07 ± 0.02	18.37 ± 0.04
SL727,LW307,KMHK1393	87.260 73	−65.012 12	0.35 ± 0.05	2.63 ± 0.20	0.88	1.82 ± 0.04	−0.88 ± 0.12	0.01 ± 0.01	18.57 ± 0.01
SL729,LW311,KMHK1399	87.334 53	−63.134 70	0.38 ± 0.06	1.42 ± 0.48	0.57	1.10 ± 0.03	−0.40 ± 0.10	0.02 ± 0.01	18.50 ± 0.01
SL738,LW314,KMHK1417	87.533 06	−64.153 52	0.21 ± 0.05	2.58 ± 0.33	1.09	1.29 ± 0.12	−0.70 ± 0.13	0.05 ± 0.03	18.42 ± 0.01
NGC2120,SL742,LW316,ESO86SC34,	87.645 99	−63.675 48	1.07 ± 0.03	2.17 ± 0.02	0.31	1.78 ± 0.04	−0.58 ± 0.06	0.00 ± 0.01	18.50 ± 0.01
LW319,KMHK1439	87.772 90	−64.187 43	0.44 ± 0.02	0.47 ± 0.14	0.03	1.10 ± 0.05	−0.70 ± 0.08	0.06 ± 0.01	18.10 ± 0.03
LW320,KMHK1447	87.840 75	−62.992 15	0.31 ± 0.03	1.39 ± 0.30	0.66	3.02 ± 0.14	−1.18 ± 0.10	0.07 ± 0.01	18.27 ± 0.01
LW323,KMHK1455	87.938 22	−63.865 62	0.59 ± 0.07	0.87 ± 0.40	0.17	1.91 ± 0.04	−0.58 ± 0.06	0.00 ± 0.01	18.36 ± 0.01
OHSC27,KMHK1469	88.122 57	−63.600 65	0.70 ± 0.06	0.79 ± 0.38	0.05	1.32 ± 0.20	−0.88 ± 0.35	0.05 ± 0.08	18.21 ± 0.20
KMHK1484	88.298 43	−63.806 91	0.48 ± 0.03	0.49 ± 0.30	0.00	0.83 ± 0.29	−0.40 ± 0.16	0.02 ± 0.10	18.47 ± 0.16
SL768,LW326,ESO86SC38,KMHK1493	88.473 78	−63.615 44	0.68 ± 0.05	3.62 ± 0.05	0.72	1.51 ± 0.04	−0.34 ± 0.03	0.00 ± 0.01	18.40 ± 0.01
DES001SC26	88.559 20	−65.147 52	0.31 ± 0.09	0.79 ± 0.49	0.41	1.35 ± 0.10	−0.88 ± 0.17	0.08 ± 0.05	18.16 ± 0.10
DES001SC25	88.654 18	−64.887 16	0.11 ± 0.04	1.12 ± 0.75	1.02	0.81 ± 0.08	−0.28 ± 0.12	0.02 ± 0.04	18.48 ± 0.14
LW332,KMHK1518	88.778 51	−64.652 82	0.33 ± 0.10	0.83 ± 0.48	0.40	1.00 ± 0.07	−0.88 ± 0.12	0.11 ± 0.02	18.41 ± 0.01
OHSC28	88.897 00	−62.345 24	0.29 ± 0.01	0.38 ± 0.12	0.13	2.63 ± 0.32	−0.58 ± 0.06	0.05 ± 0.01	18.38 ± 0.01
BSDL3181	88.970 86	−65.293 11	0.38 ± 0.06	0.73 ± 0.56	0.28	0.83 ± 0.04	−1.18 ± 0.11	0.14 ± 0.04	18.39 ± 0.02
KMHK1530	89.034 12	−63.642 78	0.17 ± 0.06	1.58 ± 0.57	0.97	2.63 ± 0.06	−0.88 ± 0.12	0.06 ± 0.01	18.50 ± 0.01
DES001SC24	89.082 72	−64.717 55	0.17 ± 0.06	1.18 ± 0.57	0.84	1.26 ± 0.33	−1.18 ± 0.09	0.12 ± 0.01	18.31 ± 0.04
BSDL3189	89.384 47	−65.343 30	0.15 ± 0.04	1.29 ± 0.58	0.94	1.91 ± 0.04	−0.58 ± 0.06	0.06 ± 0.01	18.45 ± 0.01
LW340,KMHK1548	89.397 15	−64.998 39	0.34 ± 0.06	1.19 ± 0.49	0.55	2.51 ± 0.18	−0.88 ± 0.15	0.05 ± 0.05	18.41 ± 0.10
SL798,LW344,KMHK1556	89.550 14	−63.894 50	0.22 ± 0.05	1.22 ± 0.52	0.74	2.51 ± 0.31	−0.88 ± 0.12	0.06 ± 0.02	18.20 ± 0.10
DES001SC27	89.608 03	−64.594 79	0.10 ± 0.03	1.05 ± 0.67	1.03	1.10 ± 0.16	−0.70 ± 0.26	0.06 ± 0.07	18.10 ± 0.14
NGC2162,SL814,LW351,ESO86SC47,	90.125 89	−63.721 73	0.91 ± 0.03	1.86 ± 0.05	0.31	1.29 ± 0.03	−0.88 ± 0.12	0.08 ± 0.02	18.36 ± 0.01
KMHK1593	90.466 76	−64.132 92	0.14 ± 0.03	2.34 ± 0.49	1.23	3.39 ± 0.41	−0.88 ± 0.12	0.03 ± 0.03	18.33 ± 0.01
ESO121SC03,KMHK1591	90.513 84	−60.523 79	0.47 ± 0.04	2.63 ± 0.09	0.75	9.77 ± 0.23	−1.40 ± 0.05	0.07 ± 0.01	18.14 ± 0.01
DES001SC28	90.829 90	−64.831 38	0.15 ± 0.04	1.15 ± 0.64	0.89	0.79 ± 0.10	−0.70 ± 0.08	0.08 ± 0.02	18.83 ± 0.10
NGC2193,SL839,LW387,ESO86SC57	91.572 13	−65.098 74	0.46 ± 0.05	3.29 ± 0.26	0.85	2.40 ± 0.06	−0.70 ± 0.08	0.01 ± 0.01	18.47 ± 0.01

[1]*Instituto de Física, Universidade Federal do Rio Grande do Sul, Caixa Postal 15051, Porto Alegre, RS - 91501-970, Brazil*
[2]*Laboratório Interinstitucional de e-Astronomia - LIneA, Rua Gal. José Cristino 77, Rio de Janeiro, RJ - 20921-400, Brazil*
[3]*Department of Physics, University of Surrey, Guildford GU2 7XH, UK*
[4]*Observatório Nacional, Rua Gal. José Cristino 77, Rio de Janeiro, RJ - 20921-400, Brazil*
[5]*Fermi National Accelerator Laboratory, PO Box 500, Batavia, IL 60510, USA*
[6]*Kavli Institute for Particle Astrophysics and Cosmology, PO Box 2450, Stanford University, Stanford, CA 94305, USA*
[7]*SLAC National Accelerator Laboratory, Menlo Park, CA 94025, USA*
[8]*Cerro Tololo Inter-American Observatory, National Optical Astronomy Observatory, Casilla 603, La Serena, Chile*
[9]*CNRS, UMR 7095, Institut d'Astrophysique de Paris, F-75014 Paris, France*
[10]*Department of Physics and Astronomy, University College London, Gower Street, London WC1E 6BT, UK*
[11]*Sorbonne Universités, UPMC Univ Paris 06, UMR 7095, Institut d'Astrophysique de Paris, F-75014 Paris, France*
[12]*Department of Astronomy, University of Illinois, 1002 W. Green Street, Urbana, IL 61801, USA*
[13]*National Center for Supercomputing Applications, 1205 West Clark St, Urbana, IL 61801, USA*
[14]*Institut de Ciències de l'Espai, IEEC-CSIC, Campus UAB, Carrer de Can Magrans, s/n, E-08193 Bellaterra, Barcelona, Spain*
[15]*Institut de Física d'Altes Energies (IFAE), The Barcelona Institute of Science and Technology, Campus UAB, E-08193 Bellaterra, Barcelona, Spain*
[16]*Excellence Cluster Universe, Boltzmannstr. 2, D-85748 Garching, Germany*
[17]*Faculty of Physics, Ludwig-Maximilians University, Scheinerstr. 1, D-81679 Munich, Germany*
[18]*Jet Propulsion Laboratory, California Institute of Technology, 4800 Oak Grove Dr, Pasadena, CA 91109, USA*
[19]*Department of Physics, University of Michigan, Ann Arbor, MI 48109, USA*
[20]*Center for Cosmology and Astro-Particle Physics, The Ohio State University, Columbus, OH 43210, USA*
[21]*Department of Physics, The Ohio State University, Columbus, OH 43210, USA*
[22]*Australian Astronomical Observatory, North Ryde, NSW 2113, Australia*
[23]*George P. and Cynthia Woods Mitchell Institute for Fundamental Physics and Astronomy, and Department of Physics and Astronomy, Texas A&M University, College Station, TX 77843, USA*
[24]*Department of Astronomy, The Ohio State University, Columbus, OH 43210, USA*
[25]*Department of Astronomy, University of Michigan, Ann Arbor, MI 48109, USA*
[26]*Institució Catalana de Recerca i Estudis Avançats, E-08010 Barcelona, Spain*
[27]*Institute of Cosmology and Gravitation, University of Portsmouth, Portsmouth PO1 3FX, UK*
[28]*Department of Physics and Astronomy, Pevensey Building, University of Sussex, Brighton BN1 9QH, UK*
[29]*Centro de Investigaciones Energéticas, Medioambientales y Tecnológicas (CIEMAT), Madrid, Spain*
[30]*ICTP South American Institute for Fundamental Research Instituto de Física Teórica, Universidade Estadual Paulista, São Paulo, Brazil*
[31]*Department of Physics and Astronomy, University of Pennsylvania, Philadelphia, PA 19104, USA*
[32]*Department of Physics, University of Illinois, 1110 W. Green St, Urbana, IL 61801, USA*

This paper has been typeset from a TEX/LATEX file prepared by the author.

Capítulo 4

SMCNOD

4.1 Introdução

Com o aumento do campo do DES com o catálogo Y2Q1, nossa intenção foi fazer uma busca automática por subestruturas estelares estendidas, tendo como escopo o trabalho de Torrealba et al. (2016): a descoberta de Crater II, uma galáxia anã com raio de meia-luz em torno de 30 minutos de arco (equivalente a 1,1 kpc), tornando este objeto o quarto maior satélite da Via-Láctea, sendo apenas ultrapassado pelas Nuvens de Magalhães e pela anã de Sagitário.

Com a descoberta de um objeto situado a 8 graus (relativamente distante) do centro da SMC, nossa intenção era a de determinar se este objeto, então batizado de SMCNOD (Small Magellanic Cloud Northern Over-Density), se destacaria do halo estendido de estrelas da SMC detectado por Nidever et al. 2011. Foi graças à colaboração com o DES e a presença de um outro levantamento (MagLiteS, no seu primeiro *round* de imagens) que objetiva o imageamento completo das cercanias da LMC nas bandas g e r, também utilizando a DECam, que pudemos levar a contento nosso projeto. Logo depois da descoberta da SMCNOD, os campos adjacentes foram imageados e reduzidos pela colaboração MagLiteS. Em menos de duas semanas, nós integramos os campos imageados pelo MagLiteS ao catálogo DES-Y2Q1, determinando os pontos zero para cada imagem e melhorando a fotometria se havia mais de uma observação (área de sobreposição). O catálogo final revelou que a SMCNOD é uma sobredensidade na área limite do halo estendido de estrelas. Além do DES, este paper passou pela revisão do grupo do MagLiteS, com muitos valorosos comentários por parte principalmente de Roland van der Marel, Gurtina Besla, Carme Gallart, David Martinez-Delgado, Knut Olsen e David Nidever.

A SMCNOD mostrou-se composta praticamente por uma população de 6 bilhões

de anos, comum à SMC, sendo uma pequena parte representada por uma população mais jovem. Outro fato importante é que o levantamento da região do entorno mostrou que o halo estelar estendido da SMC é uma realidade, embora tenha sido sondado apenas em campos esparsos por Nidever et al. 2011.

Um dos pontos mais importantes na descoberta deste objeto é que as interações de maré, como as que formaram a Ponte de Magalhães, sempre produzem subestruturas simétricas (ver referências no artigo anexo). Embora a Ponte de Magalhães seja conhecida há bastante tempo, não foi descoberta nenhuma outra subestrutura semelhante com tão grande escala que pudesse servir de contrapartida à formação da Ponte de Magalhães. Dada a grande extensão da SMCNOD ($6^o \times 2^o$), este objeto é um forte candidato a ser esta contrapartida para uma forte interação SMC-LMC.

4.2 Resumo das atividades desenvolvidas em relação à SMCNOD

Aqui fornecemos uma lista de tarefas desenvolvidas ao longo do artigo:

- Desenvolvimento de uma ferramenta para a detecção de sobredensidades estelares extendidas, com a detecção dos principais objetos estelares conhecidos (aglomerados globulares e galáxias anãs);
- Determinação da população da SMCNOD, via comparação visual com a isócrona e utilizando dados da literatura como referência para idade e metalicidade;
- Complementação dos dados do DES-Y2Q1 com os dados do MagLiteS, nas bandas g e r. Os dados foram primariamente reduzidos, ainda no formato da DECam, e então unidos, retiradas as fontes duplas, subtraídas as extinções e ambas as bandas e determinado o ponto-zero;
- Uma análise de densidade foi feita utilizando um filtro isocronal;
- Os dados de densidade foram comparados com os dados de Nidever et al. (2011) utilizando um campo em comum entre os dados daquele autor e nossos dados, mostrando que a SMCNOD é a maior densidade estelar àquela distância da SMC;
- Um perfil elíptico exponencial foi ajustado à SMCNOD, determinando seus componentes estruturais;

- Os mapas de gás não mostraram uma sobredensidade sensível de gás, o que pode indicar que a SMCNOD sofreu retirada de gás via tidal stripping ou que suas estrelas foram retiradas da SMC, trazendo uma quantidade muito pequena de gás;

- A função de luminosidade da SMCNOD é muito semelhante à da SMC, o que é um argumento a favor de que este objeto foi retirado por forças de maré da SMC;

- É feito uma profunda análise da literatura, indicando as origens possíveis para a SMCNOD.

A análise da SMCNOD culminou com a publicação do artigo (Pieres et al., 2017) em junho deste ano. O artigo é reproduzido na sequência deste capítulo, onde há uma maior discussão a respeito das possíveis origens da SMCNOD, bem como uma análise mais aprofundada do objeto.

Monthly Notices of the ROYAL ASTRONOMICAL SOCIETY

MNRAS **468,** 1349–1360 (2017) doi:10.1093/mnras/stx507
Advance Access publication 2017 February 28

A stellar overdensity associated with the Small Magellanic Cloud

A. Pieres,[1,2]★ B. X. Santiago,[1,2] A. Drlica-Wagner,[3] K. Bechtol,[4] R. P. van der Marel,[5] G. Besla,[6] N. F. Martin,[7,8] V. Belokurov,[9] C. Gallart,[10,11] D. Martinez-Delgado,[12] J. Marshall,[13] N. E. D. Nöel,[14] S. R. Majewski,[15] M.-R. L. Cioni,[16,17] T. S. Li,[3] W. Hartley,[18] E. Luque,[1,2] B. C. Conn,[19] A. R. Walker,[20] E. Balbinot,[14] G. S. Stringfellow,[21] K. A. G. Olsen,[22] D. Nidever,[22] L. N. da Costa,[2,23] R. Ogando,[2,23] M. Maia,[2,23] A. Fausti Neto,[2] T. M. C. Abbott,[20] F. B. Abdalla,[24,25] S. Allam,[3] J. Annis,[3] A. Benoit-Lévy,[25,26,27] A. Carnero Rosell,[2,23] M. Carrasco Kind,[28,29] J. Carretero,[30,31] C. E. Cunha,[32] C. B. D'Andrea,[33,34] S. Desai,[35] H. T. Diehl,[3] P. Doel,[25] B. Flaugher,[3] P. Fosalba,[30] J. García-Bellido,[31] D. Gruen,[32,36] R. A. Gruendl,[28,29] J. Gschwend,[2,23] G. Gutierrez,[3] K. Honscheid,[37,38] D. James,[20,39] K. Kuehn,[40] N. Kuropatkin,[3] F. Menanteau,[28,29] R. Miquel,[41,42] A. A. Plazas,[43] A. K. Romer,[44] M. Sako,[45] E. Sanchez,[46] V. Scarpine,[3] M. Schubnell,[47] I. Sevilla-Noarbe,[46] R. C. Smith,[20] M. Soares-Santos,[3] F. Sobreira,[2,48] E. Suchyta,[49] M. E. C. Swanson,[29] G. Tarle,[47] D. L. Tucker[3] and W. Wester[3]

Affiliations are listed at the end of the paper

Accepted 2017 February 23. Received 2017 February 23; in original form 2016 December 12

ABSTRACT

We report the discovery of a stellar overdensity 8° north of the centre of the Small Magellanic Cloud (SMC; Small Magellanic Cloud Northern Over-Density; SMCNOD), using data from the first 2 yr of the Dark Energy Survey (DES) and the first year of the MAGellanic SatelLITEs Survey (MagLiteS). The SMCNOD is indistinguishable in age, metallicity and distance from the nearby SMC stars, being primarily composed of intermediate-age stars (6 Gyr, Z=0.001), with a small fraction of young stars (1 Gyr, Z=0.01). The SMCNOD has an elongated shape with an ellipticity of 0.6 and a size of $\sim 6^\circ \times 2^\circ$. It has an absolute magnitude of $M_V \cong -7.7$, $r_h = 2.1$ kpc, and $\mu_V(r < r_h) = 31.2$ mag arcsec^{-2}. We estimate a stellar mass of $\sim 10^5$ M$_\odot$, following a Kroupa mass function. The SMCNOD was probably removed from the SMC disc by tidal stripping, since it is located near the head of the Magellanic Stream, and the literature indicates likely recent Large Magellanic Cloud-SMC encounters. This scenario is supported by the lack of significant H I gas. Other potential scenarios for the SMCNOD origin are a transient overdensity within the SMC tidal radius or a primordial SMC satellite in advanced stage of disruption.

Key words: galaxies: interactions – Magellanic Clouds.

1 INTRODUCTION

The Magellanic Clouds (MCs) are a rich and nearby system where we can observe dynamic evolution as well as the results of star formation throughout time. The system also includes the Magellanic Stream (MS), an H I gas stream (Mathewson, Cleary & Murray 1974) connected to the MCs spanning at least 200° on the sky (Nidever et al. 2010), where no stellar counterpart has yet been identified (Recillas-Cruz 1982; Guhathakurta & Reitzel 1998). Other important structures belonging to this system are the Magellanic Bridge, containing neutral hydrogen, stars and star clusters linking the MCs (Irwin, Demers & Kunkel 1990; Grondin, Demers & Kunkel 1992; Bica et al. 2015) and the Leading Arm (LA) or Leading Arm Feature, a gas stream on the opposite side of the MS.

★ E-mail: adriano.pieres@gmail.com; adriano.pieres@ufrgs.br

Given the higher velocities (than previously estimated) for the MCs in recent works (Kallivayalil et al. 2006a; Kallivayalil, van der Marel & Alcock 2006b; Vieira et al. 2010; Kallivayalil et al. 2013), it is thought that the MCs are completing their first passage around the Milky Way (MW). This conclusion is supported by proper motion measurements using *HST* (Kallivayalil et al. 2013) and *Gaia* data release 1 (van der Marel & Sahlmann 2016). Thus, the gravitational interaction between the Small and Large Magellanic Clouds (SMCs and LMCs, respectively) may be playing a larger role than the MW in triggering star formation.

In the recent decades, a wide range of dynamical simulations of the MCs has improved our understanding of their substructures, taking advantage of more reliable proper motion measurements, among other enhanced initial conditions (e.g. masses, gas fraction, ellipticity, stellar disc scalelength). Using *N*-body simulations, Connors, Kawata & Gibson (2006) reproduced the MS and LA as substructures formed through tidal interaction between the clouds. Their work reproduced for the first time the spatial and kinematic bifurcations in the LA and in the MS. The MCs simulations of Bekki & Chiba (2007) over the last 800 Myr are able to reproduce the off-centre bar and the H I spirals in the LMC. They also predict that a substantial number of SMC stars could be transferred to the LMC to form diffuse halo components around that galaxy. Restricting their study to the SMC, Bekki & Chiba (2009) designed chemodynamical simulations, using an SMC 'dwarf spheroidal model' (an extended H I gas disc and a spherical distribution for old stars), which they argue is a better description of the stellar and gas kinematic properties. In their fiducial model, the final distribution of old stars is more regular (spherical) than that of the younger stars (which form basically a bar-like structure). Diaz & Bekki (2012) simulate a large set of models based on proper motion data from Vieira et al. (2010) and Kallivayalil et al. (2006b,a), predicting two main encounters between the SMC and the LMC (260 Myr and 1.97 Gyr ago), suggesting a joint history for these galaxies. In their simulations, the first encounter forms two substructures: the Magellanic Bridge and a less obvious structure called Counter-Bridge. Besla et al. (2012) present two models for the Magellanic System, designed to explain the MS as the action of LMC tides on the SMC. In their models, the LMC is a one-armed spiral and features as well as a warped, off-centre stellar bar as a result of the gravitational interaction.

The possible association between the MCs and ultrafaint dwarf galaxies recently discovered in the Dark Energy Survey (DES; The Dark Energy Survey Collaboration 2005) footprint has revived the search for dwarf galaxy satellites of the LMC or SMC (Deason et al. 2015; Drlica-Wagner et al. 2015, 2016; Koposov et al. 2015; Jethwa, Erkal & Belokurov 2016; Sales et al. 2016). The recent discovery by Mackey et al. (2016) of a stellar cloud with a length of 10 kpc within the LMC tidal radius (and an additional extension farther west of the LMC) shows that the exploration of the outer area of the MCs has an important potential for new discoveries. It also reinforces the idea that newly discovered structures can be used to trace the gravitational interaction history of the MCs. Besla et al. (2016) suggest that the existence of stellar arcs and multiple spiral arms in the northern LMC periphery (without comparable counterparts in southern regions of the SMC) could be attributed to repeated close interactions between the LMC and the SMC. A large number of simulations predict clumpy substructures formed by a spheroidal distribution surrounding the SMC (see e.g. the references listed in Section 4.3), though there is no specific prediction of overdensities as large as those presented here. Nevertheless, the discovery of this structure reinforces the scenario where the LMC and the SMC have had recent and drastic encounters.

Table 1. List of bands and central positions for each MagLiteS DECam exposures used in this work.

Band	$\alpha(^\circ)$	$\delta(^\circ)$
g	14.092	−65.826
	10.690	−65.029
	7.280	−65.861
	10.804	−66.803
	9.789	−65.893
	13.324	−66.744
	16.504	−65.664
	13.055	−64.994
r	14.114	−65.815
	10.699	−65.036
	7.306	−65.856
	10.807	−66.783
	9.792	−65.893
	13.322	−66.729
	16.524	−65.653
	13.077	−65.004

In what follows, we report a stellar overdensity located 8° north of the SMC centre, hereafter referred to as the Small Magellanic Cloud Northern Over-Density (SMCNOD). The SMCNOD was discovered in data from DES and follow-up imaging was performed with the Dark Energy Camera (DECam; Flaugher et al. 2015) as part of the MAGellanic SatelLITEs Survey – MagLiteS. The data sets and criteria used to select stellar sources are discussed in Section 2. In Section 3, we describe the analysis of the stellar populations and the structure of the SMCNOD. We conclude by discussing the SMCNOD stellar population and gas content, as well as its formation and fate, in Section 4.

2 DATA

The DES data used in this work is the year-2 quick release (DES-Y2Q1) catalogue, constructed using 26 590 DECam exposures. The DES-Y2Q1 images were taken between 2013 August and 2014 February and between 2014 August and 2015 February, in the first 2 yr of the survey. The images cover most of the DES footprint (5000 square degrees), with the exception of a few hundred square degrees in the region near the South Galactic Pole. We refer to section 2 of Drlica-Wagner et al. (2015) for a detailed description of the data and the star selection criteria.

MagLiteS is a National Optical Astronomy Observatories (NOAO) community survey (NOAO proposal 2016A-0366) that is using the DECam to complete an annulus of contiguous imaging around the periphery of the Magellanic System (Drlica-Wagner et al. 2016).

The MagLiteS data used here are composed of 16 DECam 90 s exposures in the *g* and *r* bands. The positions for each MagLiteS DECam exposure are listed in Table 1. The MagLiteS exposures were taken in 2016 June 27, in an effort to enlarge DECam coverage in the SMCNOD region. MagLiteS images were reduced using the Dark Energy Survey Data Management (DESDM) pipeline, and source detection was performed separately on each exposure.

To assemble a combined DES-Y2Q1 and MagLiteS source catalogue, we first set the zero-points by comparing DES-Y2Q1 bright stars to individual MagLiteS DECam single-exposure catalogues. Since the DES-Y2Q1 is a de-reddened catalogue, we applied an extinction correction to each DES-Y2Q1 source following Schlegel, Finkbeiner & Davis (1998). Comparison

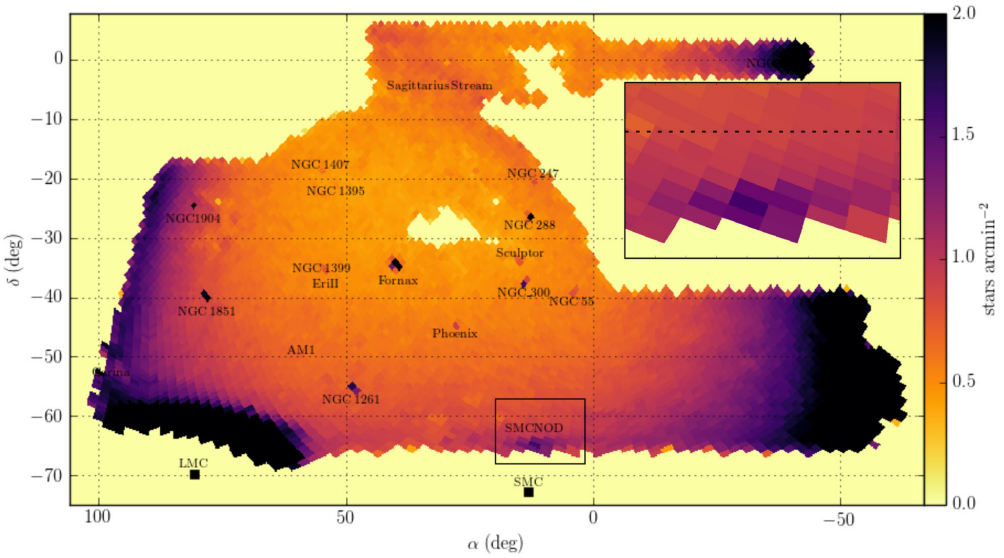

Figure 1. DES-Y2Q1 stellar density map using the HEALPIX scheme with NSIDE = 64 (0.839 square degrees), corrected by a survey coverage map and saturating at 2 stars arcmin^{-2}. Objects detected in the search for extended structures are explicitly labelled in the DES-Y2Q1 footprint. In this density map, we are counting all of the DES-Y2Q1 stars. Inserted box: zoomed view of the SMCNOD region.

stars were selected in the magnitude range of $17 < g < 21$, $|wavg\_spread\_model| < 0.003$ and $flags < 4$ in each band (g and r) in the DES-Y2Q1 catalogue. SPREAD_MODEL[1] is a morphological output from SEXTRACTOR[2] used to distinguish stars from galaxies. The prefix *wavg* means we used the weighted average of *spread_model* from individual single-epoch detections. The maximum positional deviation (object matching between DES-Y2Q1 and MagLiteS sources) was set to 1 arcsec. After adding the photometric zero-points, we joined all sources from the MagLiteS fields into a single catalogue. We then subtracted the extinction and incorporated the final MagLiteS catalogue into the DES-Y2Q1 catalogue, to create the final DES-MagLiteS stars list used in this paper. We applied the same criteria used to select DES-Y2Q1 stars to filter our final sample of stars, namely using a star/galaxy separation criterion of $|wavg\_spread\_model\_r| < 0.003 + spreaderr\_model\_r$, $flags\_\{g,r\} < 4$, and $magerr\_psf\_\{g, r\} < 1$.

Moreover, we applied a magnitude cut of $17 < g < 23$ to ensure high source detection efficiency on the DES-MagLiteS catalogue. Also, we applied a colour cut to select stellar sources with $-0.5 < g - r < 1.2$.

A single 90 s DECam exposure (the DECam exposure time for DES in g and r bands) reaches point sources with magnitudes as faint as $\{g, r\} \cong \{23.6,23.2\}$ with a signal-to-noise ratio (S/N) equal to 10. Therefore, the faint magnitude cut adopted here results in uniform depth at least down to this S/N level. We emphasize that the quoted limiting magnitudes and S/N may change slightly due to seeing and weather conditions during the observing nights.

3 ANALYSIS

The SMCNOD was discovered during a search for extended ($r_t \simeq$ 30 arcmin) and low surface brightness structures in the DES-Y2Q1 catalogue. We initially built density maps for the DES-Y2Q1 stars, partitioning the sky into equal area HEALPIX.[3] We set the pixel area to 0.839 square degrees (NSIDE = 64). We then counted all DES-Y2Q1 stars within each pixel, correcting the density in each pixel by the respective survey coverage for both g and r bands. The coverage maps were created by using a finer grid of pixels (pixel size $\cong$ 1.7 arcmin on a side, NSIDE = 2048), then checking whether or not a pixel contains any star or galaxy and finally grouping into pixels with 0.839 square degrees (NSIDE = 64), where the effective survey coverage area was computed. We then calculated the average number of stars in the eight immediately neighbouring pixels (with NSIDE = 64). The significance of any overdensity was calculated by subtracting the average counts in the neighbouring pixels and dividing the result by the square root of that average, thus yielding the number of standard deviations (following a Poisson distribution) of the star counts. For example, the least significant candidate has a star count equal to 3781, whereas the average counts of the neighbouring pixels is 1.0 star per arcmin^2 (3600 stars per square degree). Its significance is then only 3σ $((3781-3600)/\sqrt{3600})$, presenting an excess of 5 per cent above the mean star counts. We examined all candidates with significance greater than 3σ, which results in a list of 314 candidates.

The highest significance candidates were mostly known globular clusters and dwarf galaxies (see Fig. 1). However, one candidate

[1] SPREAD_MODEL is a 'normalized simplified linear discriminant between the best-fitting local point spread function model and a slightly more extended model' as described in Desai et al. (2012).
[2] http://www.astromatic.net/software/sextractor

[3] HEALPIX is an equal-area pixelization scheme for spherical surfaces (in our case, the sky) in a certain number of pixels. This number of pixels is given by 12 times the square of the parameter NSIDE, chosen by the user. See more details in http://healpix.sourceforge.net/.

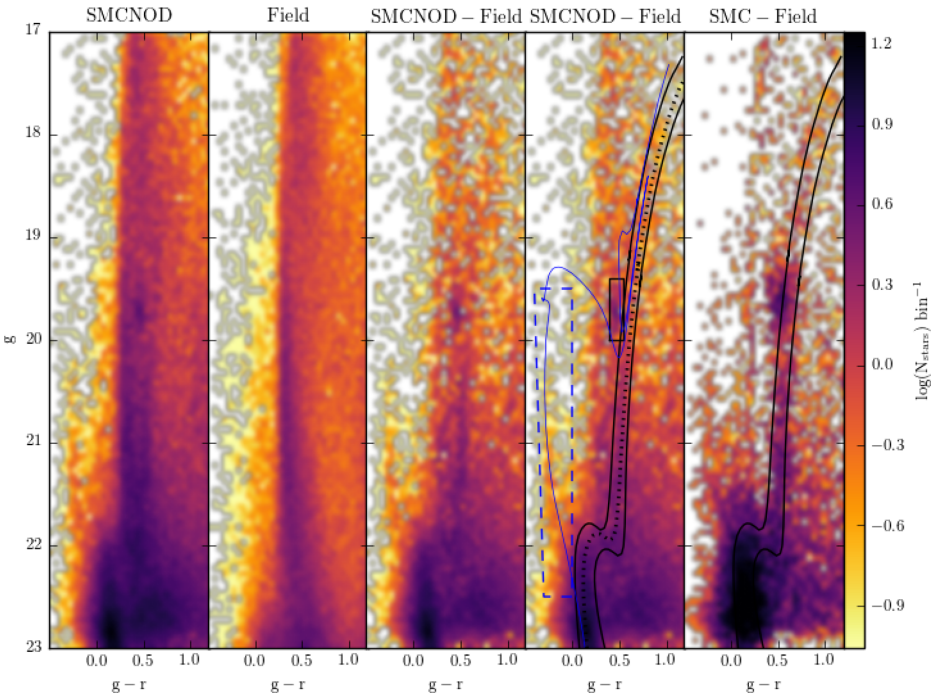

Figure 2. First panel: Hess diagram for stars in the range $6^\circ < \alpha < 15^\circ$ and $-66^\circ < \delta < -63^\circ$, which covers most of the SMCNOD. A stellar population with a turnoff at $g \approx 22$ can be clearly seen. A main sequence, sub-giant branch, RGB and RC are all discernible against the foreground Galactic stars even with no subtraction. Second panel: Hess diagram for a region at the same Galactic latitude ($b = -52.^\circ58$) as the previous one ($32^\circ < \alpha < 40^\circ$, $-64^\circ < \delta < -58.^\circ25$). Third panel: subtracted Hess diagram (object minus field). Fourth panel: same as the third panel, but featuring isochronal masks of intermediate-age (young) SMC populations bounded by the solid black (dashed blue) line, encompassing most of the SMCNOD stars by displacing the isochrone. The black rectangle denotes the RC stars. A PARSEC model with $\tau \simeq 6$ Gyr and $Z = 0.001$ ($\tau \simeq 1$ Gyr, $Z = 0.01$) is shown in dotted black (solid thin blue) line. Both models (intermediate-age and young) are displaced by a distance modulus equal to 18.96, following the SMC distance modulus obtained by de Grijs & Bono (2015). Fifth panel: sample of SMC field stars with $\delta < -67^\circ$ and $10^\circ < \alpha < 15^\circ$ minus the second Hess diagram (MW foreground stars). The data show a spread in magnitude that is comparable between the SMC stars and SMCNOD stars. The isochronal mask for intermediate-age stars is reproduced in the last panel.

located at $\alpha \cong 12^\circ$ and $\delta \cong -65^\circ$ was significantly higher (with a significance of 8σ at the highest density pixel) than the local background, and several of its neighbouring pixels emerged in the significance list, suggesting that the overdensity spans multiple pixels (insert in Fig. 1). Given its proximity to the SMC, we refer to this overdensity as the SMCNOD. This object is located in the border of the DES survey and so we performed follow-up imaging with MagLiteS to cover an extra area around SMCNOD.

In the leftmost panel of Fig. 2, we plot the g versus g-r colour–magnitude Hess diagram for the region surrounding the SMCNOD in the DES-MagLiteS catalogue, to analyse the photometric features of that putative stellar population. The second Hess diagram samples stars in a field with 20 square degrees, centred on $l = 304.^\circ60$ and $b = -52.^\circ60$ at the same Galactic latitude as the SMCNOD ($l = 284.^\circ72$, $b = -52.^\circ60$). Subtracting the first two Hess diagrams (and weighting by their respective areas) results in the third Hess diagram in Fig. 2. It is dominated by a stellar population with age $\tau \simeq 6$ Gyr and metallicity $Z = 0.001$ as attested by the overlaid PARSEC model (Bressan et al. 2012) represented by the dotted black line in the fourth panel. This model was chosen by a visual comparison to the Hess diagram in the fourth panel. A colour–magnitude diagram (CMD) mask is drawn (solid black lines) displacing the PARSEC model for intermediate-age stars in $g - r$ colour and g magnitude. The SMCNOD distance modulus is indistinguishable from that of the SMC (18.96 ± 0.02 following de Grijs & Bono 2015). A PARSEC model is also shown in the fourth panel of Fig. 2 (thin blue line) to represent the blue plume of younger stars ($\tau \simeq 1$ Gyr and Z=0.01). We note that there is some overlap between both populations (younger and intermediate-age) in the lower main sequence, red giant branch (RGB) and red clump (RC) CMD regions. In the last Hess diagram, stars from the DES-MagLiteS catalogue with $-68^\circ < \delta < -67^\circ$ and $10^\circ < \alpha < 15^\circ$ (the closest region to the SMC in the DES-MagLiteS catalogue) are sampled and the CMD mask for intermediate-age stars is reproduced to compare the SMC and SMCNOD stellar populations.

The PARSEC model for intermediate age is a good description of the SMCNOD population, and we selected stars that are more likely to belong to the object using the CMD filter described above. As a young population is also visible in the third and fourth subtracted Hess diagrams, we added an extra filter box to include the younger

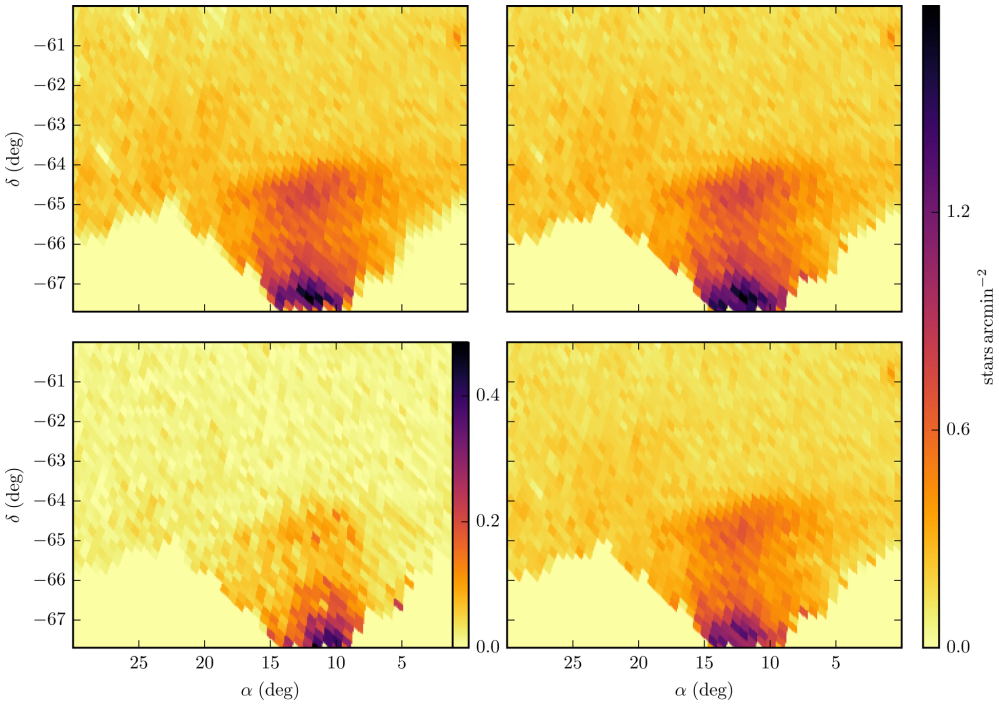

Figure 3. Top left: density map (each pixel has 14 × 14 arcmin, NSIDE=256) for stars filtered by the isochrone mask shown in the fourth panel of Fig. 2, in the field surrounding the SMCNOD. Top right: the same density map as in the left, but corrected by the coverage map. Bottom: density map for young (left) and intermediate-age (right) stellar population. Both bottom panels are corrected by the coverage map. The object in the top-right corner of each panel at α, $\delta \simeq \{1^\circ, -61^\circ\}$ is the dwarf galaxy candidate Tucana IV (Drlica-Wagner et al. 2015). Top-left panel and both right-hand panels are sharing the rightmost colourbar, while the young population is shown in a different colourbar scale, to highlight its weak contribution.

main-sequence stars. Using both CMD filters described above (for intermediate-age and young stars), we reanalyzed the stellar density distribution in the DES-MagLiteS catalogue. First, we built the stellar density map (top-left panel in Fig. 3) using NSIDE=256 (pixel size $\cong$ 14 arcmin on a side). Dividing this stellar density map by the coverage map results in the stellar density map shown in top-right panel in Fig. 3. We now see a stellar overdensity with a roughly elliptical shape, mainly composed of intermediate-age stars (comparing both bottom panels of Fig. 3) at a distance of 8° from the SMC centre ($\alpha = 13\overset{\circ}{.}000$, $\delta = -72\overset{\circ}{.}817$).

We follow the model from Noël & Gallart (2007) to compare the SMCNOD brightness to the expected SMC surface brightness extrapolated to that position. They fit the SMC surface brightness profile (in B and R bands) using three 34 arcmin × 33 arcmin fields located southwards of the SMC, at a distance of 4.7, 5.6 and 6.5 kpc (respectively, $4\overset{\circ}{.}2$, $4\overset{\circ}{.}9$ and $5\overset{\circ}{.}8$). Extrapolating their surface brightness profile out to a radial distance of 8° from the SMC centre, we derive an expected B-band surface brightness of $\mu_B = 32.4 \pm 0.3$ mag arcsec^{-2}. To compare to the SMCNOD surface brightness, we first applied a transformation of stellar magnitudes from g and r DES bands to g and r SDSS bands, following Bechtol et al. (2015):

$$g_{\rm SDSS} = g_{\rm DES} + 0.104(g_{\rm DES} - r_{\rm DES}) - 0.01 \quad (1)$$

$$r_{\rm SDSS} = r_{\rm DES} + 0.102(g_{\rm DES} - r_{\rm DES}) - 0.02. \quad (2)$$

We then converted the SDSS magnitudes from the CMD filtered stars to the B band, using the transformation equation from Jester et al. (2005):

$$B = g_{\rm SDSS} + 0.390(g_{\rm SDSS} - r_{\rm SDSS}) + 0.21. \quad (3)$$

We evaluate the integrated B flux at the SMCNOD centre, in the same HEALPIX pixels (NSIDE = 256) applied before, obtaining a surface brightness of $\mu_B = 29.7 \pm 0.17$ mag arcsec^{-2}. This is almost 3 mag brighter than expected from extrapolating the main body of the SMC based on Noël & Gallart (2007). The uncertainties were estimated using a bootstrap method, where the stars in the central pixel were randomly sorted (with replacement) to make up a new estimate of the brightness in the B band. A total of 1000 such bootstrap realizations were carried out.

Nidever et al. (2011) explored the SMC RGB distribution, using data from the MAgellanic Periphery Survey (MAPS), sampling 36 arcmin × 36 arcmin fields with the MOSAIC II Camera mounted on the CTIO 4 m Blanco telescope, and reaching as far as 12° from the SMC centre. They observed stars with Washington photometry in three bands (*DDO*51, M and T_2), as these bands are useful to discriminate MW foreground dwarfs from SMC RGB stars. The best-fitting elliptical density profile for the SMC giants sampled presents a 'break' at $7\overset{\circ}{.}5$ from the fitted centre ($\alpha = 15\overset{\circ}{.}129$, $\delta = -72\overset{\circ}{.}720$), where the density slope abruptly decreases and the distribution of giants begins to scatter around this flatter profile. In Fig. 4, we

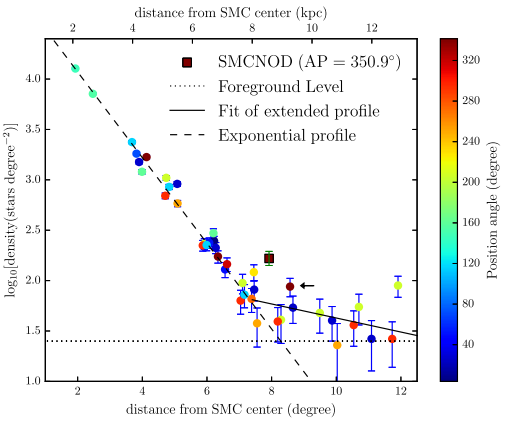

Figure 4. RGB density profile reproduced from fig. 3 of Nidever et al. (2011). The circles are the densities (as found by those authors) colour coded by position angle (from N to E). Also shown are the foreground contamination level and fitted profiles. The brown square is the density of giants as sampled in the SMCNOD centre, while the brown circle at 8.°4 (indicated by a black arrow) is the field 84S341, which overlaps with DES-MagLiteS and which was used to re-normalize DES-MagLiteS density scale. The SMC centre adopted here is at $\alpha = 15.°129$, $\delta = -72.°720$ and a distance of 61.94 kpc from the Sun (de Grijs & Bono 2015).

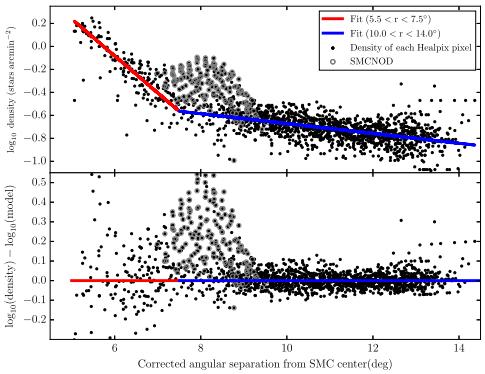

Figure 5. Top: stellar density (black dots) versus angular separation (corrected for elliptical shape and position angle) of the SMC centre. The stellar density was determined in each HEALPIX (NSIDE=256) in DES-MagLiteS, and the angular separation corresponds to the elliptical exponential model from Nidever et al. (2011). The solid red line is the fit for HEALPIX between 5.°5 and 7.°5 and solid blue line for pixels between 10.°0 and 14.°0. The grey circles are the boxes within the SMCNOD position (cells within truncation radius). Bottom: stellar density data divided by the model for all HEALPIX pixels. The SMCNOD resides at the interface between exponential models, but is discrepant from both. The radial scalelength is 1.°33 for the inner fit and 10.°13 for the outer fit.

reproduce fig. 3 from Nidever et al. (2011) using colour-coded circles according to the field position angles. The figure also reproduces the best-fitting models, both internal and external to the profile break.

To compare the density of RGB stars at the centre of the SMCNOD to the measurements of Nidever et al. (2011), we subtracted the Galactic foreground dwarf stars contaminating the RGB locus and we normalized our densities to the density profile shown in Fig. 4. This second goal is achieved with the use of the only field from Nidever et al. (2011) that overlaps the DES-MagLiteS footprint, which they name 84S341 and which is located 2.°2 away from the SMCNOD centre. Table 2 lists the positions and DES-MagLiteS stellar densities at the SMCNOD centre, at the 84S341 field and at a field far from the SMCNOD. The three fields are at nearly the same Galactic latitude and we assume that the difference in MW dwarf counts is negligible. The densities listed in the second to last column correspond to the stars falling within the intermediate-age isochrone CMD mask described earlier with an additional colour–magnitude cut of $g < 21$ applied and with no RC stars included. We refer to that filter as the RGB box. The first line in the last column represents the resulting RGB density after subtracting the foreground contamination. The bracketed density value for the 84S341 field is the RGB density actually measured by Nidever et al. (2011). The final SMCNOD RGB density (also shown in brackets) is then obtained by applying the same ratio as in the 84S341 field (166 giants degree^{-2}), placing it clearly above the density profile of any of the individual fields analysed by Nidever et al. (2011) at that angular distance (Fig. 4).

To compare the SMCNOD stellar density to the surrounding areas, we fit two models: a profile closer to the SMC than the SMCNOD (called the inner profile) and a profile more distant of the SMC than the SMCNOD (the outer profile). The distances from the SMC centre to each HEALPIX pixel were set following the Nidever et al. (2011) elliptical exponential model. The density of CMD-filtered stars was calculated in HEALPIX pixels with NSIDE = 256. We fitted the inner (outer) profile for boxes between 5.°5 and 7.°5 (between 10° and 14°) from the SMC centre. The fits provide an independent and striking confirmation of the SMC extended profile, along with the break at $\simeq 8°$ from the SMC centre. The top panel in Fig. 5 shows both inner (red line) and outer (blue line) fits for the density profiles near the SMCNOD. Dividing the density by the respective fits (bottom panel in Fig. 5), we find that the HEALPIX

Table 2. Name (first column) and position in equatorial (columns 2 and 3) and Galactic (columns 4 and 5) coordinates for three fields: the SMCNOD centre, the field overlapping (Nidever et al. 2011) and an MW foreground field at roughly the same Galactic latitude. The numbers in the second to last column are the stellar density after applying our CMD filters. The last column presents the density of giants after subtracting the MW foreground density (247 stars degree^{-2}). Numbers in brackets in the last columns are normalizing to Nidever et al. (2011), used as reference. More details are given in the text.

Field name	α (°)	δ (°)	l (°)	b (°)	ρ stars degree^{-2}	ρ giants degree^{-2}
SMCNOOD centre	12.000	−64.800	303.529	−52.317	457	210 [166]^a
84S341	6.892	−64.741	307.082	−52.194	357	110 [87.2]^b
MW foreground	19.928	−64.600	297.985	−52.256	247	–

Notes. ^{a}Density of giants estimated for the SMCNOD centre.
^{b}Density of giants from Nidever et al. (2011), used as reference. Both (^{a} and ^{b}) are plotted in Fig. 4.

Table 3. SMCNOD properties: equatorial (α and δ) and Galactic (l and b) coordinates of the centre, ellipticity, half-light radius, truncation radius, absolute magnitude and surface brightness. The last two properties are in the V band.

Property	Value	Unit
α	$12.00^{+0.08}_{-0.06}$	deg
δ	$-64.80^{+0.05}_{-0.08}$	deg
l	303.53	deg
b	−52.32	deg
ϵ	$0.60^{+0.19}_{-0.20}$	–
$r_{\rm h}$	$120.4^{+19.2}_{-3.12}$	arcmin
$r_{\rm tr}$	192 ± 20.0	arcmin
M_V	-7.7 ± 0.3	mag
$\mu_V(r < r_{\rm h})$	31.23 ± 0.21	mag arcsec^{-2}

pixels within the SMCNOD truncation radius (where the densities decrease to the level of the background density) have notably higher densities than those of the surrounding areas.

The structural parameters listed in Table 3 were fit using a marginalized likelihood approach and EMCEE, an affine-invariant ensemble sampler for Markov Chain Monte Carlo models (Foreman-Mackey et al. 2013).[4] We applied the marginalized likelihood fit to the HEALPIX pixels from Fig. 6, modelling the stellar density with a Plummer profile (Plummer 1911).

The absolute magnitude M_V was derived by adding the V flux within the ellipse bounded by the SMCNOD truncation radius converted from the g and r bands, also using equation from Jester et al. (2005):

$$V = g_{\rm SDSS} - 0.590(g_{\rm SDSS} - r_{\rm SDSS}) - 0.01. \quad (4)$$

To evaluate the V-band flux of the background, we added the flux within an ellipse with the same area shifted to 3° north of the SMCNOD and then subtracting from the SMCNOD flux in the V band. The M_V uncertainty incorporates the spatial fluctuations in the background flux and is in fact dominated by them.

The stellar mass of the SMCNOD was estimated by comparing a luminosity function (LF) from a simulated simple stellar population to the SMCNOD LF. The SMCNOD LF is subtracted from a field LF immediately above the overdensity, with equal area and located 3° north of the SMCNOD centre. The subtracted LF comprises 6068 stars within the range $21.0 \leq g \leq 23.0$, corresponding to the mass range of 0.90–0.99 $M_\odot$. A simulated simple stellar population (τ=6 Gyr and Z=0.001) with an evolved Kroupa mass function (MF; Kroupa 2001) was generated using GENCMD,[5] populating the 0.90–0.99 $M_\odot$ mass range with the same star counts as the SMCNOD subtracted LF. The mass range between 0.1 and 1.02 $M_\odot$ amounts to a stellar mass for the SMCNOD $\simeq 1.1 \times 10^5$ $M_\odot$, and its resulting M/L is very close to unity (1.07 $M_\odot/L_\odot$). The young population density is about one-tenth of the intermediate-age population density and thus the computed young population mass is included in the mass error range for SMCNOD. As a comparison, the SMCNOD has a stellar mass comparable to Galactic Globular cluster NGC 6287 (Gnedin & Ostriker 1997), but it is brighter (for NGC 6287, $M_V = -7.36$; following Harris 1996, updated 2010). Another estimate, using an evolved MF similar to that found for Palomar 5 by Koch et al. (2004), where the fainter stars were removed from the main body, yields an SMCNOD stellar mass $\simeq 8.0 \times 10^4$ $M_\odot$. These values show how the choice of an MF changes the total estimated stellar mass. Therefore, we interpret the first estimate as an upper limit for the SMCNOD stellar mass.

The dynamical mass of the SMCNOD (m) was estimated (in the case SMCNOD is bounded to the SMC) using equations (7–84) from Binney & Tremaine (2008):

$$\frac{m}{M} = 3\left(\frac{r_{\rm J}}{D}\right)^3, \quad (5)$$

where M is the SMC dynamical mass, $r_{\rm J}$ is the SMCNOD tidal radius and D is the distance between the SMC and SMCNOD centres. Assuming the SMCNOD tidal radius as 1.°5 (from the bottom panel in Fig. 5) and $D = 8°$, we determined that $m/M \cong 2.0 \times 10^{-2}$. Bekki & Stanimirović (2009) estimate that the SMC dark halo has a mass of 3×10^9 $M_\odot$ in the inner 3 kpc for a V-band mass-to-light ratio $\simeq$ 2. This mass agrees reasonably well with SMC rotation curves. Using this conservative estimate for the SMC mass, the SMCNOD dynamical mass is 6×10^7 $M_\odot$, a six hundred times greater than calculated for the stellar mass. The large disagreement between the stellar mass and the dynamical mass calculated using equation (5) is an argument favouring the SMCNOD is a structure detached from the SMC. The uncertainties in the SMCNOD dynamical mass are dominated by the errors in the SMC dynamical mass, which is estimated as about 13 per cent (Bekki & Stanimirović 2009).

The H I gas map could provide more insight into the nature of the SMCNOD, as well as a possible connection to the SMC. The H I gas column density map from the GASS Third Data Release[6] (Kalberla & Haud 2015) is shown in Fig. 7. While the LMC and the SMC H I gas contents are obvious, there is no apparent excess of gas associated with the position of the SMCNOD. We also use the GASS data to look for peaks in the velocity distribution of the gas within the velocity range from −495 to 495 km s^{-1} (1 km s^{-1} steps). The emission for one square degree centred on the SMCNOD exhibits two main peaks: 94 and 186 km s^{-1} (which are shown in Figs 8 and 9, respectively). These velocities agree with the velocity field related to the MS at the SMCNOD position, at an MS longitude $L_{\rm MS} \simeq -25°$. See for example fig. 8 in Nidever et al. (2010). We discuss details about H I gas distribution in Section 4.

4 DISCUSSION

In this section, we discuss the characteristics of the SMCNOD: we compare its stellar populations to those of the SMC (Section 4.1), its gas content (Section 4.2), possible scenarios for its origin (Section 4.3) and in the last subsection we provide a brief summary of the discovery, discussing the SMCNOD fate and some prospects for future analyses (Section 4.4).

4.1 The SMCNOD and SMC stellar populations

The $(g - r)$ colour distributions of SMCNOD and SMC stars for 3 mag ranges in the Hess diagram from Fig. 2 are shown in the left-hand panel of Fig. 10, whereas their number counts in bins of g magnitude filtered by the CMD mask and normalized (to the areas) are presented in the right-hand panel of the same figure. The colour distributions look very similar. For RC stars (solid lines), there may be a slight preference for the SMCNOD being a little bluer than the

[4] http://dan.iel.fm/emcee/current/

[5] GENCMD yields position, magnitude and errors with a simple stellar population. See details in https://github.com/balbinot/gencmd.

[6] https://www.astro.uni-bonn.de/hisurvey/gass/

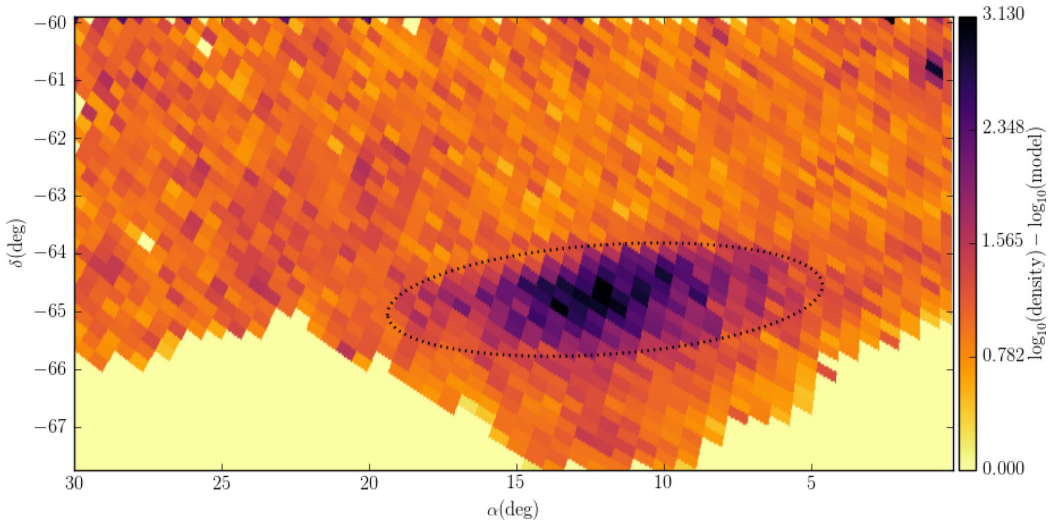

Figure 6. Ratio from Fig. 5 (bottom panel) projected on to the sky. The truncation radius from Table 3 is shown as a dotted black line.

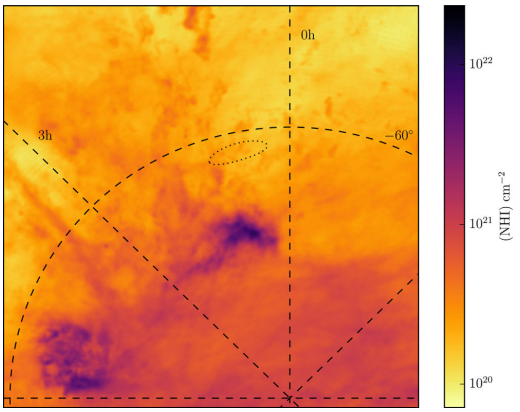

Figure 7. H I gas column density map from Kalberla & Haud (2015), in zenith equal area projection, close to the south celestial pole. A grid of equatorial coordinates (α and δ) is indicated. The SMC is close to the centre of the figure and the LMC is located near the bright spot in the lower-left corner. No significant excess of H I gas is observed at the position of the SMCNOD (dotted ellipse).

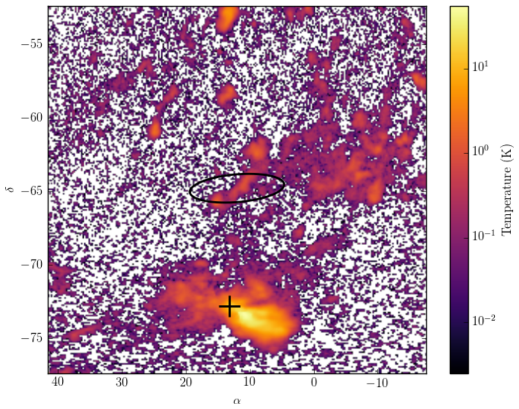

Figure 8. H I gas emission map from Kalberla & Haud (2015), in equatorial coordinates for the velocity channel 94 km s^{-1} < v_{LSR} < 95 km s^{-1}. The SMCNOD position is highlighted by an empty ellipse and the SMC centre by a plus symbol.

SMC. However, a Kolmogorov–Smirnov (KS) test indicates that the two RC populations come from the same parent distribution ($p = 0.42$). As for the LF comparison, the two distributions look similar as well.

4.2 The SMCNOD and H I gas

The results of considering the H I gas velocity channels are inconclusive. The v_{LSR}=186 km s^{-1} channel map (Fig. 9) shows a few links between the SMC and the SMCNOD, while the v_{LSR}=94 km s^{-1} channel map (Fig. 8) shows a bar-shaped gas cloud detached from the SMC main body. A looping feature is visible in the v_{LSR}=186 km s^{-1} channel map that could be the result of a weak gas inflow (from the SMC, counterclockwise). But in summary, the SMCNOD does not seem to contain a large amount of gas and it is currently unclear whether the H I gas features present in either velocity channel map are connected to it. It has been suggested that the drift rate of the MS gas away from the LMC is ∼49 km s^{-1}, as indicated by Nidever, Majewski & Butler Burton (2008). Using these results, an age of 1.74 Gyr is expected for the MS. In this sense, the gas features surrounding the SMC should be very recent (a few hundred million years or even younger), showing a complex dynamics. Taken at face value, the gas properties around the SMCNOD are more consistent with gas-poor dwarf spheroidals (Grebel, Gallagher & Harbeck 2003) and ultrafaint dwarf galaxies in the Local Group (Grcevich 2013).

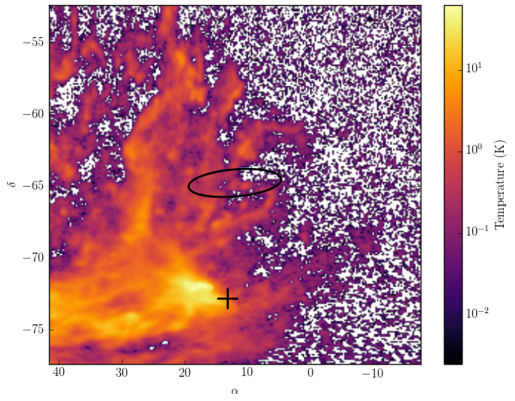

Figure 9. Same as Fig. 8 but for velocity channel equal to 186 km s^{-1} (186 km s^{-1} < v_{LSR} < 187 km s^{-1}).

4.3 The SMCNOD origin

Regarding the formation of the SMCNOD, the most likely scenario is that this structure was formed by material pulled from the SMC disc through tidal stripping, given the recent *N*-body simulations as cited in Section 1. Following the classical galactic interaction theory of Toomre & Toomre (1972), many other works predict the existence of a Magellanic Counter-Bridge as a counterpart to the Magellanic Bridge (Diaz & Bekki 2012; Dobbie et al. 2014a). In the north-west part of the SMC, a kinematical substructure discovered by Dobbie et al. (2014a) is associated with the Magellanic Counter-Bridge, as an observational counterpart. The simulations also predict a spread of stars as a result of an LMC-SMC close encounters. See for example the tidal tail in fig. 5 of Gardiner & Noguchi (1996), the set of particles located south-west of the SMC in fig. 12 from Yoshizawa & Noguchi (2003), and the SMC stellar distribution in figs 4 and 5 of Connors et al. (2006). Also, a conspicuous clump of young stars can be seen for the fiducial model simulated by Bekki & Chiba (2009) in their figs 5, 6 and 9, located 4° from the centre of the SMC, along with a stream-like feature on the opposite side. Earlier simulations present a spread of particles around the SMC, for example fig. 10 b of Fujimoto & Sofue (1976) and fig. 6 a of Murai & Fujimoto (1980). The substantial stream-like stellar overdensity in the northern periphery of the LMC centre recently discovered by Mackey et al. (2016), with characteristics similar to the SMCNOD, also corroborates this scenario for the SMCNOD formation based on close LMC-SMC interactions. Finally, a close encounter occurred ≈ 200 Myr ago is also claimed as an explanation for a 55 kpc stellar structure in the eastern SMC (Nidever et al. 2013), where likely the stars were tidally stripped from the SMC.

If the SMCNOD is the result of an LMC-SMC collision, a contemporaneous peak in star formation is expected in both galaxies. Unfortunately, the results of star formation history (SFH) analyses have large uncertainties, and there is a significant spatial variation for the SFH in the LMC (Holtzman et al. 1999; Olsen 1999; Smecker-Hane et al. 2002; Harris & Zaritsky 2009; Rubele et al. 2012) and SMC (Noël et al. 2009; Cignoni et al. 2013; Rubele et al. 2015). SFH variations are larger when based on different models (isochrones) and/or stellar tracers (RGB, carbon or variable stars) and the MCs SFH is still far from being fully characterized in spite of much work. Even so, it is interesting to note that most of the references listed above agree with a simultaneous peak in star formation rate between 4 and 6 Gyr (also discussed in Dobbie et al. 2014b), the age of the main stellar population of the SMCNOD. A complete reconstruction of the SFH of the SMCNOD (and also a comparison to the SFH of various SMC regions) is beyond the scope of this work.

Another possible scenario for the SMCNOD origin is a tidal dwarf galaxy (TDG), an object formed as described by Elmegreen, Kaufman & Thomasson (1993), where mainly gas is stripped from

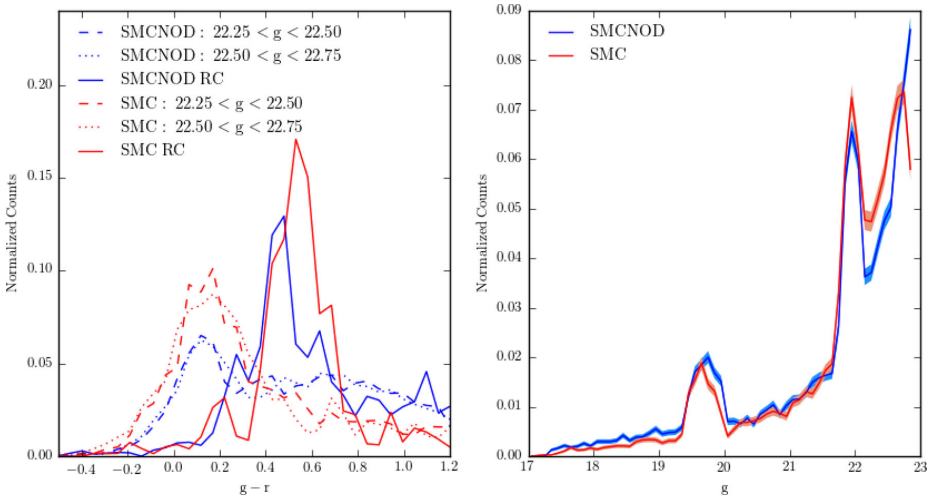

Figure 10. Histograms in bins of colour (left) and in bins of *g* magnitude (right) filtered by the CMD mask for the SMCNOD (third panel in Fig. 2) and the SMC (fifth panel in Fig. 2). In the right-hand panel, the Poissonian uncertainties are shown as shaded areas. The stellar colour distribution is very similar between the SMC and SMCNOD in the left-hand panel (comparing dotted red and blue lines and dashed red and blue lines), as well as the histogram in bins of magnitude for the stars filtered with the CMD mask in the last two panels in Fig. 2 (right-hand panel).

past mergers and resemble as dwarf galaxies, where the stars are forming during/after the main encounter. The lack of dark matter in TDGs makes them fragile, leading to short lifetimes (a few Gyr) as cohesive systems. This scenario for the SMCNOD formation is disfavoured due to its poor gas content and predominantly intermediate-age stars (at least 6 Gyr), compared to an expected young TDG stellar population (Duc 2012). On the other hand, numerical simulations by Ploeckinger et al. (2014) show TDGs could survive at least 3 Gyr, despite the lack of dark matter content. This is corroborated by the existence of the relatively old TDG VCC2062 observed by Duc et al. (2007), where its parent galaxies have likely merged.

The scenario where the SMCNOD is a primordial galaxy orbiting and/or merging with the SMC could be favoured if the stellar populations of the SMCNOD have narrower age and metallicity ranges than those of the SMC. This would make the SMCNOD more consistent with typical dwarf spheroidal galaxies.

An intriguing possibility for the origin of the SMCNOD is the 'resonant stripping' predicted by D'Onghia et al. (2009). This process allows for an efficient removal of stars in a dwarf–dwarf encounter, where the smaller dwarf loses stars by a resonance between the angular frequency of its orbit and spin, changing the ratio of the stellar to dark matter mass. Simulations also predict that dwarf-disc galaxies will evolve into compact spheroidal systems with stream-like and shell-like structures, resembling the SMCNOD shape around the SMC. Future deep photometric surveys of the SMC/LMC outskirts could reveal similar structures, testing the significance of this 'resonant stripping' in the model.

The relatively old age for most of the stars in the SMC-NOD rules out its origin as being formed by H I gas from the MS. As Nidever et al. (2008) point out, the expected age of putative MS stars should be $\simeq$2.0 Gyr, less than half of the characteristic age found for the overdensity stars. The origin of the SMCNOD younger population may or may not be attributed to the same physical mechanism as the intermediate-age population. Since the SMC-LMC interaction is known to have triggered star formation at recent times (as in the case of the Magellanic Bridge, see for example Bica et al. 2015; Noël et al. 2015), we cannot rule out that this interaction may be responsible for the younger SMCNOD population.

4.4 Summary, prospects and fate of the SMCNOD

Using DES and MagLiteS data, we have found and analysed a stellar overdensity located about 8° north of the SMC centre. The stellar density and surface brightness associated with this feature lie significantly above the values expected from the extrapolated stellar profile of the SMC itself. This is true even when we consider only the contribution from the RGB stars. Previous surveys around the SMCNOD, such as the MAPS (Nidever et al. 2011), Two Micron All Sky Survey (Skrutskie et al. 1997), Digitized Sky Survey[7] and Infrared Astronomical Satellite survey,[8] among others, did not reveal any stellar overdensity similar to the one measured here. This may be due to either their non-contiguous area or their lower photometric depth.

The fact that the structure discussed here has a density peak lying significantly in excess of the expected SMC exponential density profile (or above the combined SMC and Galactic background) and follows a roughly elliptical profile encourage us to argue that it is a distinct SMC substructure. On the other hand, the CMD analysis indicates that the stellar populations are very similar to those found in the main SMC body, and the SMCNOD lies at a similar heliocentric distance as the SMC.

The fate of the SMCNOD has interesting implications for the Magellanic System generally. If the SMCNOD is an unstable object, such as a stellar cloud, it should dissipate into the SMC main body or, if unbound to the SMC, be ejected and dissipate eventually into the Galactic field. However, for the first hypothesis to hold, the SMC truncation radius must be $\simeq$10 kpc (see the SMCNOD limits in Fig. 5) to encompass the entire stellar cloud presented here. As a reference, the truncation radius derived from chemodynamical simulations involving SMC-like objects is in the range between 5 and 7.5 kpc (Bekki & Chiba 2007, 2009; Diaz & Bekki 2012), not enough to include the entire SMCNOD.

Radial velocities and proper motions of likely stellar members will constrain systemic and internal kinematics of the SMCNOD, as well as its internal motions. Metallicities and other abundance estimates may indicate similarities and differences between the SMCNOD stars and those belonging to the main SMC body. An internal age and/or metallicity gradient (or its absence) may also constrain its nature as either a primordial or tidal object. Finally, the SMCNOD discovery shows that the Magellanic System, despite being relatively well studied, still hides surprising substructures that may be revealed with deep photometric surveys. The discovery of the SMCNOD at such a large distance from the SMC should provide an additional constraint for simulations of the Magellanic System.

[7] http://archive.stsci.edu/cgi-bin/dss_form
[8] http://irsa.ipac.caltech.edu/Missions/iras.html

ACKNOWLEDGEMENTS

We are grateful to the anonymous referee for valuable comments, which contributed to improving this paper. This paper has gone through internal review by the DES and MagLiteS Collaboration. EB acknowledges financial support from the European Research Council (ERC-StG-335936). DMD acknowledges support by Sonderforschungsbereich (SFB) 881 'The Milky Way System' of the German Research Foundation (DFB), subproject A2.

Funding for the DES Projects has been provided by the US Department of Energy, the US National Science Foundation, the Ministry of Science and Education of Spain, the Science and Technology Facilities Council of the United Kingdom, the Higher Education Funding Council for England, the National Center for Supercomputing Applications at the University of Illinois at Urbana–Champaign, the Kavli Institute of Cosmological Physics at the University of Chicago, the Center for Cosmology and Astro-Particle Physics at the Ohio State University, the Mitchell Institute for Fundamental Physics and Astronomy at Texas A&M University, Financiadora de Estudos e Projetos, Fundação Carlos Chagas Filho de Amparo à Pesquisa do Estado do Rio de Janeiro, Conselho Nacional de Desenvolvimento Científico e Tecnológico and the Ministério da Ciência, Tecnologia e Inovação, the Deutsche Forschungsgemeinschaft and the Collaborating Institutions in the DES.

The Collaborating Institutions are Argonne National Laboratory, the University of California at Santa Cruz, the University of Cambridge, Centro de Investigaciones Energéticas, Medioambientales y Tecnológicas–Madrid, the University of Chicago, University College London, the DES-Brazil Consortium, the University of Edinburgh, the Eidgenössische Technische Hochschule (ETH) Zürich, Fermi National Accelerator Laboratory, the University of Illinois at Urbana–Champaign, the Institut de Ciències de l'Espai (IEEC/CSIC), the Institut de Física d'Altes Energies, Lawrence Berkeley National Laboratory, the Ludwig-Maximilians Universität

München and the associated Excellence Cluster Universe, the University of Michigan, the NOAO, the University of Nottingham, The Ohio State University, the University of Pennsylvania, the University of Portsmouth, SLAC National Accelerator Laboratory, Stanford University, the University of Sussex, Texas A&M University and the OzDES Membership Consortium.

The DES data management system is supported by the National Science Foundation under Grant Number AST-1138766. The DES participants from Spanish institutions are partially supported by MINECO under grants AYA2012-39559, ESP2013-48274, FPA2013-47986, and Centro de Excelencia Severo Ochoa SEV-2012-0234. Research leading to these results has received funding from the European Research Council under the European Union's Seventh Framework Programme (FP7/2007-2013) including ERC grant agreements 240672, 291329 and 306478.

REFERENCES

Bechtol K. et al., 2015, ApJ, 807, 50
Bekki K., Chiba M., 2007, Publ. Astron. Soc. Aust., 24, 21
Bekki K., Chiba M., 2009, Publ. Astron. Soc. Aust., 26, 48
Bekki K., Stanimirović S., 2009, MNRAS, 395, 342
Besla G., Kallivayalil N., Hernquist L., van der Marel R. P., Cox T. J., Kereš D., 2012, MNRAS, 421, 2109
Besla G., Martínez-Delgado D., van der Marel R. P., Beletsky Y., Seibert M., Schlafly E. F., Grebel E. K., Neyer F., 2016, ApJ, 825, 20
Bica E., Santiago B., Bonatto C., Garcia-Dias R., Kerber L., Dias B., Barbuy B., Balbinot E., 2015, MNRAS, 453, 3190
Binney J., Tremaine S., 2008, Galactic Dynamics: Second Edition. Princeton Univ. Press, Princeton, NJ
Bressan A., Marigo P., Girardi L., Salasnich B., Dal Cero C., Rubele S., Nanni A., 2012, MNRAS, 427, 127
Cignoni M., Cole A. A., Tosi M., Gallagher J. S., Sabbi E., Anderson J., Grebel E. K., Nota A., 2013, ApJ, 775, 83
Connors T. W., Kawata D., Gibson B. K., 2006, MNRAS, 371, 108
D'Onghia E., Besla G., Cox T. J., Hernquist L., 2009, Nature, 460, 605
de Grijs R., Bono G., 2015, ApJ, 149, 179
Deason A. J., Wetzel A. R., Garrison-Kimmel S., Belokurov V., 2015, MNRAS, 453, 3568
Desai S. et al., 2012, ApJ, 757, 83
Diaz J. D., Bekki K., 2012, ApJ, 750, 36
Dobbie P. D., Cole A. A., Subramaniam A., Keller S., 2014a, MNRAS, 442, 1663
Dobbie P. D., Cole A. A., Subramaniam A., Keller S., 2014b, MNRAS, 442, 1680
Drlica-Wagner A. et al., 2015, ApJ, 813, 109
Drlica-Wagner A. et al., 2016, ApJ, 833, L5
Duc P.-A., 2012, in Papaderos P., Recchi S., Hensler G., eds, Astrophysics and Space Science Proceedings, Vol. 28, Dwarf Galaxies: Keys to Galaxy Formation and Evolution. Springer-Verlag, Berlin, p. 305
Duc P.-A., Braine J., Lisenfeld U., Brinks E., Boquien M., 2007, A&A, 475, 187
Elmegreen B. G., Kaufman M., Thomasson M., 1993, ApJ, 412, 90
Flaugher B. et al., 2015, AJ, 150, 150
Foreman-Mackey D., Hogg D. W., Lang D., Goodman J., 2013, PASP, 125, 306
Fujimoto M., Sofue Y., 1976, A&A, 47, 263
Gardiner L. T., Noguchi M., 1996, MNRAS, 278, 191
Gnedin O. Y., Ostriker J. P., 1997, ApJ, 474, 223
Grcevich J., 2013, PhD thesis, University of Columbia
Grebel E. K., Gallagher J. S., III, Harbeck D., 2003, AJ, 125, 1926
Grondin L., Demers S., Kunkel W. E., 1992, AJ, 103, 1234
Guhathakurta P., Reitzel D. B., 1998, in Zaritsky D., ed., ASP Conf. Ser. Vol. 136, Galactic Halos. Astron. Soc. Pac., San Francisco, p. 22
Harris W. E., 1996, AJ, 112, 1487
Harris J., Zaritsky D., 2009, AJ, 138, 1243
Holtzman J. A. et al., 1999, AJ, 118, 2262
Irwin M. J., Demers S., Kunkel W. E., 1990, AJ, 99, 191
Jester S. et al., 2005, AJ, 130, 873
Jethwa P., Erkal D., Belokurov V., 2016, MNRAS, 461, 2212
Kalberla P. M. W., Haud U., 2015, A&A, 578, A78
Kallivayalil N., van der Marel R. P., Alcock C., Axelrod T., Cook K. H., Drake A. J., Geha M., 2006a, ApJ, 638, 772
Kallivayalil N., van der Marel R. P., Alcock C., 2006b, ApJ, 652, 1213
Kallivayalil N., van der Marel R. P., Besla G., Anderson J., Alcock C., 2013, ApJ, 764, 161
Koch A., Grebel E. K., Odenkirchen M., Martínez-Delgado D., Caldwell J. A. R., 2004, AJ, 128, 2274
Koposov S. E., Belokurov V., Torrealba G., Evans N. W., 2015, ApJ, 805, 130
Kroupa P., 2001, MNRAS, 322, 231
Mackey A. D., Koposov S. E., Erkal D., Belokurov V., Da Costa G. S., Gómez F. A., 2016, MNRAS, 459, 239
Mathewson D. S., Cleary M. N., Murray J. D., 1974, ApJ, 190, 291
Murai T., Fujimoto M., 1980, PASJ, 32, 581
Nidever D. L., Majewski S. R., Butler Burton W., 2008, ApJ, 679, 432
Nidever D. L., Majewski S. R., Butler Burton W., Nigra L., 2010, ApJ, 723, 1618
Nidever D. L., Majewski S. R., Muñoz R. R., Beaton R. L., Patterson R. J., Kunkel W. E., 2011, ApJ, 733, L10
Nidever D. L., Monachesi A., Bell E. F., Majewski S. R., Muñoz R. R., Beaton R. L., 2013, ApJ, 779, 145
Noël N. E. D., Gallart C., 2007, ApJ, 665, L23
Noël N. E. D., Aparicio A., Gallart C., Hidalgo S. L., Costa E., Méndez R. A., 2009, ApJ, 705, 1260
Noël N. E. D., Conn B. C., Read J. I., Carrera R., Dolphin A., Rix H.-W., 2015, MNRAS, 452, 4222
Olsen K. A. G., 1999, AJ, 117, 2244
Ploeckinger S., Hensler G., Recchi S., Mitchell N., Kroupa P., 2014, MNRAS, 437, 3980
Plummer H. C., 1911, MNRAS, 71, 460
Recillas-Cruz E., 1982, MNRAS, 201, 473
Rubele S. et al., 2012, A&A, 537, A106
Rubele S. et al., 2015, MNRAS, 449, 639
Sales L. V., Navarro J. F., Kallivayalil N., Frenk C. S., 2016, MNRAS, 465, 1879
Schlegel D. J., Finkbeiner D. P., Davis M., 1998, ApJ, 500, 525
Skrutskie M. F. et al., 1997, in Garzon F., ed., Astrophysics and Space Science Library, Vol. 210, The Impact of Large Scale Near-IR Sky Surveys. Kluwer, Dordrecht, p. 25
Smecker-Hane T. A., Cole A. A., Gallagher J. S., III, Stetson P. B., 2002, ApJ, 566, 239
The Dark Energy Survey Collaboration, 2005, preprint (astro-ph/0510346)
Toomre A., Toomre J., 1972, ApJ, 178, 623
van der Marel R. P., Sahlmann J., 2016, ApJ, 832, L23
Vieira K. et al., 2010, AJ, 140, 1934
Yoshizawa A. M., Noguchi M., 2003, MNRAS, 339, 1135

[1]*Instituto de Física, Universidade Federal do Rio Grande do Sul, 91501-900 Porto Alegre, RS, Brazil*
[2]*Laboratório Interinstitucional de e-Astronomia - LIneA, Rua Gal. José Cristino 77, 20921-400 Rio de Janeiro, RJ, Brazil*
[3]*Fermi National Accelerator Laboratory, P.O. Box 500, Batavia, IL 60510, USA*
[4]*Large Synoptic Survey Telescope, 933 North Cherry Avenue, Tucson, AZ 85721, USA*
[5]*Space Telescope Science Institute, 3700 San Martin Drive, Baltimore, MD 21218, USA*
[6]*Steward Observatory, University of Arizona, 933 North Cherry Avenue, Tucson, AZ 85721, USA*
[7]*Observatoire astronomique de Strasbourg, Université de Strasbourg, CNRS, UMR 7550, 11 rue de l'Université, F-67000 Strasbourg, France*

[8]*Max-Planck-Institut für Astronomie, Königstuhl 17, D-69117 Heidelberg, Germany*
[9]*Institute of Astronomy, University of Cambridge, Madingley Road, Cambridge CB3 0HA, UK*
[10]*Instituto de Astrofísica de Canarias. Vía Láctea s/n. E-38200 - La Laguna, Tenerife, Canary Islands, Spain*
[11]*Department of Astrophysics, University of La Laguna. Vía Láctea s/n. E-38200 - La Laguna, Tenerife, Canary Islands, Spain*
[12]*Astronomisches Rechen-Institut, Zentrum für Astronomie der Universität Heidelberg, Mönchhofstr. 12-14, D-69120 Heidelberg, Germany*
[13]*George P. and Cynthia Woods Mitchell Institute for Fundamental Physics and Astronomy, and Department of Physics and Astronomy, Texas A&M University, College Station, TX 77843, USA*
[14]*Department of Physics, University of Surrey, Guildford GU2 7XH, UK*
[15]*Department of Astronomy, University of Virginia, Charlottesville, VA 22904-4325, USA*
[16]*University of Hertfordshire, Physics Astronomy and Mathematics, College Lane, Hatfield AL10 9AB, UK*
[17]*Leibnitz-Institut für Astrophysik Potsdam, An der Sternwarte 16, D-14482 Potsdam, Germany*
[18]*Department of Physics, ETH Zurich, Wolfgang-PauliStrasse 16, CH-8093 Zurich, Switzerland*
[19]*Research School of Astronomy & Astrophysics, Mount Stromlo Observatory, Cotter Road, Weston Creek, ACT 2611, Australia*
[20]*Cerro Tololo Inter-American Observatory, National Optical Astronomy Observatory, Casilla 603, La Serena, Chile*
[21]*Center for Astrophysics and Space Astronomy, Department of Astrophysical and Planetary Sciences, University of Colorado, 389 UCB, Boulder, CO 80309, USA*
[22]*National Optical Astronomy Observatory, 950 N. Cherry Ave, Tucson, AZ 85719, USA*
[23]*Observatório Nacional, Rua Gal. José Cristino 77, Rio de Janeiro 20921-400, RJ, Brazil*
[24]*Department of Physics and Electronics, Rhodes University, P.O. Box 94, Grahamstown 6140, South Africa*
[25]*Department of Physics & Astronomy, University College London, Gower Street, London WC1E 6BT, UK*
[26]*CNRS, UMR 7095, Institut d'Astrophysique de Paris, F-75014 Paris, France*
[27]*Sorbonne Universités, UPMC Univ Paris 06, UMR 7095, Institut d'Astrophysique de Paris, F-75014 Paris, France*
[28]*Department of Astronomy, University of Illinois, 1002 W. Green Street, Urbana, IL 61801, USA*
[29]*National Center for Supercomputing Applications, 1205 West Clark St, Urbana, IL 61801, USA*
[30]*Institut de Ciències de l'Espai, IEEC-CSIC, Campus UAB, Carrer de Can Magrans, s/n, E-08193 Bellaterra, Barcelona, Spain*
[31]*Instituto de Fisica Teorica UAM/CSIC, Universidad Autonoma de Madrid, E-28049 Madrid, Spain*
[32]*Kavli Institute for Particle Astrophysics & Cosmology, P.O. Box 2450, Stanford University, Stanford, CA 94305, USA*
[33]*Institute of Cosmology & Gravitation, University of Portsmouth, Portsmouth PO1 3FX, UK*
[34]*School of Physics and Astronomy, University of Southampton, Southampton SO17 1BJ, UK*
[35]*Department of Physics, IIT Hyderabad, Kandi, Telangana 502285, India*
[36]*SLAC National Accelerator Laboratory, Menlo Park, CA 94025, USA*
[37]*Center for Cosmology and Astro-Particle Physics, The Ohio State University, Columbus, OH 43210, USA*
[38]*Department of Physics, The Ohio State University, Columbus, OH 43210, USA*
[39]*Astronomy Department, University of Washington, Box 351580, Seattle, WA 98195, USA*
[40]*Australian Astronomical Observatory, North Ryde, NSW 2113, Australia*
[41]*Institució Catalana de Recerca i Estudis Avançats, E-08010 Barcelona, Spain*
[42]*Institut de Física d'Altes Energies (IFAE), The Barcelona Institute of Science and Technology, Campus UAB, E-08193 Bellaterra (Barcelona), Spain*
[43]*Jet Propulsion Laboratory, California Institute of Technology, 4800 Oak Grove Dr, Pasadena, CA 91109, USA*
[44]*Department of Physics and Astronomy, Pevensey Building, University of Sussex, Brighton BN1 9QH, UK*
[45]*Department of Physics and Astronomy, University of Pennsylvania, Philadelphia, PA 19104, USA*
[46]*Centro de Investigaciones Energéticas, Medioambientales y Tecnológicas (CIEMAT), Avda. Complutense, 40 E-28040, Madrid, Spain*
[47]*Department of Physics, University of Michigan, Ann Arbor, MI 48109, USA*
[48]*Universidade Federal do ABC, Centro de Ciências Naturais e Humanas, Av. dos Estados, 5001, Santo André 09210-580, SP, Brazil*
[49]*Computer Science and Mathematics Division, Oak Ridge National Laboratory, Oak Ridge, TN 37831, USA*

This paper has been typeset from a TEX/LATEX file prepared by the author.

Capítulo 5

Considerações Finais

5.1 Os aglomerados da LMC na amostra do DES

Nesta seção vamos discorrer sobre os resultados e as implicações físicas destes resultados no tocante à distribuição dos aglomerados (procura por gradientes) nesta região externa em que trabalhamos.

5.1.1 Distribuição de idade dos aglomerados da amostra

Um dos principais resultados que obtivemos com o ajuste de idade dos aglomerados foi uma distribuição aparentemente bimodal de idades, como mostrado na figura 5.1 e na figura 5.2. A última figura citada mostra claramente dois picos em $\approx$1,7 e $\approx$ 2,4 bilhões de anos para o histograma de idades.

De forma a comprovar a validade desta bimodalidade para a idade testamos primeiramente a abordagem de Kolmogorov-Smirnov para uma distribuição centrada em um único pico. Posteriormente aplicamos o mesmo teste de hipótese para dois picos. Para realizar estes testes, selecionamos a amostra de aglomerados com menos de 4 bilhões de anos e comparamos com 1000 simulações de distribuição unimodal de idade. Os resultados para uma distribuição gaussiana unimodal indicam um valor de p de 1%, muito pouco significativo utilizando como tomada de decisão $\alpha = 0{,}05$. Neste caso, podemos rejeitar a hipótese nula de que ambas as distribuições de idade (dos aglomerados reais e das simulações) têm o mesmo comportamento (provêm de Gaussianas com um único pico, centrado no melhor ajuste feito previamente).

Para o modelo de dupla Gaussiana, primeiramente se fez uma distribuição centrada em dois picos de 1,2 e 2,7 bilhões de anos, com desvio padrão de 0,3 e 0,4 bilhão de anos, respectivamente. A comparação da distribuição real com mil simulações

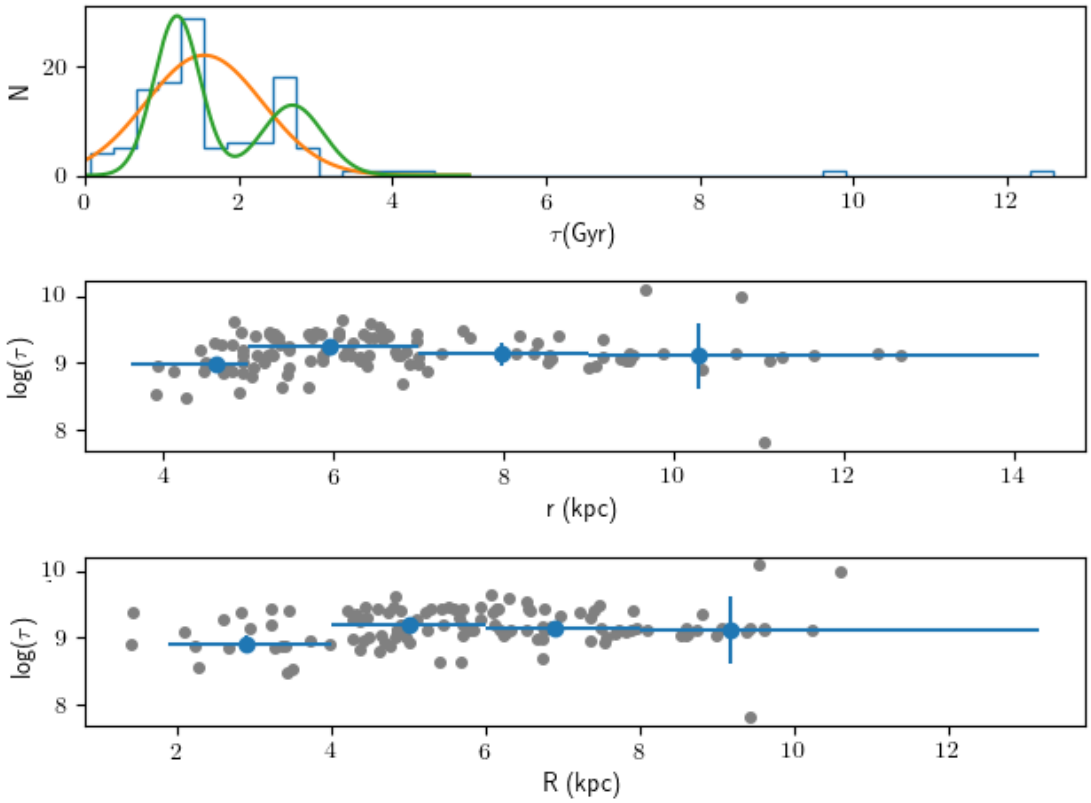

Figura 5.1: *Painel superior:* Histograma dos aglomerados mostrando uma distribuição normal unimodal e bimodal ajustadas com o método apresentado em Ashman et al. (1994). *Painel central:* Idade em função da distância do aglomerado ao centro da LMC. Círculos azuis são a média em idade em quatro amostras não homogêneas. Barras horizontais indicam o intervalo de coordenadas e as barras verticais representam o desvio padrão em idade para cada subamostra. *Painel inferior:* Idade versus coordenada cilíndrica R.

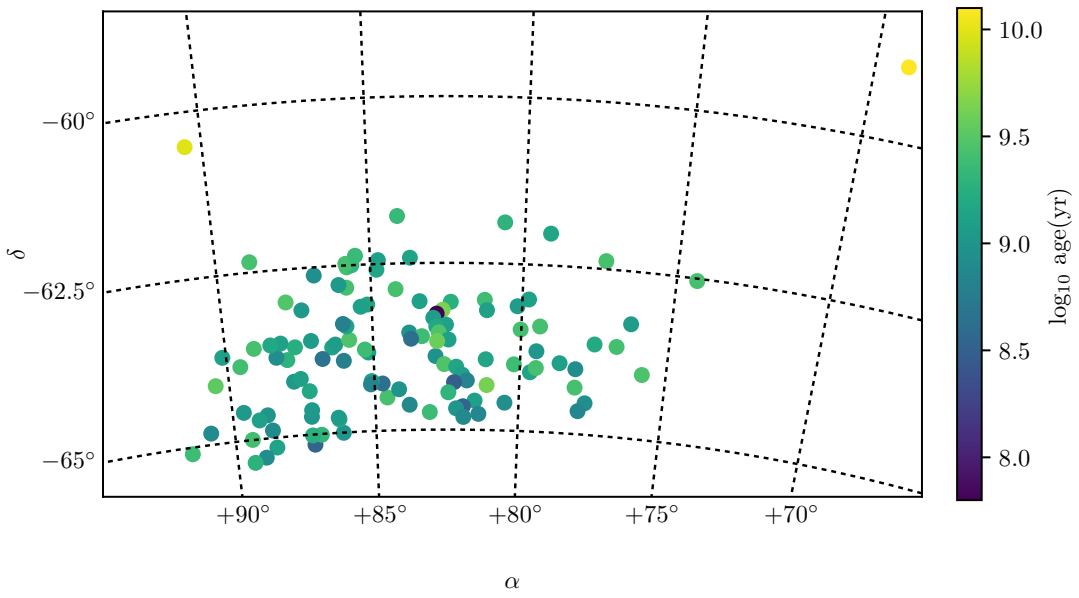

Figura 5.2: Distribuição de aglomerados no céu, de acordo com o $\log_{10}$ da idade (em anos), indicado pela cor. Embora os aglomerados distantes sejam os mais velhos, não há (pelo menos visualmente) um gradiente de idade para os aglomerados mais próximos do centro da Grande Nuvem de Magalhães (situado mais ao Sul, com declinação $-62.5°$).

mostrou um valor médio de $p = 0{,}25$, sendo a distribuição real compatível com as distribuições simuladas, de modo que não podemos rejeitar a hipótese nula de que a distribuição real e as simuladas bimodais têm o mesmo comportamento.

Sobre o modelo utilizado para a distribuição de idades (Gaussiana), poder-se-ia utilizar um outro modelo. No entanto, preferimos os mais simples. Ainda o pico de idade mais jovem mostra uma distribuição aparentemente mais abrupta tendendo a idades mais velhas do que para a tendência para as mais jovens. Desta maneira, isso poderia indicar um pico mais intenso próximo de 1,5 bilhões de anos, favorecendo uma intensa formação de aglomerados que foi diminuindo com o tempo, havendo um número menor de aglomerados imediatamente mais jovens do que imediatamente mais velhos.

Dentro da colaboração do DES, foi-nos indicado o trabalho de Ashman et al. (1994) sobre bimodalidade. No entanto, este trabalho desenvolve um arcabouço de fórmulas aplicadas a uma distribuição multivariada (mais de um pico de distribuição) mas homoscedástica (apenas um único valor de dispersão para as várias Gaussianas), o que não se aplica à distribuição de idades para os aglomerados da amostra, que nitidamente possui mais de um pico e mais de uma dispersão de idades.

Como um último teste (já a pedido do árbitro da revista Montly Notices of the Royal Astronomic Society) para a bimodalidade em idade foram feitos testes utilizando o algoritmo *Expectation-Maximization* (Dempster et al., 1977, Sundberg, 1974) para a determinação dos melhores parâmetros estatísticos (média, dispersão e participação de cada população) para a distribuição de idade dos aglomerados. Utilizamos o modelo Gaussiano como modelo estatístico para cada população em idade. O algoritmo *Expectation-Maximization* basicamente trabalha em um ciclo contendo dois passos. No primeiro passo são assumidos valores iniciais para as médias, dispersões e participação de populações. A partir destes valores, uma grade de modelos (*training set*) é calculada, com dispersão dada pelos valores iniciais. No segundo passo (*maximization*), a probabilidade para cada modelo é calculada e comparada com os dados observados. O modelo que resulta na maior probabilidade é reinserido como valor inicial no primeiro passo do algoritmo, fechando o ciclo. A convergência ocorre quando a diferença entre os valores dos parâmetros estatísticos é menor do que um valor indicado pelo usuário (geralmente 0,001). O método é robusto o suficiente para contornar problemas como valores iniciais distantes dos valores de convergência (o que basicamente vai afetar apenas o tempo computacional) e chega nos mesmos valores mesmo que os chutes iniciais sejam diferentes.

Além disso utilizamos o Critério de Informação Bayesiano (ou em inglês BIC[1]) para a tomada de decisão sobre o número de Gaussianas mais provável na distribuição de idades. Este critério foi calculado para um conjunto que vai de 1 a 7 Gaussianas e os menores valores foram 270,4 para uma Gaussiana, 258,8 para duas e 268,2 para três Gaussianas. Os centros indicados para as duas Gaussianas (com menor BIC) foram de 1,1 e 2,3 em idade, com respectivas dispersões de 0,4 e 0,6 e pesos de 0,63 e 0,37 para as respectivas populações. Uma referência mais didática para o algoritmo *Expectation-Maximization* pode ser encontrada em (Do & Batzoglou, 2008).

Dividindo a população em dois intervalos de idade (respectivamente mais jovens e mais velha que 2 bilhões de anos), os valores médios para as distâncias ao centro da LMC das duas populações, tanto em coordenadas esféricas (com coordenadas radiais r) ou em coordenadas cilíndricas (coordenadas radiais R), foram muito próximos: $\bar{r}$ = 6,87 e 6,42 kpc e $\bar{R}$ = 5,92 e 5,79 kpc respectivamente para as populações jovens e mais velhas que 2 bilhões de anos. Os aglomerados com população maior do que 10 bilhões de anos são poucos para justificar uma argumentação a favor de uma 'população velha' de aglomerados.

Simulações de Diaz & Bekki 2012 indicam dois prováveis encontros recentes entre a LMC e SMC (há 0,26 e 1,97 bilhões de anos atrás), fazendo com que a interação gravitacional entre as nuvens aumentasse consideravelmente a taxa de formação estelar. Muito provavelmente esta taxa de formação estelar não aconteceu devido à interação Via-Láctea/LMC-SMC, pois os últimos estudos (van der Marel & Kallivayalil, 2014) desfavorecem períodos maiores que 4 bilhões de anos para este encontro e são preferidos modelos de primeiro *infall*. Outro aporte interessante é que de a aproximação das Nuvens com a Via-Láctea possa ter iniciado um aumento na taxa de formação estelar. Segundo Besla et al. 2007, isso teria ocorrido num passado entre 1-3 bilhões de anos, quando então as Nuvens teriam adentrado o raio de virial da Via-Láctea.

O melhor modelo orbital descrito nas simulações de Bekki & Chiba (2005) indica uma forte interação gravitacional devido a uma passagem pericêntrica SMC-LMC ocorrida há 1,5 bilhão de anos atrás, coincidindo com um pico de idades na distribuição desta amostra. Com a provável dissolução de aglomerados mais velhos, é esperado que o pico secundário seja em uma idade mais velha, próximo do período orbital previsto para a órbita das Nuvens, em torno de 2,8 bilhão de anos. As mínimas aproximações neste modelo ocorreram recentemente ($\approx$ 200 milhões de

[1]O critério de informação Bayesiano *(BIC)* é definido por $BIC = \ln(n)k - 2\ln(\hat{L})$, onde n é o número de dados, k o número de parâmetros a serem ajustados e $\hat{L}$ é a função probabilidade para o conjunto de dados. Quanto menor o valor do BIC, mais provável é a distribuição.

anos atrás), há 1,5 bilhão de anos e há 2,8 bilhões de anos atrás. Estes últimos valores são totalmente compatíveis com as determinações dos picos de idade para a amostra aqui apresentada.

5.1.2 Distribuição de metalicidade dos aglomerados da amostra

As figuras 5.3 e 5.4 são análogas às figuras 5.1 e 5.2, porém para a metalicidade. Analisando estas figuras, podemos ver que os aglomerados com baixa metalicidade (Z <0,0004 ou [Fe/H]=-1,58 com $Z_{\odot} = 0,0152$ seguindo Grevesse & Sauval 1998) estão situados apenas na parte externa da amostra. Diferentemente da idade, a distribuição de metalicidade mostra uma clara tendência com a coordenada esférica ou cilíndrica radial, estatísticamente significante. O teste de hipótese para esta distribuição revelou um valor para $p = 10^{-5}$, rejeitando a hipótese de que não há variação de metalicidade ao longo da distância radial. Embora para um mesmo intervalo de distância haja um relativo espalhamento em metalicidade, a localização dos aglomerados mais metálicos ocorre apenas na parte interna da amostra ([Fe/H]>-0,6 ocorre apenas para r <8 kpc). E na parte externa da amostra é que estão localizados os aglomerados com mais baixa metalicidade.

5.1.3 Distribuição de avermelhamento dos aglomerados da amostra

A distribuição de avermelhamento dos aglomerados não mostra uma clara tendência na distribuição projetada no céu, como mostra a figura 5.5. Já o histograma para o avermelhamento (figura 5.6) mostra que há um grande número de aglomerados com baixo avermelhamento e um número muito pequeno supera 0,1 em E(B-V), corroborado pela alta latitude Galáctica dos aglomerados e pela distribuição dos mapas de extinção de de Schlegel et al. (1998). Não parece haver uma tendência nos aglomerados de terem um avermelhamento maior ou menor em relação à distância ao centro da LMC, tanto para a coordenada cilíndrica R ou esférica r.

5.2 A SMCNOD

O maior resultado quanto a esta parte da pesquisa foi a descoberta de uma nuvem estelar distante 8 graus ao Norte do centro da SMC. Mesmo estando na borda do

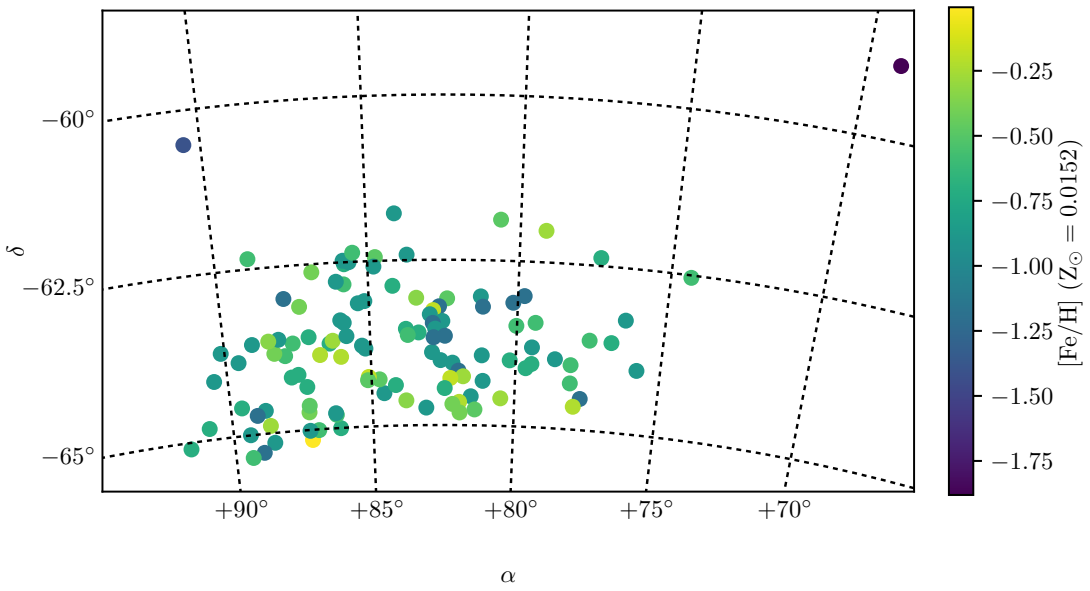

Figura 5.3: Distribuição de aglomerados no céu, de acordo com a metalicidade, indicada pela cor.

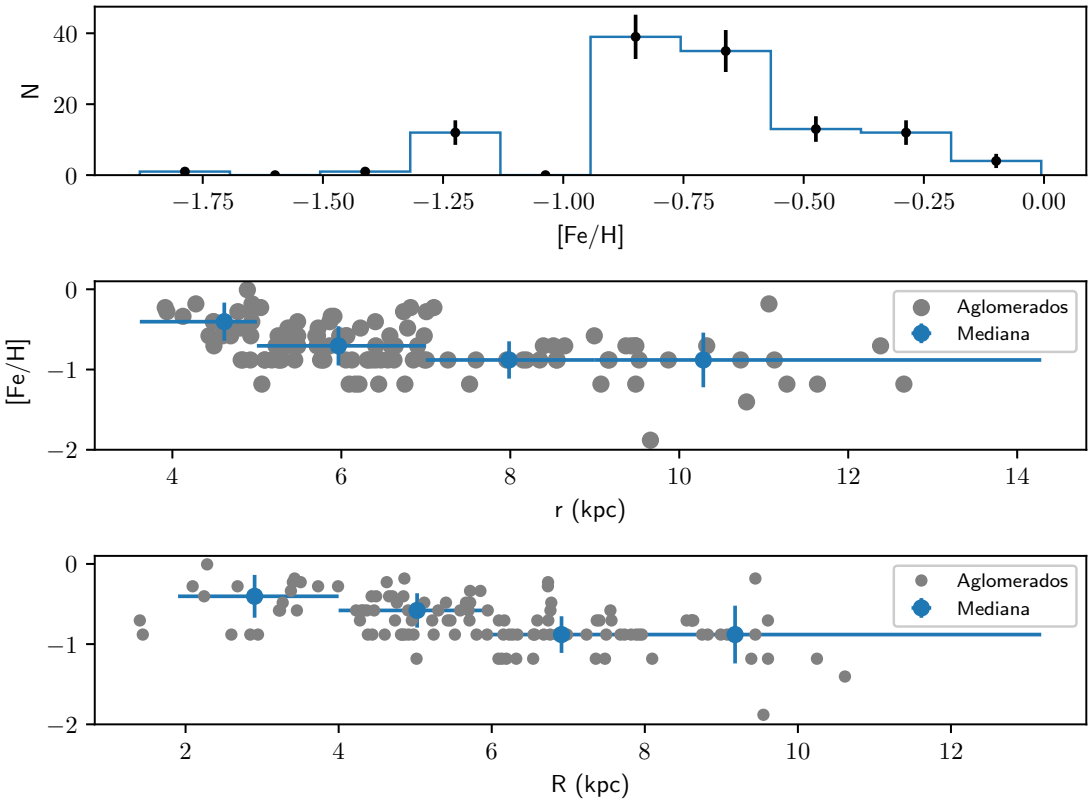

Figura 5.4: *Painel superior:* Histograma dos aglomerados com relação à metalicidade. *Painel central:* A metalicidade e a distância do aglomerado ao centro da LMC, expressa pela coordenada esférica r. *Painel inferior:* Metalicidade versus coordenada cilíndrica R.

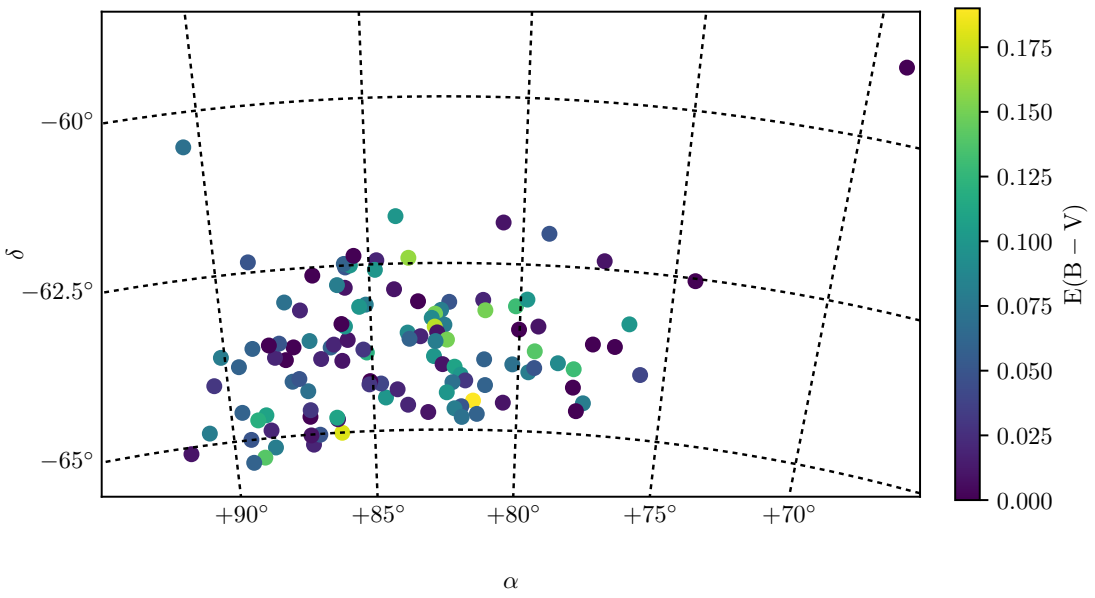

Figura 5.5: Distribuição de aglomerados no céu, de acordo com o avermelhamento, indicado pela cor.

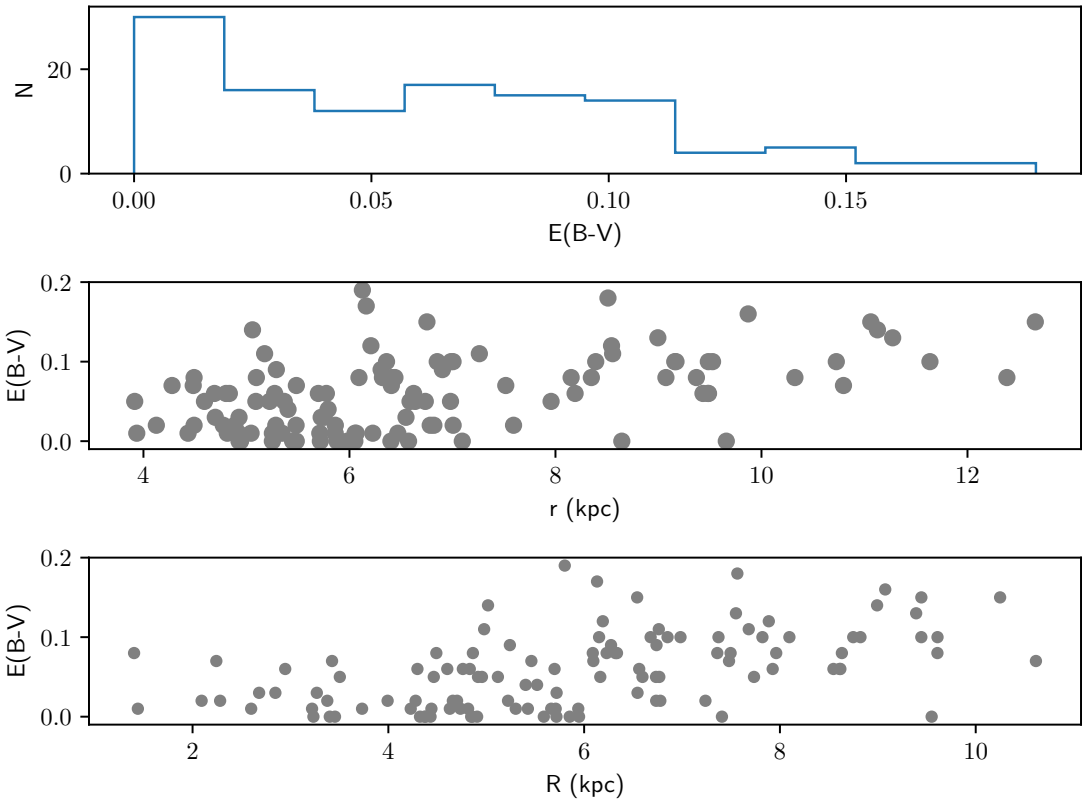

Figura 5.6: *Painel superior:* Histograma dos aglomerados com relação ao avermelhamento. *Painel central:* O avermelhamento e a distância do aglomerado ao centro da LMC, usando a coordenada esférica r. *Painel inferior:* Avermelhamento versus coordenada cilíndrica R.

footprint do DES, anexamos dados de um outro survey, logo depois da tomada das imagens, e conseguimos demonstrar que a SMCNOD é uma sobredensidade estelar situada nos limites de um halo externo de estrelas rodeando a SMC.

Utilizando um filtro isocronal com uma idade e metalicidade semelhantes às da SMC, delineamos os contornos da SMCNOD. Simulações utilizando o GENCMD mostraram que uma função de luminosidade descontaminada semelhante à da SMCNOD deve ser produzida por um objeto que tenha em torno de 10^5 $M_{\odot}$, uma massa semelhante à massa atual dos aglomerados globulares Galácticos, mas apresentando um raio de meia-luz de 2,15 kpc. Se este objeto tivesse sido detectado e depois os dados do MagLiteS tivessem indicado que este objeto se trata de um todo maior, semelhante a uma 'casca', isso poderia indicar que teríamos achado o limite do halo externo publicado por Nidever et al. (2011). No entanto, ao acoplar os dados do MagliteS aos dados do DES, o contorno da SMCNOD mostrou-se claramente independente do halo de estrelas da SMC. Isso levou-nos à conclusão que este objeto poderia ser formado pela interação entre SMC/LMC, assim como várias outras *tidal features* como o MS e a Magellanic Bridge. Ou então, esta seria um objeto como uma galáxia-anã primordial de baixíssimo brilho.

Para comparar com os dados de densidade de estrelas no RGB de Nidever et al. (2011), utilizamos um único campo em comum com os dados do autor, que utilizou o sistema de magnitudes $DDO51$, que é mais eficiente para a separação entre anãs e gigantes do RGB. Para determinar o número de estrelas do RGB naquele campo em comum, utilizamos um filtro limitado no espaço cor-magnitude, selecionando apenas estrelas mais brilhantes que g=21 e excluindo as estrelas do *Red Clump*. Subtraímos deste campo em comum as estrelas da Galáxia contaminantes, através da contagem em um outro campo, situado á mesma latitude galáctica, mas distante da SMCNOD. Chegamos então a um número de estrelas RGB ainda maior do que o informado por Nidever et al. (2011) no campo comum, devido à nossa maior contaminação. Usamos então a razão entre os dois números como fator de normalização de nossa contagem de estrelas para o perfil obtido por aqueles autores. Aplicando este fator de normalização para um campo central da SMCNOD, obtemos uma densidade de estrelas muito maior do que a densidade prevista pelos autores, demonstrando que a SMCNOD é de fato uma sobredensidade também se consideramos apenas as RGB.

Uma estimativa para a massa dinâmica da SMCNOD pode ser feita utilizando a equaçao 7-84 de Binney & Tremaine (1987), como feito no artigo publicado e chegando a uma razão de 2×10^{-2} entre a massa da SMCNOD e da SMC. Esta relação mostra que a massa dinâmica para a SMCNOD seria pelo menos 600 vezes

maior do que a massa estelar estimada para este objeto. Esta razão sugere uma quantidade importante de matéria escura neste objeto, à semelhança das galáxias-anãs esferoidais (Baumgardt & Mieske, 2008). A partir da medição da dispersão de velocidades das estrelas será possível determinar se a SMCNOD está em equilíbrio dinâmico (com base na massa e tamanho deste objeto) ou se a SMCNOD não terá vida muito longa como objeto coeso, sendo mais provável que se dissipasse como um conjunto de estrelas próximo à SMC. Desta maneira, a SMCNOD seria realmente uma *tidal feature*, com uma vida de no máximo algums dezenas de milhões de anos, dissipando suas estrelas no campo.

Analisamos também a distribuição de Hidrogênio neutro em torno de SMCNOD. Infelizmente os dados da distribuição de gás na região da SMCNOD não retornaram informações conclusivas. Não encontramos evidência, por exemplo, de uma ponte vinculando a SMCNOD com a SMC, ou mesmo de uma sobredensidade de gás coincidente com a SMCNOD, com uma velocidade diferente da esperada para a região. Fazendo uma média da emissão em um grau quadrado centrado na SMCNOD ao longo dos intervalos de velocidades (indo de -495 a 495 km/s), no mapa de HI de Kalberla & Haud (2006), as velocidades que apresentaram um pico foram de 94 e 186 km/s. Nestes dois mapas de gás, as sobredensidades do gás não formam uma figura como a esperada para a SMCNOD. Na verdade, estes dois canais de velocidades concordem com o esperado para o MS àquela posição (Nidever et al., 2010).

Capítulo 6

Conclusões

6.1 Comentários finais - Os aglomerados da LMC

Exploramos um grande número de aglomerados estelares no primeiro artigo publicado, e isso apenas foi possível graças à cobertura contínua e profunda do Dark Energy Survey. Por um lado as referências citadas sobre os aglomerados da LMC foram poucas, pois os aglomerados de nosso trabalho estão realmente distantes do centro da LMC onde os dados da literatura são muito mais abundantes. Por outro lado, a grande cobertura deste levantamento nos proporcionou um grande número de objetos, possibilitando a criação de vínculos para algumas grandezas físicas com boa precisão. Além de profunda, nossa amostra foi tratada homogeneamente, o que incorpora qualidade ao trabalho. Para citar, a razão sinal/ruído próximo de 10 alcança a magnitude 23,6 na banda g nas imagens de única exposição (90s) do DES.

O objetivo inicial desta tese foi o estudo dos aglomerados da periferia da LMC dentro do *footprint* do DES. Esse objetivo foi cumprido com a análise principalmente da posição, idade e metalicidade destes aglomerados, além obviamente da descoberta de alguns aglomerados. Basicamente nosso estudo mostrou dois picos para a idade e um grande espalhamento para a metalicidade até $r \simeq 6$ kpc, com a ausência de aglomerados mais ricos que $[Fe/H] \simeq -0.7$ além desse raio. Inicialmente poder-se-ia pensar que estas conclusões para a idade e metalicidade são contraditórias, mas ao analisar a AMR vemos que o grande espalhamento em metalicidade ocorre principalmente para os aglomerados mais jovens do que 3 bilhões de anos, o que permite conciliar a tendência radial em metalicidade com os picos em idade.

Para se reconstruir uma taxa de formação de aglomerados (em inglês *Cluster Formation Rate*) é necessário levar em conta o tempo de dissolução para os aglomerados da galáxia hospedeira. Afinal, uma contínua formação e rápida dissolução

de aglomerados em uma galáxia não traria informação a respeito do histórico de formação estelar. Baumgardt et al. (2013) compilaram um catálogo de aglomerados da LMC utilizando vários catálogos de aglomerados. Os autores compararam a frequência em idade destes aglomerados com a taxa de formação estelar global da LMC segundo Harris & Zaritsky (2009) e chegaram à conclusão que aglomerados mais velhos do que 200 milhões de anos tem a sua vida como objetos coesos diminuída em torno de 20 vezes comparada com a previsão teórica. A previsão teórica levou em conta a expulsão do gás, evolução estelar, relaxação de dois corpos, campos de maré externos, choques com o disco e encontros com GMCs. Para aglomerados mais jovens do que 200 milhões de anos os dados são facilmente explicados pela previsão teórica. Para aglomerados com idade da ordem de 2 bilhões de anos, é esperado uma frequência menor do que o observado e para aglomerados situados no *gap* de idade, são esperados aglomerados (contrapartida não confirmada pelos dados experimentais) em número aproximadamente igual aos aglomerados com 12 bilhões de anos existentes. Embora um interessante vínculo para a CFR, estas determinações são um tanto difíceis de se comparar com a nossa amostra, pois os SFH foram tomados de Harris & Zaritsky (2009), onde não há uma sobreposição com a região de nossa amostra. Também a taxa de dissolução foi calculada para uma região de até 4 kpc, bem mais interna do que nossa amostra. Embora a equação (2) daquele trabalho mostre uma pequena variação no tempo de dissolução dos aglomerados quanto ao campo de maré externo, fatores como os choques com o disco e os encontros com GMCs devem alterar significativamente o tempo de dissolução, diminuindo-o substancialmente. Desta maneira, é difícil comparar a nossa amostra de aglomerados com um número esperado de aglomerados previsto por Baumgardt et al. (2013), dada a forte dependência em posição de nossa amostra, enquanto que aquele trabalho está focado em uma amostra muito mais central. É também esperado que o tempo de dissolução de nossa amostra não seja tão curto quanto o da amostra observacional de Baumgardt et al. (2013), que segundo os autores é em torno de 20 vezes mais rápido do que as previsões teóricas.

Fazendo uma comparação dos aglomerados de nossa amostra com a população do halo da nossa Galáxia, podemos citar o trabalho de Carollo et al. (2016). Este estudo mostra um gradiente de idade para as estrela do halo Galáctico, onde as estrelas mais velhas tendem a se concentrar em regiões mais centrais e as estrelas um pouco mais jovens (mesmo assim com idade média de 9 bilhões de anos) tendem a ocupar as regiões mais externas da Galáxia. Desta forma, galáxias anãs e possivelmente aglomerados globulares velhos que adentram a Galáxia podem ser localizados

facilmente por contrastarem em idade com um halo mais jovem. Diferentemente do que ocorre na nossa Galáxia, como citado no artigo, não há significância estatística suficiente para demonstrar que há um gradiente em idade nos aglomerados da LMC, o que também não é esperado para as estrelas de campo. Isso mostra que o SFH ou a taxa de formação de aglomerados da LMC é diferente da de nossa Galáxia, exceto se houver uma mistura muito eficiente de idades quanto à posição radial.

Quanto ao enriquecimento químico, um meio onde a formação estelar é contínua vai produzir um aumento gradual em metalicidade (quanto mais jovens as estrelas, mais ricas em metal), enquanto que em um meio onde houve uma formação estelar inicial e posteriormente uma pausa, as estrelas formadas serão menos metálicas. O diagnóstico da formação estelar de Harris & Zaritsky (2009), mostra o SFH para uma série de campos da LMC. Infelizmente, como já citado, as áreas naquele trabalho são mais centrais do que a nossa amostra, então não se poderia (a rigor) comparar os dados de nossa amostra com a formação estelar indicada por aqueles autores. No entanto, é esperado que as regiões externas não apresentem uma grande variação no SFH. Também, existem características semelhantes em todas as regiões de Harris & Zaritsky (2009), evidenciando situações que ocorreram para a galáxia como um todo. Uma destas características globais para a LMC é uma época quiescente de formação estelar entre 5 e 12 bilhões de anos (o chamado *age gap*). Esta época quiescente concorda com o número de aglomerados de nossa amostra, embora grande parte de nossa amostra seja de aglomerados mais jovens do que 5 bilhões de anos, enquanto que os aglomerados bem mais velhos são apenas 2 (Aglomerado do Retículo e ESO121SC003).

A figura 6.1 sintetiza a relação idade-metalicidade para os aglomerados da LMC na amostra do DES, juntamente com dois modelos principais para o histórico de formação estelar da LMC, o modelo de Pagel & Tautvaisiene (1998) e de Harris & Zaritsky (2009). Desta forma, primeiro comparamos os resultados com os modelos propostos para a evolução química da LMC.

O modelo de Pagel & Tautvaisiene (1998) apresenta uma extensão da aplicação para a Galáxia do modelo desenvolvido pelos autores, onde um modelo analítico é aplicado envolvendo uma gradual queda (ou *inflow*) não processado de gás), formando estrelas que mais tarde expelem seu material enriquecido quimicamente no meio circundante. Alguns modelos do tipo suave (*smooth*) e do tipo explosivo (*burst*) foram desenvolvidos para ambas as nuvens (SMC e LMC). Os resultados finais mostram que o modelo mais adequado é o *bursting model*, melhor reproduzindo os dados da literatura (Olszewski et al., 1991, Girardi et al., 1995, Geisler et al., 1997, de

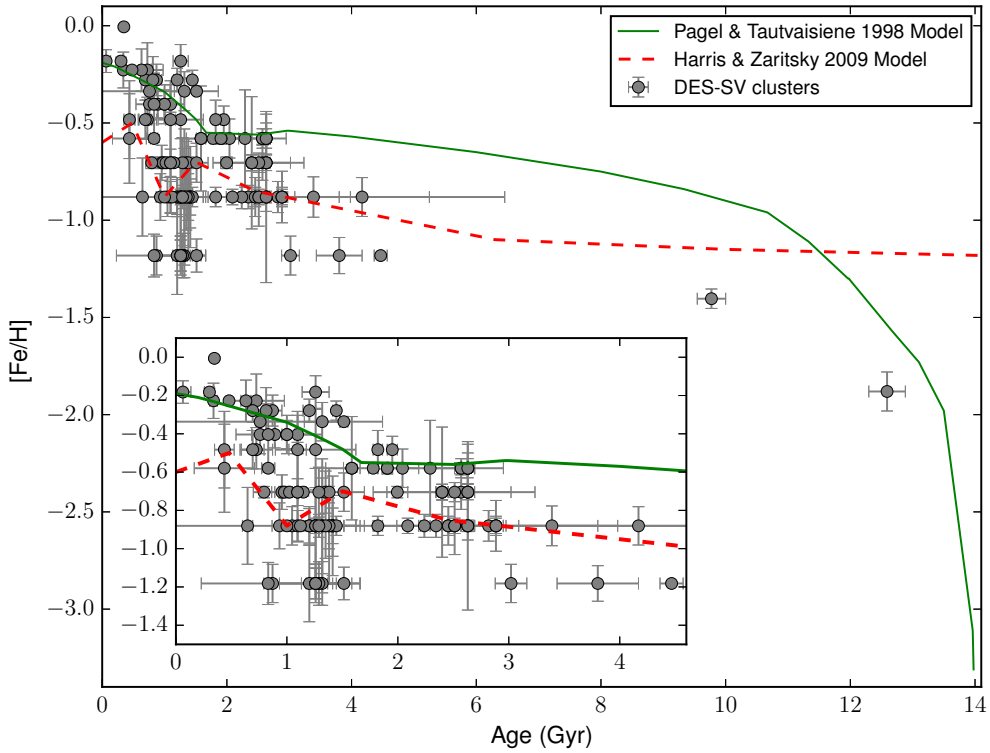

Figura 6.1: Dois modelos para o histórico de formação estelar são comparados com a relação idade-metalicidade para a amostra externa de aglomerados da LMC (círculos preenchidos). O modelo de Harris & Zaritsky (2009) é mostrado como uma linha vermelha tracejada e a linha sólida verde indica o modelo de Pagel & Tautvaisiene (1998). *Caixa:* Ampliação na região indicada mostrando os aglomerados jovens e ricos em metal comparados aos dois modelos.

Freitas Pacheco et al., 1998). Por outro lado, a taxa de formação estelar é muito semelhante para ambas as Nuvens de Magalhães, sendo que a SMC apresenta um atraso para a época quiescente (que ocorre entre 3 e 12 bilhões de anos para a LMC e entre 4 e 12,6 bilhões de anos para a SMC).

Embora os dois modelos, de Pagel & Tautvaisiene (1998) e de Harris & Zaritsky (2009), possam ser utilizados para descrever o comportamento dos aglomerados de nossa amostra, a distribuição de aglomerados no espaço de idade e metalicidade parece indicar que uma mistura dos dois modelos é a mais adequada, ou ainda que os dois modelos possam ser dados como limites para a distribuição dos aglomerados no espaço idade-metalicidade. O modelo de Pagel & Tautvaisiene (1998) parece indicar um limite superior para os aglomerados jovens e ricos em metal, enquanto que o modelo de Harris & Zaritsky (2009) se aproxima mais dos aglomerados jovens mas pobres em metal. Já os aglomerados velhos e pobres em metal são descritos (ou tendem a ser) pelo modelo de Pagel & Tautvaisiene (1998). Neste último trabalho citado, mesmo os aglomerados lá inseridos (Olszewski et al., 1991, Girardi et al., 1995, Geisler et al., 1997) espalham-se pela região em torno do *bursting model*, não apresentando um comportamento único no tocante idade-metalicidade. Uma possibilidade interessante principalmente para o modelo de Pagel & Tautvaisiene (1998) seria a determinação dos picos de SFR com base nos aglomerados de nossa amostra, realizando uma abordagem de máxima verossimilhança, o que poderia levar ao SFH desta região mais periférica da LMC.

Um comentário sobre as comparações de nossas determinações de idade, metalicidade, avermelhamento e módulo de distância. Nossas idades parecem muito semelhantes às dos autores da literatura (ver Figura 8 do artigo sobre os aglomerados da LMC). Já as metalicidades dos aglomerados parecem deslocadas para serem menos metálicas que as da literatura. Atribuímos isso a diferentes modelos, visto que há muitas determinações foram feitas comparando com modelos de pelo menos 10 anos atrás.

Se por um lado este estado quiescente fornece uma evidência da ligação entre as duas Nuvens, por outro a falta de aglomerados na LMC com idade entre 4 e 10 bilhões de anos (conhecido como o *gap* de idade), deveria existir em ambas as galáxias se assumirmos uma taxa de formação conjunta para o sistema, o que não acontece, sendo que este intervalo existe apenas na LMC. No modelo de Pagel & Tautvaisiene (1998), os valores da taxa de formação estelar são dados em termos da massa total do gás inicial da SMC e LMC, ainda contando com $inflows$ e $outflows$ de gás. Assim, vamos assumir um valor inicial para o gás de 10 bilhões de massas solares para a

LMC e de 1 bilhão de massas solares para a SMC. Inicialmente assume-se que ambas as nuvens começam com um taxa de formação alta (1,2 massas solares ao ano para a LMC e 0,07 para a SMC assumindo aqueles valores para a massa inicial de gás) entre 0 e 3 bilhões de anos (estas idades são correspondentes para a idade do Universo) que repentinamente decai em quatro bilhões de anos, mantendo-se constante em ambas as nuvens durante os seguintes 8 ou 9 bilhões de anos. Nos últimos dois bilhões de anos há um aumento súbito, que vai decaindo até o presente momento. Se o último aumento (há aproximadamente dois bilhões de anos atrás) é indício de uma aproximação entre LMC-SMC, deve-se pensar que esta aproximação (ou a esperada consequência desta na formação estelar) não ocorreu anteriormente, pois deveria ter elevado a taxa de formação estelar da mesma forma. Aqui deve-se lembrar que a reconstrução do histórico de formação estelar (em inglês *Star Formation History* ou *SFH*) é mais difícil para épocas remotas, pois os erros para a taxa de formação estelar se acumulam.

Neste sentido, pode-se assumir que as duas galáxias evoluíram juntas, no modelo de galáxia binária (*binary galaxy model*) ou então acoplaram-se recentemente, como citam os autores Bekki & Chiba (2005). Aprofundando a discussão, estes autores citam que as propriedades estruturais e cinemáticas do *Magellanic Stream* (MS) são condizentes com simulações numéricas onde as Nuvens de Magalhães permaneceram em um sistema binário nos últimos 15 bilhões de anos (Murai & Fujimoto, 1980, Gardiner et al., 1994, Gardiner & Noguchi, 1996, Yoshizawa & Noguchi, 2003). Outras previsões confirmadas destas simulações são a intensa formação estelar no disco da LMC nos últimos 200 milhões de anos (Gardiner et al., 1994) e o recente histórico de formação estelar da SMC. No entanto, alguns pontos entre estas simulações e o trabalho de Bekki & Chiba (2005) não convergem. Os trabalhos anteriormente citados desprezam a fricção dinâmica e assumem valores para a massa da LMC que, se reproduzidos no modelo de Bekki & Chiba (2005) fazem com que o sistema Magalhânico não permaneça ligado nos últimos 13 bilhões de anos. Assim, as simulações dinâmicas e hidro-dinâmicas parecem não resolver se o sistema das Nuvens de Magalhães é melhor explicado como uma galáxia binária ou foi acoplado mais tarde. Medidas de movimento próprio mais recentes como as de Kallivayalil et al. (2013), mesmo que ainda apresentando deficiências na compreensão da dinâmica das estrelas na Galáxia e nas Nuvens, parecem mais confiáveis. Estes indicam que, se o sistema LMC-SMC é tratado como ligado (pelo menos por vários bilhões de anos), modelos de primeira queda deste sistema na Galáxia são preferíveis.

O trabalho de Harris & Zaritsky (2009) sobre o SFH da LMC provém da análise

de estrelas de campo da LMC, utilizando um algoritmo para a determinação da idade conhecido como $StarFISH$. Este código basicamente compara os dados fotométricos observados (em forma de diagramas de Hess, variando conforme o número de filtros) com modelos teóricos de isócronas, utilizando as isócronas de Pádova. Os parâmetros a serem ajustados são a distância, função de massa inicial, fração de binárias, extinção interestelar e erros fotométricos. O parâmetro estatístico eleito para comparação e determinação do melhor modelo é o *chi*-quadrado. Para a determinação deste melhor modelo é utilizado uma minimização tipo $down - hill$ para o *chi*-quadrado dos parâmetros. Seus resultados mostram que a LMC apresenta um surto inicial de formação estelar e depois uma época de diminuição na formação estelar entre 5 e 12 bilhões de anos de idade. A formação estelar é então retomada em 5 bilhões de anos até a presente data com uma taxa de formação estelar de 0,2 $M_{\odot}$ por ano, com variações temporais dentro de um fator de 2 em relação à taxa anteriormente citada, até a atualidade. A retomada da formação estelar há 5 bilhões de anos atrás sugere um evento dramático no sistema Magalhânico. Entre as variações globais de formação estelar recente o trabalho cita picos em 2 bilhões, 500 milhões, 100 milhões e 12 milhões de anos atrás. Os picos de 500 milhões e 2 bilhões são simultâneos com os da SMC, sugerindo um histórico conjunto de formação estelar há pelo menos dois bilhões de anos atrás. Para a determinação deste modelo de histórico estelar foram utilizados dados do Magellanic Clouds Photometric Survey nas bandas *B, V* e *I* atingindo as magnitudes 21 e 22 para fontes puntuais, dependendo do adensamento estelar, em uma área de $8{,}5^{\circ} \times 7,5^{\circ}$ cobrindo o centro da LMC. O total de estrelas utilizadas para a determinação do histórico de formação estelar é da ordem de 5 milhões.

Diferentemente das regiões mais internas da LMC, as regiões de nossa amostra devem ter uma forte correlação entre as interações gravitacionais LMC/SMC e a formação estelar. À semelhança do bojo Galáctico (Minniti & Zoccali, 2008), a região central da LMC (barra) pode ter tido um colapso de formação estelar monolítico, e a parte periférica (a de nossa amostra) deve ter sofrido mais os efeitos de interação gravitacional LMC-SMC. Assim, a AMR e o SFH dos aglomerados da LMC devem concordar com ambas as propriedades das estrelas de campo. Infelizmente, pela nossa amostra ocupar uma área mais externa, não há trabalhos deduzindo a AMR e o SFH para a área em questão. Nossa amostra poderia ser comparada com uma AMR e SFH globais para a LMC ou então, se esta área é uma extensão de outra região (como um braço ou barra da LMC), poderia se utilizar esta região para comparar a AMR e SFH. Comparando a área coberta pela amostra do DES com as

regiões para as quais foram determinadas a SFR, podemos ver que nossa amostra é um apêndice da região delimitada por Harris & Zaritsky (2009) como o *Northwest Arm* ou uma extensão do *Blue Arm* (veja as figuras 13-15 deste paper). Embora haja variações consideráveis nas SFR para estas regiões no tocante às quantidades de SFR, ambas as regiões concordam quanto aos picos de idade (2 bilhões de anos e 400 milhões de anos), exceto por um pico recente na formação estelar (100 milhões de anos) para o *Blue Arm* inexistente no *Northwest Arm*. Mesmo com grandes margens de erro para a SFR naquele paper, este pico fica além de um sigma para ambas as regiões. A denominação de *Blue Arm* vem justamente desta possível formação estelar em 100 milhões de anos atrás, graças à detecção de número relativamente maior de estrelas azuis naquela região. Nesse sentido, nossa amostra de aglomerados mostra alguns aglomerados jovens mais pobres em metais do que a Figura 20 do paper de Harris & Zaritsky (2009), indicando que possivelmente a região amostrada pelo DES na LMC tenha sido palco de uma formação estelar mais tardia, tendo uma contribuição maior do *Blue Arm* do que do *Northwest Arm*. Cabe indicar que este pico em 100 milhões de anos também não aparece na região diametralmente oposta (SE) da LMC (Figura 14 daquele paper).

Comparando o histograma de idade dos aglomerados de nossa amostra com o SFH de Harris & Zaritsky (2009), vemos que aquela região é a única que indica timidamente dois picos em formação estelar entre 1 e 5 bilhões de anos. Mais precisamente estes picos são para as idades de 1 e $\simeq$ 3 bilhões de anos (com uma taxa de formação de $\simeq 0.1$ $M_{\odot}/yr$), enquanto que os outros picos são mais jovens do que 500 milhões de anos para esta região. Estes picos concordam muito bem com a determinação de idade de nossa amostra (1,2 e 2,7 bilhões de anos).

Nossa amostra de aglomerados da LMC pode ser considerada então como tendo uma pequena contribuição de objetos velhos e pobres em metal de uma época inicial de formação, com outros objetos de uma época de retomada de formação estelar. Levando em conta o tempo de dissolução para o pico para 3 e 1 bilhão de anos (Baumgardt et al., 2013), é esperado que o número de aglomerados criados para estas duas épocas seja praticamente o mesmo, o que nos leva a determinar as SFR como muito semelhantes e concordando com Harris & Zaritsky (2009).

A distribuição radial de aglomerados mostrada em nosso trabalho é um argumento de que os aglomerados ocupam um intervalo considerável em distância, o que concorda com o trabalho de Klein et al. 2014, onde a distribuição de estrelas RR Lyrae na LMC forma figuras tridimensionais de isodensidades aproximadamente prolatas, com o eixo maior apontando na direção da Via-Láctea. Nesta referência, o semi-eixo

maior tem um tamanho relativo de aproximadamente duas vezes o semi-eixo menor.

As simulações de Diaz & Bekki 2012 apresentam um modelo dinâmico para as Nuvens de Magalhães onde a primeira aproximação LMC-SMC (40 kpc) ocorre há 4 bilhões de anos atrás. Antes deste tempo, há cinco bilhões de anos, as duas Nuvens estariam separadas por uma distância de 120 kpc. De uma maneira similar, Besla et al. 2010 desenvolve modelos de evolução para as três galáxias (Via-Láctea, SMC e LMC) onde há uma máxima aproximação entre LMC-SMC há 1,1 e 4,6 bilhões de anos. Ambos os modelos representam bastante bem a evolução das Nuvens ao longo do tempo (inclusive apresentando características como o *Leading Arm* e o *Magellanic Stream*). Eles vinculam um aumento na formação de aglomerados à interação gravitacional entre a LMC e a SMC, o que razoavelmente explica a origem do intervalo de idades para a LMC, apenas supondo uma formação estelar inicial independente da interação gravitacional. No entanto, existem aglomerados na SMC que habitam o *gap* de idade da LMC, (por exemplo em Dias et al. 2016). Interpretando estes dados, somos levados a pensar que a interação gravitacional induz a formação estelar dependendo da massa (ou da razão entre as massas) das galáxias. Para interações entre galáxias muito diferentes em massa, a interação gravitacional deve disparar a formação estelar mais intensamente e a uma distância maior na galáxia menos massiva do que na galáxia mais massiva (assim como nos exemplos da LMC e da SMC). Esta teoria pode explicar o motivo de termos uma AMR povoada ao longo do eixo das idades para a SMC e o *gap* para a LMC. Por outro lado, se as Nuvens fossem satélites da Via-Láctea há muito tempo (ou seja, já tivessem completado várias órbitas em torno da Via-Láctea) e esta interação fosse preponderante para a formação estelar (ao invés de termos a interação entre as Nuvens como preponderante), esperaríamos um histórico de formação estelar semelhante para ambas as Nuvens.

6.2 Comentários finais - SMCNOD

6.2.1 Introdução

Para contextualizar a descoberta da SMCNOD vamos aqui descrever as principais características deste objeto, vinculando-o quanto à sua provável origem e destino. Mais do que a discussão constante no artigo publicado, aqui expandimos a discussão, suprimindo algumas referências (para evitar a repetição das referências já citadas no artigo).

6.2.2 Características principais da SMCNOD

As principais características da SMCNOD e pontos importantes no trabalho são:

- Grande área coberta pelo objeto (em torno de $6^o \times 2^o$). Para se ter uma ideia da dimensão ao longo do campo de visada, supondo uma população estelar com um intervalo de idade muito restrito, o RC da figura 10 (painel direito) do artigo publicado pode servir de referência ou indicar um limite superior para este eixo. Como as estrelas se espalham por um intervalo de 0.7 magnitudes, é esperado um intervalo de 20 kpc para grande parte das estrelas da SMCNOD. Esta estimativa deve ser tomada como um limite superior para o eixo ao longo da linha de visada, refletindo por um lado a interação deste objeto com a MW. Com um raio de meia-luz de 2.1 kpc, este é um dos maiores objetos descobertos na vizinhança da SMC.

- A SMCNOD tem um baixo conteúdo de gás, sendo que apenas dois canais de velocidade apresentaram conteúdo significativo em uma área de um grau quadrado centrado na SMCNOD. Mesmo assim, o conteúdo gasoso é pequeno se comparado com outras áreas como o centro da SMC e as figuras formadas pelo gás não estão distribuídas uniformemente ou seguindo formas arredondadas centradas na SMCNOD. Como este objeto está próximo da SMC, esta característica não é surpreendente, visto que grande parte do gás da SMC foi retirado, formando o MS, seguindo recentes simulações (Diaz & Bekki, 2012). Mesmo que a SMCNOD esteja se aproximando da SMC e portanto não tenha sido afetada pelas colisões LMC/SMC, o suposto gás original da SMCNOD pode ter sido perdido via *RAM pressure*.

- Simulações de N-corpos têm suportado um grande número de *tidal features* no entorno das Nuvens. Embora estas simulações utilizem dados recentes, ainda há grandes incertezas quanto às massas das galáxias (inclusive o conteúdo de matéria escura), massa muito grande para cada partícula (Diaz & Bekki 2012 utilizaram, por exemplo 3400 $M_\odot$ para cada partícula), sem contar o desconhecimento de todos os objetos no entorno.

- Como publicado no artigo, as populações da SMCNOD e da parte mais ao Norte da SMC (imediatamente ao Sul da SMCNOD) são muito parecidas, evidenciada tanto pela distribuição em cor quanto pela distribuição em magnitude (Figura 10 do paper). Isso demonstra uma forte correlação entre os

históricos de formação estelar dos dois objetos que deve ser levado em conta quando é discutida a origem da SMCNOD.

- Estruturas de maré ou *tidal features* tem sido encontradas no entorno das Nuvens. Assim, como foi mapeada a parte utilizando o DES, não há registro de levantamentos que mapeiem contiguamente a região Sul das Nuvens. Isso abre uma lacuna muito grande sobre as estruturas de maré nestas regiões mais distantes do centro de ambas as galáxias.

- Mesmo em uma fração pequena, a SMCNOD apresenta uma formação estelar de idade intermediária, fornecendo um vínculo interessante entre a formação estelar e a possível formação deste objeto. A população de idade intermediária parece ter sido formada em um intervalo de tempo relativamente curto, há 1 bilhão de anos atrás. Esta formação estelar pode estar associada a uma colisão LMC/SMC que pode ter sido a própria formadora da SMCNOD, caso esta se configure como uma *tidal feature*. Por outro lado, se a formação da SMCNOD ocorreu anteriormente (há alguns bilhões de anos atrás), esta população de idade intermediária pode ter se formado 'in situ' na SMCNOD ou então migrado da SMC para a SMCNOD. Caso tenha migrado, a população intermediária deveria se configurar homogeneamente como um halo em torno da SMC, mas a figura 3 do artigo mostra que há um agrupamento destas estrelas na SMCNOD, mostrando que, se elas migraram, acabaram por formar uma sobredensidade na SMCNOD.

6.2.3 Principais possibilidades para a origem da SMCNOD

Analisando estas características, as possíveis origens para a SMCNOD são:

- Material retirado da SMC a partir de uma colisão LMC/SMC, suportada pelas simulações de N-corpos. A SMCNOD se configuraria como uma estrutura de maré, podendo ser inclusive uma contrapartida à formação da MB (seria então a *Magellanic Counter-Bridge*). Embora simulações de interações entre galáxias mostrem estruturas de maré que se formam aos pares e simetricamente (Toomre & Toomre, 1972), as estruturas de maré acabam evoluindo e tomando diferentes formas, sendo que a SMCNOD, se tomada como evoluindo a partir de uma contra-partida à MB, poderia ter tomado a forma elíptica que possui atualmente. Esta teoria explica várias características da SMCNOD, como por exemplo a forma atual, o baixo conteúdo de gás, as populações semelhantes,

um burst de formação estelar anular em torno da SMC há $1,6-2.5$ bilhões de anos atrás (Harris & Zaritsky, 2004), além de outras estruturas encontradas no entorno da SMC (Nidever et al., 2013, Dobbie et al., 2014).

- Galáxia anã primordial, tendo evoluído ao lado da SMC, visto as similaridades entre as populações estelares. Embora tenhamos utilizado um filtro com uma população de 6 bilhões de anos para caracterizar a grande maioria da população estelar da SMCNOD, a presença de uma população estelar mais velha (10-12 bilhões de anos) não está descartada, apenas nos diagramas de Hess da Figura 2 do artigo publicado há uma quase completa sobreposição entre a população de 6 bilhões de anos e uma população ainda mais velha (10-12 bilhões de anos). Uma melhor caracterização da população mais velha apenas seria factível com um diagrama de Hess mais profundo, quando então poderíamos comparar as funções de luminosidade para as duas populações ou mesmo utilizarmos filtros isocronais distintos, mesmo com uma sobreposição em algumas regiões.

- Galáxia anã de maré *Tidal Dwarf Galaxy*, uma galáxia anã constituída por uma população estelar formada pelo gás retirado de uma outra galáxia. Estas galáxias, como ressaltado no artigo, tem uma sobrevida muito pequena (alguns bilhões de anos, no máximo) dado que não possuem matéria escura, sendo estruturas muito frágeis. Se a SMNCOD é uma TDG, seria esperado que o gás tivesse sido retirado da SMC há no mínimo 6 bilhões de anos, muito antes da formação do MS (estimado como em torno de 2 bilhões de anos por Nidever et al. 2010). Como são esperadas colisões SMC/LMC muito mais recentemente, não seria esperado que uma TDG formada há seis bilhões de anos atrás sobrevivesse por tão longo tempo. Além disso, as simulações de Besla et al. 2010 e de Diaz & Bekki 2012 mostram que as Nuvens estariam afastadas (> 100 kpc) há mais de 5 bilhões de anos.

- Uma última possibilidade é o *resonant stripping*, como citado por D'Onghia et al. (2009) para a origem de galáxias anãs. Este é um processo ressonante entre a frequência angular de rotação do disco da galáxia e a frequência da órbita, sendo este processo eficiente para a remoção de estrelas quando as duas grandezas têm magnitudes semelhantes e ambos os eixos estão alinhados. Este processo exige a interação entre duas galáxias anãs. Esta interação deveria ocorrer entre as duas Nuvens, gerando uma galáxia anã com baixo brilho superficial, como descrito no artigo. Maiores simulações são necessárias para demonstrar se este processo para as duas Nuvens poderia gerar um objeto

como a SMCNOD.

Caso a origem da SMCNOD esteja vinculada às Nuvens, como realmente parece sugerido pelas suas características, a explicação para a origem da SMCNOD estará vinculada a melhores simulações de N-corpos para a evolução do sistema LMC-SMC-MW. Novamente novas simulações devem explicar sua origem como uma característica da colisão entre as Nuvens, como uma contrapartida da MB (ou *Counter Bridge*). Assim como citado no artigo da SMCNOD, muitos trabalhos demonstram a existência desta contrapartida para a Ponte, pois sempre as *Tidal Features* ocorrem simetricamente (assim como as marés). Vínculos posteriores para o movimento próprio irão demonstrar qual o movimento da SMCNOD relativo à SMC, restringindo o espaço de parâmetros para a origem deste objeto. Junto com a velocidade radial, haveria um vínculo ainda maior para a determinação de uma primeira órbita deste objeto, o que colocaria um vínculo para a origem da SMCNOD.

Além disso, um levantamento no entorno mais próximo das Nuvens poderia levar à descoberta de objetos como a SMCNOD, colocando vínculos importantes para as simulações de N-corpos que têm sido feitas nas últimas décadas e que alcançam cada vez maior precisão (ver a série de simulações citadas no artigo da SMCNOD, principalmente as de Besla et al. (2010) e Diaz & Bekki (2012). Embora tratemos a SMCNOD como um objeto advindo da interação entre LMC-SMC, outras possíveis origens não estão descartadas, como por exemplo, ela ser uma galáxia primordial em formação coeva com a SMC. Anteriormente à SMCNOD, Nidever et al. (2011) já havia demonstrado a ocorrência de um halo estelar na periferia da SMC a partir de dados não contíguos ao redor da SMC. Além de Nidever et al. (2011), certamente outros objetos aguardam a descoberta, talvez semelhantes à SMCNOD ou ainda mais surpreendentes do que esta. Ainda durante o período de avaliação do trabalho dentro da colaboração, citou-se a possibilidade de a SMCNOD vir a fazer parte de uma grande estrutura semelhante a uma casca (*shell*) ao redor da SMC, o que poderia indicar uma frente de onda choque depois da máxima aproximação das duas Nuvens. Com os dados que tínhamos disponíveis, não foi possível comprovar a existência deste grande estrutura, embora ela deva ser descontínua caso exista.

Um último comentário é sobre um trabalho importante que vincula e delimita a possibilidade de as galáxias anãs descobertas no DES terem sido inicialmente formadas como satélites da LMC e/ou da SMC é o artigo de Jethwa et al. 2016. Simulações cinemáticas das nuvens e da Via-Láctea são constituídas a partir das posições atuais destas galáxias e de suas velocidades e movimentos próprios. As posições são revertidas no tempo e, posteriormente, um número extenso de partículas traçadoras

das posições das galáxias anãs são rodadas até o presente. Utilizando os dados disponíveis de velocidade radial, movimento próprio e posição, são construídas as probabilidades de pertencimento das galáxias anãs às Nuvens. Nominalmente, das quatorze galáxias anãs descobertas na área amostrada pelo DES, 7 têm probabilidade maior do que 70% de pertencerem à LMC. Apenas uma (Reticulum III) tem uma probabilidade razoáavel, de 30%, de pertencer à SMC. O trabalho de Jethwa et al. (2016) mostra o quanto esta visão dinâmica do movimento das Nuvens encontra contrapartida inclusive na amostra de galáxias anãs companheiras da Via-Láctea. As Figuras 1 e 6 daqueles autores mostram a proximidade das galáxias recém-descobertas do DES às Nuvens de Magalhães se comparadas com a distribuição das galáxias anãs no hemisfério Norte, o que evidencia uma provável origem para estas anãs. Além disso, para cobrir o entorno das Nuvens e utilizando também a DECam, lembramos que o MagLiteS está amostrando a região entre as Nuvens e o pólo celeste Sul (na parte não amostrado pelo DES), onde possíveis futuras descobertas irão inferir melhor a participação das Nuvens no senso de satélites da Via-Láctea. O trabalho de Jethwa et al. 2016 também é importante impor um vínculo à questão de satélites de satélites. Além disso, se algumas (ou muitas) galáxias-anãs tiverem este vínculo Magalhânico comprovado, isso irá agravar o problema do modelo ΛCDM conhecido como *missing satellites* ou satélites faltantes, onde a previsão do número de halos de matéria escura povoados com matéria bariônica (as galáxias anãs) é bem maior do que as observações demonstram, haja visto que um sistema como a Via-Láctea e as duas Nuvens são um sistema incomum (James & Ivory, 2011). Para uma revisão deste problema, indicamos Bullock 2010, Simon & Geha 2007. Trabalho semelhante ao de Jethwa et al. (2016) poderia ser feito também para os aglomerados recém descobertos (como os que tivemos participação como o DES1), o que poderia fornecer uma explicação para a formação destes objetos, os quais têm sido catalogados como aglomerados globulares (por exemplo, Koposov et al., 2007), mas que diferem dos aglomerados globulares da Galáxia, como os conhecemos, massivos e luminosos.

Apêndice A

Artigos publicados com contribuição

Nesta seção vou apresentar as principais contribuições aos artigos em anexo, onde figuro na lista de autores.

O artigo publicado pela colaboração do DES com as descobertas dos companheiros da Via-Láctea nos dados do primeiro ano teve nossa intensa participação quanto à determinação de idades, metalicidade, avermelhamento e módulo de distância. Por mais de uma vez apresentamos nosso trabalho nas reuniões do grupo de trabalho da Via-Láctea (MWWG). Nesta época, estávamos com os testes e validação dos programas para a determinação destes parâmetros físicos, então além de mais um teste de comparação, pudemos comparar nossos resultados com os resultados de outras abordagens pela colaboração. Foi uma intensa troca de experiências, discussão de métodos e parâmetros com outros colaboradores do DES.

The Astrophysical Journal, 807:50 (16pp), 2015 July 1 doi:10.1088/0004-637X/807/1/50

EIGHT NEW MILKY WAY COMPANIONS DISCOVERED IN FIRST-YEAR DARK ENERGY SURVEY DATA

K. Bechtol[1], A. Drlica-Wagner[2], E. Balbinot[3,4], A. Pieres[4,5], J. D. Simon[6], B. Yanny[2], B. Santiago[4,5], R. H. Wechsler[7,8,9], J. Frieman[1,2], A. R. Walker[10], P. Williams[1], E. Rozo[9,11], E. S. Rykoff[9], A. Queiroz[4,5], E. Luque[4,5], A. Benoit-Lévy[12], D. Tucker[2], I. Sevilla[13,14], R. A. Gruendl[13,15], L. N. da Costa[4,16], A. Fausti Neto[4], M. A. G. Maia[4,16], T. Abbott[10], S. Allam[2,17], R. Armstrong[18], A. H. Bauer[19], G. M. Bernstein[18], R. A. Bernstein[6], E. Bertin[20,21], D. Brooks[12], E. Buckley-Geer[2], D. L. Burke[9], A. Carnero Rosell[4,16], F. J. Castander[19], R. Covarrubias[15], C. B. D'Andrea[22], D. L. DePoy[23], S. Desai[24,25], H. T. Diehl[2], T. F. Eifler[18,26], J. Estrada[2], A. E. Evrard[27], E. Fernandez[28,29], D. A. Finley[2], B. Flaugher[2], E. Gaztanaga[19], D. Gerdes[27], L. Girardi[16], M. Gladders[1,28], D. Gruen[30,31], G. Gutierrez[2], J. Hao[2], K. Honscheid[32,33], B. Jain[18], D. James[10], S. Kent[2], R. Kron[1], K. Kuehn[34,35], N. Kuropatkin[2], O. Lahav[12], T. S. Li[23], H. Lin[2], M. Makler[36], M. March[18], J. Marshall[23], P. Martini[33,37], K. W. Merritt[2], C. Miller[27,38], R. Miquel[29,39], J. Mohr[24], E. Neilsen[2], R. Nichol[22], B. Nord[2], R. Ogando[4,16], J. Peoples[2], D. Petravick[15], A. A. Plazas[26,40], A. K. Romer[41], A. Roodman[7,10], M. Sako[18], E. Sanchez[14], V. Scarpine[2], M. Schubnell[27], R. C. Smith[10], M. Soares-Santos[2], F. Sobreira[2,4], E. Suchyta[32,33], M. E. C. Swanson[15], G. Tarle[27], J. Thaler[42], D. Thomas[22], W. Wester[2], and J. Zuntz[43]
(The DES Collaboration)
[1] Kavli Institute for Cosmological Physics, University of Chicago, Chicago, IL 60637, USA; bechtol@kicp.uchicago.edu, kadrlica@fnal.gov
[2] Fermi National Accelerator Laboratory, P.O. Box 500, Batavia, IL 60510, USA
[3] Department of Physics, University of Surrey, Guildford GU2 7XH, UK
[4] Laboratório Interinstitucional de e-Astronomia—LIneA, Rua Gal. José Cristino 77, Rio de Janeiro, RJ—20921-400, Brazil
[5] Instituto de Física, UFRGS, Caixa Postal 15051, Porto Alegre, RS—91501-970, Brazil
[6] Carnegie Observatories, 813 Santa Barbara St., Pasadena, CA 91101, USA
[7] Kavli Institute for Particle Astrophysics & Cosmology, P.O. Box 2450, Stanford University, Stanford, CA 94305, USA
[8] Department of Physics, Stanford University, 382 Via Pueblo Mall, Stanford, CA 94305, USA
[9] SLAC National Accelerator Laboratory, Menlo Park, CA 94025, USA
[10] Cerro Tololo Inter-American Observatory, National Optical Astronomy Observatory, Casilla 603, La Serena, Chile
[11] University of Arizona, Department of Physics, 1118 E. Fourth St., Tucson, AZ 85721, USA
[12] Department of Physics & Astronomy, University College London, Gower Street, London, WC1E 6BT, UK
[13] Department of Astronomy, University of Illinois, 1002 W. Green Street, Urbana, IL 61801, USA
[14] Centro de Investigaciones Energéticas, Medioambientales y Tecnológicas (CIEMAT), Madrid, Spain
[15] National Center for Supercomputing Applications, 1205 West Clark St., Urbana, IL 61801, USA
[16] Observatório Nacional, Rua Gal. José Cristino 77, Rio de Janeiro, RJ—20921-400, Brazil
[17] Space Telescope Science Institute, 3700 San Martin Drive, Baltimore, MD 21218, USA
[18] Department of Physics and Astronomy, University of Pennsylvania, Philadelphia, PA 19104, USA
[19] Institut de Ciències de l'Espai, IEEC-CSIC, Campus UAB, Facultat de Ciències, Torre C5 par-2, E-08193 Bellaterra, Barcelona, Spain
[20] Sorbonne Universités, UPMC Univ Paris 06, UMR 7095, Institut d'Astrophysique de Paris, F-75014, Paris, France
[21] CNRS, UMR 7095, Institut d'Astrophysique de Paris, F-75014, Paris, France
[22] Institute of Cosmology & Gravitation, University of Portsmouth, Portsmouth, PO1 3FX, UK
[23] George P. and Cynthia Woods Mitchell Institute for Fundamental Physics and Astronomy, and Department of Physics and Astronomy, Texas A&M University, College Station, TX 77843, USA
[24] Department of Physics, Ludwig-Maximilians-Universitat, Scheinerstr.1, D-81679 Munich, Germany
[25] Excellence Cluster universe, Boltzmannstr.2, D-85748 Garching, Germany
[26] Jet Propulsion Laboratory, California Institute of Technology, 4800 Oak Grove Dr., Pasadena, CA 91109, USA
[27] Department of Physics, University of Michigan, Ann Arbor, MI48109, USA
[28] Department of Astronomy and Astrophysics, University of Chicago, Chicago IL 60637, USA
[29] Institució Catalana de Recerca i Estudis Avançats, E-08010, Barcelona, Spain
[30] Max Planck Institute for Extraterrestrial Physics, Giessenbachstrasse, D-85748 Garching, Germany
[31] University Observatory Munich, Scheinerstrasse 1, D-81679 Munich, Germany
[32] Department of Physics, The Ohio State University, Columbus, OH 43210, USA
[33] Center for Cosmology and Astro-Particle Physics, The Ohio State University, Columbus, OH 43210, USA
[34] Australian Astronomical Observatory, North Ryde, NSW 2113, Australia
[35] Argonne National Laboratory, 9700 S. Cass Avenue, Lemont IL 60639 USA
[36] ICRA, Centro Brasileiro de Pesquisas Físicas, Rua Dr. Xavier Sigaud 150, CEP 22290-180, Rio de Janeiro, RJ, Brazil
[37] Department of Astronomy, The Ohio State University, Columbus, OH 43210, USA
[38] Department of Astronomy, University of Michigan, Ann Arbor, MI, 48109, USA
[39] Institut de Física d'Altes Energies, Universitat Autònoma de Barcelona, E-08193 Bellaterra, Barcelona, Spain
[40] Brookhaven National Laboratory, Bldg 510, Upton, NY 11973, USA
[41] Astronomy Centre, University of Sussex, Falmer, Brighton, BN1 9QH, UK
[42] Department of Physics, University of Illinois, 1110 W. Green St., Urbana, IL 61801, USA
[43] Jodrell Bank Center for Astrophysics, School of Physics and Astronomy, University of Manchester, Oxford Road, Manchester, M13 9PL, UK
Received 2015 March 9; accepted 2015 April 30; published 2015 June 30

ABSTRACT

We report the discovery of eight new Milky Way companions in $\sim$1800 deg^2 of optical imaging data collected during the first year of the Dark Energy Survey (DES). Each system is identified as a statistically significant overdensity of individual stars consistent with the expected isochrone and luminosity function of an old and metal-poor stellar population. The objects span a wide range of absolute magnitudes (M_V from -2.2 to -7.4 mag), physical

The Astrophysical Journal, 807:50 (16pp), 2015 July 1 Bechtol et al.

sizes (10−170 pc), and heliocentric distances (30−330 kpc). Based on the low surface brightnesses, large physical sizes, and/or large Galactocentric distances of these objects, several are likely to be new ultra-faint satellite galaxies of the Milky Way and/or Magellanic Clouds. We introduce a likelihood-based algorithm to search for and characterize stellar over-densities, as well as identify stars with high satellite membership probabilities. We also present completeness estimates for detecting ultra-faint galaxies of varying luminosities, sizes, and heliocentric distances in the first-year DES data.

Key words: galaxies: dwarf – Local Group

1. INTRODUCTION

Milky Way satellite galaxies provide a unique opportunity to study the low-luminosity threshold of galaxy formation and to better connect the baryonic component of galaxies with the dark matter halos in which they reside. Prior to the Sloan Digital Sky Survey (SDSS), the faintest known galaxies had luminosities of $\sim 10^5\ L_\odot$, and it was clear that the population of 12 "classical" Milky Way satellites was orders of magnitude smaller than would be naively expected in the cold dark matter paradigm (Klypin et al. 1999; Moore et al. 1999). Over the past decade, systematic searches of wide-field SDSS imaging have revealed 15 additional arcminute-scale, resolved stellar over-densities (Willman et al. 2005a, 2005b; Belokurov et al. 2006, 2007, 2008, 2009, 2010; Grillmair 2006, 2009; Sakamoto & Hasegawa 2006; Zucker et al. 2006a, 2006b; Irwin et al. 2007; Walsh et al. 2007) that have been either photometrically classified or spectroscopically confirmed as gravitationally bound "ultra-faint" galaxies (Kleyna et al. 2005; Muñoz et al. 2006; Martin et al. 2007; Simon & Geha 2007; Adén et al. 2009; Belokurov et al. 2009; Carlin et al. 2009; Geha et al. 2009; Koch et al. 2009; Walker et al. 2009; Koposov et al. 2011; Simon et al. 2011; Willman et al. 2011; Kirby et al. 2013). These ultra-faint galaxies are the smallest, least luminous, least chemically enriched, and most dark matter dominated galaxies in the known universe.

Since all known ultra-faint Milky Way satellite galaxies were discovered in SDSS, the census of these objects is almost certainly incomplete due to the partial sky coverage ($\sim 14,000\ \mathrm{deg}^2$) and photometric magnitude limit (95% complete to $r \sim 22$ mag) of that survey. While only 27 Milky Way satellite galaxies are currently known, extrapolations of the luminosity function suggest that hundreds of luminous Milky Way satellites remain to be found in current and near-future wide-field optical imaging surveys (Tollerud et al. 2008; Hargis et al. 2014; He et al. 2015).

The Dark Energy Survey (DES) is in the process of imaging $5000\ \mathrm{deg}^2$ of the southern Galactic cap in five photometric bands (Abbott et al. 2005; Diehl et al. 2014). The deep photometry of DES ($r \sim 24$ mag) will enable the detection of the faintest known satellite galaxies out to ~120 kpc (compared to the SDSS limit of ~50 kpc), and more luminous satellite galaxies out to the Milky Way virial radius (Rossetto et al. 2011). We have completed an initial search of the first year of DES data and report here on the eight most significant dwarf galaxy candidates discovered therein (Table 1). Since the physical nature of these candidates cannot be definitively determined with photometry alone, we refer to them by their discovery coordinates. If these candidates are later confirmed to be Local Group galaxies, they should be renamed after the constellation in which they reside: DES J0335.6−5403 (Reticulum II), DES J0344.3−4331 (Eridanus II), DES J2251.2−5836 (Tucana II), DES J0255.4−5406 (Horologium I), DES J2108.8−5109 (Indus I), DES J0443.8−5017 (Pictor I), DES J2339.9−5424 (Phoenix II), and DES J0222.7−5217 (Eridanus III). If any are instead globular clusters, they would be known as DES 1 through N. After the completion of this work, we learned that DES J2108.8−5109 was previously identified by Kim et al. (2015) in data from the Stromlo Milky Way Satellite Survey and designated as a likely star cluster, Kim 2.

2. DATA SET

DES is a wide-field optical imaging survey in the *griz*Y bands performed with the Dark Energy Camera (DECam; Flaugher et al. 2010, 2015; Diehl 2012). The DECam focal plane comprises 74 CCDs: 62 2k × 4k CCDs dedicated to science imaging and 12 2k × 2k CCDs for guiding, focus, and alignment. DECam is installed at the prime focus of the 4 m Blanco telescope at Cerro Tololo Inter-American Observatory. In this configuration, DECam has a hexagonal 2.°2-wide field of view and a central pixel scale of 0.263 arcseconds. The full DES survey is scheduled for 525 nights distributed over 5 years. Here, we consider data collected between 2013 August 15 and 2014 February 9 during the first year of DES.

The first internal annual release of DES data (Y1A1) consists of ~12,000 science exposures processed by the DES data management (DESDM) infrastructure (R. A. Gruendl et al. 2015, in preparation).[44] Most of the Y1A1 footprint is covered by 2–4 overlapping exposures, or "tilings," in each filter. Single exposures in a tiling are 90 s in *griz* and 45 s in *Y*. Here, we rely on the *g*- and *r*-band images for photometry, and use the *i*-band for star–galaxy separation.

The DESDM image processing pipeline consists of image detrending, astrometric calibration, nightly photometric calibration, global calibration, image coaddition, and object catalog creation, as recently summarized in Balbinot et al. (2015). We refer to Sevilla et al. (2011), Desai et al. (2012), and Mohr et al. (2012) for a more detailed description of the DES single-epoch and coadd image processing. The `SExtractor`toolkit is used to create object catalogs from the processed and coadded images (Bertin & Arnouts 1996; Bertin et al. 2011). The Y1A1 data release contains a catalog of ~131 million unique objects detected in the coadd imaging which are distributed over $1800\ \mathrm{deg}^2$. This area includes $\sim 200\ \mathrm{deg}^2$ overlapping with the Stripe 82 region of SDSS, as well as a contiguous region of $\sim 1600\ \mathrm{deg}^2$ overlapping the South Pole Telescope (SPT) footprint (Carlstrom et al. 2011). The DES imaging in the SPT region is unprecedented in depth. Figure 1 shows the coverage of Y1A1 in Galactic coordinates.

We selected stars from the Y1A1 coadd object catalog based on the *spread_model* quantity output by `SExtractor` (Desai et al. 2012). To avoid issues arising from fitting the point-spread function (PSF) across variable-depth coadded images,

[44] http://data.darkenergysurvey.org/aux/releasenotes/DESDMrelease.html

Table 1
Detection of New Satellite Galaxy Candidates in DES Y1A1

Name	α_{2000} (deg)	δ_{2000} (deg)	$m-M$	Map Sig (σ)	TS Scan	TS Fit	r_h (deg)	ϵ	ϕ (deg)	Σp_i
DES J0335.6–5403 (Ret II)	53.92	−54.05	17.5	24.6	1466	1713	$0.10^{+0.01}_{-0.01}$	$0.6^{+0.1}_{-0.2}$	72^{+7}_{-7}	338.1
DES J0344.3–4331 (Eri II)	56.09	−43.53	22.6	23.0	322	512	$0.03^{+0.01}_{-0.01}$	$0.19^{+0.16}_{-0.16}$	90^{+30}_{-30}	96.9
DES J2251.2–5836 (Tuc II)	343.06	−58.57	18.8	6.4	129	167	$0.12^{+0.03}_{-0.03}$	⋯	⋯	114.9
DES J0255.4–5406 (Hor I)	43.87	−54.11	19.7	8.2	55	81	$0.04^{+0.05}_{-0.02}$	⋯	⋯	30.6
DES J2108.8–5109 (Ind I)	317.20	−51.16	19.2	5.5	⋯	75	$0.010^{+0.002}_{-0.002}$	⋯	⋯	26.6
DES J0443.8–5017 (Pic I)	70.95	−50.28	20.5	7.1	⋯	63	$0.02^{+0.07}_{-0.01}$	⋯	⋯	19.1
DES J2339.9–5424 (Phe II)	354.99	−54.41	19.9	5.1	⋯	61	$0.02^{+0.01}_{-0.01}$	⋯	⋯	19.4
DES J0222.7–5217 (Eri III)	35.69	−52.28	19.9	5.4	⋯	57	$0.007^{+0.005}_{-0.003}$	⋯	⋯	8.9

Note. Best-fit parameters from the maximum-likelihood fit assuming the composite isochrone described in Section 3.2. Uncertainties are calculated from the the highest density interval containing 90% of the posterior distribution. "Map Sig" refers to detection significance of the candidate from the stellar density map search method (Section 3.1). "TS Scan" refers to the significance (Equation (4)) from the likelihood scan using a Plummer model spatial kernel with half-light radius $r_h = 0.^\circ 1$ (Section 3.2). "TS Fit" denotes the significance of the likelihood method using the set of best-fit parameters. Ellipticities and position angles are not quoted for lower significance candidates where they are not well constrained by the data. For objects with significant ellipticity, the half-light radius is measured along the elliptical semimajor axis. Σp_i is the estimated number of satellite member stars with $g < 23$ in the stellar catalog.

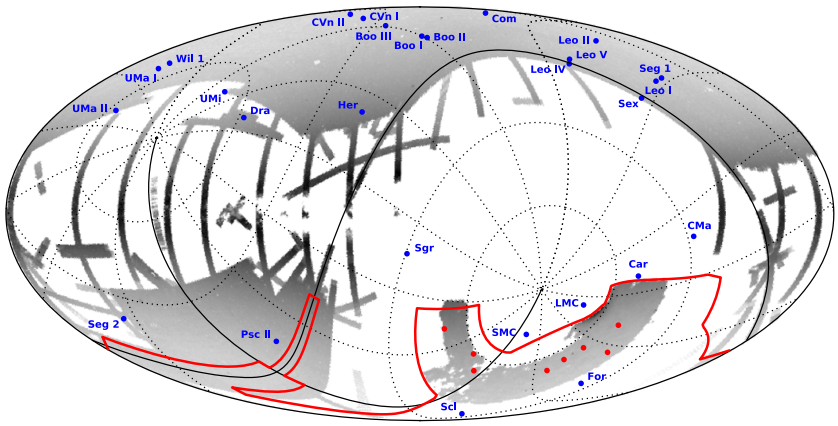

Figure 1. Locations of 27 known Milky Way satellite galaxies (blue; McConnachie 2012a) and eight DES dwarf galaxy candidates (red) in Galactic coordinates (Mollweide projection). The coordinate grid shows the equatorial coordinate system with solid lines for the equator and zero meridian. The gray scale indicates the logarithmic density of stars with $r < 22$ from SDSS and DES. The large contiguous region in the northern equatorial hemisphere shows the coverage of SDSS (Ahn et al. 2014). The full DES footprint is outlined in red, and is now partially filled in by a region of ∼1600 deg^2 near to the Magellanic Clouds and a region of ∼200 deg^2 overlapping with the SDSS Stripe 82 field along the celestial equator. Both fields were observed during the first year of DES and that compose the Y1A1 data set.

we utilized the weighted-average (*wavg*) of the *spread_model* measurements from the single-epoch exposures. Our stellar sample consists of well-measured objects with $|wavg\_spread\_model\_i| < 0.003$, $flags\_\{g, r, i\} < 4$, and $magerr\_auto\_\{g, r, i\} < 1$. We also removed objects for which the *mag_psf* and *mag_auto* measurements differ by more than 0.5 mag because this is indicative of poor object characterization.

We estimated the stellar completeness on a statistical basis over the full Y1A1 footprint by creating a test sample of high stellar purity using a color-based selection of $r - i > 1.7$. We then applied the morphology-based star selection criteria above that uses imaging in only a single band to evaluate the stellar completeness for the test sample. This approach is unbiased since the two star selection criteria are orthogonal, and benefits from a large statistical sample that is representative of the full Y1A1 data set. The stellar completeness was found to be >90% to $g \sim 22$ mag and falls to ∼50% by $g \sim 23$ mag. We validated this completeness estimate with matched spectroscopic data in the overlap region between Y1A1 and SDSS Stripe 82. Based on studies with the DAOPHOT[45] software package optimized for photometry in crowded stellar fields, we do not expect this stellar completeness to be reduced in the vicinity of DES satellite galaxy candidates relative to the Y1A1 footprint at large.

For point-like objects and a well-estimated PSF, the SExtractor *mag_psf* variables are expected to give the best measurement of stellar fluxes. However, due to the aforementioned difficulties with PSF estimation on deep coadded images, we chose instead to use the *mag_auto* measurements. The *mag_auto* measurements are found to give a less biased estimate of flux when compared to a stellar calibration sample from Pan-STARRS (Schlafly et al. 2012). Measured magnitudes are extinction corrected using the

[45] http://www.star.bris.ac.uk/∼mbt/daophot/

$E(B-V)$ dust maps from Schlegel et al. (1998). The relative calibration uncertainties are estimated via stellar-locus regression (Kelly et al. 2014) and are found to be ∼2% across the survey footprint. Uncertaities in the offsets between the DES photometric system and the AB system are estimated to be ∼1%.

3. SEARCH METHODS

Ultra-faint galaxies are discovered as arcminute-scale over-densities of individually resolved stars. The Y1A1 stellar object catalog is of such quality and depth that numerous stellar over-densities are immediately apparent from a visual scan. Several of these over-densities are not associated with any known star cluster, globular cluster, or satellite galaxy. To formalize the process of identifying new candidate satellite galaxies, we applied both (1) a simple spatial binning algorithm to facilitate inspection of the stellar density field, and (2) a matched-filter maximum-likelihood technique. These complementary approaches validated one another and the resultant list of candidates was vetted by both methods.

3.1. Stellar Density Maps

Several independent searches of the stellar density field were conducted. One approach involved direct visual inspection of coadded images. Other searches used binned stellar density maps constructed from the coadd object catalogs. As an example, we detail below how one of these maps was built and analyzed.

We began by spatially binning the stellar catalog into equal-area pixels using the `HEALPix` scheme (Górski et al. 2005).[46] We considered `HEALPix` pixel sizes of ∼0.°06 (nside = 1024) and ∼0.°11 (nside = 512) to optimize sensitivity to satellites possessing different angular sizes. Since the stellar density is greatly enhanced in regions of the Y1A1 footprint near the LMC and Galactic plane, we further grouped the stars into larger regions of ∼13 deg^2 (nside = 16) to estimate the local field density of stars. We corrected the effective solid angle of each pixel using the survey coverage, as estimated by `mangle` as part of DESDM processing (Swanson et al. 2008).[47] Several conspicuous stellar over-densities were immediately apparent after this simple spatial binning procedure.

We increase our sensitivity to ultra-faint satellite galaxies by focusing our search on regions of color–magnitude space populated by old, low-metallicity stellar populations (Koposov et al. 2008; Walsh et al. 2009). As a template, we used a `PARSEC` isochrone corresponding to a stellar population of age 12 Gyr and metallicity $Z = 0.0002$ (Bressan et al. 2012). Sensitivity to satellites at varying distances was enhanced by considering 20 logarithmically spaced steps in heliocentric distance ranging from 20 to 400 kpc (distance moduli $16.5 < M - m < 23.0$). For each step in distance, all stars within 0.2 mag of the isochrone in magnitude–magnitude space were retained while those outside the isochrone template were discarded. We then created a significance map for each ∼13 deg^2 region by computing the Poisson likelihood of finding the observed number of stars in each map pixel given a background level characterized by the local field density.

[46] http://healpix.sourceforge.net
[47] http://space.mit.edu/∼molly/mangle/

3.2. Matched-filter Maximum-likelihood Method

The simple approach described above is computationally efficient and easily generalizable. However, a more sensitive search can be performed by simultaneously modeling the spatial and photometric distributions of stars and incorporating detailed characteristics of the survey (variable depth, photometric uncertainty, etc.). One way to incorporate this information is through a maximum-likelihood analysis (Fisher 1925; Edwards 1972). Likelihood-based analyses have found broad applicability in studies of Milky Way satellites (e.g., Dolphin 2002; Martin et al. 2008a). Here we extend the maximum-likelihood approach to a wide-area search for Milky Way satellites. Similar strategies have been applied to create catalogs of galaxy clusters over wide-field optical surveys (e.g., Rykoff et al. 2014).

Our maximum-likelihood search begins by assuming that the stellar catalog in a small patch of sky represents a Poisson realization of (1) a field contribution including Milky Way foreground stars, mis-classified background galaxies, and imaging artifacts, and (2) a putative satellite galaxy. The unbinned Poisson log-likelihood function is given by

$$\log \mathcal{L} = -f\lambda + \sum_i \left(1 - p_i\right), \quad (1)$$

where i indexes the objects in the stellar sample. The value p_i can be interpreted as the probability that star i is a member of the satellite, and is computed as

$$p_i \equiv \frac{\lambda u_i}{\lambda u_i + b_i}. \quad (2)$$

Here, u represents the signal probability density function (PDF) for the satellite galaxy and is normalized to unity over the spatial and magnitude domain, $\mathcal{S}$; specifically, $\int_{\rm all} u\, d\mathcal{S} = 1$. The corresponding background density function for the field population is denoted by b.

We define the richness, λ, to be a normalization parameter representing the total number of satellite member stars with mass $>0.1 M_\odot$. In Equation (1), $f \equiv \int_{\rm obs} u\, d\mathcal{S}$ represents the fraction of satellite member stars that are within the *observable* spatial and magnitude domain of the survey, and $f\lambda$ denotes the expected number of observable satellite member stars.[48] Maximizing the likelihood with respect to the richness implies $f\lambda = \sum_i p_i$. This condition makes clear that the satellite membership probability for each star in the catalog is a natural product of the maximum-likelihood approach. These membership probabilities can be used to prioritize targeting when planning spectroscopic follow-up observations. Figure 2 highlights the use of membership probabilities to visualize a low-surface-brightness satellite galaxy candidate.

To characterize a candidate satellite galaxy, we explore the likelihood of the data, $\mathcal{D}$, as a function of a set of input model parameters, $\boldsymbol{\theta}$. The signal PDF is assumed to be separable into two independent components,

$$u\left(\mathcal{D}_i \,|\boldsymbol{\theta}\right) = u_s\left(\mathcal{D}_{s,i} \,|\boldsymbol{\theta}_s\right) \times u_c\left(\mathcal{D}_{c,i} \,|\boldsymbol{\theta}_c\right). \quad (3)$$

[48] `Mangle` maps of the survey coverage are used in the calculation of the observable fraction at each position in the sky.

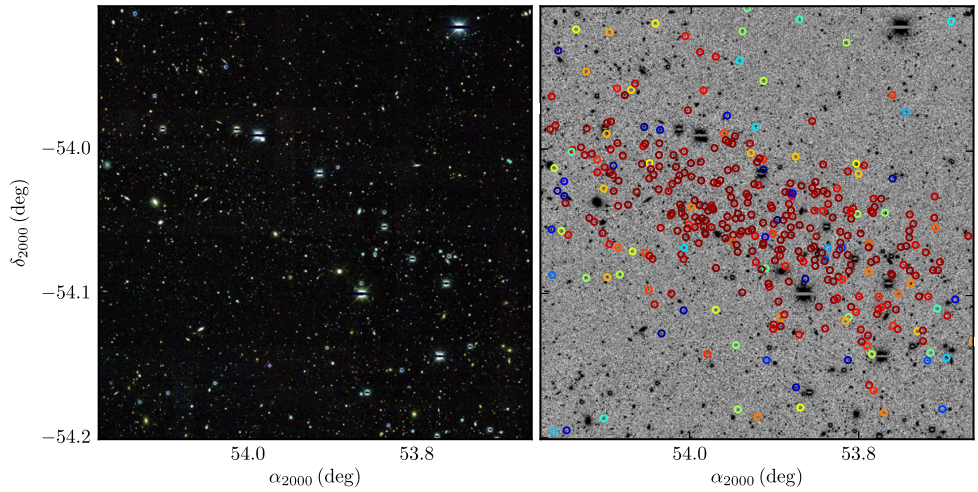

Figure 2. Left: false color *gri* coadd image of the $0.^{\circ}3 \times 0.^{\circ}3$ region centered on DES J0335.6−5403. Right: stars in the same field of view with membership probability $p_i > 0.01$ are marked with colored circles. In this color map, red signifies high-confidence association with DES J0335.6−5403 and blue indicates lower membership probability. The membership probabilities have been evaluated using Equation (2) for the best-fit model parameters listed in Table 1.

The first component, u_s, depends only on the spatial properties, while the second component, u_c, depends only on the distribution in color–magnitude space.

We modeled the spatial distribution of satellite member stars with an elliptical Plummer profile (Plummer 1911), following the elliptical coordinate prescription of Martin et al. (2008a). The Plummer profile is sufficient to describe the spatial distribution of stars in known ultra-faint galaxies (Muñoz et al. 2012b). The spatial data for catalog object i consist of spatial coordinates, $\mathcal{D}_{s,i} = \{\alpha_i, \delta_i\}$, while the parameters of our elliptical Plummer profile are the centroid coordinates, half-light radius, ellipticity, and position angle, $\boldsymbol{\theta}_s = \{\alpha_0, \delta_0, r_h, \epsilon, \phi\}$.

We modeled the color–magnitude component of the signal PDF with a set of representative isochrones for old, metal-poor stellar populations, specifically by taking a grid of isochrones from Bressan et al. (2012) spanning $0.0001 < Z < 0.001$ and $1\ \mathrm{Gyr} < \tau < 13.5\ \mathrm{Gyr}$. Our spectral data for star i consist of the magnitude and magnitude error in each of two filters, $\mathcal{D}_{c,i} = \{g_i, \sigma_{g,i}, r_i, \sigma_{r,i}\}$, while the model parameters are composed of the distance modulus, age, and metallicity describing the isochrone, $\boldsymbol{\theta}_c = \{M - m, \tau, Z\}$. To calculate the spectral signal PDF, we weight the isochrone by a Chabrier (2001) initial mass function (IMF) and densely sample in magnitude–magnitude space. We then convolve the photometric measurement PDF of each star with the PDF of the weighted isochrone. The resulting distribution represents the predicted probability of finding a star at a given position in magnitude–magnitude space given a model of the stellar system.

The background density function of the field population is empirically determined from a circular annulus surrounding each satellite candidate ($0.^{\circ}5 < r < 2.^{\circ}0$). The inner radius of the annulus is chosen to be sufficiently large that the stellar population of the candidate satellite does not bias the estimate of the field population. Stellar objects in the background annulus are binned in color–magnitude space using a cloud-in-cells algorithm and are weighted by the inverse solid angle of the annulus. The effective solid angle of the annulus is corrected to account for regions that are masked or fall below our imposed magnitude limit of $g < 23$ mag. The resulting two-dimensional histogram for the field population provides the number density of stellar objects as a function of observed color and magnitude ($\mathrm{deg}^{-2}\ \mathrm{mag}^{-2}$). This empirical determination of the background density incorporates contamination from unresolved galaxies and imaging artifacts.

The likelihood formalism above was applied to the Y1A1 data set via an automated analysis pipeline.[49] For the search phase of the algorithm, we used a radially symmetric Plummer model with half-light radius $r_h = 0.^{\circ}1$ as the spatial kernel, and a composite isochrone model consisting of four isochrones bracketing a range of ages, $\tau = \{12, 13.5\ \mathrm{Gyr}\}$, and metallicities, $Z = \{0.0001, 0.0002\}$, to bound a range of possible stellar populations. We then tested for a putative satellite galaxy at each location on a three-dimensional grid of sky position (0.7 arcmin resolution; nside = 4096) and distance modulus ($16 < M - m < 24$; 16−630 kpc).

The statistical significance at each grid point can be expressed as a Test Statistic (TS) based on the likelihood ratio between a hypothesis that includes a satellite galaxy versus a field-only hypothesis:

$$\mathrm{TS} = 2\Big[\log \mathcal{L}\Big(\lambda = \hat{\lambda}\Big) - \log \mathcal{L}\Big(\lambda = 0\Big)\Big]. \quad (4)$$

Here, $\hat{\lambda}$ is the value of the stellar richness that maximizes the likelihood. In the asymptotic limit, the null-hypothesis distribution of the TS will follow a $\chi^2/2$ distribution with one bounded degree of freedom (Chernoff 1954). We have verified that the output distribution of our implementation agrees well with the theoretical expectation by testing on simulations of the stellar field. In this case, the *local* statistical significance of a given stellar over-density, expressed in

[49] The Ultra-faint Galaxy Likelihood (UGALI) code; detailed methodology and performance to be presented elsewhere.

Table 2
Properties of DES Satellite Galaxy Candidates

Name	Distance (kpc)	M_* ($10^3 M_\odot$)	M_V (mag)	$r_{1/2}$ (pc)	$\log_{10}(\tau)$ $\log_{10}$(Gyr)	Z
DES J0335.6–5403 (Ret II)	32	$2.6^{+0.2}_{-0.2}$	-3.6 ± 0.1	55^{+5}_{-5}	10.08 ± 0.21	<0.0003
DES J0344.3–4331 (Eri II)	330	83^{+17}_{-14}	-7.4 ± 0.1	172^{+37}_{-37}	10.10 ± 0.23	<0.0006
DES J2251.2–5836 (Tuc II)	58	3^{+7}_{-1}	-3.9 ± 0.2	120^{+30}_{-30}	...	...
DES J0255.4–5406 (Hor I)	87	$2.4^{+1.4}_{-0.7}$	-3.5 ± 0.3	60^{+76}_{-30}	9.96 ± 0.21	<0.0005
DES J2108.8–5109 (Ind I)	69	$0.8^{+0.4}_{-0.4}$	-2.2 ± 0.5	12^{+2}_{-2}	...	...
DES J0443.8–5017 (Pic I)	126	$2.8^{+5.0}_{-1.7}$	-3.7 ± 0.4	43^{+153}_{-21}	10.00 ± 0.16	<0.0004
DES J2339.9–5424 (Phe II)	95	$2.8^{+1.2}_{-0.7}$	-3.7 ± 0.4	33^{+20}_{-11}	...	...
DES J0222.7–5217 (Eri III)	95	$0.9^{+0.9}_{-0.7}$	-2.4 ± 0.6	11^{+8}_{-5}	...	...

Note. Uncertainties are calculated from the the highest density interval containing 90% of the posterior distribution. Stellar masses are computed for a Chabrier initial mass function.

Gaussian standard deviations, is approximately the square root of the TS.

4. CANDIDATE SELECTION AND CHARACTERIZATION

The two search methods described in Section 3 each produce significance maps of the full Y1A1 footprint, where peaks in these maps represent the three-dimensional seed positions (α_{2000}, δ_{2000}, $M - m$) of possible satellite galaxies. Seeds were selected from the union of the search methods. Statistical significance thresholds were set at $>5\sigma$ for the stellar density map method and TS > 45 for the matched-filter maximum-likelihood method, yielding $\sim$50 seeds. Most of these were discarded as being attributed to steep gradients in the stellar density field, numerical effects near the survey boundaries, imaging artifacts, and large nearby galaxies resolved into multiple closely spaced catalog objects. For this reason, we did not pursue investigation at lower significance thresholds.

The resulting seed list was compared against catalogs of known star clusters (Harris 1996, 2010 edition; Kharchenko et al. 2013) and Milky Way satellite galaxies (McConnachie 2012a) as well as catalogs of other astrophysical objects that can produce false positives, such as large nearby galaxies (Nilson 1973; Corwin 2004) or galaxy clusters (Rykoff et al. 2014). Associated seeds include the Reticulum globular cluster, the Phoenix dwarf galaxy, AM 1, NGC 1261, NGC 1291, NGC 1553, NGC 1851, NGC 7089, NGC 7424, ESO 121-SC 003, and ESO 201-SC 010.

We explored the multi-dimensional parameter space for each unassociated seed using the `emcee` module for Markov Chain Monte Carlo (MCMC; Foreman-Mackey et al. 2013),[50] and the likelihood function described in Section 3.2 with flat priors on each of the input parameters. For each seed, we ran an MCMC chain with 100 walkers that each make 1000 steps including a burn-in stage of 50 steps. This is sufficient to sample the region of parameter space near the maximum-likelihood estimate. Only seeds with well-constrained posterior distributions enter our candidate list of new Milky Way companions.

Table 1 presents the eight most significant stellar over-densities in the Y1A1 data set consistent with being previously unknown dwarf galaxies. When comparing the significances obtained with the map-based and likelihood scan algorithms, it is worth noting that the two methods were applied assuming different size scales for the target satellites, and that kernel assumed for the likelihood scan ($r_h = 0.^\circ 1$) is larger than the majority of candidates listed in Table 1. After fitting the spatial parameters of the candidates, all are detected with high significance using the likelihood-based method. The dependence of detection efficiency on assumed kernel size is discussed is Section 5.2.

The physical characteristics of these objects, as determined by the follow-up MCMC likelihood analysis, are summarized in Table 2. The best-fit values and uncertainties are determined from the peak of the posterior distribution and the 90% highest posterior density interval (Box & Tiao 1973). A significant correlation was observed between the age of the stellar isochrone and the heliocentric distance—a degeneracy that may be expected given the evolution of the main sequence turnoff. For some DES candidates, the posterior distribution for the distance is multi-modal. The distance estimates provided in Table 2 indicate the peaks in the posterior distribution.

To compare with previously known Milky Way satellite galaxies, we convert from DES g- and r-band magnitudes to visual magnitudes using

$$\begin{aligned} g_{\rm DES} &= g_{\rm SDSS} - 0.104\left(g_{\rm SDSS} - r_{\rm SDSS}\right) + 0.01 \text{ mag} \\ r_{\rm DES} &= r_{\rm SDSS} - 0.102\left(g_{\rm SDSS} - r_{\rm SDSS}\right) + 0.02 \text{ mag} \\ \Rightarrow V &= g_{\rm DES} - 0.487\left(g_{\rm DES} - r_{\rm DES}\right) - 0.025 \text{ mag}. \end{aligned} \quad (5)$$

This transform from DES g and r magnitudes to V-band magnitudes was derived using an SDSS stellar calibration sample and the equations from Jester et al. (2005). The absolute magnitude of each satellite is calculated using the sampling formalism of Martin et al. (2008a). For bright satellites, this formalism yields a very similar estimate to the integration of the stellar luminosity function for the best-fit model. However, for fainter satellites, the uncertainty in the total magnitude can be dominated by shot noise arising from sparse sampling of the stellar population. In this case, the additional association of a single bright star can have a strong influence on the measured magnitude of a satellite. Similarly, the evolution of individual member stars can substantially change the total luminosity. To quantify the impact of shot noise on the derived luminosity estimates, we use a representative isochrone weighted by a Chabrier IMF to simulate an ensemble of satellites with similar characteristics to the observed candidates. The quoted uncertainty on the

[50] `emcee` v2.1.0: http://dan.iel.fm/emcee/current/.

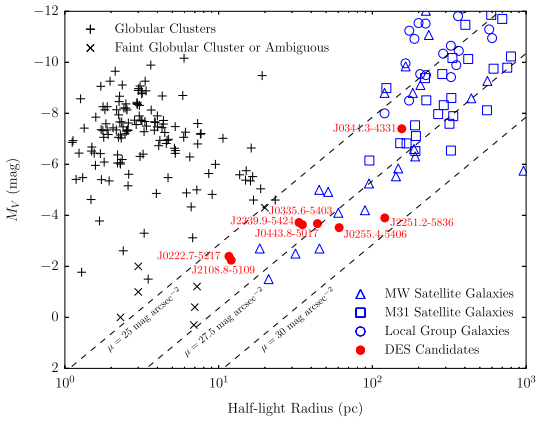

Figure 3. Local Group galaxies (McConnachie 2012a) and globular clusters (Harris 1996, 2010 edition) occupy distinct regions in the plane of physical half-light radius (geometric mean of the major and minor axes) and absolute luminosity. The majority of DES satellite candidates (red dots) are more consistent with the locus of Local Group galaxies (empty blue shapes) than with the population of Galactic globular clusters (black crosses). Several of the faintest globular clusters and systems of ambiguous classification are indicated with×marks: Koposov 1 and Koposov 2 (Koposov et al. 2007; Paust et al. 2014), Segue 3 (Belokurov et al. 2010; Fadely et al. 2011; Ortolani et al. 2013), Muñoz 1 (Muñoz et al. 2012a), Balbinot 1 (Balbinot et al. 2013), PSO J174.0675–10.8774/Crater I (Laevens et al. 2014; Belokurov et al. 2014), and Kim 1 (Kim & Jerjen 2015). Dashed lines indicate contours of constant surface brightness at $\mu = \{25, 27.5, 30\}$ mag arcsec^{-2}.

luminosity reflects the expected shot noise from stars in the magnitude range visible to DES, 17 mag $< g <$ 23 mag.

The angular and physical half-light radii listed in Tables 1 and Table 2 are both given as two-dimensional quantities. The deprojected (three-dimensional) half-light radius is a factor ∼1.3 larger than the projected half-light radius for a variety of common density profiles (Wolf et al. 2010). For objects with measured ellipticity, we report the half-light radius measured along the semimajor axis.

As illustrated in Figure 1, the DES candidates are distributed throughout the Y1A1 footprint and occupy a portion of the celestial sphere in the direction of the Magellanic Clouds where no ultra-faint galaxies were previously known. The DES candidates are widely distributed in heliocentric distance from ∼30 kpc (DES J0335.6−5403) to >300 kpc (DES J0344.3−4331).

5. DISCUSSION

Galaxies are distinguished from star clusters by having a dynamical mass that is substantially larger than the mass inferred from the luminous stellar population and/or a significant dispersion in metallicities indicative of multiple generations of star formation and a deep enough gravitational potential to retain supernova ejecta (Willman & Strader 2012). While devoted spectroscopic follow up observations are necessary to unambiguously classify these objects, the properties given in Table 2 already provide strong clues as to which candidates are most likely to be galaxies. First, the large physical sizes of most of these objects are more consistent with the locus occupied by known satellite galaxies of the Local Group than with globular clusters of the Milky Way, as shown in Figure 3. All of the DES candidates are of comparable surface brightness to the ultra-faint galaxies detected in SDSS (McConnachie 2012a). The two most compact systems, DES J2108.8−5109 and DES J0222.7−5217, fall in between the known ultra-faint galaxies and the faintest Milky Way star clusters, e.g., Koposov 1 and Koposov 2 (Koposov et al. 2007; Paust et al. 2014), Segue 3 (Belokurov et al. 2010; Fadely et al. 2011; Ortolani et al. 2013), Muñoz 1 (Muñoz et al. 2012a), Balbinot 1 (Balbinot et al. 2013), and Kim 1 (Kim & Jerjen 2015). For the most significant DES candidates, it is possible to estimate the ellipticity. Whereas globular clusters tend to have ellipticity $\lesssim$0.2 (Martin et al. 2008a; van den Bergh 2008), the best measured candidate, DES J0335.6−5403, has an ellipticity ∼0.6, which is more consistent with the population of known ultra-faint galaxies.

Further insight can be gained by fitting isochrones to the observed stellar distribution in color–magnitude space. Two independent maximum-likelihood implementations confirm that the DES candidates are generally consistent with old ($\tau \gtrsim 10$ Gyr) and metal-poor stellar populations ($Z \sim 0.0002$). The first of these analyses is the pipeline described in Section 3.2 used in a mode that varies age and metallicity in addition to spatial parameters and distance modulus in a simultaneous fit. The second color–magnitude fitting procedure adopts a similar likelihood formalism, but fits the spatial and photometric distributions of the stars in two separate phases. Instead of assuming an IMF, the second method weights the stars according to their proximity to the best-fit centroid location, and then evaluates the consistency between each star and a given isochrone in color–magnitude space given the photometric uncertainty for that star. The second method is more robust to complications that might arise from stellar incompleteness and/or imperfect modeling of the IMF. Age estimates and metallicity upper limits for four of the more significant DES candidates are reported in Table 2. Like the previously known ultra-faint dwarfs, the new DES systems are old and metal-poor (e.g., Brown et al. 2014). The latter fitting procedure has also been applied to non-extinction corrected magnitudes to independently validate the extinction values from Schlegel et al. (1998).

5.1. Review of Individual Candidates.

Brief comments on the individual galaxy candidates are provided below, and spatial maps and color–magnitude diagrams for each candidate are provided in Figures 4–11. The rightmost panels of these Figures show the satellite membership probabilities of individual stars that are assigned by the likelihood fit using a single representative isochrone with $\tau = 13.5$ Gyr and $Z = 0.0001$. Stars with high membership probabilities contribute most to the statistical significance of each candidate. The constellation designation, should these candidates be confirmed as dwarf galaxies, is listed in parenthesis.

1. *DES J0335.6–5403* (Reticulum II, Figure 4): as the nearest and most significant candidate, DES J0335.6−5403 is highly conspicuous in the Y1A1 stellar density maps, with ∼300 member stars brighter than $g \sim 23$ mag. In fact, an over-density of faint stars at this position is even visible in the much shallower Digitized Sky Survey images, although it was not detected by Whiting et al. (2007) and other searches of photographic material. Note that like the previously known ultra-faint dwarfs, DES J0335.6−5403 very likely contains several blue horizontal branch stars identified by the likelihood

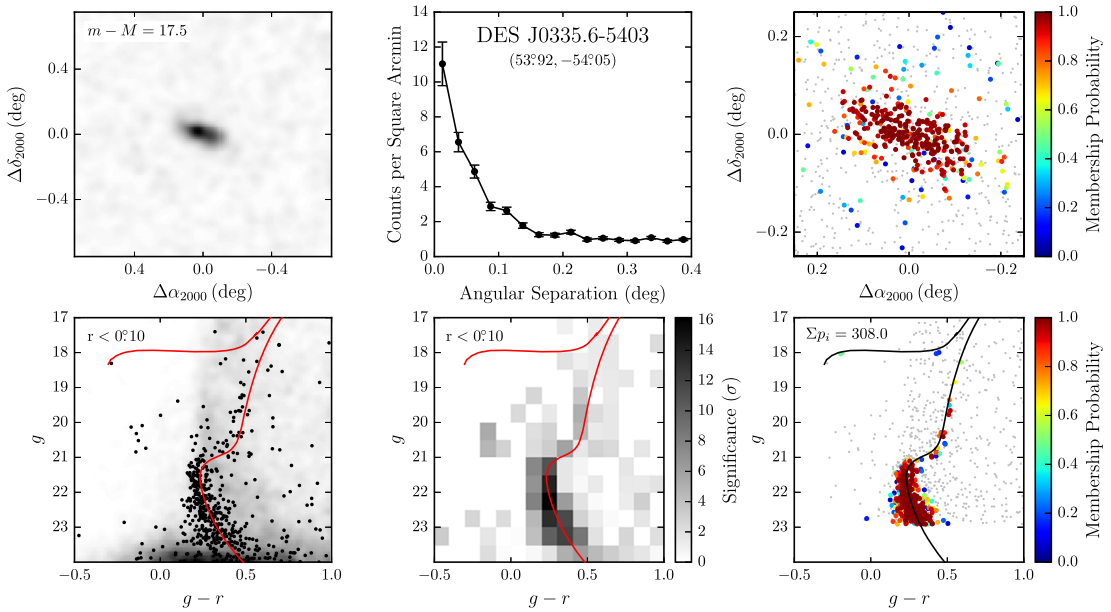

Figure 4. Stellar density and color–magnitude diagrams for DES J0335.6–5403. Top left: spatial distribution of stars with $g < 24$ mag that are within 0.1 mag of the isochrone displayed in the lower panels. The field of view is $1.^\circ5 \times 1.^\circ5$ centered on the candidate and the stellar distribution has been smoothed with a Gaussian kernel with standard deviation $0.^\circ027$. Top center: radial distribution of stars with $g - r < 1$ mag and $g < 24$ mag. Top right: spatial distribution of stars with high membership probabilities within a $0.^\circ5 \times 0.^\circ5$ field of view. Small gray points indicate stars with membership probability less than 5%. Bottom left: the color–magnitude distribution of stars within $0.^\circ1$ of the centroid are indicated with individual points. The density of the field within a 1° annulus is represented by the background two-dimensional histogram in grayscale. The red curve shows a representative isochrone for a stellar population with $\tau = 13.5$ Gyr and $Z = 0.0001$ located at the best-fit distance modulus listed in the upper left panel. Bottom center: binned significance diagram representing the Poisson probability of detecting the observed number of stars within the central $0.^\circ1$ for each bin of the color–magnitude space given the local field density. Bottom right: color–magnitude distribution of high membership probability stars.

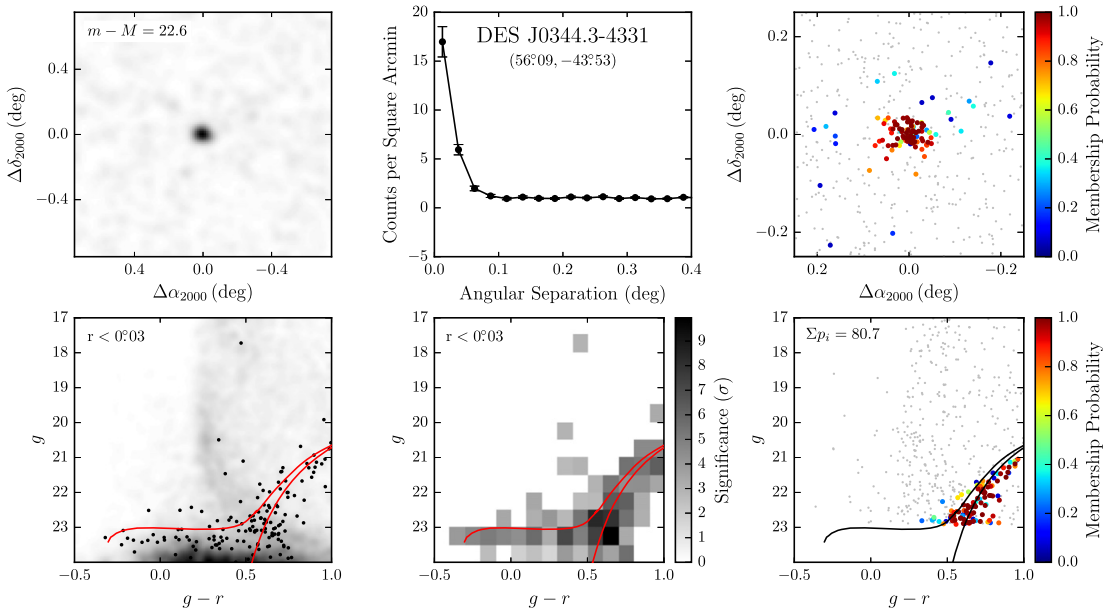

Figure 5. Analogous to Figure 4 but for DES J0344.3–4331. A large number of stars, including several probable horizontal branch members, are present at magnitudes fainter than the $g < 23$ mag threshold of our likelihood analysis. This threshold was set by the rapidly decreasing stellar completeness at fainter magnitudes. However, it is likely that extending to fainter magnitudes would cause the best-fit distance modulus of DES J0344.3–4331 to increase. Better constraints on the properties of DES J0344.3–4331 require the stellar completeness to be robustly quantified in this regime.

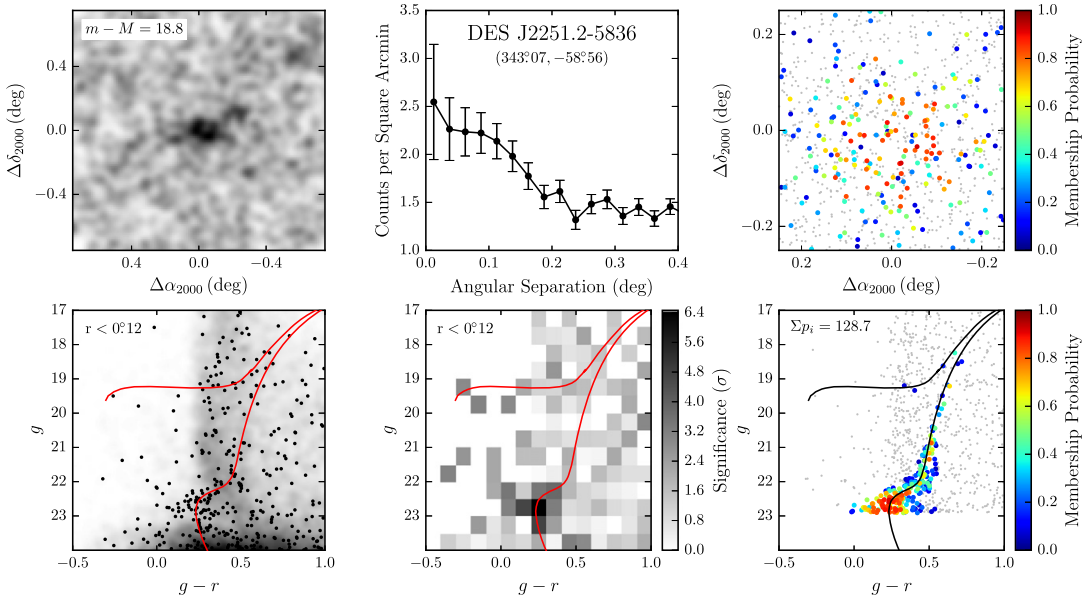

Figure 6. Analogous to Figure 4 but for DES J2251.2−5836.

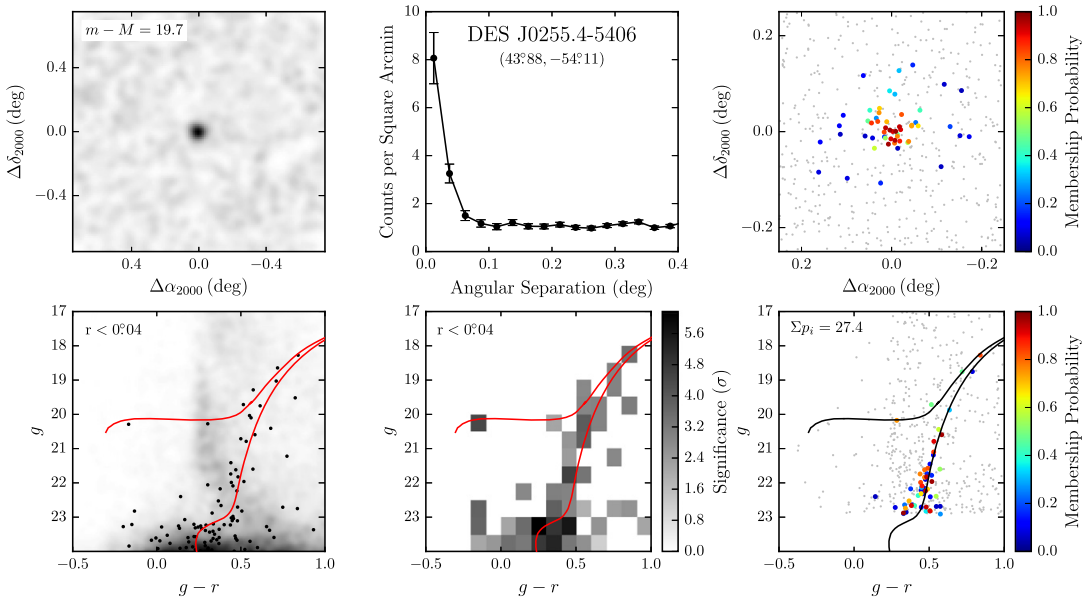

Figure 7. Analogous to Figure 4 but for DES J0255.4−5406.

procedure, two of which are relatively far from the center of the object. Given its luminosity, radius, and ellipticity, DES J0335.6−5403 is almost certainly a dwarf galaxy rather than a globular cluster. As illustrated in Figure 3, it is significantly more extended than any known faint globular cluster, and its elongated shape would also make it an extreme outlier from the Milky Way cluster population. Among known dwarfs, DES J0335.6−5403 appears quite comparable to Ursa Major II (Zucker et al. 2006a; Muñoz et al. 2010). DES J0335.6−5403 is only ∼23 kpc from the LMC, and measurements of its radial velocity and proper motion will provide strong

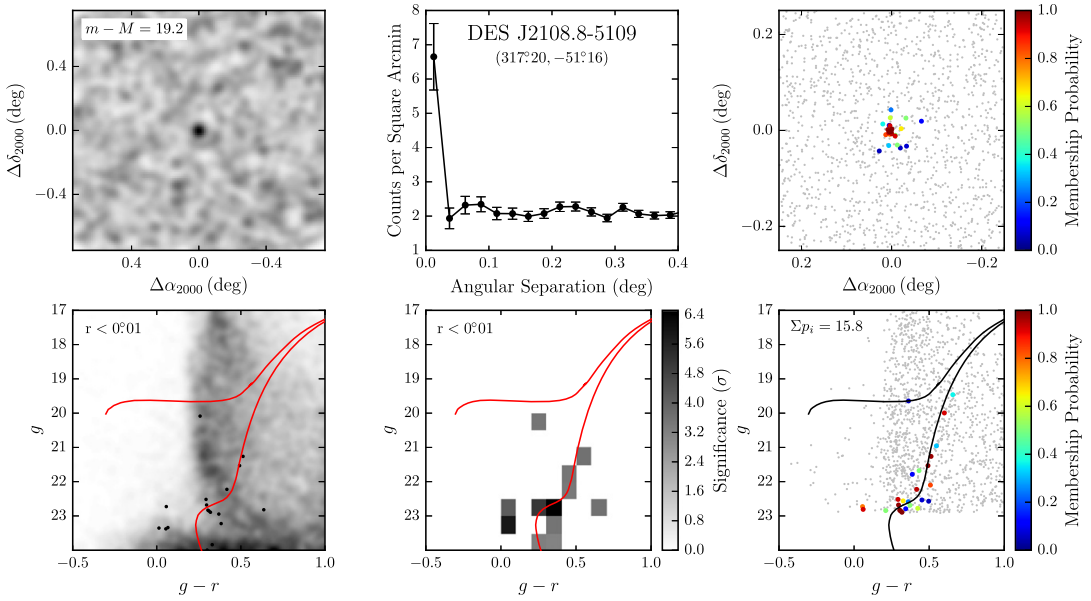

Figure 8. Analogous to Figure 4 but for DES J2108.8–5109.

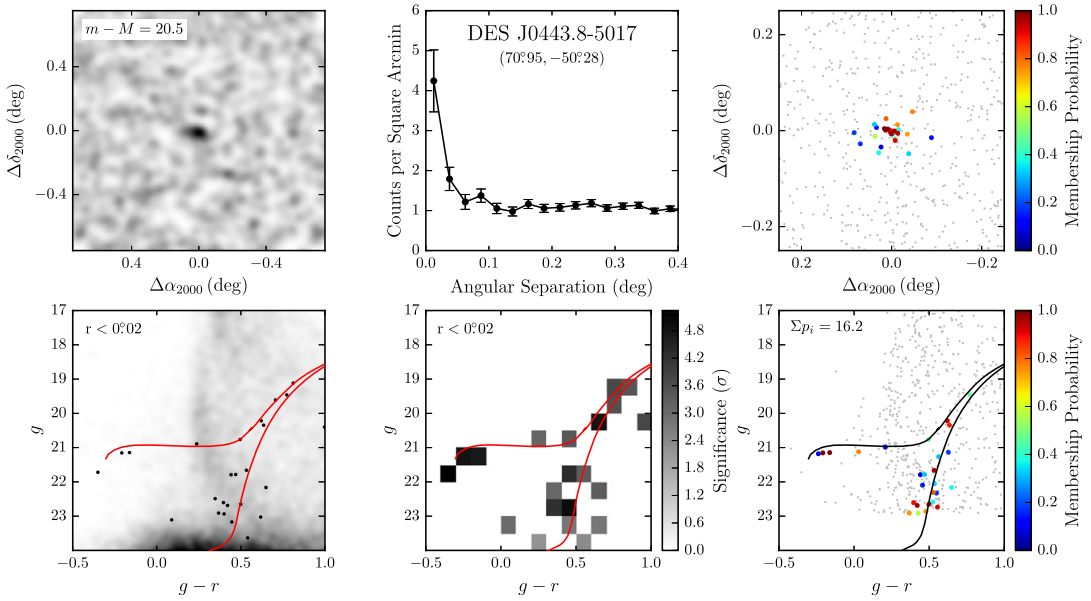

Figure 9. Analogous to Figure 4 but for DES J0443.8–5017.

clues as to whether it originated as a Milky Way satellite or fell into the Milky Way halo as part of a Magellanic group.

2. *DES J0222.7–5217* (Eridanus II, Figure 5): at a distance of >330 kpc, DES J0344.3–4331 is nearly a factor of three more distant than any known outer halo globular cluster, and its half-light radius of ∼170 pc is inconsistent with the sizes of globular clusters. It is therefore very likely that this object is a new dwarf galaxy. The color–magnitude diagram of DES J0344.3–4331 closely resembles that of another distant Milky Way satellite, Canes Venatici I, with a well-populated horizontal branch

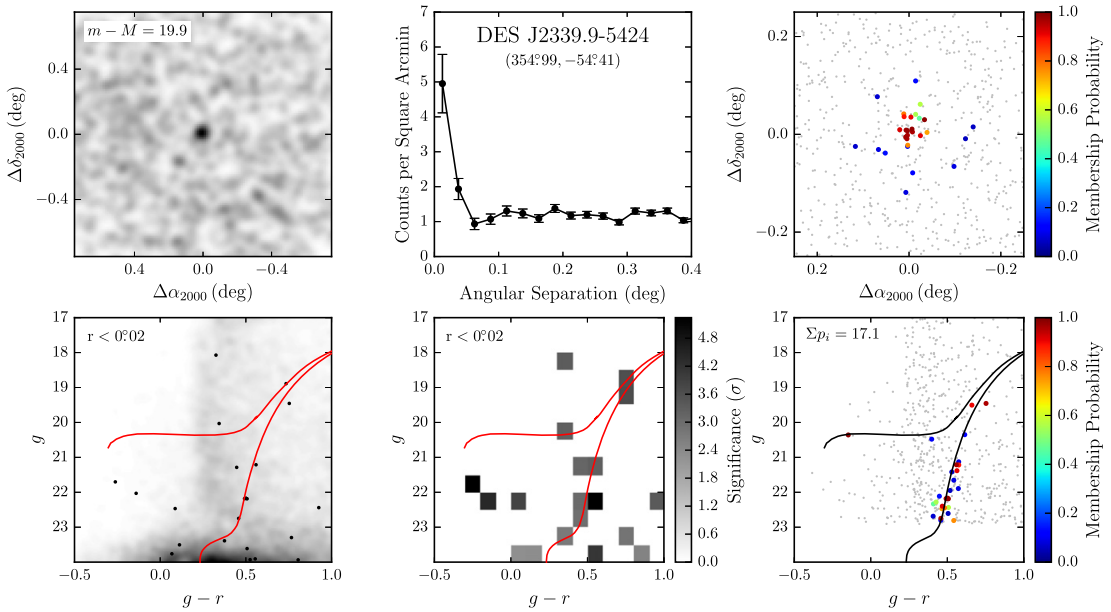

Figure 10. Analogous to Figure 4 but for DES J2339.9–5424.

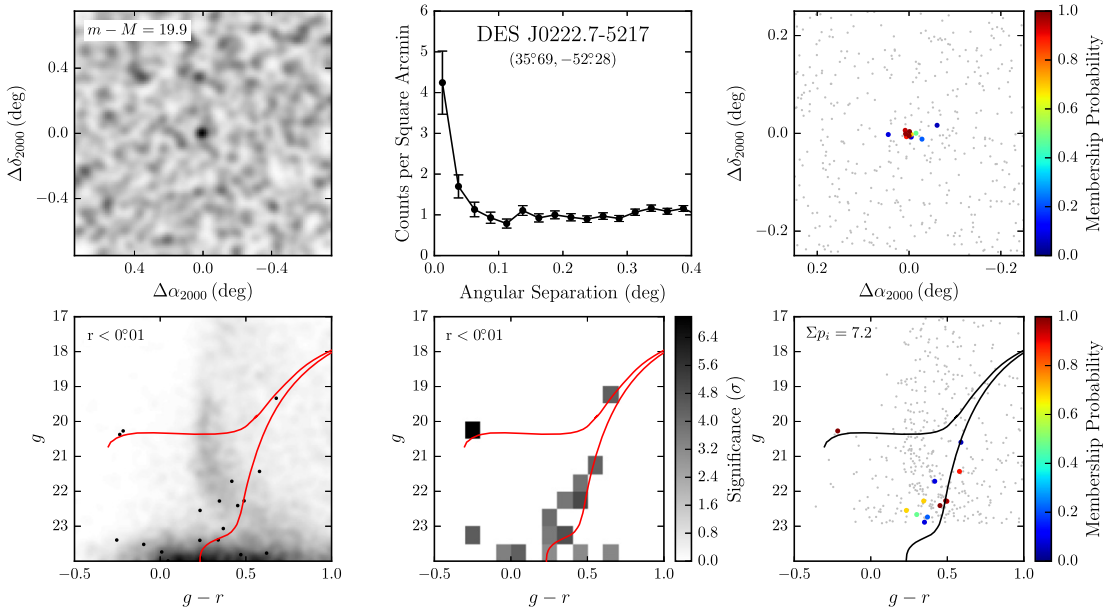

Figure 11. Analogous to Figure 4 but for DES J0222.7–5217.

covering a wide range of colors (Zucker et al. 2006b; Martin et al. 2008b; Okamoto et al. 2012). Its large distance places DES J0344.3–4331 in a very intriguing range of parameter space for studying the quenching and loss of gas in dwarf galaxies. As has been known for many years, dwarf galaxies within ∼250 kpc of the Milky Way and M31 are almost exclusively early-type galaxies with no gas or recent star formation, while dwarfs beyond that limit often have irregular morphologies, contain gas, and/or are still forming stars (e.g., Einasto et al. 1974; Blitz & Robishaw 2000; Grcevich & Putman 2009; Spekkens et al. 2014). The next most distant Milky Way dwarf galaxy, Leo T, is gas-rich and has hosted recent star formation (de Jong et al. 2008; Ryan-Weber et al.

2008); deeper optical and H I imaging to search for neutral gas and young stars in DES J0344.3−4331 has the potential to provide new insight into how gas is stripped from low-mass dwarfs and reveal the minimum mass for maintaining star formation over many Gyr. A radial velocity measurement will also shed light on if DES J0344.3−4331 has already passed close to the Milky Way or whether it is infalling for the first time. Given its distance, it is unlikely to be associated with the Magellanic Clouds. Like DES J0335.6−5403, DES J0344.3−4331 is clearly detected in Digitized Sky Survey images dating as far back as 1976.

3. *DES J2251.2-5836* (Tucana II, Figure 6): DES J2251.2−5836 is the third new satellite with a large enough size (120 pc) to be tentatively identified as a dwarf galaxy with DES multi-band photometry alone. It has a similar luminosity to DES J0335.6−5403, but is a much lower surface brightness system and is a factor of ∼2 farther away. DES J2251.2−5836 is ∼19 kpc from the LMC and ∼37 kpc from the SMC, making it a strong candidate for another member of the Magellanic group. In the surface density map in the upper left panel of Figure 6, the outer regions of DES J2251.2−5836 appear elongated and distorted. However, these features are likely a result of noise rather than real distortions (Martin et al. 2008a; Muñoz et al. 2010). The distribution of likely member stars in the upper right panel is much rounder. The high detection significance of this object demonstrates the power of the likelihood analysis to simultaneously combine spatial and color–magnitude information.
4. *DES J0255.4–5406* (Horologium I, Figure 7): DES J0255.4−5406, at a distance of ∼87 kpc, has only a sparse population of red giant branch and horizontal-branch stars visible in the DES photometry (a hint of the main sequence turnoff may be present at the detection limit). Given the small number of stars visible in the DES data, deeper imaging and spectroscopy will be needed to characterize the system more fully. Its Plummer radius of ∼60 pc establishes it as a likely dwarf galaxy, twice as extended as the largest globular clusters with comparable luminosities. DES J0255.4−5406 (perhaps along with DES J0443.8−5017 and DES J2339.9−5424; see below) is significantly farther from the Milky Way than any previously known dwarf galaxy with $M_V \lesssim -4$, suggesting that tidal stripping may not be needed to explain the low luminosities of the faintest dwarfs. On its own, the Galactocentric distance is not necessarily a good indicator of the past importance of Galactic tides in shaping the photometric and spectroscopic properties of satellites. The most important factor is the peri-Galacticon distance, which is not yet known for the new satellites. DES J0255.4−5406 is ∼40 kpc away from the Magellanic Clouds and a factor ∼2 closer to them than to the Milky Way, making it a potential Magellanic satellite. If it is (or was) associated with the Magellanic group, it is possible that tides from the LMC could have been relevant to its evolution. A measurement of the systemic velocity will help clarify whether DES J0255.4−5406 is currently near apocenter, infalling, or associated with the Magellanic system.
5. *DES J2108.8–5109* (Indus I, Figure 8): we identify DES J2108.8−5109 with Kim 2 (Kim et al. 2015). DES J2108.8−5109 is one of the faintest ($M_V \sim -2.2$ mag) and most compact ($r_h \sim 12$ pc) of the satellites discussed here. The object is visible in the coadded DES images. If it is a globular cluster, as argued by Kim et al. (2015), DES J2108.8−5109 is fainter and more extended than most of the other outer halo clusters, such as AM 1, Eridanus, Pal 3, Pal 4, and Pal 14. DES J2108.8−5109 is ∼37 kpc from the SMC, ∼55 kpc from the LMC, and ∼69 kpc from the much more massive Milky Way, so it is more likely a satellite of the Milky Way than of the Magellanic Clouds.
6. *DES J0443.8-5017* (Pictoris I, Figure 9): DES J0443.8−5017 has a large enough radius to be a likely dwarf galaxy, but the uncertainty on the radius measurement is large enough to make it also consistent with the globular cluster population. DES J0443.8−5017 has a prominent blue horizontal branch and hints of an elliptical shape, but fewer member stars are detected in the DES data. More accurate measurements of size and shape from deeper imaging, and kinematics and chemical abundances from spectroscopy, will be required to determine the nature of this object. The large distance of DES J0443.8−5017 places it far enough behind the Magellanic Clouds that it is less likely to be a Magellanic satellite than many of the other new discoveries.
7. *DES J2339.9–5424* (Phoenix II, Figure 10): DES J2339.9−5424 is quite similar to DES J0443.8−5017, but slightly smaller and closer. Again, we cannot draw firm conclusions on its nature without additional data, At ∼43 kpc from the SMC and ∼65 kpc from the LMC, it is unclear whether DES J2339.9−5424 could plausibly be a Magellanic satellite.
8. *DES J0222.7–5217* (Eridanus III, Figure 11): DES J0222.7−5217 is the most compact of the newly discovered objects in both angular and physical units. Along with DES J2108.8−5109, it is the most likely of the new discoveries to be a distant globular cluster rather than a dwarf galaxy. However, they could also be consistent with an extension of the dwarf galaxy locus to fainter magnitudes and smaller sizes. Even though it is one of the lowest luminosity system identified in the DES data so far, its compactness gives it a relatively high surface brightness, and like DES J2108.8−5109 and DES J0443.8−5017, it is clearly visible in coadded images. However, only a handful of likely member stars are resolved at the depth of the Y1A1 data, and significantly deeper imaging will be needed to better constrain its physical properties and stellar population.

5.2. Detection Completeness

Given that no additional ultra-faint Milky Way satellite galaxies have been confirmed outside of the SDSS DR7 footprint, despite the large areas of sky subsequently observed by SDSS and Pan-STARRS, it is interesting that multiple candidates have been found within the comparatively small area explored by DES thus far.[51] Without definite classifications, it is difficult to incorporate the DES candidates into

[51] The classification of PSO J174.0675–10.8774/Crater I as a globular cluster or dwarf galaxy is currently ambiguous (Belokurov et al. 2014; Laevens et al. 2014).

constraints on the luminosity function of Milky Way satellite galaxies. However, it is still possible to quantify the sensitivity of the first-year DES search using simple semi-analytic estimates of the completeness.

First, we calculated the probability that each new satellite could have been detected in the Y1A1 data. We began by generating a large number of realizations of each galaxy candidate distributed uniformly over the Y1A1 footprint. The candidates were modeled using radially symmetric Plummer profiles and the realizations included shot noise due to the limited number of stars expected to be in the observable magnitude range of DES. We then applied the simple map-based detection algorithm described in Section 3.1 to evaluate the detection efficiency. To be "detected," the satellite must possess at least 10 stars brighter than our imposed magnitude limit ($g < 23$) and a large enough surface brightness to pass the visual search selection criteria. Specifically, we considered extraction of varying sizes and computed the Poisson probability of detecting $n_{\rm satellite} + n_{\rm field}$ stars when expecting $n_{\rm field}$ stars based on the local field surface density. We tested extraction regions with sizes corresponding to the pixel areas in the map-based search algorithm ($r_{\rm ext} = \{0.^\circ 029, 0.^\circ 057\}$; Section 3.1) and the kernel size from the likelihood scan ($r_{\rm ext} = 0.^\circ 1$; Section 3.2), as well as an extraction radius set to the angular half-light radius of the simulated satellite. When computing the local field density, we selected only stars along the isochrone at the distance of the satellite with $\tau = 12$ Gyr and $Z = 0.0002$ (see Section 3.1). Table 3 summarizes the expected detection efficiencies for the DES candidates when applying a 5σ statistical significance threshold, as in our seed selection procedure for the map-based search. The results show that all of the DES candidates would have been identified over a substantial fraction of the Y1A1 footprint with non-negligible probability, and for several candidates, near certainty.

Table 3 also shows that the detection efficiency is sensitive to the size of the extraction region. Extended systems such as DES J2251.2−5836 are unlikely to found using the smallest extraction regions considered here, whereas the reverse is true for compact systems such as DES J0222.7−5217 and DES J2108.8−5109. This size dependence accounts for the low significance of the two most compact candidates, DES J0222.7−5217 and DES J2108.8−5109, in the likelihood scan (Table 1). After allowing their spatial extensions to be fit, the detection significances of these candidates increase to a level well above the our imposed threshold.

For comparison, Table 3 also provides detection efficiency estimates for previously known ultra-faint galaxies (assuming they were located in the SPT region of Y1A1 instead of their actual locations). We find that all of the SDSS ultra-faint galaxies, with the exception of the highly extended Boötes III, could have been readily detected in Y1A1. We attribute these high detection efficiencies to the deeper imaging of DES relative to SDSS and note that DES J2251.2−5836, DES J0255.4−5406, DES J2108.8−5109, and DES J0222.7−5217 have a substantially reduced detection probability when the magnitude limit is raised to $r < 22$ mag, comparable to the stellar completeness limit of SDSS.

Our Y1A1 search sensitivity can be quantified in a more general way by considering an ensemble of satellites spanning a range of luminosities, physical sizes, and heliocentric distances. Figure 12 presents the discovery potential of our Y1A1 search expressed as the detection efficiency with respect to these galaxy properties, estimated by the same method described above with $r_{\rm ext} = r_{\rm h}$. Nearby, luminous, and compact objects have a high probability of being significantly detected whereas objects that are more distant, faint, and extended are less likely to be found. The detection threshold in the plane of physical size and luminosity is nearly parallel to contours of constant surface brightness, and is weakly dependent on the distance, provided that a sufficient number of stars are detected.

Since the Y1A1 search procedure described in Section 3 is a combination of the map-based and likelihood-based search techniques, the actual completeness of our search is likely slightly higher than estimated here. We expect the likelihood method to be more sensitive to extended low surface brightness systems because it combines spatial and color–magnitude information simultaneously. As the depth of DES imaging increases (2 to 4 tilings in Y1A1 compared to 10 tilings planned after 5 years) and more advanced techniques are applied to separate stars and galaxies at faint magnitudes (e.g., Fadely et al. 2012; Soumagnac et al. 2013), we anticipate that lower surface brightness satellites will become accessible. Our present study is optimized for the detection of relatively compact ($r_0 \lesssim 0.^\circ 2$) and radially symmetric stellar overdensities. The search for extended low surface brightness features in the stellar distribution will be the focus of future work.

5.3. Total Number and Spatial Distribution of Milky Way Satellite Galaxies

The discovery of eight new dwarf galaxy candidates in $\sim$1600 deg^2 of Y1A1 not overlapping with SDSS Stripe 82 is consistent with expectations from the literature (Tollerud et al. 2008; Rossetto et al. 2011; Hargis et al. 2014; He et al. 2015). By empirically modeling the incompleteness of SDSS, Tollerud et al. 2008 predicted that 19–37 satellite galaxies could be found over the full DES footprint. More recent estimates based on high-resolution *N*-body simulations (Hargis et al. 2014) and semi-analytic galaxy formation models that include baryonic physics (He et al. 2015) predict $\sim$10 new detectable satellite galaxies in DES. Large uncertainties are associated with each of these estimates due to weak constraints on the luminosity function in the ultra-faint regime. Additionally, as noted in Section 5.1, some of the DES candidates may be globular clusters or may be associated with the Magellanic Clouds. In the latter case, it becomes more challenging to directly compare our results to the predictions above, which assume an isotropic distribution of Milky Way satellite galaxies.

A number of studies, beginning with Lynden-Bell (1976), note that many Milky Way satellite galaxies appear to be distributed on the sky along a great circle, indicating a planar three-dimensional structure rather than an ellipsoidal or spherical distribution. This great circle has a polar orientation relative to the disk of the Milky Way. The discovery of most of the SDSS ultra-faint dwarfs in the north Galactic cap region increased the apparent significance of this alignment. However, since the primary region surveyed by SDSS is located in the direction of this so-called vast polar structure (Pawlowski et al. 2012), the true anisotropy of the Milky Way satellite population is not yet clear. The next generation of deep wide-field surveys should be able to address this issue with wider sky coverage.

In this context, it is interesting to consider the locations of the eight new satellites reported here, which may increase the known Milky Way dwarf galaxy population by $\sim$30%. The

Table 3
Expected Detection Efficiencies for Milky Way Companions in DES Y1A1

Name	M_V	Distance (kpc)	r_h (deg)	Efficiency ($r_{ext} = 0.^\circ029$)	Efficiency ($r_{ext} = 0.^\circ057$)	Efficiency ($r_{ext} = 0.^\circ1$)	Efficiency ($r_{ext} = r_h$)
DES-J0335.6–5403 (Ret II)	−3.6	32	0.100	1.00	1.00	1.00	1.00
DES-J0344.3–4331 (Eri II)	−7.4	330	0.030	1.00	1.00	1.00	1.00
DES-J2251.2–5836 (Tuc II)	−3.9	58	0.120	0.25	0.98	1.00	1.00
DES-J0255.4–5406 (Hor I)	−3.5	87	0.040	0.62	0.78	0.55	0.78
DES-J2108.8–5109 (Ind I)	−2.2	69	0.010	0.96	0.69	0.18	0.97
DES-J0443.8–5017 (Pic I)	−3.7	126	0.020	0.92	0.74	0.30	0.89
DES-J2339.9–5424 (Phe II)	−3.7	95	0.020	1.00	0.96	0.74	0.99
DES-J0222.7–5217 (Eri III)	−2.4	95	0.007	0.24	0.06	0.00	0.28
Segue 1	−1.5	23	0.073	0.72	0.99	0.99	0.99
Ursa Major II	−4.2	32	0.267	0.06	0.97	1.00	1.00
Bootes II	−2.7	42	0.070	0.94	1.00	1.00	1.00
Segue 2	−2.5	35	0.057	1.00	1.00	1.00	1.00
Willman 1	−2.7	38	0.038	1.00	1.00	1.00	1.00
Coma Berenices	−4.1	44	0.100	1.00	1.00	1.00	1.00
Bootes III	−5.8	47	1.666	0.00	0.00	0.00	0.96
Bootes I	−6.3	66	0.210	1.00	1.00	1.00	1.00
Sextans	−9.3	86	0.463	1.00	1.00	1.00	1.00
Ursa Major I	−5.5	97	0.188	0.00	0.30	0.90	0.98
Hercules	−6.6	132	0.143	0.86	1.00	1.00	1.00
Leo IV	−5.8	154	0.077	1.00	1.00	1.00	1.00
Canes Venatici II	−4.9	160	0.027	1.00	1.00	1.00	1.00
Leo V	−5.2	178	0.043	1.00	1.00	1.00	1.00
Pisces II	−5.0	182	0.018	1.00	1.00	1.00	1.00
Canes Venatici I	−8.6	218	0.148	1.00	1.00	1.00	1.00

Note. Detection efficiencies are calculated from many realizations of satellites with the properties (luminosity M_V, distance, Plummer profile angular half-light radius r_h) of a given ultra-faint galaxy/candidate as they would have been observed in DES Y1A1. The simulated satellites are uniformly distributed throughout the SPT region of the Y1A1 footprint, excluding regions of high stellar density near to the LMC, i.e., ∼1600 deg^2. The rightmost columns list the detection efficiencies for extraction regions of different radii, r_{ext}. Here, a detection constitutes $>5\sigma$ stellar excess with $g < 23$ within the extraction region given the local density of the stellar field, after selecting stars that are consistent with the isochrone of an old and metal-poor stellar population at the satellite distance (i.e., following the map-based detection algorithm described in Section 3.1). The extraction region radii are choosen to reflect size scales used in the map-based search ($r_{ext} = \{0.^\circ029, 0.^\circ057\}$), likelihood scan ($r_{ext} = 0.^\circ1$; Section 3.2), and matched to the size of the satellite ($r_{ext} = r_h$). Data for previously known satellites are taken from references compiled by McConnachie (2012b).

thickness of the vast polar structure defined by Pawlowski et al. (2012) is 29 kpc, and we find that the DES satellites have a dispersion of ∼28 kpc from this plane. This result is perhaps not surprising given their proximity to the Magellanic Clouds, which played a large role in defining the original Lynden-Bell plane. In fact, the entire Y1A1 search area (with the exception of Stripe 82) is located quite close to the previously known plane of satellites. Thus, any satellite galaxies identified in this data set are necessarily close to the plane, and a selection of eight random positions within this area would likely have a similar dispersion relative to the polar structure. A more quantitative characterization of the distribution of Milky Way satellites awaits the completion of the DES survey, including areas farther away from the vast polar structure, as well as future results from Pan-STARRS.

6. CONCLUSIONS

We report on the discovery of eight new dwarf galaxy candidates associated with the Milky Way and/or Magellanic Clouds found in ∼1800 deg^2 of imaging data collected during the first year of DES. These satellites span a wide range of absolute magnitudes (−2.2 to −7.4 mag), physical sizes (10–170 pc), and heliocentric distances 30−330 kpc). The projected positions of the DES candidates are in close proximity to the Magellanic Clouds, and it is possible that some may be associated with the Magellanic system.

The nature of these systems cannot be conclusively determined with photometry alone. However, judging from their low surface brightnesses, ellipticities, and/or large distances, it is likely that several are new dwarf galaxies, in particular, DES J0335.6−5403, DES J0344.3−4331, and DES J2251.2−5836. If spectroscopically confirmed, the DES candidates may become the first ultra-faint galaxies identified outside the SDSS footprint, and would significantly increase the population of Local Group galaxies in the southern hemisphere. The proximity of DES J0335.6−5403, at ∼30 kpc, suggests that it may be an interesting target for indirect dark matter searches using gamma-ray telescopes (e.g., Ackermann et al. 2014). The implications of these candidate galaxies for indirect dark matter searches are discussed in a separate paper (Drlica-Wagner et al. 2015).

The second year of the DES survey was completed on 2015 February 15. In addition to filling in regions of non-uniform coverage in the western portion of the Y1A1 footprint, the second season expands the DES survey to encompass over 4000 deg^2. The sensitivity to ultra-faint satellite galaxies achieved with first-year DES data already exceeds that of SDSS (Section 5.2), and over the next five years, DES is expected to make an important contribution to our understanding of the Milky Way environment.

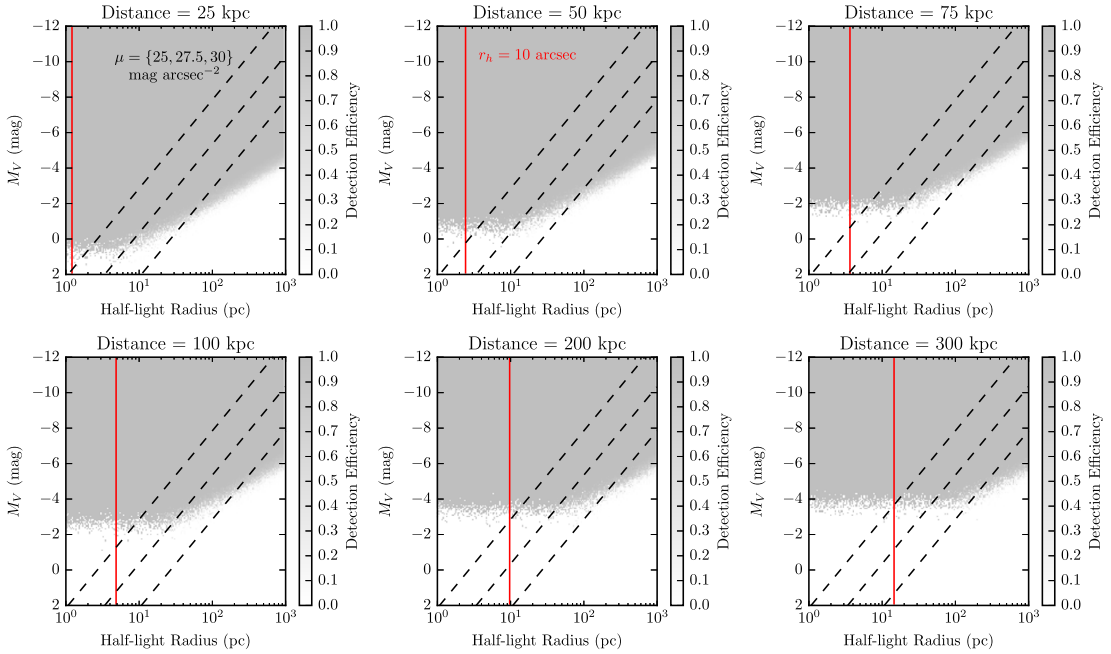

Figure 12. Sensitivity of the our Y1A1 search expressed as the detection efficiency as a function of satellite luminosity, physical size, and heliocentric distance. Each panel corresponds to a different heliocentric distance. Contours of constant surface density are indicated with dashed black lines: $\mu = \{25, 27.5, 30\}$ mag arcsec^{-2}.

During the preparation of this manuscript, we were sent an independent study by Koposov et al. using publicly released images from the first year of DES. Koposov et al. (2015) identify nine candidate satellites of the Milky Way and/or Magellanic Clouds, including eight that overlap with candidates presented here. The candidate that Koposov et al. refer to as Grus I is located outside the Y1A1 footprint in a region that was observed during the first year of DES with good image quality, but which did not have sufficient coverage in all bands to enter the coaddition stage of the standard DESDM pipeline. Therefore, the stars that comprise Grus I are not in the coadd object catalog that was used for this analysis.

We note that we have not used the coordinates shared by Koposov et al. as seeds in our analysis, nor have we tuned our search algorithms based on knowledge of the candidates reported in their work. The search methods presented here yield significance maps of the entire Y1A1 footprint, and the reported detections are the most significant points in the maps unassociated with known objects. While our final choice of 5σ for the significance threshold for reportable galaxy candidates was made after our knowledge of the results from Koposov et al., the threshold was chosen to provide as much timely information to the astronomical community as possible with minimal likelihood of false positives, rather than for agreement with the Koposov et al. detections. We conclude that the independent discovery of these Milky Way companions by two separate teams using distinct object catalogs and search algorithms strengthens the case for follow-up by the astronomical community.

We thank Sergey Koposov and collaborators for sending a copy of their submitted paper with their nine discoveries, and Helmut Jerjen for pointing out the association between Kim 2 and DES J2108.8−5109. Marla Geha provided useful comments on the presentation of these results. K.B. and A.D.W. thank Beth Willman for advice regarding the search for ultra-faint galaxies. A.D.W. thanks Ellen Bechtol for her generous hospitality during the preparation of this manuscript. We acknowledge helpful suggestions from the anonymous referee. This work made use of computational resources at the SLAC National Accelerator Laboratory and University of Chicago Research Computing Center. This material is based upon work supported by the National Science Foundation under Grant Number (1138766). A.C.R. acknowledges financial support provided by the PAPDRJ CAPES/FAPERJ Fellowship. A.A.P. was supported by DOE grant DE-AC02-98CH10886 and by JPL, run by Caltech under a contract for NASA. Funding for the DES Projects has been provided by the U.S. Department of Energy, the U.S. National Science Foundation, the Ministry of Science and Education of Spain, the Science and Technology Facilities Council of the United Kingdom, the Higher Education Funding Council for England, the National Center for Supercomputing Applications at the University of Illinois at Urbana-Champaign, the Kavli Institute of Cosmological Physics at the University of Chicago, the Center for Cosmology and Astro-Particle Physics at the Ohio State University, the Mitchell Institute for Fundamental Physics and Astronomy at Texas A&M University, Financiadora de Estudos e Projetos, Fundação Carlos Chagas Filho de Amparo à Pesquisa do Estado do Rio de Janeiro, Conselho Nacional de Desenvolvimento Científico e Tecnológico and the Ministério da Ciência, Tecnologia e Inovação, the Deutsche Forschungsgemeinschaft and the Collaborating Institutions in the Dark Energy Survey. The DES data management system is supported by the National Science Foundation under Grant Number AST-1138766. The

DES participants from Spanish institutions are partially supported by MINECO under grants AYA2012-39559, ESP2013-48274, FPA2013-47986, and Centro de Excelencia Severo Ochoa SEV-2012-0234, some of which include ERDF funds from the European Union. The Collaborating Institutions are Argonne National Laboratory, the University of California at Santa Cruz, the University of Cambridge, Centro de Investigaciones Enérgeticas, Medioambientales y Tecnológicas-Madrid, the University of Chicago, University College London, the DES-Brazil Consortium, the University of Edinburgh, the Eidgenössische Technische Hochschule (ETH) Zürich, Fermi National Accelerator Laboratory, the University of Illinois at Urbana-Champaign, the Institut de Ciències de l'Espai (IEEC/CSIC), the Institut de Física d'Altes Energies, Lawrence Berkeley National Laboratory, the Ludwig-Maximilians Universität München and the associated Excellence Cluster universe, the University of Michigan, the National Optical Astronomy Observatory, the University of Nottingham, The Ohio State University, the University of Pennsylvania, the University of Portsmouth, SLAC National Accelerator Laboratory, Stanford University, the University of Sussex, and Texas A&M University.

REFERENCES

Abbott, T., Aldering, G., Annis, J., et al. 2005, arXiv:astro-ph/0510346
Ackermann, M., Albert, A., Anderson, B., et al. 2014, PhRvD, 89, 042001
Adén, D., Feltzing, S., Koch, A., et al. 2009, A&A, 506, 1147
Ahn, C. P., Alexandroff, R., Allende Prieto, C., et al. 2014, ApJS, 211, 17
Balbinot, E., Santiago, B. X., da Costa, L., et al. 2013, ApJ, 767, 101
Balbinot, E., Santiago, B. X., Girardi, L., et al. 2015, MNRAS, 449, 1129
Belokurov, V., Irwin, M. J., Koposov, S. E., et al. 2014, MNRAS, 441, 2124
Belokurov, V., Zucker, D. B., Evans, N. W., et al. 2006, ApJL, 647, L111
Belokurov, V., Zucker, D. B., Evans, N. W., et al. 2007, ApJ, 654, 897
Belokurov, V., Walker, M. G., Evans, N. W., et al. 2008, ApJL, 686, L83
Belokurov, V., Walker, M. G., Evans, N. W., et al. 2009, MNRAS, 397, 1748
Belokurov, V., Walker, M. G., Evans, N. W., et al. 2010, ApJL, 712, L103
Bertin, E. 2011, in ASP Conf. Ser. 442, Astronomical Data Analysis Software and Systems XX, ed. I. N. Evans et al. (San Francisco, CA: ASP), 435
Bertin, E., & Arnouts, S. 1996, A&AS, 117, 393
Blitz, L., & Robishaw, T. 2000, ApJ, 541, 675
Box, G., & Tiao, G. 1973, Bayesian Inference in Statistical Analysis (Reading, MA: Addison-Wesley)
Bressan, A., Marigo, P., Girardi, L., et al. 2012, MNRAS, 427, 127
Brown, T. M., Tumlinson, J., Geha, M., et al. 2014, ApJ, 796, 91
Carlin, J. L., Grillmair, C. J., Muñoz, R. R., Nidever, D. L., & Majewski, S. R. 2009, ApJL, 702, L9
Carlstrom, J., Ade, P., Aird, K., et al. 2011, PASP, 123, 568
Chabrier, G. 2001, ApJ, 554, 1274
Chernoff, H. 1954, AnMat, 25, 573
Corwin, H. G. 2004, yCat, 7239, 0
de Jong, J. T. A., Harris, J., Coleman, M. G., et al. 2008, ApJ, 680, 1112
Desai, S., Armstrong, R., Mohr, J. J., et al. 2012, ApJ, 757, 83
Diehl, H. T., Abbott, T. M. C., Annis, J., et al. 2014, Proc. SPIE, 9149, 0
Diehl, T. 2012, PhPro, 37, 1332
Dolphin, A. E. 2002, MNRAS, 332, 91
Drlica-Wagner, A., Albert, A., Bechtol, K., et al. 2015, ApJL, submitted (arXiv:1503.02632)
Edwards, A. 1972, Likelihood: An Account of the Statistical Concept of Likelihood and Its Application to Scientific Inference (Cambridge: Cambridge Univ. Press)
Einasto, J., Saar, E., Kaasik, A., & Chernin, A. D. 1974, Natur, 252, 111
Fadely, R., Hogg, D. W., & Willman, B. 2012, ApJ, 760, 15
Fadely, R., Willman, B., Geha, M., et al. 2011, AJ, 142, 88
Fisher, R. A. 1925, PCPS, 22, 700
Flaugher, B., Diehl, H. T., Honscheid, K., et al. 2015, AJ, submitted (arXiv:1504.02900)
Flaugher, B. L., Abbott, T. M. C., Annis, J., et al. 2010, Proc. SPIE, 7735, 0
Foreman-Mackey, D., Hogg, D. W., Lang, D., & Goodman, J. 2013, PASP, 125, 306
Geha, M., Willman, B., Simon, J. D., et al. 2009, ApJ, 692, 1464
Górski, K. M., Hivon, E., Banday, A. J., et al. 2005, ApJ, 622, 759
Grcevich, J., & Putman, M. E. 2009, ApJ, 696, 385
Grillmair, C. J. 2006, ApJL, 645, L37
Grillmair, C. J. 2009, ApJ, 693, 1118
Hargis, J. R., Willman, B., & Peter, A. H. G. 2014, ApJL, 795, L13
Harris, W. E. 1996, AJ, 112, 1487
He, C., Bechtol, K., Hearin, A. P., & Hooper, D. 2015, PhRvD, 91, 063515
Irwin, M. J., Belokurov, V., Evans, N. W., et al. 2007, ApJL, 656, L13
Jester, S., Schneider, D. P., Richards, G. T., et al. 2005, AJ, 130, 873
Kelly, P. L., von der Linden, A., Applegate, D. E., et al. 2014, MNRAS, 439, 28
Kharchenko, N. V., Piskunov, A. E., Schilbach, E., Röser, S., & Scholz, R.-D. 2013, A&A, 558, A53
Kim, D., & Jerjen, H. 2015, ApJ, 799, 73
Kim, D., Jerjen, H., Milone, A. P., Mackey, D., & da Costa, G. S. 2015, ApJ, 803, 63
Kirby, E. N., Boylan-Kolchin, M., Cohen, J. G., et al. 2013, ApJ, 770, 16
Kleyna, J. T., Wilkinson, M. I., Evans, N. W., & Gilmore, G. 2005, ApJL, 630, L141
Klypin, A., Kravtsov, A. V., Valenzuela, O., & Prada, F. 1999, ApJ, 522, 82
Koch, A., Wilkinson, M. I., Kleyna, J. T., et al. 2009, ApJ, 690, 453
Koposov, S., Belokurov, V., Evans, N. W., et al. 2008, ApJ, 686, 279
Koposov, S., de Jong, J. T. A., Belokurov, V., et al. 2007, ApJ, 669, 337
Koposov, S. E., Belokurov, V., Torrealba, G., & Evans, N. W. 2015, ApJ, 805, 130
Koposov, S. E., Gilmore, G., Walker, M. G., et al. 2011, ApJ, 736, 146
Laevens, B. P. M., Martin, N. F., Sesar, B., et al. 2014, ApJL, 786, L3
Lynden-Bell, D. 1976, MNRAS, 174, 695
Martin, N. F., de Jong, J. T. A., & Rix, H.-W. 2008a, ApJ, 684, 1075
Martin, N. F., Ibata, R. A., Chapman, S. C., Irwin, M., & Lewis, G. F. 2007, MNRAS, 380, 281
Martin, N. F., Coleman, M. G., de Jong, J. T. A., et al. 2008b, ApJL, 672, L13
McConnachie, A. W. 2012a, AJ, 144, 4
McConnachie, A. W. 2012b, AJ, 144, 4
Mohr, J. J., Armstrong, R., Bertin, E., et al. 2012, Proc. SPIE, 8451, 84510D
Moore, B., Ghigna, S., Governato, F., et al. 1999, ApJL, 524, L19
Muñoz, R. R., Carlin, J. L., Frinchaboy, P. M., et al. 2006, ApJL, 650, L51
Muñoz, R. R., Geha, M., Côté, P., et al. 2012a, ApJL, 753, L15
Muñoz, R. R., Geha, M., & Willman, B. 2010, AJ, 140, 138
Muñoz, R. R., Padmanabhan, N., & Geha, M. 2012b, ApJ, 745, 127
Nilson, P. 1973, Uppsala General Catalogue of Galaxies
Okamoto, S., Arimoto, N., Yamada, Y., & Onodera, M. 2012, ApJ, 744, 96
Ortolani, S., Bica, E., & Barbuy, B. 2013, MNRAS, 433, 1966
Paust, N., Wilson, D., & van Belle, G. 2014, AJ, 148, 19
Pawlowski, M. S., Pflamm-Altenburg, J., & Kroupa, P. 2012, MNRAS, 423, 1109
Plummer, H. C. 1911, MNRAS, 71, 460
Rossetto, B. M., Santiago, B. X., Girardi, L., et al. 2011, AJ, 141, 185
Ryan-Weber, E. V., Begum, A., Oosterloo, T., et al. 2008, MNRAS, 384, 535
Rykoff, E. S., Rozo, E., Busha, M. T., et al. 2014, ApJ, 785, 104
Sakamoto, T., & Hasegawa, T. 2006, ApJL, 653, L29
Schlafly, E. F., Finkbeiner, D. P., Jurić, M., et al. 2012, ApJ, 756, 158
Schlegel, D. J., Finkbeiner, D. P., & Davis, M. 1998, ApJ, 500, 525
Sevilla, I., Armstrong, R., Bertin, E., et al. 2011, arXiv:1109.6741
Simon, J. D., & Geha, M. 2007, ApJ, 670, 313
Simon, J. D., Geha, M., Minor, Q. E., et al. 2011, ApJ, 733, 46
Soumagnac, M. T., Abdalla, F. B., Lahav, O., et al. 2013, arXiv:1306.5236
Spekkens, K., Urbancic, N., Mason, B. S., Willman, B., & Aguirre, J. E. 2014, ApJL, 795, L5
Swanson, M. E. C., Tegmark, M., Hamilton, A. J. S., & Hill, J. C. 2008, MNRAS, 387, 1391
Tollerud, E. J., Bullock, J. S., Strigari, L. E., & Willman, B. 2008, ApJ, 688, 277
van den Bergh, S. 2008, AJ, 135, 1731
Walker, M. G., Belokurov, V., Evans, N. W., et al. 2009, ApJL, 694, L144
Walsh, S. M., Jerjen, H., & Willman, B. 2007, ApJL, 662, L83
Walsh, S. M., Willman, B., & Jerjen, H. 2009, AJ, 137, 450
Whiting, A. B., Hau, G. K. T., Irwin, M., & Verdugo, M. 2007, AJ, 133, 715
Willman, B., Geha, M., Strader, J., et al. 2011, AJ, 142, 128
Willman, B., & Strader, J. 2012, AJ, 144, 76
Willman, B., Blanton, M. R., West, A. A., et al. 2005a, AJ, 129, 2692
Willman, B., Dalcanton, J. J., Martinez-Delgado, D., et al. 2005b, ApJL, 626, L85
Wolf, J., Martinez, G. D., Bullock, J. S., et al. 2010, MNRAS, 406, 1220
Zucker, D. B., Belokurov, V., Evans, N. W., et al. 2006a, ApJL, 650, L41
Zucker, D. B., Belokurov, V., Evans, N. W., et al. 2006b, ApJL, 643, L103

No artigo de descoberta do segundo ano, minha participação foi basicamente a mesma do que no primeiro ano, apenas em menor volume, dado que havia um forte envolvimento com a finalização do artigo dos aglomerados da LMC. Importante destacar que para a calibração das fontes do catálogo do segundo ano do DES (Y2Q1) foi utilizado um approach (BIGMACS) publicado por Kelly et al. 2014, que inicialmente rodamos comparando um conjunto de estrelas do DES com as estrelas do 2MASS. Mais tarde repassamos o conjunto de dados que rodamos para o conjunto de dados do DES para o grupo do portal científico do DES, e esta baseado no Locus stelar e implementado no portal científico, estando a disposição dos demais colaboradores do portal.

The Astrophysical Journal, 813:109 (20pp), 2015 November 10 doi:10.1088/0004-637X/813/2/109

EIGHT ULTRA-FAINT GALAXY CANDIDATES DISCOVERED IN YEAR TWO OF THE DARK ENERGY SURVEY

A. Drlica-Wagner[1], K. Bechtol[2,3], E. S. Rykoff[4,5], E. Luque[6,7], A. Queiroz[6,7], Y.-Y. Mao[4,5,8], R. H. Wechsler[4,5,8], J. D. Simon[9], B. Santiago[6,7], B. Yanny[1], E. Balbinot[7,10], S. Dodelson[1,11], A. Fausti Neto[7], D. J. James[12], T. S. Li[13], M. A. G. Maia[7,14], J. L. Marshall[13], A. Pieres[6,7], K. Stringer[13], A. R. Walker[12], T. M. C. Abbott[12], F. B. Abdalla[15,16], S. Allam[1], A. Benoit-Lévy[15], G. M. Bernstein[17], E. Bertin[18,19], D. Brooks[15], E. Buckley-Geer[1], D. L. Burke[4,5], A. Carnero Rosell[7,14], M. Carrasco Kind[20,21], J. Carretero[22,23], M. Crocce[22], L. N. da Costa[7,14], S. Desai[24,25], H. T. Diehl[1], J. P. Dietrich[24,25], P. Doel[15], T. F. Eifler[17,26], A. E. Evrard[27,28], D. A. Finley[1], B. Flaugher[1], P. Fosalba[22], J. Frieman[1,11], E. Gaztanaga[22], D. W. Gerdes[28], D. Gruen[29,30], R. A. Gruendl[20,21], G. Gutierrez[1], K. Honscheid[31,32], K. Kuehn[33], N. Kuropatkin[1], O. Lahav[15], P. Martini[31,34], R. Miquel[23,35], B. Nord[1], R. Ogando[7,14], A. A. Plazas[26], K. Reil[5], A. Roodman[4,5], M. Sako[17], E. Sanchez[36], V. Scarpine[1], M. Schubnell[28], I. Sevilla-Noarbe[20,36], R. C. Smith[12], M. Soares-Santos[1], F. Sobreira[1,7], E. Suchyta[31,32], M. E. C. Swanson[21], G. Tarle[28], D. Tucker[1], V. Vikram[37], W. Wester[1], Y. Zhang[28], and J. Zuntz[38]

(The DES Collaboration)

[1] Fermi National Accelerator Laboratory, P.O. Box 500, Batavia, IL 60510, USA; kadrlica@fnal.gov
[2] Wisconsin IceCube Particle Astrophysics Center (WIPAC), Madison, WI 53703, USA; keith.bechtol@icecube.wisc.edu
[3] Department of Physics, University of Wisconsin–Madison, Madison, WI 53706, USA
[4] Kavli Institute for Particle Astrophysics & Cosmology, P.O. Box 2450, Stanford University, Stanford, CA 94305, USA
[5] SLAC National Accelerator Laboratory, Menlo Park, CA 94025, USA
[6] Instituto de Física, UFRGS, Caixa Postal 15051, Porto Alegre, RS-91501-970, Brazil
[7] Laboratório Interinstitucional de e-Astronomia—LIneA, Rua Gal. José Cristino 77, Rio de Janeiro, RJ-20921-400, Brazil
[8] Department of Physics, Stanford University, 382 Via Pueblo Mall, Stanford, CA 94305, USA
[9] Carnegie Observatories, 813 Santa Barbara St., Pasadena, CA 91101, USA
[10] Department of Physics, University of Surrey, Guildford GU2 7XH, UK
[11] Kavli Institute for Cosmological Physics, University of Chicago, Chicago, IL 60637, USA
[12] Cerro Tololo Inter-American Observatory, National Optical Astronomy Observatory, Casilla 603, La Serena, Chile
[13] George P. and Cynthia Woods Mitchell Institute for Fundamental Physics and Astronomy, and Department of Physics and Astronomy, Texas A&M University, College Station, TX 77843, USA
[14] Observatório Nacional, Rua Gal. José Cristino 77, Rio de Janeiro, RJ-20921-400, Brazil
[15] Department of Physics & Astronomy, University College London, Gower Street, London, WC1E 6BT, UK
[16] Department of Physics and Electronics, Rhodes University, P.O. Box 94, Grahamstown, 6140, South Africa
[17] Department of Physics and Astronomy, University of Pennsylvania, Philadelphia, PA 19104, USA
[18] CNRS, UMR 7095, Institut d'Astrophysique de Paris, F-75014, Paris, France
[19] Sorbonne Universités, UPMC Univ Paris 06, UMR 7095, Institut d'Astrophysique de Paris, F-75014, Paris, France
[20] Department of Astronomy, University of Illinois, 1002 W. Green Street, Urbana, IL 61801, USA
[21] National Center for Supercomputing Applications, 1205 West Clark St., Urbana, IL 61801, USA
[22] Institut de Ciències de l'Espai, IEEC-CSIC, Campus UAB, Carrer de Can Magrans, s/n, E-08193 Bellaterra, Barcelona, Spain
[23] Institut de Física d'Altes Energies, Universitat Autònoma de Barcelona, E-08193 Bellaterra, Barcelona, Spain
[24] Excellence Cluster Universe, Boltzmannstr. 2, D-85748 Garching, Germany
[25] Faculty of Physics, Ludwig-Maximilians University, Scheinerstr. 1, D-81679 Munich, Germany
[26] Jet Propulsion Laboratory, California Institute of Technology, 4800 Oak Grove Dr., Pasadena, CA 91109, USA
[27] Department of Astronomy, University of Michigan, Ann Arbor, MI 48109, USA
[28] Department of Physics, University of Michigan, Ann Arbor, MI 48109, USA
[29] Max Planck Institute for Extraterrestrial Physics, Giessenbachstrasse, D-85748 Garching, Germany
[30] Universitäts-Sternwarte, Fakultät für Physik, Ludwig-Maximilians Universität München, Scheinerstr. 1, D-81679 München, Germany
[31] Center for Cosmology and Astro-Particle Physics, The Ohio State University, Columbus, OH 43210, USA
[32] Department of Physics, The Ohio State University, Columbus, OH 43210, USA
[33] Australian Astronomical Observatory, North Ryde, NSW 2113, Australia
[34] Department of Astronomy, The Ohio State University, Columbus, OH 43210, USA
[35] Institució Catalana de Recerca i Estudis Avançats, E-08010 Barcelona, Spain
[36] Centro de Investigaciones Energéticas, Medioambientales y Tecnológicas (CIEMAT), Madrid, Spain
[37] Argonne National Laboratory, 9700 South Cass Avenue, Lemont, IL 60439, USA
[38] Jodrell Bank Center for Astrophysics, School of Physics and Astronomy, University of Manchester, Oxford Road, Manchester, M13 9PL, UK

Received 2015 August 14; accepted 2015 September 22; published 2015 November 4

ABSTRACT

We report the discovery of eight new ultra-faint dwarf galaxy candidates in the second year of optical imaging data from the Dark Energy Survey (DES). Six of these candidates are detected at high confidence, while two lower-confidence candidates are identified in regions of non-uniform survey coverage. The new stellar systems are found by three independent automated search techniques and are identified as overdensities of stars, consistent with the isochrone and luminosity function of an old and metal-poor simple stellar population. The new systems are faint ($M_V > -4.7$ mag) and span a range of physical sizes (17 pc $< r_{1/2} <$ 181 pc) and heliocentric distances (25 kpc $< D_\odot <$ 214 kpc). All of the new systems have central surface brightnesses consistent with known ultra-faint dwarf galaxies ($\mu \gtrsim 27.5$ mag arcsec^{-2}). Roughly half of the DES candidates are more distant, less luminous, and/or have lower surface brightnesses than previously known Milky Way satellite galaxies. Most of the

The Astrophysical Journal, 813:109 (20pp), 2015 November 10 Drlica-Wagner et al.

candidates are found in the southern part of the DES footprint close to the Magellanic Clouds. We find that the DES data alone exclude ($p < 10^{-3}$) a spatially isotropic distribution of Milky Way satellites and that the observed distribution can be well, though not uniquely, described by an association between several of the DES satellites and the Magellanic system. Our model predicts that the full sky may hold ∼100 ultra-faint galaxies with physical properties comparable to the DES satellites and that 20%–30% of these would be spatially associated with the Magellanic Clouds.

Key words: galaxies: dwarf – Local Group

1. INTRODUCTION

The population of Milky Way satellite galaxies includes the least luminous, least chemically enriched, and most dark matter dominated galaxies in the known universe (e.g., Simon & Geha 2007; Kirby et al. 2008). Although they are extreme systems from an observational perspective, low-luminosity dwarf spheroidal galaxies are likely to be the most common galaxy type by number. This duality places the emerging population of near-field galaxies in a unique position to allow the testing of models of galaxy formation and the cold dark matter paradigm (e.g., Bullock et al. 2001), and has motivated studies ranging from the physical conditions at the time of reionization (e.g., Bullock et al. 2000; Benson et al. 2002), to the particle properties of dark matter (e.g., Ackermann et al. 2015; Geringer-Sameth et al. 2015a).

Milky Way satellite galaxies are typically discovered as arcminute-scale statistical overdensities of individually resolved stars in wide-field optical imaging surveys (Willman 2010, and the references therein). Prior to 2005, there were 12 known "classical" Milky Way satellite galaxies with absolute magnitudes in the range $-8\,\mathrm{mag} \gtrsim M_V \gtrsim -18\,\mathrm{mag}$ (McConnachie 2012). From 2005 to 2014, 15 ultra-faint satellite galaxies with $M_V \gtrsim -8\,\mathrm{mag}$ were identified in Sloan Digital Sky Survey (SDSS; York et al. 2000) data through a combination of systematic searches (Willman et al. 2005a, 2005b; Belokurov et al. 2006, 2007, 2008, 2009, 2010; Grillmair 2006, 2009; Sakamoto & Hasegawa 2006; Zucker et al. 2006a, 2006b; Irwin et al. 2007; Walsh et al. 2007) and dedicated spectroscopic follow-up observations (Kleyna et al. 2005; Muñoz et al. 2006; Martin et al. 2007; Simon & Geha 2007; Adén et al. 2009; Belokurov et al. 2009; Carlin et al. 2009; Geha et al. 2009; Koch et al. 2009; Walker et al. 2009; Koposov et al. 2011; Simon et al. 2011; Willman et al. 2011; Kirby et al. 2013). Several outer halo star clusters and/or more compact stellar systems of uncertain classification were reported during roughly the same period (e.g., Koposov et al. 2007; Walsh et al. 2009; Belokurov et al. 2010, 2014; Muñoz et al. 2012; Balbinot et al. 2013; Laevens et al. 2014; Kim & Jerjen 2015a; Kim et al. 2015b). Dwarf galaxies are distinguished from star clusters by having a dynamical mass that is substantially larger than the mass inferred from the luminous stellar population and/or a significant dispersion in stellar metallicities indicative of multiple generations of star formation and a gravitational potential deep enough to retain supernova ejecta (Willman & Strader 2012).

Since the beginning of 2015, a combination of new optical imaging surveys and a reanalysis of SDSS data have resulted in the detection of 14 additional Milky Way companions, tentatively classified as dwarf galaxies (Bechtol et al. 2015; Kim & Jerjen 2015b; Kim et al. 2015a; Koposov et al. 2015a; Laevens et al. 2015a, 2015b; Martin et al. 2015). The new galaxy candidates have been examined for their (lack of) neutral gas (Westmeier et al. 2015), possible association with the Magellanic Clouds (Deason et al. 2015; Yozin & Bekki 2015), and spatial distribution within the Galactic halo (Pawlowski et al. 2015), and have become targets for indirect dark matter searches (Drlica-Wagner et al. 2015; Geringer-Sameth et al. 2015b; Hooper & Linden 2015). The provisional classification of these stellar systems as dwarf galaxies relies on their low surface brightnesses, large physical sizes, large ellipticities, and/or large heliocentric distances. However, some of these objects lie in a region of size–luminosity space where the distinction between dwarf galaxy and globular cluster is ambiguous. Thus far, spectroscopic observations have confirmed that three of the recently discovered satellites, Reticulum II (Koposov et al. 2015b; Simon et al. 2015; Walker et al. 2015), Horologium I (Koposov et al. 2015b), and Hydra II (Kirby et al. 2015) possess the kinematic and chemical signatures of galaxies.

The Dark Energy Survey (DES; Abbott et al. 2005), which began science operations in late 2013, has already had a large impact on our census of Milky Way substructures. In the first year of DES data, nine new dwarf galaxy candidates were discovered in a region spanning less than 10% of the southern hemisphere (Bechtol et al. 2015; Kim & Jerjen 2015b; Koposov et al. 2015a).[39] Here, we present an extension of the analysis described in Bechtol et al. (2015), incorporating the second year of DES observations to expand the survey coverage from $\sim 1800\,\mathrm{deg}^2$ to $\sim 5000\,\mathrm{deg}^2$ (Figure 1). In Section 2, we discuss the data reduction and catalog generation steps applied to the two-year DES data set and the resulting unique catalog of calibrated objects. We review the various algorithms applied to the DES data to search for ultra-faint galaxies in Section 3 and describe our candidate selection criteria in Section 4. The eight most significant stellar overdensities that are unassociated with previously known systems are reported in Section 5. If these objects are confirmed to be ultra-faint dwarf galaxies, they will be named after their resident constellations—Cetus II (DES J0117–1725), Columba I (DES J0531–2801), Grus II (DES J2204–4626), Indus II (DES J2038–4609).[40] Reticulum III (DES J0345–6026), Tucana III (DES J2356–5935), Tucana IV (DES J0002–6051), and Tucana V (DES J2337–6316)—and named DES 2 through *N* if found to be globular clusters (e.g., Luque et al. 2015). We place the DES candidates in context with other known Local Group galaxies and the Magellanic system in Section 6, and we conclude in Section 7.

[39] The system Kim 2/DES J2108.8–5109/Indus I was discovered independently in a separate data set by Kim et al. (2015b) slightly before the DES announcement. With deeper observations, Kim et al concluded that this object is likely a star cluster, and we do not include it in our count of dwarf galaxy candidates.

[40] To distinguish DES J2038–4609 from Kim 2/DES J2108.8–5109/Indus I, we suggest that the new system be designated Indus II if determined to be a dwarf galaxy.

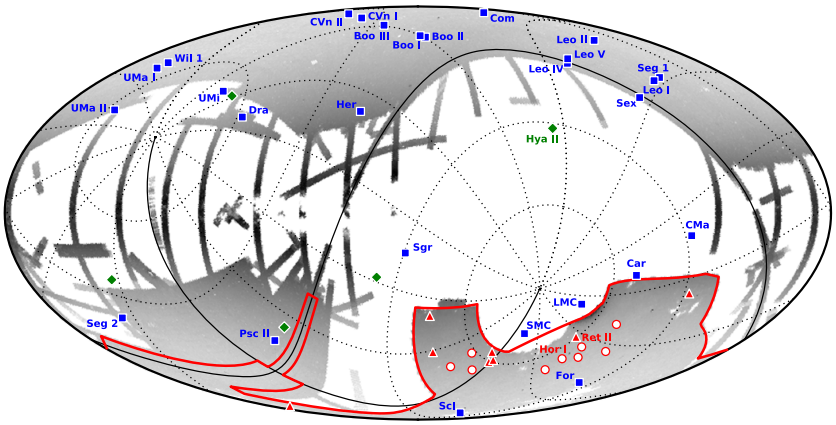

Figure 1. Locations of the eight new dwarf galaxy candidates reported here (red triangles) along with 9 previously reported dwarf galaxy candidates in the DES footprint (red circles; Bechtol et al. 2015; Kim & Jerjen 2015b; Koposov et al. 2015a), 5 recently discovered dwarf galaxy candidates located outside the DES footprint (green diamonds; Kim et al. 2015a; Laevens et al. 2015a, 2015b; Martin et al. 2015), and 27 Milky Way satellite galaxies known prior to 2015 (blue squares; McConnachie 2012). Systems that have been confirmed as satellite galaxies are individually labeled. The figure is shown in Galactic coordinates (Mollweide projection) with the coordinate grid marking the equatorial coordinate system (solid lines for the equator and zero meridian). The grayscale indicates the logarithmic density of stars with $r < 22$ from SDSS and DES. The two-year coverage of DES is $\sim$5000 deg^2 and nearly fills the planned DES footprint (outlined in red). For comparison, the Pan-STARRS 1 3π survey covers the region of sky with $\delta_{2000} > -30^\circ$ (Laevens et al. 2015a).

2. DATA SET

DES is an ongoing optical imaging survey of $\sim$5000 deg^2 in the south Galactic cap using the Dark Energy Camera (DECam; Flaugher et al. 2015) on the 4-m Blanco Telescope at Cerro Tololo Inter-American Observatory (CTIO). The DECam focal plane comprises 62 2k $\times$ 4k CCDs dedicated to science imaging and 12 2k $\times$ 2k CCDs for guiding, focus, and alignment. The DECam field of view covers 3 deg^2 with a central pixel scale of $0\farcs263$. DES is scheduled for 525 nights distributed over five years, during which period each point in the survey footprint will be imaged ten times in each of the *grizY* bands (Abbott et al. 2005).

The searches presented in Bechtol et al. (2015) and Luque et al. (2015) utilized an object catalog generated from the coadded images in the DES year-one annual release (Y1A1). To expedite the search for Milky Way satellites in year two, the present analysis uses data products derived from single-epoch imaging instead. This data set is referred to as the DES year-two quick release (Y2Q1), and its construction is summarized below.

2.1. DES Year-two Quick Release

Observations: The Y2Q1 data set consists of 26,590 DECam exposures taken during the first two years of DES observing that pass DES survey quality cuts. Slightly less than half of the DES survey area was observed during the first season (Y1; 2013 August 15–2014 February 9), with typically two to four overlapping exposures, referred to as "tilings," in each of the *grizY* filters. The second season (Y2; 2014 August 7–2015 February 15) covered much of the remaining survey area to a similar depth. Exposures taken in the *griz* bands are 90 s, while *Y*-band exposures are 45 s.

Image Reduction: The DES exposures were processed with the DES data management (DESDM) image detrending pipeline (Sevilla et al. 2011; Desai et al. 2012; Mohr et al. 2012; R.A. Gruendl et al. 2015, in preparation). This pipeline corrects for cross-talk between CCD amplifier electronics, bias level variations, and pixel-to-pixel sensitivity variations (flat-fielding). Additional corrections are made for nonlinearity, fringing, pupil, and illumination. Both the Y1 and Y2 exposures were reduced with the same image detrending pipeline used to process Y1A1.

Single-epoch Catalog Generation: Astronomical source detection and photometry were performed on a per exposure basis using the `PSFex` and `SExtractor` routines (Bertin & Arnouts 1996; Bertin 2011) in an iterative process (Mohr et al. 2012; R.A. Gruendl et al. 2015, in preparation). As part of this step, astrometric calibration was performed with `SCAMP` (Bertin 2006) by matching objects to the UCAC-4 catalog (Zacharias et al. 2013). The `SExtractor` source detection threshold was set at a signal-to-noise ratio (S/N) of S/N > 10 for the Y1 exposures, while for Y2 this threshold was lowered to S/N > 5 (the impact of this change on the stellar completeness is discussed in Section 2.2). During the catalog generation process, we flagged problematic images (e.g., CCDs suffering from reflected light, imaging artifacts, point-spread function (PSF) mis-estimation, etc.) and excluded the affected objects from subsequent analyses. The resulting photometric catalogs were ingested into a high-performance relational database system. Throughout the rest of this paper, photometric fluxes and magnitudes refer to `SExtractor` output for the PSF model fit.

Photometric Calibration: Photometric calibration was performed using the stellar locus regression technique (SLR: Ivezić et al. 2004; MacDonald et al. 2004; High et al. 2009; Gilbank et al. 2011; Coupon et al. 2012; Desai et al. 2012; Kelly et al. 2014). Our reference stellar locus was empirically derived from the globally calibrated DES Y1A1 stellar objects in the region of the Y1A1 footprint with the smallest $E(B-V)$ value from the Schlegel et al. (SFD; 1998) interstellar extinction map. We performed a $1''$ match on all Y1 and Y2 objects with S/N > 10 observed in *r*-band and at least one other band. We then applied a high-purity stellar selection

based on the weighted average of the spread_model quantity for the matched objects ($|$wavg_spread_model_$r|$ < 0.003; see below). The average zero point measured in Y1A1, $ZP_{grizY} = \{30.0, 30.3, 30.2, 29.9, 28.0\}$, was assigned to each star as an initial estimate. Starting from this coarse calibration, we began an iterative procedure to fix the color uniformity across the survey footprint. We segmented the sky into equal-area pixels using the HEALPix scheme (Górski et al. 2005). For each ∼0.2 deg^2 (resolution nside = 128) HEALPix pixel, we chose the DES exposure in each band with the largest coverage and ran a modified version of the Big MACS SLR code (Kelly et al. 2014)[41] to calibrate each star from the reference exposure with respect to the empirical stellar locus. These stars became our initial calibration standards. We then adjusted the zero points of other CCDs so that the magnitudes of the matched detections agreed with the calibration set from the reference exposure. CCDs with fewer than 10 matched stars or with a large dispersion in the magnitude offsets of matched stars ($\sigma_{ZP} > 0.1$ mag) were flagged. For each calibration star, we computed the weighted-average magnitude in each band using these new CCD zero points; this weighted-average magnitude was used as the calibration standard for the next iteration of the SLR. In the first iteration, we assigned SLR zero points to the calibration stars based on the HEALPix pixel within which they reside. In subsequent iterations, we assigned SLR zero points to the calibration stars based on a bi-linear interpolation of their positions onto the HEALPix grid of SLR zero points. After the second iteration, the color zero points were stable at the 1–2 mmag level. The absolute calibration was set against the 2MASS J-band magnitude of matched stars (making use of the stellar locus in color-space), which were de-reddened using the SFD map with a reddening law of $A_J = 0.709 \times E(B-V)_{SFD}$ from Schlafly & Finkbeiner (2011). The resulting calibrated DES magnitudes are thus already corrected for Galactic reddening by the SLR calibration.

Unique Catalog Generation: There is significant imaging overlap within the DES footprint. For our final high-level object catalog, we identified unique objects by performing a 0.″5 spatial match across all five bands. For each unique object, we calculated the magnitude in each filter in two ways: (1) taking the photometry from the single-epoch detection in the exposure with the largest effective depth,[42] and (2) calculating the weighted average (wavg) magnitude from multiple matched detections. During the catalog generation stage, we kept all objects detected in any two of the five filters (this selection is later restricted to the g- and r-band for our dwarf galaxy search). The process of combining catalog-level photometry increases the photometric precision, but does not increase the detection depth.

The resulting Y2Q1 catalog covers ∼5100 deg^2 in any single band, ∼5000 deg^2 in both the g- and r-bands, and ∼4700 deg^2 in all five bands. The coverage of the Y2Q1 data set is shown in Figure 1. The Y2Q1 catalog possesses a median relative astrometric precision of ∼40 mas per coordinate and a median absolute astrometric uncertainty of ∼140 mas per coordinate when compared against UCAC-4. The median absolute photometric calibration agrees within ∼3% with the de-reddened global calibration solution of Y1A1 in the overlap region in the $griz$ bands. When variations in the reddening law are allowed, this agreement improves to $\lesssim$1%. The color uniformity of the catalog is ∼1% over the survey footprint (tested independently with the red sequence of galaxies). The Y2Q1 catalog has a median point-source depth at an S/N = 10 of $g = 23.4$, $r = 23.2$, $i = 22.4$, $z = 22.1$, and $Y = 20.7$.

2.2. Stellar Object Sample

We selected stars observed in both the g- and r-bands from the Y2Q1 unique object catalog following the common DES prescription based on the wavg_spread_model and spreaderr_model morphological quantities (e.g., Chang et al. 2015; Koposov et al. 2015a). Specifically, our stellar sample consists of well-measured objects with $|$wavg_spread_model_$r|$ < 0.003 + spreaderr_model_r, flags_{g, r} < 4, and magerr_psf_{g, r} < 1. By incorporating the uncertainty on spread_model, it is possible to maintain high stellar completeness at faint magnitudes while achieving high stellar purity at bright magnitudes. We sacrificed some performance in our stellar selection by using the r-band spread_model, which has a slightly worse PSF than the i-band; however, relaxing the requirement on i-band coverage increased the accessible survey area.

The stellar completeness is the product of the object detection efficiency and the stellar classification efficiency. As described in Section 2.1, different source detection thresholds were applied to the individual Y1 and Y2 exposures, and accordingly, the detection efficiency for faint objects in Y2Q1 varies across the survey footprint. We used a region of the DES Science Verification data set (SVA1), imaged to full survey depth (i.e., ∼10 overlapping exposures in each of $grizY$), to estimate the object detection completeness using the individual Y1 exposures. For the Y2 exposures, we instead compared to publicly available catalogs from the Canada–France–Hawaii Telescope Lensing Survey (CFHTLenS; Erben et al. 2013). In both cases, the imaging for the reference catalog is ∼2 mag deeper than the Y2Q1 catalog. These comparisons show that the Y2Q1 object catalog is >90% complete at about 0.5 mag brighter than the S/N = 10 detection limit.

We estimated the stellar classification efficiency by comparing to CFHTLenS and by using statistical estimates from the Y2Q1 data alone. For the CFHTLenS matching, we identified probable stars in the CFHTLenS catalog using a combination of the class_star output from SExtractor and the fitclass output from the lensfit code (Heymans et al. 2012). Specifically, our CFHTLenS stellar selection was (fitclass = 1) OR (class_star > 0.98), and our galaxy selection was (fitclass = 0) OR (class_star < 0.2). Comparing against the DES stellar classification based on spread_model, we found that the Y2Q1 stellar classification efficiency exceeds 90% for $r < 23$ mag, and falls to ∼80% by $r = 24$ (Figure 2). We independently estimated the stellar classification efficiency by creating a test sample of Y2Q1 objects with high stellar purity using the color-based selection $r - i > 1.7$. We then applied the spread_model morphological stellar selection to evaluate the stellar completeness for the test sample. The stellar selection efficiency determined by the color-based selection test is in good agreement with that from the CFHTLenS comparison.

For a typical field at high Galactic latitude, the stellar purity is ∼50% at $r = 22.5$ mag, and falls to ∼10% at the faint magnitude limit (Figure 2). In other words, the majority of faint objects in the "stellar sample" are misclassified galaxies rather

[41] https://code.google.com/p/big-macs-calibrate/

[42] The effective depth is calculated from the exposure time, sky brightness, seeing, and atmospheric transmission (Neilsen et al. 2015).

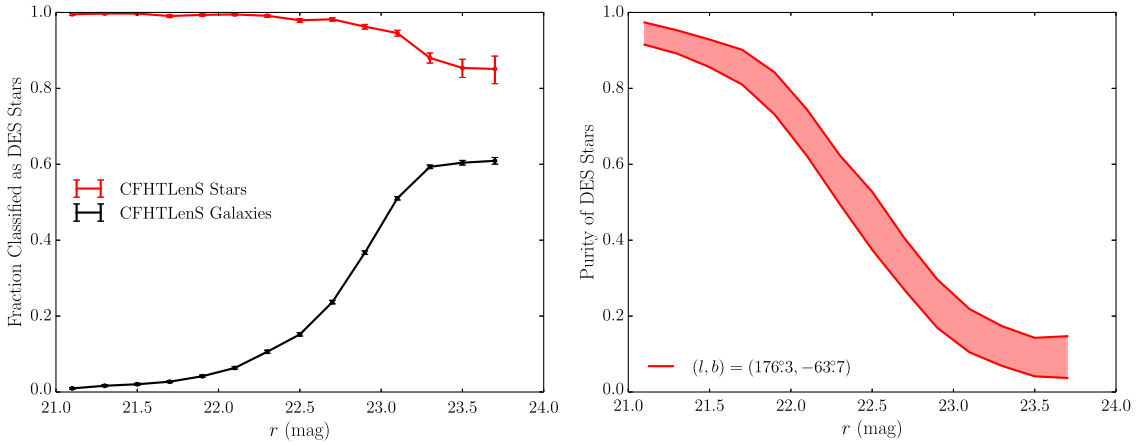

Figure 2. Performance of the morphological stellar classification based on |wavg_spread_model_r| < 0.003 + spreaderr_model_r was evaluated by comparing against deeper CFHTLenS imaging (Section 2.2). Left: fraction of CFHTLenS-classified stars and galaxies that pass our DES stellar selection criteria. Right: stellar purity evaluated in a typical high-Galactic latitude field centered at Galactic coordinates (l, b) = (176.°3, −63.°7). The shaded region represents the uncertainty associated with objects that are not confidently classified as either stars or galaxies with CFHTLenS. If a large fraction of these ambiguous objects are true stars, the inferred stellar purity for DES is near the upper bound of the indicated range.

than foreground halo stars.[43] This transition can be seen in the color–magnitude distribution diagnostic plots for individual candidates (Section 6.1).

3. SEARCH METHODS

In this section we describe three complementary search strategies that were used to identify overdensities of individually resolved stars matching the old and metal-poor populations that are characteristic of ultra-faint galaxies. Each technique used a different method to estimate the spatially varying field density and to select potential satellite member stars. The output of each search method was a set of seed coordinates, (α_{2000}, δ_{2000}, $m - M$), corresponding to statistical excesses relative to the local field density. These seeds were cross-matched between methods and examined in greater detail (Section 5).

When searching for new stellar systems, each detection algorithm applied a deep magnitude threshold ($g < 23.5$ mag or $g < 24$ mag depending on the search technique). At these faint magnitudes, our stellar sample is far from complete (Section 2.2). However, real stellar systems are dominated by faint stars, and the signal-to-noise ratio for satellite discovery can increase by including objects that are fainter than the stellar completeness limit. After candidate systems were identified, we applied a brighter magnitude threshold ($g < 23$ mag) to avoid biasing the fit results during object characterization (Section 5).

One potential concern when extending our search to very faint magnitudes is the increased contamination from misclassified galaxies (Section 2.2). However, as long as the contaminating objects have a similar statistical distribution in the target region and the surrounding area, each technique naturally incorporates the increased object density into the background estimate. There are situations where the assumption of uniformity does not apply (e.g., clusters of galaxies, variations in survey depth, gaps in coverage, etc.); therefore, when assembling our candidate list, we also examined the distribution of probable galaxies as well as stars with colors far from the expected isochrone (Section 5).

We briefly describe our three search strategies below.

3.1. Stellar Density Maps

Our most straightforward and model-independent search technique used a simple isochrone filter to facilitate visual inspection of the stellar density field. The specific algorithm was a variant of the general approach described in Section 3.1 of Bechtol et al. (2015) and follows from the methods of Koposov et al. (2008), Walsh et al. (2009), and Kim & Jerjen (2015a).

We first increased the contrast of putative satellite galaxies by selecting stars that were consistent with the isochrone of an old ($\tau = 12$ Gyr) and metal-poor ($Z = 0.0001$) stellar population (Dotter et al. 2008). Specifically, we selected stars within 0.1 mag of the isochrone locus in color–magnitude space, enlarged by the photometric measurement uncertainty of each star added in quadrature. After isochrone filtering, we smoothed the stellar density field with a 2′ Gaussian kernel. For each density peak in the smoothed map, we scanned over a range of radii (1′–18′) and computed the Poisson significance of finding the observed number of stars within each circle centered on the density peak given the local field density. This process was repeated for stellar populations at a range of distance moduli (16 mag $\leqslant m - M \leqslant$ 24 mag) and diagnostic plots were automatically generated for each unique density peak. Our nominal magnitude threshold for this search was $g < 24$ mag; however, in regions on the periphery of the survey with large variations in coverage we used a brighter threshold of $g < 23$ mag.

3.2. Matched-filter Search

Our second search strategy utilized a matched-filter algorithm (Balbinot et al. 2011, 2013; Luque et al. 2015). We began by binning objects in our stellar sample with 17 mag

[43] This conclusion differs from that of Koposov et al. (2015a), who state that low levels of contamination are observed to the magnitude limit of DES.

$< g < 24$ mag into $1' \times 1'$ spatial pixels and g versus $g-r$ color–magnitude bins of 0.01 mag $\times$ 0.05 mag. We then created a grid of possible simple stellar populations modeled with the isochrones of Bressan et al. (2012) and populated according to a Chabrier (2001) initial mass function to use as signal templates. The model grid spanned a range of distances (10 kpc $< D <$ 200 kpc), ages ($9 < \log_{10}\tau < 10.2$), and metallicities ($Z = \{0.0002, 0.001, 0.007\}$). The color–magnitude distribution of the field population was empirically determined over larger $10^\circ \times 10^\circ$ regions. For each isochrone in the grid, we then fit the normalization of the simple stellar population in each spatial pixel to create a corresponding density map for the full Y2Q1 area.

The set of pixelized density maps do not assume a spatial model for the stellar system, and can be used to search for a variety of stellar substructures (e.g., streams and diffuse clouds). To search specifically for dwarf galaxies, we convolved the density maps with Gaussian kernels having widths ranging from $0'$ (no convolution) to $9'$ and used `SExtractor` to identify compact stellar structures in those maps. This convolution and search was performed on each map for our grid of isochrones. The resulting seeds were ranked according to their statistical significance and by the number of maps in which they appeared, i.e., the number of isochrones for which an excess was observed.

3.3. Likelihood-based Search

Our third search technique was a maximum-likelihood-based algorithm that simultaneously used the full spatial and color–magnitude distribution of stars, as well as photometric uncertainties and information about the survey coverage. The likelihood was constructed from the product of Poisson probabilities for detecting each individual star given its measured properties and the parameters that describe the field population and putative satellite (Section 3.2 of Bechtol et al. 2015). When searching for new stellar systems, we used a spherically symmetric Plummer model as the spatial kernel, and a composite isochrone model consisting of four isochrones of different ages, $\tau = \{12\,\mathrm{Gyr}, 13.5\,\mathrm{Gyr}\}$, and metallicities, $Z = \{0.0001, 0.0002\}$, to bracket a range of possible stellar populations (Bressan et al. 2012). We scanned the Y2Q1 data testing for the presence of a satellite galaxy at each location on a multi-dimensional grid of sky position ($0.'7$ resolution; `HEALPix` nside = 4096), distance modulus (16 mag $< m - M <$ 23 mag), and kernel half-light radius ($r_h = \{0.^\circ03, 0.^\circ1, 0.^\circ3\}$). For the likelihood search, we restricted our magnitude range to 16 mag $< g <$ 23.5 mag as a compromise between survey depth and stellar completeness. The statistical significance of a putative galaxy at each grid point was expressed as a test statistic (TS) based on the likelihood ratio between a hypothesis that includes a satellite galaxy versus a field-only hypothesis (Equation (4) of Bechtol et al. 2015). As a part of the model fitting, the satellite membership probability is computed for every star in the region of interest. These photometric membership probabilities can be used to visualize which stars contribute to the candidate detection significance (Section 5) and have previously been used to select targets for spectroscopic follow-up (Simon et al. 2015; Walker et al. 2015).

4. CANDIDATE SELECTION

The search methods described in Section 3 each produced a set of seed locations (α_{2000}, δ_{2000}, $m - M$) for overdensities in the stellar field and a significance associated with each seed. Before performing a computationally intensive multi-parameter likelihood fit to characterize each seed, we applied a set of simple selection cuts to remove seeds that are unlikely to be new Milky Way satellites. We set detection significance thresholds at $>5.5\sigma$ for the stellar density map search and TS > 45 ($\sim 6\sigma$) for the maximum-likelihood search. For the matched-filter method, the ten highest-ranked seeds were selected from each $10^\circ \times 10^\circ$ search region. After thresholding, the union of all three search techniques yielded several hundred unique seeds. Many of these seeds were attributed to steep gradients in the stellar density field, numerical effects near the survey boundaries, and imaging artifacts. We also compared against catalogs of other astrophysical objects that produce false positives, such as large nearby galaxies (Nilson 1973; Corwin 2004) and galaxy clusters (Rykoff et al. 2014). These objects were removed from our list of candidates and we did not pursue investigation at lower significance thresholds due to an increased false positive rate.

The resulting list of seeds was matched against catalogs of known Local Group galaxies (McConnachie 2012) and star clusters (Harris 1996, 2010 edition; Kharchenko et al. 2013). Some of the most prominent stellar systems in our list of seeds were the Fornax, Phoenix, Sculptor,[44] and Tucana dwarf galaxies, and the globular clusters AM 1, Eridanus, Reticulum, Whiting 1, NGC 288, NGC 1261, NGC 1851, NGC 1904, and NGC 7089. Additionally, seed locations were compared against other stellar overdensities recently reported in the DES footprint (Bechtol et al. 2015; Kim et al. 2015b; Koposov et al. 2015a; Kim & Jerjen 2015b; Luque et al. 2015) and all 11 objects were recovered with high significance. The locations of previously known stellar systems in the DES footprint are shown in Figure 3.

As an additional test of the physical nature of the $\sim$30 highest significance unassociated seeds, we explored the posterior probability density of the likelihood with an affine invariant Markov Chain Monte Carlo (MCMC) ensemble sampler (MCMC; Foreman-Mackey et al. 2013).[45] This step was meant as a preliminary investigation of whether the posterior distribution was well-constrained by the data. We fixed the distance modulus of each object at the value that maximized the likelihood in the grid search (Section 16) and sampled the morphological parameters (center position, extension, ellipticity, and position angle) along with the richness of the putative stellar system. We imposed a Jeffreys' prior on the extension ($\mathcal{P}(a_h) \propto 1/a_h$) and flat priors on all other parameters. The posterior probability was sampled with 2.5×10^5 steps and we rejected seeds that lacked a well-defined maximum in the posterior.

The process described above resulted in the selection of eight candidate stellar systems. Six of these candidates, DES J2204–4626 (Gru I), DES J2356–5935 (Tuc III), DES J0531–2801 (Col I), DES J0002–6051 (Tuc IV), DES J0345–6026 (Ret III), and DES J2337–6316 (Tuc V), are high-confidence detections in clean regions of the survey. The additional two candidates,

[44] The center of Sculptor lies in a hole in Y2Q1 coverage, though the outskirts are still detected at high significance.
[45] `emcee` v2.1.0: http://dan.iel.fm/emcee/

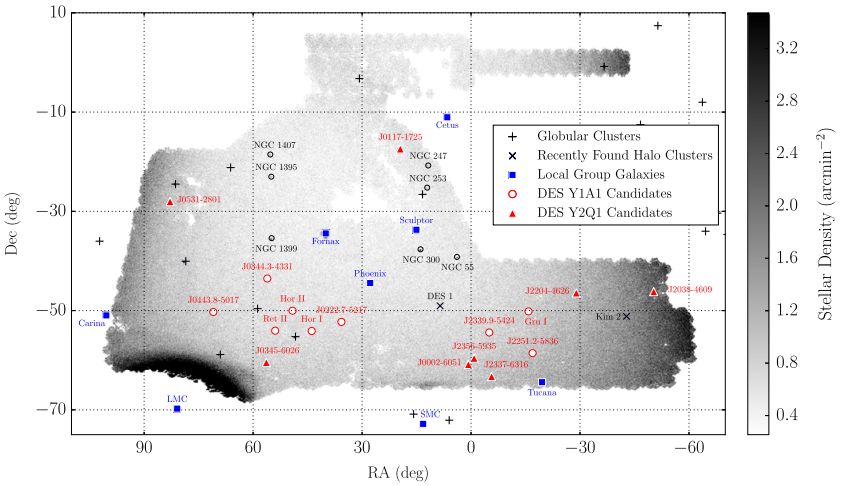

Figure 3. Cartesian projection of the density of stars observed in both the g- and r-bands with $g < 23$ and $g - r < 1$ over the DES Y2Q1 footprint (~5000 deg^2). Globular clusters are marked with "+" symbols (Harris 1996, 2010 edition), two faint outer halo clusters are marked with "×" symbols (Kim et al. 2015b; Luque et al. 2015), Local Group galaxies known prior to DES are marked with blue squares (McConnachie 2012), dwarf galaxy candidates discovered in Y1 DES data are marked with red outlined circles, and the Y2 stellar systems are marked with red triangles. The periphery of the LMC can be seen in the southeast corner of the footprint, while the Galactic stellar disk can be seen on the eastern and western edges.

Table 1
Detection of Ultra-faint Galaxy Candidates

Name	α_{2000} (deg)	δ_{2000} (deg)	$m - M$	r_h ($'$)	a_h ($'$)	ϵ	ϕ	Map Sig. (σ)	TS Scan	$\sum p_i$
DES J2204–4626 (Gru II)	331.02	−46.44	18.62 ± 0.21	$6.0^{+0.9}_{-0.5}$	…	<0.2	…	15.7	369	161
DES J2356–5935 (Tuc III)[a]	359.15	−59.60	17.01 ± 0.16	$6.0^{+0.8}_{-0.6}$	…	…	…	11.1	390	168
DES J0531–2801 (Col I)[b]	82.86	−28.03	21.30 ± 0.22	$1.9^{+0.5}_{-0.4}$	…	<0.2	…	10.5	71	33
DES J0002–6051 (Tuc IV)	0.73	−60.85	18.41 ± 0.19	$9.1^{+1.7}_{-1.4}$	$11.8^{+2.2}_{-1.8}$	$0.4^{+0.1}_{-0.1}$	11 ± 9	8.7	287	134
DES J0345–6026 (Ret III)[b]	56.36	−60.45	19.81 ± 0.31	$2.4^{+0.9}_{-0.8}$	…	<0.4	…	8.1	56	22
DES J2337–6316 (Tuc V)	354.35	−63.27	18.71 ± 0.34	$1.0^{+0.3}_{-0.3}$	$1.8^{+0.5}_{-0.6}$	$0.7^{+0.1}_{-0.2}$	30 ± 5	8.0	129	24
DES J2038–4609 (Ind II)[b]	309.72	−46.16	21.65 ± 0.16	$2.9^{+1.1}_{-1.0}$	…	<0.4	…	6.0	32	22
DES J0117–1725 (Cet II)	19.47	−17.42	17.38 ± 0.19	$1.9^{+1.0}_{-0.5}$	…	<0.4	…	5.5	53	21

Notes. Characteristics of satellite galaxy candidates discovered in DES Y2 data. Best-fit parameters from the maximum-likelihood analysis assume a Bressan et al. (2012) isochrone. Uncertainties come from the highest density interval containing 68% of the posterior distribution. The uncertainty on the distance modulus ($m - M$) also includes systematic uncertainties coming from the choice of theoretical isochrone and photometric calibration (Section 5). The azimuthally averaged half-light radius (r_h) is quoted for all candidates. For systems with evidence for asphericity (Bayes' factor > 3), we quote the ellipticity (ϵ), the position angle (ϕ), and the length of the semimajor axis of the ellipse containing half of the light ($a_h = r_h/\sqrt{1-\epsilon}$). Upper limits on the ellipticity are quoted for other candidates at 84% confidence. "Map Sig." refers to detection significance of the candidate from the stellar density map search method (Section 3.1). "TS Scan" refers to the significance (Equation (4) in Bechtol et al. 2015) from the likelihood scan (Section 3.3). $\sum p_i$ is the estimated number of satellite member stars in the DES Y2Q1 catalog with $g < 23$ mag.
[a] Fit with a spherically symmetric Plummer profile due to the possible presence of tidal tails (Section 6.1).
[b] Fit with a composite isochrone: $\tau = \{12\,\mathrm{Gyr}, 13.5\,\mathrm{Gyr}\}$, $Z = \{0.0001, 0.0002\}$ (Section 5).

DES J2038–4609 (Ind II) and DES J0117–1725 (Cet II), are lower confidence and reside in more complicated regions. In Table 1 we report the coordinates and detection significances of each of these objects.

5. CANDIDATE CHARACTERIZATION

In this section, we describe the iterative procedure used to characterize each of the eight candidate stellar systems. When fitting the new candidates, we applied a brighter magnitude threshold, $g < 23$ mag, to mitigate the impact of stellar incompleteness. The results of our characterization are shown in Tables 1 and 2.

We began by simultaneously fitting the morphological parameters and distance modulus of each candidate following the procedure described in Section 4. Best-fit values were derived from the marginalized posterior distribution and the morphological parameters were temporarily fixed at these values. We then ran a MCMC chain simultaneously sampling the distance, age, metallicity, and richness, assuming flat priors on each parameter. Significant correlations between these parameters were found, and in some cases the age and metallicity were poorly constrained (see below). To assess the error contribution from intrinsic uncertainty in the isochrone, we resample the posterior distribution using the Dartmouth isochrone family (Dotter et al. 2008). In general, the best-fit distance moduli agree to within 0.1 mag when the data were fit

Table 2
Derived Properties of Ultra-faint Galaxy Candidates

Name	ℓ (deg)	b (deg)	Distance (kpc)	M_* (10^3 $M_\odot$)	M_V (mag)	$r_{1/2}$ (pc)	τ (Gyr)	Z
DES J2204–4626 (Gru II)	351.15	−51.94	53 ± 5	$3.4^{+0.3}_{-0.4}$	−3.9 ± 0.22	93 ± 14	12.5	0.0002
DES J2356–5935 (Tuc III)[a]	315.38	−56.19	25 ± 2	$0.8^{+0.1}_{-0.1}$	−2.4 ± 0.42	44 ± 6	10.9	0.0001
DES J0531–2801 (Col I)[b]	231.62	−28.88	182 ± 18	$6.2^{+1.9}_{-1.0}$	−4.5 ± 0.17	103 ± 25	…	…
DES J0002–6051 (Tuc IV)	313.29	−55.29	48 ± 4	$2.2^{+0.4}_{-0.3}$	−3.5 ± 0.28	127 ± 24	11.6	0.0001
DES J0345–6026 (Ret III)[b]	273.88	−45.65	92 ± 13	$2.0^{+0.6}_{-0.7}$	−3.3 ± 0.29	64 ± 24	…	…
DES J2337–6316 (Tuc V)	316.31	−51.89	55 ± 9	$0.5^{+0.1}_{-0.1}$	−1.6 ± 0.49	17 ± 6	10.9	0.0003
DES J2038–4609(Ind II)[b]	353.99	−37.40	214 ± 16	$4.9^{+1.8}_{-1.6}$	−4.3 ± 0.19	181 ± 67	…	…
DES J0117–1725 (Cet II)	156.48	−78.53	30 ± 3	$0.1^{+0.04}_{-0.04}$	0.0 ± 0.68	17 ± 7	10.9	0.0002

Notes. Derived properties of the DES Y2 satellite candidates. Stellar masses (M_*) are computed for a Chabrier (2001) initial mass function. The absolute visual magnitude is derived via the procedure of Martin et al. (2008) using the transformation equations from Bechtol et al. (2015). The uncertainty on the azimuthally averaged physical half-light radius ($r_{1/2}$) includes the uncertainty in the projected half-light radius and distance. Age (τ) and metallicity (Z) values come from the peak of the posterior distribution.
[a] Fit with a spherically symmetric Plummer profile due to the possible presence of tidal tails (Section 6.1).
[b] Fit with a composite isochrone: $\tau = \{12\,\mathrm{Gyr}, 13.5\,\mathrm{Gyr}\}$, $Z = \{0.0001, 0.0002\}$ (Section 5).

by these two isochrone classes. To determine the uncertainty on the distance modulus quoted in Table 1 we started with the highest posterior density interval from the Bressan et al. (2012) isochrone fit. We then calculated a systematic component from the difference in the best-fit distance modulus derived with Bressan et al. (2012) and Dotter et al. (2008) isochrones. An additional ±0.03 mag uncertainty was added to account for uncertainty in the photometric calibration. The age and metallicity values were taken from the peak of the marginalized posterior density from the Bressan et al. (2012) isochrone fit.

For the distant systems (i.e., DES J0531–2801, DES J2038–4609, and DES J0345–6026), the main-sequence turnoff (MSTO) is fainter than the $g < 23$ mag limit imposed for our fit. In these systems, the data provide weaker constraints on the age and metallicity. We therefore fit the distance modulus using a composite of four Bressan et al. (2012) isochrones with fixed ages, $\tau = \{12\,\mathrm{Gyr}, 13.5\,\mathrm{Gyr}\}$, and metallicities, $Z = \{0.0001, 0.0002\}$. We followed the procedure above to incorporate systematic uncertainties from the choice of theoretical isochrone family and from the calibration.[46]

Fixing the distance, age, and metallicity at the values derived in the previous step, we then re-fit the morphological parameters. The best-fit values of the morphological parameters and their highest posterior density intervals are listed in Table 1. The majority of objects show no significant evidence for ellipticity, which is confirmed by calculating the Bayes factor (BF) via the Savage–Dickey density ratio (Dickey 1971; Trotta 2007). For objects with evidence for asphericity (BF > 3), we report both the elliptical Plummer radius, a_h, and the position angle, ϕ. For all objects, we report the azimuthally averaged half-light radius, r_h. In the region of DES J2356–5935 there is a linear structure visible in the filtered stellar density map, consistent with a set of tidal tails (Section 6.1). We require the spatial profile of DES J2356–5935 to be azimuthally symmetric in the MCMC fit and analyze this linear feature separately.

The best-fit parameters derived from our iterative MCMC analysis along with several additional derived properties are reported in Tables 1 and 2. The physical size of each object was calculated by propagating the uncertainty from the distance and azimuthally averaged half-light radius. Absolute magnitudes were calculated according to the prescription of Martin et al. (2008) and do not include the distance uncertainty.

The two lower-confidence candidates are located in complicated regions of the survey. DES J0117–1725 is located in a region of sparse coverage and is close to both a CCD chip gap and a larger hole in the survey. DES J2038–4609 is located in a region of non-uniform depth at the interface of Y1 and Y2 observations. Although we have attempted to account for these issues in the likelihood fit, we caution that the parameters derived for these systems may be less secure than for the other candidates.

As a final note, the iterative MCMC fitting procedure described above was also applied to the satellite galaxy candidate Grus I (Koposov et al. 2015a). Grus I was identified in Y1A1 imaging data, but was located close to a CCD chip gap in a region with sparse coverage. We reanalyzed Grus I with the additional Y2 exposures and found that its structural parameters are consistent within uncertainties with those reported by Koposov et al. (2015a).

6. DISCUSSION

Spectroscopic observations are needed to definitively classify the newly discovered stellar systems as either star clusters or ultra-faint dwarf galaxies based upon their stellar dynamics and/or metallicity dispersions. However, the distances, physical sizes, and luminosities derived from DES photometry (Table 2) already suggest a galactic classification for many of the new candidates. In Figures 4 and 5, we show the distributions of physical half-light radius heliocentric distance versus absolute magnitude for Milky Way globular clusters (Harris 1996, 2010 edition) and Local Group galaxies (McConnachie 2012). We find that all of the systems discovered in Y2Q1 fall along the established locus for nearby galaxies. Several of the new systems possess lower surface brightnesses than any confirmed ultra-faint galaxy,[47] supporting earlier conclusions that the threshold in surface brightness was an observational selection effect (Koposov et al. 2008;

[46] One notable exception is the case of DES J2038–4609, where significant constraining power comes from a set of horizontal branch (HB) stars. For DES J2038–4609 we estimated the distance uncertainty from the Bressan et al. (2012) isochrone analysis alone.

[47] A potential exception to this statement is the large, faint, and perhaps tidally disrupted object Böotes III (Carlin et al. 2009).

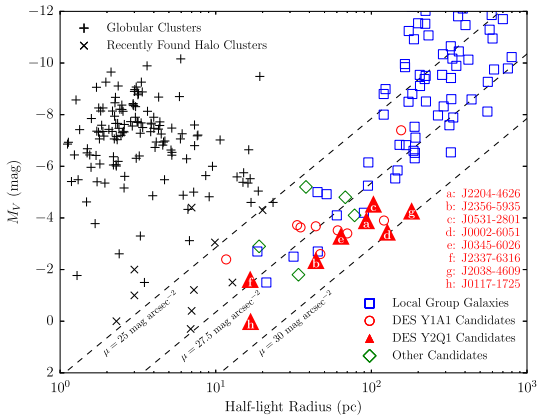

Figure 4. Local Group galaxies (McConnachie 2012) and globular clusters (Harris 1996, 2010 edition) occupy distinct regions in the plane of physical half-light radius (azimuthally averaged) and absolute magnitude. The majority of DES satellite candidates (red triangles and circles) are more consistent with the locus of Local Group galaxies (blue squares) than with the population of Galactic globular clusters (black "+"). Other recently reported dwarf galaxy candidates (green diamonds) include Hydra II (Martin et al. 2015), Triangulum II (Laevens et al. 2015b), Pegasus III (Kim et al. 2015a), Draco II, and Sagittarius II (Laevens et al. 2015a). Several outer halo star clusters and systems of ambiguous classification are indicated with "×" symbols: Koposov 1 and Koposov 2 (Koposov et al. 2007; Paust et al. 2014), Segue 3 (Belokurov et al. 2010; Fadely et al. 2011; Ortolani et al. 2013), Muñoz 1 (Muñoz et al. 2012), Balbinot 1 (Balbinot et al. 2013), Laevens 1 (Belokurov et al. 2014; Laevens et al. 2014), Laevens 3 (Laevens et al. 2015a), Kim 1 and Kim 2 (Kim & Jerjen 2015a; Kim et al. 2015b), and DES 1(Luque et al. 2015). The dashed lines indicate contours of constant surface brightness at $\mu = \{25, 27.5, 30\}$ magarcsec^{-2}.

Walsh et al. 2009). Finally, globular clusters generally have small ellipticities, $\epsilon \lesssim 0.2$ (van den Bergh 2008), while dwarf galaxies are commonly more elliptical (Martin et al. 2008). However, the ellipticities of many of the new objects are not well-constrained by the DES data and thus do not provide a strong indicator of the nature of these objects.

The spatial distribution of the new candidates within the DES footprint is suggestive of an association with the Magellanic Clouds (Section 6.3). When discussing this scenario, the coordinates of the Large Magellanic Cloud (LMC) are taken to be α_{2000}, δ_{2000}, $D_\odot$ = (80.°89, −69.°76, 49.89 kpc) (distance from de Grijs et al. 2014) and the coordinates of the Small Magellanic Cloud (SMC) are taken to be (α_{2000}, δ_{2000}, $D_\odot$) = (13.°19, − 72.°83, 61.94 kpc) (distance from de Grijs & Bono 2015).[48] While the new DES candidates reside in a region close to the Magellanic Stream, no candidate is found to be coincident with the main filament of the Stream. A similar observation was made by Koposov et al. (2015a) for the DES stellar systems discovered in Y1.

We also investigate a potential group of satellites in the constellation Tucana, consisting of DES J0002–6051 and DES J2337–6316, and the object DES J2251.2–5836 (Tuc II) discovered in Y1 data (Bechtol et al. 2015; Koposov et al. 2015a). The centroid of the Tucana group is at (α_{2000}, δ_{2000}, $D_\odot$) = (351.°90, −61.°06, 53.63 kpc), and the separation of each member from the centroid is $\lesssim$7 kpc (Table 3). This grouping of objects is projected onto a region of H I gas that is likely a secondary filament or high-velocity cloud associated with the head of the Magellanic Stream (Putman et al. 2003; McClure-Griffiths et al. 2009).

[48] Sky coordinates taken from NED: https://ned.ipac.caltech.edu

Table 3
Physical Separations of Ultra-faint Galaxy Candidates

Name	$D_\odot$ (kpc)	D_{GC} (kpc)	D_{LMC} (kpc)	D_{SMC} (kpc)	D_{Tuc} (kpc)
DES J2204–4626 (Gru II)	53	49	46	33	18
DES J2356–5935 (Tuc III)	25	23	32	38	28
DES J0531–2801 (Col I)	182	186	149	157	168
DES J0002–6051 (Tuc IV)	48	46	27	18	7
DES J0345–6026 (Ret III)	92	92	45	40	53
DES J2337–6316 (Tuc V)	55	52	29	14	3
DES J2038–4609 (Ind II)	214	208	193	170	169
DES J0117–1725 (Cet II)	30	32	46	51	40
DES J2251.2–5836 (Tuc II)	58	54	37	20	7

Note. Three-dimensional physical separation between DES satellite candidates and the LMC and SMC. Also listed is the heliocentric distance, the Galactocentric distance, and the separation to the centroid of the proposed Tucana group comprising DES J2251.2–5836, DES J0002–6051, and DES J2337–6316.

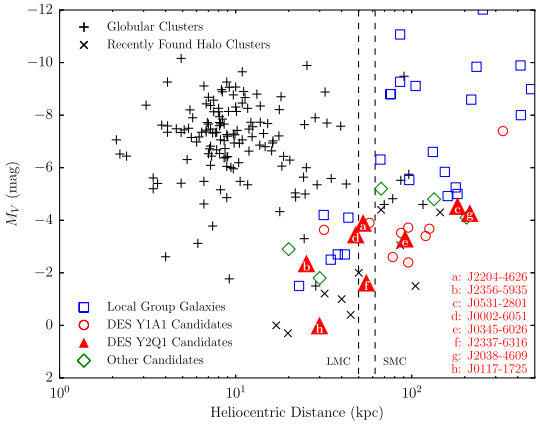

Figure 5. DES satellite galaxy candidates (red circles and triangles) have comparable luminosities to known Local Group galaxies (blue squares; McConnachie 2012) and other newly discovered galaxy candidates (green diamonds), but are typically found at larger distances. The dashed lines indicate the heliocentric distances of the LMC and SMC. Globular clusters (black "+" symbols, Harris 1996) and outer halo star clusters ("×" symbols) have been detected at comparable luminosities and distances due to their more compact nature. The constituents of each source class can be found in Figure 4.

6.1. Review of Individual Candidates

1. *DES J2204–4626* (Grus II, Figure 6): As the most significant new candidate, DES J2204–4626 has ∼161 probable member stars with $g < 23$ mag in the DES imaging. The large physical size of this system (93 pc) allows it to be tentatively classified as an ultra-faint dwarf galaxy. A clear red giant branch (RGB) and MSTO are seen in the color–magnitude diagram of DES J2204–4626. Several likely blue horizontal branch (BHB) members are seen at $g \sim 19$ mag. There is a small gap in survey coverage ∼0.°5 from the centroid of

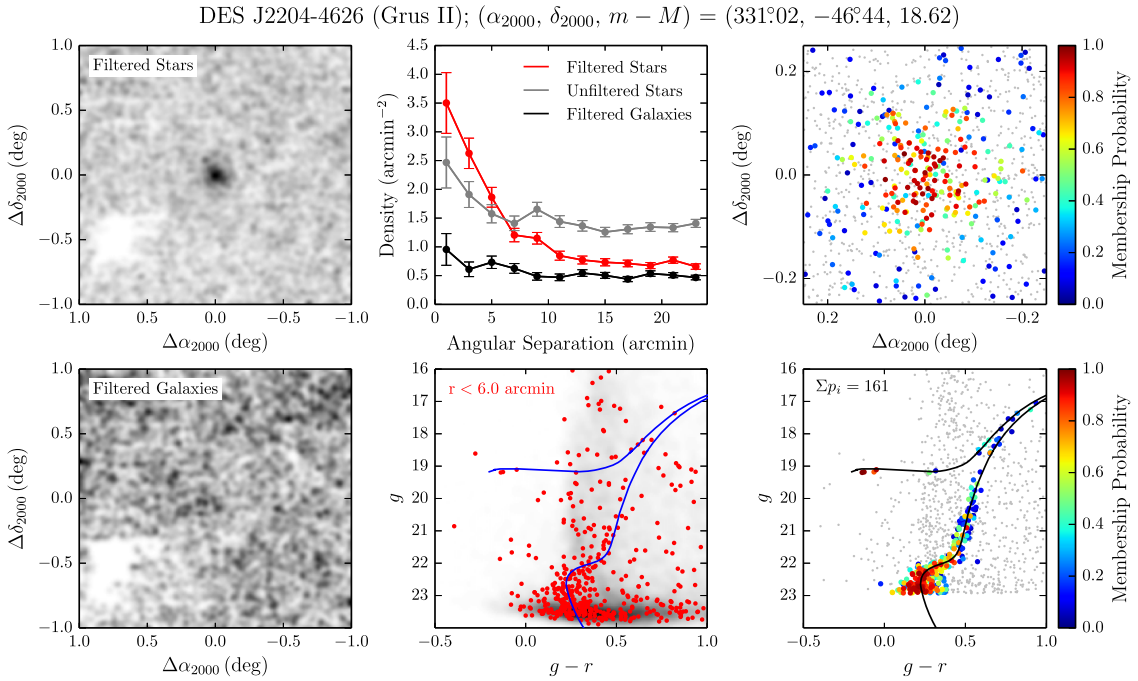

Figure 6. Stellar density and color–magnitude diagrams for DES J2204–4626 (Grus II). Top left: spatial distribution of stellar objects with $g < 24$ mag that pass the isochrone filter (see text). The field of view is 2° × 2° centered on the candidate and the stellar distribution has been smoothed by a Gaussian kernel with standard deviation 1.′2. Top center: radial distribution of objects with $g - r < 1$ mag and $g < 24$ mag: stars passing the isochrone filter (red), stars excluded from the isochrone filter (gray), and galaxies passing the isochrone filter (black). Top right: spatial distribution of stars with high membership probabilities within a 0.°5 × 0.°5 field of view. Small gray points indicate stars with membership probability less than 5%. *Bottom left*: same as top left panel, but for probable galaxies that pass the isochrone filter. Bottom center: the color–magnitude distributions of stars within 0.°1 of the centroid are indicated with individual points. The density of the field within an annulus from radii of 0.°5–1.°0 is represented by the background two-dimensional histogram in grayscale. The blue curve shows the best-fit isochrone as described in Tables 1 and 2. Bottom right: color–magnitude distribution of high membership probability stars.

DES J2204–4626, but this is accounted for in the maximum-likelihood analysis and should not significantly affect the characterization of this rich satellite.

DES J2204–4626 is from the LMC (46 kpc) and from the Galactic center (49 kpc). It is slightly closer to the SMC (33 kpc) and intriguingly close to the the group of stellar systems in Tucana (∼18 kpc). While it is unlikely that DES J2204–4626 is currently interacting with any of the other known satellites, we cannot preclude the possibility of a past association.

2. *DES J2356–5935* (Tucana III, Figure 7): DES J2356–5935 is another highly significant stellar system that presents a clearly defined main sequence and several RGB stars. The physical size and luminosity of DES J2356–5935 ($r_{1/2}$ = 44 pc, M_V = −2.4 mag) are comparable to that of the recently discovered dwarf galaxy Reticulum II. At a distance of 25 kpc, DES J2356–5935 would be among the nearest ultra-faint satellite galaxies known, along with Segue 1 (23 kpc), Reticulum II (32 kpc), and Ursa Major II (32 kpc). The relative abundance of bright stars in DES J2356–5935 should allow for an accurate spectroscopic determination of both its velocity dispersion and metallicity. DES J2356–5935 is reasonably close to the LMC and SMC (32 kpc and 38 kpc, respectively), and measurements of its systemic velocity will help to elucidate a physical association.

As mentioned in Section 5, there is an additional linear feature in the stellar density field around DES J2356–5935 that strongly influences the fitted ellipticity of this galaxy candidate. In Figure 8, we show the 6 ° × 6° region centered on DES J2356–5935, which contains this linear feature. Selecting stars with the same isochrone filter used to increase the contrast of DES J2356–5935 relative to the field population, we found a faint stellar overdensity extending ∼2° on both sides of DES J2356–5935. This feature has an FWHM of ∼0.°3 (i.e., projected dimensions of 1.7 kpc × 130 pc at a distance of 25 kpc) and is oriented ∼85° east of north. The length of the feature and the smooth density field observed with an inverted isochrone filter support the conclusion that this is a genuine stellar structure associated with DES J2356–5935.

One interpretation is that DES J2356–5935 is in the process of being tidally stripped by the gravitational potential of the Milky Way. The relatively short projected length of the putative tails may imply that DES J2356–5935 is far from its orbital pericenter (where tidal effects are strongest) and/or that stripping began recently. Despite the possible presence of tidal tails, the

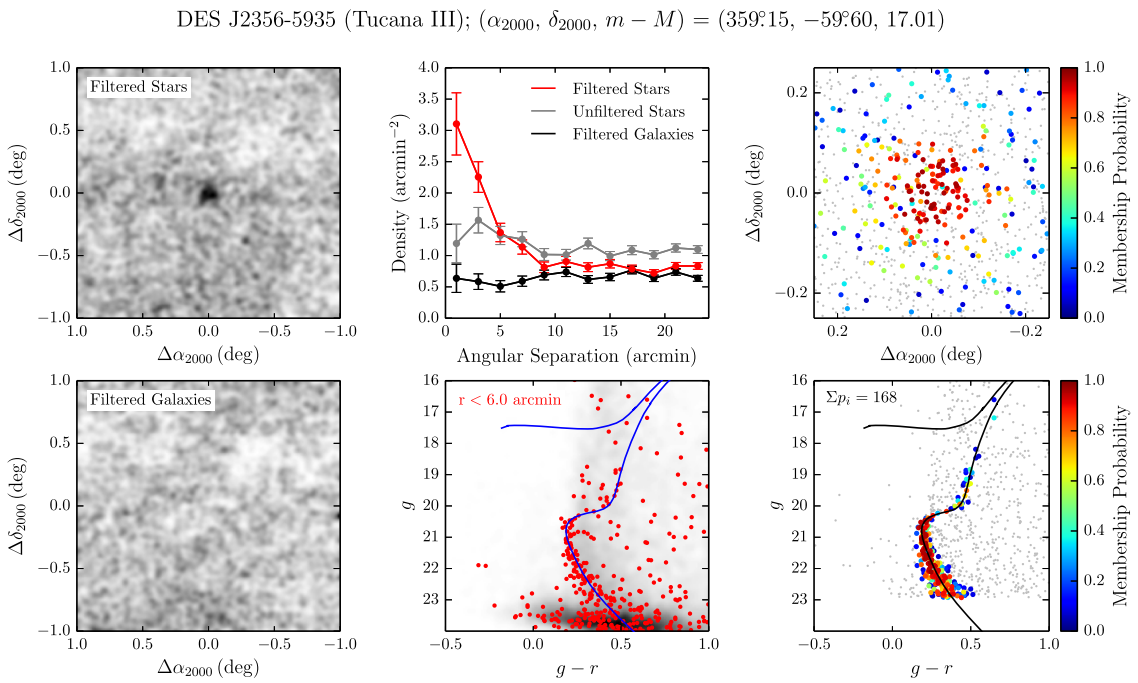

Figure 7. Analogous to Figure 6 but for DES J2356–5935 (Tucana III).

main body of DES J2356–5935 appears to be relatively round. While the proximity of DES J2356–5935 might make it an important object for indirect dark matter searches, evidence of tidal stripping would suggest that a large fraction of its outer dark matter halo has been removed. However, the mass within the stellar core (and therefore the dark matter content in the central region) can still likely be determined accurately (Oh et al. 1995; Muñoz et al. 2008; Peñarrubia et al. 2008).

3. *DES J0531–2801* (Columba I, Figure 9): DES J0531–2801 is the second most distant of the Y2 DES candidates (182 kpc) and is detected as a compact cluster of RGB stars. Both the BHB and red horizontal branch (RHB) appear to be well-populated. The distance, physical size (103 pc), and luminosity ($M_V = -4.5$ mag) of DES J0531–2801 place it in the locus of Local Group dwarf galaxies, comparable to Leo IV and CVn II (Belokurov et al. 2007). DES J0531–2801 is isolated from the other new DES systems and is likely not associated with the Magellanic system.
4. *DES J0002–6051* (Tucana IV, Figure 10): DES J0002–6051 has the largest angular size of the candidates ($r_h = 9.'1$), which at a distance of 48 kpc corresponds to a physical size of $r_{1/2} \sim 127$ pc. This large half-light radius is inconsistent with the sizes of known globular clusters (Harris 1996, 2010 edition), thus making it very likely that DES J0002–6051 is a dwarf galaxy. The measured ellipticity of DES J0002–6051, $\epsilon = 0.4$, is also consistent with a galactic classification. DES J0002–6051 is found to be 27 kpc from the LMC and 18 kpc from the SMC. DES J0002–6051 is one of the proposed members of the Tucana group, with a centroid separation of 7 kpc. Measurements of the radial velocity and proper motion of DES J0002–6051 will provide strong clues as to whether it was accreted as part of a system of satellites. Similar to DES J2356–5935 and DES J2204–4626, the MSTO of DES J0002–6051 is well-populated and clearly visible. Several possible member stars can also be seen along the HB.
5. *DES J0345–6026* (Reticulum III, Figure 11): DES J0345–6026 appears to be similar to DES J2204–4626 in its structural properties, but is more distant (heliocentric distance of 92 kpc). Like DES J2204–4626, DES J0345–6026 can be tentatively classified as a dwarf galaxy based on its physical size and low surface brightness. There is some indication of asphericity for this object; however, the ellipticity is not significantly constrained by the DES data. DES J0345–6026 has a sparsely populated RGB, a few possible RHB members, and two possible BHB members. The MSTO for DES J0345–6026 is slightly fainter than our fitting threshold of $g < 23$ mag, thus its age is poorly constrained.
6. *DES J2337–6316* (Tucana V, Figure 12): DES J2337–6316 is the second new system in the Tucana group and is the closest to the group's centroid (3 kpc). At a heliocentric distance of 55 kpc, DES J2337–6316 is also located 29 kpc from the LMC and 14 kpc from the SMC. The physical size (17 pc) and luminosity ($M_V \sim -1.6$ mag) place DES J2337–6316 in a region of the size–luminosity plane close to Segue 1, Willman 1, and Kim 2. Segue 1 and Willman 1 have sizes similar to the most extended globular clusters, but are approximately an order of magnitude less luminous. On the other hand, deep imaging of Kim 2 has led Kim et al. (2015b) to

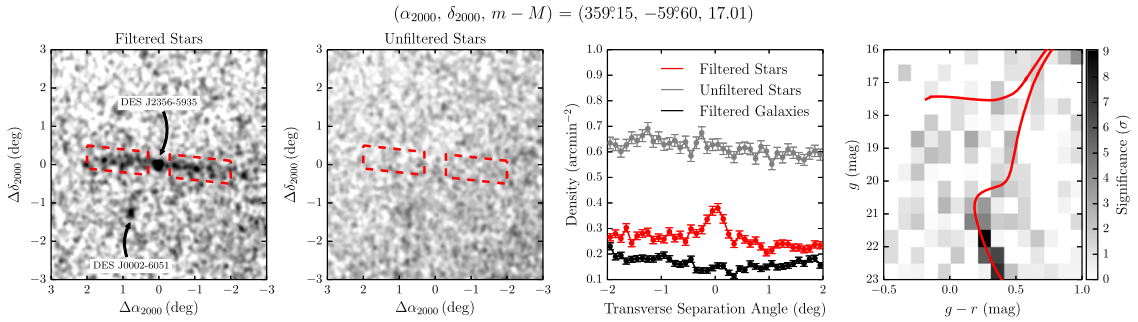

Figure 8. Possible tidal tails around DES J2356–5935 (Tucana III). Left: spatial distribution of stellar objects with $g < 23$ mag that pass the same isochrone filter as applied to visualize DES J2356–5935 (Figure 7). Red boxes highlight the positions of the tidal tails. Middle left: spatial distribution of stellar objects with $g - r < 1$ mag and $g < 23$ mag not passing the isochrone filter. Middle right: average density profiles transverse to the tidal tail axis: stars passing the isochrone filter (red), other unfiltered stars (gray), and galaxies passing the isochrone filter (black). For the density calculation, the range of included angles parallel to the tidal tails is $\pm 2.^{\circ}0$, excluding the region within $0.^{\circ}3$ of DES J2356–5935. Right: binned significance diagram representing the Poisson probability of detecting the observed number of stars within $0.^{\circ}2$ of the tidal tail axis (excluding the region within $0.^{\circ}3$ of DES J2356–5935) for each bin of the color–magnitude space given the local field density.

conclude that it is very likely a star cluster. DES J2337–6316 is one of the few new objects for which the DES data places a constraint on ellipticity. The high ellipticity, $\epsilon = 0.7$, supports a galactic classification for DES J2337–6316. Most of the high probability member stars for DES J2337–6316 are on the main sequence and fainter than $g \sim 22.5$ mag. As with other similarly faint objects, a few stars situated close to the lower RGB are also likely members. A system similar to DES J2337–6316 would have been difficult to detect in SDSS with a threshold at $r < 22$.

7. *DES J2038–4609* (Indus II, Figure 13): DES J2038–4609 is the first of the two lower-confidence candidates. The detection of this object comes predominantly from a tight clump of BHB stars at $g \sim 22$ mag and $g-r \sim 0$ mag. Three of the potential HB members are clustered within a spatial region of radius $\sim 10''$. Several additional HB and RGB stars are assigned non-zero membership probabilities by the likelihood fit, enlarging the best-fit size of this system. DES J2038–4609 is located at a boundary between the Y1 and Y2 imaging, and the effect of the deeper Y2 source detection threshold is visible when extending to magnitudes of $g > 23$ mag. The best-fit physical size of DES J2038–4609 (181 pc) would place it among the population of Local Group galaxies. Deeper imaging is needed to better characterize this candidate since the MSTO is fainter than the current DES detection threshold.
8. *DES J0117–1725* (Cetus II, Figure 14): DES J0117–1725 is the second lower-confidence candidate, being the least luminous ($M_V = 0.0 \pm 0.68$ mag) and most compact ($r_{1/2} = 17$ pc) of the new stellar systems. DES J0117–1725 is nearly two orders of magnitude fainter than globular clusters with comparable half-light radii. At a heliocentric distance of 30 kpc, DES J0117–1725 is the second nearest of the new systems. DES J0117–1725 is detected predominantly by its main sequence stars and has one potential HB member. The lack of strong features in the color–magnitude distribution of stars associated with DES J0117–1725 leads to a large degeneracy between the distance, age, and metallicity of this system. If determined to be a dwarf galaxy, DES J0117–1725 would be the least luminous known galaxy; however, the current classification of this object is ambiguous.

There are several gaps in the Y2Q1 coverage $\sim 0.^{\circ}1$ from DES J0117–1725; however, DES J0117–1725 is sufficiently compact that few member stars are expected in the region of missing coverage. These gaps are incorporated into the likelihood analysis and should have a minimal impact on the fit. The region around DES J0117–1725 was imaged in only a single r-band exposure; however, there are two to three overlapping exposures in each of the g- and i-bands. We have verified that the stellar overdensity is also apparent in the $g-i$ filter combination. Nonetheless, the properties of DES J0117–1725 should be interpreted with caution until additional imaging is acquired.

6.2. Satellite Detection Completeness

Many studies of the Milky Way satellite galaxy population require knowledge of the detection efficiency for satellites as a function of luminosity, heliocentric distance, physical size, and sky position in order to account for observational selection effects. To quantify our search sensitivity with the Y2Q1 data set, we follow the approach that Bechtol et al. (2015) applied to the DES Y1A1 coadd data. Briefly, we generated many realizations of satellite galaxies with different structural properties that are spread uniformly throughout the survey footprint, excluding regions of high stellar density near to the LMC. We then applied the map-based search algorithm to estimate the likelihood of a high-confidence detection. In the present implementation, the detection significance was evaluated as the Poisson probability of finding the "observed" number of stars within a circular region matched to the half-light radius of the simulated satellite given the effective local field density after the isochrone selection (see Section 3.1). Realizations that yield at least 10 detectable stars and produce a $>5.50\sigma$ overdensity within the half-light radius are considered "detected."

An essential input to the completeness calculation is the magnitude threshold for individual stars. For the searches described in Section 3, we used deeper magnitude thresholds (e.g., $g < 24$ mag) in order to maximize the discovery potential. A more conservative threshold, $g < 23$ mag, is selected to estimate the completeness in detecting new stellar systems

The Astrophysical Journal, 813:109 (20pp), 2015 November 10 Drlica-Wagner et al.

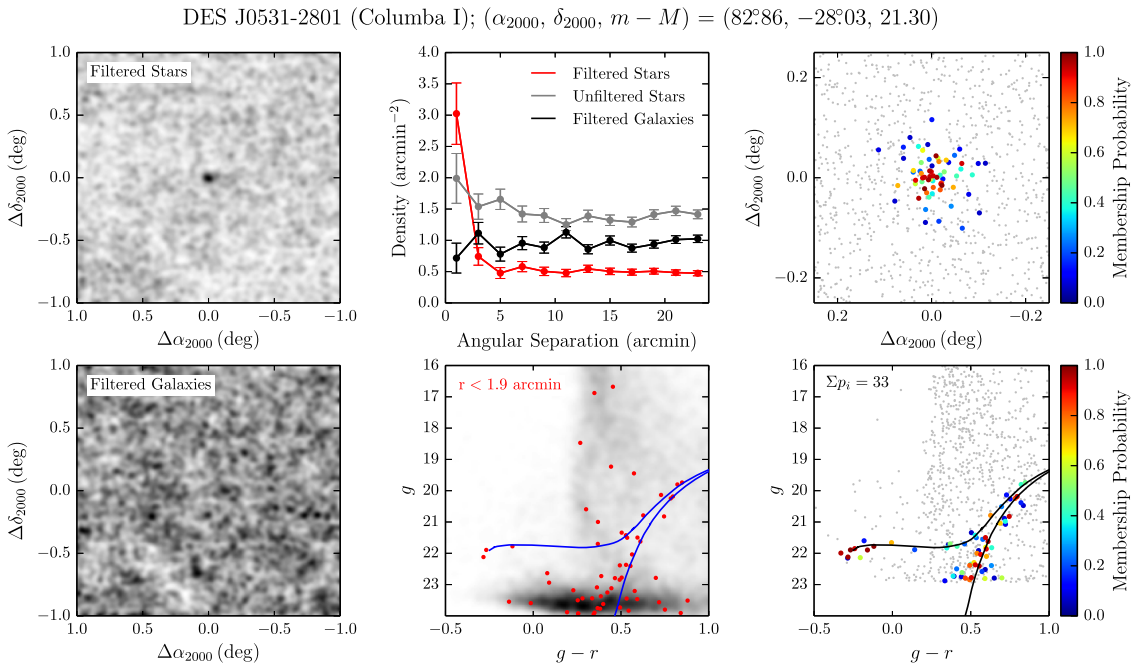

Figure 9. Analogous to Figure 6 but for DES J0531–2801 (Columba I).

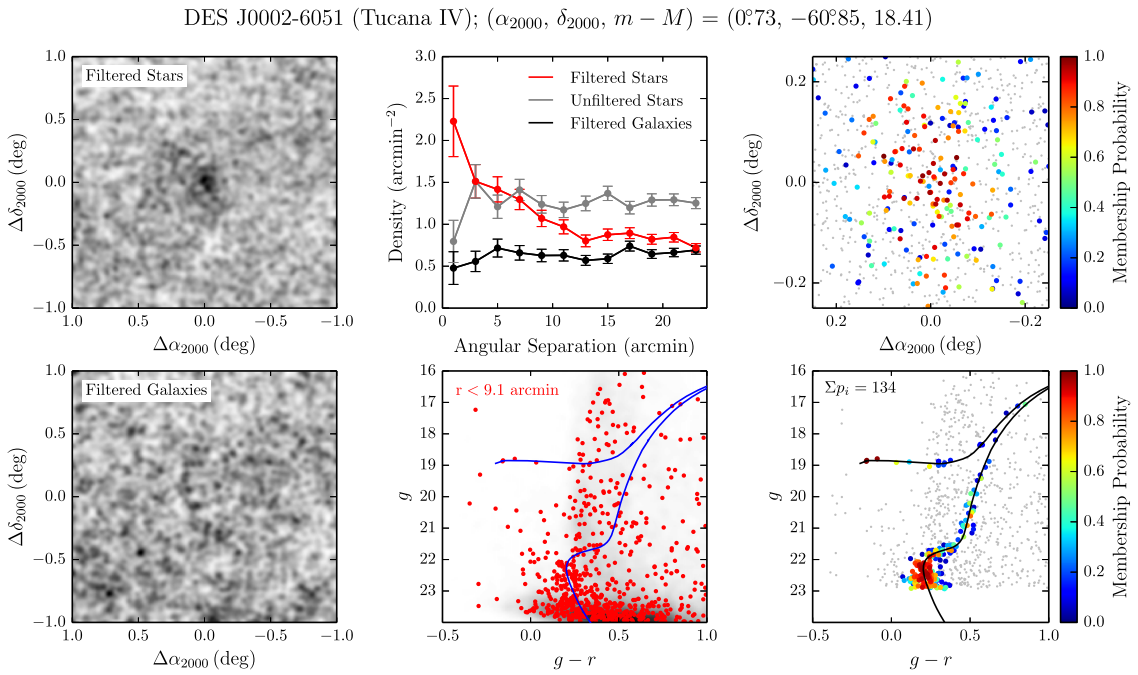

Figure 10. Analogous to Figure 6 but for DES J0002–6051 (Tucana IV).

The Astrophysical Journal, 813:109 (20pp), 2015 November 10 Drlica-Wagner et al.

DES J0345-6026 (Reticulum III); $(\alpha_{2000}, \delta_{2000}, m - M) = (56.^{\circ}36, -60.^{\circ}45, 19.81)$

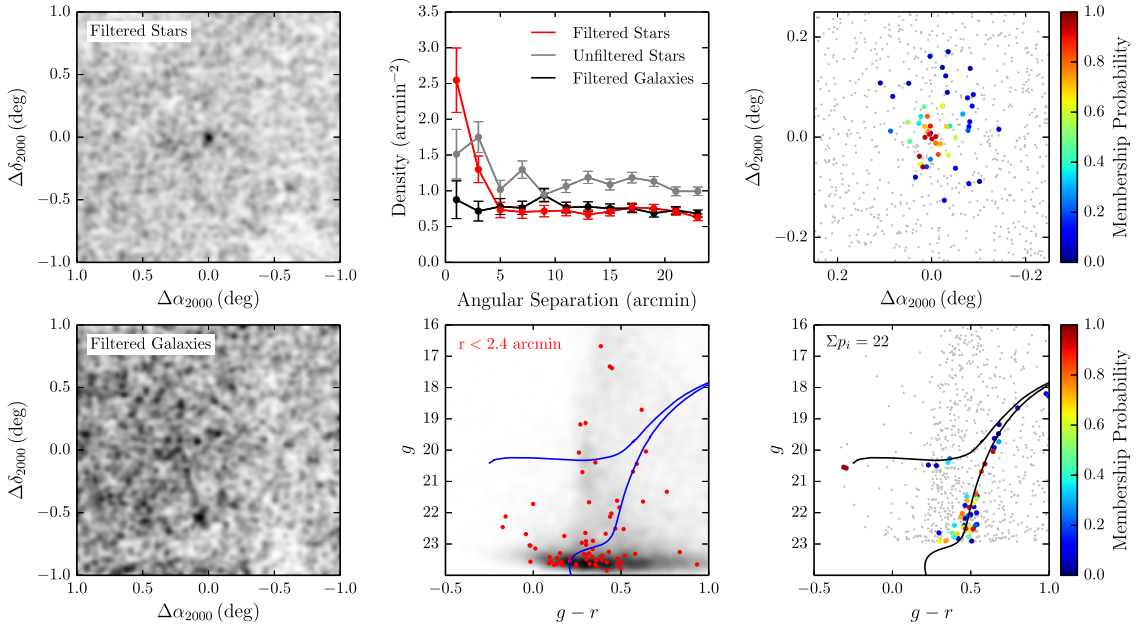

Figure 11. Analogous to Figure 6 but for DES J0345–6026 (Reticulum III).

DES J2337-6316 (Tucana V); $(\alpha_{2000}, \delta_{2000}, m - M) = (354.^{\circ}35, -63.^{\circ}27, 18.71)$

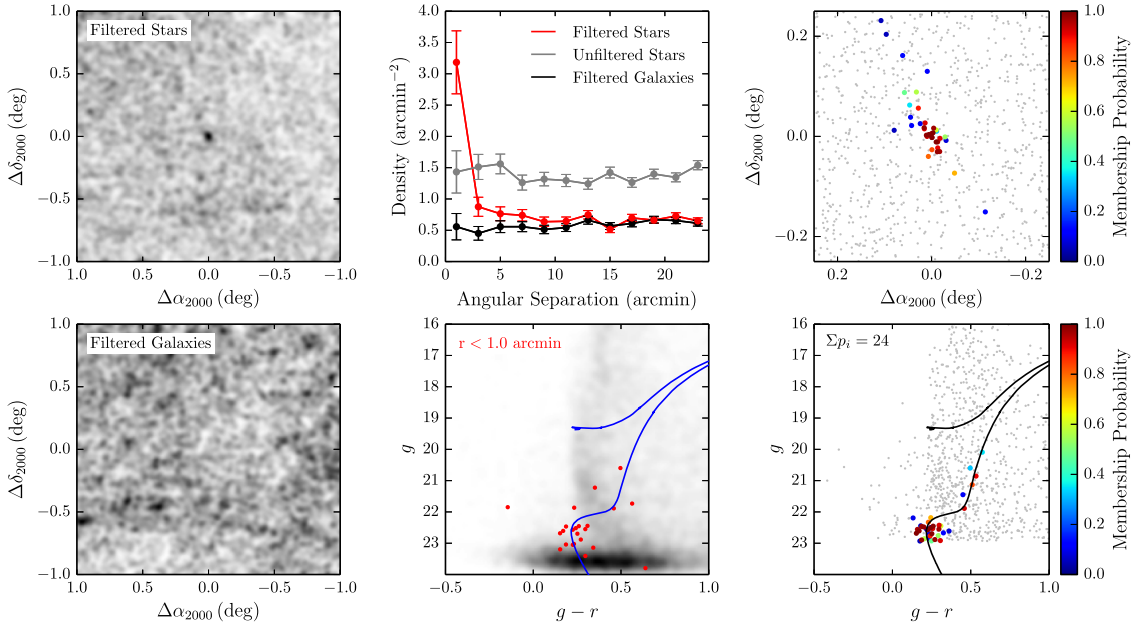

Figure 12. Analogous to Figure 6 but for DES J2337–6316 (Tucana V).

The Astrophysical Journal, 813:109 (20pp), 2015 November 10 Drlica-Wagner et al.

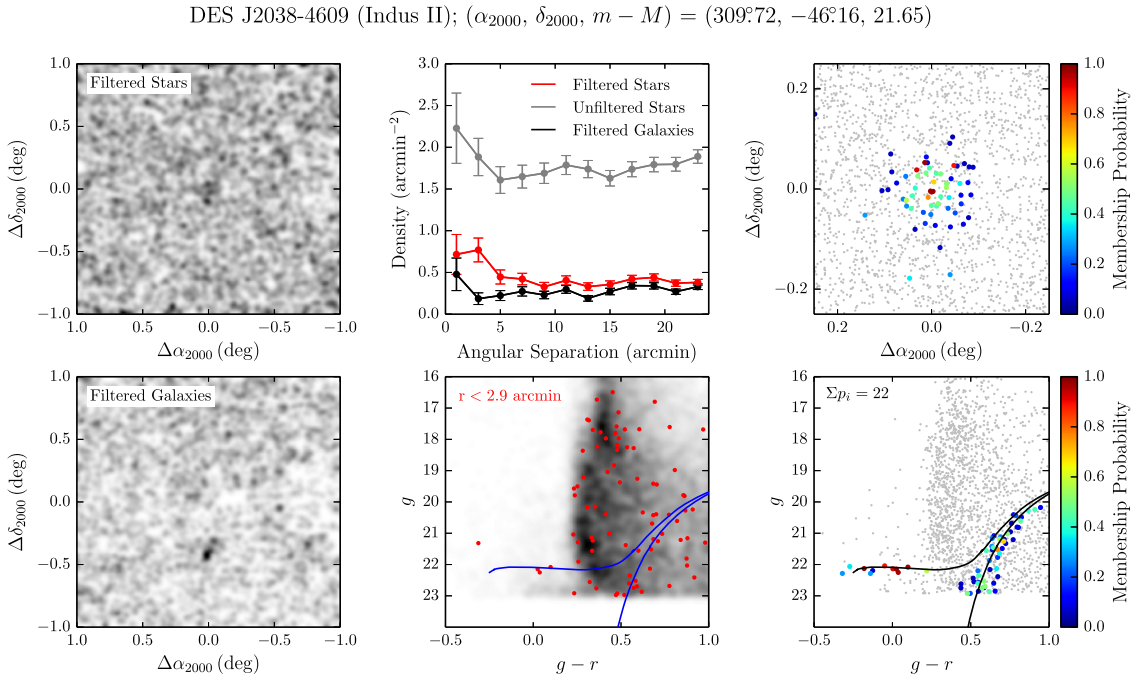

Figure 13. Analogous to Figure 6 but for DES J2038–4609 (Indus II). Note that the magnitude threshold for the smoothed counts maps and radial profiles has been raised to $g < 23$ mag due to non-uniform imaging depth in this region. DES J2038–4609 is detected primarily by a cluster of potential BHB members.

based on the following considerations. First, the Y2Q1 stellar sample is expected to be nearly complete for both Y1 and Y2 exposures at magnitudes $g \lesssim 23$ mag. Figure 3 shows that the measured stellar density in this magnitude range varies smoothly over the Y2Q1 footprint. At fainter magnitudes, discontinuities in the field density can occur in regions where exposures from Y1 and Y2 overlap (typically, more faint objects are detected in the Y2 exposures). Second, the field population with $g \gtrsim 23$ mag in high Galactic latitude regions is likely dominated by misclassified galaxies rather than halo stars, and therefore the assumption of isotropy on arcminute angular scales is compromised due to galaxy clustering. The adopted magnitude threshold matches that used in Bechtol et al. (2015), and in this case, the sensitivity estimates obtained in the prior work can be approximately scaled to the enlarged effective solid angle of the Y2Q1 data set, ∼5000 deg^2.

In Table 4, we list the expected detection efficiencies for the DES ultra-faint galaxy candidates using magnitude thresholds of $g < 23$ mag and $g < 22$ mag, which roughly correspond to the stellar completeness limits of Y2Q1 and SDSS, respectively. For the brighter threshold, several of the DES candidates have substantially reduced detection probabilities.

We note that all of the faint stellar systems that were discovered in the Y1A1 data set are also significantly detected using the Y2Q1 data set, suggesting that our present search has sensitivity comparable to previous studies.

6.3. Total Number and Distribution of Milky Way Satellite Galaxies

The detection of 17 candidate ultra-faint galaxies in the first two years of DES data is consistent with the range of predictions based on the standard cosmological model (Tollerud et al. 2008; Hargis et al. 2014). These predictions model the spatial distribution of luminous satellites from the locations of dark matter subhalos in cosmological *N*-body simulations of Local Group analogs. Significant anisotropy in the distribution of satellites is expected (Tollerud et al. 2008; Hargis et al. 2014) and likely depends on the specific accretion history of the Milky Way (Deason et al. 2015).

The proximity of the DES footprint to the Magellanic Clouds is noteworthy when considering an anisotropic distribution of satellites. The possibility that some Milky Way satellites are or were associated with the Magellanic system has been discussed for some time (Lynden-Bell 1976; D'Onghia & Lake 2008; Nichols et al. 2011; Sales et al. 2011), and the recent DES results have renewed interest in this topic (Deason et al. 2015; Koposov et al. 2015a; Wheeler et al. 2015; Yozin & Bekki 2015). The existence of structures on mass scales ranging from galaxy clusters to ultra-faint satellite galaxies is a generic prediction of hierarchical galaxy formation in the cold dark matter paradigm. However, specific predictions for the number of observable satellites of the LMC and SMC depend on the still unknown efficiency of galaxy formation in low-mass subhalos. Identifying satellites of satellites within the Local Group would support the standard cosmological model, and may provide a new opportunity to test the impact of environment on the formation of the least luminous galaxies (Wetzel et al. 2015).

Based on a study of Milky Way–LMC analogs in *N*-body simulations, Deason et al. (2015) propose a method to evaluate the probability that a given satellite was at one time associated with the LMC based upon the present three-dimensional

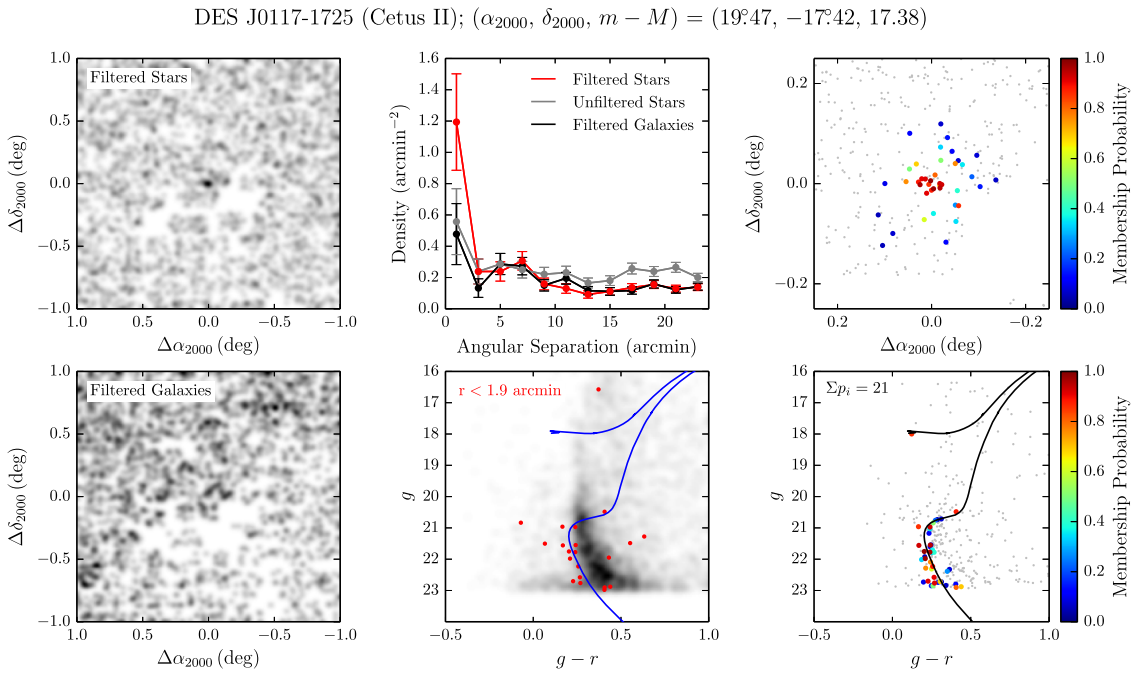

Figure 14. Analogous to Figure 6 but for DES J0117–1725 (Cetus II). Note that the magnitude threshold for the smoothed counts maps and radial profiles has been raised to $g < 23$ mag due to incomplete coverage in this region.

Table 4
Expected Detection Efficiencies for Ultra-faint Galaxy Candidates

Name	M_V	Distance (kpc)	r_h (arcmin)	Efficiency ($g < 23$ mag)	Efficiency ($g < 22$ mag)
DES J2204–4626 (Gru II)	−3.9	53	6.0	1.00	0.39
DES J2356–5935 (Tuc III)	−2.4	25	6.0	1.00	0.94
DES J0531–2801 (Col I)	−4.5	182	1.9	0.95	0.86
DES J0002–6051 (Tuc IV)	−3.5	48	9.1	0.98	0.05
DES J0345–6026 (Ret III)	−3.3	92	2.4	0.33	0.05
DES J2337–6316 (Tuc V)	−1.6	55	1.0	0.94	0.01
DES J2038–4609 (Ind II)	−4.3	214	2.9	0.26	0.00
DES J0117–1725 (Cet II)	0.0	30	1.9	0.38	0.01
Ret II	−3.6	32	6.0	1.00	1.00
DES J0344.3–4331 (Eri II)	−7.4	330	1.8	1.00	1.00
DES J2251.2–5836 (Tuc II)	−3.9	58	7.2	1.00	0.07
Hor I	−3.5	87	2.4	0.66	0.14
DES J0443.8–5017 (Pic I)	−3.7	126	1.2	0.85	0.47
DES J0222.7–5217 (Eri III)	−2.4	95	0.4	0.41	0.04
DES J2339.9–5424 (Phe II)	−3.7	95	1.2	0.99	0.77
Gru I	−3.4	120	2.0	0.21	0.04
Hor II	−2.6	78	2.1	0.26	0.01

Note. Expected detection efficiencies are provided for two magnitude thresholds roughly corresponding to the stellar completeness depths of DES Y2Q1 ($g < 23$ mag) and SDSS ($g < 22$ mag). The detection efficiencies are estimated from multiple realizations of each candidate within the DES footprint using the best-fit luminosity M_V, heliocentric distance, and azimuthally averaged half-light radius r_h, which were then analyzed with the map-based detection algorithm described in Section 3.1. The average detection probability ratio between the two threshold choices is ∼50%, implying that roughly half of the DES candidates would have been detected if they were located in the SDSS footprint.

separation between the two (Table 3). This prescription predicts that two to four of the Y2 DES candidates were associated with the LMC before infall, in addition to the two to four potentially associated satellites found in Y1 DES data. Deason et al. further suggest that a grouping of satellites near the LMC in both physical separation and velocity would imply that the Magellanic system was recently accreted onto the Milky Way since members of this group would disperse within a few Gyr.

As a population, the new DES satellite galaxy candidates do appear to be unevenly distributed within the survey footprint;

15 are located at $\delta_{2000} < -40°$, close to the Magellanic Clouds (Figure 3). A Kolmogorov–Smirnov test, shown in Figure 15, significantly rejects the hypothesis of a uniform distribution ($p = 4.3 \times 10^{-4}$). One possible explanation for non-uniformity is that some of the new systems are satellites of the LMC or SMC. Below we introduce a simple model to test this hypothesis.

We began by modeling the probability distribution for detecting a satellite galaxy as a function of sky position. In this analysis, we excluded classical Milky Way satellites and considered only satellites that have similar characteristics to those discovered by DES (i.e., are detectable at the DES Y2Q1 depth). The underlying luminosity function and the completeness as a function of luminosity, heliocentric distance, and physical size were all simplified into a two-dimensional probability distribution.

We modeled this two-dimensional probability distribution with three components: (i) an isotropic distribution of satellites associated with the main halo of the Milky Way, (ii) a population of satellites spatially associated with the LMC halo, and (iii) a population of satellites spatially associated with the SMC halo. The first component was uniform on the sky, and the latter two components were spatially concentrated around the Magellanic Clouds. We assumed spherically symmetric three-dimensional distributions of satellites centered around each of the Magellanic Clouds having power-law radial profiles with slope $\alpha = -1$ and truncation radius $r_t = 35$ kpc. These distributions were then projected onto the sky to create two-dimensional predicted density maps.

Several underlying assumptions went into this simple model. First, we assumed that the Magellanic components were concentrated enough that variations in the completeness with respect to heliocentric distance would not substantially alter the projected density maps. Second, we assumed that the truncation radii of the LMC and SMC are the same, but later test the sensitivity of our results to this choice. Third, we assumed that smaller satellites of the Milky Way do not have their own associated satellites. We note that a power-law radial profile with slope $\alpha = -1$ can be viewed as a very extended Navarro–Frenk–White profile (Navarro et al. 1997). Since the DES footprint does not cover the central regions of the Magellanic Clouds, this shallow profile yields a conservative estimate on the fraction of satellites associated with the Magellanic system.

We performed an unbinned maximum-likelihood fit of our three-component model to the distribution of observed satellites. The parameters of the likelihood function are the total number of satellites and the relative normalizations of the three components. The likelihood is defined as the product of the probabilities to detect each observed satellite given its sky position. When presenting our results, we marginalized over the ratio of the LMC component to the SMC component. This ratio is not strongly constrained by our analysis; however, there is a slight preference for a larger SMC component.

The left panel of Figure 16 shows the constraints using the sky positions of the seventeen DES satellite galaxy candidates. We find that the DES data alone reject a uniform distribution of satellites at $>3\sigma$ confidence when compared to our best-fit model. This again implies that there is either a clear overdensity of satellites around the Magellanic Clouds or that the initial assumption of isotropy around the main halo is incorrect. In Figure 15, we show the distribution of declinations for our best-fit three-component model and find good agreement with the observations ($p = 0.7$).

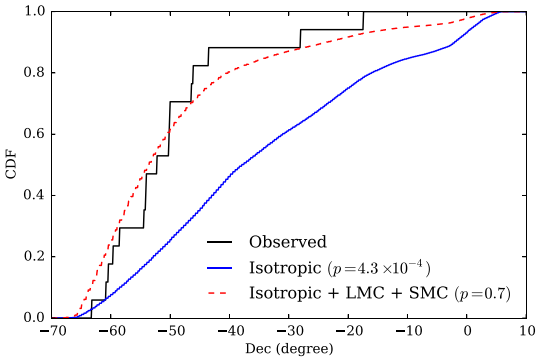

Figure 15. Cumulative distribution functions of declination values for the 17 observed satellites in the DES footprint (black), a uniform distribution given the shape of DES footprint (blue), and the best-fit model for a uniform distribution and Magellanic Cloud components (red dashed). See Section 6.3.

We next tested the sensitivity of our result to the assumed distribution of satellites around the LMC and SMC. The central panel of Figure 16 shows the 1σ contours for three different values of $r_t = \{25, 35, 45\,\mathrm{kpc}\}$, and two values of the slope, $\alpha = \{-1, -2\}$. Despite slight changes in the likelihood contours, in each case >10% of Milky Way satellites are likely to be spatially associated with the Magellanic Clouds.

We further examined the satellite population by simultaneously considering the 16 ultra-faint satellites observed in the SDSS DR10 footprint.[49] To fully combine DES and SDSS observations we would need to model the detection efficiency of SDSS relative to DES as a function of satellite distance, size, and luminosity. However, since the SDSS DR10 footprint only overlaps with the isotropic component in our model, we can again fold the complications of detection efficiency into a constant detection ratio. Our fiducial calculation assumes that 50% of the satellites discovered in DES would be detectable by SDSS, which agrees with the relative detection efficiency of the 17 DES satellites at the depth of SDSS (Table 4). The right panel of Figure 16 shows that the DES+SDSS constraints are in agreement with those from DES data alone, though the fraction of LMC and SMC satellites is more tightly constrained by including information from a large region widely separated from the Magellanic Clouds. The combined results imply that there are ∼100 satellites over the full sky that are detectable at DES Y2Q1 depth, and that 20%–30% of these might be associated with the Magellanic Clouds. Importantly, this prediction does not attempt to model the full population of Milky Way satellites beyond the DES Y2Q1 sensitivity and ignores the diminished detection efficiency close to the Galactic plane.

The Pan-STARRS team has recently identified three candidate Milky Way satellite galaxies in their 3π survey (Laevens et al. 2015a, 2015b). If this search is complete to the depth of SDSS over its full area, it is notable that so few candidates have been found. This observation alone could imply anisotropy without requiring the influence of the Magellanic Clouds. However, much of the Pan-STARRS area

[49] We include Pegasus III (Kim et al. 2015a) in the list of ultra-faint satellites from SDSS.

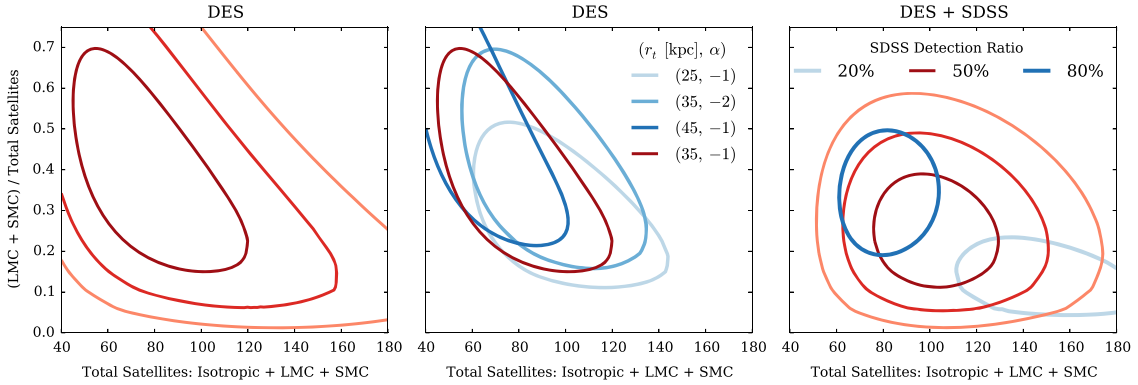

Figure 16. Maximum-likelihood fit to the spatial distribution of satellites for a model including isotropic, LMC, and SMC components (Section 6.3). The horizontal axis represents the total number of satellites detectable at DES Y2Q1 depth integrated over the entire sky (not including the classical dwarf galaxies and detection inefficiency near the Galactic plane). The vertical axis represents the fraction of these satellites associated with the Magellanic Clouds. Left: the 1σ, 2σ, and 3σ likelihood contours when considering only DES data. Center: 1σ contours for different values of the LMC and SMC truncation radius (r_t) and the slope of the radial profile (α). Right: contours of the likelihood function when SDSS observations are included. Red contours (1σ, 2σ, 3σ) assume that 50% of the satellites discovered in DES would have been detected if they were located in the SDSS footprint. This value matches the estimated detection efficiency from Table 4. We show the sensitivity of our results to the SDSS/DES detection ratio with the dark blue contour (80% detection ratio) and the light blue contour (20% detection ratio).

is located at low Galactic latitudes where the elevated foreground stellar density and interstellar extinction may present additional challenges. Under the assumption that Pan-STARRS covers the full sky with $\delta_{2000} > -30°$, $\sim$2000 deg^2 overlap with DES Y2Q1. This area of the DES footprint includes two new candidates, one of which has a large enough surface brightness to likely have been detected at SDSS depth (DES J0531–2801, see Table 4). These two candidates are located in a region of the sky that would be observed at a relatively high airmass by Pan-STARRS and may suffer from decreased detection efficiency.

From this analysis, we conclude that the distribution of satellites around the Milky Way is unlikely to be isotropic, and that a plausible component of this anisotropy is a population of satellites associated with the Magellanic Clouds. However, several alternative explanations for anisotropy in the Milky Way satellite distribution exist. For example, Milky Way satellites could be preferentially located along a three-dimensional planar structure, as has been suggested by many authors, starting with Lynden-Bell (1976). This proposed planar structure encompasses the Magellanic Clouds and many of the classical and SDSS satellites. Pawlowski et al. (2015) suggest that the satellites discovered in Y1 DES data are also well aligned with this polar structure. We note that the Y2 discoveries presented here include several objects near the SMC and may reduce the fraction of objects in close proximity to the proposed plane. An additional possibility is that the satellites are associated with the orbit of the Magellanic System and are not isotropically distributed around the Magellanic Clouds themselves (Yozin & Bekki 2015). The DES footprint covers only a fraction of the region surrounding the Magellanic Clouds and additional sky coverage may yield more satellites with similar proximity to the Magellanic system and/or help to distinguish between these various scenarios. Measurements of the relative motions of the satellites and further theoretical work will also help clarify the physical relationships between these stellar systems.

7. CONCLUSIONS

We report the discovery of six new ultra-faint galaxy candidates in a combined data set from the first two years of DES covering $\sim$5000 deg^2 of the south Galactic cap. Two additional candidates are identified in regions with incomplete or non-uniform coverage and should be viewed with lower confidence until additional imaging is obtained. The new satellites are faint ($M_V > -4.7$ mag) and span a wide range of physical sizes (17 pc $< r_{1/2} <$ 181 pc) and heliocentric distances (25 kpc $< D_\odot <$ 214 kpc). All are low surface brightness systems similar to the known ultra-faint satellite galaxies of the Milky Way, and most possess physical sizes that are large enough (>40 pc) to be provisionally classified as galaxies. Spectroscopic observations are needed to better understand and unambiguously classify the new stellar systems. A total of 17 confirmed and candidate ultra-faint galaxies have been found in the first two years of DES. Roughly half of the DES systems are sufficiently distant and/or faint to have eluded detection at survey depths comparable to SDSS.

The DES satellites are concentrated in the southern half of the survey footprint in proximity to the Magellanic Clouds. In addition, we find three satellites clustered in a Tucana group, each of which is within <10 kpc of the group centroid. We find that the DES data alone exclude ($p < 10^{-3}$) an isotropic distribution of satellites within the Milky Way halo, and that the observed distribution can be well, although not uniquely, explained by a model in which several of the observed DES satellites are associated with the Magellanic system. Under the assumption that the total satellite population can be modeled by isotropic distributions around the Milky Way, LMC, and SMC, we estimate that a total of $\sim$100 ultra-faint satellites with comparable physical characteristics to those detected by DES might exist over the full sky, with 20%–30% of these systems being spatially associated with the Magellanic Clouds.

Milky Way satellite galaxies are considered a unique population for studying the particle nature of dark matter due to their proximity, characteristically large mass-to-light ratios,

and lack of intrinsic astrophysical backgrounds. Although the dark matter content of the new stellar systems has not yet been spectroscopically confirmed, the possibility that some are dark matter dominated galaxies makes them interesting targets for indirect dark matter searches via gamma rays. No gamma-ray sources from the third *Fermi*-LAT source catalog (3FGL; Acero et al. 2015) are located within $0.^{\circ}5$ of any of the new candidates. A follow-up gamma-ray analysis of these ultra-faint galaxy candidates will be presented separately.

Future seasons of DES will not significantly increase the DES sky coverage. However, there will be considerable gains in depth from the expected 10 tilings per filter relative to the two to four in the Y2Q1 data set. This increased depth will expand the effective volume of the survey. In addition, we expect the survey uniformity to improve with the coming seasons, resulting in a cleaner list of seeds with fewer false positives. Star-galaxy separation may become a limiting factor at the future depth of DES, motivating the development of improved classification algorithms (e.g., Fadely et al. 2012; Soumagnac et al. 2015), as well as alternative search strategies, involving, for instance, the time domain (Baker & Willman 2015) or stellar velocities (Antoja et al. 2015). While it is likely that the most conspicuous Milky Way satellites in the DES footprint have been found, the most exciting phase of Milky Way science with DES is likely still to come. The wide area and growing sensitivity of DES will enable the discovery of dwarf galaxies that are fainter, farther, and have lower surface brightness.

This work made use of computational resources at SLAC National Accelerator Laboratory and the University of Chicago Research Computing Center. Some of the results in this paper have been derived using the `HEALPix` (Górski et al. 2005) package. This research made use of Astropy, a community-developed core Python package for Astronomy (Astropy Collaboration et al. 2013). We thank the anonymous referee for helpful suggestions. A.D.W. thanks Ellen Bechtol for her generous hospitality during the preparation of this manuscript. E.B. acknowledges financial support from the European Research Council (ERC-StG-335936, CLUSTERS).

Funding for the DES Projects has been provided by the U.S. Department of Energy, the U.S. National Science Foundation, the Ministry of Science and Education of Spain, the Science and Technology Facilities Council of the United Kingdom, the Higher Education Funding Council for England, the National Center for Supercomputing Applications at the University of Illinois at Urbana-Champaign, the Kavli Institute of Cosmological Physics at the University of Chicago, the Center for Cosmology and Astro-Particle Physics at the Ohio State University, the Mitchell Institute for Fundamental Physics and Astronomy at Texas A&M University, Financiadora de Estudos e Projetos, Fundação Carlos Chagas Filho de Amparo à Pesquisa do Estado do Rio de Janeiro, Conselho Nacional de Desenvolvimento Científico e Tecnológico and the Ministério da Ciência, Tecnologia e Inovação, the Deutsche Forschungsgemeinschaft and the Collaborating Institutions in the Dark Energy Survey.

The Collaborating Institutions are Argonne National Laboratory, the University of California at Santa Cruz, the University of Cambridge, Centro de Investigaciones Energéticas, Medioambientales y Tecnológicas-Madrid, the University of Chicago, University College London, the DES-Brazil Consortium, the University of Edinburgh, the Eidgenössische Technische Hochschule (ETH) Zürich, Fermi National Accelerator Laboratory, the University of Illinois at Urbana-Champaign, the Institut de Ciències de l'Espai (IEEC/CSIC), the Institut de Física d'Altes Energies, Lawrence Berkeley National Laboratory, the Ludwig-Maximilians Universität München and the associated Excellence Cluster universe, the University of Michigan, the National Optical Astronomy Observatory, the University of Nottingham, The Ohio State University, the University of Pennsylvania, the University of Portsmouth, SLAC National Accelerator Laboratory, Stanford University, the University of Sussex, and Texas A&M University.

The DES data management system is supported by the National Science Foundation under grant Number AST-1138766. The DES participants from Spanish institutions are partially supported by MINECO under grants AYA2012-39559, ESP2013-48274, FPA2013-47986, and Centro de Excelencia Severo Ochoa SEV-2012-0234. Research leading to these results has received funding from the European Research Council under the European Union's Seventh Framework Programme (FP7/2007-2013), including ERC grant agreements 240672, 291329, and 306478.

REFERENCES

Abbott, T., Aldering, G., Annis, J., et al. 2005, arXiv:astro-ph/0510346
Acero, F., Ackermann, M., Ajello, M., et al. 2015, ApJS, 218, 23
Ackermann, M., et al. 2015, PRL, in press (arXiv:1503.02641)
Adén, D., Feltzing, S., Koch, A., et al. 2009, A&A, 506, 1147
Antoja, T., Mateu, C., Aguilar, L., et al. 2015, MNRAS, 453, 541
Astropy Collaboration, Robitaille, T. P., Tollerud, E. J., et al. 2013, A&A, 558, A33
Baker, M., & Willman, B. 2015, AJ, in press (arXiv:1507.00734)
Balbinot, E., Santiago, B. X., da Costa, L. N., Makler, M., & Maia, M. A. G. 2011, MNRAS, 416, 393
Balbinot, E., Santiago, B. X., da Costa, L., et al. 2013, ApJ, 767, 101
Bechtol, K., Drlica-Wagner, A., Balbinot, E., et al. 2015, ApJ, 807, 50
Belokurov, V., Irwin, M. J., Koposov, S. E., et al. 2014, MNRAS, 441, 2124
Belokurov, V., Walker, M. G., Evans, N. W., et al. 2008, ApJL, 686, L83
Belokurov, V., Walker, M. G., Evans, N. W., et al. 2009, MNRAS, 397, 1748
Belokurov, V., Walker, M. G., Evans, N. W., et al. 2010, ApJL, 712, L103
Belokurov, V., Zucker, D. B., Evans, N. W., et al. 2006, ApJL, 647, L111
Belokurov, V., Zucker, D. B., Evans, N. W., et al. 2007, ApJ, 654, 897
Benson, A. J., Frenk, C. S., Lacey, C. G., Baugh, C. M., & Cole, S. 2002, MNRAS, 333, 177
Bertin, E. 2006, in ASP Conf. Ser. 351, Astronomical Data Analysis Software and Systems XV, ed. C. Gabriel et al. (San Francisco, CA: ASP), 112
Bertin, E. 2011, in ASP Conf. Ser. 442, Astronomical Data Analysis Software and Systems XX, ed. I. N. Evans et al. (San Francisco, CA: ASP), 435
Bertin, E., & Arnouts, S. 1996, A&AS, 117, 393
Bressan, A., Marigo, P., Girardi, L., et al. 2012, MNRAS, 427, 127
Bullock, J. S., Kravtsov, A. V., & Weinberg, D. H. 2000, ApJ, 539, 517
Bullock, J. S., Kravtsov, A. V., & Weinberg, D. H. 2001, ApJ, 548, 33
Carlin, J. L., Grillmair, C. J., Muñoz, R. R., Nidever, D. L., & Majewski, S. R. 2009, ApJL, 702, L9
Chabrier, G. 2001, ApJ, 554, 1274
Chang, C., Busha, M. T., Wechsler, R. H., et al. 2015, ApJ, 801, 73
Corwin, H. G. 2004, yCat, 7239, 0
Coupon, J., Kilbinger, M., McCracken, H. J., et al. 2012, A&A, 542, A5
de Grijs, R., & Bono, G. 2015, AJ, 149, 179
de Grijs, R., Wicker, J. E., & Bono, G. 2014, AJ, 147, 122
Deason, A. J., Wetzel, A. R., Garrison-Kimmel, S., & Belokurov, V. 2015, MNRAS, 453, 3568
Desai, S., Armstrong, R., Mohr, J. J., et al. 2012, ApJ, 757, 83
Dickey, J. M. 1971, Ann. Math. Statist., 42, 204
D'Onghia, E., & Lake, G. 2008, ApJL, 686, L61
Dotter, A., Chaboyer, B., Jevremović, D., et al. 2008, ApJS, 178, 89
Drlica-Wagner, A., Albert, A., Bechtol, K., et al. 2015, ApJL, 809, L4
Erben, T., Hildebrandt, H., Miller, L., et al. 2013, MNRAS, 433, 2545
Fadely, R., Hogg, D. W., & Willman, B. 2012, ApJ, 760, 15

Fadely, R., Willman, B., Geha, M., et al. 2011, AJ, 142, 88
Flaugher, B., Diehl, H. T., Honscheid, K., et al. 2015, AJ, submitted (arXiv:1504.02900)
Foreman-Mackey, D., Hogg, D. W., Lang, D., & Goodman, J. 2013, PASP, 125, 306
Geha, M., Willman, B., Simon, J. D., et al. 2009, ApJ, 692, 1464
Geringer-Sameth, A., Koushiappas, S. M., & Walker, M. G. 2015a, PhRvD, 91, 083535
Geringer-Sameth, A., Walker, M. G., Koushiappas, S. M., et al. 2015b, PhRvL, 115, 081101
Gilbank, D. G., Gladders, M. D., Yee, H. K. C., & Hsieh, B. C. 2011, AJ, 141, 94
Górski, K. M., Hivon, E., Banday, A. J., et al. 2005, ApJ, 622, 759
Grillmair, C. J. 2006, ApJL, 645, L37
Grillmair, C. J. 2009, ApJ, 693, 1118
Hargis, J. R., Willman, B., & Peter, A. H. G. 2014, ApJL, 795, L13
Harris, W. E. 1996, AJ, 112, 1487
Heymans, C., van Waerbeke, L., Miller, L., et al. 2012, MNRAS, 427, 146
High, F. W., Stubbs, C. W., Rest, A., Stalder, B., & Challis, P. 2009, AJ, 138, 110
Hooper, D., & Linden, T. 2015, arXiv:1503.06209
Irwin, M. J., Belokurov, V., Evans, N. W., et al. 2007, ApJL, 656, L13
Ivezić, Ž., Lupton, R. H., Schlegel, D., et al. 2004, AN, 325, 583
Kelly, P. L., von der Linden, A., Applegate, D. E., et al. 2014, MNRAS, 439, 28
Kharchenko, N. V., Piskunov, A. E., Schilbach, E., Röser, S., & Scholz, R.-D. 2013, A&A, 558, A53
Kim, D., & Jerjen, H. 2015a, ApJ, 799, 73
Kim, D., & Jerjen, H. 2015b, ApJL, 808, L39
Kim, D., Jerjen, H., Mackey, D., da Costa, G. S., & Milone, A. P. 2015a, ApJL, 804, L44
Kim, D., Jerjen, H., Milone, A. P., Mackey, D., & da Costa, G. S. 2015b, ApJ, 803, 63
Kirby, E. N., Boylan-Kolchin, M., Cohen, J. G., et al. 2013, ApJ, 770, 16
Kirby, E. N., Simon, J. D., & Cohen, J. G. 2015, ApJ, 810, 56
Kirby, E. N., Simon, J. D., Geha, M., Guhathakurta, P., & Frebel, A. 2008, ApJL, 685, L43
Kleyna, J. T., Wilkinson, M. I., Evans, N. W., & Gilmore, G. 2005, ApJL, 630, L141
Koch, A., Wilkinson, M. I., Kleyna, J. T., et al. 2009, ApJ, 690, 453
Koposov, S., Belokurov, V., Evans, N. W., et al. 2008, ApJ, 686, 279
Koposov, S., de Jong, J. T. A., Belokurov, V., et al. 2007, ApJ, 669, 337
Koposov, S. E., Belokurov, V., Torrealba, G., & Evans, N. W. 2015a, ApJ, 805, 130
Koposov, S. E., Casey, A. R., Belokurov, V., et al. 2015b, ApJ, in press (arXiv:1504.07916)
Koposov, S. E., Gilmore, G., Walker, M. G., et al. 2011, ApJ, 736, 146
Laevens, B. P. M., Martin, N. F., Bernard, E. J., et al. 2015a, ApJ, submitted (arXiv:1507.07564)
Laevens, B. P. M., Martin, N. F., Ibata, R. A., et al. 2015b, ApJL, 802, L18
Laevens, B. P. M., Martin, N. F., Sesar, B., et al. 2014, ApJL, 786, L3
Luque, E., Queiroz, A., Santiago, B., et al. 2015, MNRAS, in press (arXiv:1508.02381)
Lynden-Bell, D. 1976, MNRAS, 174, 695
MacDonald, E. C., Allen, P., Dalton, G., et al. 2004, MNRAS, 352, 1255
Martin, N. F., de Jong, J. T. A., & Rix, H.-W. 2008, ApJ, 684, 1075
Martin, N. F., Ibata, R. A., Chapman, S. C., Irwin, M., & Lewis, G. F. 2007, MNRAS, 380, 281
Martin, N. F., Nidever, D. L., Besla, G., et al. 2015, ApJL, 804, L5
McClure-Griffiths, N. M., Pisano, D. J., Calabretta, M. R., et al. 2009, ApJS, 181, 398
McConnachie, A. W. 2012, AJ, 144, 4
Mohr, J. J., Armstrong, R., Bertin, E., et al. 2012, Proc. SPIE, 8451, 84510D
Muñoz, R. R., Carlin, J. L., Frinchaboy, P. M., et al. 2006, ApJL, 650, L51
Muñoz, R. R., Geha, M., Côté, P., et al. 2012, ApJL, 753, L15
Muñoz, R. R., Majewski, S. R., & Johnston, K. V. 2008, ApJ, 679, 346
Navarro, J. F., Frenk, C. S., & White, S. D. M. 1997, ApJ, 490, 493
Neilsen, E., Bernstein, G., Gruendl, R., & Kent, S. 2015, Limiting Magnitude, τ, $T_{\rm eff}$, and Image Quality in DES Year 1, Tech. Rep. FERMILAB-TM-2610-AE-CD (Batavia, IL: Fermi National Accelerator Laboratory)
Nichols, M., Colless, J., Colless, M., & Bland-Hawthorn, J. 2011, ApJ, 742, 110
Nilson, P. 1973, Uppsala General Catalogue of Galaxies (Uppsala: Royal Society of Sciences in Uppsala)
Oh, K. S., Lin, D. N. C., & Aarseth, S. J. 1995, ApJ, 442, 142
Ortolani, S., Bica, E., & Barbuy, B. 2013, MNRAS, 433, 1966
Paust, N., Wilson, D., & van Belle, G. 2014, AJ, 148, 19
Pawlowski, M. S., McGaugh, S. S., & Jerjen, H. 2015, MNRAS, 453, 1047
Peñarrubia, J., Navarro, J. F., & McConnachie, A. W. 2008, ApJ, 673, 226
Putman, M. E., Staveley-Smith, L., Freeman, K. C., Gibson, B. K., & Barnes, D. G. 2003, ApJ, 586, 170
Rykoff, E. S., Rozo, E., Busha, M. T., et al. 2014, ApJ, 785, 104
Sakamoto, T., & Hasegawa, T. 2006, ApJL, 653, L29
Sales, L. V., Navarro, J. F., Cooper, A. P., et al. 2011, MNRAS, 418, 648
Schlafly, E. F., & Finkbeiner, D. P. 2011, ApJ, 737, 103
Schlegel, D. J., Finkbeiner, D. P., & Davis, M. 1998, ApJ, 500, 525
Sevilla, I., Armstrong, R., Bertin, E., et al. 2011, in Proc. DPF-2011 Conf., Providence, RI, 8–13 August 2011
Simon, J., Drlica-Wagner, A., Li, T. S., et al. 2015, ApJ, 808, 95
Simon, J. D., & Geha, M. 2007, ApJ, 670, 313
Simon, J. D., Geha, M., Minor, Q. E., et al. 2011, ApJ, 733, 46
Soumagnac, M. T., Abdalla, F. B., Lahav, O., et al. 2015, MNRAS, 450, 666
Tollerud, E. J., Bullock, J. S., Strigari, L. E., & Willman, B. 2008, ApJ, 688, 277
Trotta, R. 2007, MNRAS, 378, 72
van den Bergh, S. 2008, AJ, 135, 1731
Walker, M. G., Belokurov, V., Evans, N. W., et al. 2009, ApJL, 694, L144
Walker, M. G., Mateo, M., Olszewski, E. W., et al. 2015, ApJ, 808, 108
Walsh, S. M., Jerjen, H., & Willman, B. 2007, ApJL, 662, L83
Walsh, S. M., Willman, B., & Jerjen, H. 2009, AJ, 137, 450
Westmeier, T., Staveley-Smith, L., Calabretta, M., et al. 2015, MNRAS, 453, 338
Wetzel, A. R., Deason, A. J., & Garrison-Kimmel, S. 2015, ApJ, 807, 49
Wheeler, C., Oñorbe, J., Bullock, J. S., et al. 2015, MNRAS, 453, 1305
Willman, B. 2010, AdAst, 2010, 21
Willman, B., Blanton, M. R., West, A. A., et al. 2005a, AJ, 129, 2692
Willman, B., Dalcanton, J. J., Martinez-Delgado, D., et al. 2005b, ApJL, 626, L85
Willman, B., Geha, M., Strader, J., et al. 2011, AJ, 142, 128
Willman, B., & Strader, J. 2012, AJ, 144, 76
York, D. G., Adelman, J., Anderson, J. E., Jr., et al. 2000, AJ, 120, 1579
Yozin, C., & Bekki, K. 2015, MNRAS, 453, 2302
Zacharias, N., Finch, C. T., Girard, T. M., et al. 2013, AJ, 145, 44
Zucker, D. B., Belokurov, V., Evans, N. W., et al. 2006a, ApJL, 650, L41
Zucker, D. B., Belokurov, V., Evans, N. W., et al. 2006b, ApJL, 643, L103

Este artigo foi publicado no começo do período de meu doutorado e contou com dados de fotometria que foram compartilhados no artigo de Pieres et al. (2016). A determinação da completeza estelar da amostra do catálogo dos dados de verificação científica do DES neste artigo (Figuras 2 e 3) foi feita com base na fotometria apresentada nesta tese. Além disso, contribuí também no processo de revisão interna do paper.

MNRAS **449,** 1129–1145 (2015) doi:10.1093/mnras/stv356

The LMC geometry and outer stellar populations from early DES data

Eduardo Balbinot,[1,2,3★] B. X. Santiago,[2,3] L. Girardi,[4] A. Pieres,[2,3] L. N. da Costa,[3,5] M. A. G. Maia,[3,5] R. A. Gruendl,[6,7] A. R. Walker,[8] B. Yanny,[9] A. Drlica-Wagner,[9] A. Benoit-Levy,[10] T. M. C. Abbott,[8] S. S. Allam,[9,11] J. Annis,[9] J. P. Bernstein,[12] R. A. Bernstein,[13] E. Bertin,[14] D. Brooks,[10] E. Buckley-Geer,[9] A. Carnero Rosell,[3,5] C. E. Cunha,[15] D. L. DePoy,[16] S. Desai,[17,18] H. T. Diehl,[9] P. Doel,[10] J. Estrada,[9] A. E. Evrard,[19,20,14] A. Fausti Neto,[3] D. A. Finley,[9] B. Flaugher,[9] J. A. Frieman,[9,18] D. Gruen,[17,21] K. Honscheid,[22] D. James,[8] K. Kuehn,[23] N. Kuropatkin,[9] O. Lahav,[10] M. March,[24] J. L. Marshall,[16] C. Miller,[19,20] R. Miquel,[25,26] R. Ogando,[3,5] J. Peoples,[9] A. Plazas,[27] V. Scarpine,[9] M. Schubnell,[12] I. Sevilla-Noarbe,[28] R. C. Smith,[8] M. Soares-Santos,[9] E. Suchyta,[22] M. E. C. Swanson,[7] G. Tarle,[19] D. L. Tucker,[9] R. Wechsler[18,29] and J. Zuntz[30]

Affiliations are listed at the end of the paper

Accepted 2015 February 17. Received 2015 February 17; in original form 2014 October 9

ABSTRACT

The Dark Energy Camera has captured a large set of images as part of Science Verification (SV) for the Dark Energy Survey (DES). The SV footprint covers a large portion of the outer Large Magellanic Cloud (LMC), providing photometry 1.5 mag fainter than the main sequence turn-off of the oldest LMC stellar population. We derive geometrical and structural parameters for various stellar populations in the LMC disc. For the distribution of all LMC stars, we find an inclination of $i = -38.^{\circ}14 \pm 0.^{\circ}08$ (near side in the north) and a position angle for the line of nodes of $\theta_0 = 129.^{\circ}51 \pm 0.^{\circ}17$. We find that stars younger than ∼4 Gyr are more centrally concentrated than older stars. Fitting a projected exponential disc shows that the scale radius of the old populations is $R_{>4\,\mathrm{Gyr}} = 1.41 \pm 0.01$ kpc, while the younger population has $R_{<4\,\mathrm{Gyr}} = 0.72 \pm 0.01$ kpc. However, the spatial distribution of the younger population deviates significantly from the projected exponential disc model. The distribution of old stars suggests a large truncation radius of $R_{\mathrm{t}} = 13.5 \pm 0.8$ kpc. If this truncation is dominated by the tidal field of the Galaxy, we find that the LMC is $\simeq 24^{+9}_{-6}$ times less massive than the encircled Galactic mass. By measuring the Red Clump peak magnitude and comparing with the best-fitting LMC disc model, we find that the LMC disc is warped and thicker in the outer regions north of the LMC centre. Our findings may either be interpreted as a warped and flared disc in the LMC outskirts, or as evidence of a spheroidal halo component.

Key words: stars: statistics – Magellanic Clouds – galaxies: stellar content.

1 INTRODUCTION

The Milky Way (MW) satellite system offers a variety of examples of dwarf galaxies. Most of its members are essentially gas-free and contain mainly old stars (McConnachie 2012). The evolution of these systems is closely related to the formation of the Galaxy and the process of mass assembly of the large-scale structures in the Universe (Klypin et al. 1999; Moore et al. 1999; Stewart et al. 2008). On the other hand, the Large and Small Magellanic Clouds (LMC and SMC, respectively) are the closest low-mass, gas-rich (Grcevich & Putman 2009) interacting systems. The main features tracing the interaction history of the clouds are the H I Magellanic Stream (Mathewson, Cleary & Murray 1974), and Bridge (Hindman, Kerr & McGee 1963). A counterpart of the Stream was found and named the Leading Arm (Putman et al. 1998). The formation of these structures is a subject of great debate. Recent simulations favour a scenario where the Stream, Bridge, and Leading Arm are remains

★ E-mail: e.balbinot@surrey.ac.uk

from the close interaction between the LMC and SMC before falling into the MW potential (Besla et al. 2012; Kallivayalil et al. 2013).

The Clouds' star formation history (SFH) also reflects their close interaction history. It is possible to identify multiple periods of enhanced star formation that are arguably correlated with close encounter between the Clouds (Holtzman et al. 1999; Javiel, Santiago & Kerber 2005; Rubele et al. 2012; Meschin et al. 2014). Evidence of such events is imprinted in the stellar population which, due to the proximity of the Magellanic System, is resolved into individual stars with medium sized ground-based telescopes. Enhanced star formation is also demonstrated by the extensive star cluster system throughout the Magellanic Clouds (MCs). The clusters in this system span a very broad range in age and metallicity (Kerber & Santiago 2009). Evidence of an age-gap (Jensen, Mould & Reid 1988) may support a relationship between the formation/disruption rate of star clusters and the intergalactic interaction history. In this sense, the star clusters in the LMC may give hints to how the intergalactic interaction affects the evolution of star cluster systems (Renaud & Gieles 2013).

Despite being the nearest interacting system of galaxies, the Magellanic System still has only a small angular fraction observed to the photometric depth of its old main sequence turn-off (MSTO). Deep observations suggest that the LMC stellar populations extend beyond an angular distance of 15° from its centre (Majewski et al. 2009). There is also kinematic evidence for a dynamically warm stellar component consistent with a halo (Minniti et al. 2003) that has its major axis oriented with the disc (Alves 2004).

Very few studies are available in the outskirts of the LMC. Weinberg & Nikolaev (2001) report an exponential scalelength of $R_s \sim 1.4$ kpc with no significant distinction between a young and old disc; however, their sample is from the 2 Micron All-Sky Survey (2MASS; Skrutskie et al. 2006), which is very shallow and does not allow for a clear age selection. Saha et al. (2010) report a smaller scalelength of $R_s = 1.15$ kpc based on an optical survey. They argue in favour of a truncation radius of $R_t \sim 14$ kpc. Their sample is limited to only a few fields and their analysis does not use age selected stellar samples.

A new generation of photometric surveys is now coming to the Southern hemisphere, allowing for the first time a complete view of the Magellanic System. One of them is the Dark Energy Survey (DES)[1], which will observe the outskirts of the LMC, SMC, and most of the Magellanic Stream over the course of five years. DES is a photometric survey with the primary goal of measuring the dark energy equation of state. To achieve this goal, the survey will employ four independent cosmological probes: galaxy clusters, baryon acoustic oscillations, weak lensing, and Type Ia supernovae (Flaugher 2005). The total survey area is ∼5000 deg^2 reaching a magnitude limit of $i \sim 24$. The photometric system adopted for DES comprises the filters g, r, i, z, which are similar to the ones used in the Sloan Digital Sky Survey (Fukugita et al. 1996), with the addition of the Y passband, which provides synergy with the VISTA Hemisphere Survey (McMahon 2012) and the VISTA Magellanic Clouds survey (Cioni et al. 2011). The DES footprint will overlap with several other surveys in the Southern hemisphere allowing a multiwavelength approach to various astrophysical problems.

An early release of DES Science Verification (SV) data was made available to the DES collaboration recently. The data cover ∼200 deg^2 of the southern sky and sample regions as close as 4° north from the LMC centre. The photometric catalogue from this release reaches ∼1.5 mag fainter than the old MSTO of the LMC (which is at $g \sim 22$), allowing for a detailed study of the resolved stellar population of this galaxy.

In this paper, we use the DES SV data to study the LMC geometry and density profile as traced by stellar components with a characteristic age range. We model the distribution of stars using a simple projected exponential disc and perform a formal fit. We discuss the presence of a possible truncation radius and its implication for the LMC mass. As an alternative probe of the LMC geometry we use Red Clump (RC) stars as a distance indicator and a ruler for the LMC thickness. This paper is organized as follows. In Section 2, we present a brief introduction to the DES SV data. In Section 3, we discuss the quality of the photometry and address issues due to completeness and survey coverage. In Section 4, we describe the disc model and the fitting procedure used to find the geometrical parameters of the LMC. Section 5 shows our efforts to use the RC as a distance and thickness estimator. In Section 6, we summarize and discuss the implications of the results found in this paper.

2 DECam AND DES SCIENCE VERIFICATION

The Dark Energy Camera (DECam) (Flaugher et al. 2010) was constructed in order to carry out the DES. This instrument has a focal plane comprised of 74 CCDs: 62 2k × 4k CCDs dedicated to science imaging and 12 2k × 2k CCDs for guiding, focus, and alignment. The camera is also equipped with a five element optical corrector and a sophisticated cryogenic cooling system. DECam is installed at the prime focus of the Cerro Tololo Inter-American Observatory (CTIO) 4 m Blanco telescope. In this configuration, DECam has a 2.2 degree-wide field-of-view (FoV) and a central pixel scale of 0.263 pixel^{-1}. In typical site conditions, the Blanco telescope plus DECam yield an imaging point spread function with full-width half-maximum (FWHM) of 0.9 parsec, which is adequately sampled by the pixel scale.

DECam was commissioned in 2012 September and began operations in 2012 November, with the DES SV campaign covering a period of three months. The DES SV data are intended to test capabilities of the camera, the data transfer infrastructure, and the data processing. All images taken during SV are public; however, the catalogues generated by the collaboration are proprietary.

2.1 Data reduction

The DES data management (DESDM) team was responsible for the reduction of the SV images. Here, we will give a brief description of the reduction process. For a complete description, we refer to Sevilla et al. (2011), Desai et al. (2012), and Mohr et al. (2012).

The DESDM data reduction pipeline consists of the following steps.

Image detrending: this step includes correction for cross-talk between CCD amplifier electronics, bias level correction, correction for pixel-to-pixel sensitivity variation (flat-fielding), as well as corrections for non-linearity, fringing, pupil, and illumination.

Astrometric calibration: in this step, bright known stars are identified in a given image using SExtractor (Bertin & Arnouts 1996). The position of these stars in the focal plane is used to find the astrometric solution with the aid of the software scamp (Bertin 2006) through comparison to UCAC-4 (Zacharias et al. 2013).

Nightly photometric calibration: several reference stars are observed each night, and a photometric equation is derived for that night. This equation takes into account a zero-point, a colour term, and an airmass term for each of the DECam science CCDs.

[1] http://www.darkenergysurvey.org/

Table 1. Here, we show a subset of the SExtractor parameters measured for the co-added DECam SV data. We also show any selection criteria that were made.

Parameter name	Selection
RA	–
DEC	–
MAG_AUTO_*	≤ 26.0 in g and r
MAGERR_AUTO_*	–
SPREAD_MODEL_*	$\lvert$SPREAD_MODEL_I$\rvert \leq 0.002$
FLAGS_*	≤ 3 in g and r

Note. The * symbol refers to all passbands available.

Global calibration: relative photometric calibration of the DES survey area is done with repeated observations of the same star in overlapping DECam exposures using a method similar to that described in Glazebrook et al. (1994). The relative magnitudes are anchored to a small set of absolutely calibrated reference stars within the same area called tertiary standards which come from observations on photometric nights. They are then calibrated relative to known equatorial belt standards observed on the same night with the same filter set (Tucker et al. 2007). The current accuracy of the relative and absolute systems is a few per cent, and is expected to improve as the DES survey covers larger contiguous areas. DES calibration was checked using the Star Locus Regression technique (Kelly et al. 2014). This analysis revealed that zero-point offsets are typically less than 0.05 mag in g, r, i, and z across the DES footprint observed so far.

Coaddition: in order to increase the signal-to-noise ratio, exposures are combined. This has the advantage of mitigating transient objects, such as cosmic rays and satellite trails. This step requires the placement of the images in a common reference projection. The software SWarp (Bertin et al. 2002) was used and the co-addition process was done in segments of the sky called *tiles*. At this stage the flux is corrected according to the photometric calibration described above.

Cataloging: for each co-added *tile* source detection and model-fitting photometry is performed using PSFEx and SExtractor (Bertin & Arnouts 1996; Bertin 2011) on a combined r, i, and z image. Object fluxes and many other characteristics are calculated in the individual g, r, i, z, Y frames. These catalogues are ingested into a high-performance data base system.

The final catalogue is available for the DES collaboration through a data base query client. There are approximately 900 parameters measured for each source identified by SExtractor. In Table 1, we list a few parameters relevant to this work. In the same table, we also list any comments about the parameter and the quality cuts applied.

3 THE SV DATA

By the end of the SV campaign, DECam had obtained images in five passbands of a region with roughly 300 deg^2, for which 200 deg^2 are contiguous. The contiguous region covers the northern outskirts of the LMC. This region overlaps an eastern portion of the South Pole Telescope (SPT) footprint (Carlstrom et al. 2011). Hence, we call it SPT-E for simplicity.

In this section, we will discuss several aspects of the SV data and how it is suitable for the analysis we propose.

3.1 Photometry

Currently, the deepest and most homogeneous magnitude measurement resulting from the DESDM pipeline is MAG_AUTO, which is computed using the flux inside a Kron radius (Kron 1980). The Kron radius is dependent on how extended a source is, hence the aperture is variable, but it is essentially the same for all stars, given that there are no significant spatial dependence in the image quality, which is the case for DES observations. Thus, MAG_AUTO is roughly equivalent to a simple aperture magnitude but less sensitive to seeing variations. We adopt the following notation throughout the paper: g is the MAG_AUTO magnitude measured for the g passband. This also applies for the magnitudes measured in r, i, z, Y.

The raw DESDM catalogue has approximately 10^8 sources with $g \leq 24.6$. This list includes spurious detections like satellite trails, star wings, cosmic rays, etc. To exclude such detections from our catalogue, we adopt a simple cut in the FLAGS parameter. We select only sources that simultaneously have FLAGS_G and FLAGS_R ≤ 3, which selects objects that are not saturated and do not contain any bad pixel. The FLAGS code is the same as the one adopted by SExtractor. The number of sources left after this cut is $\sim 9 \times 10^7$.

We check the stability of the photometric calibration provided by DESDM by comparing the RC peak colour at different points of the SPT-E that contain LMC stars. For all bands, we found a maximum scatter of 0.02 mags around the RC peak colour.

The following model was adopted to describe the photometric uncertainties from the DECam SV data.

$$\sigma(\mathrm{mag}) = a + \exp\left(\frac{\mathrm{mag} - b}{c}\right). \quad (1)$$

By fitting the above equation to a sample of 0.01 per cent randomly chosen stars from the SPT-E region, we find the error curves shown in Fig. 1. The coefficients for each curve are given on Table 2, where we also show the 10 per cent uncertainty magnitude for each band. Along with these values, we also give some basic information about the filter central wavelength and extinction coefficients at those wavelengths from Cardelli, Clayton & Mathis (1989).

3.2 Star/Galaxy separation

The DES collaboration has generated several data sets for validating and testing the DESDM system (Mohr et al. 2012). These data sets were simulations of the actual observations. To create these *mock* observations, input catalogues of artificial galaxies and stars were generated (Rossetto et al. 2011; Balbinot et al. 2012; Busha, in preparation). The mock observations included a time varying seeing, realistic shapes for the galaxies, and variations to the focal plane of DECam. These images were fed into the DESDM reduction pipeline and an output catalogue was generated, which was then released to the collaboration to perform tests of their scientific algorithms.

Tests with a set of such simulations, called Data Challenge 5 (DC5) by the collaboration, have been carried out in order to assess how different star–galaxy classification parameters perform. A summary of this comparison is shown in Rossetto et al. (2011). The main conclusion is that SPREAD_MODEL (Desai et al. 2012; Bouy et al. 2013) performs better in terms of purity and completeness than other typically employed classifiers such as CLASS_STAR and FLUX_RADIUS (Bertin & Arnouts 1996). Later, Soumagnac et al. (2013) developed a more sophisticated star–galaxy separation algorithm; however, this algorithm must be trained on a data set where true stars and galaxies are known. Implementation of such methods is being considered collaboration wide. For

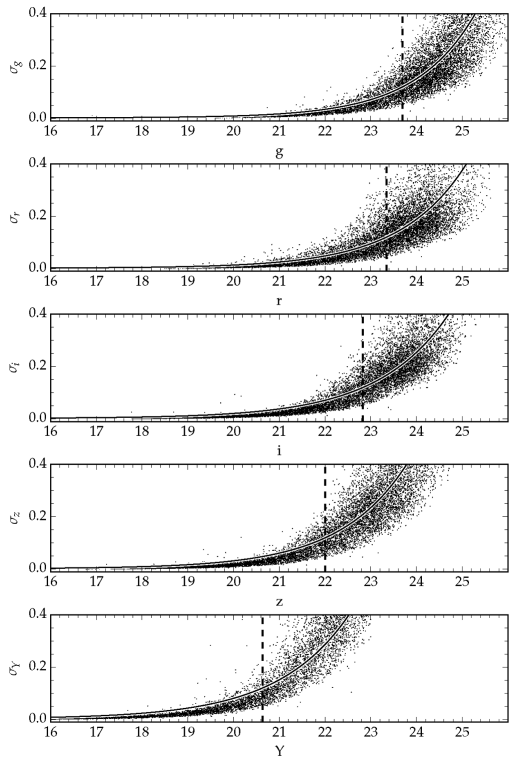

Figure 1. Magnitude versus uncertainty for a sample of 0.01 per cent of the total number of stars in the DECam SV region. The solid curve shows the best-fitting error model. The coefficients are given in Table 2. The dashed line shows the 10 per cent uncertainty magnitude.

Table 2. Some general photometric system information: the central wavelength (λ_c) in nanometres, the extinction as a fraction of the extinction in the Johnson V passband (assuming $R_V = 3.1$ and a Cardelli et al. (1989) extinction curve for the MW), and the value of the magnitude corresponding to a typical signal-to-noise ratio of 10. In the last three columns, the coefficients of the best-fitting error model are shown.

Filter	λ_c (nm)	A_λ/A_V	$m_{10\,\mathrm{per\,cent}}$	(a, b, c)
g	479	1.199	23.94	(0.001, 26.41, 1.25)
r	641	0.837	23.76	(0.001, 26.34, 1.27)
i	781	0.635	22.75	(0.003, 25.52, 1.34)
z	924	0.462	22.03	(0.003, 24.75, 1.43)
Y	1008	0.400	20.50	(0.009, 23.45, 1.40)

simplicity, we choose to use SPREAD_MODEL measured in the i band as the star–galaxy separator. The cut-off criterion for selecting stars is |SPREAD_MODEL_I| ≤ 0.002. From test on DC5, this cut is found to correspond to a simultaneous stellar completeness and purity of $\simeq$80 per cent for objects with $g < 23$ (Rossetto et al. 2011). From this point further we call objects that match this cut-off criteria *stars*. It is worth mentioning that at $g = 23$ we expect $\sim$20 per cent of contamination from galaxies in our sample. However, the large-scale distribution of these objects is homogeneous and is unlikely to significantly affect the findings of this paper.

3.3 Completeness

To independently assess the completeness of the DESDM catalogue, we conducted a few experiments using DAOPHOT (Stetson 1987). This photometry code is known to perform very well in extremely crowded regions such as the cores of globular clusters (Balbinot et al. 2009). Hence, at the typical density of LMC field stars it should yield a fairly complete catalogue. This DAOPHOT catalogue may be compared to the one produced by DESDM as an approximation to a complete catalogue and giving an estimate of the completeness as function of magnitude. This is not the most accurate approach to this problem; however, it is much simpler than performing artificial star experiments across several hundred squared degrees.

We performed DAOPHOT photometry on 51 fields, 50 of which contained an LMC star cluster in its centre. The 51st field was selected as far away as available in the SPT-E data in order to sample a region where there are few or no LMC stars. The fields selected are subregions of the co-added images encompassing 6.75 arcmin $\times$ 6.75 arcmin each, with the exception of the 51st field, which has 18 arcmin $\times$ 36 arcmin. The first 50 fields were selected in order to assess the completeness not only in regions with a density of stars typical of the LMC, but also with varying density, such as the inner regions of a star cluster. A broader discussion about this subject will be presented in a future paper. The 51st field was selected in order to compare the performance of the DESDM reduction pipeline in a region with little or no crowding. The position of each of the all 51 fields is marked on Fig. 2. On average DESDM and DAOPHOT photometry agree within 0.02 in g and r.

To compare the number of stars as a function of magnitude, we cut both the DESDM and DAOPHOT catalogues at the 3 per cent photometric uncertainty level. This cut happens at $g \simeq 23.5$. To separate stars from galaxies in DAOPHOT, we adopted a cut in the *sharpness* parameter which behaves similarly to SPREAD_MODEL.

In Fig. 3 top panel, we show the ratio between the number of stars detected by DESDM and DAOPHOT ($N_{\mathrm{DES}}/N_{\mathrm{DAOPHOT}}$) averaged in magnitude bins for the 51 fields discussed above. The solid line shows the average value at a given magnitude bin. The shaded region shows the standard deviation. In the two bottom panels in the same figure, we show the value of $N_{\mathrm{DES}}/N_{\mathrm{DAOPHOT}}$ as a function of angular separation to the LMC centre. We show this for two magnitude bins: $21.8 < g \leq 22.6$ and $22.6 < g \leq 23.3$ (also indicated in the figure). From Fig. 3, we notice that the average completeness drops as a function of increasing magnitude, as expected. The completeness remains roughly constant as a function of angular separation to the LMC centre with a spread of the same order as the one shown in the shaded region of the top panel. We conclude that the completeness has little spatial dependence at least up to magnitudes as faint as $g \sim 23$.

Despite the good performance in moderately crowded fields (i.e. LMC field population), we observed that in the inner regions of star clusters the DESDM sample is highly incomplete reaching less than 40 per cent completeness for $g = 19$ and dropping to zero for fainter magnitudes. This will be further explored in future publications.

We note that where the completeness is most important to our results regarding truncation radii and scalelengths, i.e. at distances farther away from the centre of the LMC, the star density is low enough that crowding effects do not affect the sample selection as shown in Fig. 3.

From the completeness analysis described above, we conclude that in the DESDM catalogue completeness does not depend strongly on source density, except in extremely crowded

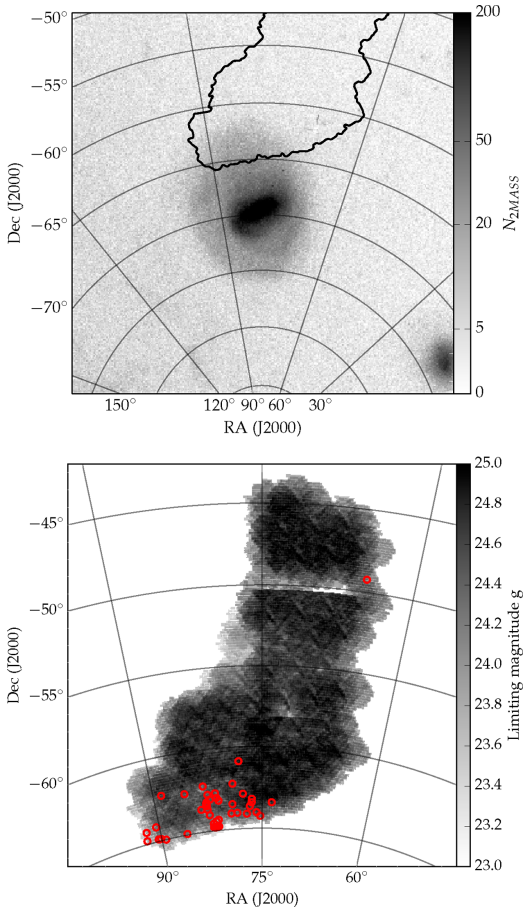

Figure 2. Top panel: Gnomonic projection of the number of 2MASS stars that are consistent with AGB and RGB stars according to Yang et al. (2007). The projection is centred in the LMC centre. Part of the SMC is visible in the lower-right corner. The solid contour shows an approximate footprint of the southern part of the SPT-E region of the DES SV data. Bottom panel: Gnomonic projection of a $N_{side} = 4096$ HEALPIX map of the g magnitude limit MANGLE mask for the SPT-E region quoted above. Holes and unobserved regions are masked and shown in white. Red circles mark the position of the fields selected for assessing the survey completeness.

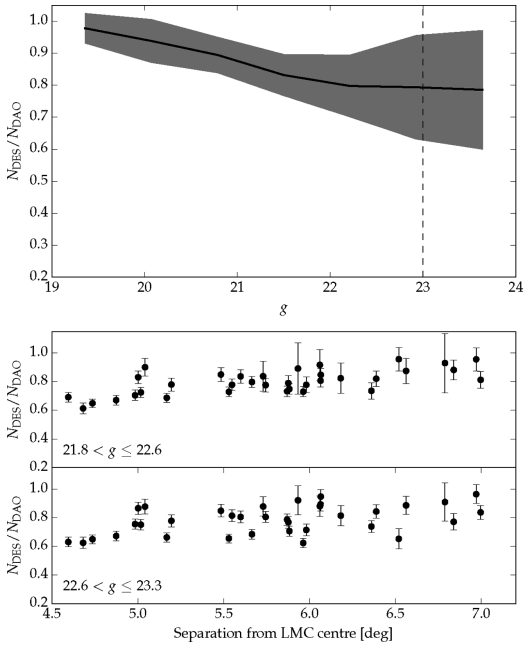

Figure 3. Top panel: we show the ratio of stars detected by DESDM and DAOPHOT as a function of g magnitude. The solid line shows the average for the 51 fields analysed. The shaded region shows the standard deviation for the 51 fields. The dashed vertical line shows the faintest magnitude limit used in this work. Bottom panels: black circles show the same ratio as in the top panel but now as a function of angular separation to the LMC centre for two magnitude bins (indicated in the captions). The error bars are computed using the Poisson uncertainty.

environments such as the central parts of stars clusters. From visual inspection and through comparison with state-of-the-art crowded field photometry methods we find no strong evidence for large-scale variations in the stellar completeness in the SPT-E region, thus allowing us to properly access the spatial distribution of stars across its footprint, either from the LMC or from the MW.

3.4 Mangle masks

We use the MANGLE software (Swanson et al. 2008) to track the survey coverage and limiting magnitude. Along with the release of the DESDM catalogues, a set of MANGLE masks was also provided. These masks contain information about the limiting magnitude in each patch of the sky, as well as other key information about data quality. The magnitude limit is computed as the detection limit of a point source with signal-to-noise ratio S/N = 10. The noise is estimated from the variance and level of the sky on a patch of the sky. To measure the flux an aperture of 1 arcsec radius is used; this yields a magnitude measurement called `MAG_APER_4`. For a complete description of the masks, we refer to Swanson et al. (2012).

In Fig. 2, we show the number of asymptotic giant branch (AGB) and red giant branch (RGB) stars found in 2MASS according to Yang et al. (2007) with the southern limits of the SPT-E region overplotted (top panel). We also show an approximation of the magnitude limit MANGLE mask for the SPT-E region (bottom panel). It is an approximation in the sense that it uses the value of the MANGLE mask at the central position of each pixel in the sky. The grey-scale represents the magnitude limit at each point of the footprint. Holes caused by bright stars or other image imperfections are displayed as well. These regions have a magnitude limit of zero, hence going out of the grey-scale range. The white colour in the figure represents regions that were not observed. The figure uses a HEALPIX pixelization (Górski et al. 2005) with $N_{side} = 4096$ and a Gnomonic projection centred at $(\alpha, \delta) = (75^\circ, -55^\circ)$.

The approximate mask discussed above allows us to deal with the full SPT-E mask in a much faster way and at the same time to provide a very good approximation of the general properties of the survey, such as coverage and magnitude limits. The coverage mask is simply a HEALPIX map with the value of 1 for pixels that were observed and 0 for those that were not or were masked for some reason. The coverage mask originally did not contain holes due to star clusters. To mask these regions, we conducted a visual search

for star clusters in the SPT-E and used the position of each cluster to add a hole in the mask (i.e. a region with coverage equals to zero).

The approximated masks were used to remove stars residing in regions where the following criteria were met: (i) a limiting g or r magnitude brighter than 23; (ii) coverage value equal to 0. The additional trimming for zero mask values was necessary because the original catalogue was limited by the *exact* masks, not the approximated ones.

The above section outlines the process of trimming the catalogue to select objects that are likely stars and to keep only regions with deep photometry that were not affected by artefacts in the survey. This catalogue, as well as the mask associated with it, will be used in the remainder of this paper.

4 THE LMC GEOMETRY

Classically, the LMC is classified as an Irregular Dwarf Galaxy, although it has several major components of a spiral galaxy such as a disc and a bar. It is, perhaps, more appropriate to classify this galaxy as a highly perturbed spiral galaxy. Its morphology departs so much from a classical Irregular Dwarf that it has been established that the LMC is the prototype of a class of dwarf galaxies called Magellanic Irregular (de Vaucouleurs & Freeman 1972). These galaxies are characterized by being gas-rich, one-armed spirals with off-centre bars.

The SMC is the closest neighbour to the LMC. Together they form the Magellanic System. Recent dynamical modelling (Besla et al. 2012) and high precision tangential velocity measurements (Kallivayalil et al. 2013) point to the need for updated thinking with regard to the origins of the Magellanic System. The centre of mass spatial velocity of these galaxies is very close to the escape velocity of the MW, thus suggesting that the system is not gravitationally bound to the MW. The same models also predict the formation of the Magellanic Bridge and Stream as a result of the interaction of the LMC with the SMC, generating long arms of debris in the same fashion as the Antennae system.

Despite the growing number of simulations and high precision velocity measurements, a few aspects of the LMC geometry, such as the presence of a spheroidal halo (Majewski et al. 2009), and the warping and flaring of the disc (Subramaniam & Subramanian 2009) remain uncertain to some degree. New large area surveys in the Southern hemisphere are beginning to shed light on these uncertainties.

Here, we study the LMC disc geometry using a very simple approach. We try to model its stellar density using a circular exponential disc. This disc is inclined relative to the sky plane by the angle i. To compute the expected number of stars ρ as a function of α and δ we use the transformations found in Weinberg & Nikolaev (2001). For the sake of clarity, we give the expression for the heliocentric distance t to a given point of the disc with coordinates (α, δ).

$$t(\alpha,\delta) = -R_{\rm LMC}\cos i \times \{\cos\delta\sin(\alpha-\alpha_0)\sin\theta\sin i + [\sin\delta\cos\delta_0 - \cos\delta\sin\delta_0\cos(\alpha-\alpha_0)]\cos\theta\sin i - [\cos\delta\cos\delta_0\cos(\alpha-\alpha_0) + \sin\delta\sin\delta_0]\cos i\}^{-1}, \quad (2)$$

where (α_0, δ_0) is the central coordinate of the LMC, i is the disc inclination, $R_{\rm LMC}$ is the heliocentric distance to the LMC centre, and θ the position angle (PA) of the minor axis. In the reference frame adopted here, the inclination i has negative values when the north side of the LMC is closer to us. In the reference frame adopted, the i angle is reversed to what is typically adopted in the literature.

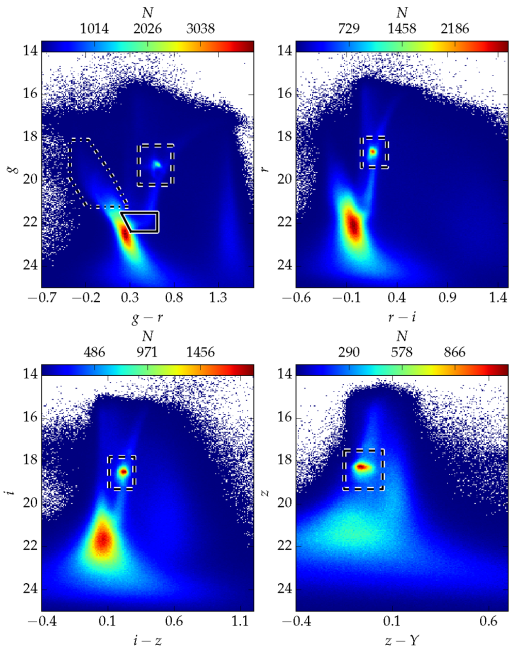

Figure 4. The Hess diagrams in each set of colour and magnitude available in the DES photometric system. In the top-left panel, we also show the colour–magnitude polygons used to select stars consistent with a young/intermediate (dot–dashed polygon) and old (solid polygon) stellar population. The boxes (dashed) used for the selection of RC stars are shown in all panels.

The density of stars is simply given by

$$\rho(\alpha,\delta) = \rho_0 t(\alpha,\delta)^2 \exp(-R/R_{\rm s}) + \rho_{\rm BG} f(\alpha,\delta), \quad (3)$$

where R is the radial distance in the disc plane, $R_{\rm s}$ is the scalelength of the exponential disc, $\rho_0 t(\alpha_0, \delta_0)$ is the central density, and $\rho_{\rm BG}$ is the density of background/foreground stars. The function $f(\alpha, \delta)$ is a third degree polynomial which takes into account the spatial variation of MW field stars.

Five parameters are used to model the disc geometry: the LMC central coordinates (α_0, δ_0), its distance to the Sun ($R_{\rm LMC}$), the inclination i, and the PA θ. Additionally, three parameters describe the density of stars along this disc: the central density ρ_0, the scale radius $R_{\rm s}$, and the density scale of background stars $\rho_{\rm BG}$.

To simplify the problem and to better accommodate the fact that the observations are all on the northern side of the MCs, we make a few assumptions. The LMC centre is kept fixed at the Nikolaev et al. (2004) value of $(\alpha_0, \delta_0) = (79.^\circ40, -69.^\circ03)$. The heliocentric distance to the LMC centre $R_{\rm LMC} = 49.9$ kpc is adopted from the most recent review about the subject (de Grijs, Wicker & Bono 2014).

With the machinery to produce LMC disc models, we proceed to a formal fit to the observed distribution of stars in the SPT-E region. This fit was performed on three samples of stars. The selections were made based on PARSEC (Bressan et al. 2012) stellar evolution models. The first is made only of stars older than 4 Gyr, selected using a colour–magnitude cut shown in Fig. 4. The second sample

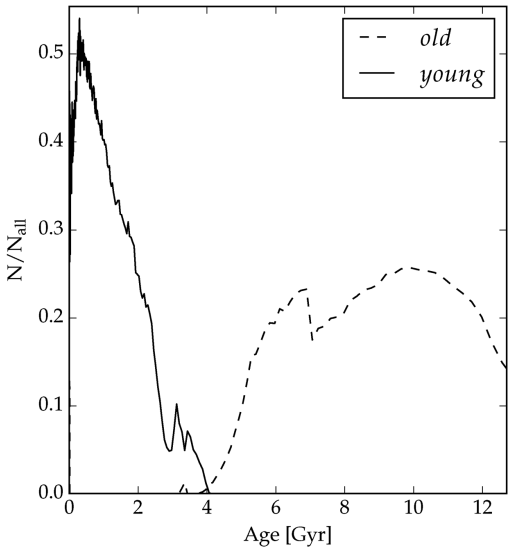

Figure 5. Ratio of the number of young (old) to all stars as a function of age. The ratio was computed using a constant SFR and a Piatti & Geisler (2013) AMR.

selects only stars younger than 4 Gyr. The third sample is made of stars that fall within the limits $17 < g < 23$ and $-0.5 < g - r < 1.0$. We name these samples *old*, *young*, and *all* for simplicity. In Fig. 5, we show the ratio of *old* (*young*) and *all* stars for a simulated LMC stellar population that assumes a constant star formation rate (SFR) and a Piatti & Geisler (2013) age–metallicity relation (AMR). Photometric errors were simulated according to equation (1) and Table 2. We observe that the colour–magnitude cuts chosen are able to create two samples with virtually no age overlap.

Using a TRILEGAL (Girardi et al. 2005) simulation, we modelled the expected MW stellar population in the SPT-E region. Assuming the same colour cuts as the ones used to select the three stellar populations quoted above, we fit the density of stars as a function of RA and Dec using a third-order polynomial, $f(\alpha, \delta)$. The best-fitting polynomial for each of the stellar populations cuts is later used to account for foreground contamination while fitting the LMC disc. This polynomial is scaled by $\rho_{\rm BG}$ since the colour–magnitude cuts are not perfectly consistent with the theoretical prediction of TRILEGAL.

To count stars in the sky plane, we adopt the HEALPIX pixelization scheme with $N_{\rm side} = 512$ which yields a constant pixel area across the sky of $\sim$0.013 deg^2. The maps built in this scheme for each stellar sample described above are shown in the left-hand panel of Figs 6–8.

The best-fitting disc model was obtained through a Markov Chain Monte Carlo (MCMC) technique. We used the code EMCEE (Foreman-Mackey et al. 2013) in its version 2.0.0. The test statistics chosen is a binned Poisson log-likelihood model (Dolphin 2002). We refer the reader to these authors for details on the MCMC and statistics used. This is the most appropriate test statistics for data-model comparison since we are dealing with counts that are subject to shot noise, especially in the outermost regions of the LMC. Our MCMC run uses a total of 30 walkers that make 1000 steps each for the *burn-in* phase. After the *burn-in*, we let the walkers advance 5000 more steps each, sufficient to well sample the parameter space and converge to the maxima.

This fitting procedure was repeated for each stellar population (*all, old,* and *young*), yielding the parameters shown on Table 3. In this table, we chose to present the PA of the line of nodes $\theta_0 = \theta + 90^\circ$. This is the quantity most often presented in the literature.

The boxes chosen to select a given stellar population in the colour–magnitude diagram (CMD) assume that the stars are all at the same distance to us. This is not strictly the case for the LMC stars, which are spread across a disc plane inclined relative to the sky plane. To test how this distance spread affects our disc fit, we correct the magnitude of each star using the best-fitting disc models so as to bring the stars to a common distance. This common distance is chosen as the mean distance to the disc in the SPT-E. Using these distance corrected magnitudes we perform the CMD box selections again. For all the CMD based selections an increase of <1 per cent in the number of stars inside the CMD box is observed. Using this distance corrected sample we rerun the fitting procedure and find that the largest change in the parameters is a 5 per cent increase in the inclination. The remaining disc parameters are more stable. We adopt the difference on the parameters found in this experiment as the systematic uncertainty in our parameter estimation. We show these variations as the uncertainties in parenthesis in Table 3.

The left-hand panel of Fig. 6 a HEALPIX map in Gnomonic projection shows the logarithm of the number of stars for the *all* stellar population. Overplotted we show the best-fitting disc model as iso-density lines. On the right-hand side of the figure, we show the sampled probability distribution function for each parameter after marginalization. In light blue we mark the point of maximum probability density, which indicates the maximum likelihood solution. Note that the samples are distributed in a fairly symmetric way around the maxima, yielding symmetric error bars. Figs 7 and 8 are similar to the figure described above, but showing different age-selected populations.

We notice that the *old* population spreads out to declinations of $\sim -55^\circ$, while the *young* population is much more abruptly truncated at $\sim -60^\circ$. This points to different scale radii for these populations. In Table 3, we give a summary of the parameters that best fit each case. Here, we see that the distributions have significantly different values of $R_{\rm s}$ while retaining similar values for the purely geometrical parameters θ_0 and i.

The difference in the scalelength is much more obvious in Fig. 9 where we show, for each stellar population, the average number of stars per HEALPIX pixel in bins of distance along the LMC disc. We also show the best-fitting disc model for each of the stellar populations, this model includes the MW foreground stars (i.e. the term $\rho_{\rm BG} f(\alpha, \delta)$ in equation 2). We notice that the *old* (triangles and dot–dashed line) profile is much more extended than the *young* one (crosses and dotted line). It is also remarkable that the LMC *old* density profile is well fit without the need for other components such as a spheroidal halo. However, the *young* profile is not very well described by the disc model. This could also account for the value found for its inclination, which is not in good agreement with the literature (van der Marel & Cioni 2001; Nikolaev et al. 2004; Rubele et al. 2012). In the same figure, the solid line shows the contribution of MW stars, we notice that the slope in the number of stars at the outskirts of the LMC can be accounted by for the spatial variation in the number of MW field stars. Due to the large number of stars in each radial bin, the Poisson uncertainty is very low. These uncertainties are only visible, as error bars, on the inset plot, where the outer parts of the *old* population profile is shown.

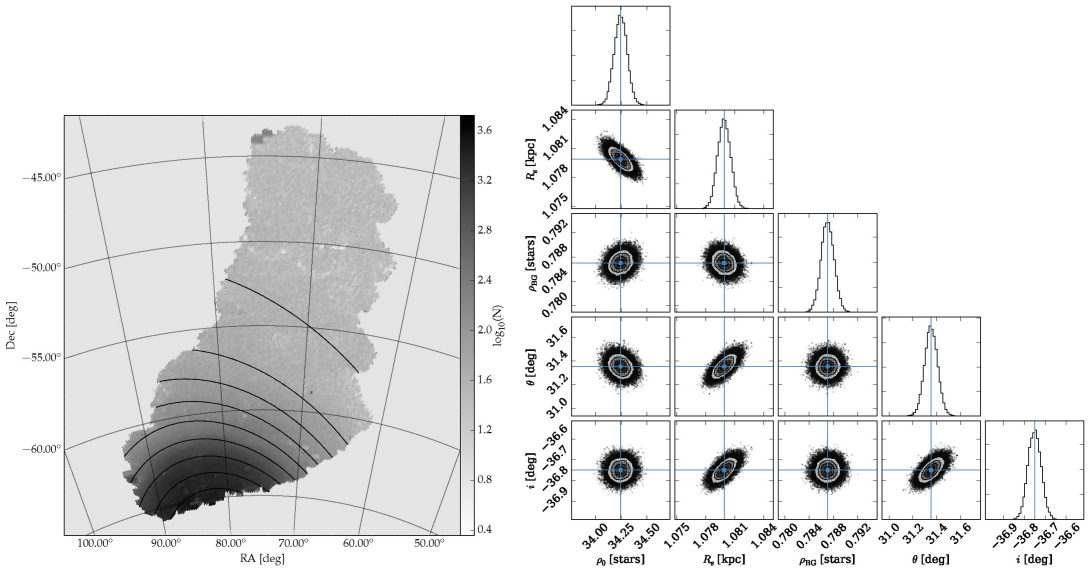

Figure 6. Left-hand panel: map showing the number of stars from the all sample in grey-scale. The stars used to build this map are those that fall inside a simple colour cut of $-0.5 < g - r < 1.0$ and $g < 23$. The solid isodensity contours show the best exponential disc model. The contours start at $\log_{10}(N) = 3.3$ and progress in steps of 0.3 dex. Right-hand panels: the marginalization for the different disc model pairs of parameters. The solid blue cross-hair shows the position of the best solution. The contours show the 1σ, 2σ, and 3σ confidence levels. The histograms in the diagonal panels show the marginalization over each single parameter. Again the blue line shows the point of maximum likelihood.

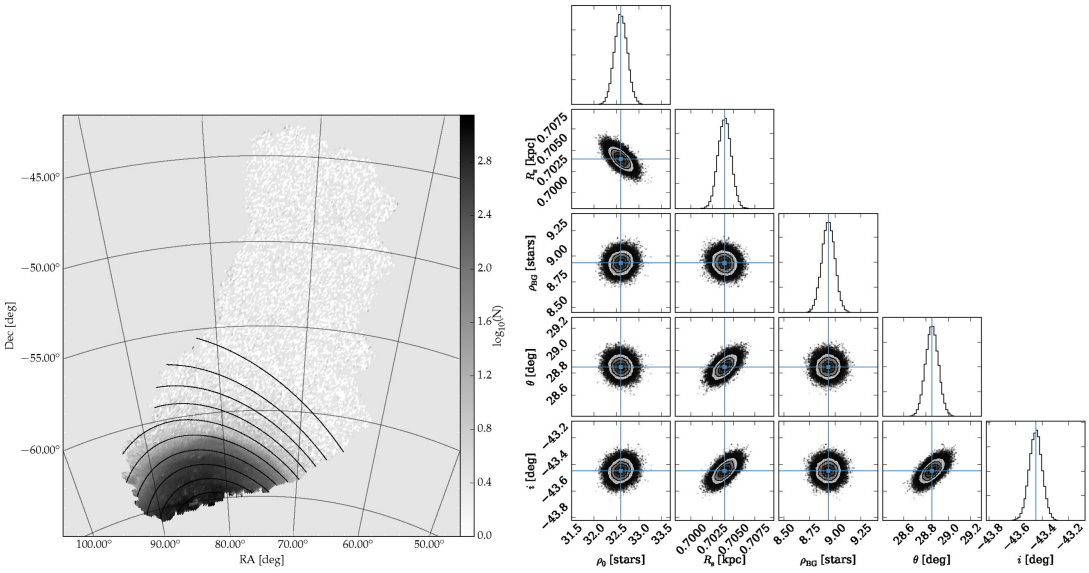

Figure 7. Similar to Fig. 6 but for the young stellar population. The isodensity contours start at $\log_{10}(N) = 2.9$ and progress in steps of 0.4 dex.

We notice from Table 3 that the statistical uncertainties in the disc parameters are quite small. This is caused by the relatively poor description that our disc model gives of the LMC stellar population, especially the *young* population. In Fig. 9 this becomes apparent where we observe that the models deviate significantly from the observations, even when the uncertainties are considered. This can point to the case where there are other systematic effects that were not taken into account. One cause of such effects might be the spatial variation of the star–galaxy classifier. However, the classifier adopted here is very stable especially at bright magnitudes ($g < 22.5$), thus being improbable to be a significant source of error. Also, spatial changes in the completeness of the survey are unlikely

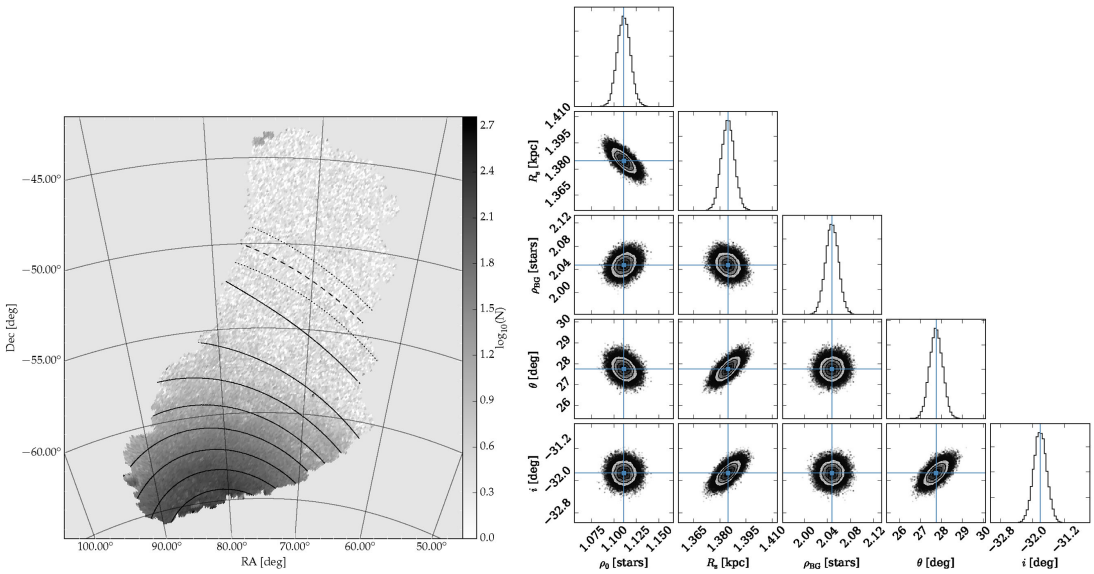

Figure 8. Similar to Fig. 6 but for the old stellar population. The isodensity contours start at $\log_{10}(N) = 2.5$ and progress in steps of 0.35 dex. In the left-hand panel, we also show the truncation radius (R_t) position as the dashed contour, and the dotted contours show the uncertainty in R_t.

Table 3. A summary of the best-fitting disc models parameters for each stellar population. The uncertainties are the 3σ confidence level that arises from the MCMC analysis. The uncertainties in parenthesis are obtained from the difference between the fit with and without correcting the magnitudes by the heliocentric distance to each point of the LMC disc. NOTE: our definition of inclination (i) has the opposite sign than what is typically found in the literature.

Population	Age (Gyr)	θ_0 (deg)	i (deg)	R_s (kpc)	ρ_0 (stars pixel^{-1} kpc^{-2})	ρ_{BG}
All	–	$129.51 \pm 0.17(\pm1.08)$	$-38.14 \pm 0.08(\pm1.59)$	$1.09 \pm 0.01(\pm0.02)$	$26.41 \pm 0.14(\pm0.59)$	$0.80 \pm 0.03(\pm0.67)$
Young	0–4	$125.93 \pm 0.20(\pm0.09)$	$-44.19 \pm 0.14(\pm1.80)$	$0.72 \pm 0.01(\pm0.00)$	$22.86 \pm 0.28(\pm1.33)$	$9.06 \pm 0.18(\pm0.00)$
Old	4–13	$127.40 \pm 1.02(\pm0.59)$	$-32.94 \pm 0.39(\pm1.25)$	$1.41 \pm 0.01(\pm0.00)$	$0.89 \pm 0.02(\pm0.05)$	$2.08 \pm 0.04(\pm0.01)$

to cause a large change in the number of stars per HEALPIX pixel (see Section 3.3). Evidence indicates that the deviations from the fitted disc model are real features of the LMC structure. These features are more apparent for the *young* stellar population, which is most likely to hold signs of disc perturbations such as spiral arms.

We use the *old* population profile to probe the total extent of the LMC. We define the truncation radius as the radius where the observed density profile reaches becomes indistinguishable from the MW foreground population. In the inset plot of Fig. 9, we observe that for $\log(R/\mathrm{kpc}) > 1.13$ the profile can be explained solely by the MW contribution. The uncertainty on this truncation radius (R_t) is taken as the size of the radial bin, which is 0.8 kpc. This yields a $R_t = 13.5 \pm 0.8$ kpc.

If we assume that the LMC luminous component is tidally truncated by the MW potential, we can use the simple theoretical tidal radius formula (Binney & Tremaine 2008), given by

$$R_t = d_{LMC} \left(\frac{M_{LMC}}{2M_{MW}(d < d_{LMC})} \right)^{1/3}, \quad (4)$$

we find the following relation for the LMC mass (M_{LMC}) and the MW mass (M_{MW}) encircled within a radius equal to the Galactocentric distance of the LMC (d_{LMC}):

$$M_{MW}(d < d_{LMC}) = 24.5^{+8.8}_{-6.4} \times M_{LMC}, \quad (5)$$

where the Sun is assumed to be at a distance of $d_\odot = 8.0$ kpc from the MW centre. This yields a d_{LMC} of 49.4 ± 2.1 kpc. The uncertainty in this value was considered for the result in equation (5). The distance to the Sun is taken as a compromise between two recent determinations from Eisenhauer et al. (2005) and Gillessen et al. (2009). The adoption of $d_\odot = 8.5$ kpc would increase d_{LMC} by ~ 0.03 per cent, leading to an insignificant increase in R_t. Thus, we choose to disregard the uncertainty in $d_\odot$.

To further support our claim that there are very few LMC stars beyond 13 kpc, we show in Fig. 10 the Hess diagrams at different bins of angular separation from the LMC centre. The upper and lower bound of each bin is indicated in each panel. We apply a simple decontamination algorithm in order to remove the contribution of MW stars. The decontamination was done by selecting a region with angular distance greater than $\theta = 20^\circ$. A Hess diagram of this region was constructed. These Hess diagrams were area weighted and subtracted from the Hess diagram of each angular separation bin shown in Fig. 10. This process assumes that the contribution of LMC stars at angular distances larger than 20° is negligible.

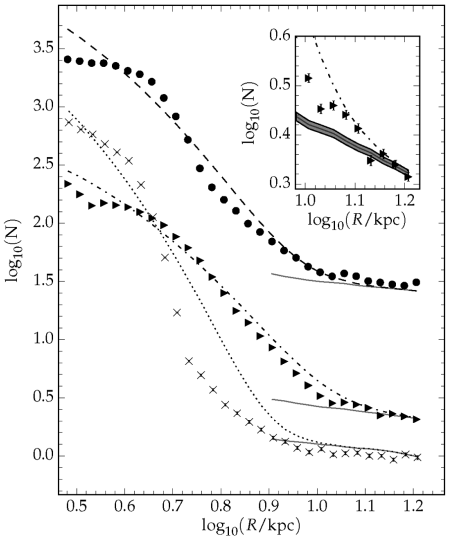

Figure 9. The black circles show the averaged number of stars from the all sample per HEALPIX pixel in different bins of distances along the LMC disc. The triangles (crosses) show the same but for the old (young) sample. The dashed, dot–dashed, and dotted lines show the best-fitting disc model for the all, old, and young populations, including the term $\rho_{\rm BG} f(\alpha, \delta)$ that accounts for the contamination of MW stars. In the inset plot, we show the outer tail of the old profile. The solid line shows the MW contribution and the shaded region shows its uncertainty, propagated from the uncertainty in $\rho_{\rm BG}$. The error bar represents the Poission uncertainty on the number of counts per bin.

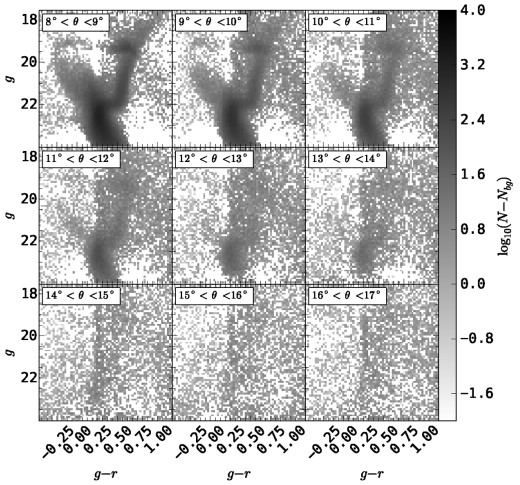

Figure 10. Hess diagrams in $g - r$ versus g for different angular distance ranges (indicated in the top-left of each panel). The contribution from MW stars has been removed as described in the text.

We again assume that the MW stellar population varies very little throughout the SPT-E.

In Fig. 10 we note, from visual inspection, that the LMC population in the bottom central panel is indistinguishable from the noise in the Hess diagram. This panel corresponds to angular separations between 15° and 16°. This range corresponds to distances from 10.5 to 11.2 kpc along the disc plane, which are intermediate between the truncations radius of the *old* and *young* population. This does not mean the complete absence of LMC stars. However, it shows that at this range of distances the LMC populations is too low in number to be distinguishable by eye from the MW foreground stars.

With the aid of the GALPY[2] (Bovy 2010) suite for galactic dynamics, we compute a three component MW potential with an NFW halo (Navarro, Frenk & White 1996), a Miyamoto–Nagai disc (Miyamoto & Nagai 1975), and a Hernquist bulge (Hernquist 1990) following the same recipe as in Bovy et al. (2012). This potential was normalized such as to yield a Solar circular velocity of 220 km s^{-1} at the Galactocentric distance of 8 kpc. We obtain that the enclosed MW mass inside a sphere centred in the MW with radius $d_{\rm LMC}$ is $5.6 \times 10^{11}\,{\rm M}_\odot$. Using the result from equation (5) and propagating the uncertainties in $R_{\rm t}$, we obtain an LMC mass of $M_{\rm LMC} = 2.3^{+0.8}_{-0.6} \times 10^{10}\,{\rm M}_\odot$.

According to the set of simulations by Kallivayalil et al. (2013), the combination of MW and LMC masses found in this work would favour a scenario where the Magellanic System is in its first pericentric passage. However, it is not clear if there is enough time for the LMC to develop a truncation radius without finishing a complete orbit around the MW and if this truncation would affect its luminous component. We would like to stress that the calculations presented in our work are subject to many uncertainties, especially with respect to our knowledge of the MW mass profile at large distances.

5 THE LMC RC AS A DISTANCE ESTIMATOR

The peak magnitude of the RC is used widely in astronomy as a standard candle to determine distances of old and intermediate age star clusters. RC stars are He-burning stars of mass $M \lesssim 2\,{\rm M}_\odot$; they develop an electron degenerate core after the main sequence, and as a consequence have to increase their core up to a critical mass of $\sim$0.46 M$_\odot$ before helium can be ignited. The almost-constancy of their helium-core masses determines that they all share similar (but not constant) luminosities in their central helium burning phase.

Using the RC peak magnitude as a standard candle, we define the distance modulus μ_0 with the following equation:

$$\mu_0 = m_\lambda^{\rm RC} - M_\lambda^{\rm RC} - A_\lambda - \Delta M_\lambda^{\rm RC}, \qquad (6)$$

where A_λ is the extinction, $M_\lambda^{\rm RC}$ is the absolute magnitude of the RC peak, and $\Delta M_\lambda^{\rm RC}$ is a correction in the absolute magnitude due to population mixing effects. Here, λ represents the observational filters ($\lambda = g, r, i, z$).

If one is to determine μ_0, the terms A_λ and $\Delta M_\lambda^{\rm RC}$ must be inferred. Here, we choose to correct the magnitudes for extinction using the Schlegel, Finkbeiner & Davis (1998) dust maps. For the time being we will assume that $\Delta M_\lambda^{\rm RC}$ is zero. This assumption will be addressed in more detail later.

To probe μ_0 as a function of position in the LMC, we subdivided the sky in HEALPIX pixels using the pixelization scheme with $N_{\rm side} = 128$. This gives a pixel area of $\sim$0.21 deg^2. We choose a larger pixel than the previous section since the RC is much less populated than the main sequence. To measure the peak apparent magnitude of the RC in a given passband ($m_\lambda^{\rm RC}$), we compute the number count of stars as a function of magnitude ($N(m_\lambda)$) for stars

[2] http://github.com/jobovy/galpy

that have colours and magnitudes limited by the dashed boxes in Fig. 4. The CMD region occupied by RC stars was selected visually.

To build $N(m_\lambda)$ the bin size is chosen according to the method described in Knuth (2006), which is based on optimization of a Bayesian fitness function across fixed-width bins. This avoids issues that may arise from oversampling or undersampling the number of bins. The values of $N(m_\lambda)$ are fitted by means of a non-linear least-square algorithm using a second-order polynomial plus a Gaussian. This function is given by the following equation:

$$N(m_\lambda) = a + bm_\lambda + cm_\lambda^2 + d\exp\left[\frac{-(m_\lambda^{\rm RC} - m_\lambda)^2}{2\sigma_\lambda^2}\right], \quad (7)$$

where a, b, c are the coefficients of the polynomial, d is the normalization of the Gaussian and σ_λ is the standard deviation of the magnitudes around the RC peak.

The uncertainty on $m_\lambda^{\rm RC}$ is taken from the covariance matrix of the least-square fit.

It is convenient to define the heliocentric distance to points in the LMC disc as a function of the so called line of maximum distance gradient. This line connects points on the disc plane with the most rapidly varying distance from us, hence its name. The distance along this line is the deprojected distance between a point in the disc to the line of nodes. The distances along this line are given by the y component of equation (A3) of Weinberg & Nikolaev (2001). The line of maximum distance gradient has a PA given by θ (equation 2) and it is oriented approximately in the NE–SW direction. Showing the heliocentric distance to points in the LMC disc as a function of the position in the line of maximum distance gradient is the equivalent of showing an edge-on view of the LMC.

To infer the absolute magnitude of the RC ($M_\lambda^{\rm RC}$), we could adopt the prediction from synthetic stellar populations based on stellar evolution models. However, simulations using PARSEC (Bressan et al. 2012) models agree well with the disc models found in this work. A small magnitude offset can be seen in Fig. 11, where the solid black line shows the best-fitting disc model and the grey points are the inferred distance modulus based on theoretical values of $M_\lambda^{\rm RC}$.

Despite the small offset in the theoretical value of $M_\lambda^{\rm RC}$, we chose to determine $M_\lambda^{\rm RC}$ by matching the expected distance modulus from our best-fitting disc model to the observed values of the RC peak magnitude. This matching was done using stars that are between 3 and 4 kpc along the LMC line of maximum distance gradient. We compute the median value of m_λ in this distance range and subtract from that the heliocentric distance expected from the disc model at 3.5 kpc from the LMC centre. This offset is determined for all passbands. The value obtained is then used to compute the RC-based distances consistently with our disc model. These distances are shown as the black points in Fig. 11 and the error bars are propagated from the RC peak fit.

In Fig. 12, we show the distributions of $m_\lambda^{\rm RC}$ on the sky, for $\lambda = g, r, i, z$. The lines show the direction of maximum gradient and the line of nodes obtained from our best disc model fit using the *all* stellar population. We notice that the entire sampled region in this work is on the same side (near side) of the LMC disc major axis. There is a global trend in the sense that for all passbands the nearest points to us are located in the north-east edge of the LMC. Another remarkable feature present in all maps is that the north edge of the LMC is systematically more distant than what is expected for the disc model. This effect is noticeable in all passbands.

The discrepancies observed in the maps described above may be due to population mixing in RC stars. The RC luminosity depends slightly on the age and metallicity of the stars (Girardi 1999; Girardi & Salaris 2001). This fact makes the RC of a stellar population older than ∼3 Gyr dimmer as a function of age. The exact amount of dimming depends on the metallicity and on the passband used. A detailed discussion about how the RC magnitude of simple stellar populations varies with age and metallicity may be found in Girardi & Salaris (2001).

In the case of the LMC, we would like to know how the RC magnitude changes as a function of the SFH, therefore mapping $\Delta M_\lambda^{\rm RC}$ at different positions in the LMC. However, it is known that the LMC SFH is very complex and varies spatially (Meschin et al. 2014), therefore rendering this a very difficult task.

To assess the amplitude of the populations mixing effect over the RC magnitudes, we conducted a series of synthetic stellar population experiments. These simulations assume that the LMC follows an AMR given by Piatti & Geisler (2013) with a spread of 0.15 dex in [Fe/H]. We also assume that stars in the LMC follow a Kroupa initial mass function (Kroupa 2001). To generate synthetic magnitudes for a set of simulated stars we adopt the PARSEC (Bressan et al. 2012) isochrones in the DES photometric system. Our grid of models has a step of 0.01 in $\log_{10}$(age/yr) and 0.0002 in Z in the range [0.0002, 0.001] and 0.001 for Z in the range [0.001, 0.020]. Photometric uncertainties were included according to equation (1) and Table 2. The simulations were made in the framework of the open-source code GENCMD.[3]

We adopt three SFHs that are modelled according to what has been found by Meschin et al. (2014) for the outer regions of the LMC (red squares in Fig. 12). The simulated SFHs contain two events of star formation that were modelled as Gaussian peaks in SFR. The young peak is centred on an age of 2.5 Gyr with a width of 1 Gyr, while the second is centred on 9 Gyr with a width of 1.5 Gyr. The first adopted SFH gives equal amplitude to each star forming event, the second gives twice the amplitude to the older event, and the third gives twice the amplitude to the younger event. The largest difference for the RC peak magnitude was observed between the models with asymmetric peaks in the SFH. We use this difference to estimate the maximum value for $\Delta M_\lambda^{\rm RC}$ which was found to be 0.06, 0.06, 0.07, and 0.11 for g, r, i, z, respectively. The dashed lines in Fig. 11 show the maximum expected deviations due to populations mixing effects.

We notice that the RC distance variations are very similar to the one expected from the best-fitting disc model. However, there are very discrepant points that the disc model cannot account for, even when population mixing effects are considered. We also notice that the distance moduli determined using different passbands are consistent.

From the RC distributions, we may also extract information about the thickness of the LMC disc. This information is embedded in σ_λ shown in equation (7). However, this quantity is also affected by the intrinsic scatter of the RC and by photometric uncertainty. The RC simulations described above incorporate this intrinsic scatter (σ_i) convolved with the photometric one ($\sigma_{\rm phot}$). In our simulations, we measure this quantity ($\sqrt{\sigma_i^2 + \sigma_{\rm phot}^2}$) and we find that this quantity has a mean value of 0.11, 0.12, 0.13, 0.13 for g, r, i, and z, respectively. Finally, the last contributions comes from the depth of the disc along the line of sight itself ($\sigma_{\rm depth}$). Thus, we may write

$$\sigma_{\rm depth}^2 = \sigma_\lambda^2 - \sigma_{\rm phot}^2 - \sigma_i^2. \quad (8)$$

In Fig. 13, we show $\sigma_{\rm depth}$ as a function of the distance along the LMC disc. The error bars are taken from the covariance matrix

[3] https://github.com/balbinot/genCMD

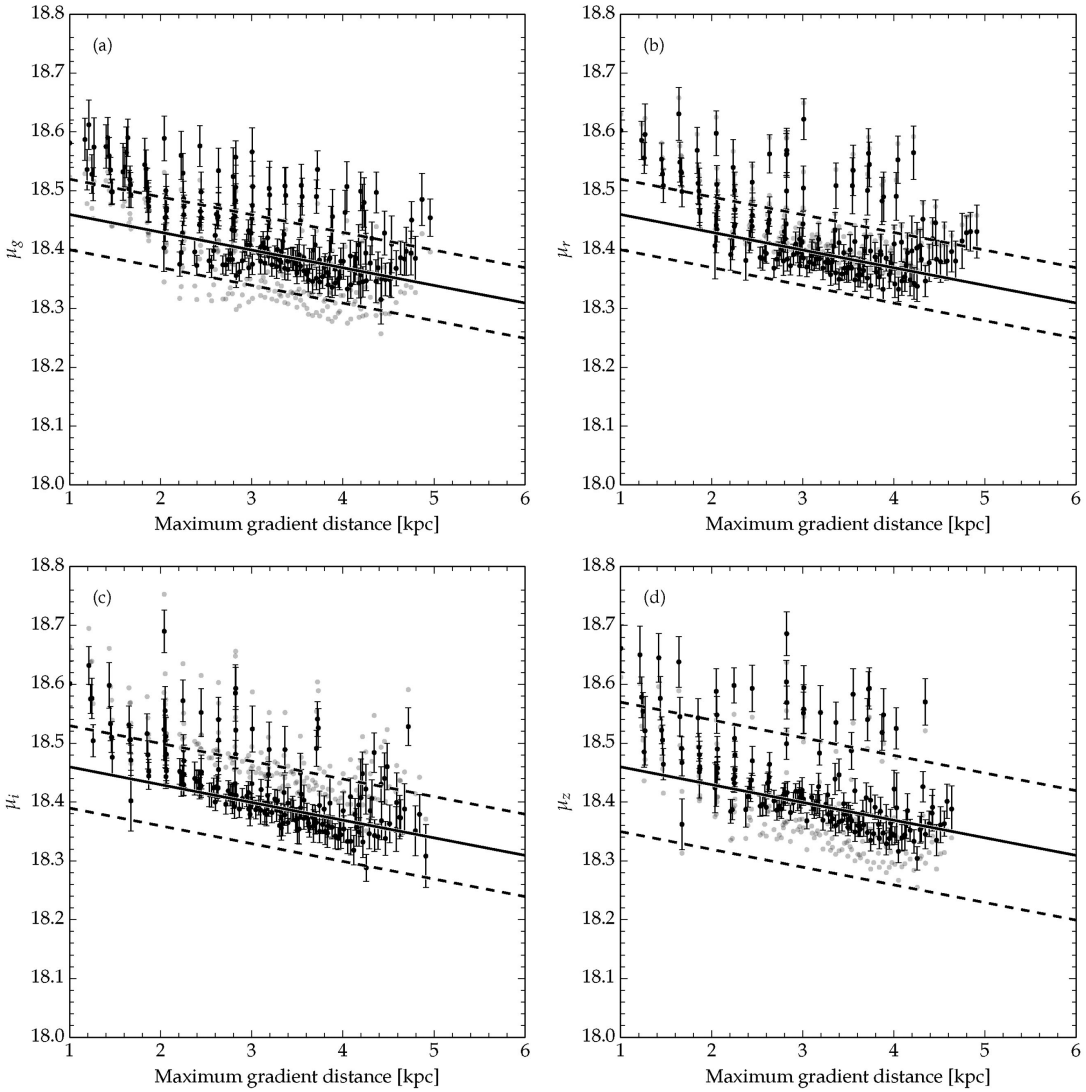

Figure 11. The distance modulus as a function of the distance along the maximum gradient line (∼ NE–SW). The black circles are the measured distance modulus in each HEALPIX pixel, as describe in the text. The error bars shows the 1 σ_m for each measured point. The solid line shows the behaviour expected from the best-fitting disc model for the all population. The dashed line shows the maximum magnitude variation expected from populations mixing effects. The grey points are the distance modulus inferred using the theoretical RC absolute magnitude. Panels a, b, c, and d show the distance modulus determination using the filters *g*, *r*, *i*, and *z*, respectively.

obtained on the least-square fit of the RC distribution as given by equation (7). We took averages of $\sigma_{\rm depth}$ in bins of 0.5 kpc, which are shown as the black circles. The error bar is the standard deviation of the values of $\sigma_{\rm depth}$ in each distance bin. For distances less than ∼4.5 kpc, we observe a constant depth of ∼0.08 mag (1.8 kpc) measured in *r*, *i*, and *z* while the *g* band yields a value of 0.12 mag (2.8 kpc). The depth in *r*, *i*, and *z* passbands tends to increase by ∼0.02 mag (∼0.5 kpc) towards the edge of the LMC. The slight difference in the *g* band depth might be due to the underestimate of the intrinsic RC magnitude spread. This effect may be due to changes in the metallicity of the LMC field populations towards its edge (Majewski et al. 2009), leading to the formation of a horizontal branch instead of a RC. The *g* band is more affected since it is more sensitive to hotter stars.

6 DISCUSSION AND SUMMARY

To the best of our knowledge, this paper is the first to show a clear distinction in the structure of the LMC disc for stellar populations of different ages. Meschin et al. (2014) report signs of an age gradient,

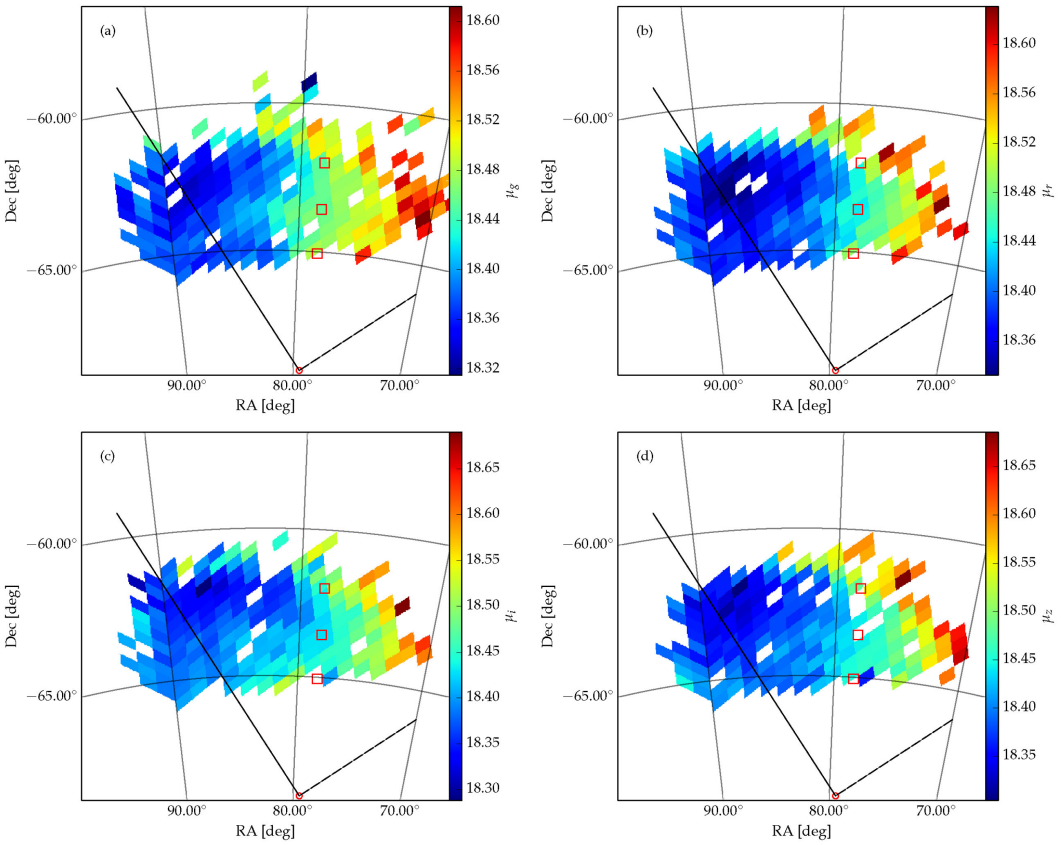

Figure 12. Gnomonic projection of $N_{\rm side} = 128$ maps showing the distance modulus measured in each the g, r, i,and z passband. On every panel the solid line shows the direction of the maximum distance gradient (θ) and the dashed line the direction of the line of nodes (θ_0) expected from the best-fitting disc model for the all population. The red squares are the fields studied by Meschin et al. (2014). The red circle is the LMC centre adopted in this work. Panels a, b, c, and d show the distance modulus determination using the filters g, r, i, and z, respectively.

but did not derive the structural properties for different age components of the LMC. Previous studies, based on large spectroscopic samples, reported a clear kinematic distinction between different stellar types and attributed that to an age difference in their samples (van der Marel, Kallivayalil & Besla 2009, and references therein). Here, we confirm this distinction based only on stellar photometry alone.

The disc models obtained in this work are in agreement with what has been reported in the literature (e.g. Weinberg & Nikolaev 2001; Nikolaev et al. 2004; Saha et al. 2010; Rubele et al. 2012). We observe a significant difference between disc models fitted using stars younger and older than 4 Gyr. The most striking difference is found in the scalelength ($R_{\rm s}$), which suggests a star formation that follows the outside-in paradigm. The summary of the disc models parameters can be found in Table 3.

The *young* population is poorly described by an exponential disc model. It presents a prominent feature that strongly deviates from an exponential profile truncated at ∼8 kpc. The *young* and *old* LMC disc have a clear distinction in the level of substructures. The younger stars are known to have peculiar spiral arms that have most likely been formed in the last SMC–LMC encounter (Staveley-Smith et al. 2003; Olsen & Massey 2007; Bekki 2009). This could explain why the *young* disc cannot be well described by our disc model.

On the other hand, the *old* disc extends over ∼13 scalelengths. Our results for the scalelength and truncation radius are similar to what Saha et al. (2010) found. The authors report $R_{\rm s} \simeq 1.15$ and a truncation radius that is ∼12 times this value, which is very similar to our determination. If we assume that the truncation radius of the *old* disc is caused by the tidal field of the MW, we obtain an LMC mass that is $M_{\rm LMC} = 2.3^{+0.8}_{-0.6} \times 10^{10}\,{\rm M}_{\odot}$. This mass is strongly dependent on the efficiency with which the MW potential tidally truncates the LMC stellar distribution. Even if the Clouds are in their first pericentric passage, their orbit is predicted to be past the pericentre, which could allow the formation of a tidal limit (Besla, private communication). Also, (Gan et al. 2010) showed that subhaloes in their first pericentric passage may undergo substantial mass loss. We also point out that in the case where the MW tidal field efficiently strips the dark matter and luminous components, our estimate of the LMC mass is reliable. However, in the case

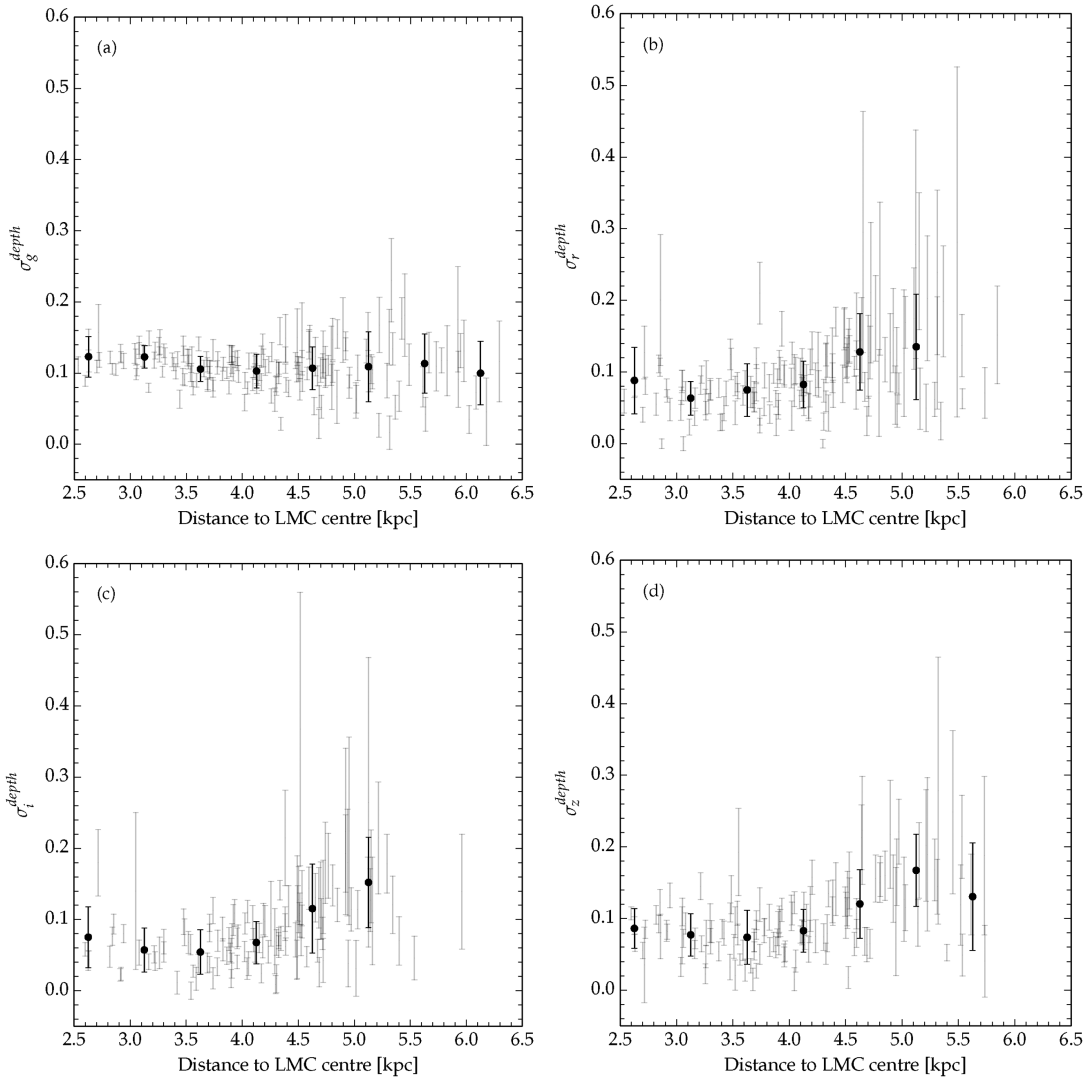

Figure 13. Disc depth as a function of distance to the LMC centre. The grey error bars show the $\sigma_{\rm depth}$ measured for each HEALPIX pixel shown on Fig. 12. The dark circles are the average over 0.5 kpc and the error bar the standard deviation. Panels a,b,c, and d are for determinations using the filters *g*, *r*, *i*, and, *z* respectively.

where dark matter is still present in an extended halo, our estimate of the LMC mass sets only a lower limit. The absolute mass value is also dependent on the MW mass profile, but the relative LMC to MW encircled mass is not. New more precise determinations of the MW mass in its outer regions will help to more accurately constrain the LMC mass.

The dynamical mass determination by van der Marel & Kallivayalil (2014) suggests $M_{\rm LMC}(R < 8.7\ {\rm kpc}) = (1.7 \pm 0.7) \times 10^{10}\,{\rm M}_\odot$ that can be extrapolated to the mass inside our truncation radius of $M_{\rm LMC}(R < R_{\rm t}) = (3.5 \pm 1.4) \times 10^{10}\,{\rm M}_\odot$ assuming a flat rotation curve. This value is within the error bars of our mass determination, suggesting that the truncation radius found in this work has a tidal origin.

Through the fit of the RC peak magnitude, we observe that a few regions coherently grouped in the north of the LMC are systematically more distant than what is expected by an inclined circular disc model. While Olsen & Salyk (2002) found that regions of the south-east LMC are systematically closer, we find that the northern LMC disc behaves in the opposite sense. This is the classic case for a galaxy with warped disc. We demonstrate, through the use of synthetic stellar population models, that the offsets from the disc model are larger than what is expected from population mixing effects.

Using the same synthetic stellar populations quoted above, we are able to compute the theoretical magnitude scatter of RC stars. This allows us to disentangle the contribution of the intrinsic scatter from the one caused by the disc thickness. We measure a thickness

ranging from 1.8 to 2.8 kpc in the inner parts of the LMC and which increases by 0.5 kpc in its outer parts. If we assume that the disc follows an exponential profile in height, we obtain that the scaleheight ranges from 1.3 to 1.9 kpc, increasing by 0.3 kpc in the outer parts. This slight increase towards the outskirts can be interpreted as the *flaring* of the disc. van der Marel & Cioni (2001) argue that this kind of behaviour is expected if the LMC disc is tidally perturbed by the MW potential. The disc thickening may also be explained solely by LMC dynamical models (Besla et al. 2012), where the old stellar component is expected to form a dynamically hotter component. The fact that we only observe it on the edge of the LMC may be due to the steep truncation of the *young* disc, allowing us to measure a thickness that is dominated by the *old* population only in the LMC outskirts.

The analysis presented in this work points to a scenario where there are two distinct disc components in the LMC. One is composed of old stars (>4 Gyr) and possesses a smooth, extended profile out to dozens of scalelengths. The second component is composed of younger stars (<4 Gyr) and appears to be perturbed and much less extended. We find signs of *warp* and *flare* towards the outskirts of the LMC, both of which have been reported previously (Olsen & Salyk 2002; Subramaniam & Subramanian 2009).

An alternative scenario for the disc *warp* and *flare* is the existence of a hot halo composed of *old* stars, while the disc could contain both populations. Because the *old* population is more *spatially* extended, this scenario would explain the outward increase in the thickness of the RC as the *young* disc fades, therefore accounting for the 'flare' signal. Besides the *flaring*, the *old* spheroidal component would lead to a systematic variation on the heliocentric distances across the LMC in the sense of bringing them closer to the heliocentric distance of the LMC centre on both sides of the galaxy, also mimicking a *warp* effect.

The fact that the *old* disc is well fitted by a single exponential disc favours the scenario where there is no detectable stellar halo and older stars form a thicker disc. Also the fact that the hot halo has only been possibly detected in the central regions of the LMC (Minniti et al. 2003) raises doubts about the existence of such a stellar component. To investigate the existence of a halo component, a more detailed study must be carried out in the LMC outskirts in order to isolate its extremely sparse stellar population. This kind of study should employ more sophisticated CMD decontamination methods such as the ones used to detect streams and tidal tails (Rockosi et al. 2002).

The upcoming years promise to greatly increase our understanding of the Magellanic system. With the data already observed during the DES SV campaign, we have the ability to study a vast number of LMC star clusters and their three-dimensional distribution in the galaxy. The field LMC population may also be used to infer a very detailed, and spatially dependent SFH.

Upcoming DES observations will cover a large portion of the Magellanic Stream allowing for the discovery and characterization of its stellar component, if it exists. Additionally, DES will continue to map the outskirts of the LMC and SMC. This novel data set will certainly reveal some of the many puzzles of the Magellanic system.

ACKNOWLEDGEMENTS

This paper has gone through internal review by the DES collaboration.

We are grateful for the extraordinary contributions of our CTIO colleagues and the DECam, Commissioning and Science Verification teams in achieving the excellent instrument and telescope conditions that have made this work possible. The success of this project also relies critically on the expertise and dedication of the DES Data Management group.

Funding for the DES Projects has been provided by the US Department of Energy, the US National Science Foundation, the Ministry of Science and Education of Spain, the Science and Technology Facilities Council of the United Kingdom, the Higher Education Funding Council for England, the National Center for Supercomputing Applications at the University of Illinois at Urbana-Champaign, the Kavli Institute of Cosmological Physics at the University of Chicago, Financiadora de Estudos e Projetos, Fundação Carlos Chagas Filho de Amparo à Pesquisa do Estado do Rio de Janeiro, Conselho Nacional de Desenvolvimento Científico e Tecnológico and the Ministério da Ciência e Tecnologia, the Deutsche Forschungsgemeinschaft and the Collaborating Institutions in the Dark Energy Survey.

The Collaborating Institutions are Argonne National Laboratory, the University of California at Santa Cruz, the University of Cambridge, Centro de Investigaciones Energeticas, Medioambientales y Tecnologicas-Madrid, the University of Chicago, University College London, the DES-Brazil Consortium, the Eidgenössische Technische Hochschule (ETH) Zürich, Fermi National Accelerator Laboratory, the University of Edinburgh, the University of Illinois at Urbana-Champaign, the Institut de Ciencies de l'Espai (IEEC/CSIC), the Institut de Fisica d'Altes Energies, Lawrence Berkeley National Laboratory, the Ludwig-Maximilians Universität and the associated Excellence Cluster Universe, the University of Michigan, the National Optical Astronomy Observatory, the University of Nottingham, The Ohio State University, the University of Pennsylvania, the University of Portsmouth, SLAC National Accelerator Laboratory, Stanford University, the University of Sussex, and Texas A&M University.

The DES participants from Spanish institutions are partially supported by MINECO under grants AYA2009-13936, AYA2012-39559, AYA2012-39620, and FPA2012-39684, which include FEDER funds from the European Union.

DG was supported by SFB-Transregio 33 'The Dark Universe' by the Deutsche Forschungsgemeinschaft (DFG) and the DFG cluster of excellence 'Origin and Structure of the Universe'.

JZ acknowledges support from the European Research Council in the form of a Starting Grant with number 240672.

REFERENCES

Alves D. R., 2004, ApJ, 601, L151

Balbinot E., Santiago B. X., Bica E., Bonatto C., 2009, MNRAS, 396, 1596

Balbinot E., Santiago B., Girardi L., da Costa L. N., Maia M. A. G., Pellegrini P. S. S., Makler M., 2012, in Ballester P., Egret D., Lorente N. P. F., eds, ASP Conf. Ser. Vol. 461, Astronomical Data Analysis Software and Systems XXI. Astron. Soc. Pac., San Francisco, p. 287

Bekki K., 2009, in Van Loon J. T., Oliveira J. M., eds, Proc. IAU Symp. 256 The Magellanic System: Stars, Gas, and Galaxies. Cambridge Univ. Press, Cambridge, p. 105

Bertin E., 2006, in Gabriel C., Arviset C., Ponz D., Enrique S., eds, ASP Conf. Ser. Vol. 351, Astronomical Data Analysis Software and Systems XV. Astron. Soc. Pac., San Francisco. p. 112

Bertin E., 2011, in Evans I. N., Accomazzi A., Mink D. J., Rots A. H., eds, ASP Conf. Ser. Vol. 442, Astron. Soc. Pac., San Francisco, p. 435

Bertin E., Arnouts S., 1996, A&AS, 117, 393

Bertin E., Mellier Y., Radovich M., Missonnier G., Didelon P., Morin B., 2002, in Bohlender D. A., Durand D., Handley T. H., eds, ASP Conf. Ser. Vol. 281, Astronomical Data Analysis Software and Systems XI. Astron. Soc. Pac., San Francisco, p. 228

Besla G., Kallivayalil N., Hernquist L., van der Marel R. P., Cox T. J., Kereš D., 2012, MNRAS, 421, 2109
Binney J., Tremaine S., 2008, Galactic Dynamics, 2nd edn. Princeton Univ. Press, Princeton, NJ
Bouy H., Bertin E., Moraux E., Cuillandre J.-C., Bouvier J., Barrado D., Solano E., Bayo A., 2013, A&A, 554, A101
Bovy J., 2010, ApJ, 725, 1676
Bovy J., Rix H.-W., Liu C., Hogg D. W., Beers T. C., Lee Y. S., 2012, ApJ, 753, 148
Bressan A., Marigo P., Girardi L., Salasnich B., Dal Cero C., Rubele S., Nanni A., 2012, MNRAS, 427, 127
Cardelli J. A., Clayton G. C., Mathis J. S., 1989, ApJ, 345, 245
Carlstrom J. E. et al., 2011, PASP, 123, 568
Cioni M.-R. L. et al., 2011, A&A, 527, A116
de Grijs R., Wicker J. E., Bono G., 2014, AJ, 147, 122
de Vaucouleurs G., Freeman K. C., 1972, Vistas Astron., 14, 163
Desai S. et al., 2012, ApJ, 757, 83
Dolphin A. E., 2002, MNRAS, 332, 91
Eisenhauer F. et al., 2005, ApJ, 628, 246
Flaugher B., 2005, Int. J. Mod. Phys. A, 20, 3121
Flaugher B. L. et al., 2010, in McLean I. S., K. Ramsay S. K., Takami H., eds, Proc. SPIE Conf. Ser. Vol. 7735, Ground-based and Airborne Instrumentation for Astronomy III. SPIE, Bellingham, p. 77350D
Foreman-Mackey D., Hogg D. W., Lang D., Goodman J., 2013, PASP, 125, 306
Fukugita M., Ichikawa T., Gunn J. E., Doi M., Shimasaku K., Schneider D. P., 1996, AJ, 111, 1748
Gan J., Kang X., van den Bosch F. C., Hou J., 2010, MNRAS, 408, 2201
Gillessen S., Eisenhauer F., Fritz T. K., Bartko H., Dodds-Eden K., Pfuhl O., Ott T., Genzel R., 2009, ApJ, 707, L114
Girardi L., 1999, MNRAS, 308, 818
Girardi L., Salaris M., 2001, MNRAS, 323, 109
Girardi L., Groenewegen M. A. T., Hatziminaoglou E., da Costa L., 2005, A&A, 436, 895
Glazebrook K., Peacock J. A., Collins C. A., Miller L., 1994, MNRAS, 266, 65
Górski K. M., Hivon E., Banday A. J., Wandelt B. D., Hansen F. K., Reinecke M., Bartelmann M., 2005, ApJ, 622, 759
Grcevich J., Putman M. E., 2009, ApJ, 696, 385
Hernquist L., 1990, ApJ, 356, 359
Hindman J. V., Kerr F. J., McGee R. X., 1963, Aust. J. Phys., 16, 570
Holtzman J. A. et al., 1999, AJ, 118, 2262
Javiel S. C., Santiago B. X., Kerber L. O., 2005, A&A, 431, 73
Jensen J., Mould J., Reid N., 1988, ApJS, 67, 77
Kallivayalil N., van der Marel R. P., Besla G., Anderson J., Alcock C., 2013, ApJ, 764, 161
Kelly P. L. et al., 2014, MNRAS, 439, 28
Kerber L. O., Santiago B. X., 2009, in Van Loon J. T., Oliveira J. M., eds, Proc. IAU Symp. Vol. 256, The Magellanic System: Stars, Gas, and Galaxies. Cambridge Univ. Press, Cambridge, p. 391
Klypin A., Kravtsov A. V., Valenzuela O., Prada F., 1999, ApJ, 522, 82
Knuth K. H., 2006, preprint (arXiv:physics/0605197)
Kron R. G., 1980, ApJS, 43, 305
Kroupa P., 2001, MNRAS, 322, 231
McConnachie A. W., 2012, AJ, 144, 4
McMahon R., 2012, in Proc. Science from the Next Generation Imaging and Spectroscopic Surveys, ESO Garching, 15–18 October 2012. Available online at: http://www.eso.org/sci/meetings/2012/surveys2012/program.html, id.37
Majewski S. R., Nidever D. L., Muñoz R. R., Patterson R. J., Kunkel W. E., Carlin J. L., 2009, in Van Loon J. T., Oliveira J. M., eds, Proc. IAU Symp. Vol. 256, The Magellanic System: Stars, Gas, and Galaxies. Cambridge Univ. Press, Cambridge, p. 51
Mathewson D. S., Cleary M. N., Murray J. D., 1974, ApJ, 190, 291
Meschin I., Gallart C., Aparicio A., Hidalgo S. L., Monelli M., Stetson P. B., Carrera R., 2014, MNRAS, 438, 1067
Minniti D., Borissova J., Rejkuba M., Alves D. R., Cook K. H., Freeman K. C., 2003, Science, 301, 1508
Miyamoto M., Nagai R., 1975, PASJ, 27, 533
Mohr J. J. et al., 2012, in Radziwill N. M., Chiozzi G., eds, Proc. SPIE Conf. Ser. Vol. 8451, Software and Cyberinfrastructure for Astronomy II. SPIE, Bellingham, p. 84510D
Moore B., Ghigna S., Governato F., Lake G., Quinn T., Stadel J., Tozzi P., 1999, ApJ, 524, L19
Navarro J. F., Frenk C. S., White S. D. M., 1996, ApJ, 462, 563
Nikolaev S., Drake A. J., Keller S. C., Cook K. H., Dalal N., Griest K., Welch D. L., Kanbur S. M., 2004, ApJ, 601, 260
Olsen K. A. G., Massey P., 2007, ApJ, 656, L61
Olsen K., Salyk C., 2002, AJ, 124, 2045
Piatti A. E., Geisler D., 2013, AJ, 145, 17
Putman M. E. et al., 1998, Nature, 394, 752
Renaud F., Gieles M., 2013, MNRAS, 431, L83
Rockosi C. M. et al., 2002, AJ, 124, 349
Rossetto B. M. et al., 2011, AJ, 141, 185
Rubele S. et al., 2012, A&A, 537, A106
Saha A. et al., 2010, AJ, 140, 1719
Schlegel D. J., Finkbeiner D. P., Davis M., 1998, ApJ, 500, 525
Sevilla I. et al., 2011, preprint (arXiv:1109.6741)
Skrutskie M. F. et al., 2006, AJ, 131, 1163
Soumagnac M. T. et al., 2013, preprint (arXiv:1306.5236)
Staveley-Smith L., Kim S., Calabretta M. R., Haynes R. F., Kesteven M. J., 2003, MNRAS, 339, 87
Stetson P. B., 1987, PASP, 99, 191
Stewart K. R., Bullock J. S., Wechsler R. H., Maller A. H., Zentner A. R., 2008, ApJ, 683, 597
Subramaniam A., Subramanian S., 2009, ApJ, 703, L37
Swanson M. E. C., Tegmark M., Hamilton A. J. S., Hill J. C., 2008, MNRAS, 387, 1391
Swanson M., Tegmark M., Hamilton A., Hill C., 2012, Astrophysics Source Code Library, record ascl:1202.005
Tucker D. L. et al., 2007, in Sterken C., ed., ASP Conf. Ser. Vol. 364, The Future of Photometric, Spectrophotometric and Polarimetric Standardization. Astron. Soc. Pac., San Francisco, p. 187
van der Marel R. P., Cioni M.-R. L., 2001, AJ, 122, 1807
van der Marel R. P., Kallivayalil N., 2014, ApJ, 781, 121
van der Marel R. P., Kallivayalil N., Besla G., 2009, in Van Loon J. T., Oliveira J. M., eds, Proc. IAU Symp. Vol. 256, The Magellanic System: Stars, Gas, and Galaxies. Cambridge Univ. Press, Cambridge, p. 81
Weinberg M. D., Nikolaev S., 2001, ApJ, 548, 712
Yang C.-C., Gruendl R. A., Chu Y.-H., Mac Low M.-M., Fukui Y., 2007, ApJ, 671, 374
Zacharias N., Finch C. T., Girard T. M., Henden A., Bartlett J. L., Monet D. G., Zacharias M. I., 2013, AJ, 145, 44

[1]*Department of Physics, University of Surrey, Guildford GU2 7XH, UK*
[2]*Departamento de Astronomia, Universidade Federal do Rio Grande do Sul, Av. Bento Gonçalves 9500, Porto Alegre 91501-970, RS, Brazil*
[3]*Laboratório Interinstitucional de e-Astronomia - LIneA, Rua Gal. José Cristino 77, Rio de Janeiro, RJ 20921-400, Brazil*
[4]*Osservatorio Astronomico di Padova INAF, Vicolo dell'Osservatorio 5, I-35122 Padova, Italy*
[5]*Observatório Nacional, Rua Gal. José Cristino 77, Rio de Janeiro, RJ 20921-400, Brazil*
[6]*Astronomy Department, University of Illinois, 1002 W Green St, Urbana, IL 61801, USA*
[7]*National Center for Supercomputing Applications, University of Illinois, 1205 W Clark St, Urbana, IL 61801, USA*
[8]*Cerro Tololo Inter-American Observatory, National Optical Astronomy Observatory, Casilla 603, La Serena, Chile*
[9]*Fermi National Accelerator Laboratory, PO Box 500, Batavia, IL 60510, USA*
[10]*Department of Physics & Astronomy, University College London, Gower Street, London WC1E 6BT, UK*
[11]*Space Telescope Science Institute (STScI), 3700 San Martin Drive, Baltimore, MD 21218, USA*

[12]*Argonne National Laboratory, 9700 South Cass Avenue, Lemont, IL 60439, USA*
[13]*Carnegie Observatories, 813 Santa Barbara St, Pasadena, CA 91101, USA*
[14]*Institut d'Astrophysique de Paris, Univ. Pierre et Marie Curie & CNRS UMR7095, F-75014 Paris, France*
[15]*Kavli Institute for Particle Astrophysics and Cosmology, Stanford University, 452 Lomita Mall, Stanford, CA 94305, USA*
[16]*George P. and Cynthia Woods Mitchell Institute for Fundamental Physics and Astronomy, and Department of Physics and Astronomy, Texas A&M University, College Station, TX 77843, USA*
[17]*Department of Physics, Ludwig-Maximilians-Universität, Scheinerstr. 1, D-81679 München, Germany*
[18]*Excellence Cluster Universe, Boltzmannstr. 2, D-85748 Garching, Germany*
[19]*Department of Physics, University of Michigan, Ann Arbor, MI 48109, USA*
[20]*Department of Astronomy, University of Michigan, Ann Arbor, MI 48109, USA*
[21]*Max Planck Institute for Extraterrestrial Physics, Giessenbachstrasse, D-85748 Garching, Germany*
[22]*Department of Physics, The Ohio State University, Columbus, OH 43210, USA*
[23]*Australian Astronomical Observatory, North Ryde, NSW 2113, Australia*
[24]*Department of Physics and Astronomy, Center for Particle Cosmology, University of Pennsylvania, 209 South 33rd Street, Philadelphia, PA 19104, USA*
[25]*Institut de Física d'Altes Energies, Universitat Autònoma de Barcelona, E-08193 Bellaterra (Barcelona), Spain*
[26] *Institució Catalana de Recerca i Estudis Avançats, E-08010 Barcelona, Spain*
[27]*Brookhaven National Laboratory, Bldg 510, Upton, NY 11973, USA*
[28]*Centro de Investigaciones Energéticas, Medioambientales y Tecnológicas (CIEMAT), Av. Complutense 40, E-28040 Madrid, Spain*
[29]*SLAC National Accelerator Laboratory, Menlo Park, CA 94025, USA*
[30]*Jodrell Bank Centre for Astrophysics, University of Manchester, Alan Turing Building, Manchester, M13 9PL, UK*

This paper has been typeset from a TEX/LATEX file prepared by the author.

Neste artigo foi feita a aplicação das abordagens de máxima probabilidade aos parâmetros estruturais do aglomerado DES1 utilizando o perfil de King e exponencial, ambos elípticos, bem como aos parâmetros físicos idade, metalicidade, avermelhamento, módulo de distância e magnitude absoluta. Para a magnitude absoluta do aglomerado, comparamos a função de luminosidade do aglomerado com a função de luminosidade dos modelos de Padova (Bressan et al., 2012), para estrelas até a magnitude $g = 23$, evitando magnitudes fracas onde a completeza é muito abaixo da unidade.

MNRAS **458,** 603–612 (2016) doi:10.1093/mnras/stw302
Advance Access publication 2016 February 9

Digging deeper into the Southern skies: a compact Milky Way companion discovered in first-year Dark Energy Survey data

E. Luque,[1,2⋆] A. Queiroz,[1,2] B. Santiago,[1,2⋆] A. Pieres,[1,2] E. Balbinot,[2,3] K. Bechtol,[4] A. Drlica-Wagner,[5] A. Fausti Neto,[2] L. N. da Costa,[2,6] M. A. G. Maia,[2,6] B. Yanny,[5] T. Abbott,[7] S. Allam,[5] A. Benoit-Lévy,[8] E. Bertin,[9,10] D. Brooks,[8] E. Buckley-Geer,[5] D. L. Burke,[11,12] A. Carnero Rosell,[2,6] M. Carrasco Kind,[13,14] J. Carretero,[15,16] C. E. Cunha,[11] S. Desai,[17,18] H. T. Diehl,[5] J. P. Dietrich,[17,18] T. F. Eifler,[19,20] D. A. Finley,[5] B. Flaugher,[5] P. Fosalba,[15] J. Frieman,[5,21] D. W. Gerdes,[22] D. Gruen,[23,24] G. Gutierrez,[5] K. Honscheid,[25,26] D. J. James,[7] K. Kuehn,[27] N. Kuropatkin,[5] O. Lahav,[8] T. S. Li,[28] M. March,[19] J. L. Marshall,[28] P. Martini,[25,29] R. Miquel,[16,30] E. Neilsen,[5] R. C. Nichol,[31] B. Nord,[5] R. Ogando,[2,6] A. A. Plazas,[20] A. K. Romer,[32] A. Roodman,[11,12] E. Sanchez,[33] V. Scarpine,[5] M. Schubnell,[22] I. Sevilla-Noarbe,[13,33] R. C. Smith,[7] M. Soares-Santos,[5] F. Sobreira,[2,5] E. Suchyta,[25,26] M. E. C. Swanson,[14] G. Tarle,[22] J. Thaler,[34] D. Tucker,[5] A. R. Walker[7] and Y. Zhang[22]

Affiliations are listed at the end of the paper

Accepted 2016 February 5. Received 2016 February 5; in original form 2015 August 8

ABSTRACT

We use the first-year Dark Energy Survey (DES) data down to previously unprobed photometric depths to search for stellar systems in the Galactic halo, therefore complementing the previous analysis of the same data carried out by our group earlier this year. Our search is based on a matched filter algorithm that produces stellar density maps consistent with stellar population models of various ages, metallicities, and distances over the survey area. The most conspicuous density peaks in these maps have been identified automatically and ranked according to their significance and recurrence for different input models. We report the discovery of one additional stellar system besides those previously found by several authors using the same first-year DES data. The object is compact, and consistent with being dominated by an old and metal-poor population. DES 1 is found at high significance and appears in the DES images as a compact concentration of faint blue point sources. Assuming different spatial profile parameterizations, the best-fitting heliocentric distance and total absolute magnitude in the range of 77.6–87.1 kpc and $-3.00 \lesssim M_V \lesssim -2.21$, respectively. The half-light radius of this object, $r_h \sim 10$ pc and total luminosity are consistent with it being a low-mass halo cluster. It is also found to have a very elongated shape ($\epsilon \sim 0.57$). In addition, our deeper probe of DES first-year data confirms the recently reported satellite galaxy candidate Horologium II as a significant stellar overdensity. We also infer its structural properties and compare them to those reported in the literature.

Key words: globular clusters: general – globular clusters: individual (DES 1) – galaxies: dwarf.

1 INTRODUCTION

The census of Milky Way (MW) satellites has grown rapidly over the past 15 yr. Several of these newly found objects are star systems with very low luminosities ($-3.0 \lesssim M_V \lesssim 0$) and small half-light radii

⋆ E-mail: elmer.luque@ufrgs.br (EL); basilio.santiago@ufrgs.br (BS)

(<10 pc), being more consistent with star clusters (Koposov et al. 2007; Belokurov et al. 2010; Fadely et al. 2011; Muñoz et al. 2012; Balbinot et al. 2013). These clusters are thought to be suffering stellar mass-loss via dynamical processes such as tidal disruption or evaporation (Koposov et al. 2007; Kim & Jerjen 2015a). The number of dwarf galaxies around the MW has also increased significantly, from the 11 classical dwarfs known until the late 1990s, up to a total of 27 which were known by early this year (McConnachie 2012), thanks in large part to the Sloan Digital Sky Survey (SDSS). Several of the dwarfs found with SDSS are very low-luminosity systems with high M/L, thus representing some of the most dark matter rich objects (Simon & Geha 2007).

At the larger luminosities typical of globular clusters (GCs), $-10 \lesssim M_V \lesssim -5$ mag, different cluster sub-populations classified by their position, kinematics, and horizontal branch (HB) morphology have been known for several decades (Zinn 1985, 1993; Milone et al. 2014). The so-called young halo clusters may have originated in dwarf galaxies accreted by the MW (Zinn 1993; Lee, Demarque & Zinn 1994; Marino et al. 2014, 2015). Both types of objects seem to share a vast planar structure around the Galaxy, which also encloses several stellar and gaseous streams of clusters and dwarf galaxies (Pawlowski, Pflamm-Altenburg & Kroupa 2012; Pawlowski, McGaugh & Jerjen 2015). The accretion origin of part of the MW system of GCs is also supported by the fact that several of them are found to have positions and kinematics that relate them to the Sagittarius dwarf galaxy (Law & Majewski 2010). On the other hand, at the much lower luminosities ($M_V \geq -7.4$ mag) of the recent satellite discoveries, the very distinction between star clusters and dwarf satellites may become less clear, as attested by their respective loci in size and luminosity space. It is therefore important to pursue a complete census of faint stellar systems inhabiting the Galactic halo, and to characterize them in terms of structure, stellar populations, and dark matter content. Extrapolations of the SDSS results over the entire sky and over the currently known luminosity function of MW dwarfs indicate that this census is still very incomplete (Tollerud et al. 2008; Hargis, Willman & Peter 2014).

A very recent boost to the number of known MW satellites has been brought by the Dark Energy Survey (DES; Abbott et al. 2005). Using the first internal release of DES co-add data (Y1A1), Bechtol et al. (2015) reported on the discovery of eight new MW satellites over a solid angle of 1800 deg^2 in the southern equatorial hemisphere. Six of these systems have sizes and optical luminosities clearly consistent with the low-luminosity dwarfs previously detected in SDSS. The case for the other two objects is less clear. In a parallel effort, Koposov et al. (2015) reported nine new MW satellites using the same DES imaging data, including the same eight and one additional object. One of the objects in common between these two searches, Kim 2, had in fact been previously found by Kim et al. (2015) using data from the Stromlo MW Satellite Survey. In addition to that, Kim & Jerjen (2015b) have discovered yet another object using Y1A1 data, Horologium II. The Panoramic Survey Telescope and Rapid Response System 1 and the Survey of the Magellanic Stellar History have also been responsible for several recent discoveries of MW satellites (Laevens et al. 2014, 2015a,b; Martin et al. 2015).

As described in Bechtol et al. (2015), several complementary search strategies have been implemented within the DES Collaboration to search for stellar sub-structures. In Bechtol et al. (2015), we used a conservative star selection to ensure high stellar purity and completeness as well as a uniform field density over the survey footprint. The present work extends the results presented in Bechtol et al. (2015) by including stars at fainter magnitudes and by considering a broader range of spatial extensions as well as ages and metallicities for the stellar populations composing new satellite systems. We also describe in detail the application of another search algorithm to the Y1A1 co-add data. Together, these analysis updates have enabled the discovery of a new candidate stellar cluster, DES J0034−4902, which we call DES 1, and the confirmation of Horologium II as a physical stellar system. In Section 2, we describe the first-year DES data used. In Section 3, we describe the matched-filter (MF) algorithm applied to find the new systems. The new discovery is presented in Section 4. In Section 5, we report on the detection and characterization of Horologium II. Our final remarks are given in Section 6.

2 DES DATA

DES is a wide-field imaging programme expected to cover about 5000 deg^2 in the *grizY* bands down to $\simeq$ 24.6th magnitude (at S/N $\simeq$ 10 for galaxies in g band; Abbott et al. 2005) in the southern equatorial hemisphere for a period of five years. It uses the Dark Energy Camera (DECam), a 3 deg^2 (2.°2 diameter) mosaic camera with 0.263 arcsec pixels on the prime focus of the Cerro Tololo Inter-American Observatory (CTIO) Blanco 4 m telescope (Flaugher et al. 2015). The DECam images are reduced by the DES Data Management (DESDM) team, which has developed a pipeline to process the data from basic single exposure instrumental corrections all the way to catalogue creation from calibrated co-added images. Here, we use the DES year one co-add catalogue data (Y1A1), taken from 2013 August to 2014 February. For more details on Y1A1 and DESDM, we refer to Sevilla et al. (2011), Mohr et al. (2012), and Gruendl et al., in preparation. The stellar sample used in this work was drawn using the SExtractor parameters `FLAGS`, `SPREAD_MODEL`, and point spread function (`PSF`) magnitudes (Bertin & Arnouts 1996; Desai et al. 2012; Bouy et al. 2013). We used a source quality criterion of `FLAGS` ≤ 3 over the *gri* filters. To avoid issues arising from fitting the `PSF` across variable-depth co-added images, we utilized the weighted-average (`WAVG`) of the `SPREAD_MODEL` measurements from the single-epoch exposures (for details, see Bechtol et al. 2015).

As mentioned above, Kim & Jerjen (2015b) have discovered one stellar object (Horologium II) in Y1A1 data that was not initially identified by Bechtol et al. (2015), or by Koposov et al. (2015). We believe that a primary reason for the non-detection of this object is that most of the probable member stars are fainter than $g \simeq 23$ mag, which is where Bechtol et al. (2015) set the faint-end threshold to search of stellar objects. This conservative threshold was set to ensure high stellar purity and completeness, as well as a uniform field density over the survey footprint.

In this work, we adopt a selection in `WAVG_SPREAD_MODEL` intended to increase stellar completeness relative to the analysis of Bechtol et al. (2015), specifically, i-band |`WAGV_SPREAD_MODEL`| < 0.003 + `WAVG_SPREADERR_MODEL`. A bright (faint) g magnitude limit of `WAVG_MAG_PSF` = 17 (`WAVG_MAG_PSF` = 24) was also applied. The faint limit is 1 mag deeper than used by Bechtol et al. (2015). In order to prevent point sources with extreme colours (including red dwarfs from the Galactic disc) from contaminating the sample, a colour cut at $-0.5 \leq g - r \leq 1.2$ was also used.

We estimated stellar completeness as follows. We first obtained a completeness curve that quantifies the stellar detection efficiency. This is determined by applying daophot to fields around DES 1 and Horologium II in the g and r filters. The fields selected are sub-regions of the co-added images encompassing

8.67 arcmin × 8.67 arcmin each. We then added sets of 450 artificial stars at a time, with 10 realizations for each filter from $\{g, r\} = 18$ mag down to 27 mag. These artificial stars were reduced in the same way as the real image, following the same IRAF tasks and PSF model. In addition, we have obtained a stellar completeness following the method described in Bechtol et al. (2015). This method basically quantifies the stellar classification efficiency. As in Bechtol et al. (2015), we have created a test sample of high stellar purity around from DES 1 and Horologium II using a colour-based selection ($r - i > 1.7$). We then applied the morphology-based star selection criteria (see above in the text) to evaluate the classification efficiency for the test sample. Our final stellar completeness was the product of the detection and classification efficiencies. The stellar completeness was found to be >90 per cent to $r \sim 23$ mag and falls to ∼80 per cent by $r \sim 24$ mag.

3 SEARCH METHOD

As discussed in Bechtol et al. (2015), several independent search methods were used in the original analysis of Y1A1 data. In this section, we describe in detail a different method, which was the one primarily used in this work.

3.1 Matched filter

The MF technique has several applications for signal processing. In the context of astronomy, it has been used to detect low-density features and populations in imaging data (Rockosi et al. 2002; Szabo et al. 2011). We here use it to search for new star clusters and dwarf galaxies following on the work by Balbinot et al. (2011).

The number of stars as a function of position on the sky (α,δ) and of colour (c) and magnitude (m) may be generally described as

$$n(\alpha, \delta, c, m) = n_{\rm cl}(\alpha, \delta, c, m) + n_{\rm bg}(\alpha, \delta, c, m). \quad (1)$$

The first term on the right-hand side corresponds to the contribution by the cluster (cl) we want to discover, whereas the second term represents the background (bg), which includes foreground halo stars and background unresolved galaxies. We then split these terms into a normalization term and a probability distribution function (PDF):

$$n_{\rm cl}(\alpha, \delta, c, m) = \zeta_{\rm cl}(\alpha, \delta) f_{\rm cl}(c, m), \quad (2)$$

where $\zeta_{\rm cl}$ and $f_{\rm cl}$ are the number normalization and PDF on the colour–magnitude diagram (CMD) plane, respectively, for the stellar population to be found. The stellar population may be extended in space (as in a stream), but we explicitly assume that its CMD is the same everywhere. As for the background stars, Galactic structure models show that both the number density and CMD vary as a function of position across the sky (Jurić et al. 2008). Therefore, we write

$$n_{\rm bg}(\alpha, \delta, c, m) = \zeta_{\rm bg}(\alpha, \delta) f_{\rm bg}(\alpha, \delta, c, m). \quad (3)$$

With the definitions above, equation (1) then becomes

$$n(\alpha, \delta, c, m) = \zeta_{\rm cl}(\alpha, \delta) f_{\rm cl}(c, m) + \zeta_{\rm bg}(\alpha, \delta) f_{\rm bg}(\alpha, \delta, c, m). \quad (4)$$

We bin stars into spatial pixels of area of 1.0 arcmin × 1.0 arcmin, indexed by i, and colour–magnitude bins of 0.01 mag × 0.05 mag, indexed by j. Details on the construction of the $f_{\rm cl}$ and $f_{\rm bg}$ PDFs are found in Section 3.2 and Section 3.3, respectively. With this notation,

$$n(i, j) = \zeta_{\rm cl}(i) f_{\rm cl}(j) + \zeta_{\rm bg}(i) f_{\rm bg}(i, j). \quad (5)$$

Table 1. Parameter grid used to simulate SSPs for the search of star systems in DES Y1 footprint.

Parameters	Lower limit	Upper limit	steps
log(Age)	9.0	10.2	0.3
Distance (kpc)	10	200	10
Metallicity, Z	0.0002, 0.001, and 0.007		

The left-hand side is the expected number of stars in a given spatial pixel and CMD bin. If the actual number of stars observed in a catalogue is $N(i, j)$, the variance between data and model is

$$s^2(i) = \sum_j \frac{[N(i, j) - \zeta_{\rm cl}(i) f_{\rm cl}(j) - \zeta_{\rm bg}(i) f_{\rm bg}(i, j)]^2}{\zeta_{\rm bg}(i) f_{\rm bg}(i, j)}. \quad (6)$$

The term in the denominator expresses the expected Poisson fluctuation in the star counts, which, for simplicity, we assume to be dominated by the background. Minimizing the variance and solving for $\zeta_{\rm cl}(i)$, we have the number of observed stars that, according to the model given by equation (4), are consistent with the model.

$$\zeta_{\rm cl}(i) = \frac{\sum_j N(i, j) f_{\rm cl}(j)/f_{\rm bg}(i, j)}{\sum_j f_{\rm cl}^2(j)/f_{\rm bg}(i, j)} - \frac{\zeta_{\rm bg}(i)}{\sum_j f_{\rm cl}^2(j)/f_{\rm bg}(i, j)}. \quad (7)$$

The output of the filter application is a stellar density map of stars which are probable cluster members stars, i.e. $\zeta_{\rm cl}(i)$. In practice, $f_{\rm bg}(i, j)$ is generated from our target stellar catalogue itself. We do that under the assumption that the contamination by any yet to be detected cluster, dwarf galaxy, or stellar stream, does not change the background PDF. As for the object PDF, we make use of simulated samples, as described in the next sub-section.

3.2 Model grid

Since we do not know a priori what stellar populations we will find, we create a grid of simple stellar populations (SSPs) with the code GENCMD.[1] GENCMD uses PARSEC isochrones by Bressan et al. (2012) for different assumed distances and randomly selects stellar masses following a predefined initial mass function (IMF). Currently, we are adopting a Kroupa (2001) IMF for that purpose. Given each stellar mass, we interpolate among the isochrone entries to draw absolute magnitudes in the desired filters. These are converted into *measured* apparent magnitudes using the assumed model distance, magnitude uncertainties taken from Y1A1, and the reddening map of Schlegel, Finkbeiner & Davis (1998). Positions on the sky may also be simulated assuming different profile models. We simulate several SSPs at various ages, metallicities and distances covering a broader range of isochrone choices, including younger and higher metallicity stellar populations, than those adopted in Bechtol et al. (2015). The parameter grid of these simulations is presented in Table 1.

3.3 Object detection

We apply the MF method as presented in Section 3.1 to the stellar catalogue using each of the SSPs in the model grid described in Section 3.2. In practice, the sky is partitioned into ∼10° × 10° cells to account for local variations in the background CMD, which is empirically derived from the stars in each individual cell. This

[1] https://github.com/balbinot/gencmd

procedure generates one density map for every sky cell and for every point in the model grid.

The maps are then convolved with Gaussian spatial kernels of different sizes $\{\sigma = 0.0$ arcmin (no convolution) to $\sigma = 9.0$ arcmin$\}$ to highlight sub-structure on scales typical of star clusters and ultrafaint dwarf galaxies. In particular, smaller spatial kernels are suitable for the detection of more compact stellar systems. Our range of spatial kernel sizes complements those adopted by Bechtol et al. (2015).

As it is not practical to visually inspect all the resulting maps from the large number of combinations of sky cells, SSP models, and spatial convolution kernels, we use the SExtractor code to automatically search for density peaks. In fact, the convolution kernels are applied from within SExtractor itself as we run it on maps of different sky regions resulting from different SSP models. Any object found by SExtractor in each map is recorded. Objects are then ranked according to the number of times they are detected by SExtractor. This is done separately for each sky cell and convolution kernel. The SExtractor parameters for the search were defined as those that maximized the recovery of simulated objects of different sizes and richness inserted into the DES stellar catalogue.

The first 10 objects in each region of the sky and for each convolution kernel are visually inspected to identify the most likely candidates. We visually checked the stellar density map around them, the Poisson statistical significance above the background represented by their associated stellar peak, their number density profile and CMD. The density maps, significance and density profiles provide a basic assessment of the overdensities being found. The CMD helps us judge if this overdensity is consistent with a stellar population. All these diagnostic tools are shown in the next section for DES 1.

We validated the detection method described above, which we call sparsex, by applying it to simulated SSPs superposed on real SDSS and DES data. We also tried to recover faint MW satellites previously discovered in SDSS data. In particular, we have chosen 17 objects found in SDSS data (11 dwarf galaxies and six star clusters) that are characterized as distant and ultrafaint objects. sparsex detected all these stellar objects at the top of the object ranking lists. The rate of success for simulated stellar systems with similar properties was the same. Finally, sparsex detected all eight satellites reported by Bechtol et al. (2015) and Horologium II reported by Kim & Jerjen (2015b). The latter is discussed in more detail in Section 5. The ninth object detected by Koposov et al. (2015) is in a region of Y1 data that is not included in the Y1A1 co-add due to limited coverage in some of the DES filters.

Table 2 lists the central position (α_0, δ_0), the peak Poisson significance and ranking position of objects detected by sparsex in Y1A1 data. The objects reported by Bechtol et al. (2015), Koposov et al. (2015), and Kim & Jerjen (2015b) are shown in the top nine lines in Table 2. DES 1 is also included. The Poisson significance profile is built by taking the ratio of the number of stars internal to each radius[2] r and in excess of the background ($N_{\rm bgd}$), $N_{\rm obj}$, to the expected fluctuation in the same background, i.e., $N_{\rm obj}/\sqrt{N_{\rm bgd}}$. $N_{\rm obj} = (N_{\rm obs} - N_{\rm bgd})$, where $N_{\rm obs}$ is the total number of observed stars. $N_{\rm bgd}$ is computed within an annulus at 30.0 arcmin $< r <$ 34.0 arcmin from each object. To avoid a low stellar statistic, we have built the Poisson significance profile using a cumulative radius of 1.0 arcmin centred on the object.

[2] For the initial sub-structure search, we evaluate the detection significance assuming circular symmetry.

Table 2. sparsex validation in Y1A1 data. Column 1: name of object. Column 2: right ascension. Column 3: declination. Column 4: ranking position. Column 5: peak Poisson significance.

Name	α_0 (deg)	δ_0 (deg)	Rank	Peak[a] significance
Ret II	53.92	−54.05	1.0	38.9
Eri II	56.09	−43.53	1.0	46.0
Tuc II	343.06	−58.57	1.0	9.1
Hor I	43.87	−54.11	1.0	24.1
Kim 2	317.20	−51.16	1.0	11.3
Pic I	70.95	−50.28	1.0	12.0
Phe II	354.99	−54.41	1.0	11.3
Eri III	35.69	−54.28	5.0	16.1
Hor II	49.12	−50.01	2.0	7.7
DES 1	8.50	−49.04	4.0	11.6

[a] Adopting a circular symmetry.

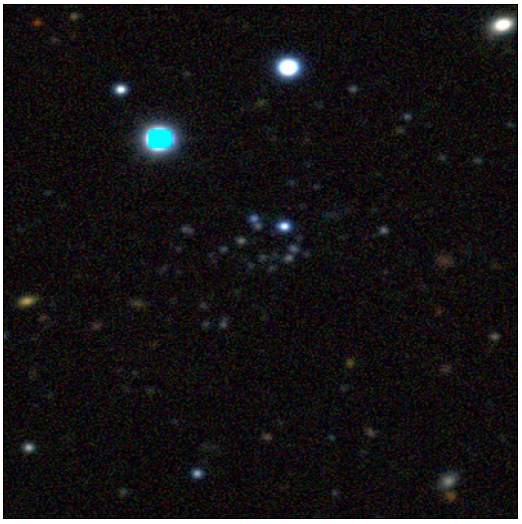

Figure 1. DES co-add image cutout of DES 1 taken from the DES Science portal. The image is 1.78 arcmin × 1.78 arcmin centred on DES 1. The R,G,B channels correspond to the i, r, g bands.

4 DES 1

DES 1 stands out as the most conspicuous new candidate from our search. It is also directly seen as an overdensity of blue stellar sources in the DES co-add images (Fig. 1). In Fig. 2, we show the number density of stars on the sky around this object (top panels). The left-hand panel shows all classified stellar sources, as described in Section 2, and the middle one shows only those close to the best-fitting isochrone (see Fig. 5 and associated discussion later in the text). A clear overdensity is seen in both. The elliptical Poisson significance profile[3] shows the higher peak at about 1.0 arcmin from the centre of DES 1 (see explanation in Section 3.3). This peak is clearly enhanced by filtering the stars according to our best-fitting

[3] The elliptical Poisson significance profile is built using the best-fitting structural parameters presented in this same section. Note that the semimajor axis of the ellipse, which we represent by the letter a, is equivalent to the elliptical radius defined in Martin, de Jong & Rix (2008).

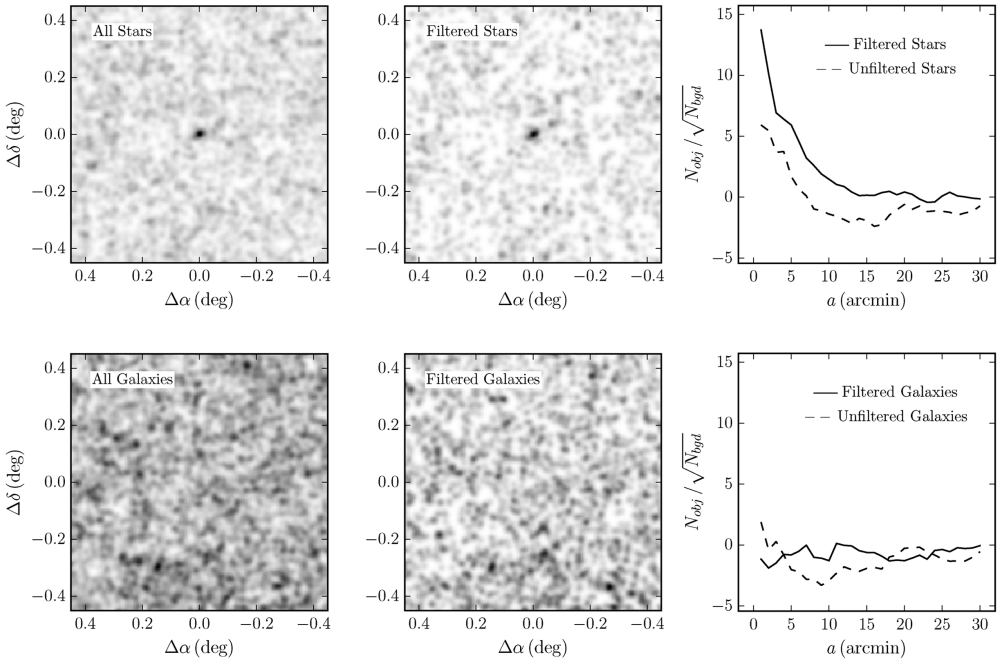

Figure 2. Top left panel: on-sky number density map of stellar sources around candidate DES 1. All stars are included. Top middle panel: similar to previous panel, but now only stars which lie close to the best-fitting isochrone shown in Fig. 5 are used. Density maps have been smoothed with a Gaussian kernel with standard deviation 0.°03. Top right panel: elliptical Poisson significance as a function of semimajor axis a from the centre of DES 1. The solid [dashed] line correspond to isochrone filtered [not pass the filter (unfiltered)] stars as indicated. The corresponding panels at the bottom show the same plots but using the distribution of sources classified as galaxies. *Note*. The centre was determined from the best-fitting exponential profile (see Table 3).

CMD model, discussed below. The bottom panels of Fig. 2 show that there is not an overdensity of galaxies at the position of DES 1, and therefore it is unlikely that misclassified galaxies can account for the apparent stellar overdensity.

We use a maximum-likelihood technique to infer structural and CMD parameters for DES 1. To estimate the structural properties for DES 1, we use two density profile models: exponential and empirical King (King 1962). The exponential profile has five free parameters: central RA (α_0) and Dec. (δ_0), position angle θ, ellipticity ϵ, and exponential scale r_e, whereas the King profile has six free parameters: α_0, δ_0, θ, ϵ, core radius r_c, and tidal radius r_t. We follow the same method as Martin et al. (2008) to find the best-fitting solution. For the parameter uncertainties, we follow a slight variant of Martin et al. (2008). The covariance between parameters is included in our uncertainty calculations via the profile likelihood technique (Sprott 2000, Section 4.5). We use 2σ (95.4 per cent confidence interval) to represent the structural and CMD parameter uncertainties.

The CMD fits weight each star by their membership probabilities p taken from the best profile fits. A threshold of $p \geq 1$ per cent is also adopted. We then use the CMDs of the most likely members of the system to fit an isochrone model, whose free parameters are: age, [Fe/H], $(m - M)_0$, and A_V. The method is based on finding the peak likelihood in a series of model grids, as described in detail by Pieres et al. (2015).

In Fig. 3, we show the results of the exponential profile fit to DES 1. The first three panels show the likelihood values projected on individual planes of this five-dimensional space, which all show well-defined peaks. The corresponding parameter values and their uncertainties (computed as discussed in Martin et al. 2008 and Pieres et al. 2015) are listed in Table 3. The last panel shows the individual stars coded by their membership probabilities. We note that DES 1 is a quite elongated object ($\epsilon \simeq 0.7$). Fig. 4 shows a binned density profile compared to the best-fitting exponential model. In both cases, we took into account the ellipticity. The central density of DES 1 is $\simeq 200$ stars arcmin^{-2}. A clear excess of stars relative to the background is seen out to $\simeq 2.0$ arcmin. In Fig. 4, we also show the best-fitting elliptical King profile. The set of structural parameters and their uncertainties determined by the maximum-likelihood fit are presented in Table 3. A visual inspection in Fig. 4 suggests that the King model best describes the central region and the excess stars seen out to $\simeq 2.0$ arcmin. We compute an estimate of half-mass radius[4] (r_h) for the King profile as follows. First, we have subtracted the expected number of field stars coinciding with DES 1, to obtain N_{DES1}, where N_{DES1} is the number of stars that belong to DES 1. We then compute r_h as the semimajor axis of the ellipse which contains $N_{DES1}/2$ stars (Balbinot et al. 2013). We obtain $r_h = 0.'39^{+0.13}_{-0.02}$ arcmin. The structural parameters determined by the exponential and King profiles agree within the uncertainties (see Table 3), confirming that DES 1 is a compact and quite elongated object.

The CMD for this candidate is shown on the left-hand panel of Fig. 5. Only stars inside an ellipse with semimajor axis $a = 2.0$ arcmin are shown. The middle panel shows the field

[4] To determine the half-mass radius, we have used the parameters determined from the best fit of King profile (see Table 3).

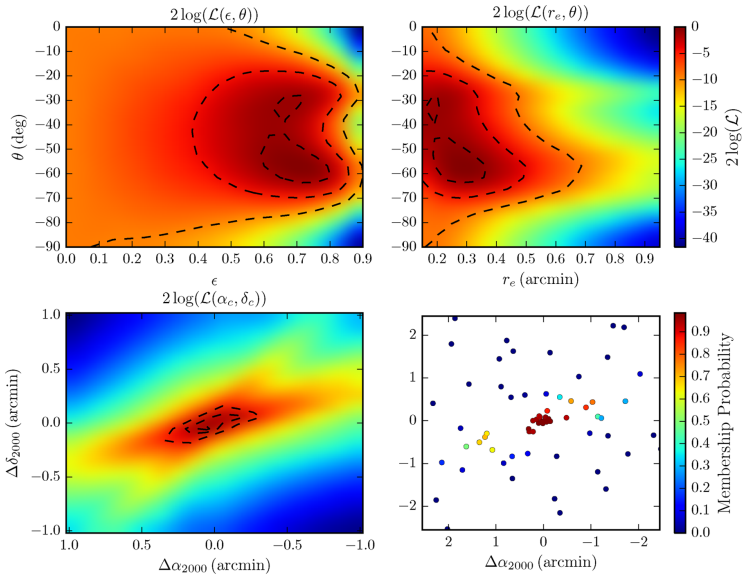

Figure 3. Upper left panel: likelihood map for DES 1 projected on to the position angle and eccentricity plane. Upper right: likelihood map for DES 1 projected on to the position angle and exponential scale plane. Lower left: likelihood map for DES 1 projected on to the central equatorial coordinates plane. The 1σ, 2σ and 3σ contour lines are shown. Lower right: spatial map of stars with probability larger than 1 per cent to belong to DES 1 colour-coded by probability. The best-fitting parameters are listed in Table 3.

Table 3. Properties of DES 1.

Parameters	Exponential profile	King profile
α_0 (J2000)	$00^h33^m59^s.7 \pm 9^s.4$	$00^h33^m59^s.6 \pm 1^s.4$
δ_0 (J2000)	$-49°02'20''.0 \pm 3''.6$	$-49°02'19''.8 \pm 2''.1$
$D_\odot$ (kpc)	$\sim$87.1	$\sim$77.6
r_e	$0'.23 \pm 0'.17$	–
θ (deg)	-57.9 ± 26.0	-52.5 ± 22.8
ϵ	0.69 ± 0.24	0.53 ± 0.22
Σ_c	204.98 ± 35.81	522.38 ± 88.30
Σ_{bgd}	2.02 ± 0.01	2.02 ± 0.01
r_h (arcmin)	0.39 ± 0.28^a	$0.39^{+0.13}_{-0.02}$
r_h (pc)	9.88 ± 7.09^b	$9.88^{+2.93}_{-0.45}{}^c$
M_V	$-3.00^{+0.66}_{-0.41}$	$-2.21^{+0.71}_{-0.48}$
TS	134.7	–
PS	13.7 ± 4.1	11.6 ± 3.9
r_c	–	$0'.08 \pm 0'.04$
r_t	–	$10'.75 \pm 5'.6$
[Fe/H]^d	-1.88 ± 0.25	-1.88 ± 0.05
log (Age)	10.00 ± 0.09	10.00 ± 0.06
A_V	0.0 ± 0.04	0.10 ± 0.07
$(m-M)_0$	19.70 ± 0.36	19.45 ± 0.11

[a]Using the relation, $r_h = 1.68 r_e$ (Martin et al. 2008).
[b]Adopting a distance of 87.1 kpc.
[c]Adopting a distance of 77.6 kpc.
[d]Adopting $Z_\odot = 0.0152$ (Bressan et al. 2012).
Note. Σ_c and Σ_{bgd} have units stars arcmin^{-2}.

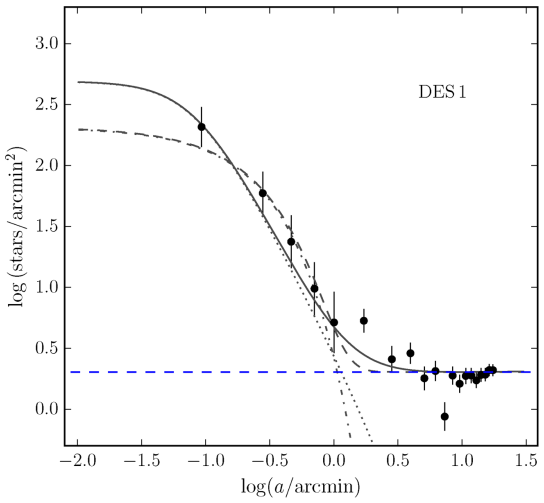

Figure 4. Solid points show a binned version of the density profile of DES 1, constructed in elliptical annuli using the derived structural parameters from the best-fit exponential profile (see Table 3). The error bars are 1σ Poisson uncertainties. Dot–dashed and dotted lines represent the best-fitting of exponential and King profiles, respectively. The horizontal dashed line shows the background level. Dashed and solid lines are the combination of the background level with the exponential and King profiles, respectively.

CMD in an elliptical annulus of equal area, whose inner semi-major axis is equal to 20.0 arcmin. The best-fitting isochrones derived from the likely members based on an exponential profile (solid line) and a King profile (dashed line) are also shown in Fig. 5; parameter values are listed in Table 3. Also shown are the sequences bracketing the best-fitting isochrone fit at a distance of $\sqrt{0.1^2 + \texttt{MAG\_ERR}^2 + \texttt{COL\_ERR}^2}$ on the CMD plane, where MAG_ERR and COL_ERR are the mean photometric uncertainties along the CMD axes. The 0.1 within the square root is a minimum isochrone mask width. It is meant to avoid

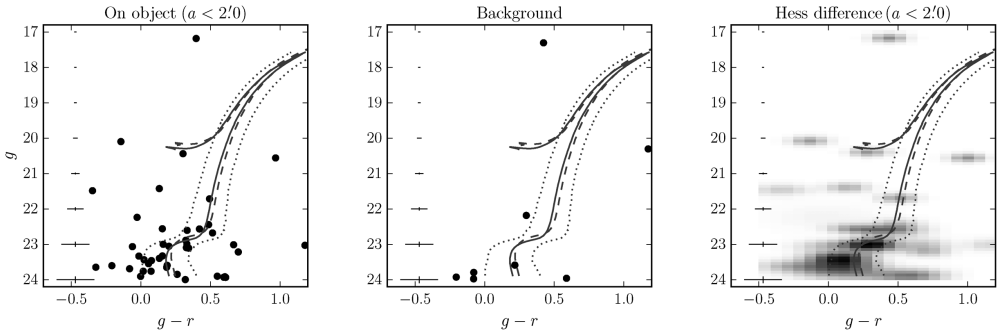

Figure 5. Left-hand panel: CMD of stars within an ellipse with semimajor axis $a = 2.0$ arcmin from the centre of DES 1. The best-fitting PARSEC isochrones (Bressan et al. 2012) are shown, along with ridge lines meant to bracket the most likely members. The best-fitting isochrone derived using the most likely stars as taken from an exponential profile is shown as a solid line, whereas the dashed line represents the best-fitting isochrone using the corresponding stars from a King profile. Middle panel: CMD of background stars in an elliptical annulus of equal area on the sky as the previous panel. Right-hand panel: Hess diagram of the CMD difference between stars within $a = 2.0$ arcmin and background stars (25.0 arcmin $< a <$ 40.0 arcmin). The mean photometric error is shown in the extreme left of each panel.

too narrow isochrone masks at the bright magnitudes, where uncertainties are small. We use the CMD space between them to filter the most likely cluster stars. See the middle and right-hand panels of Fig. 2 for a density map and an elliptical Poisson significance profile of objects inside this isochrone filter, respectively. The CMD difference relative to the background field, in their respective elliptical areas on the sky, is shown as the Hess diagram in the right-hand panel of Fig. 5. The main-sequence turn-off (MSTO) and sub-giant branch (SGB) are clearly visible.

As previously mentioned, we summarize the inferred properties of DES 1 in Table 3. The table lists positions, structural parameters, central (Σ_c) and background (Σ_{bgd}) densities, half-light radius (r_h), distance ($D_\odot$), absolute magnitude (M_V), test statistic (TS), peak Poisson significance (PS) value, core radius (r_c), and tidal radius (r_t), as well as best-fitting CMD parameters. The TS is based on the likelihood ratio between a hypothesis that includes an object versus a field-only hypothesis (see Bechtol et al. 2015).

In addition, we use Y2Q1[5] data to determine the properties of DES 1, but adopting a different magnitude threshold, $g < 23$ mag. By using a maximum-likelihood that simultaneously fits the profile (assuming a Plummer model) and the distance (but assuming an age of 12 Gyrs and a spread in metallicities), we obtain a distance modulus of $(m - M)_0 = 19.6$, in agreement with the method described earlier. The alternative r_h, however, is larger, $r_h \simeq 0.7$ arcmin. This value is marginally consistent with the previous ones reported here. Visual fits were also independently made to the object's CMD. Again, the results agree well with those from the maximum-likelihood fits shown on the table: log(Age) = 9.9, [Fe/H] = -1.88, $A_V = 0.03$, and $(m - M)_0 = 19.9$.

The quoted M_V estimate was computed by integrating overall masses along the best-fitting model isochrone assuming a Kroupa (2001) IMF, and normalizing the number of objects by those observed in the CMD with $r < 23$ mag and which fall in the isochrone filter. The star counts were corrected for sample incompleteness. As we count stars in $r < 23$ mag, the main source of uncertainty is due to small number of stars that are detected in the DES imaging.

[5] The Y2Q1 (year-two quick release) data set consists of exposures taken in the first and second years of DES. This data set is derived from single-epoch imaging instead (for details, see Drlica-Wagner et al. 2015).

We then calculate the uncertainty by estimating the upper and lower limits for the integrated V magnitude. We convert from DES g and r magnitudes to V magnitudes using

$$g_{SDSS} = g_{DES} + 0.104(g_{DES} - r_{DES}) - 0.01$$
$$r_{SDSS} = r_{DES} + 0.102(g_{DES} - r_{DES}) - 0.02$$
$$V = g_{SDSS} - 0.59(g_{SDSS} - r_{SDSS}) - 0.01. \quad (8)$$

This transform from DES g and r magnitudes to V-band magnitudes was derived using an SDSS stellar calibration sample and the equations from Jester et al. (2005) (see Bechtol et al. 2015).

5 HOROLOGIUM II

As mentioned earlier, Kim & Jerjen (2015b) report an additional MW satellite besides those found by Bechtol et al. (2015) and Koposov et al. (2015). Our reanalysis of Y1A1 presented here confirms this object, Horologium II, as a real stellar system. In fact, once we allow for a deeper magnitude threshold, as explained in Section 2, we detect it not only with the method described in Section 3 but also with the maximum-likelihood satellite search method described in Bechtol et al. (2015).

Fig. 6 shows the same information as Fig. 2, but now for Horologium II. A clear overdensity of stars is seen in the density map on the sky. The statistical significance of this overdensity is close to nine times the expected Poisson fluctuation in the background.

We have used the maximum-likelihood method to fit the spatial and CMD distributions as in the previous section. Table 4 lists the structural and isochrone parameters. The latter were derived from the most likely member stars when assuming an exponential profile.

The left-hand panel of Fig. 7 shows the CMD for Horologium II within an ellipse with semimajor axis $a = 3.0$ arcmin. The middle panel shows the background CMD in an elliptical annulus of equal area, whose inner semimajor axis is equal to 30.0 arcmin. The best-fitting PARSEC (Bressan et al. 2012) isochrone is shown. The sequences bracketing the best-fitting isochrone are also shown. The MSTO, SGB, and red giant branch are visible. Note that the CMD of Horologium II shows two stars that may belong to the HB. However, our maximum-likelihood fit assigns these stars a low probability of membership to Horologium II. The right-hand

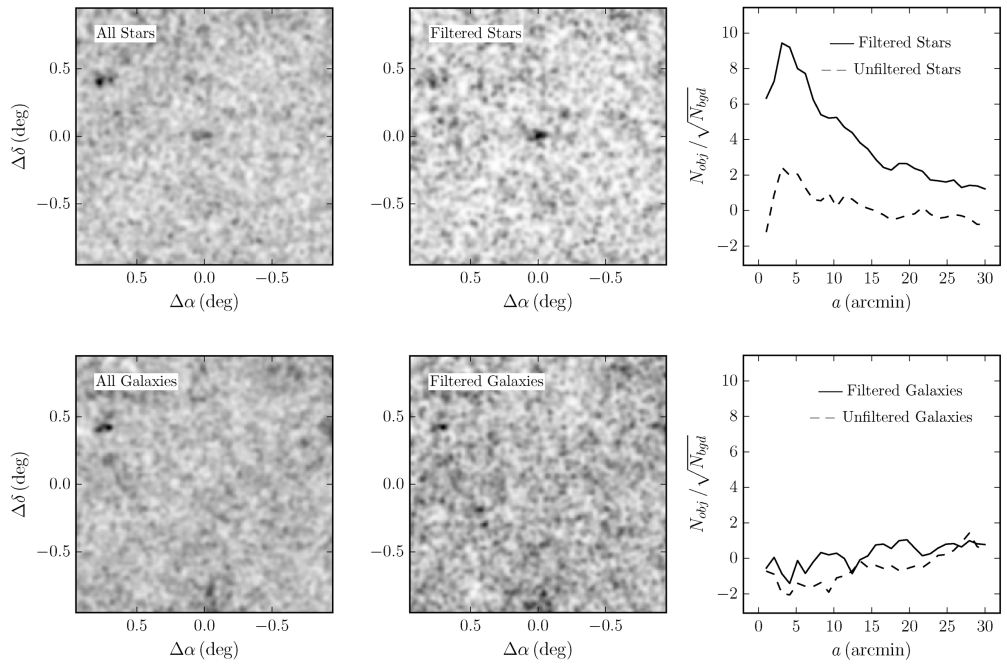

Figure 6. All panels are the same as those in Fig. 2 but now for the Horologium II satellite dwarf.

Table 4. Properties of Horologium II.

Parameters	Exponential profile
α_0 (J2000)	$03^h16^m27\overset{s}{.}6 \pm 39\overset{s}{.}3$
δ_0 (J2000)	$-50°00'36\overset{''}{.}7 \pm 46\overset{''}{.}7$
$D_\odot$ (kpc)	∼79.4
r_e	$1\overset{'}{.}32 \pm 0\overset{'}{.}45$
θ (deg)	106.3 ± 55.0
ϵ	0.57 ± 0.41
Σ_c (stars arcmin^{-2})	7.76 ± 1.29
Σ_{bgd} (stars arcmin^{-2})	1.80 ± 0.01
r_h	$2\overset{'}{.}22 \pm 0\overset{'}{.}76^a$
r_h (pc)	51.27 ± 17.55^b
M_V	$-2.72^{+0.67}_{-0.41}$
TS	52.3
PS	9.2 ± 2.7
[Fe/H]	-1.18 ± 0.24^c
log (Age)	9.88 ± 0.06
A_V	0.03 ± 0.11
$(m - M)_0$	19.50 ± 0.21

[a]Using the relation, $r_h = 1.68 r_e$ (Martin et al. 2008).
[b]Adopting a distance of 79.4 kpc.
[c]Adopting $Z_\odot = 0.0152$ (Bressan et al. 2012).

panel shows a binned elliptical density profile for Horologium II as a function of semimajor axis. For the centre of the overdensity, we adopt the value determined from the maximum-likelihood fit using an exponential profile. The best-fitting elliptical exponential profile is also overplotted.

Our distance, size, ellipticity, and absolute luminosity estimates are in good agreement (within 1σ) with those from the discovery paper by Kim & Jerjen (2015b). The position angle is within 2σ of its quoted value. The largest discrepancies occur for the isochrone parameters. We fit the observed CMD of Horologium II to a younger and more metal-rich PARSEC model than Kim & Jerjen (2015b). However, our likelihood function over the metallicity and age plane exhibits a tail of high-likelihood values towards lower Z and older ages. The discrepancy may also be related to the fact that our listed redenning value comes out of the maximum-likelihood CMD fit, whereas the values from Schlegel et al. (1998) maps (with corrections from Schlafly & Finkbeiner 2011) are used in the discovery paper.

6 CONCLUSIONS

In this paper, we make a deeper probe on the DES Y1A1 catalogue in search for additional Galactic satellites besides those previously reported by the collaboration (Bechtol et al. 2015). We report the discovery of a new stellar system in the MW halo, using catalogues based on first-year data from the DES. We have explored the data at least 1 mag deeper ($g < 24$ mag) than previously done in Bechtol et al. (2015). The candidate adds to the 11 previously identified systems found using DECam images (Bechtol et al. 2015; Kim & Jerjen 2015b; Kim et al. 2015; Koposov et al. 2015; Martin et al. 2015). We also confirm the dwarf galaxy candidate Horologium II, originally discovered by Kim & Jerjen (2015b), as a significant overdensity in the Y1A1 catalogue. Our best-fitting structural parameters for Horologium II are in general agreement with the ones derived by those authors, although the isochrone fit points to a younger and more metal-rich object than previously reported.

DES 1 is detected as a significant stellar overdensity both spatially and on the CMD plane. Isochrone fits based on two different methods show that it is made up of old and metal poor stars, as commonly observed in MW satellites found in the Galactic halo.

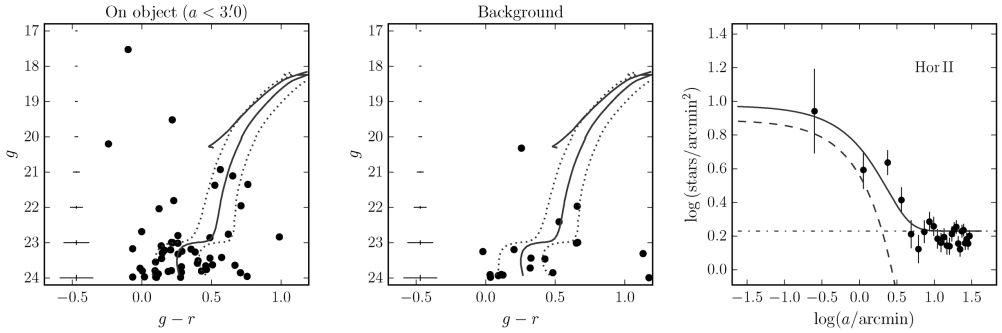

Figure 7. Left-hand panel: CMD of stars within an ellipse with semimajor axis $a = 3.0$ arcmin from the centre of Horologium II. The maximum-likelihood PARSEC (Bressan et al. 2012) isochrone fit is shown, along with ridge lines meant to bracket the most likely members. Middle panel: CMD of background stars in an elliptical annulus of equal area on the sky as the previous panel. The mean photometric error is shown in the extreme left of these panels. Right-hand panel: solid points show the binned density profile for Horologium II, constructed in elliptical annuli using the derived structural parameters from the best-fitting exponential profile (see Table 4). Error bars are based on a Poisson statistics. The dashed line shows the best fit of exponential profile, the horizontal dot–dashed line shows the background level, and the solid line represents the combination of both.

Maximum-likelihood fits of the King profile from DES 1 yield a core radius of $r_c \simeq 0.08$ arcmin, which at a distance $\simeq 77.6$ kpc corresponds to a physical size of $r_h \simeq 9.88$ pc. Its estimated distance places this faint cluster candidate as one of farthest away from the Sun. The absolute magnitude has been determined using a similar approach as Koposov et al. (2015), yielding $M_V \simeq -2.21$ for DES 1. Taken together, the physical size and luminosity place DES 1 in the locus occupied by low-luminosity star clusters. DES 1 is also significantly elongated [$\epsilon \simeq 0.69$ (Exponential), $\epsilon \simeq 0.53$ (King)], something that is apparent not only from the both profiles fit, but also from the distribution of the stars on the sky (Figs 1 and 3). It is, in fact, the most elongated halo cluster known to date, although, given the error bars, its ellipticity is marginally consistent with those of Kim 1, Laevens 3 (see Kim & Jerjen 2015a; Laevens et al. 2015b, respectively). The very high inferred ellipticity suggests that DES 1 is in dynamical process of tidal disruption, despite its large distance, and makes it a very interesting object for deeper imaging and spectroscopic follow up.

Due to the low number of probable member stars detected in the DES imaging, it is difficult to extract more reliable information about DES 1 at this stage. Steps to acquire deeper imaging of this object are already under way.

A search for satellites in data collected by the DES during its second season, including new areas sky, is under way. It is likely that additional new stellar systems will be discovered soon.

ACKNOWLEDGEMENTS

This paper has gone through internal review by the DES collaboration.

Funding for the DES Projects has been provided by the US Department of Energy, the US National Science Foundation, the Ministry of Science and Education of Spain, the Science and Technology Facilities Council of the United Kingdom, the Higher Education Funding Council for England, the National Center for Supercomputing Applications at the University of Illinois at Urbana-Champaign, the Kavli Institute of Cosmological Physics at the University of Chicago, the Center for Cosmology and Astro-Particle Physics at the Ohio State University, the Mitchell Institute for Fundamental Physics and Astronomy at Texas A&M University, Financiadora de Estudos e Projetos, Fundação Carlos Chagas Filho de Amparo à Pesquisa do Estado do Rio de Janeiro, Conselho Nacional de Desenvolvimento Científico e Tecnológico and the Ministério da Ciência, Tecnologia e Inovação, the Deutsche Forschungsgemeinschaft and the Collaborating Institutions in the DES. The DESDM system is supported by the National Science Foundation under Grant Number AST-1138766. The DES participants from Spanish institutions are partially supported by MINECO under grants AYA2012-39559, ESP2013-48274, FPA2013-47986, and Centro de Excelencia Severo Ochoa SEV-2012-0234, some of which include ERDF funds from the European Union.

The Collaborating Institutions are Argonne National Laboratory, the University of California at Santa Cruz, the University of Cambridge, Centro de Investigaciones Enérgeticas, Medioambientales y Tecnológicas-Madrid, the University of Chicago, University College London, the DES-Brazil Consortium, the University of Edinburgh, the Eidgenössische Technische Hochschule (ETH) Zürich, Fermi National Accelerator Laboratory, the University of Illinois at Urbana-Champaign, the Institut de Ciències de l'Espai (IEEC/CSIC), the Institut de Física d'Altes Energies, Lawrence Berkeley National Laboratory, the Ludwig-Maximilians Universität München and the associated Excellence Cluster Universe, the University of Michigan, the National Optical Astronomy Observatory, the University of Nottingham, The Ohio State University, the University of Pennsylvania, the University of Portsmouth, SLAC National Accelerator Laboratory, Stanford University, the University of Sussex, and Texas A&M University.

The DES data management system is supported by the National Science Foundation under Grant Number AST-1138766. The DES participants from Spanish institutions are partially supported by MINECO under grants AYA2012-39559, ESP2013-48274, FPA2013-47986, and Centro de Excelencia Severo Ochoa SEV-2012-0234.

Research leading to these results has received funding from the European Research Council under the European Union's Seventh Framework Programme (FP7/2007-2013) including ERC grant agreements 240672, 291329, and 306478.

EB acknowledges financial support from the European Research Council (ERC-StG-335936, CLUSTERS).

REFERENCES

Abbott T. et al., 2005, (arXiv:Astrophysics:e-prints)
Balbinot E., Santiago B. X., da Costa L. N., Makler M., Maia M. A. G., 2011, MNRAS, 416, 393
Balbinot E. et al., 2013, ApJ, 767, 101
Bechtol K. et al., 2015, ApJ, 807, 50
Belokurov V. et al., 2010, ApJ, 712, L103
Bertin E., Arnouts S., 1996, A&AS, 117, 393
Bouy H., Bertin E., Moraux E., Cuillandre J.-C., Bouvier J., Barrado D., Solano E., Bayo A., 2013, A&A, 554, A101
Bressan A., Marigo P., Girardi L., Salasnich B., Dal Cero C., Rubele S., Nanni A., 2012, MNRAS, 427, 127
Desai S. et al., 2012, ApJ, 757, 83
Drlica-Wagner A. et al., 2015, ApJ, 813, 109
Fadely R., Willman B., Geha M., Walsh S., Muñoz R. R., Jerjen H., Vargas L. C., Da Costa G. S., 2011, AJ, 142, 88
Flaugher B. et al., 2015, AJ, 150, 150
Hargis J. R., Willman B., Peter A. H. G., 2014, ApJ, 795, L13
Jester S. et al., 2005, AJ, 130, 873
Jurić M. et al., 2008, ApJ, 673, 864
Kim D., Jerjen H., 2015a, ApJ, 799, 73
Kim D., Jerjen H., 2015b, ApJ, 808, L39
Kim D., Jerjen H., Milone A. P., Mackey D., Da Costa G. S., 2015, ApJ, 803, 63
King I., 1962, AJ, 67, 471
Koposov S. et al., 2007, ApJ, 669, 337
Koposov S. E., Belokurov V., Torrealba G., Evans N. W., 2015, ApJ, 805, 130
Kroupa P., 2001, MNRAS, 322, 231
Laevens B. P. M. et al., 2014, ApJ, 786, L3
Laevens B. P. M. et al., 2015a, ApJ, 802, L18
Laevens B. P. M. et al., 2015b, ApJ, 813, 44
Law D. R., Majewski S. R., 2010, ApJ, 718, 1128
Lee Y.-W., Demarque P., Zinn R., 1994, ApJ, 423, 248
McConnachie A. W., 2012, AJ, 144, 4
Marino A. F. et al., 2014, MNRAS, 442, 3044
Marino A. F. et al., 2015, MNRAS, 450, 815
Martin N. F., de Jong J. T. A., Rix H.-W., 2008, ApJ, 684, 1075
Martin N. F. et al., 2015, ApJ, 804, L5
Milone A. P. et al., 2014, ApJ, 785, 21
Mohr J. J. et al., 2012, in Radziwill N. M., Chiozzi G., eds, Proc. SPIE Conf. Ser. Vol. 8451, Software and Cyberinfrastructure for Astronomy II. SPIE, Bellingham, p. 84510D
Muñoz R. R., Geha M., Côté P., Vargas L. C., Santana F. A., Stetson P., Simon J. D., Djorgovski S. G., 2012, ApJ, 753, L15
Pawlowski M. S., Pflamm-Altenburg J., Kroupa P., 2012, MNRAS, 423, 1109
Pawlowski M. S., McGaugh S. S., Jerjen H., 2015, MNRAS, 453, 1047
Pieres A. et al., 2015, preprint (arXiv:1512.01032)
Rockosi C. M. et al., 2002, AJ, 124, 349
Schlafly E. F., Finkbeiner D. P., 2011, ApJ, 737, 103
Schlegel D. J., Finkbeiner D. P., Davis M., 1998, ApJ, 500, 525
Sevilla I. et al., 2011, preprint (arXiv:1109.6741)
Simon J. D., Geha M., 2007, ApJ, 670, 313
Sprott D. A., 2000, Statistical Inference in Science. Springer-Verlag, Berlin
Szabo T., Pierpaoli E., Dong F., Pipino A., Gunn J., 2011, ApJ, 736, 21
Tollerud E. J., Bullock J. S., Strigari L. E., Willman B., 2008, ApJ, 688, 277
Zinn R., 1985, ApJ, 293, 424
Zinn R., 1993, in Smith G. H., Brodie J. P., eds, ASP Conf. Ser. Vol. 48, The Globular Cluster-Galaxy Connection. Astron. Soc. Pac., San Francisco, p. 38

[1]*Instituto de Física, UFRGS, Caixa Postal 15051, Porto Alegre, RS 91501-970, Brazil*
[2]*Laboratório Interinstitucional de e-Astronomia – LIneA, Rua Gal. José Cristino 77, Rio de Janeiro, RJ 20921-400, Brazil*
[3]*Department of Physics, University of Surrey, Guildford GU2 7XH, UK*
[4]*Kavli Institute for Cosmological Physics, University of Chicago, Chicago, IL 60637, USA*
[5]*Fermi National Accelerator Laboratory, PO Box 500, Batavia, IL 60510, USA*
[6]*Observatório Nacional, Rua Gal. José Cristino 77, Rio de Janeiro, RJ 20921-400, Brazil*
[7]*Cerro Tololo Inter-American Observatory, National Optical Astronomy Observatory, Casilla 603, La Serena, Chile*
[8]*Department of Physics and Astronomy, University College London, Gower Street, London WC1E 6BT, UK*
[9]*CNRS, UMR 7095, Institut d'Astrophysique de Paris, F-75014 Paris, France*
[10]*Sorbonne Universités, UPMC Univ Paris 06, UMR 7095, Institut d'Astrophysique de Paris, F-75014, Paris, France*
[11]*Kavli Institute for Particle Astrophysics & Cosmology, PO Box 2450, Stanford University, Stanford, CA 94305, USA*
[12]*SLAC National Accelerator Laboratory, Menlo Park, CA 94025, USA*
[13]*Department of Astronomy, University of Illinois, 1002 W. Green Street, Urbana, IL 61801, USA*
[14]*National Center for Supercomputing Applications, 1205 West Clark St, Urbana, IL 61801, USA*
[15]*Institut de Ciéncies de l'Espai, IEEC-CSIC, Campus UAB, Carrer de Can Magrans, s/n, E-08193 Bellaterra, Barcelona, Spain*
[16]*Institut de Física d'Altes Energies, Universitat Autònoma de Barcelona, E-08193 Bellaterra, Barcelona, Spain*
[17]*Excellence Cluster Universe, Boltzmannstr. 2, D-85748 Garching, Germany*
[18]*Faculty of Physics, Ludwig-Maximilians University, Scheinerstr. 1, D-81679 Munich, Germany*
[19]*Department of Physics and Astronomy, University of Pennsylvania, Philadelphia, PA 19104, USA*
[20]*Jet Propulsion Laboratory, California Institute of Technology, 4800 Oak Grove Dr., Pasadena, CA 91109, USA*
[21]*Kavli Institute for Cosmological Physics, University of Chicago, Chicago, IL 60637, USA*
[22]*Department of Physics, University of Michigan, Ann Arbor, MI 48109, USA*
[23]*Max Planck Institute for Extraterrestrial Physics, Giessenbachstrasse, D-85748 Garching, Germany*
[24]*Universitäts-Sternwarte, Fakultät für Physik, Ludwig-Maximilians Universität München, Scheinerstr. 1, D-81679 München, Germany*
[25]*Center for Cosmology and Astro-Particle Physics, The Ohio State University, Columbus, OH 43210, USA*
[26]*Department of Physics, The Ohio State University, Columbus, OH 43210, USA*
[27]*Australian Astronomical Observatory, North Ryde, NSW 2113, Australia*
[28]*George P. and Cynthia Woods Mitchell Institute for Fundamental Physics and Astronomy, and Department of Physics and Astronomy, Texas A&M University, College Station, TX 77843, USA*
[29]*Department of Astronomy, The Ohio State University, Columbus, OH 43210, USA*
[30]*Institució Catalana de Recerca i Estudis Avançats, E-08010 Barcelona, Spain*
[31]*Institute of Cosmology and Gravitation, University of Portsmouth, Portsmouth PO1 3FX, UK*
[32]*Department of Physics and Astronomy, Pevensey Building, University of Sussex, Brighton BN1 9QH, UK*
[33]*Centro de Investigaciones Energéticas, Medioambientales y Tecnológicas (CIEMAT), Madrid, Spain*
[34]*Department of Physics, University of Illinois, 1110 W. Green St, Urbana, IL 61801, USA*

This paper has been typeset from a TEX/LATEX file prepared by the author.

Neste artigo nosso maior trabalho foi na revisão interna na colaboração, inserindo correções e comentários sobre o artigo.

The Astrophysical Journal, 820:58 (8pp), 2016 March 20 doi:10.3847/0004-637X/820/1/58

THE PHOENIX STREAM: A COLD STREAM IN THE SOUTHERN HEMISPHERE

E. Balbinot[1], B. Yanny[2], T. S. Li[3], B. Santiago[4,5], J. L. Marshall[3], D. A. Finley[2], A. Pieres[4,5], T. M. C. Abbott[6], F. B. Abdalla[7], S. Allam[2], A. Benoit-Lévy[7], G. M. Bernstein[8], E. Bertin[9,10], D. Brooks[7], D. L. Burke[11,12], A. Carnero Rosell[5,13], M. Carrasco Kind[14,15], J. Carretero[16,17], C. E. Cunha[11], L. N. da Costa[5,13], D. L. DePoy[3], S. Desai[18,19], H. T. Diehl[2], P. Doel[7], J. Estrada[2], B. Flaugher[2], J. Frieman[2,20], D. W. Gerdes[21], D. Gruen[22,23], R. A. Gruendl[14,15], K. Honscheid[24,25], D. J. James[6], K. Kuehn[26], N. Kuropatkin[2], O. Lahav[7], M. March[8], P. Martini[24,27], R. Miquel[17,28], R. C. Nichol[29], R. Ogando[5,13], A. K. Romer[30], E. Sanchez[31], M. Schubnell[21], I. Sevilla-Noarbe[14,31], R. C. Smith[6], M. Soares-Santos[2], F. Sobreira[2,5], E. Suchyta[24,25], G. Tarle[21], D. Thomas[29], D. Tucker[2], and A. R. Walker[6]
(The DES Collaboration)
[1] Department of Physics, University of Surrey, Guildford GU2 7XH, UK; e.balbinot@surrey.ac.uk
[2] Fermi National Accelerator Laboratory, P.O. Box 500, Batavia, IL 60510, USA
[3] George P. and Cynthia Woods Mitchell Institute for Fundamental Physics and Astronomy, and Department of Physics and Astronomy, Texas A&M University, College Station, TX 77843, USA
[4] Instituto de Física, UFRGS, Caixa Postal 15051, Porto Alegre, RS—91501-970, Brazil
[5] Laboratório Interinstitucional de e-Astronomia—LIneA, Rua Gal. José Cristino 77, Rio de Janeiro, RJ—20921-400, Brazil
[6] Cerro Tololo Inter-American Observatory, National Optical Astronomy Observatory, Casilla 603, La Serena, Chile
[7] Department of Physics & Astronomy, University College London, Gower Street, London, WC1E 6BT, UK
[8] Department of Physics and Astronomy, University of Pennsylvania, Philadelphia, PA 19104, USA
[9] CNRS, UMR 7095, Institut d'Astrophysique de Paris, F-75014, Paris, France
[10] Sorbonne Universités, UPMC Univ Paris 06, UMR 7095, Institut d'Astrophysique de Paris, F-75014, Paris, France
[11] Kavli Institute for Particle Astrophysics & Cosmology, P.O. Box 2450, Stanford University, Stanford, CA 94305, USA
[12] SLAC National Accelerator Laboratory, Menlo Park, CA 94025, USA
[13] Observatório Nacional, Rua Gal. José Cristino 77, Rio de Janeiro, RJ—20921-400, Brazil
[14] Department of Astronomy, University of Illinois, 1002 W. Green Street, Urbana, IL 61801, USA
[15] National Center for Supercomputing Applications, 1205 West Clark Street, Urbana, IL 61801, USA
[16] Institut de Ciències de l'Espai, IEEC-CSIC, Campus UAB, Carrer de Can Magrans, s/n, E-08193 Bellaterra, Barcelona, Spain
[17] Institut de Física d'Altes Energies, Universitat Autònoma de Barcelona, E-08193 Bellaterra, Barcelona, Spain
[18] Excellence Cluster universe, Boltzmannstr. 2, D-85748 Garching, Germany
[19] Faculty of Physics, Ludwig-Maximilians University, Scheinerstr. 1, D-81679 Munich, Germany
[20] Kavli Institute for Cosmological Physics, University of Chicago, Chicago, IL 60637, USA
[21] Department of Physics, University of Michigan, Ann Arbor, MI 48109, USA
[22] Max Planck Institute for Extraterrestrial Physics, Giessenbachstrasse, D-85748 Garching, Germany
[23] Universitäts-Sternwarte, Fakultät für Physik, Ludwig-Maximilians Universität München, Scheinerstr. 1, D-81679 München, Germany
[24] Center for Cosmology and Astro-Particle Physics, The Ohio State University, Columbus, OH 43210, USA
[25] Department of Physics, The Ohio State University, Columbus, OH 43210, USA
[26] Australian Astronomical Observatory, North Ryde, NSW 2113, Australia
[27] Department of Astronomy, The Ohio State University, Columbus, OH 43210, USA
[28] Institució Catalana de Recerca i Estudis Avançats, E-08010 Barcelona, Spain
[29] Institute of Cosmology & Gravitation, University of Portsmouth, Portsmouth, PO1 3FX, UK
[30] Department of Physics and Astronomy, Pevensey Building, University of Sussex, Brighton, BN1 9QH, UK
[31] Centro de Investigaciones Energéticas, Medioambientales y Tecnológicas (CIEMAT), Madrid, Spain
Received 2015 September 10; accepted 2016 February 5; published 2016 March 17

ABSTRACT

We report the discovery of a stellar stream in the Dark Energy Survey Year 1 (Y1A1) data. The discovery was made through simple color–magnitude filters and visual inspection of the Y1A1 data. We refer to this new object as the Phoenix stream, after its resident constellation. After subtraction of the background stellar population we detect a clear signal of a simple stellar population. By fitting the ridge line of the stream in color–magnitude space, we find that a stellar population with age $\tau = 11.5 \pm 0.5$ Gyr and [Fe/H] < -1.6, located 17.5 ± 0.9 kpc from the Sun, gives an adequate description of the stream stellar population. The stream is detected over an extension of $8\overset{\circ}{.}1$ (2.5 kpc) and has a width of ∼54 pc assuming a Gaussian profile, indicating that a globular cluster (GC) is a probable progenitor. There is no known GC within 5 kpc that is compatible with being the progenitor of the stream, assuming that the stream traces its orbit. We examined overdensities (ODs) along the stream, however, no obvious counterpart-bound stellar system is visible in the coadded images. We also find ODs along the stream that appear to be symmetrically distributed—consistent with the epicyclic OD scenario for the formation of cold streams—as well as a misalignment between the northern and southern part of stream. Despite the close proximity we find no evidence that this stream and the halo cluster NGC 1261 have a common accretion origin linked to the recently found EriPhe OD.

Key words: Galaxy: halo – Galaxy: structure

1. INTRODUCTION

Our understanding of the structure of the Galactic halo has evolved considerably in the past two decades, largely thanks to deep and homogeneous photometric surveys, such as the Two Micron All Sky Survey (Skrutskie et al. 2006) and the Sloan Digital Sky Survey (SDSS; Ahn et al. 2014). The stellar halo is

The Astrophysical Journal, 820:58 (8pp), 2016 March 20

now known to be inhabited by a variety of spatial and kinematic stellar substructure, from globular clusters (GCs) and dwarf galaxies to extended stellar clouds and streams (see, e.g., Willman et al. 2005; Belokurov et al. 2006, 2007). In fact, recent simulations based on hierarchical models of structure formation predict that most halo stars were brought by the disruption of the Galactic substructures (Bullock et al. 2001).

The thin and cold stellar streams found in the Galaxy often span tens of degrees on the sky and originate from the tidal effects of the host on the progenitor, whether a GC or a dwarf galaxy. Perhaps the most conspicuous examples of Galactic streams are those associated with the Pal 5 GC and the Sagittarius dwarf (Odenkirchen et al. 2001; Newberg et al. 2002). The tidal nature of such streams makes them useful probes of the dark matter distribution across the halo (Johnston et al. 2005; Küpper et al. 2015). Detailed modeling of a stream's position, distance, kinematics, gaps, and overdensities (ODs) in extended cold streams also leads to constraints on the amount of dark matter fragments orbiting the halo, known as subhalos (Yoon et al. 2011; Ngan et al. 2015), on the progenitor's properties and on Galactic parameters (Koposov et al. 2010).

The Dark Energy Survey (DES; The Dark Energy Survey Collaboration 2005) is an ongoing deep ($g \sim 24.7$) photometric survey in the southern hemisphere that started its planned 5-year mission of collecting data in 2013. Despite the mission's focus on cosmology, DES data have already produced a wealth of results pertaining to resolved stellar populations in the Galaxy and its vicinity, including the analysis of the structure and stellar populations in the outskirts of the Large Magellanic Cloud (LMC; Balbinot et al. 2015), the identification of new Galactic companions (Bechtol et al. 2015; Drlica-Wagner et al. 2015; Kim & Jerjen 2015; Koposov et al. 2015; Luque et al. 2016), and the development of a new search for variable stars exclusively based on DES data (D. Hatt et al. 2016, in preparation).

Here we report on the discovery of the first cold stellar stream using DES data. In Section 2 we give more details about DES, the data used, and the search algorithm. Our results are presented in Section 3 and our conclusions are in Section 4.

2. DATA ANALYSIS

DES is a wide-field optical imaging survey using broad photometric bands (*grizY*) performed with the Dark Energy Camera (DECam; described in detail in Flaugher et al. 2015). The DECam focal plane is comprised of 74 CCDs: 62 2k × 4k CCDs dedicated to science imaging and 12 2k × 2k CCDs for guiding, focus, and alignment. DECam is installed at the prime focus of the 4 m Blanco telescope at the Cerro Tololo Inter-American Observatory. In this configuration, DECam has a $2\overset{\circ}{.}2$ wide field-of-view and a central pixel scale of 0.263 arcseconds. The full DES survey is scheduled for 525 nights distributed over five years. Here, we consider data from the first year of DES obtained between 2013 August 15 and 2014 February 9.

The first internal annual release of DES data (Y1A1) comprises the data products obtained from the processing of a subset of wide-field and supernova-field data accumulated during the first year of DES operations (Diehl et al. 2014). Briefly, the image processing pipeline consists of image detrending (crosstalk correction, bias subtraction, flat-fielding, etc.), astrometric calibration, nightly photometric calibration, global calibration, image coaddition, and object catalog creation. For a more detailed description of the DESDM image processing pipeline, we refer to Desai et al. (2012) and Mohr et al. (2012), and for a recent overview, Balbinot et al. (2015). The SExtractor toolkit is used to create image catalogs from the processed and coadded images (Bertin 2011; Bertin & Arnouts 1996). The number of overlapping exposures in Y1A1 varies, but most of the footprint has at least three coadded exposures. The Y1A1 coadd object catalog contains ∼131 million unique objects spread over $\sim 1800\,\mathrm{deg}^2$. This area includes $\sim 200\,\mathrm{deg}^2$ overlapping with the Stripe-82 region of SDSS, as well as a contiguous region of $\sim 1600\,\mathrm{deg}^2$ overlapping with the South Pole Telescope footprint.

We perform stellar selection on the Y1A1 coadd object catalog based on the *spread_model* quantity output of SExtractor (Desai et al. 2012). To avoid issues arising from fitting the PSF across variable depth coadded images, we utilize the weighted-average (wavg) of the *spread_model* measurements from the single-epoch exposures. Our stellar sample consists of well-measured objects with $|wavg\_spread\_model\_i| < 0.003$, $flags_{\{g,r,i\}} < 4$, and $magerr\_auto\_\{g, r, i\} < 1$ (henceforth referred to as "stars"). Our stellar completeness is >90% down to magnitude $g \sim 22$, at which point it drops to ∼50% by $g \sim 23$ (Bechtol et al. 2015).

Stars are extinction-corrected according to Schlegel et al. (1998), with the scaling correction from Schlafly & Finkbeiner (2011), assuming the extinction curve from Cardelli et al. (1989) and a calibration at infinity, that is, we assume that the light of every object in our sample crosses the full extent of the dust column measured in the dust maps.

From this point all magnitudes considered in this paper are corrected for the extinction.

2.1. Search Method

Using the objects classified as stars according to the criteria described in the previous section, we apply narrow color filters to isolate interesting stellar types such as old turnoff stars and horizontal branch (HB) stars. To avoid issues related to the inhomogeneous photometric depth of the survey and saturation of bright stars, we only use stars with magnitudes $17 < g < 23$. We find that this magnitude limit yields a sample that has a completeness that is fairly constant across the footprint and produces a smoothly varying density for the field stars.

For each color-selected catalog we build a sky "density map." Throughout this paper we use density maps to refer to maps where we show the number of sources per pixel (N) in a Cartesian projection. The pixel size is made explicit whenever necessary. The pixel area is corrected for changes in solid angle with declination. These density maps are visually inspected for ODs. In Figure 1 we show the particularly interesting density map for stars with $0.2 < (g - r) < 0.6$ and $20 < g < 23$, which mainly selects turnoff and upper main-sequence stars from an old (>10 Gyr) simple stellar population (SSP), according to Bressan et al. (2012). Several features are noticeable, such as the GC NGC 1261, the Phoenix dwarf galaxy (Canterna & Flower 1977), and two of the recently discovered dwarf galaxies (Bechtol et al. 2015; Koposov et al. 2015): Reticulum II (Ret II) and Eridanus II (Eri II). These objects are labeled with their names in the figure. A linear structure is also visible near the Phoenix dwarf extending from $(\alpha, \delta) \simeq (20^\circ, -57^\circ)$ to $(27^\circ, -45^\circ)$. This structure is

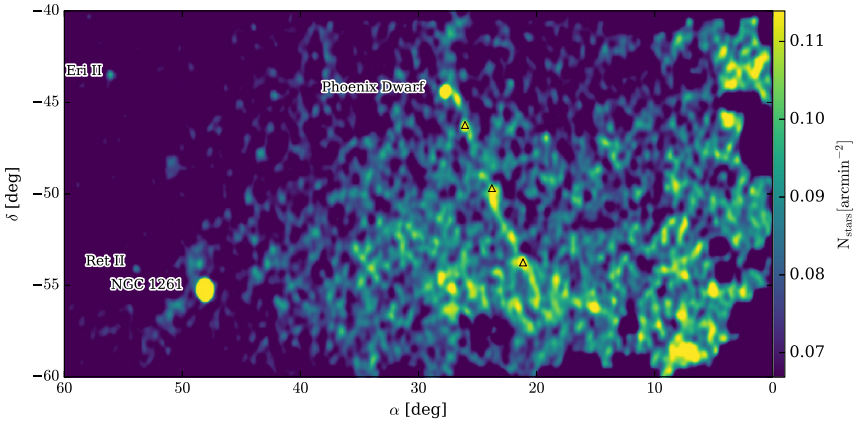

Figure 1. Y1A1 density map for stars with $0.2 < (g - r) < 0.6$ and $20 < g < 23$. The open triangles show the anchor points adopted for the stream. Other interesting objects are labeled in the figure. This density map was convolved with a 2×1 pixel Gaussian. Each pixel has a size of $4\farcm5 \times 2\farcm8$.

highlighted by open triangles marking high density points along the stream candidate.

In the same figure, a large OD of stars is visible between the stream candidate and NGC 1261. This feature is the Eridanus–Phoenix (EriPhe) OD and it is discussed in detail in a simultaneous publication (Li et al. 2016).

3. RESULTS

By means of the method outlined in the previous section we perform a visual search for stellar ODs. This search, conducted over the full Y1A1 footprint, has revealed only one[32] stream candidate, which is shown in Figure 1. For simplicity, we refer to this candidate stream as the Phoenix stream due to its proximity to the Phoenix constellation.

To study the stellar population that comprises the Phoenix stream we define a line passing through the center of the stream using anchor points along the stream (three open triangles in Figure 1). We then select stars inside a box defined by the stream central line with an offset of $\pm 0\fdg8$ in R.A. We name this selection *on stream*. To compare with the typical Milky Way (MW) stellar population at this position in the sky we select stars in boxes that are offset by $\pm 1\fdg5$ with respect to the central one and have the same width as the *on stream* region. We name these selections *off stream east* and *west*. For each region described above we compute the solid angle normalized Hess diagram. We use Mangle masks (Swanson et al. 2008) to compute the solid angle of each box, taking into account possible holes in the survey footprint. In Figure 2 we show the Hess diagram of the *on stream* minus the average diagram of the two *off stream* ones in logarithmic scale.

From the decontaminated Hess diagram shown in Figure 2 we estimate that the stream has ∼500 stars that fall within the photometric limits of DES. This decontaminated Hess diagram was smoothed using a Gaussian kernel with a dispersion of 0.06×0.2 in color and magnitude, respectively. This step is required due to the low number of stars in the stream and allows us to define the ridge line shown as the red circles in Figure 2. The ridge line is defined as the peak value of counts in color for each magnitude bin, the bin size for the ridge line construction being twice as large as the one used for the Hess diagram. Magnitude bins with low counts or peak values that obviously depart from the bulk of the stream stars are

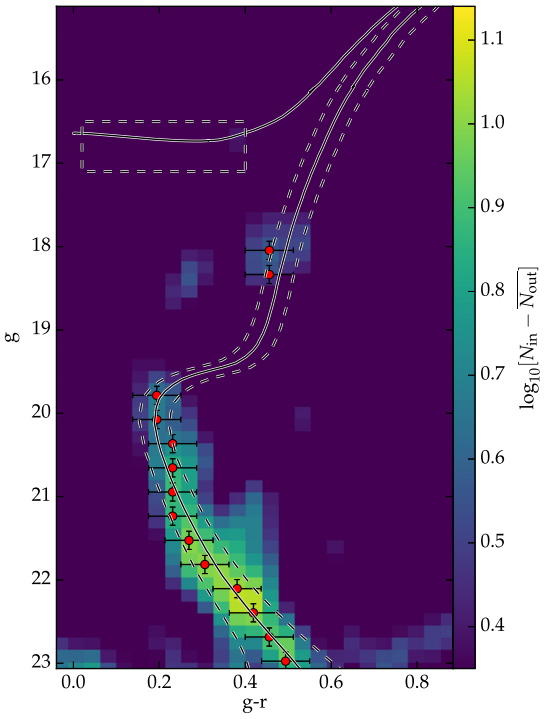

Figure 2. Decontaminated Hess diagram of the stream candidate. The decontamination process is described in detail in the text. The solid line shows an 11.5 Gyr and [Fe/H] = −1.9 PARSEC isochrone (Bressan et al. 2012). The dashed lines show the color–magnitude diagram (CMD) region selected to isolate stream stars, including a box to select horizontal branch (HB) stars. The red dots with error bars form the ridge line used to perform the isochrone fit.

[32] Recently Mackey et al. (2015) reported a 10 kpc-long stream associated with the LMC using a similar data set as the one in this work. We confirm this detection, however, its tidal origin is still uncertain.

Table 1
Phoenix Stream Parameter Summary

Name	Value	Unit	Description
τ	11.5 ± 0.5	Gyr	Age
[Fe/H]	<-1.6	dex	Metallicity
$d_{\odot}$	17.5 ± 0.9	kpc	Heliocentric distance
d_{GC}	18.4 ± 0.9	kpc	Galactocentric distance[a]
σ	54	pc	Stream width[b]
$(\alpha, \delta)_{start}$	(20, −57)	deg	Stream begin point
$(\alpha, \delta)_{end}$	(27, −45)	deg	Stream end point
Θ	8.1	deg	Stream length

Notes.
[a] Computed using $R_{\odot} = 8.3$ kpc.
[b] Assuming a Gaussian profile.

discarded. We define the error bars as equal to the Gaussian kernel size, which is always larger than the photometric errors in the magnitude range shown. This choice of error bar accounts for the broadening of the Hess diagram due to the smoothing process. Using the typical photometric error would yield unrealistically small uncertainty estimates that would propagate into the stellar evolution model fitting, described below.

We compare the ridge line to different PARSEC stellar evolution models (Bressan et al. 2012) by computing the minimum distance from each ridge line point to a given model. The model grid has a resolution of 0.01 in $\log_{10}(\tau/\mathrm{year})$ in the range from 9 to 10.16 and 0.0002 in Z in the range from 0.0001 to 0.001, where τ and Z are age and metallicity. The distance modulus was explored in the range from 15 to 18 in steps of 0.01. For each parameter combination we compute the probability that a given ridge line point was drawn from the isochrone at its minimum distance position to that given point. The probability is computed assuming a normal distribution with a 1σ dispersion as indicated by the error bars. All ridge line points are given the same weight. An obvious improvement would be to weight these points by a mass function (MF). However, the MF of a stream is likely very different from an initial MF and can vary along the stream itself (Koch et al. 2004). For this reason, we leave the study of the MF of the stream to future works with deeper photometry and more accurate membership probabilities.

We calculate a likelihood function for our model by multiplying the individual probabilities of each ridge line point. We define the best model as the one maximizing the likelihood and the parameters' uncertainties are derived using the profile likelihood technique (e.g., Rolke et al. 2005). To estimate the 90% confidence interval of each fitter parameter we find the value of that parameter where the log-likelihood (maximized with respect to the other parameters) decreases by 2.71/2 from its maximum value. We find that the stream population is well described by a model with $(m - M) = 16.21 \pm 0.11$ (or $d_{\odot} = 17.5 \pm 0.9$ kpc), $\log_{10}(\tau/\mathrm{yr}) = 10.06 \pm 0.02$ (or $\tau = 11.5 \pm 0.5$ Gyr), and $Z < 0.0004$ (or [Fe/H] < -1.6). The best-fit model is shown in Figure 2 as the solid black line. Note that the lowest metallicity available in our model grid is still consistent with the stream color–magnitude diagram (CMD), thus we are only able to define a upper bound for the metallicity. We summarize the stream parameters in Table 1.

We use the best-fit model to define a region in the CMD where stream stars are more likely to be. This region is shown as the dashed line in Figure 2. The locus shown in the figure was defined by color-shifting the best-fit model by twice the typical color error at each magnitude value. We also consider that the color uncertainty at magnitudes brighter than $g = 21$ is constant and equal to 0.03.

In Figure 3 we show the density map for stars (left panel) built using the color selection described above but only for stars with $20 < g < 23$. The best-fit model describes the stream population in the full domain of colors and magnitudes observed; however, we find that the HB, sub-giant branch, and red giant branch are very sparsely populated. Including these stars in the CMD selection adds more noise than signal to our density maps. In the same figure, we also show the density map, using the same selection as before, but for sources classified as galaxies (center panel). On the rightmost panel we show a reddening map from Schlegel et al. (1998). In the last two panels the solid line shows the position of the stream. We notice no obvious features in the galaxy or reddening distribution that could mimic the presence of the stream.

3.1. Possible Progenitors

In order to investigate any possible progenitors for the new stream we assume that streams are approximate tracers of the progenitor's orbit (Bovy 2014). We also exploit the property of spherically symmetric potentials in which orbits should be confined to a plane containing the center of such a potential (Binney & Tremaine 2008). The same is approximately true for axisymmetric potentials (Johnston et al. 1996). For more complex potentials this assumption only holds close to the progenitor itself. There is evidence that the MW potential, at least in its inner parts, is well-approximated by an axisymmetric potential (see Küpper et al. 2015). The Phoenix stream lies at 18.4 kpc from the Galactic center where the MW potential should be reasonably spherical (Bell et al. 2008; Deason et al. 2011; Küpper et al. 2015). Under the assumption that the stream formed through the interaction with the MW potential only, we expect that it should be confined to a plane passing through the center of the Galaxy. When observed from the center of the MW this plane is described by a great circle.

To define such a plane we choose three anchor points along the stream. These points are defined by their Galactic coordinates and the heliocentric distance to the stream. We find the plane that contains the anchor points and the MW center. And finally we find the circle oriented the same way as the plane that intersects all anchor points. In order to intersect all three anchor points we must apply corrections to their heliocentric distances, which were so far considered all identical.

We find that a heliocentric distance gradient of ∼1 kpc is necessary for a circular orbit to intersect all three anchor points. In order to check this possible distance gradient we build two separate decontaminated Hess diagrams, following the same procedure outlined in Section 3: one using stars north of $\delta = -56°$ and the other using stars south of this same declination value. Using the ridge line of each of these new Hess diagrams we proceed with the fitting process; however, this time we keep the metallicity and age fixed at the best-fit values found previously using the full stream length. We find that the best-fit distance modulus for the north part of the stream is 16.19 ± 0.12, and 16.35 ± 0.12 in the south. This is

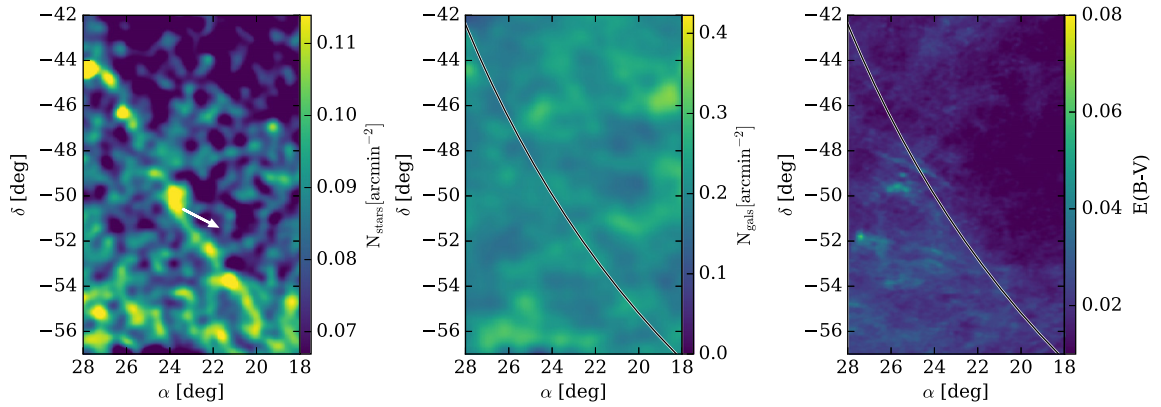

Figure 3. Left panel: density map after applying the color–magnitude selection shown in Figure 2. The white arrow points toward the MW center. Center panel: density map using the same filter as the previous panel but built using sources classified as galaxies. Right panel: $E(B-V)$ color excess map from Schlegel et al. (1998) and Schlafly & Finkbeiner (2011). In the last two maps the solid line shows the position of the stream as seen in the stellar density map. All maps use a pixel size of $4\farcm5 \times 2\farcm8$.

consistent with, but does not require, the ∼1 kpc gradient required for a circular orbit. We conclude that a distance gradient cannot be ruled out for the stream. Detailed spectroscopic observations must be used to isolate stream member stars based on radial velocities and chemical composition and confirm this scenario. For the purpose of looking for possible progenitors close to the stream we will assume a circular orbit.

Using the best-fit circular orbit described above, we look for possible known GCs that are not in the Y1A1 footprint that could be progenitors. This approach does not explore other kinds of orbits, which are more likely: however, it does provide a useful approach for searching for progenitors in the close vicinity of the stream. In Figure 4 we show the best-fit great circle in an all-sky Aitoff Galactic projection. We also show known GCs with galactocentric distances between 15 and 25 kpc, distances consistent with the stream distance. We find that no GC is consistent with this stream under the assumption of a circular orbit.

Another possible scenario is that the progenitor has completely dissolved and only its remains are visible along the stream. To investigate possible progenitors for this stream we first look for ODs on the stream. We start by creating a reference frame where the horizontal axis is oriented along the stream, similar to what has been adopted by Majewski et al. (2003) for the Sagittarius stream. To create such a reference frame we use two Euler angles that define two consecutive rotations (ϕ, θ). The angles were determined by finding the plane that intersects the anchor stream points in Equatorial coordinates. The new reference frame has an azimuthal component (Λ) with an arbitrary origin that is defined in the range $[0, 2\pi)$, and an elevation component (β) defined in the range $[-\frac{\pi}{2}, \frac{\pi}{2}]$. The values of ϕ and θ adopted are $-29\fdg698$ and $72\fdg247$, respectively.

In Figure 5 we show the density map of color-selected stars in the coordinate system described above. We also show the average density map in projection onto the β (left panel) and Λ (top panel) axes. The Λ projection is shown for stars that lie within $\sigma = 0\fdg18$ from the stream centroid in β, where σ is the standard deviation with respect to the stream median line. The stream median line is defined in the stream coordinate system

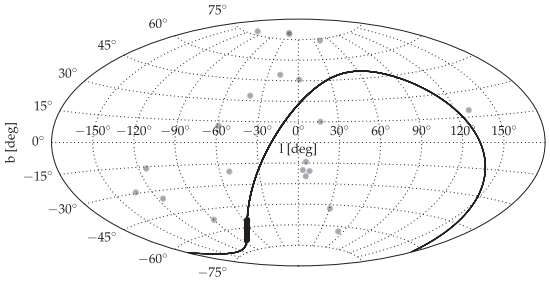

Figure 4. Aitoff projection in Galactic coordinates. The gray circles show GCs with galactocentric distances between 15 and 25 kpc. The solid line shows the great circle that best fits the Phoenix stream, the portion of the stream observed is highlighted with a broader line.

as the peak in the β projected density. We also show the β projection for stars south (green dashed line) and north (blue dashed line) of the central OD. We notice an offset of $\sim 0\fdg14$ in β between the north and south portions of the stream.

The stream width depends on two sets of factors. The first and more obvious is the progenitor's size and velocity dispersion. The second is the shape of the gravitational potential. For instance, triaxial potentials tend to increase the fanning of stream stars significantly (Pearson et al. 2015; Price-Whelan et al. 2016). However, there is evidence that the inner halo of the Galaxy is relatively spherical (Küpper et al. 2015) out to ∼20 kpc, thus allowing us to assume the stream width maps only to the progenitor size and velocity dispersion. Using the stream coordinate system, we determine that it has an on-sky width of $\sigma = 0\fdg18$, which translates to ∼54 pc at its distance. Typically, 50 pc is consistent with the tidal radius of the MW halo GCs. The fact that the stream forms a thin coherent structure that is several kiloparsecs long makes it plausible that the progenitor was in fact a GC.

From the density projected in the Λ coordinate we explore the presence of ODs as possible progenitors. We label these ODs in the top panel of Figure 5. First we call attention to C1 and C2, which have a slight offset with respect to each other in the β direction, showing hints of trailing and leading tail

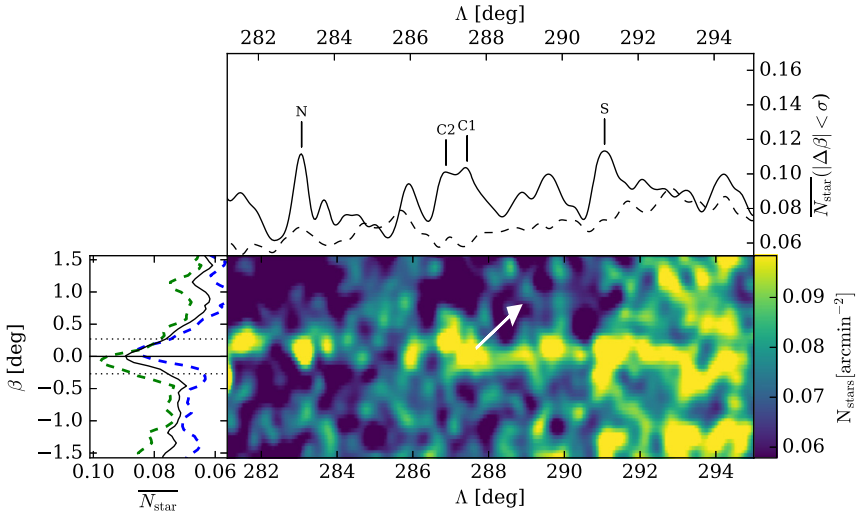

Figure 5. Bottom right panel: density map in the stream's coordinate system built using color–magnitude selected stars. The white arrow points toward the MW center. The pixel size is the same as in Figure 1. The dashed lines shown in Figure 2 encompass the region of the CMD from which stars were selected. The left panel shows the average density map value in projection onto the β axis, the solid horizontal line marks the position of the stream centroid, and the dotted lines show the $\pm 1\sigma$ limits. The green (blue) dashed line shows the same kind of β projection but for the south (north) part of the stream. The top panel shows the average density map value in projection along the Λ axis. The latter is built using only stars that are within $\pm 1\sigma$ of the centroid of the stream. Vertical solid lines mark the position of candidate progenitors. In this panel the dashed line shows the typical background contribution, computed using stars within $\pm 1\sigma$ of a center line offset 5σ from the stream's original center line.

Table 2
Overdensity Positions

OD	R.A. (deg)	Decl. (deg)	l (deg)	b (deg)	Λ (deg)	β (deg)	$\Delta\overline{\rm C1C2}$ (deg)	σ
C1	23.75	−49.89	285.68	−65.76	287.50	0.00	···	5.1
C2	23.77	−50.40	286.16	−65.28	286.94	0.22	···	5.0
N	26.15	−46.34	277.74	−68.10	283.16	−0.09	4.10	7.1
S	21.23	−53.70	292.10	−62.72	291.11	0.03	4.17	5.0

misalignment with respect to the orbit (Bovy 2014). Apart from C1 and C2 we find two other peaks, one to the north (N) and another to the south (S) of the central ODs. These ODs stand out when compared to the typical background counts (dashed line in Figure 5). We compute the typical local background noise at the position of the north (south) OD by taking the standard deviation of the background counts in the north (south) portion of the stream. We find that both ODs (N & S) peak densities stand out more than 4σ with respect to the background. The significance values are listed on Table 2.

The fact that ODs N and S are approximately equally separated from the central OD could point to epicyclic ODs such as the ones reported in Küpper et al. (2015) for Palomar 5. Table 2 summarizes the positions and angular separation of the ODs with regard to the central peaks. From this table we observe that ODs to the north are systematically at higher β than those in the south, hinting at the misalignment mentioned above.

Using the misalignment of the northern and southern portions of the stream (hinted in Figure 5), we may infer from geometrical considerations alone that its northern part is closer to the MW center, hence being formed by stars that leave the progenitor through the inner part of its orbit, forming a leading tail. By construction, the south portion forms the trailing tail. From this argument, we conclude that the stream is moving from south to north.

All ODs were visually inspected in the coadded images and catalog; however, we could not identify any stellar system (e.g., GC) that might have given origin to the stream. This result is very puzzling, especially if the scenario described above is to be confirmed. The fact that no progenitor is found, but classic signs of cold tail formation were observed, could indicate that a progenitor was fully disrupted very recently.

4. CONCLUSIONS

We report the discovery of a stellar stream in the southern hemisphere. Through the visual fit of stellar evolution models we find that this stream is comprised of an old (11.5 ± 0.5 Gyr) metal-poor ([Fe/H] < -1.6) population that is 17.5 kpc away from the Sun and 18.4 kpc from the Galactic center. Though close in projection, the Phoenix stream is not related to the Phoenix galaxy, which lies 440 kpc from the Sun (Karachentsev et al. 2004).

Through the extrapolation of the stream outside the Y1A1 footprint, we found no known GC that could be its progenitor; however, more eccentric and/or non-planar orbits were not considered.

We also investigate the distribution of ODs along the stream, in search of a progenitor. We find that none of the ODs have any obvious stellar OD associated with them when coadded images were inspected. We find that the ODs with high significance display a symmetric pattern with respect to a central OD. This central OD shows some hints of misalignment perpendicular to the orbit direction, which could indicate the position of the progenitor.

A diffuse stellar OD that nearly overlaps with the Phoenix stream has recently been found in the DES data (Li et al. 2016). This OD (EriPhe) was previously hinted at by Carballo-Bello et al. (2014) as an anomalous background population close to NGC 1261. EriPhe and NGC 1261 share a similar heliocentric distance as the Phoenix stream. Using GALPY (Bovy 2015) and literature proper motions for NGC 1261 (Dambis 2006), we integrate the cluster orbit and find that it roughly aligns with the Phoenix stream and that its motion is retrograde with respect to the solar motion. The close proximity of NGC 1261 and the orbit alignment with the stream may suggest that they could share a common origin with the EriPhe OD. However, the stream appears not to be in a retrograde orbit, favoring a scenario where the stream is independent of EriPhe or NGC 1261. For an extended discussion about this scenario we refer to Li et al. (2015).

We thank Carl Grillmair for pointing out that our original derivation of the direction of motion of the stream was incorrect, and that the stream is actually moving in a prograde direction about the Galaxy.

Funding for the DES Projects has been provided by the U.S. Department of Energy, the U.S. National Science Foundation, the Ministry of Science and Education of Spain, the Science and Technology Facilities Council of the United Kingdom, the Higher Education Funding Council for England, the National Center for Supercomputing Applications at the University of Illinois at Urbana-Champaign, the Kavli Institute of Cosmological Physics at the University of Chicago, the Center for Cosmology and Astro-Particle Physics at the Ohio State University, the Mitchell Institute for Fundamental Physics and Astronomy at Texas A&M University, Financiadora de Estudos e Projetos, Fundação Carlos Chagas Filho de Amparo à Pesquisa do Estado do Rio de Janeiro, Conselho Nacional de Desenvolvimento Científico e Tecnológico and the Ministério da Ciência, Tecnologia e Inovação, the Deutsche Forschungsgemeinschaft, and the Collaborating Institutions in the Dark Energy Survey.

The Collaborating Institutions are Argonne National Laboratory, the University of California at Santa Cruz, the University of Cambridge, Centro de Investigaciones Energéticas, Medioambientales y Tecnológicas-Madrid, the University of Chicago, University College London, the DES-Brazil Consortium, the University of Edinburgh, the Eidgenössische Technische Hochschule (ETH) Zürich, Fermi National Accelerator Laboratory, the University of Illinois at Urbana-Champaign, the Institut de Ciències de l'Espai (IEEC/CSIC), the Institut de Física d'Altes Energies, Lawrence Berkeley National Laboratory, the Ludwig-Maximilians Universität München and the associated Excellence Cluster universe, the University of Michigan, the National Optical Astronomy Observatory, the University of Nottingham, The Ohio State University, the University of Pennsylvania, the University of Portsmouth, SLAC National Accelerator Laboratory, Stanford University, the University of Sussex, and Texas A&M University.

The DES data management system is supported by the National Science Foundation under grant No. AST-1138766. The DES participants from Spanish institutions are partially supported by MINECO under grants AYA2012-39559, ESP2013-48274, FPA2013-47986, and Centro de Excelencia Severo Ochoa SEV-2012-0234, some of which include ERDF funds from the European Union. Research leading to these results has received funding from the European Research Council under the European Union's Seventh Framework Programme (FP7/2007-2013), including ERC grant agreements 240672, 291329, and 306478.

This research made use of Astropy, a community-developed core Python package for Astronomy (Astropy Collaboration et al. 2013).

E. Balbinot acknowledges financial support from the European Research Council (ERC-StG-335936, CLUSTERS).

This paper has undergone internal review by the DES collaboration.

REFERENCES

Ahn, C. P., Alexandroff, R., Allende Prieto, C., et al. 2014, ApJS, 211, 17
Astropy Collaboration, Robitaille, T. P., Tollerud, E. J., et al. 2013, A&A, 558, A33
Balbinot, E., Santiago, B. X., Girardi, L., et al. 2015, MNRAS, 449, 1129
Bechtol, K., Drlica-Wagner, A., Balbinot, E., et al. 2015, ApJ, 807, 50
Bell, E. F., Zucker, D. B., Belokurov, V., et al. 2008, ApJ, 680, 295
Belokurov, V., Zucker, D. B., Evans, N. W., et al. 2006, ApJL, 647, L111
Belokurov, V., Zucker, D. B., Evans, N. W., et al. 2007, ApJ, 654, 897
Bertin, E. 2011, in ASP Conf. Ser. 442, Astronomical Data Analysis Software and Systems XX, ed. I. N. Evans et al. (San Francisco, CA: ASP), 435
Bertin, E., & Arnouts, S. 1996, A&AS, 117, 393
Binney, J., & Tremaine, S. 2008, Galactic Dynamics (2nd ed.; Princeton, NJ: Princeton Univ. Press)
Bovy, J. 2014, ApJ, 795, 95
Bovy, J. 2015, ApJS, 216, 29
Bressan, A., Marigo, P., Girardi, L., et al. 2012, MNRAS, 427, 127
Bullock, J. S., Kravtsov, A. V., & Weinberg, D. H. 2001, ApJ, 548, 33
Canterna, R., & Flower, P. J. 1977, ApJL, 212, L57
Carballo-Bello, J. A., Sollima, A., Martínez-Delgado, D., et al. 2014, MNRAS, 445, 2971
Cardelli, J. A., Clayton, G. C., & Mathis, J. S. 1989, ApJ, 345, 245
Dambis, A. K. 2006, A&AT, 25, 185
Deason, A. J., Belokurov, V., & Evans, N. W. 2011, MNRAS, 416, 2903
Desai, S., Armstrong, R., Mohr, J. J., et al. 2012, ApJ, 757, 83
Diehl, H. T., Abbott, T. M. C., Annis, J., et al. 2014, Proc. SPIE, 9149, 0
Drlica-Wagner, A., Bechtol, K., Rykoff, E. S., et al. 2015, ApJ, 813, 109
Flaugher, B., Diehl, H. T., Honscheid, K., et al. 2015, AJ, 150, 150
Johnston, K. V., Hernquist, L., & Bolte, M. 1996, ApJ, 465, 278
Johnston, K. V., Law, D. R., & Majewski, S. R. 2005, ApJ, 619, 800
Karachentsev, I. D., Karachentseva, V. E., Huchtmeier, W. K., & Makarov, D. I. 2004, AJ, 127, 2031
Kim, D., & Jerjen, H. 2015, ApJL, 808, L39
Koch, A., Grebel, E. K., Odenkirchen, M., Martínez-Delgado, D., & Caldwell, J. A. R. 2004, AJ, 128, 2274
Koposov, S. E., Belokurov, V., Torrealba, G., & Wyn Evans, N. 2015, ApJ, 805, 130
Koposov, S. E., Rix, H.-W., & Hogg, D. W. 2010, ApJ, 712, 260
Küpper, A. H. W., Balbinot, E., Bonaca, A., et al. 2015, ApJ, 803, 80
Li, T. S., Balbinot, E., Mondrik, N., et al. 2016, ApJ, 817, 135
Luque, E., Queiroz, A., Santiago, B., et al. 2016, MNRAS, 458, 603
Mackey, D., Koposov, S. E., Erkal, D., et al. 2015, MNRAS, in press (arXiv:1508.01356)
Majewski, S. R., Skrutskie, M. F., Weinberg, M. D., & Ostheimer, J. C. 2003, ApJ, 599, 1082
Mohr, J. J., Armstrong, R., Bertin, E., et al. 2012, Proc. SPIE, 8451, 84510D
Newberg, H. J., Yanny, B., Rockosi, C., et al. 2002, ApJ, 569, 245
Ngan, W., Bozek, B., Carlberg, R. G., et al. 2015, ApJ, 803, 75
Odenkirchen, M., Grebel, E. K., Rockosi, C. M., et al. 2001, ApJL, 548, L165

Pearson, S., Küpper, A. H. W., Johnston, K. V., & Price-Whelan, A. M. 2015, ApJ, 799, 28
Price-Whelan, A. M., Johnston, K. V., Valluri, M., et al. 2016, MNRAS, 455, 1079
Rolke, W. A., López, A. M., & Conrad, J. 2005, NIMPA, 551, 493
Schlafly, E. F., & Finkbeiner, D. P. 2011, ApJ, 737, 103
Schlegel, D. J., Finkbeiner, D. P., & Davis, M. 1998, ApJ, 500, 525
Skrutskie, M. F., Cutri, R. M., Stiening, R., et al. 2006, AJ, 131, 1163
Swanson, M. E. C., Tegmark, M., Hamilton, A. J. S., & Hill, J. C. 2008, MNRAS, 387, 1391
The Dark Energy Survey Collaboration 2005, arXiv:astro-ph/0510346
Willman, B., Dalcanton, J. J., Martinez-Delgado, D., et al. 2005, ApJL, 626, L85
Yoon, J. H., Johnston, K. V., & Hogg, D. W. 2011, ApJ, 731, 58

Neste artigo fizemos em colaboração com o primeiro autor uma série de modificações nos códigos de determinação dos parãmetros estruturais e físicos dos dois objetos descobertos no paper. Neste trabalho utilizamos uma abordagem estatisticamente distinta para a determinação dos parâmetros dos objetos, baseada na probabilidade marginalizada, ao invés das abordagens anteriores que se baseavam na máxima probabilidade. Além disso a nova abordagem utiliza um conjunto amostrador afim e invariante do tipo Monte Carlo para cadeias de Markov (Foreman-Mackey et al., 2013), muito mais rápido e que possibilita a inserção de novos parâmetros de ajuste sem alcançar tempos proibitivos para rodadas. Além disso, implementamos determinações de massa para os objetos descobertos, com contribuições nos códigos de ambos os lados (nossas e do primeiro autor). Além disso, testes foram indispensáveis na comparação dos resultados entre estas abordagens (máxima probabilidade via força bruta e probabilidade marginalizada via Markov Chain Monte Carlo).

MNRAS **468,** 97–108 (2017)
Advance Access publication 2017 February 17
doi:10.1093/mnras/stx405

The Dark Energy Survey view of the Sagittarius stream: discovery of two faint stellar system candidates

E. Luque,[1,2]★ A. Pieres,[1,2] B. Santiago,[1,2]★ B. Yanny,[3] A. K. Vivas,[4] A. Queiroz,[1,2] A. Drlica-Wagner,[3] E. Morganson,[5] E. Balbinot,[6] J. L. Marshall,[7] T. S. Li,[7] A. Fausti Neto,[2] L. N. da Costa,[2,8] M. A. G. Maia,[2,8] K. Bechtol,[9] A. G. Kim,[10] G. M. Bernstein,[11] S. Dodelson,[3,9] L. Whiteway,[12] H. T. Diehl,[3] D. A. Finley,[3] T. Abbott,[4] F. B. Abdalla,[12,13] S. Allam,[3] J. Annis,[3] A. Benoit-Lévy,[12,14,15] E. Bertin,[14,15] D. Brooks,[12] D. L. Burke,[16,17] A. Carnero Rosell,[2,8] M. Carrasco Kind,[5,18] J. Carretero,[19,20] C. E. Cunha,[16] C. B. D'Andrea,[21,22] S. Desai,[23] P. Doel,[12] A. E. Evrard,[24,25] B. Flaugher,[3] P. Fosalba,[19] D. W. Gerdes,[25] D. A. Goldstein,[10,26] D. Gruen,[16,17] R. A. Gruendl,[5,18] G. Gutierrez,[3] D. J. James,[4] K. Kuehn,[27] N. Kuropatkin,[3] O. Lahav,[12] P. Martini,[28,29] R. Miquel,[20,30] B. Nord,[3] R. Ogando,[2,8] A. A. Plazas,[31] A. K. Romer,[32] E. Sanchez,[33] V. Scarpine,[3] M. Schubnell,[25] I. Sevilla-Noarbe,[33] R. C. Smith,[4] M. Soares-Santos,[3] F. Sobreira,[2,34] E. Suchyta,[35] M. E. C. Swanson,[5] G. Tarle,[25] D. Thomas[21] and A. R. Walker[4]

Affiliations are listed at the end of the paper

Accepted 2017 February 14. Received 2017 February 14; in original form 2016 August 13

ABSTRACT

We report the discovery of two new candidate stellar systems in the constellation of Cetus using the data from the first two years of the Dark Energy Survey (DES). The objects, DES J0111−1341 and DES J0225+0304, are located at a heliocentric distance of ∼25 kpc and appear to have old and metal-poor populations. Their distances to the Sagittarius orbital plane, ∼1.73 kpc (DES J0111−1341) and ∼0.50 kpc (DES J0225+0304), indicate that they are possibly associated with the Sagittarius dwarf stream. The half-light radius ($r_h \simeq 4.55$ pc) and luminosity ($M_V \simeq +0.3$) of DES J0111−1341 are consistent with it being an ultrafaint stellar cluster, while the half-light radius ($r_h \simeq 18.55$ pc) and luminosity ($M_V \simeq -1.1$) of DES J0225+0304 place it in an ambiguous region of size–luminosity space between stellar clusters and dwarf galaxies. Determinations of the characteristic parameters of the Sagittarius stream, metallicity spread ($-2.18 \lesssim$ [Fe/H] $\lesssim -0.95$) and distance gradient (23 kpc $\lesssim D_\odot \lesssim$ 29 kpc), within the DES footprint in the Southern hemisphere, using the same DES data, also indicate a possible association between these systems. If these objects are confirmed through spectroscopic follow-up to be gravitationally bound systems and to share a Galactic trajectory with the Sagittarius stream, DES J0111−1341 and DES J0225+0304 would be the first ultrafaint stellar systems associated with the Sagittarius stream. Furthermore, DES J0225+0304 would also be the first confirmed case of an ultrafaint satellite of a satellite.

Key words: globular clusters: general – galaxies: dwarf.

1 INTRODUCTION

The Sagittarius dwarf galaxy was discovered relatively recently due to its position on the far side of the Milky Way (MW; Ibata, Gilmore & Irwin 1994). Its extended morphology towards the MW plane suggested the existence of extra tidal features (Johnston, Spergel

★ E-mail: elmer.luque@ufrgs.br. (EL); basilio.santiago@ufrgs.br (BS)

& Hernquist 1995; Lynden-Bell & Lynden-Bell 1995; Mateo et al. 1996). The Two Micron All-Sky Survey (2MASS) and the Sloan Digital Sky Survey (SDSS) made it clear that this dwarf is responsible for the most conspicuous tidal stellar substructure present in the Galactic halo (Newberg et al. 2002; Majewski et al. 2003).

Deeper photometric and spectroscopic data, specifically with SDSS, have allowed the morphological, structural and kinematic properties of the Sagittarius stream to be disentangled from MW substructure (Newberg et al. 2003, 2007; Belokurov et al. 2006, 2014; Yanny et al. 2009). This wealth of data was used by Law & Majewski (2010a) to model the MW gravitational potential and to find some evidence in favour of triaxiality (i.e. flattening).

Belokurov et al. (2006) demonstrated that the Sagittarius stream in the northern Galactic hemisphere bifurcates into brighter and fainter components separated by up to $\sim 15^\circ$ on the sky. More recently, Koposov et al. (2012) have shown that a bifurcation also appears in the Sagittarius tails in the southern Galactic hemisphere. This fainter branch had comparatively more metal-poor stars and a simpler mix of stellar populations than the main structure. The southern bifurcation, extending at least 30° on the sky, was confirmed using Panoramic Survey Telescope and Rapid Response System 1 (Pan-STARRS) data by Slater et al. (2013). The authors found evidence that the fainter substructure is 5 kpc closer to the Sun than the brighter one, similar to the behaviour seen in the northern Galactic hemisphere. They also argue that the distance between the streams agrees with the predictions of the *N*-body simulations presented by Law & Majewski (2010a). Based on their model, the same authors also identify MW satellites, dwarf galaxies and globular clusters (GCs) that may be physically associated with the Sagittarius dwarf. In particular, the Sagittarius dwarf has been observed to contain at least four GCs (NGC 6715, Arp 2, Terzan 7 and Terzan 8) within its main body (Da Costa & Armandroff 1995; Bellazzini, Ferraro & Ibata 2003). However, different studies have proposed several GCs to likely be associated with the Sagittarius stream (e.g. Bellazzini et al. 2003; Dotter et al. 2010; Forbes & Bridges 2010; Dotter, Sarajedini & Anderson 2011; Carballo-Bello et al. 2014; Sbordone et al. 2015). Even open clusters (OCs) have been suggested as members of the Sagittarius family (e.g. Carraro et al. 2004; Carraro & Bensby 2009). It is likely that additional GCs and OCs may have been stripped from Sagittarius during prolonged interaction with the MW and now lie scattered throughout the Galactic halo. In a recent analysis based on new models of the tidal disruption of the Sagittarius dwarf, Law & Majewski (2010b) found that several of the candidates proposed in the literature have non-negligible probability of belonging to the Sagittarius dwarf. However, calculating the expected quantity of false associations in the sample, they proposed that only five GCs (Arp 2, NGC 6715, NGC 5634, Terzan 8 and Whiting 1) are almost certainly associated with the Sagittarius dwarf; an additional four (Berkeley 29, NGC 5053, Pal 12 and Terzan 7) are moderately likely to be associated.

It now appears that stars left over from the accretion of the Sagittarius dwarf entirely wrap around the Galactic Centre. Recent spectroscopic analysis by Hyde et al. (2015), for instance, finds over 100 good stream candidates with metallicities in the range $-0.97 < [\mathrm{Fe/H}] < -0.59$ spread over 142°. De Boer, Belokurov & Koposov (2015) analyse the stream in the SDSS Stripe 82 region with both photometry and spectroscopy, finding a tight age–metallicity relation. They also show that the fainter branch is old (>9 Gyr) and metal-poor ($[\mathrm{Fe/H}] < -1.3$), while the dominant branch has stars covering large ranges in age and metallicity.

In this paper, we explore the tidal tails of Sagittarius within the Dark Energy Survey (DES; The Dark Energy Survey Collaboration 2005) footprint in the Southern hemisphere. This data set is $\sim$2 mag (in the *g* band) deeper than other large surveys covering this part of the sky (e.g. Pan-STARRS or SDSS). DES is a wide-field imaging survey of the Southern hemisphere that has recently finished its third year of data taking, from an expected total of 5 yr (Diehl et al. 2016). We also identify two previously undiscovered ultrafaint stellar systems whose inferred ages, metallicities and distances make it likely that they are associated with Sagittarius. In Section 2, we present the DES data. In Section 3, we discuss the properties of the Sagittarius stream as probed by those data. In Section 4, we present a method used to search for star clusters and other stellar systems in the DES footprint. In Section 5, we report on the identification of the two star system candidates whose properties make them likely to have been stripped from the Sagittarius dwarf. If DES J0111−1341 is confirmed to be a stellar cluster, it will be named DES 2, whereas DES J0225+0304 will be named Cetus III if found to be a dwarf galaxy. Our final remarks are then presented in Section 6.

2 DES DATA

DES is a wide-field optical imaging survey of 5000 deg^2 in the southern equatorial hemisphere in the *grizY* bands. DES is scheduled for 525 nights distributed over 5 yr. It uses the Dark Energy Camera (DECam), a 3 deg^2 (2.°2 diameter) mosaic camera with 0.263 arcsec pixels on the prime focus of the 4-metre Blanco telescope at Cerro Tololo Inter-American Observatory (Flaugher et al. 2015). The DES data management (DESDM) uses an image-processing pipeline that consists of image detrending, astrometric calibration, nightly photometric calibration, global calibration, image coaddition and object catalogue creation. For a more detailed description, we refer to Sevilla et al. (2011), Desai et al. (2012) and Mohr et al. (2012). Here, we use DES Y2Q1 (year-two quick release) data derived from single-epoch imaging. This catalogue is derived from 26 590 DECam exposures taken during the first 2 yr of DES observing and has a median point-source depth at an S/N = 10 of $g = 23.4$, $r = 23.2$, $i = 22.4$, $z = 22.1$ and $Y = 20.7$. The resulting calibrated DES magnitudes are already corrected for Galactic reddening by the stellar locus regression (SLR) calibration (see Drlica-Wagner et al. 2015).

The stellar sample used in this work was drawn using SExtractor parameters `FLAGS`, `SPREAD_MODEL` and `PSF` magnitudes (Bertin & Arnouts 1996; Bertin 2011; Bouy et al. 2013). Briefly, `FLAGS` tells for instance if an object is saturated or has been truncated at the edge of the image, while `SPREAD_MODEL` is the main star/galaxy separator. We used the weighted average (`WAVG`) of the `SPREAD_MODEL` measurements from the individual exposures of each source. A source quality criterion of `FLAGS` < 4 over the *g* and *r* filters was also applied. To increase stellar completeness, we selected sources in the *r* band with $|$`WAVG_SPREAD_MODEL`$| <$ $0.003 +$ `SPREADERR_MODEL`. A bright (faint) *g* magnitude limit of `WAVG_MAG_PSF` $= 17$ (`WAVG_MAG_PSF` $= 24$) was also applied. In order to prevent point sources with extreme colours (including red dwarfs from the Galactic disc) from contaminating the sample, a colour cut at $-0.5 \leq g - r \leq 1.2$ was also used. Drlica-Wagner et al. (2015) show that our Y2Q1 stellar classification efficiency exceeds 90 per cent for $r < 23$ mag, and falls to $\sim$80 per cent by $r < 24$ mag, whereas contamination by galaxies is $\sim$40 per cent for 23 mag and increases to $\sim$60 per cent by $r < 24$ mag.

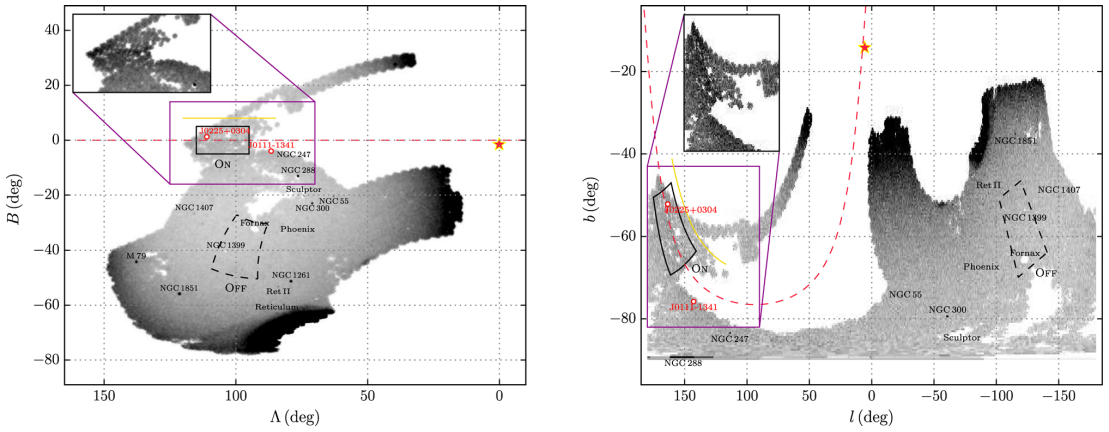

Figure 1. Density map of stars with $17 < g < 23$ and $-0.5 < g - r < 1.2$ from the DES Y2Q1 footprint in two different coordinate systems. The left-hand panel is shown in a coordinate system defined by the orbit of the Sagittarius dwarf (Majewski et al. 2003; Belokurov et al. 2014), while the right-hand panel is in Galactic coordinates (l, b). The current location of the Sagittarius dwarf is indicated by a red star. The red dashed line traces the Sagittarius tidal tail (Majewski et al. 2003). At the top left of each panel, we show an inset of the density map where the stream is more visible. Overdensities of some GCs (Harris 2010) and dwarf galaxies (McConnachie 2012; Bechtol et al. 2015; Koposov et al. 2015a) are also indicated. The new stellar system candidates discovered, DES J0111−1341 and DES J0225+0304, are marked with red circles. The ON region (solid lines) defined by $95^\circ < \Lambda < 115^\circ$ and $-5^\circ < B < 5^\circ$ represents the best-sampled region of the Sagittarius stream, whereas the OFF region (dashed lines) represents the region of stars used for the background with the same Galactic latitude as the ON region. The Fornax dwarf galaxy and NGC 1399 were masked to avoid overestimating the density of our sample of background stars (OFF region). These regions are used to construct the Hess diagrams in Figs 3 and 4. The yellow solid line, as shown in both panels, indicates the position of the faint branch of the Sagittarius stream in the DES footprint (see Section 3.1).

3 SAGITTARIUS STREAM IN THE SOUTHERN HEMISPHERE

In Fig. 1, we show a density map of stars with $17 < g < 23$ and $-0.5 < g - r < 1.2$ from the DES Y2Q1 footprint in two different coordinate systems. The colour cut was performed to exclude stars from the Galactic disc and possibly spurious objects that can contaminate our sample. The left-hand panel is in the coordinate system aligned with the Sagittarius stream (Λ, B) (Majewski et al. 2003; Belokurov et al. 2014), while the right-hand panel is in Galactic coordinates (l, b). Several overdensities are noticeable, such as some GCs (Harris 2010), dwarf galaxies (McConnachie 2012) and the recently discovered dwarf galaxy Reticulum II (Bechtol et al. 2015; Koposov et al. 2015a). The Sagittarius stream in the Southern hemisphere (trailing tail) is also visible between $90^\circ \lesssim \Lambda \lesssim 120^\circ$ and $-15^\circ \lesssim B \lesssim 12^\circ$ in Sagittarius coordinates and between $120^\circ \lesssim l \lesssim 190^\circ$ and $-80^\circ \lesssim b \lesssim -45^\circ$ in Galactic coordinates (see the inset maps on the top left of each panel). In the same figure, we show with red circles two new stellar system candidates, DES J0111−1341 and DES J0225+0304. Given their physical locations, these new candidates are possibly associated with the Sagittarius stream (discussed in Section 4). In this figure, we also show ON and OFF regions. The ON region (solid lines) defined by $95^\circ \leq \Lambda \leq 115^\circ$ and $-5^\circ \leq B \leq 5^\circ$ represents the best-sampled region of the Sagittarius stream, while the OFF region (dashed lines) represents the sample of background[1] stars located at the same Galactic latitude as the ON region. These regions are used in our colour–magnitude diagram (CMD) analysis presented in Sections 3.2 and 3.3. Finally, the yellow solid line represents the position of a possible secondary peak previously identified by Koposov et al. (2012, see discussion in the next section).

We emphasize that our analysis of the Sagittarius stream is focused on determining, using DES data, its basic characteristic parameters, such as metallicity, age and distance ranges so that they can be compared to the properties inferred for the newly discovered systems, DES J0111−1341 and DES J0225+0304. The compatibility between stream stars and these newly found systems helps shed light on their possible physical association.

3.1 Inferred number of stars

The Sagittarius stream is known to display substructures, like its bright and faint branches, in both the northern and southern Galactic hemispheres (Newberg et al. 2003; Belokurov et al. 2006; Yanny et al. 2009; Koposov et al. 2012). In particular, in the southern Galactic hemisphere, parallel to the bright branch, but ∼10° away, the faint branch is found (Koposov et al. 2012). We start by analysing variations in stellar number counts along and across the Sagittarius stream as covered by DES, in search for any clear branching of the stream in this region. In the left-hand panel of Fig. 1, we show the density map of the Sagittarius stream in the coordinate system approximately aligned with the orbit of Sagittarius (Λ, B) as described in Majewski et al. (2003) and Belokurov et al. (2014). We selected stars inside an area defined by $95^\circ < \Lambda < 115^\circ$ and $-15^\circ < B < 12^\circ$. We name this region the *stream sample*. This chosen region is a compromise between reaching a reasonably homogeneous stream coverage along both streams and still keeping a sizeable area within the DES footprint. To subtract the expected number of background stars coinciding with the *stream sample* region, we selected stars inside a region that is offset by $\Delta l = 80^\circ$ with respect to the centre of the *stream sample* region. These regions[2]

[1] We refer to these stars as 'background', though they are dominantly composed of MW foreground stars.

[2] These two regions are not shown in Fig. 1 to avoid confusion with the ON and OFF regions used in Sections 3.2 and 3.3.

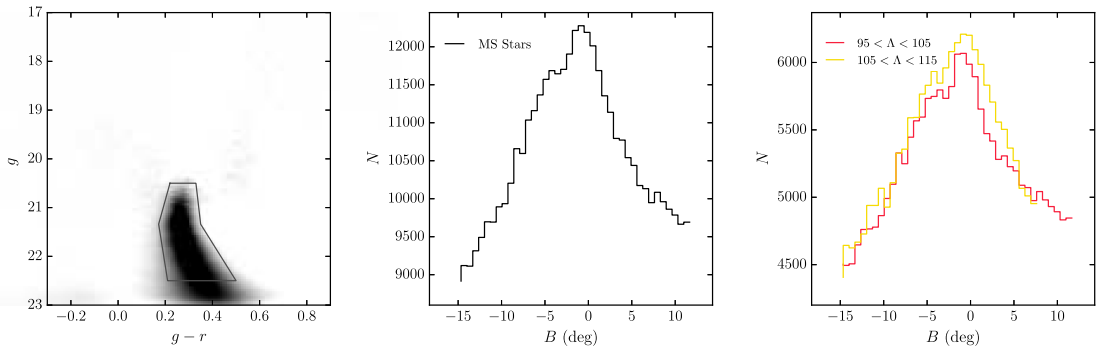

Figure 2. Left-hand panel: decontaminated Hess diagram constructed with stars within a region defined by $95^\circ < \Lambda < 115^\circ$ and $-15^\circ < B < 12^\circ$. The solid lines on the CMD plane are used to select MS stars belonging to the Sagittarius stream. Middle panel: number of MS stars (using the selected stars in the previous panel) along the Sagittarius stream ($95^\circ < \Lambda < 115^\circ$). The expected position of the faint stream (Koposov et al. 2012) is at $B \sim 8^\circ$. Right-hand panel: number of MS stars for two regions along the stream from $95^\circ < \Lambda < 105^\circ$ and $105^\circ < \Lambda < 115^\circ$ as indicated. The faint stream is seen only at $95^\circ < \Lambda < 105^\circ$ due to the current coverage of the DES footprint (see Fig. 1).

have approximately the same area and are from approximately the same Galactic latitude ($b \sim -59^\circ$) in order to maintain similar background density. For each region described above, we constructed the Hess diagram. In the left-hand panel of Fig. 2, we show the decontaminated Hess diagram calculated as the difference between the Hess diagrams of both regions weighted by their respective areas.[3] We use the HEALPIX software to determine the effective area in each region. In order to obtain a sample of representative stars of the Sagittarius stream, we weight each star of the *stream sample* region by its probability of being a member of the Sagittarius stream, $w = n_i/m_i$, where n_i (m_i) represents the number of stars in a given cell of the Hess diagram, with bins of 0.01 mag × 0.05 mag, after (before) subtracting the background stars. We consider that all the stars in a given cell of the Hess diagram have the same weight. The solid lines in the CMD plane on the left-hand panel of Fig. 2 select main-sequence (MS) stars associated with the stream. We then use the weights of these stars to analyse the variation of the number of stars along and across the stream. The results are shown in the middle and right-hand panels of Fig. 2. We use the HEALPIX software to compute the area actually covered by the Y2Q1 footprint and thus to compensate the number of stars for the area loss.

Koposov et al. (2012) find evidence for a faint stream at $B \sim 8^\circ$–10°. The DES footprint covers this area only from $95^\circ < \Lambda < 105^\circ$. The red histogram in the right-hand plot in Fig. 2 shows the number of MS stars within this region in bins of B; within this area, our data show a suggestion of an excess of stars that could be attributed to the faint stream. At Sagittarius longitudes $105^\circ < \Lambda < 115^\circ$, DES does not cover the secondary stream ($5^\circ < B < 12^\circ$); however, where DES has coverage ($-15^\circ < B < 5^\circ$), the number of MS stars (yellow histogram) is consistent with those at $95^\circ < \Lambda < 105^\circ$ (red histogram). Scaling the number of stars to the full range ($-15^\circ < B < 12^\circ$), we infer a number of MS stars for $95^\circ < \Lambda < 115^\circ$ as shown in the middle panel. The possible excess of stars observed at $B \sim 8^\circ$ (middle and right-hand panels in Fig. 2) only is visible when we use bin sizes between $0.^\circ6 \lesssim \Delta B \lesssim 0.^\circ7$; otherwise, this latter is not evident. Therefore, in this paper, we do not claim a detection of the branching of the stream.

[3] We replace negative values in the decontaminated Hess diagram by zero.

3.2 Metallicity spread

The Sagittarius stream in the northern Galactic hemisphere and the celestial equator (Stripe 82) is known for having a metallicity range (e.g. Koposov et al. 2012; De Boer et al. 2015; Hyde et al. 2015). In particular, using photometric and spectroscopic data within the SDSS Stripe 82 region (region in common with the DES footprint), Koposov et al. (2012) determined that the stars belonging to the bright and faint branches cover a metallicity range from $-2 \lesssim$ [Fe/H] $\lesssim 0$, while De Boer et al. (2015) determined a metallicity range from $-2.5 \lesssim$ [Fe/H] $\lesssim -0.3$. However, the brighter branch contains substantial numbers of metal-rich stars as compared to the fainter branch (Koposov et al. 2012).

We now turn to a global analysis of the stellar populations contributing to the Sagittarius stream. We first use the red giant branch (RGB) stars to find a spread in metallicity as follows. First, we selected stars inside a region defined by $95^\circ < \Lambda < 115^\circ$ and $-5^\circ < B < 5^\circ$ (ON region; left-hand panel of Fig. 1). The more restricted range in B is meant to further reduce sky coverage effects and to avoid any possible contamination by the faint branch. Using these stars, we have constructed and decontaminated a Hess diagram representative of the Sagittarius stream. The left-hand and middle panels of Fig. 3 show the Hess diagrams for the ON and OFF regions, respectively. They contain 185 558 and 117 860 stars (within an isochrone filter[4]), respectively. These regions are from approximately the same Galactic latitude (see right-hand panel of Fig. 1). The decontaminated Hess diagram shown in the right-hand panel of Fig. 3 was calculated as the difference between the Hess diagrams of the ON and OFF regions weighted by their respective areas. It contains a total of 87 810 stars. We use the HEALPIX software to determine the effective area in each region. In the decontaminated Hess diagram, we can identify MS, RGB and some younger population stars.

We select stars within the decontaminated CMD region defined by $0.4 < g - r < 0.8$ and $19.3 < g < 20.5$. For each interval of ∼0.4 mag along the CMD, we count stars as a function of colour and

[4] The isochrone filter is constructed by using the best-fitting isochrone determined for mean colour values (see Fig. 3). For isochrone filter details, we refer to Luque et al. (2016).

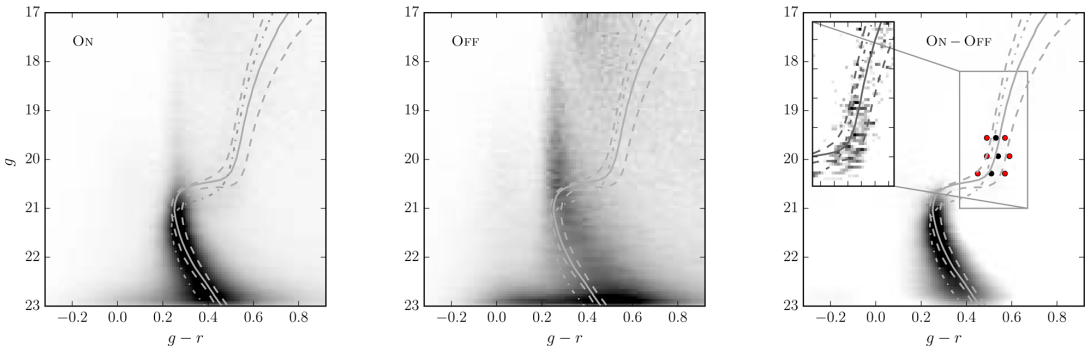

Figure 3. Left-hand panel: Hess diagram constructed with stars within a region of the Sagittarius stream defined by $95^\circ < \Lambda < 115^\circ$ and $-5^\circ < B < 5^\circ$ (ON region; Fig. 1). Middle panel: Hess diagram of the background constructed with stars within the OFF region (Fig. 1). Right-hand panel: difference Hess diagram between the ON and OFF regions. The solid black (red) circles represent the mean colour (standard deviation) values of RGB stars as a function of the colour $(g - r)$ for different ranges of magnitude. The mean colour value (μ) and standard deviation (σ) obtained from the Gaussian fit are $\mu = 0.527 \pm 0.002$ and $\sigma = 0.043 \pm 0.002$ (top circles), $\mu = 0.544 \pm 0.003$ and $\sigma = 0.051 \pm 0.005$ (middle circles), $\mu = 0.509 \pm 0.004$ and $\sigma = 0.061 \pm 0.006$ (lower circles). The solid line, in each panel, represents the best-fitting isochrone (Bressan et al. 2012) determined from mean colour values. The lower (top) dashed line represents the 1σ (-1σ) isochrone. From the bottom up, the isochrone parameters are $\log(\text{Age}) = 9.98$, $D_\odot = 24.5$ kpc and $[\text{Fe/H}] = -0.95$ (lower dashed line), $\log(\text{Age}) = 10.02$, $D_\odot = 24.5$ kpc and $[\text{Fe/H}] = -1.34$ (solid line), $\log(\text{Age}) = 10.12$, $D_\odot = 24.5$ kpc and $[\text{Fe/H}] = -2.18$ (top dashed line). In addition, an isochrone model with $[\text{Fe/H}] = -2.18$, $\log(\text{Age}) = 10.12$ and $(m - M)_0 = 17.31$ parameters is also overplotted on each panel (dot–dashed line; see Sections 3.2 and 3.3).

use the PYTHON package scipy.optimize[5] to fit a Gaussian distribution to determine the mean colour value and the associated standard deviation. The peak and 1σ deviations from it are shown as the black and red dots in the right-hand panel of Fig. 3. We then choose a set of PARSEC isochrone (Bressan et al. 2012) models that visually agree with the RGB mean and associated $\pm 1\sigma$ colours resulting from the Gaussian fits as well as the observed main-sequence turn-off (MSTO) and MS loci. This is done by imposing the following restrictions to the isochrones: (i) the model age and metallicity must respect the tight age–metallicity relation by De Boer et al. (2015) and (ii) a single distance must be used for the three sets of points along the RGB, MS and MSTO loci.

The best-fitting isochrones for the mean values and standard deviations (as described above) are shown in Fig. 3. Our results show that the stream population is old but displays a significant metallicity spread. While the peak RGB locus is consistent with $[\text{Fe/H}] = -1.34$, their redder and bluer ends are more metal-rich ($[\text{Fe/H}] = -0.98$) and metal-poor ($[\text{Fe/H}] = -2.18$), respectively. The metallicity spread found in this analysis is also much larger than the photometric errors ($\sigma_{g-r} \simeq 0.01$ for RGB stars at $g \simeq 20$) and uncertainty in calibration[6] [$\Delta(g - r) = 0.013$ for the ON region], which again attests to its reality. However, metallicity determinations in the literature (Koposov et al. 2012; De Boer et al. 2015) suggest that the Sagittarius stream in the Stripe 82 region contains more metal-rich stars than our determinations.

3.3 Distance gradient

Distance determinations for different regions of the Sagittarius stream in the northern Galactic hemisphere were performed by different authors (e.g. Belokurov et al. 2006; Correnti et al. 2010). Recent studies of the Sagittarius stream in the southern Galactic hemisphere were performed by Koposov et al. (2012) and Slater et al. (2013). Using SDSS Data Release 8, Koposov et al. (2012) determined a distance gradient from 22.08 ($\Lambda \simeq 97.^\circ5$) to 27.2 kpc ($\Lambda \simeq 112.^\circ5$), whereas Slater et al. (2013), using Pan-STARRS data, determined a distance gradient from 29.5 ($\Lambda \simeq 102^\circ$) to 33.1 kpc ($\Lambda \simeq 110^\circ$). We note a discrepancy in determining the distance gradient between the two groups. While it is true that both groups use red clump (RC) stars to determine the distance gradient along of the Sagittarius stream, the difference lies in the absolute magnitude value assumed in these determinations. To compare our results with the literature, we show only results within our region of analysis, $95^\circ < \Lambda < 115^\circ$. In this section, we perform an independent estimate of the distance gradient along the Sagittarius stream in the southern Galactic hemisphere, so as to compare it to those previous studies.

For each interval of $2.^\circ5$ in Λ, we construct a Hess diagram along the Sagittarius stream (ON region; left-hand panel of Fig. 1), eight in total. To decontaminate each one of the Hess diagrams by removing the background stars, we first divide the OFF region in subregions approximately equal to those used in the ON region, maintaining the same Galactic latitude. We then follow the same procedure described in Section 3.2. The results are shown in Fig. 4.

We estimated the distance gradient along the stream as follows. For each interval in Λ (see the text above), we first select CMD stars with $0.4 < g - r < 0.8$. For two intervals of magnitude, we count stars as a function of colour and fit a Gaussian distribution to determine the mean colour value (μ). The choice of only two intervals of magnitude is due to low statistics of RGB stars present in all the CMDs. By applying this restriction, we obtain ∼150 stars in each magnitude interval. The peak values are shown as black solid dots in Fig. 4. We then use a set of PARSEC isochrone (Bressan et al. 2012) models that visually fit the RGB mean values resulting from the Gaussian fits as well as the observed MSTO and MS loci. This is done by again imposing the restriction that the model age and metallicity respect the age–metallicity relation by

[5] http://docs.scipy.org/doc/scipy-0.17.0/reference/optimize.html

[6] The uncertainty in calibration was determined by comparing the SLR calibration for Y2Q1 against external catalogues (2MASS and AAVSO Photometric All-Sky Survey, APASS-DR9). The latter transformed to DES filters.

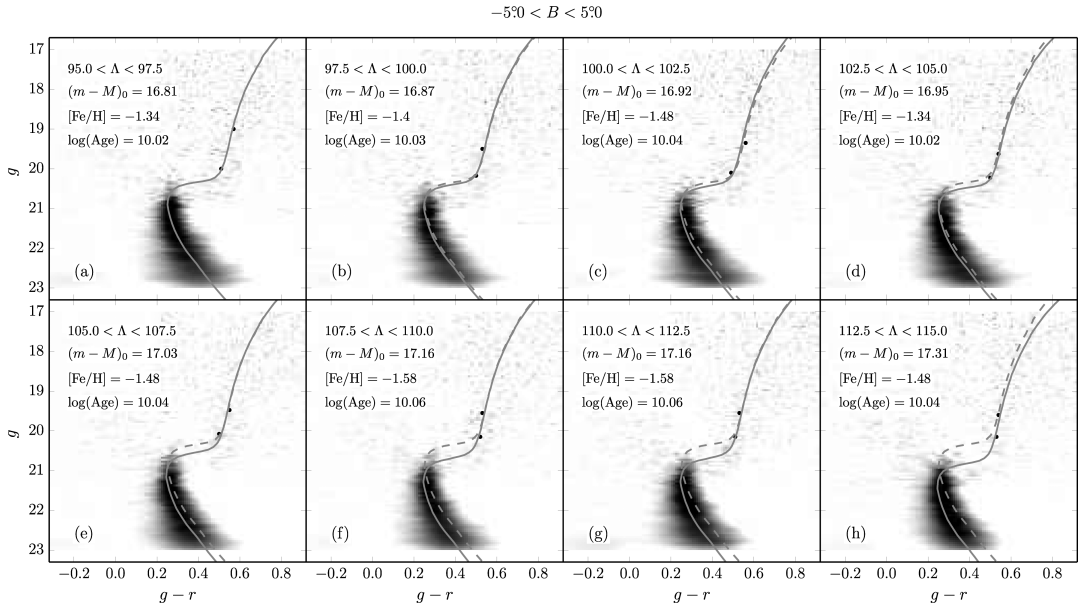

Figure 4. Hess diagrams, after decontamination from the background contribution, constructed along the Sagittarius stream (ON region) from 95° < Λ < 97.°5 to 112.°5 < Λ < 115° as indicated on each panel. The solid black dots represent the mean colour values of the Gaussian fit on RGB stars. The best-fitting isochrone (Bressan et al. 2012) using the method described in Section 3.3 is overplotted on each panel with a solid line. The isochrone parameters are also indicated on each panel. For comparison, in panels (b) through (h) is overplotted (with a dashed line) the nearest isochrone model [from panel (a)].

De Boer et al. (2015). The best-fitting isochrones using the method described above are superposed on to the decontaminated Hess diagrams (Fig. 4). Our best-fitting isochrones show a distance gradient along the Sagittarius stream from ∼23 kpc for 95° < Λ < 97.°5 and ∼29 kpc for 112.°5 < Λ < 115°. We estimate distance uncertainties in each Λ interval by varying the age and metallicity of the PARSEC isochrones around the best-fitting case (but still bound to the same age–metallicity relation) and redoing the visual isochrone fit. We estimate a mean distance uncertainty of ±0.3 kpc. Therefore, our results are in agreement with those obtained by Koposov et al. (2012).

To quantify the effect of the distance gradient along the stream on the metallicity spread (see Section 3.2), we overplotted in Fig. 3 the same isochrone model that best fits the -1σ Gaussian locus ([Fe/H] = −2.18, log (Age) = 10.12; dots shown on the blue side of the RGB locus), but now shifted to $(m - M)_0 = 17.31 = 29$ kpc (dot–dashed line). This distance corresponds to the maximum value determined in the analysis of the distance gradient. We conclude that a variation in distance as large as is inferred in this section does not account for the observed colour spread on the RGB (see Fig. 3).

4 SUBSTRUCTURE SEARCH AND OBJECT DETECTION

Many more than 17 objects were selected by our compact overdensity search techniques, stellar density maps, likelihood-based search and SPARSEX. Only 17 of them have been published[7] (Bechtol et al. 2015; Drlica-Wagner et al. 2015; Luque et al. 2016). A careful reanalysis of the promising candidates detected by the SPARSEX code has revealed two new candidate stellar systems in addition to those reported by Drlica-Wagner et al. (2015, see discussion in the next section). In this section, we briefly review SPARSEX.

The SPARSEX code is an overdensity detection algorithm, which is based on the matched-filter (MF) method (Balbinot et al. 2011; Luque et al. 2016). Briefly, we begin by binning stars into spatial pixels of 1.0 arcmin × 1.0 arcmin and colour–magnitude bins of 0.01 mag × 0.05 mag. We then create a grid of simple stellar populations (SSPs) with the code GENCMD.[8] We use GENCMD along with PARSEC isochrones (Bressan et al. 2012) and an initial mass function (IMF) of Kroupa (2001). We simulate several SSPs in a range of ages [9.0 ≤ log (Age) ≤ 10.2], metallicities ($Z = \{0.0002, 0.001, 0.007\}$) and distance ($10 \leq D_{\odot} \leq 200$ kpc). To account for local variations in the background CMD, we partition the sky into 10° × 10° regions. We then apply SPARSEX on the stellar catalogue in every sky region using the grid of the SSPs. This procedure generates one density map for each SSP model within a sky region.

To search for stellar clusters and dwarf galaxies, we convolved the set density maps with Gaussian spatial kernels of different sizes,[9] from $\sigma = 0$ (no convolution) to 9 arcmin. To automatically detect overdensities in each map, we use the SEXTRACTOR code (Bertin & Arnouts 1996). Finally, we selected stellar object candidates based

[7] Thus far, spectroscopic observations have confirmed that Reticulum II (Koposov et al. 2015b; Simon et al. 2015; Walker et al. 2015), Horologium I (Koposov et al. 2015b) and Tucana II (Walker et al. 2016) are indeed dwarf galaxies.

[8] https://github.com/balbinot/gencmd

[9] As mentioned in Luque et al. (2016), our range of spatial kernel sizes complements those adopted by the other two substructure search techniques. This range of kernel sizes and all possible combinations of parameters, age, metallicity and distance allows us to detect compact objects as GCs, as well as extended objects such as dwarf galaxies.

on two criteria: (1) according to the number of times that the SSP models are detected. In this case, the 10 highest ranked candidates in each region of the sky and each convolution kernel were visually analysed. (2) According to the statistical significance of the excess number of stars relative to the background: we built a significant profile in a cumulative way, in incremental steps of 1.0 arcmin in radius, centred on each candidate. We then applied a simple cut in significance. All candidates with significance thresholds $>5\sigma$ were visually analysed to discard artificial objects as well as contamination by faint galaxies (Luque et al. 2016).

Applying the method described above on DES Y2Q1 data, we successfully recovered with high significance all 19 stellar objects that have been recently reported in DES data (Bechtol et al. 2015; Drlica-Wagner et al. 2015; Kim & Jerjen 2015b; Kim et al. 2015; Koposov et al. 2015a; Luque et al. 2016). Additionally, we detected two new candidate stellar systems potentially associated with the Sagittarius stream, DES J0111−1341 and DES J0225+0304. The physical properties derived for DES J0111−1341 reveal that this candidate is consistent with being an ultrafaint stellar cluster, whereas DES J0225+0304 is more consistent with being a dwarf galaxy candidate (see discussion in the next section).

5 DES J0111−1341 AND DES J0225+0304

DES J0111−1341 and DES J0225+0304 were detected with high statistical significance, 8.2σ and 7.5σ, respectively. A Test Statistic (TS) for these candidates was also determined in an independent manner. The TS is based on the likelihood ratio between a hypothesis that includes an object versus a field-only hypothesis (Bechtol et al. 2015, equation 4). This analysis has revealed a TS ~ 15 ($\sim 4\sigma$) for both candidates. We do not observe an obvious overdensity of sources classified as galaxies, which reduces the possibility that the detected overdensities are caused by misclassified faint galaxies.

We use the maximum likelihood technique to determine the structural and CMD parameters. To estimate the structural parameters, we assume that the spatial distribution of stars of both objects follows an exponential profile model. Following the convention of Martin, de Jong & Rix (2008), we parametrize this model with six free parameters: central coordinates α_0 and δ_0, position angle θ, ellipticity ϵ, exponential scale radius r_e and background density Σ_{bgd}. For CMD fits, we first weighted each star by the membership probability p taken from the exponential density profile (Pieres et al. 2016). We then selected all the stars with a threshold of $p \geq 1$ per cent to fit an isochrone model. The free parameters age, $(m-M)_0$ and Z are simultaneously determined by this fitting method (for details, see Luque et al. 2016; Pieres et al. 2016). To explore the parameter space, we use the EMCEE module for Markov Chain Monte Carlo (MCMC; Foreman-Mackey et al. 2013)[10] sampling. We use MCMC to determine the best-fitting parameters for both the exponential profile and isochrone models. The absolute magnitudes were calculated using the prescription of Luque et al. (2016). The inferred properties of DES J0111−1341 and DES J0225+0304 are listed in Table 1.

5.1 DES J0111−1341

DES J0111−1341 is the candidate detected with most statistical significance ($\sim 8.2\sigma$) in our sample of promising candidates. In the top-left panel of Fig. 5, we show the density map constructed using stars inside the isochrone filter. For comparison, we show in the top middle panel the density map of objects classified as galaxies. Note the prominent stellar overdensity centred on DES J0111−1341. The top-right panel shows the elliptical significance profile. It is defined as the ratio of the number of stars inside a given ellipse and in excess of the background (N_{bgd}), N_{obj}, to the expected fluctuation in the same background, i.e. $N_{obj}/\sqrt{N_{bgd}}$. $N_{obj} = (N_{obs} - N_{bgd})$, where N_{obs} is the total number of observed stars. We build the elliptical significance profile using cumulative ellipses with semimajor axis a centred on the object. N_{bgd} is computed within an elliptical annulus at 30 arcmin $< a <$ 34 arcmin from DES J0111−1341 (Luque et al. 2016). Note that the higher peak of significance (PS) is clearly steeper for the filtered stars according to our best-fitting isochrone model. In the same figure, the CMD for DES J0111−1341 is shown in the bottom-left panel. Only stars inside an ellipse with semimajor axis $a = 2r_h$ are shown. The CMD shows predominantly MS stars. The bottom middle panel shows the CMD of background stars contained within an elliptical annulus of equal area as the previous panel. In both CMDs, we show the filter based on our best-fitting isochrone (see Luque et al. 2016). The Hess difference between the stars inside an ellipse with semimajor axis $a = 2r_h$ and background stars (20.0 arcmin $< a <$ 35.0 arcmin), this latter scaled to the same area, is shown in the bottom-right panel. In Fig. 6, we show the binned stellar density profile for DES J0111−1341. The best-fitting exponential model is also overplotted. In both cases, we took into account the ellipticity of the object.

The physical size ($r_h \sim 4.55$ pc) of DES J0111−1341 is comparable with the size of GCs associated with the Sagittarius stream]. However, its luminosity ($M_V \sim +0.3$) is inconsistent with this class of objects]. Therefore, its low luminosity and small size place DES J0111−1341 among the MW ultrafaint stellar clusters (see size–luminosity plane, Fig. 9). In particular, its luminosity is comparable to Kim 1 ($M_V \sim +0.3$; Kim & Jerjen 2015a). However, DES J0111−1341 is fainter than DES 1 (Luque et al. 2016),

Table 1. Properties of DES J0111−1341 and DES J0225+0304.

Parameters	DES J0111−1341	DES J0225+0304	Unit
α_0 (J2000)	$01:11:10.3^{+0.40}_{-0.48}$	$02:25:42.4^{+1.52}_{-1.60}$	h: m: s
δ_0 (J2000)	$-13:41:05.4^{+5.4}_{-6.6}$	$03:04:10.1^{+45.6}_{-39.6}$	◦: ′: ″
l	142.83	163.58	deg
b	−75.79	−52.20	deg
Λ	86.61	111.02	deg
B	−3.97	1.24	deg
θ	$-53.24^{+31.70}_{-23.24}$	$31.25^{+11.48}_{-13.39}$	deg
ϵ	$0.27^{+0.20}_{-0.17}$	$0.61^{+0.14}_{-0.23}$	
Σ_{bgd}	$1.040^{+0.001}_{-0.001}$	$1.679^{+0.002}_{-0.002}$	$\frac{\text{stars}}{\text{arcmin}^2}$
$D_\odot$	$26.5^{+1.3}_{-1.3}$	$23.8^{+0.7}_{-0.5}$	kpc
r_h[a]	$0.59^{+0.17}_{-0.12}$	$2.68^{+1.33}_{-0.70}$	arcmin
r_h	$4.55^{+1.33}_{-0.95}$[b]	$18.55^{+9.22}_{-4.86}$[c]	pc
M_V	$+0.3^{+0.9}_{-0.6}$	$-1.1^{+0.5}_{-0.3}$	mag
D_{orb}	∼1.73	∼0.50	kpc
[Fe/H][d]	$-1.38^{+0.07}_{-0.05}$	$-1.26^{+0.03}_{-0.03}$	
log (Age)	$10.06^{+0.02}_{-0.02}$	$10.07^{+0.01}_{-0.01}$	
$(m-M)_0$	$17.12^{+0.11}_{-0.11}$	$16.88^{+0.06}_{-0.05}$	

Notes. [a]Using the relation $r_h = 1.68 r_e$ (Martin et al. 2008).
[b]Adopting a distance of 26.5 kpc.
[c]Adopting a distance of 23.8 kpc.
[d]Adopting $Z_\odot = 0.0152$ (Bressan et al. 2012).

[10] http://dan.iel.fm/emcee/current/

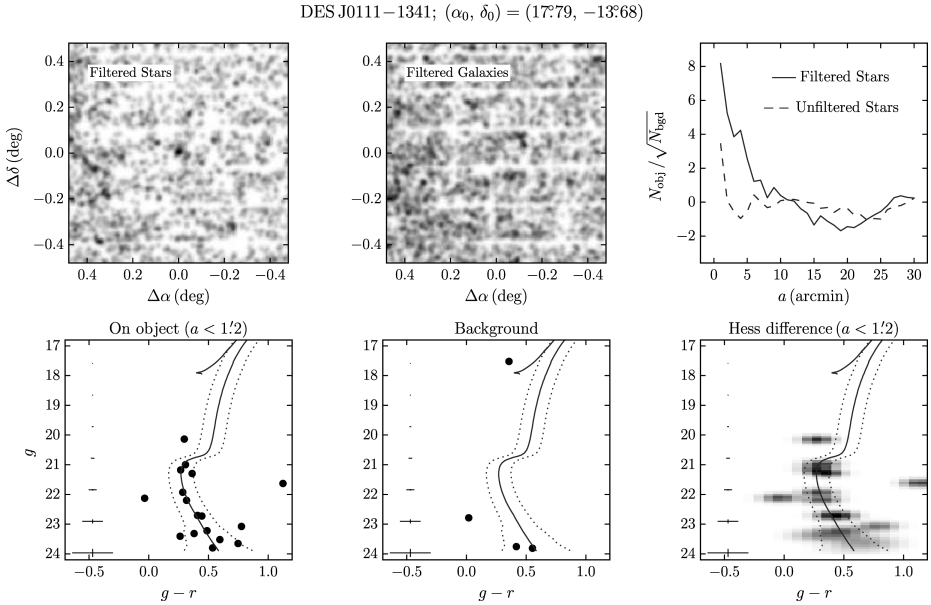

Figure 5. Top-left panel: on-sky number density map of stars around DES J0111−1341. Only stars that lie close to the best-fitting isochrone are included. Top middle panel: similar to the previous panel, but now for galaxies. Top-right panel: elliptical significance as a function of semimajor axis a from the centre of DES J0111−1341. The solid [dashed] line corresponds to isochrone-filtered [not pass the filter (unfiltered)] stars. Lower-left panel: CMD of stars within an ellipse with semimajor axis $a = 2r_h$ from the centre of DES J0111−1341. In this and the other two bottom panels, the best-fitting PARSEC isochrone (Bressan et al. 2012) is shown, along with ridge lines meant to bracket the most likely members. Lower middle panel: CMD of background stars in an elliptical annulus of equal area on the sky as the previous panel. Lower right panel: Hess diagram of the CMD difference between stars within $a = 2r_h$ and background stars (20.0 arcmin $< a <$ 35.0 arcmin). The mean photometric error is shown in the extreme left of each lower panel.

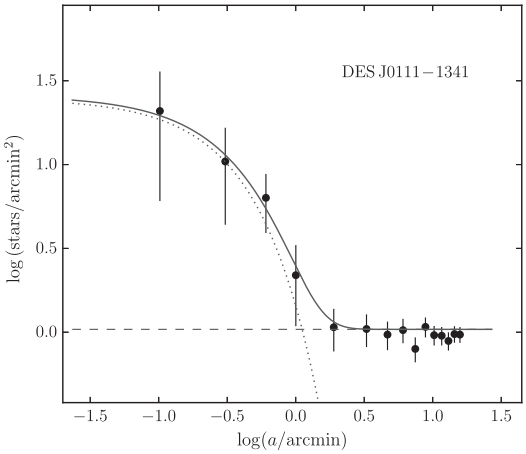

Figure 6. Solid points show a binned version of the density profile of DES J0111−1341, constructed in elliptical annuli using the derived structural parameters from the best-fitting exponential profile (see Table 1). The error bars are 1σ Poisson uncertainties. The dotted line represents the best-fitting exponential profile. The horizontal dashed line shows the background level. The solid line is the combination of the background level with the exponential profile.

Koposov 1, Koposov 2 (Koposov et al. 2007) and Muñoz 1 (Muñoz et al. 2012).

5.2 DES J0225+0304

Figs 7 and 8 show the analogous information as Figs 5 and 6 for DES J0225+0304. The physical size ($r_h \sim 18.55$ pc) and luminosity ($M_V \sim -1.1$) place it in an ambiguous region of size–luminosity space between stellar clusters and dwarf galaxies (see Fig. 9). DES J0225+0304 is elongated ($\epsilon \sim 0.61$) and has a physical size similar to an extended GC or a very small faint dwarf galaxy. In fact, the physical size, luminosity and ellipticity of DES J0225+0304 are comparable to the properties of the Tucana V stellar system ($r_h \simeq 17$ pc, $M_V \simeq -1.6$ and $\epsilon \simeq 0.7$; Drlica-Wagner et al. 2015).

5.3 Association with the Sagittarius stream

As mentioned in Section 3, DES J0111−1341 and DES J0225+0304 are probably associated with the Sagittarius dwarf stream. Their log (Age), [Fe/H] and $D_\odot$ (see Table 1) are well bracketed by the age, metallicity and distance ranges determined in Section 3.2 for the stream. In fact, the inferred ages and metallicities are very similar for both DES J0111−1341 and DES J0225+0304, and agree very well with the isochrone fit to the mean RGB colours of the stream, log (Age) = 10.02, [Fe/H] = −1.34 and $D_\odot = 24.5$ kpc.

To better explore this association, we estimate the distance of the two new candidates to the Sagittarius orbital plane (D_{orb}). For

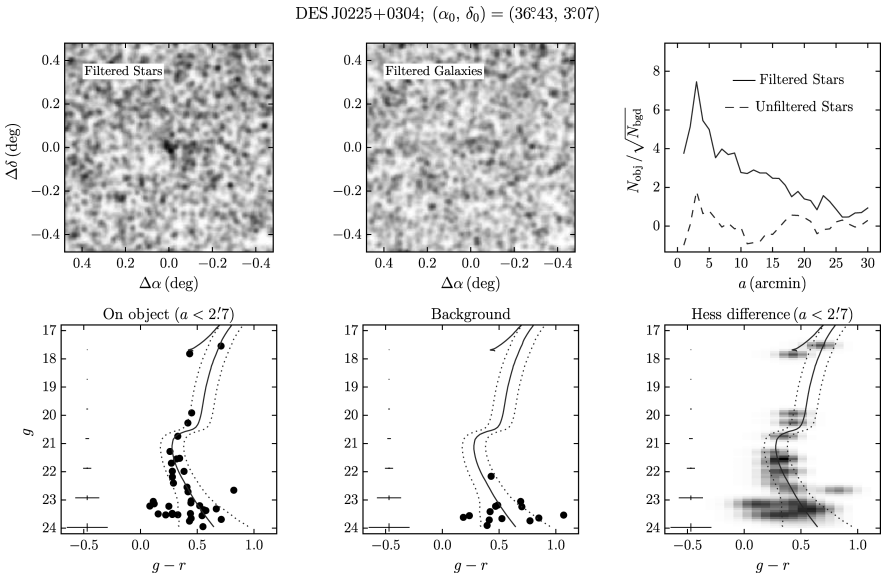

Figure 7. Top-left panel: on-sky number density map of stars around DES J0225+0304. Only stars that lie close to the best-fitting isochrone are included. Top middle panel: similar to the previous panel, but now for galaxies. Top-right panel: elliptical significance as a function of semimajor axis a from the centre of DES J0225+0304. The solid (dashed) line corresponds to isochrone-filtered [not pass the filter (unfiltered)] stars. Lower-left panel: CMD of stars within an ellipse with semimajor axis $a = 1r_h$ from the centre of DES J0225+0304. In this and the other two bottom panels, the best-fitting PARSEC isochrone (Bressan et al. 2012) is shown, along with ridge lines meant to bracket the most likely members. Lower-middle panel: CMD of background stars in an elliptical annulus of equal area on the sky as the previous panel. Lower-right panel: Hess diagram of the CMD difference between stars within $a = 1r_h$ and background stars (25.0 arcmin $< a <$ 45.0 arcmin). The mean photometric error is shown in the extreme left of each lower panel.

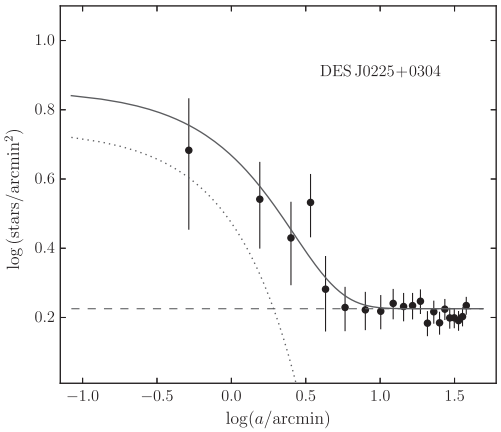

Figure 8. Solid points show a binned version of the density profile of DES J0225+0304, constructed in elliptical annuli using the derived structural parameters from the best-fitting exponential profile (see Table 1). The error bars are 1σ Poisson uncertainties. The dotted line represents the best-fitting exponential profile. The horizontal dashed line shows the background level. The solid line is the combination of the background level with the exponential profile.

this purpose, we use the best-fitting Sagittarius orbital plane[11] determined by Majewski et al. (2003). We then obtain a distance of ∼1.73 and ∼0.50 kpc for DES J0111−1341 and DES J0225+0304, respectively. When we compare the D_{orb} of the new candidates with the D_{orb} determined for GCs associated with the Sagittarius dwarf (Bellazzini et al. 2003, and references therein), we note that DES J0111−1341 has a D_{orb} similar to that of Terzan 7 (∼1.89 kpc), whereas the D_{orb} of DES J0225+0304 is comparable to that of NGC 6715 (∼0.45 kpc). These results indicate that both DES J0111−1341 and DES J0225+0304 are very close indeed to the Sagittarius plane, something that strongly increases the likelihood of their association with the Sagittarius stream. However, there are GCs spatially compatible with the orbit of Sagittarius (e.g. NCG 4147 and NGC 288) but not associated with Sagittarius when their radial velocities and proper motions are considered (Law & Majewski 2010b). This suggests that the spectroscopic determination of the radial velocity and the proper motion of these systems are both crucial to confirm that association.

We use a random sampling technique to give a statistical argument for this possible association. For this purpose, we use the sample of known star clusters and dwarf galaxies from various recent sources (Harris 2010; McConnachie 2012; Balbinot et al. 2013; Laevens et al. 2014, 2015a,b; Bechtol et al. 2015; Drlica-Wagner et al. 2015; Koposov et al. 2015a; Kim & Jerjen 2015a; Kim et al. 2015, 2016; Martin et al. 2015; Luque et al. 2016). The null hypothesis assumes that the stellar systems from our sample are not associated with the Sagittarius dwarf galaxy; thus, we removed the four GCs confirmed to be associated with the Sagittarius dwarf (NGC 6715, Arp 2, Terzan 7 and Terzan 8). First, we calculate the D_{orb} for each stellar system. We then randomly selecttwo systems from the sample, assigning an equal selection probability to each system. After performing 10^6 selections, we estimate a 0.08 probability of finding two stellar systems with $D_{orb} \leq 1.73$ kpc. While it is true that this

[11] The best-fitting plane was performed by using M-giant stars detected in 2MASS data (for details, see Majewski et al. 2003).

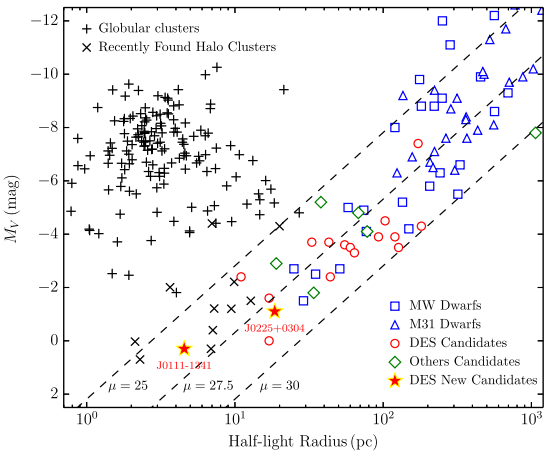

Figure 9. Absolute magnitude as a function of half-light radius. MW GCs ('+' symbols; Harris 2010), outer halo clusters with ambiguous classification ('×' symbols; Koposov et al. 2007; Belokurov et al. 2010; Muñoz et al. 2012; Balbinot et al. 2013; Laevens et al. 2014, 2015b; Kim & Jerjen 2015a; Kim et al. 2015, 2016; Luque et al. 2016), MW dwarf galaxies (blue squares; McConnachie 2012), M 31 dwarf galaxies (blue triangles; McConnachie 2012), previously reported dwarf galaxy candidates in the DES footprint (red circles; Bechtol et al. 2015; Drlica-Wagner et al. 2015), other recently reported dwarf galaxies (green diamond; Kim & Jerjen 2015a; Laevens et al. 2015a,b; Martin et al. 2015; Torrealba et al. 2016) and DES new candidates (red stars) are shown. Note that DES J0111−1341 clearly lies inside the region inhabited by ultrafaint stellar clusters, whereas DES J0225+0304 occupies the ambiguous region between stellar clusters and dwarf galaxies. The dashed lines indicate contours of constant surface brightness at $\mu = \{25, 27.5, 30\}$ mag arsec^{-2}.

probability value is not negligible, these randomly drawn pairs of objects are not necessarily as close to the Sagittarius orbit as our candidates.

6 CONCLUSIONS

In this paper, we report the discovery of two new candidate stellar systems in the constellation of Cetus using DES Y2Q1 data. These objects add to the 19 star systems that have been found in the first 2 yr of DES (Bechtol et al. 2015; Drlica-Wagner et al. 2015; Kim & Jerjen 2015b; Koposov et al. 2015a; Luque et al. 2016). DES J0111−1341 is a compact ($r_h \sim 4.55$ pc) and ultrafaint ($M_V \sim +0.3$) stellar cluster, whereas DES J0225+0304 is faint ($M_V \sim -1.1$) and has a physical size ($r_h \sim 18.55$ pc) comparable to a very small faint dwarf galaxy. These new stellar systems appear to be at a heliocentric distance $D_\odot \sim 25$ kpc.

There are several lines of evidence that suggest that our new candidates are associated with the Sagittarius stream: (i) they lie on the edges of the Sagittarius stream, as can be seen in Fig. 1 (red circles). (ii) The CMD parameters (age, metallicity and distance) determined for these new candidates lie within the metallicity and age range determined for the Sagittarius stream using the same DES data (Section 3.2). In particular, they are consistent with the parameters inferred by fitting the mean CMD locus of the stream stars. (iii) The distances D_{orb} of our candidates to the Sagittarius orbital plane, ∼1.73 kpc (DES J0111−1341) and ∼0.50 kpc (DES J0225+0304), are comparable to GCs previously associated with the Sagittarius dwarf, more specifically Terzan 7 and NGC 6715 (Bellazzini et al. 2003). Therefore, we speculate that these candidates are likely associated with the Sagittarius stream. However, the spectroscopic determination of the radial velocity and proper motion of these substructures will be very useful to confirm this hypothesis. Furthermore, the dynamic mass, derived from the velocity dispersion, will help to confirm the nature of our candidates. If all of our hypotheses are confirmed, DES J0225+0304 would be the first ultrafaint dwarf galaxy associated with the Sagittarius dwarf stream. It would also be the first confirmed case of an ultrafaint satellite of a satellite.

As for the properties of the stream itself, the star count histograms constructed across the Sagittarius stream show a possible excess of stars at $B \sim 8°$. However, this putative excess is only clearly visible when we use bin sizes of $0.^\circ6 \lesssim \Delta B \lesssim 0.^\circ7$. Therefore, we do not claim a detection of the branching of the stream. We found no further direct evidence of additional stream substructures to those already known to exist.

Finally, decontaminated Hess diagrams of the Sagittarius stream allowed us to determine a metallicity spread ($-2.18 \lesssim$ [Fe/H] $\lesssim -0.95$) as well as a distance gradient (23 kpc $\lesssim D_\odot \lesssim$ 29 kpc). This suggests that the stream is composed of more than one stellar population. Our determination of distance gradient is consistent with those determined by Koposov et al. (2012). However, metallicity determinations in the literature suggest that the stream in the celestial equator contains more metal-rich stars than those determined in this work (see e.g. Koposov et al. 2012; De Boer et al. 2015).

In the future, DES will acquire additional imaging data in this region, allowing even more significant studies of the region in which the Sagittarius stream crosses the equator.

ACKNOWLEDGEMENTS

This paper has gone through internal review by the DES collaboration.

Funding for the DES Projects has been provided by the US Department of Energy, the US National Science Foundation, the Ministry of Science and Education of Spain, the Science and Technology Facilities Council of the United Kingdom, the Higher Education Funding Council for England, the National Center for Supercomputing Applications at the University of Illinois at Urbana-Champaign, the Kavli Institute of Cosmological Physics at the University of Chicago, the Center for Cosmology and Astro-Particle Physics at the Ohio State University, the Mitchell Institute for Fundamental Physics and Astronomy at Texas A&M University, Financiadora de Estudos e Projetos, Fundação Carlos Chagas Filho de Amparo à Pesquisa do Estado do Rio de Janeiro, Conselho Nacional de Desenvolvimento Científico e Tecnológico and the Ministério da Ciência, Tecnologia e Inovação, the Deutsche Forschungsgemeinschaft and the Collaborating Institutions in the DES. The DES data management system is supported by the National Science Foundation under Grant Number AST-1138766. The DES participants from Spanish institutions are partially supported by MINECO under grants AYA2012-39559, ESP2013-48274, FPA2013-47986 and Centro de Excelencia Severo Ochoa SEV-2012-0234, some of which include ERDF funds from the European Union.

The Collaborating Institutions are Argonne National Laboratory, the University of California at Santa Cruz, the University of Cambridge, Centro de Investigaciones Enérgeticas, Medioambientales y Tecnológicas-Madrid, the University of Chicago, University College London, the DES-Brazil Consortium, the University of Edinburgh, the Eidgenössische Technische Hochschule

(ETH) Zürich, Fermi National Accelerator Laboratory, the University of Illinois at Urbana-Champaign, the Institut de Ciències de l'Espai (IEEC/CSIC), the Institut de Física d'Altes Energies, Lawrence Berkeley National Laboratory, the Ludwig-Maximilians Universität München and the associated Excellence Cluster Universe, the University of Michigan, the National Optical Astronomy Observatory, the University of Nottingham, the Ohio State University, the University of Pennsylvania, the University of Portsmouth, SLAC National Accelerator Laboratory, Stanford University, the University of Sussex and Texas A&M University.

The DES data management system is supported by the National Science Foundation under Grant Number AST-1138766. The DES participants from Spanish institutions are partially supported by MINECO under grants AYA2012-39559, ESP2013-48274, FPA2013-47986 and Centro de Excelencia Severo Ochoa SEV-2012-0234.

Research leading to these results has received funding from the European Research Council under the European Union's Seventh Framework Programme (FP7/2007-2013) including ERC grant agreements 240672, 291329 and 306478.

EB acknowledges financial support from the European Research Council (ERC-StG-335936, CLUSTERS).

REFERENCES

Balbinot E., Santiago B. X., da Costa L. N., Makler M., Maia M. A. G., 2011, MNRAS, 416, 393
Balbinot E. et al., 2013, ApJ, 767, 101
Bechtol K. et al., 2015, ApJ, 807, 50
Bellazzini M., Ferraro F. R., Ibata R., 2003, AJ, 125, 188
Belokurov V. et al., 2006, ApJ, 642, L137
Belokurov V. et al., 2010, ApJ, 712, L103
Belokurov V. et al., 2014, MNRAS, 437, 116
Bertin E., 2011, in Evans I. N., Accomazzi A., Mink D. J., Rots A. H., eds, ASP Conf. Ser. Vol. 442, Astronomical Data Analysis Software and Systems XX. Astron. Soc. Pac., San Francisco, p. 435
Bertin E., Arnouts S., 1996, A&AS, 117, 393
Bouy H., Bertin E., Moraux E., Cuillandre J.-C., Bouvier J., Barrado D., Solano E., Bayo A., 2013, A&A, 554, A101
Bressan A., Marigo P., Girardi L., Salasnich B., Dal Cero C., Rubele S., Nanni A., 2012, MNRAS, 427, 127
Carballo-Bello J. A., Sollima A., Martínez-Delgado D., Pila-Díez B., Leaman R., Fliri J., Muñoz R. R., Corral-Santana J. M., 2014, MNRAS, 445, 2971
Carraro G., Bensby T., 2009, MNRAS, 397, L106
Carraro G., Bresolin F., Villanova S., Matteucci F., Patat F., Romaniello M., 2004, AJ, 128, 1676
Correnti M., Bellazzini M., Ibata R. A., Ferraro F. R., Varghese A., 2010, ApJ, 721, 329
Da Costa G. S., Armandroff T. E., 1995, AJ, 109, 2533
De Boer T. J. L., Belokurov V., Koposov S., 2015, MNRAS, 451, 3489
Desai S. et al., 2012, ApJ, 757, 83
Diehl H. T. et al., 2016, in Peck A. B., Seaman R. L., Benn C. R., eds, Proc. SPIE Conf. Ser. Vol. 9910, Observatory Operations: Strategies, Processes, and Systems VI. SPIE, Bellingham, p. 99101D
Dotter A. et al., 2010, ApJ, 708, 698
Dotter A., Sarajedini A., Anderson J., 2011, ApJ, 738, 74
Drlica-Wagner A. et al., 2015, ApJ, 813, 109
Flaugher B. et al., 2015, AJ, 150, 150
Forbes D. A., Bridges T., 2010, MNRAS, 404, 1203
Foreman-Mackey D., Hogg D. W., Lang D., Goodman J., 2013, PASP, 125, 306
Harris W. E., 2010, preprint (arXiv:1012.3224)
Hyde E. A. et al., 2015, ApJ, 805, 189
Ibata R. A., Gilmore G., Irwin M. J., 1994, Nature, 370, 194
Johnston K. V., Spergel D. N., Hernquist L., 1995, ApJ, 451, 598
Kim D., Jerjen H., 2015a, ApJ, 799, 73
Kim D., Jerjen H., 2015b, ApJ, 808, L39
Kim D., Jerjen H., Milone A. P., Mackey D., Da Costa G. S., 2015, ApJ, 803, 63
Kim D., Jerjen H., Mackey D., Da Costa G. S., Milone A. P., 2016, ApJ, 820, 119
Koposov S. et al., 2007, ApJ, 669, 337
Koposov S. E. et al., 2012, ApJ, 750, 80
Koposov S. E., Belokurov V., Torrealba G., Evans N. W., 2015a, ApJ, 805, 130
Koposov S. E. et al., 2015b, ApJ, 811, 62
Kroupa P., 2001, MNRAS, 322, 231
Laevens B. P. M. et al., 2014, ApJ, 786, L3
Laevens B. P. M. et al., 2015a, ApJ, 802, L18
Laevens B. P. M. et al., 2015b, ApJ, 813, 44
Law D. R., Majewski S. R., 2010a, ApJ, 714, 229
Law D. R., Majewski S. R., 2010b, ApJ, 718, 1128
Luque E. et al., 2016, MNRAS, 458, 603
Lynden-Bell D., Lynden-Bell R. M., 1995, MNRAS, 275, 429
McConnachie A. W., 2012, AJ, 144, 4
Majewski S. R., Skrutskie M. F., Weinberg M. D., Ostheimer J. C., 2003, ApJ, 599, 1082
Martin N. F., de Jong J. T. A., Rix H.-W., 2008, ApJ, 684, 1075
Martin N. F. et al., 2015, ApJ, 804, L5
Mateo M., Mirabal N., Udalski A., Szymanski M., Kaluzny J., Kubiak M., Krzeminski W., Stanek K. Z., 1996, ApJ, 458, L13
Mohr J. J. et al., 2012, in Radziwill N. M., Chiozzi G., eds, Proc. SPIE Conf. Ser. Vol. 8451, Software and Cyberinfrastructure for Astronomy II. SPIE, Bellingham, p. 84510D
Muñoz R. R., Geha M., Côté P., Vargas L. C., Santana F. A., Stetson P., Simon J. D., Djorgovski S. G., 2012, ApJ, 753, L15
Newberg H. J. et al., 2002, ApJ, 569, 245
Newberg H. J. et al., 2003, ApJ, 596, L191
Newberg H. J., Yanny B., Cole N., Beers T. C., Re Fiorentin P., Schneider D. P., Wilhelm R., 2007, ApJ, 668, 221
Pieres A. et al., 2016, MNRAS, 461, 519
Sbordone L. et al., 2015, A&A, 579, A104
Sevilla I. et al., 2011, preprint (arXiv:1109.6741)
Simon J. D. et al., 2015, ApJ, 808, 95
Slater C. T. et al., 2013, ApJ, 762, 6
The Dark Energy Survey Collaboration, 2005, preprint (arXiv:e-prints)
Torrealba G., Koposov S. E., Belokurov V., Irwin M., 2016, MNRAS, 459, 2370
Walker M. G., Mateo M., Olszewski E. W., Bailey J. I., III, Koposov S. E., Belokurov V., Evans N. W., 2015, ApJ, 808, 108
Walker M. G. et al., 2016, ApJ, 819, 53
Yanny B. et al., 2009, ApJ, 700, 1282

[1]*Instituto de Física, UFRGS, Caixa Postal 15051, Porto Alegre, RS 91501-970, Brazil*
[2]*Laboratório Interinstitucional de e-Astronomia - LIneA, Rua Gal. José Cristino 77, Rio de Janeiro, RJ 20921-400, Brazil*
[3]*Fermi National Accelerator Laboratory, P. O. Box 500, Batavia, IL 60510, USA*
[4]*Cerro Tololo Inter-American Observatory, National Optical Astronomy Observatory, Casilla 603, La Serena, Chile*
[5]*National Center for Supercomputing Applications, 1205 West Clark St, Urbana, IL 61801, USA*
[6]*Department of Physics, University of Surrey, Guildford GU2 7XH, UK*
[7]*George P. and Cynthia Woods Mitchell Institute for Fundamental Physics and Astronomy, and Department of Physics and Astronomy, Texas A&M University, College Station, TX 77843, USA*
[8]*Observatório Nacional, Rua Gal. José Cristino 77, Rio de Janeiro, RJ 20921-400, Brazil*
[9]*Kavli Institute for Cosmological Physics, University of Chicago, Chicago, IL 60637, USA*

[10] *Lawrence Berkeley National Laboratory, 1 Cyclotron Road, Berkeley, CA 94720, USA*
[11] *Department of Physics and Astronomy, University of Pennsylvania, Philadelphia, PA 19104, USA*
[12] *Department of Physics & Astronomy, University College London, Gower Street, London WC1E 6BT, UK*
[13] *Department of Physics and Electronics, Rhodes University, PO Box 94, Grahamstown 6140, South Africa*
[14] *CNRS, UMR 7095, Institut d'Astrophysique de Paris, F-75014 Paris, France*
[15] *Sorbonne Universités, UPMC Univ Paris 06, UMR 7095, Institut d'Astrophysique de Paris, F-75014 Paris, France*
[16] *Kavli Institute for Particle Astrophysics & Cosmology, P. O. Box 2450, Stanford University, Stanford, CA 94305, USA*
[17] *SLAC National Accelerator Laboratory, Menlo Park, CA 94025, USA*
[18] *Department of Astronomy, University of Illinois, 1002 W. Green Street, Urbana, IL 61801, USA*
[19] *Institut de Ciències de l'Espai, IEEC-CSIC, Campus UAB, Carrer de Can Magrans, s/n, E-08193 Bellaterra, Barcelona, Spain*
[20] *Institut de Física d'Altes Energies (IFAE), The Barcelona Institute of Science and Technology, Campus UAB, E-08193 Bellaterra, Barcelona, Spain*
[21] *Institute of Cosmology & Gravitation, University of Portsmouth, Portsmouth PO1 3FX, UK*
[22] *School of Physics and Astronomy, University of Southampton, Southampton SO17 1BJ, UK*
[23] *Department of Physics, IIT Hyderabad, Kandi, Telangana 502285, India*
[24] *Department of Astronomy, University of Michigan, Ann Arbor, MI 48109, USA*
[25] *Department of Physics, University of Michigan, Ann Arbor, MI 48109, USA*
[26] *Department of Astronomy, University of California, Berkeley, 501 Campbell Hall, Berkeley, CA 94720, USA*
[27] *Australian Astronomical Observatory, North Ryde, NSW 2113, Australia*
[28] *Center for Cosmology and Astro-Particle Physics, The Ohio State University, Columbus, OH 43210, USA*
[29] *Department of Astronomy, The Ohio State University, Columbus, OH 43210, USA*
[30] *Institució Catalana de Recerca i Estudis Avançats, E-08010 Barcelona, Spain*
[31] *Jet Propulsion Laboratory, California Institute of Technology, 4800 Oak Grove Dr, Pasadena, CA 91109, USA*
[32] *Department of Physics and Astronomy, Pevensey Building, University of Sussex, Brighton BN1 9QH, UK*
[33] *Centro de Investigaciones Energéticas, Medioambientales y Tecnológicas (CIEMAT), E-28040 Madrid, Spain*
[34] *Universidade Federal do ABC, Centro de Ciências Naturais e Humanas, Av. dos Estados, 5001, Santo André, SP 09210-580, Brazil*
[35] *Computer Science and Mathematics Division, Oak Ridge National Laboratory, Oak Ridge, TN 37831, USA*

This paper has been typeset from a TEX/LATEX file prepared by the author.

Bibliografia

[1] ABELL, G. O. Globular Clusters and Planetary Nebulae Discovered on the National Geographic Society-Palomar Observatory Sky Survey. **Publications of the Astronomical Society of the Pacific**, v. 67, p. 258–261, August 1955.

[2] ASHMAN, K. M., BIRD, C. M., ZEPF, S. E. Detecting bimodality in astronomical datasets. **Astronomical Journal**, v. 108, p. 2348–2361, December 1994.

[3] BAHCALL, J. N., SONEIRA, R. M. The universe at faint magnitudes. I - Models for the galaxy and the predicted star counts. **Astrophysical Journal Supplement Series**, v. 44, p. 73–110, September 1980.

[4] BALBINOT, E., SANTIAGO, B. X., DA COSTA, L., MAIA, M. A. G., MAJEWSKI, S. R., NIDEVER, D., ROCHA-PINTO, H. J., THOMAS, D., WECHSLER, R. H., YANNY, B. A New Milky Way Halo Star Cluster in the Southern Galactic Sky. **Astrophysical Journal**, v. 767, p. 101, April 2013.

[5] BALBINOT, E., SANTIAGO, B. X., GIRARDI, L., PIERES, A., DA COSTA, L. N., MAIA, M. A. G., GRUENDL, R. A., WALKER, A. R., YANNY, B., DRLICA-WAGNER, A., BENOIT-LEVY, A., ABBOTT, T. M. C., ALLAM, S. S., ANNIS, J., BERNSTEIN, J. P., BERNSTEIN, R. A., BERTIN, E., BROOKS, D., BUCKLEY-GEER, E., ROSELL, A. C., CUNHA, C. E., DEPOY, D. L., DESAI, S., DIEHL, H. T., DOEL, P., ESTRADA, J., EVRARD, A. E., NETO, A. F., FINLEY, D. A., FLAUGHER, B., FRIEMAN, J. A., GRUEN, D., HONSCHEID, K., JAMES, D., KUEHN, K., KUROPATKIN, N., LAHAV, O., MARCH, M., MARSHALL, J. L., MILLER, C., MIQUEL, R., OGANDO, R., PEOPLES, J., PLAZAS, A., SCARPINE, V., SCHUBNELL, M., SEVILLA-NOARBE, I., SMITH, R. C., SOARES-SANTOS, M., SUCHYTA, E., SWANSON, M. E. C., TARLE, G., TUCKER, D. L., WECHSLER, R., ZUNTZ, J. The LMC geometry and outer stellar populations

from early DES data. **Monthly Notices of the Royal Astronomical Society**, v. 449, p. 1129–1145, May 2015.

[6] BALBINOT, E., SANTIAGO, B. X., KERBER, L. O., BARBUY, B., DIAS, B. M. S. Probing the Large Magellanic Cloud age gap at intermediate cluster masses. **Monthly Notices of the Royal Astronomical Society**, v. 404, p. 1625–1632, May 2010.

[7] BARAFFE, I., CHABRIER, G., ALLARD, F., HAUSCHILDT, P. H. Evolutionary models for solar metallicity low-mass stars: mass-magnitude relationships and color-magnitude diagrams. **Astronomy and Astrophysics**, v. 337, p. 403–412, September 1998.

[8] BATTANER, E., FLORIDO, E. The Rotation Curve of Spiral Galaxies and its Cosmological Implications. **Fundamental Cosmic Physics**, v. 21, p. 1–154, 2000.

[9] BAUMGARDT, H., KROUPA, P. A comprehensive set of simulations studying the influence of gas expulsion on star cluster evolution. **Monthly Notices of the Royal Astronomical Society**, v. 380, p. 1589–1598, October 2007.

[10] BAUMGARDT, H., KROUPA, P., PARMENTIER, G. The influence of residual gas expulsion on the evolution of the Galactic globular cluster system and the origin of the Population II halo. **Monthly Notices of the Royal Astronomical Society**, v. 384, p. 1231–1241, March 2008.

[11] BAUMGARDT, H., MAKINO, J. Dynamical evolution of star clusters in tidal fields. **Monthly Notices of the Royal Astronomical Society**, v. 340, p. 227–246, March 2003.

[12] BAUMGARDT, H., MIESKE, S. High mass-to-light ratios of ultra-compact dwarf galaxies - evidence for dark matter? **Monthly Notices of the Royal Astronomical Society**, v. 391, p. 942–948, December 2008.

[13] BAUMGARDT, H., PARMENTIER, G., ANDERS, P., GREBEL, E. K. The star cluster formation history of the LMC. **Monthly Notices of the Royal Astronomical Society**, v. 430, p. 676–685, March 2013.

[14] BECHTOL, K., DRLICA-WAGNER, A., BALBINOT, E., PIERES, A., SIMON, J. D., YANNY, B., SANTIAGO, B., WECHSLER, R. H., FRIEMAN, J.,

WALKER, A. R., WILLIAMS, P., ROZO, E., RYKOFF, E. S., QUEIROZ, A., LUQUE, E., BENOIT-LÉVY, A., TUCKER, D., SEVILLA, I., GRUENDL, R. A., DA COSTA, L. N., FAUSTI NETO, A., MAIA, M. A. G., ABBOTT, T., ALLAM, S., ARMSTRONG, R., BAUER, A. H., BERNSTEIN, G. M., BERNSTEIN, R. A., BERTIN, E., BROOKS, D., BUCKLEY-GEER, E., BURKE, D. L., CARNERO ROSELL, A., CASTANDER, F. J., COVAR-RUBIAS, R., D'ANDREA, C. B., DEPOY, D. L., DESAI, S., DIEHL, H. T., EIFLER, T. F., ESTRADA, J., EVRARD, A. E., FERNANDEZ, E., FINLEY, D. A., FLAUGHER, B., GAZTANAGA, E., GERDES, D., GIRARDI, L., GLADDERS, M., GRUEN, D., GUTIERREZ, G., HAO, J., HONSCHEID, K., JAIN, B., JAMES, D., KENT, S., KRON, R., KUEHN, K., KUROPATKIN, N., LAHAV, O., LI, T. S., LIN, H., MAKLER, M., MARCH, M., MARSHALL, J., MARTINI, P., MERRITT, K. W., MILLER, C., MIQUEL, R., MOHR, J., NEILSEN, E., NICHOL, R., NORD, B., OGANDO, R., PEOPLES, J., PETRAVICK, D., PLAZAS, A. A., ROMER, A. K., ROODMAN, A., SAKO, M., SANCHEZ, E., SCARPINE, V., SCHUBNELL, M., SMITH, R. C., SOARES-SANTOS, M., SOBREIRA, F., SUCHYTA, E., SWANSON, M. E. C., TARLE, G., THALER, J., THOMAS, D., WESTER, W., ZUNTZ, J., DES COLLABORATION, . Eight New Milky Way Companions Discovered in First-year Dark Energy Survey Data. **Astrophysical Journal**, v. 807, p. 50, July 2015.

[15] BEERS, T. C., SOMMER-LARSEN, J. Kinematics of metal-poor stars in the galaxy. **Astrophysical Journal Supplement Series**, v. 96, p. 175–221, January 1995.

[16] BEKKI, K., CHIBA, M. Formation and evolution of the Magellanic Clouds - I. Origin of structural, kinematic and chemical properties of the Large Magellanic Cloud. **Monthly Notices of the Royal Astronomical Society**, v. 356, p. 680–702, January 2005.

[17] BELOKUROV, V., WALKER, M. G., EVANS, N. W., FARIA, D. C., GILMORE, G., IRWIN, M. J., KOPOSOV, S., MATEO, M., OLSZEWSKI, E., ZUCKER, D. B. Leo V: A Companion of a Companion of the Milky Way Galaxy? **Astrophysical Journal Letters**, v. 686, p. L83, October 2008.

[18] BELOKUROV, V., WALKER, M. G., EVANS, N. W., GILMORE, G., IRWIN, M. J., JUST, D., KOPOSOV, S., MATEO, M., OLSZEWSKI, E., WATKINS,

L., WYRZYKOWSKI, L. Big Fish, Little Fish: Two New Ultra-faint Satellites of the Milky Way. **Astrophysical Journal Letters**, v. 712, p. L103–L106, March 2010.

[19] BELOKUROV, V., WALKER, M. G., EVANS, N. W., GILMORE, G., IRWIN, M. J., MATEO, M., MAYER, L., OLSZEWSKI, E., BECHTOLD, J., PICKERING, T. The discovery of Segue 2: a prototype of the population of satellites of satellites. **Monthly Notices of the Royal Astronomical Society**, v. 397, p. 1748–1755, August 2009.

[20] BELOKUROV, V., ZUCKER, D. B., EVANS, N. W., KLEYNA, J. T., KOPOSOV, S., HODGKIN, S. T., IRWIN, M. J., GILMORE, G., WILKINSON, M. I., FELLHAUER, M., BRAMICH, D. M., HEWETT, P. C., VIDRIH, S., DE JONG, J. T. A., SMITH, J. A., RIX, H.-W., BELL, E. F., WYSE, R. F. G., NEWBERG, H. J., MAYEUR, P. A., YANNY, B., ROCKOSI, C. M., GNEDIN, O. Y., SCHNEIDER, D. P., BEERS, T. C., BARENTINE, J. C., BREWINGTON, H., BRINKMANN, J., HARVANEK, M., KLEINMAN, S. J., KRZESINSKI, J., LONG, D., NITTA, A., SNEDDEN, S. A. Cats and Dogs, Hair and a Hero: A Quintet of New Milky Way Companions. **Astrophysical Journal**, v. 654, p. 897–906, January 2007.

[21] BELOKUROV, V., ZUCKER, D. B., EVANS, N. W., WILKINSON, M. I., IRWIN, M. J., HODGKIN, S., BRAMICH, D. M., IRWIN, J. M., GILMORE, G., WILLMAN, B., VIDRIH, S., NEWBERG, H. J., WYSE, R. F. G., FELLHAUER, M., HEWETT, P. C., COLE, N., BELL, E. F., BEERS, T. C., ROCKOSI, C. M., YANNY, B., GREBEL, E. K., SCHNEIDER, D. P., LUPTON, R., BARENTINE, J. C., BREWINGTON, H., BRINKMANN, J., HARVANEK, M., KLEINMAN, S. J., KRZESINSKI, J., LONG, D., NITTA, A., SMITH, J. A., SNEDDEN, S. A. A Faint New Milky Way Satellite in Bootes. **Astrophysical Journal Letters**, v. 647, p. L111–L114, August 2006.

[22] BERTIN, E., ARNOUTS, S. SExtractor: Software for source extraction. **Astronomy and Astrophysics Supplement Series**, v. 117, p. 393–404, June 1996.

[23] BESLA, G., KALLIVAYALIL, N., HERNQUIST, L., ROBERTSON, B., COX, T. J., VAN DER MAREL, R. P., ALCOCK, C. Are the Magellanic Clouds on Their First Passage about the Milky Way? **Astrophysical Journal**, v. 668, p. 949–967, October 2007.

[24] BESLA, G., KALLIVAYALIL, N., HERNQUIST, L., VAN DER MAREL, R. P., COX, T. J., KEREŠ, D. Simulations of the Magellanic Stream in a First Infall Scenario. **Astrophysical Journal Letters**, v. 721, p. L97–L101, October 2010.

[25] BICA, E., GEISLER, D., DOTTORI, H., CLARIÁ, J. J., PIATTI, A. E., SANTOS, J. F. C., JR. Ages and Metallicities of Star Clusters and Surrounding Fields in the Outer Disk of the Large Magellanic Cloud. **Astronomical Journal**, v. 116, p. 723–737, August 1998.

[26] BICA, E., SANTIAGO, B., BONATTO, C., GARCIA-DIAS, R., KERBER, L., DIAS, B., BARBUY, B., BALBINOT, E. Bridge over troubled gas: clusters and associations under the SMC and LMC tidal stresses. **Monthly Notices of the Royal Astronomical Society**, v. 453, p. 3190–3202, November 2015.

[27] BINGGELI, B., CAMERON, L. M. Dwarf galaxies in the Virgo cluster. I - The systematic photometric properties of early-type dwarfs. **Astronomy and Astrophysics**, v. 252, p. 27–52, December 1991.

[28] BINNEY, J., TREMAINE, S. **Galactic Dynamics**, Princeton series in astrophysics: Princeton University Press, 1987.

[29] BINNEY, J., TREMAINE, S. **Galactic Dynamics: Second Edition**, Princeton Series in Astrophysics: Princeton University Press, 2011.

[30] BISSANTZ, N., GERHARD, O. Spiral arms, bar shape and bulge microlensing in the Milky Way. **Monthly Notices of the Royal Astronomical Society**, v. 330, p. 591–608, March 2002.

[31] BOTHUN, G., IMPEY, C., MALIN, D. Extremely Low Surface Brightness Galaxies. In: BULLETIN OF THE AMERICAN ASTRONOMICAL SOCIETY, v. 18 of **Bulletin of the American Astronomical Society**, p. 958, September 1986.

[32] BOVY, J., RIX, H.-W., SCHLAFLY, E. F., NIDEVER, D. L., HOLTZMAN, J. A., SHETRONE, M., BEERS, T. C. The Stellar Population Structure of the Galactic Disk. **Astrophysical Journal**, v. 823, p. 30, May 2016.

[33] BRESSAN, A., MARIGO, P., GIRARDI, L., SALASNICH, B., DAL CERO, C., RUBELE, S., NANNI, A. PARSEC: stellar tracks and isochrones with

the PAdova and TRieste Stellar Evolution Code. **Monthly Notices of the Royal Astronomical Society**, v. 427, p. 127–145, November 2012.

[34] BROMM, V., LARSON, R. B. The First Stars. **Annual Review of Astronomy and Astrophysics**, v. 42, p. 79–118, September 2004.

[35] BULLOCK, J. S. Notes on the Missing Satellites Problem. **ArXiv e-prints**, September 2010.

[36] CARLSTROM, J. E., ADE, P. A. R., AIRD, K. A., BENSON, B. A., BLEEM, L. E., BUSETTI, S., CHANG, C. L., CHAUVIN, E., CHO, H.-M., CRAWFORD, T. M., CRITES, A. T., DOBBS, M. A., HALVERSON, N. W., HEIMSATH, S., HOLZAPFEL, W. L., HRUBES, J. D., JOY, M., KEISLER, R., LANTING, T. M., LEE, A. T., LEITCH, E. M., LEONG, J., LU, W., LUEKER, M., LUONG-VAN, D., MCMAHON, J. J., MEHL, J., MEYER, S. S., MOHR, J. J., MONTROY, T. E., PADIN, S., PLAGGE, T., PRYKE, C., RUHL, J. E., SCHAFFER, K. K., SCHWAN, D., SHIROKOFF, E., SPIELER, H. G., STANISZEWSKI, Z., STARK, A. A., TUCKER, C., VANDERLINDE, K., VIEIRA, J. D., WILLIAMSON, R. The 10 Meter South Pole Telescope. **Publications of the Astronomical Society of the Pacific**, v. 123, p. 568, May 2011.

[37] CAROLLO, D., BEERS, T. C., PLACCO, V. M., SANTUCCI, R. M., DENISSENKOV, P., TISSERA, P. B., LENTNER, G., ROSSI, S., LEE, Y. S., TUMLINSON, J. The age structure of the Milky Way's halo. **Nature Physics**, v. 12, p. 1170–1176, December 2016.

[38] CARRERA, R., GALLART, C., HARDY, E., APARICIO, A., ZINN, R. The Chemical Enrichment History of the Large Magellanic Cloud. **Astronomical Journal**, v. 135, p. 836–849, March 2008.

[39] CARRETTA, E., BRAGAGLIA, A., GRATTON, R. G., RECIO-BLANCO, A., LUCATELLO, S., D'ORAZI, V., CASSISI, S. Properties of stellar generations in globular clusters and relations with global parameters. **Astronomy and Astrophysics**, v. 516, p. A55, June 2010.

[40] CARROLL, BRADLEY W., OSTLIE, DALE A. **An Introduction to Modern Astrophysics**. 2nd (international).ed.: 2007.

[41] CATCHPOLE, R. M., WHITELOCK, P. A., GLASS, I. S. The Distribution of Stars Within Two Degrees of the Galactic Centre. **Monthly Notices of the Royal Astronomical Society**, v. 247, p. 479–490, December 1990.

[42] CHABRIER, G. Galactic Stellar and Substellar Initial Mass Function. **Publications of the Astronomical Society of the Pacific**, v. 115, p. 763–795, July 2003.

[43] CHOWDHURY, A., CHENGALUR, J. N. Angular momentum content in gas-rich dwarf galaxies. **Monthly Notices of the Royal Astronomical Society**, v. 467, p. 3856–3863, June 2017.

[44] CROWTHER, P. A., CABALLERO-NIEVES, S. M., BOSTROEM, K. A., MAíZ APELLÁNIZ, J., SCHNEIDER, F. R. N., WALBORN, N. R., ANGUS, C. R., BROTT, I., BONANOS, A., DE KOTER, A., DE MINK, S. E., EVANS, C. J., GRÄFENER, G., HERRERO, A., HOWARTH, I. D., LANGER, N., LENNON, D. J., PULS, J., SANA, H., VINK, J. S. The R136 star cluster dissected with Hubble Space Telescope/STIS. I. Far-ultraviolet spectroscopic census and the origin of He II λ1640 in young star clusters. **Monthly Notices of the Royal Astronomical Society**, v. 458, p. 624–659, May 2016.

[45] DADDI, E., BOURNAUD, F., WALTER, F., DANNERBAUER, H., CARILLI, C. L., DICKINSON, M., ELBAZ, D., MORRISON, G. E., RIECHERS, D., ONODERA, M., SALMI, F., KRIPS, M., STERN, D. Very High Gas Fractions and Extended Gas Reservoirs in z = 1.5 Disk Galaxies. **Astrophysical Journal**, v. 713, p. 686–707, April 2010.

[46] DARK ENERGY SURVEY COLLABORATION, , ABBOTT, T., ABDALLA, F. B., ALLAM, S., ALEKSIĆ, J., AMARA, A., BACON, D., BALBINOT, E., BANERJI, M., BECHTOL, K., BENOIT-LÉVY, A., BERNSTEIN, G. M., BERTIN, E., BLAZEK, J., DODELSON, S., BONNETT, C., BROOKS, D., BRIDLE, S., BRUNNER, R. J., BUCKLEY-GEER, E., BURKE, D. L., CAPOZZI, D., CAMINHA, G. B., CARLSEN, J., CARNERO-ROSELL, A., CAROLLO, M., CARRASCO-KIND, M., CARRETERO, J., CASTANDER, F. J., CLERKIN, L., COLLETT, T., CONSELICE, C., CROCCE, M., CUNHA, C. E., D'ANDREA, C. B., DA COSTA, L. N., DAVIS, T. M., DESAI, S., DIEHL, H. T., DIETRICH, J. P., DOEL, P., DRLICA-WAGNER, A., ETHERINGTON, J., ESTRADA, J., EVRARD, A. E., FABBRI, J., FINLEY, D. A., FLAUGHER, B., FOSALBA, P., FOLEY, R. J., FRIEMAN, J.,

GARCíA-BELLIDO, J., GAZTANAGA, E., GERDES, D. W., GIANNANTONIO, T., GOLDSTEIN, D. A., GRUEN, D., GRUENDL, R. A., GUARNIERI, P., GUTIERREZ, G., HARTLEY, W., HONSCHEID, K., JAIN, B., JAMES, D. J., JELTEMA, T., JOUVEL, S., KESSLER, R., KING, A., KIRK, D., KRON, R., KUEHN, K., KUROPATKIN, N., LAHAV, O., LI, T. S., LIMA, M., LIN, H., MAIA, M. A. G., MAKLER, M., MANERA, M., MARASTON, C., MARSHALL, J. L., MARTINI, P., MCMAHON, R. G., MELCHIOR, P., MERSON, A., MILLER, C. J., MIQUEL, R., MOHR, J. J., MORICE-ATKINSON, X., NAIDOO, K., NEILSEN, E., NICHOL, R. C., NORD, B., OGANDO, R., OSTROVSKI, F., PALMESE, A., PAPADOPOULOS, A., PEIRIS, H., PEOPLES, J., PLAZAS, A. A., PERCIVAL, W. J., REED, S. L., ROMER, A. K., ROODMAN, A., ROSS, A., ROZO, E., RYKOFF, E. S., SADEH, I., SAKO, M., SÁNCHEZ, C., SANCHEZ, E., SANTIAGO, B., SCARPINE, V., SCHUBNELL, M., SEVILLA-NOARBE, I., SHELDON, E., SMITH, M., SMITH, R. C., SOARES-SANTOS, M., SOBREIRA, F., SOUMAGNAC, M., SUCHYTA, E., SULLIVAN, M., SWANSON, M., TARLE, G., THALER, J., THOMAS, D., THOMAS, R. C., TUCKER, D., VIEIRA, J. D., VIKRAM, V., WALKER, A. R., WECHSLER, R. H., WESTER, W., WELLER, J., WHITEWAY, L., WILCOX, H., YANNY, B., ZHANG, Y., ZUNTZ, J. The Dark Energy Survey: more than dark energy - an overview. **Monthly Notices of the Royal Astronomical Society**, March 2016.

[47] DAVIDGE, T. J., MCCONNACHIE, A. W., FARDAL, M. A., FLIRI, J., VALLS-GABAUD, D., CHAPMAN, S. C., LEWIS, G. F., RICH, R. M. The recent stellar archeology of m31—the nearest red disk galaxy. **The Astrophysical Journal**, v. 751, n. 1, p. 74, 2012.

[48] DE FREITAS PACHECO, J. A., BARBUY, B., IDIART, T. Age and metallicity of star clusters in the Magellanic Clouds. **Astronomy and Astrophysics**, v. 332, p. 19–24, April 1998.

[49] DE GRIJS, R., ANDERS, P. How well do we know the age and mass distributions of the star cluster system in the Large Magellanic Cloud? **Monthly Notices of the Royal Astronomical Society**, v. 366, p. 295–307, February 2006.

[50] DE GRIJS, R., WICKER, J. E., BONO, G. Clustering of Local Group Distances: Publication Bias or Correlated Measurements? I. The Large Magellanic Cloud. **Astronomical Journal**, v. 147, p. 122, May 2014.

[51] DE VAUCOULEURS, G., DE VAUCOULEURS, A., CORWIN, H. G., JR., BUTA, R. J., PATUREL, G., FOUQUÉ, P. **Third Reference Catalogue of Bright Galaxies. Volume I: Explanations and references. Volume II: Data for galaxies between 0^h and 12^h. Volume III: Data for galaxies between 12^h and 24^h.**: 1991.

[52] DEMPSTER, A. P., LAIRD, N. M., RUBIN, D. B. Maximum likelihood from incomplete data via the em algorithm. **Journal of the Royal Statistical Society. Series B (Methodological)**, v. 39, n. 1, p. 1–38, 1977.

[53] DESAI, S., ARMSTRONG, R., MOHR, J. J., SEMLER, D. R., LIU, J., BERTIN, E., ALLAM, S. S., BARKHOUSE, W. A., BAZIN, G., BUCKLEY-GEER, E. J., COOPER, M. C., HANSEN, S. M., HIGH, F. W., LIN, H., LIN, Y.-T., NGEOW, C.-C., REST, A., SONG, J., TUCKER, D., ZENTENO, A. The Blanco Cosmology Survey: Data Acquisition, Processing, Calibration, Quality Diagnostics, and Data Release. **Astrophysical Journal**, v. 757, p. 83, September 2012.

[54] DIAS, B., KERBER, L., BARBUY, B., BICA, E., ORTOLANI, S. SMC west halo: a slice of the galaxy that is being tidally stripped?. Star clusters trace age and metallicity gradients. **Astronomy and Astrophysics**, v. 591, p. A11, June 2016.

[55] DIAS, W. S., ALESSI, B. S., MOITINHO, A., LÉPINE, J. R. D. New catalogue of optically visible open clusters and candidates. **Astronomy and Astrophysics**, v. 389, p. 871–873, July 2002.

[56] DIAZ, J. D., BEKKI, K. The Tidal Origin of the Magellanic Stream and the Possibility of a Stellar Counterpart. **Astrophysical Journal**, v. 750, p. 36, May 2012.

[57] DISNEY, M. J. Visibility of galaxies. **Nature**, v. 263, p. 573–575, October 1976.

[58] DO, CHUONG B, BATZOGLOU, SERAFIM. What is the expectation maximization algorithm? **Nat Biotech**, v. 26, n. 8, p. 897–899, August 2008.

[59] DOBBIE, P. D., COLE, A. A., SUBRAMANIAM, A., KELLER, S. Red giants in the Small Magellanic Cloud - I. Disc and tidal stream kinematics. **Monthly Notices of the Royal Astronomical Society**, v. 442, p. 1663–1679, August 2014.

[60] D'ONGHIA, E., BESLA, G., COX, T. J., HERNQUIST, L. Resonant stripping as the origin of dwarf spheroidal galaxies. **Nature**, v. 460, p. 605–607, July 2009.

[61] DRLICA-WAGNER, A., BECHTOL, K., ALLAM, S., TUCKER, D. L., GRUENDL, R. A., JOHNSON, M. D., WALKER, A. R., JAMES, D. J., NIDEVER, D. L., OLSEN, K. A. G., WECHSLER, R. H., CIONI, M. R. L., CONN, B. C., KUEHN, K., LI, T. S., MAO, Y.-Y., MARTIN, N. F., NEILSEN, E., NOEL, N. E. D., PIERES, A., SIMON, J. D., STRINGFELLOW, G. S., VAN DER MAREL, R. P., YANNY, B. An Ultra-faint Galaxy Candidate Discovered in Early Data from the Magellanic Satellites Survey. **Astrophysical Journal Letters**, v. 833, p. L5, December 2016.

[62] DRLICA-WAGNER, A., BECHTOL, K., RYKOFF, E. S., LUQUE, E., QUEIROZ, A., MAO, Y.-Y., WECHSLER, R. H., SIMON, J. D., SANTIAGO, B., YANNY, B., BALBINOT, E., DODELSON, S., FAUSTI NETO, A., JAMES, D. J., LI, T. S., MAIA, M. A. G., MARSHALL, J. L., PIERES, A., STRINGER, K., WALKER, A. R., ABBOTT, T. M. C., ABDALLA, F. B., ALLAM, S., BENOIT-LÉVY, A., BERNSTEIN, G. M., BERTIN, E., BROOKS, D., BUCKLEY-GEER, E., BURKE, D. L., CARNERO ROSELL, A., CARRASCO KIND, M., CARRETERO, J., CROCCE, M., DA COSTA, L. N., DESAI, S., DIEHL, H. T., DIETRICH, J. P., DOEL, P., EIFLER, T. F., EVRARD, A. E., FINLEY, D. A., FLAUGHER, B., FOSALBA, P., FRIEMAN, J., GAZTANAGA, E., GERDES, D. W., GRUEN, D., GRUENDL, R. A., GUTIERREZ, G., HONSCHEID, K., KUEHN, K., KUROPATKIN, N., LAHAV, O., MARTINI, P., MIQUEL, R., NORD, B., OGANDO, R., PLAZAS, A. A., REIL, K., ROODMAN, A., SAKO, M., SANCHEZ, E., SCARPINE, V., SCHUBNELL, M., SEVILLA-NOARBE, I., SMITH, R. C., SOARES-SANTOS, M., SOBREIRA, F., SUCHYTA, E., SWANSON, M. E. C., TARLE, G., TUCKER, D., VIKRAM, V., WESTER, W., ZHANG, Y., ZUNTZ, J., DES COLLABORATION, . Eight Ultra-faint Galaxy Candidates Discovered in Year Two of the Dark Energy Survey. **Astrophysical Journal**, v. 813, p. 109, November 2015.

[63] DUC, P.-A. Birth, Life and Survival of Tidal Dwarf Galaxies. **Astrophysics and Space Science Proceedings**, v. 28, p. 305, 2012.

[64] DUC, P.-A., BRINKS, E., WINK, J. E., MIRABEL, I. F. Gas segregation in the interacting system ARP 105. **Astronomy and Astrophysics**, v. 326, p. 537–553, October 1997.

[65] EBELING, H., STEPHENSON, L. N., EDGE, A. C. Jellyfish: Evidence of Extreme Ram-pressure Stripping in Massive Galaxy Clusters. **Astrophysical Journal Letters**, v. 781, p. L40, February 2014.

[66] FEITZINGER, J. V., SCHMIDT-KALER, T., ISSERSTEDT, J. Space orientation and translational motion of the Large Magellanic Cloud. **Astronomy and Astrophysics**, v. 57, p. 265–271, May 1977.

[67] FERGUSON, H. C., BINGGELI, B. Dwarf elliptical galaxies. **Astronomy and Astrophysics Reviews**, v. 6, p. 67–122, November 1994.

[68] FISHER, R.A. **Statistical methods for research workers**: Edinburgh Oliver & Boyd, 1925.

[69] FLAUGHER, B., DIEHL, H. T., HONSCHEID, K., ABBOTT, T. M. C., ALVAREZ, O., ANGSTADT, R., ANNIS, J. T., ANTONIK, M., BALLESTER, O., BEAUFORE, L., BERNSTEIN, G. M., BERNSTEIN, R. A., BIGELOW, B., BONATI, M., BOPRIE, D., BROOKS, D., BUCKLEY-GEER, E. J., CAMPA, J., CARDIEL-SAS, L., CASTANDER, F. J., CASTILLA, J., CEASE, H., CELA-RUIZ, J. M., CHAPPA, S., CHI, E., COOPER, C., DA COSTA, L. N., DEDE, E., DERYLO, G., DEPOY, D. L., DE VICENTE, J., DOEL, P., DRLICA-WAGNER, A., EITING, J., ELLIOTT, A. E., EMES, J., ESTRADA, J., FAUSTI NETO, A., FINLEY, D. A., FLORES, R., FRIEMAN, J., GERDES, D., GLADDERS, M. D., GREGORY, B., GUTIERREZ, G. R., HAO, J., HOLLAND, S. E., HOLM, S., HUFFMAN, D., JACKSON, C., JAMES, D. J., JONAS, M., KARCHER, A., KARLINER, I., KENT, S., KESSLER, R., KOZLOVSKY, M., KRON, R. G., KUBIK, D., KUEHN, K., KUHLMANN, S., KUK, K., LAHAV, O., LATHROP, A., LEE, J., LEVI, M. E., LEWIS, P., LI, T. S., MANDRICHENKO, I., MARSHALL, J. L., MARTINEZ, G., MERRITT, K. W., MIQUEL, R., MUÑOZ, F., NEILSEN, E. H., NICHOL, R. C., NORD, B., OGANDO, R., OLSEN, J., PALAIO, N., PATTON, K., PEOPLES, J., PLAZAS, A. A., RAUCH, J., REIL, K., RHEAULT, J.-P., ROE, N. A., ROGERS, H., ROODMAN, A., SANCHEZ, E., SCARPINE, V., SCHINDLER, R. H., SCHMIDT, R., SCHMITT, R., SCHUBNELL, M., SCHULTZ, K., SCHURTER, P., SCOTT, L., SERRANO,

S., SHAW, T. M., SMITH, R. C., SOARES-SANTOS, M., STEFANIK, A., STUERMER, W., SUCHYTA, E., SYPNIEWSKI, A., TARLE, G., THALER, J., TIGHE, R., TRAN, C., TUCKER, D., WALKER, A. R., WANG, G., WATSON, M., WEAVERDYCK, C., WESTER, W., WOODS, R., YANNY, B., DES COLLABORATION, . The Dark Energy Camera. **Astronomical Journal**, v. 150, p. 150, November 2015.

[70] FORBES, D. A., KROUPA, P. What Is a Galaxy? Cast Your Vote Here. **Publications of the Astronomical Society of Australia**, v. 28, p. 77–82, March 2011.

[71] FOREMAN-MACKEY, D., HOGG, D. W., LANG, D., GOODMAN, J. emcee: The MCMC Hammer. **Publications of the Astronomical Society of the Pacific**, v. 125, p. 306–312, March 2013.

[72] FRIAÇA, A.B.C.S. **Astronomia: Uma Visão Geral do Universo Vol. 28**: EDUSP, 2000.

[73] GARDINER, L. T., NOGUCHI, M. N-body simulations of the Small Magellanic Cloud and the Magellanic Stream. **Monthly Notices of the Royal Astronomical Society**, v. 278, p. 191–208, January 1996.

[74] GARDINER, L. T., SAWA, T., FUJIMOTO, M. Numerical Simulations of the Magellanic System - Part One - Orbits of the Magellanic Clouds and the Global Gas Distribution. **Monthly Notices of the Royal Astronomical Society**, v. 266, p. 567, February 1994.

[75] GEISLER, D., BICA, E., DOTTORI, H., CLARIA, J. J., PIATTI, A. E., SANTOS, J. F. C., JR. A Search for Old Star Clusters in the Large Magellanic Cloud. **Astronomical Journal**, v. 114, p. 1920, November 1997.

[76] GERHARD, O. Dynamical Masses, Time-scales and Evolution of Star Clusters. In: MASSIVE STELLAR CLUSTERS, Lançon, A., Boily, C. M., editores, v. 211 of **Astronomical Society of the Pacific Conference Series**, p. 12, 2000.

[77] GIELES, M., PORTEGIES ZWART, S. F. The distinction between star clusters and associations. **Monthly Notices of the Royal Astronomical Society**, v. 410, p. L6–L7, January 2011.

[78] GILLESSEN, S., EISENHAUER, F., TRIPPE, S., ALEXANDER, T., GENZEL, R., MARTINS, F., OTT, T. Monitoring Stellar Orbits Around the Massive Black Hole in the Galactic Center. **Astrophysical Journal**, v. 692, p. 1075–1109, February 2009.

[79] GILMORE, G., REID, N. New light on faint stars. III - Galactic structure towards the South Pole and the Galactic thick disc. **Monthly Notices of the Royal Astronomical Society**, v. 202, p. 1025–1047, March 1983.

[80] GILMORE, G., WILKINSON, M. I., WYSE, R. F. G., KLEYNA, J. T., KOCH, A., EVANS, N. W., GREBEL, E. K. The Observed Properties of Dark Matter on Small Spatial Scales. **Astrophysical Journal**, v. 663, p. 948–959, July 2007.

[81] GIRARDI, L., CHIOSI, C., BERTELLI, G., BRESSAN, A. Age distribution of LMC clusters from their integrated UBV colors: history of star formation. **Astronomy and Astrophysics**, v. 298, p. 87, June 1995.

[82] GLOVER, S. The Formation Of The First Stars In The Universe. **Space Science Reviews**, v. 117, p. 445–508, April 2005.

[83] GOWARDHAN, A., RIECHERS, D. A., DADDI, E., PAVESI, R., DANNERBAUER, H., CARILLI, C. High Dense Gas Fraction in a Gas-rich Star-forming Galaxy at z = 1.2. **Astrophysical Journal**, v. 838, p. 136, April 2017.

[84] GRACZYK, D., PIETRZYŃSKI, G., THOMPSON, I. B., GIEREN, W., PILECKI, B., KONORSKI, P., UDALSKI, A., SOSZYŃSKI, I., VILLANOVA, S., GÓRSKI, M., SUCHOMSKA, K., KARCZMAREK, P., KUDRITZKI, R.-P., BRESOLIN, F., GALLENNE, A. The Araucaria Project. The Distance to the Small Magellanic Cloud from Late-type Eclipsing Binaries. **Astrophysical Journal**, v. 780, p. 59, January 2014.

[85] GREVESSE, N., SAUVAL, A. J. Standard Solar Composition. **Space Science Reviews**, v. 85, p. 161–174, May 1998.

[86] GRILLMAIR, C. J. Detection of a 60deg-long Dwarf Galaxy Debris Stream. **Astrophysical Journal Letters**, v. 645, p. L37–L40, July 2006.

[87] GRILLMAIR, C. J. Four New Stellar Debris Streams in the Galactic Halo. **Astrophysical Journal**, v. 693, p. 1118–1127, March 2009.

[88] GUNN, J. E., GOTT, J. R., III. On the Infall of Matter Into Clusters of Galaxies and Some Effects on Their Evolution. **Astrophysical Journal**, v. 176, p. 1, August 1972.

[89] HANSON, D., HOOVER, S., CRITES, A., ADE, P. A. R., AIRD, K. A., AUSTERMANN, J. E., BEALL, J. A., BENDER, A. N., BENSON, B. A., BLEEM, L. E., BOCK, J. J., CARLSTROM, J. E., CHANG, C. L., CHIANG, H. C., CHO, H.-M., CONLEY, A., CRAWFORD, T. M., DE HAAN, T., DOBBS, M. A., EVERETT, W., GALLICCHIO, J., GAO, J., GEORGE, E. M., HALVERSON, N. W., HARRINGTON, N., HENNING, J. W., HILTON, G. C., HOLDER, G. P., HOLZAPFEL, W. L., HRUBES, J. D., HUANG, N., HUBMAYR, J., IRWIN, K. D., KEISLER, R., KNOX, L., LEE, A. T., LEITCH, E., LI, D., LIANG, C., LUONG-VAN, D., MARSDEN, G., MCMAHON, J. J., MEHL, J., MEYER, S. S., MOCANU, L., MONTROY, T. E., NATOLI, T., NIBARGER, J. P., NOVOSAD, V., PADIN, S., PRYKE, C., REICHARDT, C. L., RUHL, J. E., SALIWANCHIK, B. R., SAYRE, J. T., SCHAFFER, K. K., SCHULZ, B., SMECHER, G., STARK, A. A., STORY, K. T., TUCKER, C., VANDERLINDE, K., VIEIRA, J. D., VIERO, M. P., WANG, G., YEFREMENKO, V., ZAHN, O., ZEMCOV, M. Detection of B-Mode Polarization in the Cosmic Microwave Background with Data from the South Pole Telescope. **Physical Review Letters**, v. 111, n. 14, p. 141301, October 2013.

[90] HARRIS, J., ZARITSKY, D. The Star Formation History of the Small Magellanic Cloud. **Astronomical Journal**, v. 127, p. 1531–1544, March 2004.

[91] HARRIS, J., ZARITSKY, D. The Star Formation History of the Large Magellanic Cloud. **Astronomical Journal**, v. 138, p. 1243–1260, November 2009.

[92] HARRIS, W. E. A Catalog of Parameters for Globular Clusters in the Milky Way. **Astronomical Journal**, v. 112, p. 1487, October 1996a.

[93] HARRIS, W. E. VizieR Online Data Catalog: Globular Clusters in the Milky Way (Harris, 1996). **VizieR Online Data Catalog**, v. 7195, November 1996b.

[94] HILKER, M., INFANTE, L., VIEIRA, G., KISSLER-PATIG, M., RICHTLER, T. The central region of the Fornax cluster. II. Spectroscopy and radial velocities of member and background galaxies. **Astronomy and Astrophysics Supplement Series**, v. 134, p. 75–86, January 1999.

[95] HUBBLE, E. P. Extragalactic nebulae. **Astrophysical Journal**, v. 64, December 1926.

[96] HUCHRA, J., PUGHE, W., KLEINMANN, S., SKRUTSKI, M., WEINBERG, M., BEICHMAN, C., CHESTER, T. The 2 Micron All Sky Survey. In: UNVEILING LARGE-SCALE STRUCTURES BEHIND THE MILKY WAY, Balkowski, C., Kraan-Korteweg, R. C., editores, v. 67 of **Astronomical Society of the Pacific Conference Series**, p. 41, 1994.

[97] IBATA, R. A., LEWIS, G. F., CONN, A. R., IRWIN, M. J., MCCONNACHIE, A. W., CHAPMAN, S. C., COLLINS, M. L., FARDAL, M., FERGUSON, A. M. N., IBATA, N. G., MACKEY, A. D., MARTIN, N. F., NAVARRO, J., RICH, R. M., VALLS-GABAUD, D., WIDROW, L. M. A vast, thin plane of corotating dwarf galaxies orbiting the Andromeda galaxy. **Nature**, v. 493, p. 62–65, January 2013.

[98] IRWIN, M. J., BELOKUROV, V., EVANS, N. W., RYAN-WEBER, E. V., DE JONG, J. T. A., KOPOSOV, S., ZUCKER, D. B., HODGKIN, S. T., GILMORE, G., PREMA, P., HEBB, L., BEGUM, A., FELLHAUER, M., HEWETT, P. C., KENNICUTT, R. C., JR., WILKINSON, M. I., BRAMICH, D. M., VIDRIH, S., RIX, H.-W., BEERS, T. C., BARENTINE, J. C., BREWINGTON, H., HARVANEK, M., KRZESINSKI, J., LONG, D., NITTA, A., SNEDDEN, S. A. Discovery of an Unusual Dwarf Galaxy in the Outskirts of the Milky Way. **Astrophysical Journal Letters**, v. 656, p. L13–L16, February 2007.

[99] JAMES, P. A., IVORY, C. F. On the scarcity of Magellanic Cloud like satellites. **Monthly Notices of the Royal Astronomical Society**, v. 411, p. 495–504, February 2011.

[100] JEANS, J. H. The Stability of a Spherical Nebula. **Philosophical Transactions of the Royal Society of London Series A**, v. 199, p. 1–53, 1902.

[101] JETHWA, P., ERKAL, D., BELOKUROV, V. A Magellanic origin of the DES dwarfs. **Monthly Notices of the Royal Astronomical Society**, v. 461, p. 2212–2233, September 2016.

[102] JURIĆ, M., IVEZIĆ, Ž., BROOKS, A., LUPTON, R. H., SCHLEGEL, D., FINKBEINER, D., PADMANABHAN, N., BOND, N., SESAR, B., ROCKOSI,

C. M., KNAPP, G. R., GUNN, J. E., SUMI, T., SCHNEIDER, D. P., BARENTINE, J. C., BREWINGTON, H. J., BRINKMANN, J., FUKUGITA, M., HARVANEK, M., KLEINMAN, S. J., KRZESINSKI, J., LONG, D., NEILSEN, E. H., JR., NITTA, A., SNEDDEN, S. A., YORK, D. G. The Milky Way Tomography with SDSS. I. Stellar Number Density Distribution. **Astrophysical Journal**, v. 673, p. 864–914, February 2008.

[103] KAFLE, PRAJWAL RAJ, SHARMA, SANJIB, LEWIS, GERAINT F., BLAND-HAWTHORN, JOSS. On the shoulders of giants: Properties of the stellar halo and the milky way mass distribution. **The Astrophysical Journal**, v. 794, n. 1, p. 59, 2014.

[104] KALBERLA, P. M. W., HAUD, U. Global properties of the HI high velocity sky. A statistical investigation based on the LAB survey. **Astronomy and Astrophysics**, v. 455, p. 481–498, August 2006.

[105] KALLIVAYALIL, N., VAN DER MAREL, R. P., BESLA, G., ANDERSON, J., ALCOCK, C. Third-epoch Magellanic Cloud Proper Motions. I. Hubble Space Telescope/WFC3 Data and Orbit Implications. **Astrophysical Journal**, v. 764, p. 161, February 2013.

[106] KARTTUNEN, H., KRÖGER, P., OJA, H., POUTANEN, M., DONNER, K.J. **Fundamental Astronomy**, Physics and Astronomy Online Library: Springer Berlin Heidelberg, 2003.

[107] KEEL, W. C., KENNICUTT, R. C., JR., HUMMEL, E., VAN DER HULST, J. M. The effects of interactions on spiral galaxies. I - Nuclear activity and star formation. **Astronomical Journal**, v. 90, p. 708–730, May 1985.

[108] KELLY, P. L., VON DER LINDEN, A., APPLEGATE, D. E., ALLEN, M. T., ALLEN, S. W., BURCHAT, P. R., BURKE, D. L., EBELING, H., CAPAK, P., CZOSKE, O., DONOVAN, D., MANTZ, A., MORRIS, R. G. Weighing the Giants - II. Improved calibration of photometry from stellar colours and accurate photometric redshifts. **Monthly Notices of the Royal Astronomical Society**, v. 439, p. 28–47, March 2014.

[109] KIM, D., JERJEN, H., MILONE, A. P., MACKEY, D., DA COSTA, G. S. Discovery of a Faint Outer Halo Milky Way Star Cluster in the Southern Sky. **Astrophysical Journal**, v. 803, p. 63, April 2015.

[110] KIM, S., STAVELEY-SMITH, L., DOPITA, M. A. An H I Aperture Mosaic Survey of the Large Magellanic Cloud. In: MAGELLANIC CLOUDS AND OTHER DWARF GALAXIES, Richtler, T., Braun, J. M., editores, p. 169–172, December 1998.

[111] KLEIN, C. R., CENKO, S. B., MILLER, A. A., NORMAN, D. J., BLOOM, J. S. Probing the distance and morphology of the Large Magellanic Cloud with RR Lyrae stars. **ArXiv e-prints**, May 2014.

[112] KOPOSOV, S., DE JONG, J. T. A., BELOKUROV, V., RIX, H.-W., ZUCKER, D. B., EVANS, N. W., GILMORE, G., IRWIN, M. J., BELL, E. F. The Discovery of Two Extremely Low Luminosity Milky Way Globular Clusters. **Astrophysical Journal**, v. 669, p. 337–342, November 2007.

[113] KOPOSOV, S. E., BELOKUROV, V., TORREALBA, G., EVANS, N. W. Beasts of the Southern Wild : Discovery of nine Ultra Faint satellites in the vicinity of the Magellanic Clouds. **Astrophysical Journal**, v. 805, p. 130, June 2015.

[114] KROUPA, P. On the variation of the initial mass function. **Monthly Notices of the Royal Astronomical Society**, v. 322, p. 231–246, April 2001.

[115] KUTNER, M.L. **Astronomy: A Physical Perspective**: Cambridge University Press, 2003.

[116] LADA, C. J., LADA, E. A. Embedded Clusters in Molecular Clouds. **Annual Review of Astronomy and Astrophysics**, v. 41, p. 57–115, 2003.

[117] LAMERS, H. J. G. L. M., GIELES, M., BASTIAN, N., BAUMGARDT, H., KHARCHENKO, N. V., PORTEGIES ZWART, S. An analytical description of the disruption of star clusters in tidal fields with an application to Galactic open clusters. **Astronomy and Astrophysics**, v. 441, p. 117–129, October 2005.

[118] LAW, D. R., MAJEWSKI, S. R., JOHNSTON, K. V. Evidence for a Triaxial Milky Way Dark Matter Halo from the Sagittarius Stellar Tidal Stream. **Astrophysical Journal Letters**, v. 703, p. L67–L71, September 2009.

[119] LAWRENCE, A., ROWAN-ROBINSON, M., LEECH, K., JONES, D. H. P., WALL, J. V. High-luminosity IRAS galaxies. I - The proportion of IRAS galaxies in interacting systems. **Monthly Notices of the Royal Astronomical Society**, v. 240, p. 329–348, September 1989.

[120] LEBOFSKY, M. J., RIEKE, G. H. The stellar population at the galactic center. In: THE GALACTIC CENTER, Backer, D. C., editor, v. 155 of **American Institute of Physics Conference Series**, p. 79–82, April 1987.

[121] LEE, Y.-W., JOO, J.-M., SOHN, Y.-J., REY, S.-C., LEE, H.-C., WALKER, A. R. Multiple stellar populations in the globular cluster ω Centauri as tracers of a merger event. **Nature**, v. 402, p. 55–57, November 1999.

[122] LIVANOU, E., DAPERGOLAS, A., KONTIZAS, M., NORDSTRÖM, B., KONTIZAS, E., ANDERSEN, J., DIRSCH, B., KARAMPELAS, A. Age - metallicity relation in the Magellanic Clouds clusters. **Astronomy and Astrophysics**, v. 554, p. A16, June 2013.

[123] LUTZ, K. A., KILBORN, V. A., CATINELLA, B., KORIBALSKI, B. S., BROWN, T. H., CORTESE, L., DÉNES, H., JÓZSA, G. I. G., WONG, O. I. The HIX galaxy survey I: Study of the most gas rich galaxies from HIPASS. **Monthly Notices of the Royal Astronomical Society**, v. 467, p. 1083–1097, May 2017.

[124] MAGRINI, L., RANDICH, S., KORDOPATIS, G., PRANTZOS, N., ROMANO, D., CHIEFFI, A., LIMONGI, M., FRANÇOIS, P., PANCINO, E., FRIEL, E., BRAGAGLIA, A., TAUTVAIŠIENĖ, G., SPINA, L., OVERBEEK, J., CANTAT-GAUDIN, T., DONATI, P., VALLENARI, A., SORDO, R., JIMÉNEZ-ESTEBAN, F. M., TANG, B., DRAZDAUSKAS, A., SOUSA, S., DUFFAU, S., JOFRÉ, P., GILMORE, G., FELTZING, S., ALFARO, E., BENSBY, T., FLACCOMIO, E., KOPOSOV, S., LANZAFAME, A., SMILJANIC, R., BAYO, A., CARRARO, G., CASEY, A. R., COSTADO, M. T., DAMIANI, F., FRANCIOSINI, E., HOURIHANE, A., LARDO, C., LEWIS, J., MONACO, L., MORBIDELLI, L., SACCO, G., SBORDONE, L., WORLEY, C. C., ZAGGIA, S. The Gaia-ESO Survey: radial distribution of abundances in the Galactic disc from open clusters and young-field stars. **Astronomy and Astrophysics**, v. 603, p. A2, June 2017.

[125] MARINO, A. F., MILONE, A. P., PIOTTO, G., VILLANOVA, S., BEDIN, L. R., BELLINI, A., RENZINI, A. A double stellar generation in the globular cluster NGC 6656 (M 22). Two stellar groups with different iron and s-process element abundances. **Astronomy and Astrophysics**, v. 505, p. 1099–1113, October 2009.

[126] MARTIN, N. F., DE JONG, J. T. A., RIX, H.-W. A Comprehensive Maximum Likelihood Analysis of the Structural Properties of Faint Milky Way Satellites. **Astrophysical Journal**, v. 684, p. 1075–1092, September 2008.

[127] MATEO, M. L. Dwarf Galaxies of the Local Group. **Annual Review of Astronomy and Astrophysics**, v. 36, p. 435–506, 1998.

[128] MCCONNACHIE, A. W. The Observed Properties of Dwarf Galaxies in and around the Local Group. **Astronomical Journal**, v. 144, p. 4, July 2012.

[129] MCCONNACHIE, A. W., IRWIN, M. J., FERGUSON, A. M. N., IBATA, R. A., LEWIS, G. F., TANVIR, N. Distances and metallicities for 17 Local Group galaxies. **Monthly Notices of the Royal Astronomical Society**, v. 356, p. 979–997, January 2005.

[130] MCMILLAN, PAUL J. The mass distribution and gravitational potential of the milky way. **Monthly Notices of the Royal Astronomical Society**, v. 465, n. 1, p. 76–94, 2017.

[131] MESCHIN, I., GALLART, C., APARICIO, A., HIDALGO, S. L., MONELLI, M., STETSON, P. B., CARRERA, R. Spatially resolved LMC star formation history - I. Outside in evolution of the outer LMC disc. **Monthly Notices of the Royal Astronomical Society**, v. 438, p. 1067–1080, February 2014.

[132] MIESKE, S., HILKER, M., JORDÁN, A., INFANTE, L., KISSLER-PATIG, M., REJKUBA, M., RICHTLER, T., CÔTÉ, P., BAUMGARDT, H., WEST, M. J., FERRARESE, L., PENG, E. W. The nature of UCDs: Internal dynamics from an expanded sample and homogeneous database. **Astronomy and Astrophysics**, v. 487, p. 921–935, September 2008.

[133] MILONE, A. P., BEDIN, L. R., PIOTTO, G., ANDERSON, J. Multiple stellar populations in Magellanic Cloud clusters. I. An ordinary feature for intermediate age globulars in the LMC? **Astronomy and Astrophysics**, v. 497, p. 755–771, April 2009.

[134] MILONE, A. P., BEDIN, L. R., PIOTTO, G., ANDERSON, J., KING, I. R., SARAJEDINI, A., DOTTER, A., CHABOYER, B., MARíN-FRANCH, A., MAJEWSKI, S., APARICIO, A., HEMPEL, M., PAUST, N. E. Q., REID, I. N., ROSENBERG, A., SIEGEL, M. The ACS Survey of Galactic Globular Clusters. III. The Double Subgiant Branch of NGC 1851. **Astrophysical Journal**, v. 673, p. 241–250, January 2008.

[135] MINNITI, D., ZOCCALI, M. The Galactic bulge: a review. In: FORMATION AND EVOLUTION OF GALAXY BULGES, Bureau, M., Athanassoula, E., Barbuy, B., editores, v. 245 of **IAU Symposium**, p. 323–332, July 2008.

[136] MISGELD, I., HILKER, M. Families of dynamically hot stellar systems over 10 orders of magnitude in mass. **Monthly Notices of the Royal Astronomical Society**, v. 414, p. 3699–3710, July 2011.

[137] MOHR, J. J., ARMSTRONG, R., BERTIN, E., DAUES, G., DESAI, S., GOWER, M., GRUENDL, R., HANLON, W., KUROPATKIN, N., LIN, H., MARRINER, J., PETRAVIC, D., SEVILLA, I., SWANSON, M., TOMASHEK, T., TUCKER, D., YANNY, B. The Dark Energy Survey data processing and calibration system. In: SOFTWARE AND CYBERINFRASTRUCTURE FOR ASTRONOMY II, v. 8451 of **Proceedings of SPIE**, p. 84510D, September 2012.

[138] MULLER, E., STAVELEY-SMITH, L., ZEALEY, W., STANIMIROVIĆ, S. High-resolution HI observations of the Western Magellanic Bridge. **Monthly Notices of the Royal Astronomical Society**, v. 339, p. 105–124, February 2003.

[139] MURAI, T., FUJIMOTO, M. The Magellanic Stream and the Galaxy with a Massive Halo. **Publications of the Astronomical Society of Japan**, v. 32, p. 581, 1980.

[140] NAVARRO, J. F., FRENK, C. S., WHITE, S. D. M. The Structure of Cold Dark Matter Halos. **Astrophysical Journal**, v. 462, p. 563, May 1996.

[141] NIDEVER, D. L., MAJEWSKI, S. R., BUTLER BURTON, W., NIGRA, L. The 200° Long Magellanic Stream System. **Astrophysical Journal**, v. 723, p. 1618–1631, November 2010.

[142] NIDEVER, D. L., MAJEWSKI, S. R., MUÑOZ, R. R., BEATON, R. L., PATTERSON, R. J., KUNKEL, W. E. Discovery of a Large Stellar Periphery Around the Small Magellanic Cloud. **Astrophysical Journal Letters**, v. 733, p. L10, May 2011.

[143] NIDEVER, D. L., MONACHESI, A., BELL, E. F., MAJEWSKI, S. R., MUÑOZ, R. R., BEATON, R. L. A Tidally Stripped Stellar Component of the Magellanic Bridge. **Astrophysical Journal**, v. 779, p. 145, December 2013.

[144] NIDEVER, D. L., OLSEN, K., WALKER, A. R., VIVAS, A. K., BLUM, R. D., KALEIDA, C., CHOI, Y., CONN, B. C., GRUENDL, R. A., BELL, E. F., BESLA, G., MUNOZ, R. R., GALLART, C., MARTIN, N. F., OLSZEWSKI, E. W., SAHA, A., MONACHESI, A., MONELLI, M., DE BOER, T. J. L., JOHNSON, L. C., ZARITSKY, D., STRINGFELLOW, G. S., VAN DER MAREL, R. P., CIONI, M.-R. L., JIN, S., MAJEWSKI, S. R., MARTINEZ-DELGADO, D., MONTEAGUDO, L., NOEL, N. E. D., BERNARD, E. J., KUNDER, A., CHU, Y.-H., BELL, C. P. M., SANTANA, F., FRECHEM, J., MEDINA, G. E., PARKASH, V., SERON, J., HAYES, C. SMASH - Survey of the MAgellanic Stellar History. **ArXiv e-prints**, January 2017.

[145] NIKOLAEV, S., DRAKE, A., KELLER, S., COOK, K., DALAL, N., GRIEST, K., KANBUR, S. Geometry of the LMC Disk: Results from MACHO and 2MASS. In: AMERICAN ASTRONOMICAL SOCIETY MEETING ABSTRACTS, v. 33 of **Bulletin of the American Astronomical Society**, p. 1382, December 2001.

[146] NOËL, N. E. D., GALLART, C. Stellar Populations in the Outskirts of the Small Magellanic Cloud: No Outer Edge Yet. **Astrophysical Journal Letters**, v. 665, p. L23–L26, August 2007.

[147] OLSEN, K. A. G., ZARITSKY, D., BLUM, R. D., BOYER, M. L., GORDON, K. D. A Population of Accreted Small Magellanic Cloud Stars in the Large Magellanic Cloud. **Astrophysical Journal**, v. 737, p. 29, August 2011.

[148] OLSZEWSKI, E. W., SCHOMMER, R. A., SUNTZEFF, N. B., HARRIS, H. C. Spectroscopy of giants in LMC clusters. I - Velocities, abundances, and the age-metallicity relation. **Astronomical Journal**, v. 101, p. 515–537, February 1991.

[149] OWERS, MATT S., COUCH, WARRICK J., NULSEN, PAUL E. J., RANDALL, SCOTT W. Shocking tails in the major merger abell 2744. **The Astrophysical Journal Letters**, v. 750, n. 1, p. L23, 2012.

[150] PAGEL, B. E. J., TAUTVAISIENE, G. Chemical evolution of the Magellanic Clouds: analytical models. **Monthly Notices of the Royal Astronomical Society**, v. 299, p. 535–544, September 1998.

[151] PAWLOWSKI, M. S., KROUPA, P. The rotationally stabilized VPOS and predicted proper motions of the Milky Way satellite galaxies. **Monthly Notices of the Royal Astronomical Society**, v. 435, p. 2116–2131, November 2013.

[152] PAWLOWSKI, M. S., KROUPA, P., JERJEN, H. Dwarf galaxy planes: the discovery of symmetric structures in the Local Group. **Monthly Notices of the Royal Astronomical Society**, v. 435, p. 1928–1957, November 2013.

[153] PAWLOWSKI, M. S., PFLAMM-ALTENBURG, J., KROUPA, P. The VPOS: a vast polar structure of satellite galaxies, globular clusters and streams around the Milky Way. **Monthly Notices of the Royal Astronomical Society**, v. 423, p. 1109–1126, June 2012.

[154] PEÑARRUBIA, J., GÓMEZ, F. A., BESLA, G., ERKAL, D., MA, Y.-Z. A timing constraint on the (total) mass of the Large Magellanic Cloud. **Monthly Notices of the Royal Astronomical Society**, v. 456, p. L54–L58, February 2016.

[155] PEÑARRUBIA, J., MA, Y.-Z., WALKER, M. G., MCCONNACHIE, A. A dynamical model of the local cosmic expansion. **Monthly Notices of the Royal Astronomical Society**, v. 443, p. 2204–2222, September 2014.

[156] PFEFFER, J., BAUMGARDT, H. Ultra-compact dwarf galaxy formation by tidal stripping of nucleated dwarf galaxies. **Monthly Notices of the Royal Astronomical Society**, v. 433, p. 1997–2005, August 2013.

[157] PIATTI, A. E., DE GRIJS, R., RUBELE, S., CIONI, M.-R. L., RIPEPI, V., KERBER, L. The VMC survey - XV. The Small Magellanic Cloud-Bridge connection history as traced by their star cluster populations. **Monthly Notices of the Royal Astronomical Society**, v. 450, p. 552–563, June 2015.

[158] PIATTI, A. E., GEISLER, D. The Age-Metallicity Relationship of the Large Magellanic Cloud Field Star Population from Wide-field Washington Photometry. **Astronomical Journal**, v. 145, p. 17, January 2013.

[159] PIERES, A., SANTIAGO, B., BALBINOT, E., LUQUE, E., QUEIROZ, A., DA COSTA, L. N., MAIA, M. A. G., DRLICA-WAGNER, A., ROODMAN, A., ABBOTT, T. M. C., ALLAM, S., BENOIT-LÉVY, A., BERTIN, E., BROOKS, D., BUCKLEY-GEER, E., BURKE, D. L., ROSELL, A. C., KIND,

M. C., CARRETERO, J., CUNHA, C. E., DESAI, S., DIEHL, H. T., EIFLER, T. F., FINLEY, D. A., FLAUGHER, B., FOSALBA, P., FRIEMAN, J., GERDES, D. W., GRUEN, D., GRUENDL, R. A., GUTIERREZ, G., HONSCHEID, K., JAMES, D. J., KUEHN, K., KUROPATKIN, N., LAHAV, O., LI, T. S., MARSHALL, J. L., MARTINI, P., MILLER, C. J., MIQUEL, R., NICHOL, R. C., NORD, B., OGANDO, R., PLAZAS, A. A., ROMER, A. K., SANCHEZ, E., SCARPINE, V., SCHUBNELL, M., SEVILLA-NOARBE, I., SMITH, R. C., SOARES-SANTOS, M., SOBREIRA, F., SUCHYTA, E., SWANSON, M. E. C., TARLE, G., THALER, J., THOMAS, D., TUCKER, D. L., WALKER, A. R. Physical properties of star clusters in the outer LMC as observed by the DES. **Monthly Notices of the Royal Astronomical Society**, v. 461, p. 519–541, September 2016.

[160] PIERES, A., SANTIAGO, B. X., DRLICA-WAGNER, A., BECHTOL, K., MAREL, R. P. V. D., BESLA, G., MARTIN, N. F., BELOKUROV, V., GALLART, C., MARTINEZ-DELGADO, D., MARSHALL, J., NÖEL, N. E. D., MAJEWSKI, S. R., CIONI, M.-R. L., LI, T. S., HARTLEY, W., LUQUE, E., CONN, B. C., WALKER, A. R., BALBINOT, E., STRINGFELLOW, G. S., OLSEN, K. A. G., NIDEVER, D., DA COSTA, L. N., OGANDO, R., MAIA, M., NETO, A. F., ABBOTT, T. M. C., ABDALLA, F. B., ALLAM, S., ANNIS, J., BENOIT-LÉVY, A., ROSELL, A. C., KIND, M. C., CARRETERO, J., CUNHA, C. E., D'ANDREA, C. B., DESAI, S., DIEHL, H. T., DOEL, P., FLAUGHER, B., FOSALBA, P., GARCíA-BELLIDO, J., GRUEN, D., GRUENDL, R. A., GSCHWEND, J., GUTIERREZ, G., HONSCHEID, K., JAMES, D., KUEHN, K., KUROPATKIN, N., MENANTEAU, F., MIQUEL, R., PLAZAS, A. A., ROMER, A. K., SAKO, M., SANCHEZ, E., SCARPINE, V., SCHUBNELL, M., SEVILLA-NOARBE, I., SMITH, R. C., SOARES-SANTOS, M., SOBREIRA, F., SUCHYTA, E., SWANSON, M. E. C., TARLE, G., TUCKER, D. L., WESTER, W. A stellar overdensity associated with the Small Magellanic Cloud. **Monthly Notices of the Royal Astronomical Society**, v. 468, p. 1349–1360, June 2017.

[161] PIOTTO, G., MILONE, A. P., ANDERSON, J., BEDIN, L. R., BELLINI, A., CASSISI, S., MARINO, A. F., APARICIO, A., NASCIMBENI, V. Hubble Space Telescope Reveals Multiple Sub-giant Branch in Eight Globular Clusters. **Astrophysical Journal**, v. 760, p. 39, November 2012.

[162] PRUGNIEL, P., BICA, E., ALLOIN, D. Structure and Metallicity of Low-Luminosity Early-Type Galaxies. In: MORPHOLOGICAL AND PHYSICAL CLASSIFICATION OF GALAXIES, Longo, G., Capaccioli, M., Busarello, G., editores, v. 178 of **Astrophysics and Space Science Library**, p. 261, 1992.

[163] REICHARDT, C. L., STALDER, B., BLEEM, L. E., MONTROY, T. E., AIRD, K. A., ANDERSSON, K., ARMSTRONG, R., ASHBY, M. L. N., BAUTZ, M., BAYLISS, M., BAZIN, G., BENSON, B. A., BRODWIN, M., CARLSTROM, J. E., CHANG, C. L., CHO, H. M., CLOCCHIATTI, A., CRAWFORD, T. M., CRITES, A. T., DE HAAN, T., DESAI, S., DOBBS, M. A., DUDLEY, J. P., FOLEY, R. J., FORMAN, W. R., GEORGE, E. M., GLADDERS, M. D., GONZALEZ, A. H., HALVERSON, N. W., HARRINGTON, N. L., HIGH, F. W., HOLDER, G. P., HOLZAPFEL, W. L., HOOVER, S., HRUBES, J. D., JONES, C., JOY, M., KEISLER, R., KNOX, L., LEE, A. T., LEITCH, E. M., LIU, J., LUEKER, M., LUONG-VAN, D., MANTZ, A., MARRONE, D. P., MCDONALD, M., MCMAHON, J. J., MEHL, J., MEYER, S. S., MOCANU, L., MOHR, J. J., MURRAY, S. S., NATOLI, T., PADIN, S., PLAGGE, T., PRYKE, C., REST, A., RUEL, J., RUHL, J. E., SALIWANCHIK, B. R., SARO, A., SAYRE, J. T., SCHAFFER, K. K., SHAW, L., SHIROKOFF, E., SONG, J., SPIELER, H. G., STANISZEWSKI, Z., STARK, A. A., STORY, K., STUBBS, C. W., ŠUHADA, R., VAN ENGELEN, A., VANDERLINDE, K., VIEIRA, J. D., VIKHLININ, A., WILLIAMSON, R., ZAHN, O., ZENTENO, A. Galaxy Clusters Discovered via the Sunyaev-Zel'dovich Effect in the First 720 Square Degrees of the South Pole Telescope Survey. **Astrophysical Journal**, v. 763, p. 127, February 2013.

[164] RICH, R. M., SHARA, M. M., ZUREK, D. New Photometry for the Intermediate-Age Large Magellanic Cloud Globular Cluster NGC 2121 and the Nature of the LMC Age Gap. **Astronomical Journal**, v. 122, p. 842–848, August 2001.

[165] RYKOFF, E. S., DES CLUSTER WORKING GROUP, . DES Galaxy Cluster Results. In: AMERICAN ASTRONOMICAL SOCIETY MEETING ABSTRACTS #223, v. 223 of **American Astronomical Society Meeting Abstracts**, p. 141.06, January 2014.

[166] SAHU, K. C., CASERTANO, S., BOND, H. E., VALENTI, J., ED SMITH, T., MINNITI, D., ZOCCALI, M., LIVIO, M., PANAGIA, N., PISKUNOV, N., BROWN, T. M., BROWN, T., RENZINI, A., RICH, R. M., CLARKSON,

W., LUBOW, S. Transiting extrasolar planetary candidates in the Galactic bulge. **Nature**, v. 443, p. 534–540, October 2006.

[167] SAKAMOTO, T., HASEGAWA, T. Discovery of a Faint Old Stellar System at 150 kpc. **Astrophysical Journal Letters**, v. 653, p. L29–L32, December 2006.

[168] SALIM, S., RICH, R. M., CHARLOT, S., BRINCHMANN, J., JOHNSON, B. D., SCHIMINOVICH, D., SEIBERT, M., MALLERY, R., HECKMAN, T. M., FORSTER, K., FRIEDMAN, P. G., MARTIN, D. C., MORRISSEY, P., NEFF, S. G., SMALL, T., WYDER, T. K., BIANCHI, L., DONAS, J., LEE, Y.-W., MADORE, B. F., MILLIARD, B., SZALAY, A. S., WELSH, B. Y., YI, S. K. UV Star Formation Rates in the Local Universe. **Astrophysical Journal Supplement Series**, v. 173, p. 267–292, December 2007.

[169] SANDAGE, A. The Color-Magnitude Diagrams of Galactic and Globular Clusters and their Interpretation as Age Groups. **Ricerche Astronomiche**, v. 5, p. 41, 1958.

[170] SANDAGE, A. **The Hubble Atlas of Galaxies**: 1961.

[171] SANDAGE, A., BINGGELI, B. Studies of the Virgo cluster. III - A classification system and an illustrated atlas of Virgo cluster dwarf galaxies. **Astronomical Journal**, v. 89, p. 919–931, July 1984.

[172] SANDAGE, A., BINGGELI, B., TAMMANN, G. A. Studies of the Virgo Cluster - Part Five - Luminosity Functions of Virgo Cluster Galaxies. **Astronomical Journal**, v. 90, p. 1759–1771, September 1985.

[173] SANDERS, D. B., SOIFER, B. T., ELIAS, J. H., MADORE, B. F., MATTHEWS, K., NEUGEBAUER, G., SCOVILLE, N. Z. Ultraluminous infrared galaxies and the origin of quasars. **Astrophysical Journal**, v. 325, p. 74–91, February 1988.

[174] SARAJEDINI, A. Three Populous Clusters Discovered in the Large Magellanic Cloud Age Gap. **Astronomical Journal**, v. 116, p. 738–747, August 1998.

[175] SBORDONE, L., SALARIS, M., WEISS, A., CASSISI, S. Photometric signatures of multiple stellar populations in Galactic globular clusters. **Astronomy and Astrophysics**, v. 534, p. A9, October 2011.

[176] SCHLEGEL, D. J., FINKBEINER, D. P., DAVIS, M. Maps of Dust Infrared Emission for Use in Estimation of Reddening and Cosmic Microwave Background Radiation Foregrounds. **Astrophysical Journal**, v. 500, p. 525–553, June 1998.

[177] SCHNEIDER, P. **Extragalactic Astronomy and Cosmology: An Introduction**: Springer, 2006.

[178] SCHÖNRICH, R., BINNEY, J. Chemical evolution with radial mixing. **Monthly Notices of the Royal Astronomical Society**, v. 396, p. 203–222, June 2009.

[179] SIMON, J. D., GEHA, M. The Kinematics of the Ultra-faint Milky Way Satellites: Solving the Missing Satellite Problem. **Astrophysical Journal**, v. 670, p. 313–331, November 2007.

[180] SPARKE, L.S., GALLAGHER, J.S. **Galaxies in the Universe: An Introduction**: Cambridge University Press, 2000.

[181] SPROTT, D.A. **Statistical Inference in Science**, Springer Series in Statistics: Springer New York, 2000.

[182] STETSON, P. B. DAOPHOT - A computer program for crowded-field stellar photometry. **Publications of the Astronomical Society of the Pacific**, v. 99, p. 191–222, March 1987.

[183] STEVENS, J. A., AMURE, M., GEAR, W. K. Dust in spiral galaxies: global properties. **Monthly Notices of the Royal Astronomical Society**, v. 357, p. 361–380, February 2005.

[184] SUBRAMANIAN, S., SUBRAMANIAM, A. An estimate of the structural parameters of the Large Magellanic Cloud using red clump stars. **Astronomy and Astrophysics**, v. 520, p. A24, September 2010.

[185] SUBRAMANIAN, S., SUBRAMANIAM, A. The 3D structure of the Small Magellanic Cloud. In: ASTRONOMICAL SOCIETY OF INDIA CONFERENCE SERIES, v. 3 of **Astronomical Society of India Conference Series**, p. 144, 2011.

[186] SUNDBERG, ROLF. Maximum likelihood theory for incomplete data from an exponential family. **Scandinavian Journal of Statistics**, v. 1, n. 2, p. 49–58, 1974.

[187] TACCONI, L. J., GENZEL, R., NERI, R., COX, P., COOPER, M. C., SHAPIRO, K., BOLATTO, A., BOUCHÉ, N., BOURNAUD, F., BURKERT, A., COMBES, F., COMERFORD, J., DAVIS, M., SCHREIBER, N. M. F., GARCIA-BURILLO, S., GRACIA-CARPIO, J., LUTZ, D., NAAB, T., OMONT, A., SHAPLEY, A., STERNBERG, A., WEINER, B. High molecular gas fractions in normal massive star-forming galaxies in the young Universe. **Nature**, v. 463, p. 781–784, February 2010.

[188] TELLES, E., TERLEVICH, R. **High-resolution CCD surface photometry of H II galaxies.** 1994.

[189] THUAN, T. X., MARTIN, G. E. Blue compact dwarf galaxies. I - Neutral hydrogen observations of 115 galaxies. **Astrophysical Journal**, v. 247, p. 823–848, August 1981.

[190] TOLLERUD, E. J., BULLOCK, J. S., GRAVES, G. J., WOLF, J. From Galaxy Clusters to Ultra-faint Dwarf Spheroidals: A Fundamental Curve Connecting Dispersion-supported Galaxies to Their Dark Matter Halos. **Astrophysical Journal**, v. 726, p. 108, January 2011.

[191] TOOMRE, A., TOOMRE, J. Galactic Bridges and Tails. **Astrophysical Journal**, v. 178, p. 623–666, December 1972.

[192] TORREALBA, G., KOPOSOV, S. E., BELOKUROV, V., IRWIN, M. The feeble giant. Discovery of a large and diffuse Milky Way dwarf galaxy in the constellation of Crater. **Monthly Notices of the Royal Astronomical Society**, April 2016.

[193] TRUMPLER, R. J. Preliminary results on the distances, dimensions and space distribution of open star clusters. **Lick Observatory Bulletin**, v. 14, p. 154–188, 1930.

[194] TUCKER, D. L., ANNIS, J. T., LIN, H., KENT, S., STOUGHTON, C., PEOPLES, J., ALLAM, S. S., MOHR, J. J., BARKHOUSE, W. A., NGEOW, C., ALAM, T., BELDICA, C., CAI, D., DAUES, G., PLANTE, R., MILLER, C., SMITH, C., SUNTZEFF, N. B. The Photometric Calibration of the Dark Energy Survey. In: THE FUTURE OF PHOTOMETRIC, SPECTROPHOTOMETRIC AND POLARIMETRIC STANDARDIZATION, Sterken, C., editor, v. 364 of **Astronomical Society of the Pacific Conference Series**, p. 187, April 2007.

[195] VADER, J. P., CHABOYER, B. The RSA survey of dwarf galaxies, 1: Optical photometry. **Astronomical Journal**, v. 108, p. 1209–1243, October 1994.

[196] VAN DER MAREL, R. P., CIONI, M.-R. L. Magellanic Cloud Structure from Near-Infrared Surveys. I. The Viewing Angles of the Large Magellanic Cloud. **Astronomical Journal**, v. 122, p. 1807–1826, October 2001.

[197] VAN DER MAREL, R. P., KALLIVAYALIL, N. Third-epoch Magellanic Cloud Proper Motions. II. The Large Magellanic Cloud Rotation Field in Three Dimensions. **Astrophysical Journal**, v. 781, p. 121, February 2014.

[198] DOKKUM, PIETER G.VAN , ROMANOWSKY, AARON J., ABRAHAM, ROBERTO, BRODIE, JEAN P., CONROY, CHARLIE, GEHA, MARLA, MERRITT, ALLISON, VILLAUME, ALEXA, ZHANG, JIELAI. Spectroscopic confirmation of the existence of large, diffuse galaxies in the coma cluster. **The Astrophysical Journal Letters**, v. 804, n. 1, p. L26, 2015.

[199] VAN LOON, J. T., GILMORE, G. F., OMONT, A., BLOMMAERT, J. A. D. L., GLASS, I. S., MESSINEO, M., SCHULLER, F., SCHULTHEIS, M., YAMAMURA, I., ZHAO, H. S. Infrared stellar populations in the central parts of the Milky Way galaxy. **Monthly Notices of the Royal Astronomical Society**, v. 338, p. 857–879, February 2003.

[200] WALKER, M. G., PEÑARRUBIA, J. A Method for Measuring (Slopes of) the Mass Profiles of Dwarf Spheroidal Galaxies. **Astrophysical Journal**, v. 742, p. 20, November 2011.

[201] WALSH, S. M., JERJEN, H., WILLMAN, B. A Pair of Boötes: A New Milky Way Satellite. **Astrophysical Journal Letters**, v. 662, p. L83–L86, June 2007.

[202] WEGG, C., GERHARD, O., PORTAIL, M. The structure of the Milky Way's bar outside the bulge. **Monthly Notices of the Royal Astronomical Society**, v. 450, p. 4050–4069, July 2015.

[203] WILLMAN, B., BLANTON, M. R., WEST, A. A., DALCANTON, J. J., HOGG, D. W., SCHNEIDER, D. P., WHERRY, N., YANNY, B., BRINKMANN, J. A New Milky Way Companion: Unusual Globular Cluster or Extreme Dwarf Satellite? **Astronomical Journal**, v. 129, p. 2692–2700, June 2005a.

[204] WILLMAN, B., DALCANTON, J. J., MARTINEZ-DELGADO, D., WEST, A. A., BLANTON, M. R., HOGG, D. W., BARENTINE, J. C., BREWINGTON, H. J., HARVANEK, M., KLEINMAN, S. J., KRZESINSKI, J., LONG, D., NEILSEN, E. H., JR., NITTA, A., SNEDDEN, S. A. A New Milky Way Dwarf Galaxy in Ursa Major. **Astrophysical Journal Letters**, v. 626, p. L85–L88, June 2005b.

[205] WILLMAN, B., STRADER, J. "Galaxy," Defined. **Astronomical Journal**, v. 144, p. 76, September 2012.

[206] WRIGHT, E. L., EISENHARDT, P. R. M., MAINZER, A. K., RESSLER, M. E., CUTRI, R. M., JARRETT, T., KIRKPATRICK, J. D., PADGETT, D., MCMILLAN, R. S., SKRUTSKIE, M., STANFORD, S. A., COHEN, M., WALKER, R. G., MATHER, J. C., LEISAWITZ, D., GAUTIER, T. N., III, MCLEAN, I., BENFORD, D., LONSDALE, C. J., BLAIN, A., MENDEZ, B., IRACE, W. R., DUVAL, V., LIU, F., ROYER, D., HEINRICHSEN, I., HOWARD, J., SHANNON, M., KENDALL, M., WALSH, A. L., LARSEN, M., CARDON, J. G., SCHICK, S., SCHWALM, M., ABID, M., FABINSKY, B., NAES, L., TSAI, C.-W. The Wide-field Infrared Survey Explorer (WISE): Mission Description and Initial On-orbit Performance. **Astronomical Journal**, v. 140, p. 1868–1881, December 2010.

[207] YORK, D. G., ADELMAN, J., ANDERSON, J. E., JR., ANDERSON, S. F., ANNIS, J., BAHCALL, N. A., BAKKEN, J. A., BARKHOUSER, R., BASTIAN, S., BERMAN, E., BOROSKI, W. N., BRACKER, S., BRIEGEL, C., BRIGGS, J. W., BRINKMANN, J., BRUNNER, R., BURLES, S., CAREY, L., CARR, M. A., CASTANDER, F. J., CHEN, B., COLESTOCK, P. L., CONNOLLY, A. J., CROCKER, J. H., CSABAI, I., CZARAPATA, P. C., DAVIS, J. E., DOI, M., DOMBECK, T., EISENSTEIN, D., ELLMAN, N., ELMS, B. R., EVANS, M. L., FAN, X., FEDERWITZ, G. R., FISCELLI, L., FRIEDMAN, S., FRIEMAN, J. A., FUKUGITA, M., GILLESPIE, B., GUNN, J. E., GURBANI, V. K., DE HAAS, E., HALDEMAN, M., HARRIS, F. H., HAYES, J., HECKMAN, T. M., HENNESSY, G. S., HINDSLEY, R. B., HOLM, S., HOLMGREN, D. J., HUANG, C.-H., HULL, C., HUSBY, D., ICHIKAWA, S.-I., ICHIKAWA, T., IVEZIĆ, Ž., KENT, S., KIM, R. S. J., KINNEY, E., KLAENE, M., KLEINMAN, A. N., KLEINMAN, S., KNAPP, G. R., KORIENEK, J., KRON, R. G., KUNSZT, P. Z., LAMB, D. Q., LEE, B., LEGER, R. F., LIMMONGKOL, S., LINDENMEYER, C., LONG, D. C.,

LOOMIS, C., LOVEDAY, J., LUCINIO, R., LUPTON, R. H., MACKINNON, B., MANNERY, E. J., MANTSCH, P. M., MARGON, B., MCGEHEE, P., MCKAY, T. A., MEIKSIN, A., MERELLI, A., MONET, D. G., MUNN, J. A., NARAYANAN, V. K., NASH, T., NEILSEN, E., NESWOLD, R., NEWBERG, H. J., NICHOL, R. C., NICINSKI, T., NONINO, M., OKADA, N., OKAMURA, S., OSTRIKER, J. P., OWEN, R., PAULS, A. G., PEOPLES, J., PETERSON, R. L., PETRAVICK, D., PIER, J. R., POPE, A., PORDES, R., PROSAPIO, A., RECHENMACHER, R., QUINN, T. R., RICHARDS, G. T., RICHMOND, M. W., RIVETTA, C. H., ROCKOSI, C. M., RUTHMANSDORFER, K., SANDFORD, D., SCHLEGEL, D. J., SCHNEIDER, D. P., SEKIGUCHI, M., SERGEY, G., SHIMASAKU, K., SIEGMUND, W. A., SMEE, S., SMITH, J. A., SNEDDEN, S., STONE, R., STOUGHTON, C., STRAUSS, M. A., STUBBS, C., SUBBARAO, M., SZALAY, A. S., SZAPUDI, I., SZOKOLY, G. P., THAKAR, A. R., TREMONTI, C., TUCKER, D. L., UOMOTO, A., VANDEN BERK, D., VOGELEY, M. S., WADDELL, P., WANG, S.-I., WATANABE, M., WEINBERG, D. H., YANNY, B., YASUDA, N., SDSS COLLABORATION, . The Sloan Digital Sky Survey: Technical Summary. **Astronomical Journal**, v. 120, p. 1579–1587, September 2000.

[208] YOSHIZAWA, A. M., NOGUCHI, M. The dynamical evolution and star formation history of the Small Magellanic Cloud: effects of interactions with the Galaxy and the Large Magellanic Cloud. **Monthly Notices of the Royal Astronomical Society**, v. 339, p. 1135–1154, March 2003.

[209] YOUNG, L. M., BUREAU, M., DAVIS, T. A., COMBES, F., MCDERMID, R. M., ALATALO, K., BLITZ, L., BOIS, M., BOURNAUD, F., CAPPELLARI, M., DAVIES, R. L., DE ZEEUW, P. T., EMSELLEM, E., KHOCHFAR, S., KRAJNOVIĆ, D., KUNTSCHNER, H., LABLANCHE, P.-Y., MORGANTI, R., NAAB, T., OOSTERLOO, T., SARZI, M., SCOTT, N., SERRA, P., WEIJMANS, A.-M. The ATLAS^{3D} project - IV. The molecular gas content of early-type galaxies. **Monthly Notices of the Royal Astronomical Society**, v. 414, p. 940–967, June 2011.

[210] ZARITSKY, D., GONZALEZ, A. H., ZABLUDOFF, A. I. Local Group Dwarf Galaxies and the Fundamental Manifold of Spheroids. **Astrophysical Journal Letters**, v. 642, p. L37–L40, May 2006a.

[211] ZARITSKY, D., GONZALEZ, A. H., ZABLUDOFF, A. I. The Fundamental Manifold of Spheroids. **Astrophysical Journal**, v. 638, p. 725–738, February 2006b.

[212] ZINN, R. The globular cluster system of the galaxy. IV - The halo and disk subsystems. **Astrophysical Journal**, v. 293, p. 424–444, June 1985.

[213] ZUCKER, D. B., BELOKUROV, V., EVANS, N. W., KLEYNA, J. T., IRWIN, M. J., WILKINSON, M. I., FELLHAUER, M., BRAMICH, D. M., GILMORE, G., NEWBERG, H. J., YANNY, B., SMITH, J. A., HEWETT, P. C., BELL, E. F., RIX, H.-W., GNEDIN, O. Y., VIDRIH, S., WYSE, R. F. G., WILLMAN, B., GREBEL, E. K., SCHNEIDER, D. P., BEERS, T. C., KNIAZEV, A. Y., BARENTINE, J. C., BREWINGTON, H., BRINKMANN, J., HARVANEK, M., KLEINMAN, S. J., KRZESINSKI, J., LONG, D., NITTA, A., SNEDDEN, S. A. A Curious Milky Way Satellite in Ursa Major. **Astrophysical Journal Letters**, v. 650, p. L41–L44, October 2006a.

[214] ZUCKER, D. B., BELOKUROV, V., EVANS, N. W., WILKINSON, M. I., IRWIN, M. J., SIVARANI, T., HODGKIN, S., BRAMICH, D. M., IRWIN, J. M., GILMORE, G., WILLMAN, B., VIDRIH, S., FELLHAUER, M., HEWETT, P. C., BEERS, T. C., BELL, E. F., GREBEL, E. K., SCHNEIDER, D. P., NEWBERG, H. J., WYSE, R. F. G., ROCKOSI, C. M., YANNY, B., LUPTON, R., SMITH, J. A., BARENTINE, J. C., BREWINGTON, H., BRINKMANN, J., HARVANEK, M., KLEINMAN, S. J., KRZESINSKI, J., LONG, D., NITTA, A., SNEDDEN, S. A. A New Milky Way Dwarf Satellite in Canes Venatici. **Astrophysical Journal Letters**, v. 643, p. L103–L106, June 2006b.

[215] ZWICKY, F. Compact and dispersed cosmic matter. Part II. **Advances in Astronomy and Astrophysics**, v. 7, p. 227–283, 1970.

[216] ZWICKY, F., ZWICKY, M. A. **Catalogue of selected compact galaxies and of post-eruptive galaxies**: 1971.